



Local Hemodynamic Microenvironment in Bioresorbable Scaffolds

ERHAN TENEKECIOĞLU

Local Hemodynamic Microenvironment in Bioresorbable Scaffolds

Erhan Tenekecioglu

Local Hemodynamic Microenvironment in Bioresorbable Scaffolds

Dissertation, Erasmus University Rotterdam, The Netherlands

ISBN: 978-625-00-0718-1

Author: Erhan Tenekecioglu

Printing and layout: Marmara Baskı, Bursa, Turkey

Copyright © 2022 Erhan Tenekecioglu, Rotterdam, The Netherlands

All rights reserved. No parts of this thesis may be reproduced, stored, in a retrieval system, or transmitted in any form or by any means, electronical, mechanical, photocopying, recording or otherwise without prior permission of the author or copyright owning journal.

Financial support by Erasmus Medical Center – Erasmus University Rotterdam and Medis are gratefully acknowledged.

**Local Hemodynamic Microenvironment in
Bioresorbable Scaffolds
De lokale hemodynamische condities op micro-schaal in
Bioresorbeerbare Vasculaire Stents**

Thesis

to obtain the degree of Doctor from the
Erasmus University Rotterdam

by command of the
rector magnificus

Prof.dr. A.L. Bredenoord

and in accordance with the decision of the Doctorate Board.

The public defence shall be held on

Wednesday 22nd of June 2022 at 15.30 hrs

by

Erhan Tenekecioğlu
born in Batman, Turkey

Doctoral Committee:

Promotors: prof. dr. R.J.M. van Geuns
prof. dr. P.W.J.C. Serruys

Other Members: dr.ir. F. Gijsen
dr.ir. J. Wentzel
prof. dr. J.H.C. Reiber

Copromotor: dr. Y. Onuma

Thesis outline
Erhan Tenekecioglu, MD.
**“Local Hemodynamic Microenvironment in Bioresorbable
Scaffolds”**

Table of contents

Part A: Bioresorbable Scaffolds

Part B: Preclinical assessment of shear stress in bioresorbable vascular scaffolds

Part C: Clinical assessment of shear stress in bioresorbable vascular scaffolds

Part D: Summary and conclusions

Part E: Appendices

TABLE OF CONTENTS

Chapter 1

General introduction and outline of the thesis	13
------------------------------------------------	----

Part A: Bioresorbable Scaffolds

Chapter 2

Bioresorbable scaffolds: a new paradigm in percutaneous coronary intervention	24
Differential aspects between cobalt-chromium everolimus drug-eluting stent and Absorb everolimus bioresorbable vascular scaffold: from bench to clinical use	48
Optimization of percutaneous coronary intervention: Indispensables for bioresorbable scaffolds	84

Chapter 3

Intracoronary Optical Coherence Tomography: Clinical and Research Applications and Intravascular Imaging Software Overview	124
Randomized comparison of Absorb bioresorbable vascular scaffold and Mirage microfiber sirolimus eluting scaffold using multi-modality imaging	152

Part B: Preclinical assessment of shear stress in bioresorbable vascular scaffolds

Chapter 4

Assessment of the hemodynamic characteristics of Absorb BVS in a porcine coronary artery model	186
Corrigendum to “Assessment of the hemodynamic characteristics of Absorb BVS in a porcine coronary artery model.”	203
Hemodynamic analysis of a novel bioresorbable scaffold in porcine coronary artery model	208
Non-Newtonian pulsatile shear stress assessment: a method to differentiate bioresorbable scaffold platforms	228

Chapter 5

Preclinical assessment of the endothelial shear stress in porcine-based models following implantation of two different bioresorbable scaffolds: effect of scaffold design on the local hemodynamic micro-environment **236**

Difference in hemodynamic microenvironment in vessels scaffolded with Absorb BVS and Mirage BRMS: insights from a preclinical endothelial shear stress study **242**

Chapter 6

Strut protrusion and shape impact on endothelial shear stress: insights from pre-clinical study comparing Mirage and Absorb bioresorbable scaffolds **270**

The effect of strut thickness on shear stress distribution in a preclinical model **290**

Post-implantation shear stress assessment: an emerging tool for differentiation of bioresorbablescaffolds **295**

Part C: Clinical assessment of shear stress in bioresorbable vascular scaffolds

Chapter 7

Expert Recommendations on the assessment of wall shear stress in human coronary arteries: existing methodologies, technical considerations, and clinical applications **318**

Chapter 8

The Nidus for Possible Thrombus Formation: Insight from the Micro-Environment of Bioabsorbable Vascular Scaffold **372**

The Effect of Strut Protrusion on Shear Stress Distribution: Hemodynamic Insights From a Prospective Clinical Trial **376**

The impact of plaque type on strut embedment / protrusion and shear stress distribution in bioresorbable scaffold. **382**

Chapter 9

Five-year follow-up of underexpanded and overexpanded bioresorbable scaffolds: self-correction and impact on shear stress **404**

Improvement in local hemodynamics 5 years after implantation of a coronary bioresorbable scaffold: a pulsatile non-Newtonian shear stress analysis **408**

Endothelial shear stress 5 years after implantation of a coronary bioresorbable scaffold **412**

Early strut protrusion and late neointima thickness in the Absorb bioresorbable scaffold: a serial wall shear stress analysis up to five years **440**

Chapter 10

Endothelial Shear Stress and Vascular Remodeling in Bioresorbable Scaffold and Metallic Stent **466**

Part D: Summary and conclusions

Samenvatting en conclusies **497**

Part E: Appendices

Appendices **516**

Authors and affiliations

Curriculum vitae

PhD portfolio

List of publications

Acknowledgement

Local Hemodynamic Microenvironment in Bioresorbable Scaffolds

Erhan Tenekecioglu

Abstract

A new paradigm in the treatment of coronary artery disease has started with fully bioresorbable scaffolds. The ultimate goal is opening the stenotic vessel segments without any remnant following the resorption of the scaffold providing the recovery of vascular physiology at follow up. However, following first favorable results in the clinical trials, BRS has demonstrated significant concerns in terms of adverse events; at 3 year follow up Absorb Biovascular Scaffold (Absorb BVS, Abbott Vascular, Santa Clara, California, USA), the leading BRS, has shown an increased device thrombosis in ABSORB II trial. Owing to some inherent material properties, polymeric BRS have some drawbacks in mechanical properties as compared to metallic stents. To reduce the adverse clinical events of BRS, beside the procedural improvement, the design of these coronary devices is critically important. From the flow dynamics point of view, the thickness of the struts, strut design, embedment status of the struts, macro design of the vascular scaffold to be more flow “compatible” are the key points for a hemodynamically favorable coronary stent/scaffold. The primary goals of the present thesis are as follows: 1) To emphasize a paradigm shift in the treatment of coronary artery disease through bioresorbable scaffolds, 2) To apply shear stress analysis in different types of bioresorbable scaffolds in a preclinical setting, 3) To investigate shear stress in bioresorbable scaffolds in a clinical setting, 4) To give an overview for shear stress analysis methodologies, technical considerations and clinical applications.

Chapter 1

General introduction and outline of the thesis

Erhan Tenekecioglu

Coronary artery disease and shear stress

Coronary artery disease is the leading underlying cause of death over the world. Atherosclerosis, the major cause of coronary artery disease, is a chronic inflammatory disease particularly large and medium sized arteries.¹ Even though all the vascular system of the body is exposed to the systemic risk factors such as hyperlipidemia, smoking, hypertension and diabetes, atherosclerotic lesions emerge in the specific regions of the arterial system, like side branch regions, the outer wall of the bifurcations, inner wall of the curvatures.² These locations represent the zones of flow disturbance and growing evidence has shown that such local hemodynamic forces play a crucial role in the localization of atherosclerosis.^{3, 4} Endothelial shear stress (ESS) is the most pivotal metric of such local hemodynamic forces. ESS is a flow generated, blood pressure-derived tensile stress that has indispensable critical role in the regulation of the vascular biology and diseases.

ESS demonstrates its effect on the vascular biology according to its magnitudes; disturbed and low ESS yields an environment for atherosclerotic disease formation and progression whereas moderate or physiological ESS has a protective function in the atherosclerosis.⁵ While under 1.0 Pa defines low ESS, the range of 1.0-7.0 defines moderate or physiological ESS. Over 7.0 Pa, ESS has a destructive property on the vascular wall and atherosclerotic plaques. Local flow disturbances are the zones of low ESS where several mechanobiological reactions take place to initiate or to carry forward an atherosclerotic lesion.⁶ On the other hand, moderate/physiological ESS has a role on the vascular homeostasis keeping the vascular cells in a quiescent mode.

Bioresorbable scaffolds and changes in local hemodynamic microenvironment following stent/scaffold implantation

In 1977, the balloon angioplasty for percutaneous treatment of the coronary artery disease was the first revolution. However, following plain balloon angioplasty, there were restenosis in high rates. After several years metallic stents were introduced as a solution for the restenosis following balloon angioplasty, which was the second revolution in percutaneous treatment of the coronary artery disease. Despite the treatment with metallic cages, restenosis at follow up emerged as a serious problem after stenting. The third revolution was introduction of the drug-eluting stents. The anti-proliferative drug over the inside surface of the stent prevents neointimal proliferation and re-stenosis at follow up. The last revolutionary

step in the percutaneous treatment of the coronary artery disease has been the bioresorbable stents/scaffolds (BRS). Temporary scaffolding of the diseased vessel segment with recovery of the vasomotricity was the triggering point of biodegradable stents.

The implantation of the BRS have introduced some concerns into the field; the thick struts and wide footprints of the BRS caused local flow disturbances within the treated vessel segments. Those local hemodynamic changes were not so small to be underestimated. Another point is the embedment of the struts of the BRS; thicker struts prevent the embedment of the struts deeper into the vessel wall. Less embedded, in other words more protruded struts of the BRS aggravate the flow disturbances over the luminal surface in the treated vessel segment. Lower shear stress besides the struts may induce thrombus formations and diffusion of the LDL cholesterol and other substances into the intima of the vessel wall. Higher shear stress on top of the struts prevent the endothelization of the struts which may increase the thrombosis risk at follow up.

OUTLINE OF THE THESIS: LOCAL HEMODYNAMIC MICROENVIRONMENT IN BIORESORBABLE SCAFFOLDS

A new paradigm in the treatment of coronary artery disease has started with fully biodegradable scaffolds. The ultimate goal is opening the stenotic vessel segments without any remnant following the resorption of the scaffold providing the recovery of vascular physiology at follow up. However, following first favorable results in the clinical trials, BRS has demonstrated significant concerns in terms of adverse events; at 3 year follow up Absorb Biovascular Scaffold (Absorb BVS, Abbott Vascular, Santa Clara, California, USA), the leading BRS, has shown an increased device thrombosis in ABSORB II trial.

Owing to some inherent material properties, polymeric BRS have some drawbacks in mechanical properties as compared to metallic stents.^{7,8} To reduce the adverse clinical events of BRS, beside the procedural improvement, the design of these coronary devices is critically important. From the flow dynamics point of view, the thickness of the struts, streamline designed strut, deep embedded struts, macro design of the vascular scaffold to be more flow “compatible” are key points for a hemodynamically favorable coronary stent/scaffold. The primary goals of the present thesis are as follows:

- To emphasize a paradigm shift in the treatment of coronary artery disease through bioresorbable scaffolds

- To apply shear stress analysis in different types of bioresorbable scaffolds in a preclinical setting
- To investigate shear stress in bioresorbable scaffolds in a clinical setting
- To give an overview for shear stress analysis methodologies, technical considerations and clinical applications.

Part A: Bioresorbable Scaffolds

The implantation of a metallic drug-eluting stent is the current standard practice for the treatment of coronary artery disease. Bioresorbable scaffold is a paradigm shift in the percutaneous coronary intervention. Although the metallic DES have significantly reduced re-stenosis ratio, they have substantial drawbacks including hypersensitivity reaction to the polymer that provokes local inflammation, neo-atherosclerotic lesion formation that may conduce late stent failure and they may preclude surgical revascularization and distort vessel physiology. Bioresorbable scaffolds have been introduced to overcome these limitations by scaffolding the vessel temporarily and disappear after a meanwhile. In **Chapter 2**, we give information about BRS comparing it with metallic DES and different structural properties require some peculiar methods during implantation of polymeric scaffolds.

Intracoronary imaging has been indispensable for optimal implantation of coronary stents/scaffolds. It gives valuable information about vessel wall and lumen preceding implantation. During implantation, intracoronary imaging, in particular optical coherence tomography (OCT) can elaborate the apposition status of the stent/scaffold over the vessel wall. In **Chapter 3** we will introduce the clinical and research applications of OCT with software options of this microscopic imaging technique. We will give information also about a novel BRS technology, Mirage Microfiber Sirolimus-Eluting Scaffold, in comparison with Absorb BVS using different imaging modalities including OCT.

Part B: Preclinical assessment of shear stress in bioresorbable vascular scaffolds

Implantation of a stent/scaffold alters the local hemodynamic micro environment substantially. A new surface with a geometrical structure impedes the local blood flow and induce flow disruptions as it run over this new luminal surface. In **Chapter 4**, we will evaluate the hemodynamic characteristics of Absorb BVS in healthy preclinical vessel models. Computational fluid dynamic (CFD) studies provide unique opportunity to investigate these

rheological effects of implanted stents/scaffolds. Despite Newtonian steady flow simulation, incorporating shear-thinning blood rheology non-Newtonian pulsatile flow simulation gives more realistic data about the local shear stress distribution. In chapter 4, we will also assess the effect of thinner struts with similar quadratic design of another novel BRS, ArterioSorb scaffold in comparison with Absorb BVS with thicker struts, using non-Newtonian flow simulation.

In **Chapter 5**, we will evaluate the impact of Absorb BVS and a novel BRS with thinner circular struts, Mirage scaffold, on local flow dynamics following implantation in healthy animal coronary arteries. We will compare the effect of different strut designs of different bioresorbable scaffolds. In **Chapter 6**, we will investigate the effect of strut shape and strut protrusion on endothelial shear stress in preclinical vessels treated with Absorb BVS and Mirage bioresorbable scaffolds. In this study, we will do the histopathological analysis of 2 animals and demonstrate the effect of different BRS on neointimal healing. In the following section of this chapter, we will compare Absorb BVS and a novel BRS, ArterioSorb, in terms of local shear stress distribution. ArterioSorb has quadratic strut design thinner than in Absorb BVS.

Part C: Clinical assessment of shear stress in bioresorbable vascular scaffolds

In this part we will evaluate shear stress in bioresorbable scaffolds in clinical models. In **Chapter 7**, we will discuss about a consensus on the assessment of shear stress in clinical cases. In this consensus paper, there will be the current methodologies, technical considerations and clinical applications for shear stress analysis. In **Chapter 8**, we will evaluate the effect of thicker struts in Absorb BVS on local shear stress distribution in diastolic and systolic cardiac phases. We will see that, even in maximum coronary perfusion in diastole, there are some dark blue zones beside the thick struts in BRS implanted vessel segment. In following section, we will analyze strut protrusion and the impact of strut protrusion on shear stress in clinical subjects from a prospective clinical study comparing Absorb BVS and Mirage BRS. In the last section of this chapter, we will evaluate the effect of underlying plaque type on strut embedment and shear stress distribution in BRS implanted vessel segments. Due to different histomorphometric properties, the treated atherosclerotic plaques allow different strut embedment depths.

In **Chapter 9**, we will demonstrate the long-term effect of shear stress in the vessel segments implanted with Absorb BVS in clinical subjects. In the first section of this chapter, there are clinical cases of underexpansion and overexpansion of Absorb BVS and the response of local shear stress in underexpanded and overexpanded vessel segments. In the following section, we will evaluate the alteration in shear stress distribution and vascular geometry at long-term following implantation of Absorb BVS. The unique point of this analysis is the use of pulsatile flow conditions and a non-Newtonian model of blood behavior, where these simulations are of unprecedented scope and detail. In the following section, we will assess the effect of strut protrusion on shear stress post-implantation and long-term neointimal thickness response. It's proposed that the magnitude of the strut protrusion would determine the post-implantation shear stress and both acute shear stress distribution and strut protrusion would figure out the neointimal thickness at 5 years follow up.

In **Chapter 10**, we will evaluate the effect of shear stress on vessel remodeling in Absorb BVS and metallic DES implanted cases. This analysis is the first evaluating the polymeric BRS and the metallic stents in terms of their effects on the vessel wall in the subjects from a randomized clinical trial.

Part D: Summary and conclusions

Samenvatting van het proefschrift (Dutch)

Summary of the thesis

Conclusions

Part E: Appendices

Authors and affiliations

Curriculum vitae

PhD portfolio

List of publications

Acknowledgement

REFERENCES:

1. Ross R. Atherosclerosis--an inflammatory disease. *The New England journal of medicine* 1999;**340**(2):115-26.
2. VanderLaan PA, Reardon CA, Getz GS. Site specificity of atherosclerosis: site-selective responses to atherosclerotic modulators. *Arteriosclerosis, thrombosis, and vascular biology* 2004;**24**(1):12-22.
3. Stone PH, Coskun AU, Yeghiazarians Y, Kinlay S, Popma JJ, Kuntz RE, Feldman CL. Prediction of sites of coronary atherosclerosis progression: In vivo profiling of endothelial shear stress, lumen, and outer vessel wall characteristics to predict vascular behavior. *Current opinion in cardiology* 2003;**18**(6):458-70.
4. Cunningham KS, Gotlieb AI. The role of shear stress in the pathogenesis of atherosclerosis. *Laboratory investigation; a journal of technical methods and pathology* 2005;**85**(1):9-23.
5. Wentzel JJ, Chatzizisis YS, Gijzen FJ, Giannoglou GD, Feldman CL, Stone PH. Endothelial shear stress in the evolution of coronary atherosclerotic plaque and vascular remodelling: current understanding and remaining questions. *Cardiovascular research* 2012;**96**(2):234-43.
6. Harrison DG, Widder J, Grumbach I, Chen W, Weber M, Searles C. Endothelial mechanotransduction, nitric oxide and vascular inflammation. *Journal of internal medicine* 2006;**259**(4):351-63.
7. Sotomi Y, Suwannasom P, Tenekecioglu E, Tateishi H, Abdelghani M, Serruys PW, Onuma Y. Differential aspects between cobalt-chromium everolimus drug-eluting stent and Absorb everolimus bioresorbable vascular scaffold: from bench to clinical use. *Expert review of cardiovascular therapy* 2015;**13**(10):1127-45.
8. Ormiston JA, Webber B, Ubod B, Darremont O, Webster MW. An independent bench comparison of two bioresorbable drug-eluting coronary scaffolds (Absorb and DESolve) with a durable metallic drug-eluting stent (ML8/Xpedition). *EuroIntervention : journal of EuroPCR in collaboration with the Working Group on Interventional Cardiology of the European Society of Cardiology* 2015;**11**(1):60-7.

Chapter 2

**Bioresorbable scaffolds: a new paradigm
In percutaneous coronary intervention**

**Differential aspects between cobalt-
chromium everolimus drug-eluting stent
and Absorb everolimus bioresorbable
vascular scaffold: from bench to clinical
use**

**Optimization of percutaneous coronary
intervention: Indispensables for
bioresorbable scaffolds**

Bioresorbable scaffolds: a new paradigm in percutaneous coronary intervention

Erhan Tenekecioglu, Vasim Farooq, Christos V. Bourantas, Rafael Cavalcante Silva, Yoshinobu Onuma, Mustafa Yilmaz, Patrick W. Serruys

BMC Cardiovasc Disord. 2016; 16:38.

ABSTRACT

Numerous advances and innovative therapies have been introduced in interventional cardiology over the recent years, since the first introduction of balloon angioplasty, but bioresorbable scaffold is certainly one of the most exciting and attracting one. Despite the fact that the metallic drug-eluting stents have significantly diminished the re-stenosis ratio, they have considerable limitations including the hypersensitivity reaction to the polymer that can cause local inflammation, the risk of neo-atherosclerotic lesion formation which can lead to late stent failure as well as the fact that they may preclude surgical revascularization and distort vessel physiology. Bioresorbable scaffolds overcome these limitations as they have the ability to dissolve after providing temporary scaffolding which safeguards vessel patency. In this article we review the recent developments in the field and provide an overview of the devices and the evidence that support their efficacy in the treatment of CAD. Currently 3 devices are CE marked and in clinical use. Additional 24 companies are developing these kinds of coronary devices. Most frequently used material is PLLA followed by magnesium.

BACKGROUND

The need for Bioresorbable scaffolds

Plain 'old' balloon angioplasty (POBA) was first performed by Andreas Roland Grüntzig in 1977 and heralded the first revolution in the percutaneous treatment of coronary artery disease (CAD).¹ Despite the success in dilating and restoring coronary flow to diseased coronary vessels, enthusiasm to this ground-breaking technology was hampered by issues related to acute vessel closure secondary to iatrogenic coronary dissection (occurring in approximately 30–40 % of cases) and restenosis secondary to elastic re-coil, constrictive remodeling, and neointimal hyperplasia.²⁻⁵ Bare metal stents (BMS) heralded the second revolution in the treatment of CAD as means to overcome the limitations of POBA. BMS resolved the issue of acute vessel occlusion by sealing the dissection flaps and prevented elastic recoil and constrictive remodeling. Two landmark studies - BENESTENT and STRESS trials - demonstrated the superiority of bare metal stents (BMS) over POBA.⁶⁻⁸ Nevertheless, indigenous limitations of BMS such as the neointimal hyperplasia and consequent the increased risk of in-stent

restenosis (ISR) precluded the widespread adoption of this technology, particularly in more complex CAD and diabetics.⁹⁻¹²

Drug eluting stents (DES) – the third revolution in interventional cardiology – were conceived as means to tackle the iatrogenic issue of excessive neointimal hyperplasia and reduce the risk of restenosis. Land-mark studies of the first generation sirolimus-eluting Bx Velocity stents demonstrated the dramatic reduction in the excessive hyperplastic healing response and risk of restenosis compared to BMS.^{13, 14} Subsequently the indications for DES rapidly expanded, with the use of DES in more complex CAD and higher risk patient groups. Despite the promising results associated with the first-generation DES, safety issues arose, in particular the risk of late stent thrombosis, quoted as 0.53 % per year, with a cumulative incidence of 3.3 % at 4 years.^{15, 16} The primary concerns with the first generation DES were related 1) to the lack of biocompatibility of the drug eluting polymer leading to a persistent inflammatory response beyond the drug eluting period of the device, 2) to a risk of a continued neointimal response and risk of a 'late-catch up' phenomenon and late ISR, and 3) to a delayed/incomplete healing, and risk of late/very late stent thrombosis. In addition, other issues were identified including, stent malapposition (early or late acquired), the risk of early or late stent fracture, neoatherosclerotic lesion formation and late DES failure, and the permanent metallic caging causing abnormal vasomotion.¹⁷ With the latter, abnormal vasoconstriction responses to acetylcholine at the sites distal to the DES were identified, implying the abnormal function of the endothelial layer. Although newer generation DES, with more biocompatible polymers, overcame many of the safety issues related to first generation DES, these concerns were not completely resolved especially the longer-term risk of DES failure secondary to neoatherosclerosis.¹⁸⁻²⁰ Bioresorbable scaffolds (BRS) – heralded as the fourth revolution in interventional cardiology – were thus designed to overcome the perceived limitations of DES by providing a temporary support to the vessel wall, whilst simultaneously allowing for the release of an anti-proliferative drug to limit the excessive response, in order to potentially allow the vessel to heal and restore its physiological function.

Development of bioresorbable scaffolds

Historically biodegradable materials for implants which serve as a temporary function have been used in therapeutic medicine in areas that include wound closure – such as absorbable surgical sutures made from glycolic and lactic acid orthopedic devices, dental procedures,

cardiovascular surgery, intestinal surgery, urology, nerve repair, drug delivery and oncology, and were designed to overcome the disadvantages of permanent metallic-based devices.²¹

In so far as application with BRS, this concept is still in its infancy. Identifying the appropriate bioresorbable materials to allow for temporary scaffolding of the vessel wall to seal dissections and prevent recoil and allowing for drug elution to limit the healing response has proven to be a major challenge. In addition, the ideal BRS should have as thin struts as possible to limit the healing response whilst providing adequate radial support for a 3–6 month period to limit recoil and constrictive remodeling, and have as low crossing profile as possible and be flexible enough to allow delivery in more challenging anatomical disease.

Various types of materials have been used in BRS development (**Table 1**). Amongst them poly-L-lactic acid (PLLA) and magnesium appear to be the most promising and reached clinical use. PLLA is the most commonly used material for manufacturing BRS. The degradation of PLLA is by hydrolysis of the ester bonds into small particles that are phagocytosed by macrophages into lactic acid and metabolized through the Krebs cycle into carbon dioxide and water.²² Magnesium is mixed with rare earth metals to allow it to have thinner struts and control the degradation process. In addition, magnesium has been reported to have potential antithrombotic properties emanating from its electronegative charge during degradation.^{23, 24} One of the reported challenges associated with magnesium alloys has been the too rapid degradation of the material before the end of the healing process with the consequent risk of early vessel recoil and restenosis.²⁵

The potential benefits of bioresorbable scaffolds

BRS allow for successful acute revascularization of coronary artery stenosis and in preliminary studies, they have been shown to be associated with low rates of repeat revascularisation and major adverse cardiac events (MACE) during the early follow-up period.²⁶ The main advantage of the BRS is that following complete bioresorption, no foreign body remains in the vessel wall at long term follow-up, which may mitigate the increased long term risk of stent thrombosis seen with the first generation DES.^{22, 27, 28} In addition, a potential issue of late catch-up in restenosis secondary to a persistent low grade inflammatory response to the polymer/device, even evident with newer generation DES²⁹, may be mitigated with BRS since no material remains following bioresorption.

Table 1 Summary of the design and structure of clinically tested bioresorbable scaffolds

Scaffold	Strut material	Coating material	Eluted drug	Strut thickness (μm)	Resorption (month)	Current status
Igaki-Tamai	PLLA	None	None	170	24–36	CE mark for peripheral use
AMS-1	Mg	None	None	165	<4	Discontinued
DREAMS-1	Mg	PLGA	Paclitaxel	125	9	Clinical trials
DREAMS-2	Mg	PLLA	Sirolimus	150	9	Clinical trials
Absorb BVS 1.0	PLLA	PDLLA	Everolimus	156	18–24	Discontinued
Absorb BVS 1.1	PLLA	PDLLA	Everolimus	156	24–48	CE mark
Absorb BVS-New generation	PLLA	PDLLA	Everolimus	<100	NA	NA
DeSolve	PLLA	None	Myolimus	150	12–24	CE mark
DeSolve 100	PLLA	PLLA	Novolimus	100	24	CE mark
IDEAL biostent	Polymer salicylate	Salicylate	Sirolimus	175	>12	Clinical trials
REVA	PTD-PC	None	None	200	24	Discontinued
ReZolve	PTD-PC	None	Sirolimus	115–230	4–6	Clinical trials
ReZolve2	PTD-PC	None	Sirolimus	100	48	Clinical trials
Fantom	PTD-PC	-	Sirolimus	125	36	Clinical trials
Fortitude	semicrystalline polylactide	-	None	150–200	3–6	Clinical trials
Mirage BRMS	PLLA	-	Sirolimus	125–150	14	Clinical trials
MeRes	PLLA	PDLLA	Sirolimus	100	24	Clinical trials
Xinsorb	PLLA	PDLLA	Sirolimus	160	24–36	Clinical trial
ART 18AZ	PDLLA	None	None	170	3–6	Clinical trials

Mg magnesium, PLLA poly-L-lactic acid, PDLLA poly-DL-lactic acid, BVS bioresorbable vascular scaffold
 SA/AA salicylic acid/adipic acid, PTD-PC, poly-tyrosine-derived polycarbonate, CE Conformité
 Européenne. NA not available

The enhanced mechanical flexibility of the Absorb BRS (compared to metallic DES) allows for increased conformability to the original vessel wall geometry, which may have an advantageous influence on coronary blood flow and its biomechanical properties.³⁰

Additionally, the bioresorption process allows for malapposed struts or jailed struts over the side-branch to resolve at follow-up.³⁰ Furthermore, the treated vessel has been shown to potentially restore its vasomotor function a year following Absorb BRS implantation, when the structural integrity of the Absorb device has been appropriately lost.³¹ Conversely, endothelial dysfunction has been shown to persist with DES.³¹ Another useful property of BRS is that it allows for a non-invasive imaging (e.g. multi-slice coronary computed tomography [MSCT]) without any significant imaging artefacts. Additionally, BRS potentially allows the surgeons to attach anastomoses to the scaffolded segments once the bioresorption process has been completed.

Bioresorbable scaffolds currently in use

Absorbable magnesium stent (AMS)

Magnesium (Mg) is an essential element for several enzymes in human body and a co-factor for ATPase. The balloon-expandable Absorbable Metal Stent (AMS-1) (Biotronik, Berlin, Germany) (**Fig. 1**) was the first metallic bioresorbable scaffold. The radial strength of the device allowed for low elastic recoil (<8 %), a high collapse pressure (0.8 bar), and minimal



Figure 1. Design of bioresorbable scaffolds in clinical or preclinical

shortening after inflation (<5 %).³² In preclinical studies, rapid endothelialization of the device and degradation into inorganic salts was reported within 60 days^{33, 34} (**Fig. 2**).^{33, 34} In the prospective, multicenter, non-randomized, Clinical Performance and Angiographic Results of Coronary Stenting with Absorbable Metal Stents (PROGRESS AMS) pilot study (63 patients with single de novo lesions, 71 AMS), no death, MI or stent thrombosis was reported at 12 months follow-up, with the treated vessel attaining its vasoreactivity within 4-months. The device was however associated with an unacceptable incidence of repeat revascularisation (target lesion revascularization [TLR] rates 23.8 % and 45 % at 4 months and 12 months respectively), which was similar to POBA.³² Intravascular ultrasound (IVUS) imaging revealed that the late lumen loss (LLL) (1.08 mm at 4-months) was due to recoil secondary to inadequate radial force that was ascribed to be secondary to the too rapid degradation of the device. Afterwards the device was redesigned predominantly to slow down the bioresorption process, so as to retain its mechanical strength for longer in order to prevent early vessel recoil. Several design iterations have emerged: AMS-2 and AMS-3. The AMS-2 scaffold had a more refined Mg alloy which gave it a higher collapse pressure (1.5 bar compared with 0.8 bar for AMS-1), approximately 30 % thinner struts (from 165 μm [AMS 1] to 125 μm), and importantly, a longer bioresorption process – with a 2–3 times slower degradation process. The AMS-3 ‘DREAMS’ (Drug Eluting Absorbable Metal Scaffold) device uses a similar platform as the AMS-2 and includes a biodegradable polymer that allows for drug elution. The DREAMS device provides vessel scaffolding and paclitaxel drug elution for a period of 3 months (Fig. 1). DREAMS was tested in clinical setting in the BIOSOLVE-I study.³⁵ In this prospective, multicenter, non-randomized trial, 46 patients with a single de novo lesion with a reference diameter 3.0–3.5 mm were recruited. In total, 47 DREAMS devices were successfully implanted. At 6-months the TLR rate was 4.3 % and the LLL was 0.64 ± 0.50 mm. At this same time point, improvements in the scaffolded segment angulation were evident, from $14.9 \pm 12.0^\circ$ post-procedurally, to $26.1 \pm 15.9^\circ$ at follow-up.³⁵ Further modification of the DREAMS device alloy - made from a WE43 alloy with 6-crown 2-link design - have allowed for a slower bioresorption and dismantling process. The DREAMS-2 device has a strut thickness of 150 μm and incorporates tantalum based radiopaque markers at both ends to allow for more precise post-dilatation. In addition, the DREAMS-2 device was coated with a bioresorbable polylactic acid polymer (7 μm) and a limus based anti-proliferative drug (sirolimus at a dose of 1.4 $\mu\text{g}/\text{mm}^2$) – which was shown to have a more potent anti-

proliferative effect compared to paclitaxel. DREAMS-2 has completed preclinical evaluation and is currently being investigated in the BIOSOLVE-II study (n = 120).

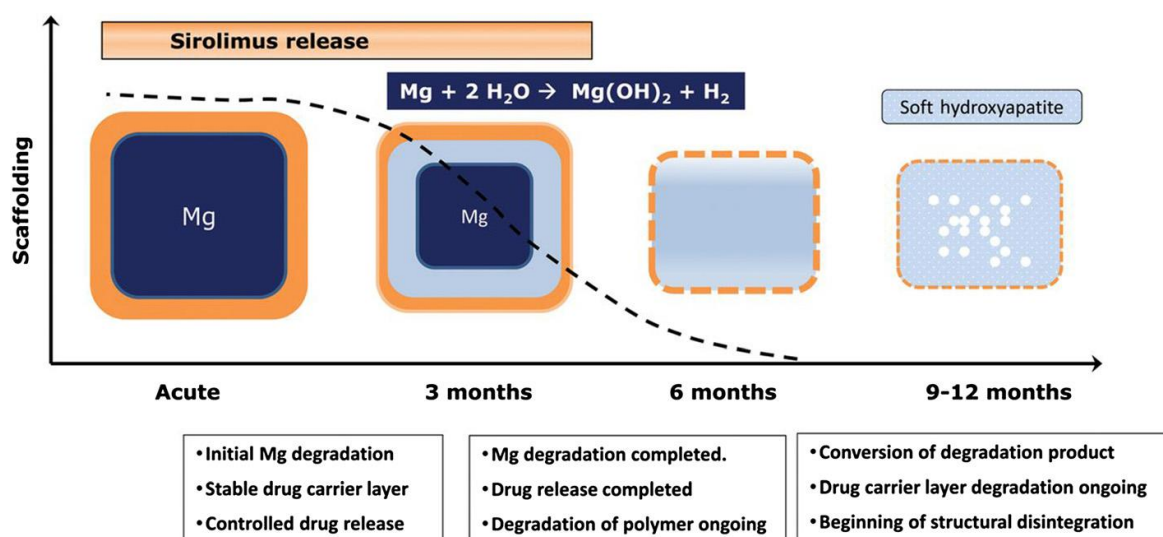


Figure 2. Device functionality of drug-eluting absorbable metal scaffold over time. (Reprinted from European Heart Journal with permission from Oxford University Press)

Polymeric scaffolds

The Igaki-Tamai scaffold

The Igaki-Tamai scaffold (Kyoto Medical Planning Co., Ltd., Kyoto, Japan) was the first BRS used in humans, and is a PLLA-based, non-drug eluting and a heat treated self-expandable device.³⁶ For the initial expansion of the device, the contrast was heated up to 80 °C and applied through the delivery balloon. Final expansion of the device was achieved at body temperature after 20–30 min following device implantation. In vivo the device took 18–24 months to fully disappear. To allow for visualization during the follow-up, two radiopaque cylindrical gold markers were placed at both ends of the device. A pilot study examining the efficacy of this device (15 patients, 19 lesions, 25 stents), demonstrated no MACE or ST within 30 days and only 1 repeat PCI at the 6-month follow-up. The mean stent cross-sectional area increased from $7.42 \pm 1.51 \text{ mm}^2$ at baseline to $8.18 \pm 2.42 \text{ mm}^2$ ($P = 0.086$) at 3 months, and $8.13 \pm 2.52 \text{ mm}^2$ at 6 months follow-ups ($p = 0.30$).³⁶ Notably, there was no significant neointimal hyperplasia on IVUS. IVUS also demonstrated no significant stent recoil at day-1 but evidence of stent expansion at 3-months following implantation.

In a second study of 50 elective patients (63 lesions, 84 stents), IVUS follow up at 3-year demonstrated complete absence of the struts. In addition, angiographic mean diameter

stenosis was 25 % compared to 38 %, 29 %, and 26 % at 6, 12, and 24 months, respectively. At 4-year follow-up, the overall and MACE-free and survival free rates were 97.7 % and 82.0 % respectively.³⁷ Ten-year clinical follow-up demonstrated freedom from cardiac death, non-cardiac death, and MACE at 98 %, 87 %, and 48 %, respectively.³⁸ Angiographic long term follow-up demonstrated no changes in the minimal lumen diameter (MLD): 1-year mean MLD 2.01 mm; 10-year mean MLD 2.06 mm. Only 2 ST events were reported at 10-year follow-up. Concerns with regards to this device arose from the use of heat to induce self-expansion, which may cause arterial wall necrosis leading to an exaggerated neointimal hyperplastic response or increased risk of platelet adhesion and scaffold thrombosis. Another concern of this device was that it required an 8-French guiding catheter. The PERSEUS study led to the biodegradable peripheral Igaki-Tamai scaffolds to be used in Europe for peripheral cases.³⁹

The REVA stent, a poly carbonate scaffold

The REVA scaffold (REVA Medical, Inc., San Diego, CA, USA) is a poly (iodinated desamino tyrosyl-tyrosine ethyl ester) carbonate device composed of iodinated-desaminotyrosinetyrosine. Following absorption, water, carbon dioxide, ethanol and iodinated-desaminotyrosinetyrosine are the end products from the Krebs cycle and excreted from the body. The REVA scaffold has no anti-proliferative drug coating and the bioresorption time is nearly 36 months. The slide and locking design prevented deformation and weakening of the polymer during scaffold deployment (**Fig. 1**). The radial force of the REVA scaffold has been reported to be greater than the MULTILINK BMS.⁴⁰ In the RESORB study, in which 27 patients with de novo lesions were enrolled, acute gain in lumen diameter and vessel shrinkage were satisfactory following device implantation. The mean diameter stenosis pre- and post-implantation were 70 % and 5.9 % respectively. The pre-implantation and post-implantation lumen diameters were 0.88 ± 0.39 mm and 2.76 ± 0.36 mm, respectively. Despite these results, at 6-months follow-up LLL was 1.81 mm and TLR was 66.7 %, predominantly secondary to vessel recoil since the neo-intimal hyperplasia response was shown to be similar compared to BMS.⁴¹ Following these findings, the scaffold has been redesigned and the second-generation ReZolve stent has stiff radiopaque polymer, a spiral 'slide and lock' mechanism and is coated with the antiproliferative drug sirolimus. In the RESTORE study, with 50 patients at 12 months follow-up, acute recoil was 3.8 ± 6.7 %, and LLL was 0.29 ± 0.33 mm at 12 months. At 6 months there were 2 MACE events in 12 patients.⁴² Further improvements

in the design of the scaffold have concluded in REVA's current product. ReZolve2 is being tested in the Safety and Performance Study of the ReZolve2 Sirolimus-Eluting Bioresorbable Coronary Scaffold study (RESTORE-II) (n = 125).⁴³ The company has presented a new clinical trial program named FANTOM investigating Fantom bioresorbable scaffold with thinner strut thickness.⁴⁴

Poly salicylic acid stent: IDEAL BRS

The IDEAL BRS (Xenogenics Corp.; Canton, Massachusetts, United States) has a backbone made of polylactide anhydride mixed with a polymer of salicylic acid and sebacic acid. The backbone is coated with salicylate that controls the release of the antiproliferative drug sirolimus (8.3 µg/mm). With salicylate and sirolimus, the scaffold has potentially both anti-inflammatory and antiproliferative properties.⁴⁵ The IDEAL BRS was initially tested in humans (11 patients) in 2009. In this first experience, there was negligible neointimal suppression and a significant reduction in lumen area that was associated with problems relating to the dose release kinetics of sirolimus – namely that it was eluted too rapidly, with a surface area dose of only a quarter compared to Cypher drug eluting stent.⁴⁶ The new generation IDEAL BioStent device has been designed with a lower profile to aid delivery, as well as optimising the dose release kinetics of sirolimus. Preclinical studies of the IDEAL BioStent device are underway.

Myolimus-eluting Poly-L-Lactic acid scaffold: DESolve

The DESolve Myolimus-Eluting Bioresorbable Coronary Scaffold System has a poly L-lactic acid (PLLA) backbone and is coated with myolimus (3 mg/mm) - a sirolimus analogue. In porcine studies, the radial strength was sufficiently provided over a 3 month period, and the resorption phase was completed at up to 2-years.⁴⁷ In the multicenter DESolve-I FIM trial, which recruited 16 patients implanted with polylactide-based bioresorbable scaffold coated with bioabsorbable polymer eluting myolimus, the incidence of acute recoil was 6.4 % and the LLL was 0.19 mm at 6 months. Post-procedural IVUS analyses demonstrated a mean scaffold area 5.35 mm² and a mean lumen area of 5.35 mm². Six-month IVUS analyses did not significantly differ from the baseline IVUS with a mean scaffold area 5.61 mm² and mean lumen area 5.10 mm². Six-month optical coherence tomography (OCT) examination at follow-up demonstrated that 98.7 % of the struts to be covered by neointima. One-year clinical follow up demonstrated 3 MACE, 1 target vessel MI and 1 TLR; no patient was reported to have had a scaffold thrombosis [47]. In the multi-center, prospective DESolve Nx trial, 120 patients were

treated with the DESolve Nx device - a PLLA-based polymer scaffold that is coated with novolimus (5 mg/mm), which is an active metabolite of sirolimus.^{48, 49} Recruitment of patients in the trial has been completed and clinical follow-up is still on-going. DESolve Nx trial was successful in demonstrating the safety and efficacy of the DESolve scaffold, with a low 6-month LLL by QCA (0.20 ± 0.32 mm), low 6-month IVUS % volume obstruction (5 %), low 6-month neointimal hyperplasia (NIH) thickness by OCT (0.10 mm), sustained neointimal suppression through 18 months follow-up, low 24-month MACE rate (7.4 %), no reported late acquired incomplete strut apposition (ISA) by IVUS / OCT at 6 months and high percentage of strut coverage by OCT at 6 months (98.8 %).^{48, 49} The preclinical study for the next generation scaffold named DESolve 100 with reduced strut thickness (100 μ m) is ongoing.

Everolimus-eluting Poly-L-lactic acid scaffold (Absorb BVS)

The Abbott Vascular everolimus eluting bioresorbable vascular scaffold (ABSORB BVS) (Abbott Vascular, Santa Clara, CA, USA) has a backbone of PLLA, coated with layer of a 1:1 mixture of an amorphous matrix of poly-D, L-lactide (PDLLA) and an antiproliferative drug everolimus (8.2 μ g/mm). The PDLLA controls the release of everolimus, 80 % of which is eluted at the end of the first month following implantation. The first version of Absorb BVS (Absorb BVS 1.0) had a strut thickness of 150 μ m, a crossing profile of 1.4 mm, and constituted of circumferential out-of-phase zigzag hoops, with the struts linked directly together by thin and straight connections. In the first human study, ABSORB (n = 30), multimodality intravascular imaging including IVUS, IVUS-virtual histology (IVUS-VH), palpography and OCT were performed at 6-month and 2-years follow up. At 6-month clinical follow-up, there was only one ischemic driven major adverse event (non Q-wave myocardial infarction); in the following 42-months there were no reported MACE events.^{22, 50} At the 4-year clinical follow-up there was no ST.⁵¹ At 5-years the overall MACE event rate was 3.4 %. At 6-months follow-up LLL was 0.44 mm. The reduction in lumen area was 16.6 %, and the late recoil was 11.7 %.⁵² The loss of radial strength with bioresorption, that was considered a consequence of scaffold shrinkage (6.94 ± 1.70 mm² to 6.29 ± 1.47 mm² at the 6 months follow-up), prompted the redesign of the scaffold. The re-designed Absorb BVS 1.1 had a strut design with in-phase hoops and straight links to provide additional radial support, and an updated polymer to provide additional mechanical strength for the scaffold.⁵³ The second generation ABSORB BVS was evaluated in the ABSORB Cohort B study. The studied population was divided into 2 groups;

the first group (B1) had QCA, IVUS, IVUS palpography, IVUS-VH, IVUS echogenicity, and OCT at 6 months and 2 years. The second group (B2) had the same follow-up imaging processes at 1 and at 3 years. At 2 year clinical follow up overall MACE was 9.0 %.⁵⁴ In Cohort B1, IVUS analyses demonstrated the minimal lumen area to decrease during the 6-months follow-up (baseline: $6.60 \pm 1.22 \text{ mm}^2$, 6-month: $5.99 \pm 1.61 \text{ mm}^2$, $P < 0.005$), and to remain stable between 6-months and 2-years follow-up (6-month: $6.37 \pm 1.12 \text{ mm}^2$, 24-month: $5.99 \pm 1.61 \text{ mm}^2$, $P = 0.26$). On OCT evaluation, the scaffold area progressively increased (baseline: $7.47 \pm 1.18 \text{ mm}^2$, 6-months: $7.70 \pm 1.34 \text{ mm}^2$, 2-years $8.34 \pm 1.83 \text{ mm}^2$).

In Cohort B2, the mean scaffold area did not significantly change between post-implantation and 12-months in OCT and IVUS examinations. The vessel vasomotion was tested with the application of acetylcholine or methylergonovine and the lumen measurements during these tests elicited restoration of the vasomotion at 12 months after scaffold implantation.⁵⁵ At two years, intracoronary administration of nitrate was performed and a significant ($p = 0.035$) but modest ($0.034 \pm 0.09 \text{ mm}$) vasodilatation was demonstrated. At three years, the vasodilatation was improved ($0.054 \pm 0.12 \text{ mm}$, $p = 0.005$).⁵⁶ Subsequently, preliminary results from the international, multi-center ABSORB EXTEND single arm study demonstrated an incidence of MACE of 7.3 %, ischemia driven TLR of 4.0 %, and stent thrombosis of 0.8 %, in 250 patients with 24 months of clinical follow-up.⁵⁷

ABSORB II constitutes the first randomized controlled trial comparing the efficacy and safety of a 2nd generation bioresorbable scaffold (Absorb, Abbott Vascular, Santa Clara, CA, USA) with a contemporary DES (Xience, Abbott Vascular, Santa Clara, CA, USA). The ABSORB II trial had a 2:1 single-masked design, recruiting 501 patients with stable and unstable angina symptoms to treatment with an everolimus eluting bioresorbable scaffold or a contemporary everolimus eluting metallic DES. The procedural details of the study were shown in **Table 2**. The co-primary endpoints of nitrate-induced vasomotion and changes in minimum lumen diameter (in-stent late loss) are to be reported at 3 years. Secondary outcomes recently reported at 1 year demonstrated no difference in major adverse cardiovascular events (defined as death, myocardial infarction or target lesion revascularization) between patients treated with a bioresorbable or a contemporary metallic DES (5 % vs. 3 %, $P = 0.35$). In addition, cumulative rates of first new or worsening angina were reported to be lower with the bioresorbable scaffold group compared to contemporary metallic DES (22 % vs. 30 %, $P = 0.001$).

p = 0.04), whereas the performance during maximum exercise and angina status by Seattle Angina Questionnaire were reported to be similar.⁵⁷

Table 2 Procedural details of ABSORB II trial

	Bioresorbable scaffold group (n = 335)	Metallic stent group (n = 166)	Difference (95 % CI)	p
Number of lesions	364	182		
Balloon dilatation prior to device implantation	364 (100 %)	180 (99 %)	1.10 % (-0.21, 3.92)	0.11
Planned overlap with the same type of device	56 (15 %)	20 (11 %)	4.40 % (-1.93, 9.94)	0.16
Additional implantation with the same device	14 (4 %)	11 (6.0)	-2.20 % (-6.91, 1.44)	0.25
More than one study device implanted	70 (19 %)	27 (15 %)	4.40 % (-2.57, 10.62)	0.21
Nominal size of study device (mm)	3.01 (0.31)	3.05 (0.28)	-0.04 (-0.10, 0.01)	0.10
Balloon dilatation after device implantation	221 (61 %)	107 (59 %)	1.92 % (-6.66, 10.67)	0.67
Nominal diameter of balloon used (mm)	3.08 (0.34)	3.16 (0.36)	-0.08 (-0.14, 0.01)	0.02
Maximum balloon pressure used (atm)	14.23 (3.43)	15.03 (3.33)	-0.80 (-1.4, -0.2)	0.01
Diameter of balloon used (mm)	3.29 (0.35)	3.35 (0.37)	-0.06 (-0.14, 0.02)	0.15
Angiographic acute recoil of device following implantation per device (mm)	0.19 (0.19)	0.19 (0.18)	-0.00 (-0.04, 0.03)	0.85
Device success				
Clinical device success	361 (99 %)	182 (100 %)	-0.82 % (-2.39, 1.31)	0.55
Clinical procedural success	322 (96 %)	164 (99 %)	-2.68 % (-5.46, 0.80)	0.16

In ABSORB II, pre-procedure mean lumen area in the BVS and metallic stent groups were reported to be similar $4.84 \pm 1.39 \text{ mm}^2$ and $5.02 \pm 1.47 \text{ mm}^2$, respectively ($p = 0.16$). The post-procedure mean lumen area were $6.06 \pm 1.44 \text{ mm}^2$ and $6.85 \pm 1.60 \text{ mm}^2$ respectively ($p < 0.001$). Post-procedure acute gain in minimum lumen diameter was significantly larger in metallic stent group than in BRS group ($1.46 \pm 0.38 \text{ mm}$ vs $1.15 \pm 0.38 \text{ mm}$, respectively; $p < 0.001$). Post-procedure in-stent/in-scaffold diameter stenosis was larger in BRS group than in metallic stent group ($16 \pm 7 \%$ vs $10 \pm 5 \%$, respectively; $p < 0.001$). In post-procedure IVUS analyses, post-procedure mean lumen area was significantly less in BVS group than in metallic stent group ($6.06 \pm 1.44 \text{ mm}^2$ vs $6.85 \pm 1.60 \text{ mm}^2$, respectively; $p < 0.001$). Post-procedure minimal lumen area ($5.73 \pm 1.51 \text{ mm}^2$ vs $4.89 \pm 1.38 \text{ mm}^2$, $p < 0.001$) and post-procedural acute gain in minimal lumen area ($3.60 \pm 1.34 \text{ mm}^2$ vs $2.85 \pm 1.25 \text{ mm}^2$, $p < 0.001$) were higher in metallic stent group than in BVS group (**Table 3**). The incidence of definite scaffold thrombosis was 0.6 % in BRS and 0 % in metallic stent group ($p = 1.0$). At the end of the first year the incidence of MI was 15 (4 %) in the BRS group and 2 (1 %) patients in the metallic stent group ($p = 0.06$), and were mostly non Q-wave MI. There were two scaffold thrombosis, one within 24 h of implantation and the second on the 2nd day.⁵⁷ In the POLAR ACS registry [58], Absorb BVS was implanted in selected patients with unstable angina, non ST-elevated myocardial infarction (NSTEMI) and ST-elevated myocardial infarction (STEMI). 100 patients were followed up for 1 year with two MACE reported, namely periprocedural MI. At the very least this small registry demonstrated the potential feasibility of the Absorb BVS in the treatment of ACS.⁵⁸

Other bioresorbable scaffolds under clinical investigation

ART bioresorbable scaffold

The ART BRS (Arterial Remodeling Technologies; Noisy le Roi, France) is made from a PDLLA amorphous polymer. Notably the device does not contain an anti-proliferative drug. The device retains its structural integrity and scaffolding properties for a period of 5–7 months; the bioresorption ends within 18 months. In animal studies, there was no MACE reported and acute recoil rates were similar with BMS, with the mean lumen area and external elastic lamina area being increased at 9-months on IVUS evaluation.^{59, 60} Based on these promising

results, the Arterial Remodeling Transient Dismantling Vascular Angioplasty (ARTDIVA)⁶¹ first in man trial (ClinicalTrials.gov Identifier: NCT01761578) was launched aiming to evaluate the safety and efficacy of the ART18Z bioresorbable scaffold in the treatment of patients with CAD.⁶¹ In this trial 30 patients with a single de novo lesion were recruited in 5 medical centers in France. The mean diameter of reference vessel pre-procedure was 2.55 ± 0.30 mm, minimal luminal diameter was 0.99 ± 0.23 mm, the diameter stenosis was 61 ± 8 % and the lesion length was 7.54 ± 1.24 mm. At 6-months follow-up, in-stent diameter stenosis was 12 ± 7 % in-segment diameter stenosis was 17 ± 5 % and angiographic recoil was 4.3 %. During this follow-up period there was 1 ischemia driven TLR and 2 non-ischemia driven TLR, no MI and stroke/TIA [62].⁶²

Xinsorb BRS

The Xinsorb BRS (Huaan Biotechnology; Laiwu, China) is a fully bioresorbable sirolimus-eluting scaffold (strut thickness 160 μ m) that consists of PLLA, polylactide- co-glycolide, and poly-L-lactide-co-e-caprolactone. 78 % of sirolimus is released from the Xinsorb BRS within 14 days [63].⁶³

In a comparison study between Xinsorb BRS and the Excel DES (JW Medical; Shandong, China) implanted in the coronaries of porcine models, there was no significant difference in percentage diameter stenosis (%DS) in the Xinsorb BRS compared to the Excel DES (18.6 % vs. 21.4 % at 30 days; $p > 0.05$ and 24.5 % vs. 27.7 % at 90 days; $p > 0.05$, respectively).⁶⁴ At 3-month follow-up OCT imaging demonstrated significant neointimal hyperplasia in porcine models.

Subsequently the LLL and %DS were noticeably reduced. At 1-month follow-up, proximal, in-scaffold, and distal LLL of scaffold were 0.53 ± 0.41 mm, 0.68 ± 0.42 mm and 0.65 ± 0.24 mm, while the %DS were 9.5 ± 7.7 %, 17.6 ± 16.8 % and 10.5 ± 7.4 % respectively. At 3-months, proximal, in-scaffold, and distal LLL were 0.23 ± 0.48 mm, 0.77 ± 0.48 mm and 0.11 ± 0.35 mm, while %DS were 14.5 ± 9.4 %, 31.9 ± 13.6 % and 5.4 ± 3.6 % respectively. At 12-months, proximal, in-scaffold, and distal LLL were -0.13 ± 0.45 mm, 0.28 ± 0.41 mm and 0.18 ± 0.48 mm, while %DS were 2.4 ± 2.9 %, 14.1 ± 9.1 % and 8.6 ± 8.7 % respectively. At 18-month, proximal, in-scaffold, and distal LLL were 0.37 ± 0.57 mm, 0.09 ± 0.31 mm and -0.01 ± 0.41 mm, while %DS were 3.9 ± 4.6 %, 13.7 ± 7.3 % and 6.9 ± 5.2 % respectively. Lumen area at 18-month was significantly larger than that at 3-month with a constant scaffold area.⁶⁵ In Xinsorb FIM trial (n=30 patients), at 6-months follow-up, LLL was 0.18 ± 0.21 mm. In

scaffolded segments, the diameter stenosis was 10.0 ± 4.2 % at post-implantation and 10.6 ± 6.6 % at 6-months follow-up ($p = 0.70$). At 6-months OCT follow-up ($n = 19$) the luminal area was 6.03 ± 0.76 mm², scaffold area was 7.74 ± 0.62 mm², in-scaffold area obstruction was 22.1 ± 6.1 %, neointimal thickness was 0.07 ± 0.04 mm with no thrombus detected. The 6-month IVUS follow-up revealed a mean vessel area 14.37 ± 0.90 mm², mean neointimal area 3.11 ± 0.19 mm², mean scaffold area 9.36 ± 0.21 mm² and mean luminal area 6.26 ± 0.26 mm².⁶⁶

Mirage bioresorbable micro-fiber scaffold

Mirage Bioresorbable Micro-fiber Scaffold (Mirage BRMS, Manli Cardiology Singapore) is a PLLA-based sirolimus eluting scaffold. The device incorporates a helix coil design that provides high flexibility with a strut thickness of 125 μ m in scaffolds with diameter ≤ 3 mm, and of 150 μ m in scaffolds with diameter ≥ 3.5 mm. Mirage BRMS has a low crossing profile (0.044" – 0.058"), and relatively short bioresorption time (~ 14 months). Results of a porcine study were encouraging; namely no in-scaffold restenosis at 6-month follow-up, 99 % of the struts were covered while the mean NIH thickness on top of covered struts was 0.08 ± 0.03 mm at 6-month follow-up.⁶⁷ Frequency of covered and uncovered struts per lesion were 99.85 ± 0.33 % and 0.15 ± 0.33 % respectively. The frequency of malapposed struts per lesion was 0.03 ± 0.08 %, and malapposition strut-to-lumen distance was 0.28 mm (there was only one malapposed strut at 6-month follow-up). In QCA analysis, MLD and % DS was 2.34 ± 0.49 mm and 2.13 ± 0.47 mm, 17.1 ± 11.4 % and 22.8 ± 15.0 %, at post-procedure and at 6-months, respectively. At 6-months, LLL was 0.21 ± 0.20 mm and late recoil was 0.16 ± 0.12 mm. Both in-scaffold and in-segment angiographic binary restenosis ratios were 0 % at 6-month [67]. Patient enrolment in FIM trial was completed in September 2014 and the results are expected to be presented at the end of 2015.

Table 3 Angiographic and IVUS/IVUS-VH outcomes of ABSORB II trial

	Bioresorbable scaffold group (n=335)	Metallic stent group (n=166)	Difference (95 % CI)	p
Angiographic analysis				
Lesion length obstruction (mm)	13.8 (6.5)	13.8 (6.6)	0.00 (-1.18, 1.18)	1.00
Total scaffolded/stented length (mm)	21.1 (8.8)	20.9 (7.4)	0.24 (-1.17, 1.65)	0.74
Reference vessel diameter				
Pre-procedure diameter (mm)	2.59 (0.38)	2.63 (0.40)	-0.03 (-0.10, 0.04)	0.36
Post-procedure diameter (mm)	2.64 (0.36)	2.80 (0.34)	-0.16 (-0.22, -0.09)	<0.001
Minimum lumen diameter				
Pre-procedure diameter (mm)	1.07 (0.32)	1.05 (0.32)	0.02 (-0.03, 0.08)	0.44
Post-procedure in-stent or in-scaff old diameter (mm)	2.22 (0.33)	2.50 (0.33)	-0.28 (-0.34, -0.22)	<0.001
In-stent/in-scaff old acute gain (mm)	1.15±0.38	1.46±0.38	-0.30 (-0.37, -0.24)	<0.001
Diameter stenosis				
Pre-procedure percent diameter stenosis (%)	59±11 %	60±12 %	-1.07 (-3.11, 0.97)	0.30
Post-procedure in-stent/in-scaffold diameter stenosis (%)	16±7 %	10±5 %	5.37 (4.38, 6.36)	<0.001
Pre-procedural fibrotic tissue (%)	31.47±11.39	30.62±11.42	0.85 (-1.33, 3.04)	0.44
Pre-procedural fibrofatty tissue (%)	47.43±16.91	48.55±16.86	-1.12 (-4.35, 2.11)	0.50
Pre-procedural necrotic core (%)	16.20±6.86	16.15±6.90	0.05 (-1.27, 1.37)	0.94
Pre-procedural dense calcium (%)	4.90±4.73	4.68±4.10	0.22 (-0.61, 1.05)	0.60
Vessel area				
Pre-procedure area (mm ²)	11.51±3.40	12.34±3.42	-0.83 (-1.47, -0.19)	0.02
Post-procedure area (mm ²)	13.17±3.55	14.28±3.59	-1.11 (-1.78, -0.44)	0.001
Plaque area				
Pre-procedure plaque area (mm ²)	6.67±2.52	7.30±2.68	0.6 (-1.12, 0.13)	0.01
Post-procedure plaque area (mm ²)	7.11±2.46	7.43±2.44	-0.32 (-0.78, 0.14)	0.18
Mean lumen area				
Pre-procedure mean lumen area (mm ²)	4.84±1.39	5.02±1.47	-0.19 (-0.47, 0.08)	0.16
Post-procedure mean lumen area (mm ²)	6.06±1.44	6.85±1.60	-0.80 (-1.09, -0.50)	<0.001
Minimal lumen area				
Pre-procedure minimal lumen area (mm ²)	2.04±0.72	2.13±0.83	-0.10 (-0.25, 0.05)	0.20
Post-procedure minimal lumen area (mm ²)	4.89±1.38	5.73±1.51	-0.84 (-1.12, -0.57)	<0.001
Acute gain in minimal lumen area (mm ²)	2.85±1.25	3.60±1.34	-0.75 (-0.99, -0.50)	<0.001

CONCLUSION

For the last 20 years percutaneous coronary revascularization has evolved, with the current premise that stent implantation to be the standard of care in appropriately selected patients.⁶⁸ Considering that coronary stenting with metallic devices may result in persistent inflammation and endothelial dysfunction, an issue that has been reduced but not eliminated with newer generation DES⁶⁹, the temporary scaffold that would safeguard vessel patency and then it would disappear, appears as the ideal solution for treating CAD.⁷⁰ These devices at the very least have to provide comparable performances to contemporary DES in the short term, with the potential promise of enhanced longer term benefits due to freeing the vessel wall from the metallic cage and allowing the vessel to potentially restore its vascular function (vessel vasomotion) adaptive shear stress and would permit late luminal enlargement, and late expansive remodeling. Ongoing, and future randomized trials assessing the efficacy of the multitude of bioresorbable scaffolds – currently 16 different scaffolds are being developed and under investigation – will ultimately determine the clinical value of this fourth revolution in interventional cardiology.

Acknowledgements

We would like to acknowledge Yapping Zhang for her intellectual input and careful review of the literature. We would like to thank the investigators of ABSORB A, ABSORB B and ABSORB II who have contributed by their investigation to the progression of the field.

REFERENCES

1. Gruntzig A. Transluminal dilatation of coronary-artery stenosis. *Lancet (London, England)*. 1978;1:263.
2. Farooq V, Gogas BD and Serruys PW. Restenosis: delineating the numerous causes of drug-eluting stent restenosis. *Circulation Cardiovascular interventions*. 2011;4:195-205.
3. Gruntzig AR, Senning A and Siegenthaler WE. Nonoperative dilatation of coronary-artery stenosis: percutaneous transluminal coronary angioplasty. *The New England journal of medicine*. 1979;301:61-8.
4. Sigwart U, Urban P, Golf S, Kaufmann U, Imbert C, Fischer A and Kappenberger L. Emergency stenting for acute occlusion after coronary balloon angioplasty. *Circulation*. 1988;78:1121-7.
5. Roubin GS, Cannon AD, Agrawal SK, Macander PJ, Dean LS, Baxley WA and Breland J. Intracoronary stenting for acute and threatened closure complicating percutaneous transluminal coronary angioplasty. *Circulation*. 1992;85:916-27.
6. Serruys PW, Strauss BH, Beatt KJ, Bertrand ME, Puel J, Rickards AF, Meier B, Goy JJ, Vogt P, Kappenberger L and et al. Angiographic follow-up after placement of a self-expanding coronary-artery stent. *The New England journal of medicine*. 1991;324:13-7.
7. Serruys PW, de Jaegere P, Kiemeneij F, Macaya C, Rutsch W, Heyndrickx G, Emanuelsson H, Marco J, Legrand V, Materne P and et al. A comparison of balloon-expandable-stent implantation with balloon angioplasty in patients with coronary artery disease. Benestent Study Group. *The New England journal of medicine*. 1994;331:489-95.
8. Fischman DL, Leon MB, Baim DS, Schatz RA, Savage MP, Penn I, Detre K, Veltri L, Ricci D, Nobuyoshi M and et al. A randomized comparison of coronary-stent placement and balloon angioplasty in the treatment of coronary artery disease. Stent Restenosis Study Investigators. *The New England journal of medicine*. 1994;331:496-501.
9. Hoffmann R, Mintz GS, Dussaillant GR, Popma JJ, Pichard AD, Satler LF, Kent KM, Griffin J and Leon MB. Patterns and mechanisms of in-stent restenosis. A serial intravascular ultrasound study. *Circulation*. 1996;94:1247-54.
10. Gordon PC, Gibson CM, Cohen DJ, Carrozza JP, Kuntz RE and Baim DS. Mechanisms of restenosis and redilation within coronary stents--quantitative angiographic assessment. *Journal of the American College of Cardiology*. 1993;21:1166-74.
11. Karas SP, Gravanis MB, Santoian EC, Robinson KA, Anderberg KA and King SB, 3rd. Coronary intimal proliferation after balloon injury and stenting in swine: an animal model of restenosis. *Journal of the American College of Cardiology*. 1992;20:467-74.
12. Dussaillant GR, Mintz GS, Pichard AD, Kent KM, Satler LF, Popma JJ, Wong SC and Leon MB. Small stent size and intimal hyperplasia contribute to restenosis: a volumetric intravascular ultrasound analysis. *Journal of the American College of Cardiology*. 1995;26:720-4.
13. Sousa JE, Costa MA, Abizaid AC, Rensing BJ, Abizaid AS, Tanajura LF, Kozuma K, Van Langenhove G, Sousa AG, Falotico R, Jaeger J, Popma JJ and Serruys PW. Sustained suppression of neointimal proliferation by sirolimus-eluting stents: one-year angiographic and intravascular ultrasound follow-up. *Circulation*. 2001;104:2007-11.
14. Stone GW, Ellis SG, Cox DA, Hermiller J, O'Shaughnessy C, Mann JT, Turco M, Caputo R, Bergin P, Greenberg J, Popma JJ and Russell ME. A polymer-based, paclitaxel-eluting stent in patients with coronary artery disease. *The New England journal of medicine*. 2004;350:221-31.

15. Daemen J, Wenaweser P, Tsuchida K, Abrecht L, Vaina S, Morger C, Kukreja N, Juni P, Sianos G, Hellige G, van Domburg RT, Hess OM, Boersma E, Meier B, Windecker S and Serruys PW. Early and late coronary stent thrombosis of sirolimus-eluting and paclitaxel-eluting stents in routine clinical practice: data from a large two-institutional cohort study. *Lancet (London, England)*. 2007;369:667-78.
16. Wenaweser P, Daemen J, Zwahlen M, van Domburg R, Juni P, Vaina S, Hellige G, Tsuchida K, Morger C, Boersma E, Kukreja N, Meier B, Serruys PW and Windecker S. Incidence and correlates of drug-eluting stent thrombosis in routine clinical practice. 4-year results from a large 2-institutional cohort study. *Journal of the American College of Cardiology*. 2008;52:1134-40.
17. Virmani R, Guagliumi G, Farb A, Musumeci G, Grieco N, Motta T, Mihalcsik L, Tsepili M, Valsecchi O and Kolodgie FD. Localized hypersensitivity and late coronary thrombosis secondary to a sirolimus-eluting stent: should we be cautious? *Circulation*. 2004;109:701-5.
18. Serruys PW, Onuma Y, Garg S, Vranckx P, De Bruyne B, Morice MC, Colombo A, Macaya C, Richardt G, Fajadet J, Hamm C, Schuijjer M, Rademaker T, Wittebols K and Stoll HP. 5-year clinical outcomes of the ARTS II (Arterial Revascularization Therapies Study II) of the sirolimus-eluting stent in the treatment of patients with multivessel de novo coronary artery lesions. *Journal of the American College of Cardiology*. 2010;55:1093-101.
19. Hofma SH, van der Giessen WJ, van Dalen BM, Lemos PA, McFadden EP, Sianos G, Ligthart JM, van Essen D, de Feyter PJ and Serruys PW. Indication of long-term endothelial dysfunction after sirolimus-eluting stent implantation. *European heart journal*. 2006;27:166-70.
20. Togni M, Windecker S, Cocchia R, Wenaweser P, Cook S, Billinger M, Meier B and Hess OM. Sirolimus-eluting stents associated with paradoxical coronary vasoconstriction. *Journal of the American College of Cardiology*. 2005;46:231-6.
21. Shalaby W, Shalaby KJLB. *Absorbable and Biodegradable Polymers*. 1 ed: CRC Press; 2003.
22. Ormiston JA, Serruys PW, Regar E, Dudek D, Thuesen L, Webster MW, Onuma Y, Garcia-Garcia HM, McGreevy R and Veldhof S. A bioabsorbable everolimus-eluting coronary stent system for patients with single de-novo coronary artery lesions (ABSORB): a prospective open-label trial. *Lancet (London, England)*. 2008;371:899-907.
23. Heublein B, Rohde R, Kaese V, Niemeyer M, Hartung W and Haverich A. Biocorrosion of magnesium alloys: a new principle in cardiovascular implant technology? *Heart (British Cardiac Society)*. 2003;89:651-6.
24. Waksman R, Pakala R, Kuchulakanti PK, Baffour R, Hellinga D, Seabron R, Tio FO, Wittchow E, Hartwig S, Harder C, Rohde R, Heublein B, Andrae A, Waldmann KH and Haverich A. Safety and efficacy of bioabsorbable magnesium alloy stents in porcine coronary arteries. *Catheterization and cardiovascular interventions : official journal of the Society for Cardiac Angiography & Interventions*. 2006;68:607-17; discussion 618-9.
25. Department. UdSdPM.
http://www.dist.unina.it/doc/seminari/corso_Auricchio/biomaterials.pdf.
2015:http://www.dist.unina.it/doc/seminari/corso_Auricchio/biomaterials.pdf.
26. Brugaletta S, Radu MD, Garcia-Garcia HM, Heo JH, Farooq V, Girisic C, van Geuns RJ, Thuesen L, McClean D, Chevalier B, Windecker S, Koolen J, Rapoza R, Miquel-Hebert K, Ormiston J and Serruys PW. Circumferential evaluation of the neointima by optical coherence tomography after ABSORB bioresorbable vascular scaffold implantation: can the scaffold cap the plaque? *Atherosclerosis*. 2012;221:106-12.

27. Joner M, Finn AV, Farb A, Mont EK, Kolodgie FD, Ladich E, Kutys R, Skorija K, Gold HK and Virmani R. Pathology of drug-eluting stents in humans: delayed healing and late thrombotic risk. *Journal of the American College of Cardiology*. 2006;48:193-202.
28. Onuma Y, Serruys PW, Perkins LE, Okamura T, Gonzalo N, Garcia-Garcia HM, Regar E, Kamberi M, Powers JC, Rapoza R, van Beusekom H, van der Giessen W and Virmani R. Intracoronary optical coherence tomography and histology at 1 month and 2, 3, and 4 years after implantation of everolimus-eluting bioresorbable vascular scaffolds in a porcine coronary artery model: an attempt to decipher the human optical coherence tomography images in the ABSORB trial. *Circulation*. 2010;122:2288-300.
29. Garg S, Serruys P, Onuma Y, Dorange C, Veldhof S, Miquel-Hebert K, Sudhir K, Boland J, Huber K, Garcia E and te Riele JA. 3-year clinical follow-up of the XIENCE V everolimus-eluting coronary stent system in the treatment of patients with de novo coronary artery lesions: the SPIRIT II trial (Clinical Evaluation of the Xience V Everolimus Eluting Coronary Stent System in the Treatment of Patients with de novo Native Coronary Artery Lesions). *JACC Cardiovascular interventions*. 2009;2:1190-8.
30. Verheye S, Ormiston JA, Stewart J, Webster M, Sanidas E, Costa R, Costa JR, Jr., Chamie D, Abizaid AS, Pinto I, Morrison L, Toyloy S, Bhat V, Yan J and Abizaid A. A next-generation bioresorbable coronary scaffold system: from bench to first clinical evaluation: 6- and 12-month clinical and multimodality imaging results. *JACC Cardiovascular interventions*. 2014;7:89-99.
31. Brugaletta S, Heo JH, Garcia-Garcia HM, Farooq V, van Geuns RJ, de Bruyne B, Dudek D, Smits PC, Koolen J, McClean D, Dorange C, Veldhof S, Rapoza R, Onuma Y, Bruining N, Ormiston JA and Serruys PW. Endothelial-dependent vasomotion in a coronary segment treated by ABSORB everolimus-eluting bioresorbable vascular scaffold system is related to plaque composition at the time of bioresorption of the polymer: indirect finding of vascular reparative therapy? *European heart journal*. 2012;33:1325-33.
32. Erbel R, Di Mario C, Bartunek J, Bonnier J, de Bruyne B, Eberli FR, Erne P, Haude M, Heublein B, Horrigan M, Ilesley C, Bose D, Koolen J, Luscher TF, Weissman N and Waksman R. Temporary scaffolding of coronary arteries with bioabsorbable magnesium stents: a prospective, non-randomised multicentre trial. *Lancet (London, England)*. 2007;369:1869-1875.
33. Barlis P, Tanigawa J and Di Mario C. Coronary bioabsorbable magnesium stent: 15-month intravascular ultrasound and optical coherence tomography findings. *European heart journal*. 2007;28:2319.
34. Ghimire G, Spiro J, Kharbanda R, Roughton M, Barlis P, Mason M, Ilesley C, Di Mario C, Erbel R, Waksman R and Dalby M. Initial evidence for the return of coronary vasoreactivity following the absorption of bioabsorbable magnesium alloy coronary stents. *EuroIntervention : journal of EuroPCR in collaboration with the Working Group on Interventional Cardiology of the European Society of Cardiology*. 2009;4:481-4.
35. Haude M, Erbel R, Erne P, Verheye S, Degen H, Bose D, Vermeersch P, Wijnbergen I, Weissman N, Prati F, Waksman R and Koolen J. Safety and performance of the drug-eluting absorbable metal scaffold (DREAMS) in patients with de-novo coronary lesions: 12 month results of the prospective, multicentre, first-in-man BIOSOLVE-I trial. *Lancet (London, England)*. 2013;381:836-44.
36. Tamai H, Igaki K, Kyo E, Kosuga K, Kawashima A, Matsui S, Komori H, Tsuji T, Motohara S and Uehata H. Initial and 6-month results of biodegradable poly-L-lactic acid coronary stents in humans. *Circulation*. 2000;102:399-404.
37. Tsuji T. Four-year follow-up of the biodegradable stent (Igaki-Tamai stent). *Circulation journal : official journal of the Japanese Circulation Society*. 2004;68:135.

38. Nishio S. Long-term (> 10 years) clinical outcomes of first-in-man biodegradable poly-L-lactic acid coronary stents. *EuroPCR*. 2010.
39. Biamino G. Treatment of SFA lesions with PLLA biodegradable stents: results of the PERSEUS study. *Journal of endovascular therapy : an official journal of the International Society of Endovascular Specialists*. 2005;12:5.
40. R S. *Cardiovascular Revascularization Therapies 2007*.
41. E G. Bioabsorbable stent: the Boston Scientific and REVA technology. *EuroPCR*.
42. RA C. REVA ReZolve clinical program update. *Transcatheter Cardiovascular Therapeutics*. 2012.
43. ReZolve2 Clinical Investigation (RESTORE II).
44. A A. *Cardiovascular Research Technologies*. 2015.
45. Jabara R, Chronos N and Robinson K. Novel bioabsorbable salicylate-based polymer as a drug-eluting stent coating. *Catheterization and cardiovascular interventions : official journal of the Society for Cardiac Angiography & Interventions*. 2008;72:186-94.
46. Jabara R, Pendyala L, Geva S, Chen J, Chronos N and Robinson K. Novel fully bioabsorbable salicylate-based sirolimus-eluting stent. *EuroIntervention : journal of EuroPCR in collaboration with the Working Group on Interventional Cardiology of the European Society of Cardiology*. 2009;5 Suppl F:F58-64.
47. S V. First-in-man results with a sirolimus-eluting bioresorbable PLLA-based vascular scaffold. *Transcatheter Cardiovasc Therapeutics*.
48. S V. DESolve Nx Novolimus-Eluting PLLA-Based BRS: First Report of the 6-month OCT and 12-month Clinical and Imaging Result. *Transcatheter Cardiovasc Therapeutics*. 2013.
49. A A. Prospective, Multicenter Evaluation of the DESolve Novolimus-Eluting Bioresorbable Coronary Scaffold: Imaging Outcomes and 2-Year Clinical Results. *Transcatheter Cardiovasc Therapeutics*. 2014.
50. Serruys PW, Ormiston JA, Onuma Y, Regar E, Gonzalo N, Garcia-Garcia HM, Nieman K, Bruining N, Dorange C, Miquel-Hebert K, Veldhof S, Webster M, Thuesen L and Dudek D. A bioabsorbable everolimus-eluting coronary stent system (ABSORB): 2-year outcomes and results from multiple imaging methods. *Lancet (London, England)*. 2009;373:897-910.
51. Onuma Y, Serruys PW, Ormiston JA, Regar E, Webster M, Thuesen L, Dudek D, Veldhof S and Rapoza R. Three-year results of clinical follow-up after a bioresorbable everolimus-eluting scaffold in patients with de novo coronary artery disease: the ABSORB trial. *EuroIntervention : journal of EuroPCR in collaboration with the Working Group on Interventional Cardiology of the European Society of Cardiology*. 2010;6:447-53.
52. Tanimoto S, Serruys PW, Thuesen L, Dudek D, de Bruyne B, Chevalier B and Ormiston JA. Comparison of in vivo acute stent recoil between the bioabsorbable everolimus-eluting coronary stent and the everolimus-eluting cobalt chromium coronary stent: insights from the ABSORB and SPIRIT trials. *Catheterization and cardiovascular interventions : official journal of the Society for Cardiac Angiography & Interventions*. 2007;70:515-23.
53. Garg S and Serruys P. Biodegradable stents and non-biodegradable stents. *Minerva cardioangiologica*. 2009;57:537-65.
54. Ormiston JA, Serruys PW, Onuma Y, van Geuns RJ, de Bruyne B, Dudek D, Thuesen L, Smits PC, Chevalier B, McClean D, Koolen J, Windecker S, Whitbourn R, Meredith I, Dorange C, Veldhof S, Hebert KM, Rapoza R and Garcia-Garcia HM. First serial assessment at 6 months and 2 years of the second

generation of absorb everolimus-eluting bioresorbable vascular scaffold: a multi-imaging modality study. *Circulation Cardiovascular interventions*. 2012;5:620-32.

55. Serruys PW, Onuma Y, Dudek D, Smits PC, Koolen J, Chevalier B, de Bruyne B, Thuesen L, McClean D, van Geuns RJ, Windecker S, Whitbourn R, Meredith I, Dorange C, Veldhof S, Hebert KM, Sudhir K, Garcia-Garcia HM and Ormiston JA. Evaluation of the second generation of a bioresorbable everolimus-eluting vascular scaffold for the treatment of de novo coronary artery stenosis: 12-month clinical and imaging outcomes. *Journal of the American College of Cardiology*. 2011;58:1578-88.

56. Serruys PW, Onuma Y, Garcia-Garcia HM, Muramatsu T, van Geuns RJ, de Bruyne B, Dudek D, Thuesen L, Smits PC, Chevalier B, McClean D, Koolen J, Windecker S, Whitbourn R, Meredith I, Dorange C, Veldhof S, Hebert KM, Rapoza R and Ormiston JA. Dynamics of vessel wall changes following the implantation of the absorb everolimus-eluting bioresorbable vascular scaffold: a multi-imaging modality study at 6, 12, 24 and 36 months. *EuroIntervention : journal of EuroPCR in collaboration with the Working Group on Interventional Cardiology of the European Society of Cardiology*. 2014;9:1271-84.

57. Serruys PW, Chevalier B, Dudek D, Cequier A, Carrie D, Iniguez A, Dominici M, van der Schaaf RJ, Haude M, Wasungu L, Veldhof S, Peng L, Staehr P, Grundeken MJ, Ishibashi Y, Garcia-Garcia HM and Onuma Y. A bioresorbable everolimus-eluting scaffold versus a metallic everolimus-eluting stent for ischaemic heart disease caused by de-novo native coronary artery lesions (ABSORB II): an interim 1-year analysis of clinical and procedural secondary outcomes from a randomised controlled trial. *Lancet (London, England)*. 2015;385:43-54.

58. Dudek D, Rzeszutko L, Zasada W, Depukat R, Siudak Z, Ochala A, Wojakowski W, Przewlocki T, Zmudka K, Kochman J, Lekston A and Gasior M. Bioresorbable vascular scaffolds in patients with acute coronary syndromes: the POLAR ACS study. *Polskie Archiwum Medycyny Wewnetrznej*. 2014;124:669-77.

59. Lafont A and Durand E. A.R.T.: concept of a bioresorbable stent without drug elution. *EuroIntervention : journal of EuroPCR in collaboration with the Working Group on Interventional Cardiology of the European Society of Cardiology*. 2009;5 Suppl F:F83-7.

60. Durand E, Lemitre M, Couty L, Sharkawi T, Brasselet C, Vert M and Lafont A. Adjusting a polymer formulation for an optimal bioresorbable stent: a 6-month follow-up study. *EuroIntervention : journal of EuroPCR in collaboration with the Working Group on Interventional Cardiology of the European Society of Cardiology*. 2012;8:242-9.

61. J F. The ART, stent: design and early first-in-man experiences. *Transcatheter Cardiovasc Therapeutics*. 2012.

62. A L. ARTDIVA. *BRS 2014*. 2014.

63. Shen L, Wang Q, Wu Y-z, Xie J, Zhang F and Ge L. Preliminary evaluation of fully bioabsorbable PLLA sirolimus eluting stents in a porcine model. *Chin J Intervent Cardiol*. 2009;19:301-305.

64. Shen L WQ, Wu Y, Xie J, Ge J. Short-term effects of sirolimus eluting fully bioabsorbable polymeric coronary stents in a porcine model. . *Transcatheter Cardiovasc Therapeutics*. 2011.

65. Wu Y SL, Yao Z, Ge L, Wang Q, Qian J. Long-term Angiographic and Optical Coherence Tomography Follow-up of XINSORB Scaffold in Porcine Coronary Model. *Transcatheter Cardiovasc Therapeutics 2014*.

66. J. G. BRS Under Development III – The XINSORB BRS. *Transcatheter Cardiovasc Therapeutics*. 2014.

67. T. S. The Mirage Bioresorbable Microfiber Scaffold (BRMS) Manli Cardiology. . *Transcatheter Cardiovasc Therapeutics*. 2014.

68. Windecker S, Kolh P, Alfonso F, Collet JP, Cremer J, Falk V, Filippatos G, Hamm C, Head SJ, Juni P, Kappetein AP, Kastrati A, Knuuti J, Landmesser U, Laufer G, Neumann FJ, Richter DJ, Schauerte P, Sousa Uva M, Stefanini GG, Taggart DP, Torracca L, Valgimigli M, Wijns W and Witkowski A. 2014 ESC/EACTS guidelines on myocardial revascularization. *EuroIntervention : journal of EuroPCR in collaboration with the Working Group on Interventional Cardiology of the European Society of Cardiology*. 2015;10:1024-94.
69. Mitsutake Y, Ueno T, Ikeno F, Yokoyama S, Sasaki K-i, Ohtsuka M, Nakayoshi T, Itaya N, Chibana H and Sasaki M. Second-generation everolimus-eluting stents demonstrate better vascular function, less thrombus formation, and less yellow intima than first-generation drug-eluting stents. *AsiaIntervention*. 2015;1:33-40.
70. Serruys PW. Innovations: resetting our thinking to solve problems. *EuroIntervention : journal of EuroPCR in collaboration with the Working Group on Interventional Cardiology of the European Society of Cardiology*. 2014;10:413.

Differential aspects between cobalt-chromium everolimus drug-eluting stent and Absorb everolimus bioresorbable vascular scaffold: from bench to clinical use

Yohei Sotomi, Pannipa Suwannasom, Erhan Tenekecioglu, Hiroki Tateishi, Mohammad Abdelghani, Patrick W Serruys, Yoshinobu Onuma

Expert Rev Cardiovasc Ther. 2015;13(10):1127-45.

ABSTRACT

Drug-eluting stents have significantly improved the outcomes of percutaneous coronary intervention by substantially reducing in-stent restenosis and stent thrombosis. However, a potential limitation of these stents is the permanent presence of a metallic foreign body within the artery, which may cause vascular inflammation, restenosis, thrombosis, neoatherosclerosis, permanent impairment of the physiological vasomotor function and interference with potential future grafting of the stented segment. Bioresorbable scaffolds have the potential to overcome these limitations as they provide temporary scaffolding and then disappear, liberating the treated vessel from its cage and restoring pulsatility, cyclical strain, physiological shear stress and mechanotransduction. This article presents a comparison between the most widespread bioresorbable vascular scaffold 'Absorb BVS' and second-generation drug-eluting stent (cobalt chromium everolimus-eluting stent) from bench to clinical use.

BACKGROUND

The need for Bioresorbable scaffolds

Introduction

The invention of balloon angioplasty as a percutaneous treatment for obstructive coronary disease by Andreas Gruntzig in 1977 was a huge forward leap in cardiovascular medicine, and undoubtedly will always be remembered as a revolution in the field of revascularization [1,2]. The advent of bare metal stenting and the landmark BENESTENT and STRESS trials have established bare metal stenting as the second revolution in interventional cardiology.[3,4] This technology provided a solution to acute vessel occlusion by sealing the dissection flaps and preventing recoil. However, since the vessel was caged with metal, late luminal enlargement and advantageous vascular remodeling could no longer occur. Another problem, namely that of late stent thrombosis, was also first described.[5] To solve the problem of in-stent restenosis, drug eluting stents (DES) were introduced. The introduction of DES was thus dubbed the third revolution in interventional cardiology. Both large scale randomized trials and all-comer registries showed excellent results in terms of the need for repeat revascularisation. However, the early enthusiasm has been tempered in recent years following

widespread concerns regarding the increased risk of late and very late stent thrombosis.[6-11] Registries of all comers treated with DES showed late stent thrombosis rates of 0.53% per year, with a continued increase to 3% over four years.[12-14] Post-mortem pathological specimens of drug eluting stents revealed significant numbers of uncovered struts with evidence of a persistent inflammatory reaction around the stent struts.[15-18] The 2nd generation DES solved some parts of these problems, and the frequency of stent thrombosis in the 2nd generation DES (Everolimus-eluting stent: EES) was improved to 0.7% at a mean follow-up of 21.7 months. [19]

All these problems are anticipated to be solved with the advent of fully biodegradable scaffolds. This new technology, heralded the fourth revolution in interventional cardiology, offers the possibility of transient scaffolding of the vessel to prevent acute vessel closure and recoil whilst also transiently eluting an antiproliferative drug to counteract the constrictive remodeling and excessive neointimal hyperplasia (**Table 1**). This new era in interventional cardiology could be viewed as the era of Vascular Reparative Therapy (VRT), with fully bioresorbable devices.

The purpose of this review is to provide insights from the bench to clinical data between 2nd generation DES and polymeric bioresorbable scaffolds, especially the most widespread DES, Cobalt chromium everolimus-eluting stent (CoCr-EES) and bioresorbable vascular scaffold “Absorb BVS” (Abbott Vascular, Santa Clara CA, USA).

Table 1. Potential benefit of BRS over metallic DES

	1st generation DES	2nd generation DES	BRS
Acute occlusion	+	+	+
Acute recoil	+	+	+
Acute thrombosis	+	+	+
Sub-acute thrombosis	+	+	+
Late thrombosis	-	±	?
Very late thrombosis	-	-	+/?
Neointimal hyperplasia	+	+	+
Adaptive (expansive) remodeling	-	-	+
Restoration of vasomotion	-	-	+
Late luminal enlargement	-	-	+

DES = drug eluting stents, BRS = bioresorbable scaffolds

'+' indicates positive/beneficial effect, '-' indicates negative/no effect, '±' indicates neutral or uncertain effect, '?' indicates lack of definite evidence

1. Theoretical advantages of bioresorbable scaffolds

Theoretical advantages of BRS stem from transient vessel support without rigid caging. The potential benefits of BRS over current metallic DES technology proposed by authors are summarized as follows:

1. A reduction in long-term adverse events from permanent materials.

As drug elution and scaffolding are temporary until the vessel has healed, no foreign material potentially triggering very late stent thrombosis (such as non-endothelialised struts and drug polymers) [17] could persist of the long-term.

2. The removal, through bioresorption, of the stented vessel's rigid caging.

This can facilitate the return of vasomotion, adaptive shear stress, late luminal enlargement and late expansive remodeling. Furthermore, this might also reduce the problems of jailing the ostium of side branches as seen with permanent metallic stent struts.

3. Suitability for future treatment options.

The treatment of complex multi-vessel disease frequently results in the use of multiple long DES, which results in so called "full metal jacket" stenting.[20] In such cases, repeat revascularization – either percutaneous or surgical, is potentially challenging because of the metallic caging by previously implanted stents. The use of a BRS implies no restriction to future percutaneous or surgical revascularization.

4. Allowing the use of non-invasive imaging techniques such as computed tomographic (CT) angiography or magnetic resonance imaging (MRI) for follow-up.

Presently, metallic stents can cause a blooming effect with these imaging modalities making interpretation more difficult.[21] The PLLA scaffold should not restrict the use of CT or MRI as it is non-metallic. Even with metallic BVS such as magnesium or iron, CT and MRI can be efficiently used once bioresorption is completed. CT has provided reliable assessment of the angiographic results up to 3 to 5 years after translucent scaffold implantation. [22,23]

5. Reservoir for the local delivery of drugs.

Since the duration of bioresorption is modifiable, according to the type of polymers/co-polymers, a tuned elution of multiple drugs can potentially be achievable (e.g. early elution of antiproliferative agent from a coated polymer and chronic elution of anti-inflammatory or other agent from the backbone polymer).

6. Relief of anxiety of implanted foreign materials

The use of BVS eliminates patients' concerns of having an implant in their bodies for the rest

of their lives.[24]

7. Pediatric application

Congenital heart disease, e.g. pulmonary stenosis or aortopulmonary collateral[25], can be potentially treated with bioresorbable scaffold. After bioresorption, scaffolded arteries can re-adopt a natural growth pattern. However, this indication for the treatment is still off-label, and the long-term results need to be monitored.

2. Bioresorption process of Absorb BVS

The bioresorption process of Absorb BVS is completed in 36 months. (**Figure 1**) First, polylactides are hydrophilic thus water can penetrate the implant. Second, depolymerisation by hydrolysis is observed as a reduction in molecular weight, which starts from the time of implantation and gradually progresses and is completed at 36-months. Thirdly, polymer fragmentation into segments of low-weight polymer due to the scission of amorphous tie chains linking the crystalline regions, resulting in subsequent gradual loss of the radial strength, which starts from 6-month after implantation and is completed at 12-month after implantation. Final process is assimilation or dissolution of monomers. The soluble monomer (e.g., L-lactate) is changed into pyruvate which eventually enters the Krebs cycle and is further converted into carbon dioxide and water, eliminated by the lung and kidney.

3. Insights from preclinical studies comparing Absorb BVS and metallic stents

Early and long-term histology

Vorpahl et al reported the histological comparison between Absorb BVS and 1st generation DES, CYPHER[®] sirolimus-eluting stent (SES) implanted in the iliac arteries of rabbit models.[26] Twenty-five New Zealand white rabbits received an Absorb bioresorbable vascular scaffold (Absorb BVS, 1.0 and 1.1) or SES in the iliac arteries. They were evaluated at 1-, 3-, 6-, and 36-months. Re-endothelialisation assessed at one month was incomplete in both Absorb BVS and SES by scanning electron microscopy, with a trend towards greater coverage in SES (endothelialisation above strut: 60.6% vs. 32.2%, $P = 0.10$). However, light microscopic analysis revealed greater endothelial coverage in Absorb BVS than in SES at 36 months (100.0% vs. 93.3%, $P = 0.05$). Inflammation scores were comparable between arteries implanted with Absorb BVS and SES at three months (1.1 vs. 1.1, $P = 0.99$), which decreased over time in the Absorb BVS implanted arteries (36 months: 0.0 vs. 0.2, $P = 0.05$). At 36 months, Absorb BVS were completely resorbed, and resorption sites were replaced by connective tissue.

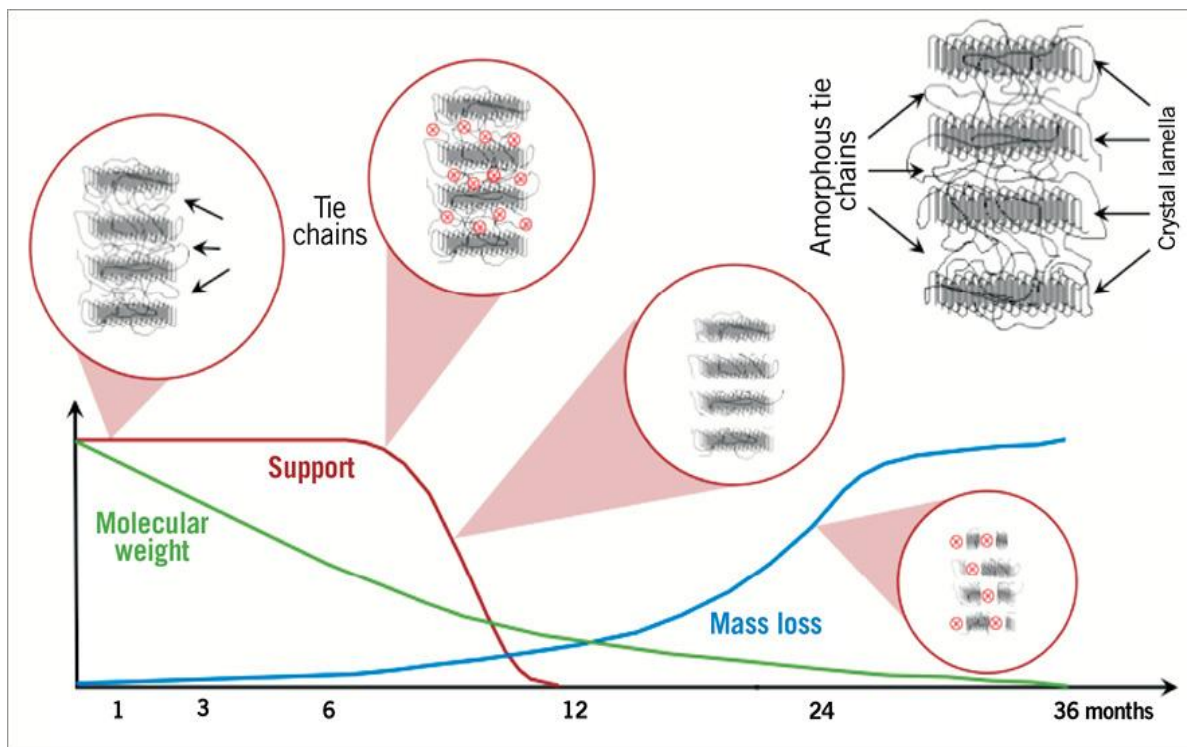


Figure 1 Bioresorption process of Absorb BVS

The Absorb bioresorbable vascular scaffold poly-L-lactide bioresorption process up to 36 months, when the polymeric device is expected to be fully resorbed. 1) Polymer hydration following implantation. Poly lactides are hydrophilic thus water can penetrate the implant. 2) Depolymerisation by hydrolysis, observed as a reduction in molecular weight (green line). 3) Polymer fragmentation into segments of low-weight polymer due to the scission of amorphous tie chains linking the crystalline regions, resulting in subsequent gradual loss of the radial strength (red line). 4) Assimilation or dissolution of monomers. The soluble monomer (e.g., L-lactate) is changed into pyruvate which eventually enters the Krebs cycle and is further converted into carbon dioxide and water, eliminated by the lung and kidney. Reprinted from *EuroIntervention*. 2014; 9:1271-84. Serruys PW et al., Dynamics of vessel wall changes following the implantation of the absorb everolimus-eluting bioresorbable vascular scaffold: a multi-imaging modality study at 6, 12, 24 and 36 months. Copyright (2014), with permission from Europa Digital & Publishing.

Onuma et al reported optical coherence tomography (OCT) findings with corresponding histology in the porcine coronary artery model immediately post-implantation and at 28 days and 2, 3, and 4 years after Absorb BVS implantation. [27] Twenty-eight days after BVS implantation, 82% of the struts had the preserved box appearance on OCT, which corresponded to intact polymeric struts. Two years after BVS implantation, OCT images demonstrated that 80% of the struts still had a preserved box appearance. Nonetheless, the corresponding histological images and polymer degradation assessment with gel permeation chromatography showed that the polymeric struts could be considered to be fully resorbed and replaced by proteoglycan. At 3 years, the absolute count of discernible struts was reduced

by $\approx 50\%$, and the no-longer-discernible strut footprints on OCT seemed to correspond in histology to complete integration into the surrounding arterial wall.

At 4 years, only one sixth of the struts were discernible in OCT with a dissolved black or dissolved bright box appearance, which were minimally discernible in histology. Indiscernible struts in OCT could confirm the integrated strut footprints seen at 4 years.

Otsuka et al reported the serial histologic changes (1-42 months) of Absorb BVS and 2nd generation DES, XIENCE V[®], CoCr-EES in 136 nonatherosclerotic porcine models. [28] Absorb BVS demonstrated comparable safety to CoCr-EES in a normal porcine coronary artery model ≤ 42 months after implantation with low-grade inflammation and fibrin deposition. Although inflammation scores were generally greater for Absorb BVS than CoCr-EES from 6 to 36 months, the scores progressively declined after 18 months in Absorb BVS ($P < 0.001$). Both devices exhibited absent or minimal inflammation at 42 months. Histomorphometric analyses showed late lumen and vessel enlargement in Absorb BVS-implanted arteries starting after 12 months. Histomorphologic changes of Absorb BVS dismantling were observed after 12 months, and resorption sites of Absorb BVS were poorly discernible to essentially absent at 42 months. Gel permeation chromatography analysis confirmed that degradation of Absorb BVS was complete by 36 months.

Overlap

Preclinical data in a porcine model [29] revealed that there is a delay in coverage of overlapping Absorb BVS struts compared with overlapping CoCr-EES struts. At 28 days in the overlap, OCT analyses indicated 80.1% of Absorb BVS and 99.4% of CoCr-EES overlapping struts to be covered ($P < 0.0001$), corresponding to histological observations of struts with cellular coverage of 75.4% and 99.6%, respectively ($p < 0.001$). At 90 days, Absorb BVS and CoCr-EES overlapping struts demonstrated $> 99\%$ strut coverage by OCT and histology, with no evidence of a significant inflammatory process, and comparable % volume obstructions. The larger strut thickness of the Absorb BVS (157 μm) is likely to be the main mechanism for the delayed coverage of overlapping Absorb BVS struts at early phase (28-day follow-up), compared with the thinner CoCr-EES struts (89 μm). In addition, it is likely that the larger strut thickness of the Absorb BVS lead to a greater neointimal response compared with the thinner-strut.

4. Difference in device design and mechanical properties between Absorb BVS and CoCr-EES

Absorb BVS and CoCr-EES have different device design and mechanical properties. The

external diameter of the Absorb BVS at deployment is greater than that of CoCr-EES because of their thicker struts (157 μm vs. 89 μm). [30] In latest recent bench test report by Ormiston et al, the 3.0 mm stent and scaffold radial strength were assessed by pressure required to reduce cross-section area by 25%. The CoCr-EES has greater radial strength than Absorb BVS (1.6 \pm 0.1 atm vs. 1.4 \pm 0.2 atm, $P = 0.02$ by Mercy test) [30]. If Absorb BVS is over-stretched beyond its designed limits, it may lose some of its radial strength and may even fracture [31,32].

Absorb BVS (1.1) has been shown to be more flexible compared to CoCr-EES. [33] One test of flexibility is the three-point bend test, where the ends of the crimped scaffold are fixed and a normal force is imposed at the center-point of the device using an Instron (Illinois Tool Works Inc., Glenview, IL, USA). The maximum compressive load required to deflect the device by 1.1 mm is one key measure of flexibility, where a lower force suggests greater flexibility. Despite the fact that the strut thickness of Absorb BVS (3.0 mm device) is greater than that of CoCr-EES (3.0 mm device), the maximum compressive load for Absorb BVS is statistically significantly lower than that for CoCr-EES (0.58 N vs. 0.78 N, $P = 0.004$). Better flexibility of Absorb BVS results in altering vessel angulation and curvature to a lesser degree (better conformability) and consequently has a modest effect on flow dynamics and shear stress distribution in the scaffolded segment and the scaffold edges. [34-36]

As summarized in **Table 2**, the mechanical properties of Absorb BVS except for flexibility are numerically inferior to those of CoCr-EES. However, the performance of Absorb BVS is similar to those of CoCr-EES and sufficient for clinical use, which has already extensively investigated by clinical trials. In addition, Absorb BVS offers transient mechanical support to resist acute vessel recoil, and at a later stage would be fully resorbed, leading to restoration of the vessel's biological properties as mentioned as theoretical advantages.

5. Techniques used for implantation and sizing

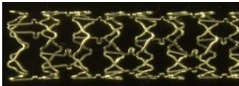
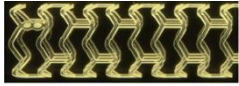
Due to the inherent difference of the mechanical properties as described above, the technique used for implantation of Absorb device has to be different from that of metallic stents to avoid the acute mechanical complications and to achieve maximum acute efficacy of the polymeric device. This should be considered during lesion preparation, device implantation, and post-dilatation process. Absorb BVS is made from polymer with less radial [30] and tensile strength. [37] The expansion of Absorb BVS, therefore, depends on optimal pre-dilatation while direct implantation of DES, without predilation, is allowed in simple lesions. Data from a small study

showed that the Absorb BVS expansion was improved by pre-dilatation.[38] The pressure applied during scaffold implantation also needs to be gradually titrated and upon the scaffold balloon reach target pressure that of different from CoCr-EES which could inflate with high pressure and no requirement for pressure maintenance for 30 seconds. Post-dilatation process is also different between Absorb BVS and CoCr-EES, the size of post-dilatation balloon should not be above 0.5 mm of nominal Absorb BVS diameter. On the other hand, the recommended post-dilatation limit provided by manufacturers for metal DES is generally 0.5-0.75 mm above the stent nominal size. [39] A summary of technical consideration is shown in **Table 3**.

Lesion selection

As the largest commercially available size of Absorb BVS is 3.5 mm at nominal pressure, the vessel diameter above 4.0 mm should not be targeted because of the risk of extensive malapposition[40]. The device should not be implanted into the lesions which cannot be adequately prepared such as heavily-calcified and unsatisfactorily pre-dilatated lesions. The calcified plaques could impair Absorb BVS expansion[41], increase rates of malapposition[38] and might elongate the scaffold during deployment.[41] The accumulated evidences on using debulking strategies in heavy calcified lesions are mainly obtained from single-center experience and case reports.[42] The safety of cutting balloon or rotational atherectomy before Absorb BVS implantation is uncertain. However, cutting balloon use may ease the optimal apposition of bioresorbable vascular scaffold in in-stent stenosis. [42] With regards to the complex lesions such as bifurcation lesions requiring two-stent technique, left main lesions, chronic total occlusions and coronary bypass graft degeneration and in-stent restenosis, available data was derived from case reports [42-46], and clinical outcomes are still uncertain. The implantation techniques for complex lesions are so far based on experts' consensus [47].

Table 2. Comparison in mechanical properties between Absorb BVS and CoCr-EES

	CoCr-EES (3.0 mm device)	Absorb BVS (1.1) (3.0 mm device)
Material	Cobalt chromium + durable fluoropolymer	poly-L-lactic acid + poly-D,L-lactic acid
Elongation at break [37]	40%	2-6%
Tensile modulus of elasticity [37]	210-235 GPa	3.1-3.7 GPa
Tensile strength [37]	1449 MPa	60-70 MPa
Strut design		
Peak per hoop	6	6
Connector per hoop	3	3
Width [35]	89-112 μm	140-191 μm
Strut thickness	89 μm	157 μm
Vessel wall area coverage [30]	13%	27%
Crossing profile [30]	1.14 \pm 0.01 mm	1.43 \pm 0.02 mm
Acute recoil [30]	\approx 0.10 mm	\approx 0.18 mm
Radial strength [†] [30]	1.6 \pm 0.1 atm	1.4 \pm 0.2 atm
Flexibility [‡] [33]	\approx 0.78 N	\approx 0.58 N
Potential circular diameter of a cell [30]	4.2 mm	3.0 mm
Safety limit of NC balloon size and pressure to avoid fracture		
Main branch [69]	5.5 mm at 22 atm	3.8 mm at 20 atm
Side branch [69]	3.0 mm at 22 atm	2.0 mm 14 atm / 3.0 mm 10 atm
mini-KBPD [70]	3.0 / 3.0 mm up to 20 atm	3.0 / 3.0 mm at 5 atm

Abbreviation: BVS, bioresorbable vascular scaffold; CoCr-EES, Cobalt chromium everolimus eluting stent; NC balloon, non-compliant balloon; KBPD, kissing balloon post-dilatation

Table 3. Technical notes for Absorb BVS implantation [modified from Rzeszutko Ł, et al[52], Everaert B et al[40]] and Tamburino C, et al[47]

Technical consideration	Detail
1. Lesion selection	<p>Avoid tortuous segment or excessive calcification to prevent device dislodgement.</p> <p>Scarce clinical data for bifurcation lesion, left main, chronic total occlusion, coronary bypass graft or in-stent restenosis.</p>
2. Device size selection	<p>i) QCA-Dmax [proximal and distal Dmax] Proximal and distal Dmax values in the range: 2.0-3.0 mm – Absorb BVS 2.5 mm should be chosen, 2.5-3.3 mm – Absorb BVS 3.0 mm should be chosen, 3.0-3.8 mm – Absorb BVS 3.5 mm should be chosen.</p> <p>ii) One of the values outside of the range – the choice of the scaffold diameter depends on the physician’s decision.</p> <p>iii) IVUS and OCT are not required but may be useful in doubt of true reference vessel diameter.</p>
3. Device length	<p>The length should cover 2 mm of healthy vessel, in case of long lesion, the overlapped length should be 1-4 mm.</p>
4. Predilatation	<p>i) Pre-dilatation is mandatory with balloon size should be 0.25 to 0.5 mm smaller than the planned Absorb BVS.</p> <p>ii) NC balloon with equal size to planned scaffold considered to be used only persistent %DS > 40% after first attempt of pre-dilatation</p>
5. Device delivery	<p>i) Apply with constant tension and avoid dotter technique.</p> <p>ii) Repeated introduction of the retracted scaffold is forbidden and a new device should be used.</p>
6. Device deployment	<p>Progressive inflation by 2 atm every 5 s minimal total time of inflation is 30 s, RBP should not be exceeded.</p>
7. Post-dilation	<p>i) Previously, it was recommended post-dilatation should be done only in cases of evident residual stenosis and performed by high pressure using NC balloon whose diameter should not exceed 0.5 mm over the nominal value of Absorb BVS).</p> <p>ii) Some data supported frequent post-dilatation to avoid under expansion of the device</p> <p>iii) Upon scaffold deployment, one should aim to obtain <10% residual stenosis, full scaffold expansion and optimal wall apposition.</p>

Absorb BVS size selection

In the early experience with Absorb BVS implantation, only one size (3.0x18 mm) was available and had strict upper limit of expansion. Therefore, a strict protocol did not allow to enroll patients with an interpolated reference vessel diameter (RVD) <2.5 mm or >3.3 mm. However, the interpolated-RVD does not assume the actual lumen dimensions of the predicted “landing zone” and is highly influenced by proximal or distal side branches not included in the

scaffolded segment. The interpolated-RVD frequently underestimated the maximal lumen diameter within the scaffolded region as observed by OCT[48]. OCT sub-studies demonstrated an increased frequency of malapposition when Absorb BVS was implanted in a too large vessel. Attempts to correct persistent malapposition could potentially increase the risk of scaffold disruption[49], particularly when the device has already reached its maximum limit of expansion. On the other hand, an excess of proximal and/or distal edge dissections was observed when the Absorb BVS was implanted in vessels smaller than the device nominal size[48]. The proximal and distal maximal lumen diameters to the MLD (Dmax values) were introduced to guide the appropriate device size selection. The chance of oversizing was lower by Dmax compared to RVD (2.9% vs. 16.7%, $P = 0.002$). A trend towards a lower incidence of implantations in small (< 2.5 mm) vessels could also be achieved using the same strategy (26.9% vs. 39.2%, $P = 0.057$). Notably, there was a significant decrease of implantations in large (> 3.3 mm) vessels (3.7% vs. 16.7%, $P = 0.002$) in the ABSORB Extend study in comparison to cohort B[50]. Another point of concern is that scaffold over sizing in small vessels might result in polymeric strut under-expansion and over-paving of the vessel (larger scaffold footprint).[51] Thus, it is mandatory to precisely evaluate vessel size and appropriately select scaffold nominal diameter. Consideration to use intravascular imaging during BVS implantation has not yet been addressed in large controlled trial.

Implantation technique and post-dilatation

Since the bulky crossing profile of Absorb BVS might cause a difficulty crossing culprit/target/candidate lesions, a back-up support guiding catheter or extension together with an extra-support wire or a buddy wire may be imperative. It should be noted that small size Absorb BVS (2.5 mm and 3.0 mm) can be delivered in a 5-in-6-Fr guide extension but requires preloading into extension tube outside the patient's body. For Absorb BVS size 3.5 mm, it can only be loaded through a 6-in-7 Fr guide extension system.[47]

During the procedure, the implantation should last at least 30 s with gradual pressure increase by 2 ATM every 5 second without exceeding the maximal acceptable pressure determined by the rated burst pressure value described in the leaflet[47,52]. Currently, operators with a large experience of BRS implantation are intuitively promoting a strategy of a high-pressure post-dilatation with a NC balloon size 0.25 or 0.5 mm larger than the nominal size of the device. Despite that the bench test showed that Absorb BVS had a larger acute gain[30], the real world

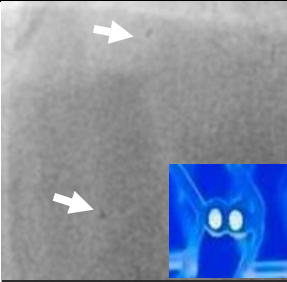

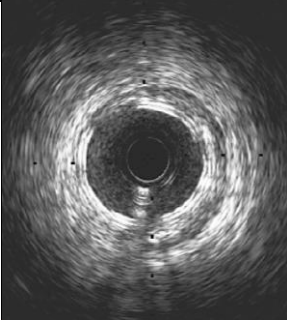
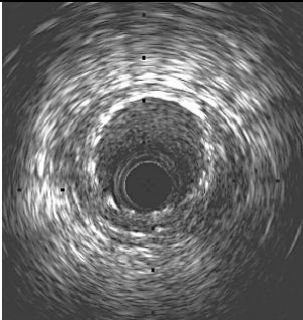
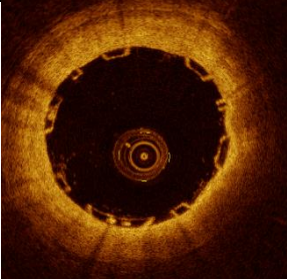
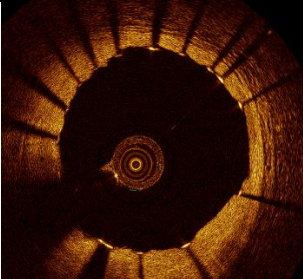


acute gain in randomized controlled trial (RCT) (ABSORB-II) was lower[53]. This is due to the fact that, in the real world, dilatation pressure and balloon diameter at the highest pressure during implantation or post-dilatation were higher and larger in the metallic stent group. Therefore, the more aggressive strategy could be applied during Absorb BVS implantation on both scaffold deployment and post-dilatation with cautious to the safety limit of size and pressure.

6. Multi-modality imaging of the Absorb BVS and CoCr-EES

The Absorb BVS presents important differences with respect to metallic stents when imaged by both invasive and non-invasive techniques. Details of the differences in each imaging modalities are summarized in **Table 4**. Absorb BVS has the unique ability to provide a temporary scaffold that is necessary to maintain the patency of the vessel after intervention, then gradually degrades.

Therefore, this novel technology has required new imaging modalities and methodology for the assessment of its efficacy in comparison to the metallic stents. In Absorb cohort studies (Cohort A and Cohort B), multimodality imaging using QCA, IVUS, OCT and MSCT was extensive. IVUS provides true vessel size and calcification in both superficial and deep location. The major drawback of IVUS after Absorb BVS implantation is that it has a poor capacity and reproducibility to detect malapposed struts, acute scaffold disruption, side-branch strut, protrusion and dissection compared with OCT.[49,54,55] Therefore, IVUS is suitable to use for optimization of scaffold size selection while OCT with its excellent axial resolution can assess strut apposition, edge dissection and change of strut characteristic post-implantation and on long-term follow-up. Since there were 4 imaging modalities used to evaluate stent efficacy in early Absorb trials, individual imaging techniques (especially OCT and IVUS) showed considerable discrepancies. The delineation of the luminal contour on IVUS after scaffold implantation relies mainly on the bright interface created by the presence of polymeric struts while lumen dimension from OCT truly reflects and delineates the endoluminal interface of the vessel wall behind the polymeric struts. Therefore, post-procedure, IVUS-mean lumen area was smaller than OCT-based measurements. At follow-up, the neointimal tissue (in between and on top of struts) is exquisitely detectable by OCT, showing the struts encapsulated by the neointima, whereas the lumen boundaries detected by IVUS were mainly determined by the blooming brightness of the polymeric struts that have not been resorbed.

Table 4. Imaging comparison between Absorb BVS and CoCr-EES in multimodalities

	Absorb BVS		CoCr-EES	
QCA		Radiopaque platinum markers at both ends (diameter of 244 μm with 156 μm thickness are separated by a distance of 147 μm) with translucency of scaffold.		Fully radiopaque for a whole length of device.
IVUS		Struts appear as parallel lines without acoustic shadowing because ultrasonic waves pass through the struts with a small reflection from the luminal and abluminal surfaces.		Struts appears as echo reflective and provide a distinctive ultrasound appearance.
OCT		A "black box" area surrounded by bright reflecting frames without backside shadowing.		A reflective leading structures with backside shadowing.
MSCT		Radiolucent except for two metallic markers located at both extremities. Therefore, it enables to delineate lumen contours of the treated vessel.		Difficult to evaluate due to blooming artifacts caused by metallic stent struts that may impair Coronary lumen visualization and quantification of lumen narrowing.

This potentially explains the larger lumen area as assessed by IVUS at follow-up compared to OCT.[23] The head-to-head comparison among multimodality imaging (QCA, IVUS, OCT, MSCT) in Absorb Cohort A, B and Extend showed that mean lumen area measured by MSCT was comparable to QCA, and statistically lower than IVUS and OCT.[56] The stent/scaffold efficacy was tested and described by various imaging techniques. A summary of the parameter(s) used to determine the efficacy of scaffold/stent is listed in **Table 5**.

7. Clinical Evaluation

First in man trials (Absorb Cohort A and B)

The first generation of Absorb BVS (1.0) (Absorb Cohort A) [57] showed a slightly higher acute recoil than conventional metallic platform stents. At 6 months, an 11.8% reduction in scaffold area and a 24.3% decrease in minimal luminal area were documented and dubbed “late recoil.” Reinforcement of the mechanical performance of the device and extension of its mechanical integrity up to 6 months were regarded as potential improvements of this technology. To enhance the mechanical strength of the struts and to reduce immediate and late recoil, the strut design and the manufacturing process of the polymer were modified in the revised version, Absorb BVS (1.1).

In Absorb Cohort B [Absorb BVS (1.1)], the mean and minimum scaffold areas significantly increased and compensated for the increase in neointimal hyperplasia - resulting in an increase of mean lumen area from 1 to 3 years with an unchanged minimal lumen area from 1 to 3 years. The total plaque area showed a biphasic change with an increase between the 1 and 2-year and a plaque reduction between the 2 and 3-year follow-up. Angiographic late luminal loss between 1 and 3 years remained unchanged with a binary in-segment restenosis of 6% for the entire Absorb cohort B. The restoration of the vasodilatory capacity was shown to be an ongoing process over time. At 6 months, no significant vasomotion could be documented in a sequential test combining ergonovine and nitrates.[58] At 1 to 3 years, vasodilatation was accentuated and the overall effect was highly significant [37], however, the clinical relevance is unclear. Major adverse cardiac events rate at 3 years seemed to be comparable with DES. [23] Since this was limited to the relatively simple lesions, further investigations are still needed to clarify the safety and efficacy for complex lesions.

Head-to-head comparison in RCT

The only published RCT comparing Absorb BVS and CoCr-EES is Absorb II trial. [53] IVUS and QCA data of ABSORB II trial are summarized in **Table 5**. Anginal status (as assessed by the Seattle Angina Questionnaire) [59], and secondary clinical endpoints did not differ between treatment groups, whereas the cumulative rate of recurrent or worsening angina was lower in the Absorb BVS group than in the CoCr-EES group. The 1-year composite device orientated endpoint was similar between Absorb BVS and CoCr-EES groups. However, it is necessary to note that these are the secondary endpoints of the trial and the study was not powered to

discriminate between Absorb BVS and CoCr-EES regarding these outcomes. The primary endpoint of the study (vasomotion at 3 years) will be available in the near future. Absorb III/IV, Absorb China, and Absorb Japan pivotal trials are ongoing for regulatory approval, and their primary results will be also presented later in this year.

Table 5. Device efficacy evaluated by multi-imaging modality

Parameter	Imaging Modality	Comment	Time	Absorb BVS	CoCr-EES	Efficacy comparison
Acute gain	Angiography (QCA)	data on RCT[53]	post-procedure	1.23±0.38 mm	1.32±0.26 mm	S
Acute gain in MLA	IVUS	data on RCT[53]	post-procedure	2.85±1.25 mm ²	3.60 ±1.34 mm ²	S
Acute percent recoil	Angiography (QCA)	data on observational study[71]	post-procedure	6.8 (2.8-11.1)	6.08(0-10.2)	NS
Late loss	Angiography (QCA)	data on propensity score matching[72]	2 years	0.26±0.19 mm	0.22±0.22 mm	NS
Net gain	Angiography (QCA)	data on propensity score matching[72]	2 years	0.97±0.40 mm	1.10±0.35 mm	NS
Percentage diameter stenosis	Angiography (QCA)	data on RCT[53]	post-procedure	16%±7%	10%±5%	S
Curvature	Angiography (QCA)	data on propensity score matching[72]	2 years	21%±7%	15%±9%	S
Vasomotion assessed by Ach	Angiography (QCA)	data on RCT[53]	post-procedure	0.29±0.23 cm ⁻¹	0.24±0.19 cm ⁻¹	S
	Angiography (QCA)	scaffolded segments react by vasomotion to Ach and methylergonovine as early at 12 months, due to the partial subsidence of the	12 months and 24 months	Overall change -1.44% (-7.35, +2.56); P = 0.303. 12 M: -5.46% (-8.25, +1.86) vs. 24 M: +2.14% (-2.58, +8.80), P = 0.038	NA	NA

(continued)

Parameter	Imaging Modality	Comment	Time	Absorb BVS	CoCr-EES	Efficacy comparison
Vasomotion assessed by NTG	Angiography (QCA)	radial force of the scaffolded vessel.[73] patients at 24 months exhibited a significant increase in the MLD after NTG administration compared with patients at 12 months. The response to nitrates tended to be greater in patients with a normal response to Ach.[73]	12 months and 24 months	Overall change +0.41% (-3.77, +5.52) 12 M: -0.60% (-5.46, +3.91) vs. 24 M: +5.79% (+1.41, +12.0), P = 0.032	NA	NA
Mean Lumen area	IVUS	data on RCT[53]	post-procedure 1 year	6.06 ± 1.44 mm ²	6.85 ± 1.60 mm ²	S
Minimal Lumen area	OCT	data on observation study[74]	post-procedure 1 year	5.90 ± 1.68 mm ²	6.16 ± 2.02 mm ²	NS
Mean plaque area	IVUS	data on RCT[53]	post-procedure 1 year	4.89 ± 1.38 mm ²	5.73 ± 1.51 mm ²	S
	OCT	data on observation study[74]	post-procedure 1 year	4.98 ± 1.87 mm ²	4.31 ± 1.41 mm ²	NS
	IVUS	data on RCT[53]	post-procedure	7.11 ± 2.46 mm ²	7.43 ± 2.44 mm ²	NS

(continued)

Parameter	Imaging Modality	Comment	Time	Absorb BVS	CoCr-EES	Efficacy comparison
Residual area stenosis	OCT	data on propensity score matching and OCT guide stent/scaffold implantation.[75]	post-procedure	20.2 ± 7.5	21.7 ± 9.9	NS
	OCT	data on observation study[74]	1 year	40.5 ± 15.9	28.7 ± 15.6	S
Eccentricity and Symmetry Index	IVUS	geometrical parameters did not seem to generate clinical events in short term follow-up (6 months).[76]	post-procedure	EI 0.88 ± 0.03 SI 0.31 ± 0.06	EI 0.92 ± 0.03 SI 0.26 ± 0.07	S
	OCT	When OCT is used to guide and optimize Absorb scaffold implantation, eccentricity index was similar to those observed after deployment of second-generation metallic drug-eluting stents.[75]	post-procedure	EI 0.85 ± 0.08 SI 0.33 ± 0.08	Metallic DES (EES, ZES) EI 0.86 ± 0.04 SI 0.38 ± 0.37	NS
Neointimal hyperplasia area	IVUS	data on propensity score matching[72]	2 years	0.26 ± 0.28 mm ²	0.27 ± 0.37 mm ²	NS
	OCT	data on observation study[74]	1 year	0.84 ± 0.51 mm ²	0.78 ± 0.32 mm ²	NS

(continued)

Parameter	Imaging Modality	Comment	Time	Absorb BVS	CoCr-EES	Efficacy comparison
Incomplete strut apposition area	OCT	data on observation study[74]	1 year	0.11 ± 0.29 mm ²	0.02 ± 0.07 mm ²	NS
Thickness of tissue coverage	OCT	data on observation study[74]	1 year	136.1 ± 71.4 mm ²	120.6 ± 46.0 mm ²	NS
Percentage of uncovered strut	OCT	data on observation study[74]	1 year	4.50%	5.30%	NS

Abbreviation: BVS-bioresorbable vascular scaffold; EI-eccentricity index; FFR-fractional flow reserve; IVUS-intravascular ultrasound; IQR-interquartile range 1st -3rd; MLA-minimal lumen area; MLD-minimal lumen diameter; MSCT-multislice computed tomography; NS-non-significant; OCT-optical coherence tomography; QCA-quantitative coronary angiography; RCT-randomized controlled trial; S-significant; SI-symmetry index

Clinical outcomes in complex lesions or high-risk populations

Although lesion selection in the initial studies was limited to simple lesions, a variety of lesion types are currently considered to be the target of Absorb BVS. However, no randomized data is available to compare the safety and efficacy of Absorb BVS and DES in patients with complex lesions and/or high-risk clinical profiles. So far, the only available clinical data stem from small case series/case reports and small registries. A summary of clinical data of high-risk patients/lesions treated with Absorb BVS is presented in **Table 6**. In short, the application of Absorb BVS is limited in left main, bifurcation, and saphenous vein graft lesions due to mechanical limitations as well as limited size variation. It seems that Absorb BVS implantation is feasible and may be as efficient as drug-eluting stents in short term in population presenting with ST-elevation myocardial infarction (STEMI) or acute coronary syndrome, and in patients with chronic total occlusions. Currently two RCTs (AIDA and COMPARE ABSORB trials) are ongoing to test the non-inferiority of Absorb BVS to the CoCr-EES in short term and to test superiority in long term, in all-comer/more-comer population.

Stent/scaffold thrombosis

Recently, there is a potential concern for an increased rate of early scaffold thrombosis, when an Absorb device is used in complex lesions. In the European multicenter GHOST-EU registry[60], the authors reported that the rate of definite/probable scaffold thrombosis was 2.1% (definite scaffold thrombosis: 1.8%, probable scaffold thrombosis: 0.3%) in an all-comers population at six months. The rates of early and midterm scaffold thrombosis, mostly clustered within 30 days were not negligible. However, when all published data including the GHOST-EU registry were combined, overall scaffold thrombosis rate was 1.22% in all-comers, 0.94% in stable angina pectoris, 2.16% in non-ST elevation acute coronary syndrome and 1.22% in STEMI, which seems not too far from the clinical results of typical 2nd generation DES (**Table 7**).[61] In the first randomized comparison of ABSORB II and DES [53], the rate of definite scaffold/stent thrombosis at 1-year follow-up was 0.6% in Absorb BVS (one acute and one subacute case) and 0% in CoCr-EES ($P = 1.0$), and the rate of definite/probable scaffold/stent thrombosis was 0.9% in Absorb BVS and 0% in CoCr-EES ($P = 0.55$). Further randomized studies may confirm these scaffold thrombosis rates in the future.

Diabetes Mellitus

Diabetes Mellitus causes systemic microvascular and macrovascular complications including coronary artery disease that ultimately contributes to cardiovascular mortality. DES

considerably reduces the need for repeat revascularization in diabetic patients compared with bare-metal stents. [62] The presence of diabetes, however, has still been associated with an increased risk of adverse clinical events after PCI with DES. [63,64] The best type of DES for the treatment of diabetic patients remains unclear. BVS could be a novel approach to the treatment of coronary artery disease in diabetic patients as it provides transient vessel support and drug delivery to the vessel wall. Muramatsu et al [65] investigated the clinical outcomes of diabetic patients treated with Absorb BVS or CoCr-EES. After propensity score matching, at 1-year follow-up, DM patients treated with BVS had a similar incidence of the device-oriented composite endpoint (DoCE) compared with those treated with EES (3.9% vs. 6.4%, $P = 0.38$). There were no differences in the incidence of definite or probable scaffold/stent thrombosis (1.0% for BVS vs. 1.7% for EES, $P = 1.0$).

ST segment elevation myocardial infarction

From a physiological perspective, the absence of permanent vessel caging facilitates the restoration of vasomotor function, adaptive shear stress, cyclic strain, and late lumen enlargement. These physiological advantages of Absorb BVS appear particularly appealing for the treatment of STEMI. There were three studies comparing Absorb BVS with CoCr-EES in STEMI population. The largest study is reported by Brugaletta et al. [66] The cumulative incidence of DoCE did not differ between BVS and EES or BMS groups at 1 year (4.1% vs. 4.1%, HR: 0.99 [95% CI: 0.23 to 4.32], $P = 0.994$; vs. 5.9%, HR: 0.50 [95% CI: 0.13 to 1.88], $P = 0.306$, respectively). Definite/probable BVS thrombosis rate was numerically higher either at 1 year (2.4% vs. 1.4%, $P = 0.948$; vs. 1.7%, $P = 0.825$, respectively), as compared with EES or BMS. The results of other studies [67,68] also suggested the favorable profile of Absorb BVS implanted during primary PCI in selected patients with STEMI.

Table 6. Clinical outcomes in complex lesions or high-risk populations

Target	Study design	Trial / author	Patient number	Follow-up	Clinical outcomes Composite Endpoint	MI	TLR	Probable/definite ST
All-comer	Multicenter registry	GHOST-EU registry[60]	1189 patients with BVS	6-month	TLF: 4.4%	2.0%	2.5%	2.1%
	Multicenter registry	Absorb EXTEND[77]	512 patients with BVS	1-year	MACE: 4.3%	2.9%	1.8%	0.8%
	Single center registry	the AMC Single Centre Real World PCI Registry[78]	135 patients with BVS	6-month	TVF: 8.5%	3.0%	6.3%	3.0%
	Single center registry	Azzalini et al. [79]	339 patients with BVS	N/A	N/A	N/A	N/A	1.2%
Complex lesion (moderate/severe calcified lesion, bifurcation, CTO)	Multicenter registry	Mattesini et al. [75]	35 patients 50 lesions with BVS vs. 38 patients 50 lesions with DES	8.5±2.8-month vs. 17.3±8.7-month	N/A	N/A	N/A	N/A
Bifurcation	Case report	Džavík et al. [80]	1 patient with BVS and EES Provisional T stent (BVS at main branch, EES at side branch)	N/A	N/A	N/A	N/A	N/A

(continued)

Target	Study design	Trial / author	Patient number	Follow-up	Clinical outcomes Composite Endpoint	MI	TLR	Probable/definite ST
	Case series	Grundeken et al. [81]	11 patients with both BVS and Tryton	6-month	MACE: 20%	0%	20%	0%
Chronic total occlusion	Single center registry	CTO-ABSORB pilot study [82]	35 patients with BVS	6-month	0%	0%	0%	0%
Left main	Case report	Miyazaki et al. [83,84] Grundeken et al. [85] Fernández et al. [86] Sato et al. [87]	4 case reports treated with BVS 1 case report at follow-up (BVS re-stenosis)	N/A	N/A	N/A	N/A	N/A
3 vessel disease	No publication							

(continued)

Target	Study design	Trial / author	Patient number	Follow-up	Clinical outcomes Composite Endpoint	MI	TLR	Probable/definite ST
Small vessels	Multicenter registry	Diletti et al. [88]	101 patients with BVS (RVD<2.5mm 41patients vs. RVD≥2.5mm 60 patients)	2-year	MACE: 7.3% vs. 10.2% (P=0.74)	4.9% vs. 1.7% (P=0.57)	2.4% vs. 8.5% (P=0.40)	0% vs. 0%
Acute coronary syndrome (UAP, NSTEMI, STEMI)	Single center registry	POLAR ACS study [89]	100 patients with BVS (46 UAP, 38 NSTEMI, 16 STEMI)	1-year	MACE: 4.0%	1.0%	1.0%	1.0%
	Single center registry	Gori et al. [90]	150 patients with BVS vs. 103 patients with EES (BVS: 24 UAP, 60 NSTEMI, 66 STEMI) (EES: 20 UAP, 46 NSTEMI, 37 STEMI)	1-month	MACE: 10.7% vs. 15.5% (P>0.8)	4.0% vs. 3.9% (P=1.0)	N/A	2.7% vs. 2.9% (P=1.0)
STEMI	PS matching comparison	BVS-EXAMINATION Study [66]	290 patients with BVS vs. 290 patients with EES vs. 290 patients with BMS	1-year	DoCE: 4.1% vs. 4.1% vs. 5.9% (P=NS)	2.1% vs. 1.4% vs. 1.0%	1.7% vs. 1.4% vs. 3.4%	2.4% vs. 1.4% vs. 1.7%
	PS matching comparison	Italian ABSORB Registry (BVS-RAI) [91]	122 patients with BVS vs. 441 patients with EES	6-month	PoCE: 4.9% vs. 7.0% (P=0.4)	4.1% vs. 2.0% (P=0.2)	4.1% vs. 4.5% (P=0.8)	2.5% vs. 1.4% (P=0.4)

(continued)

Target	Study design	Trial / author	Patient number	Follow-up	Clinical outcomes Composite Endpoint	MI	TLR	Probable/definite ST
	Multicenter registry	Prague 19 [67]	40 patients with BVS vs. 57 patients with DES	6-month	Composite endpoints of death, any MI & TVR 5.0% vs. 7.0% (P=0.67)	N/A	N/A	N/A
	Single center registry	Wiebe et al. [92]	25 patients with BVS	6-month	MACE: 8.3%	4.2%	0%	0%
	Single center registry	BVS STEMI first study [93]	49 patients with BVS	30-day	TLF: 0%	0%	0%	0%
Saphenous vein graft	Case report	Yew et al. [94]	1 patient with BVS	N/A	N/A	N/A	N/A	N/A
Diabetes mellitus	PS matching comparison	A Pooled Analysis of the ABSORB and the SPIRIT Trials [65]	102 DM patients with BVS vs. 172 DM patients with EES	1-year	DoCE: 3.9% vs. 6.4% (P=0.38)	2.9% vs. 2.9% (P=1.0)	2.0% vs. 4.1% (P=0.49)	1.0% vs. 1.7% (P=1.0)
In-stent restenosis	Multicenter registry	Ielasi et al. [95]	25 patients with BVS for 30 ISR lesions	7-month	MACE: 8.0%	4.0%	8.0%	0%

Abbreviations: BMS, bare metal stent; BVS, bioresorbable vascular scaffold; DAPT, dual antiplatelet therapy; DM, diabetes mellitus; DoCE, device-oriented composite endpoint; EES, everolimus-eluting stent; MACE, major adverse cardiac event; MI, myocardial infarction; N/A, not applicable; NSTEMI, non-ST-elevation myocardial infarction; PS, propensity score; ST, stent/scaffold thrombosis; STEMI, ST-elevation myocardial infarction; PoCE, patient-oriented composite endpoint; TLF, target lesion failure; TLR, target lesion revascularization; TVF, target vessel failure; TVR, target vessel revascularization, UAP, unstable angina pectoris.

Table 7. The rate of scaffold thrombosis in individual populations

Study (Journal/ international congress)	Population	Follow up	Total, N	Acute		Subacute ST in total, N (%)	Early ST in total, N (%)	ST in total, N (%)	SAP, N	ST in SAP, N (%)	ACS, N	ST in ACS, N (%)	STEMI, N	ST in STEMI, N (%)
				ST in total, N (%)	N (%)									
Kraak et al.[78], AMC Single Centre	All-comers	6M	135	0(0%)	3 (2.2%)	3 (2.2%)	3 (2.2%)	4 (3.0%)	82	1 (1.2%)	53	3 (5.7%)	17	0 (0%)
ABSORB FIRST (euroPCR2014)	All-comers	1M	800	0(0%)	2 (0.3%)	2 (0.3%)	2 (0.3%)	2 (0.3%)	295	N/A	505	N/A	N/A	N/A
Azzalini et al. (euroPCR2014)	All-comers	N/A	339	0 (0%)	4 (1.2%)	4 (1.2%)	4 (1.2%)	4 (1.2%)	N/A	3 (N/A)	N/A	0 (N/A)	N/A	1 (N/A)
Abizaïd et al.[77] ABSORB EXTEND	SAP	12M	512	0 (0%)	2 (0.4%)	2 (0.4%)	2 (0.4%)	4 (0.8%)	512	4 (0.8%)	-	-	-	-
Serruys et al.[23], ABSORB B	SAP	36M	101	0 (0%)	0 (0%)	0 (0%)	0 (0%)	0 (0%)	101	0 (0%)	-	-	-	-
Onuma et al.[22], ABSORB A	SAP	60M	30	0 (0%)	0 (0%)	0 (0%)	0 (0%)	0 (0%)	30	0 (0%)	-	-	-	-
CORONARY CTO (euroPCR2014)	SAP	6M	35	0 (0%)	0 (0%)	0 (0%)	0 (0%)	0 (0%)	35	0 (0%)	-	-	-	-
Serruys et al.[53], ABSORB II	SAP / UAP	12M	335	1 (0.3)	1 (0.3)	1 (0.3)	2 (0.6)	3 (0.9%)	267	3 (1.1%)	68	0 (0%)	-	-
ASSURE registry (euroPCR2014)	SAP / UAP	12M	183	0 (0%)	0 (0%)	0 (0%)	0 (0%)	0 (0%)	144	0 (0%)	39	0 (0%)	-	-
BVS EXPAND (euroPCR2014)	SAP / UAP	6M	200	0 (0%)	0 (0%)	0 (0%)	0 (0%)	4 (2.2%)	N/A	N/A	N/A	N/A	-	-
Gori et al[90] POLAR ACS (euroPCR2014)	ACS	1M	150	1 (0.7%)	1 (0.7%)	1 (0.7%)	2 (1.4%)	4 (2.7%)	-	-	150	4 (2.7%)	66	N/A
	ACS	12M	100	0 (0%)	0 (0%)	0 (0%)	0 (0%)	0 (0%)	-	-	100	0 (0%)	16	0 (0%)

(continued)

Study (Journal / international congress)	Population	Follow up	Total, N	Acute ST in total, N (%)		Subacute ST in total, N (%)	Early ST in total, N (%)	ST in total, N (%)	SAP, N	ST in SAP, N (%)	ACS, N	ST in ACS, N (%)	STEMI, N	ST in STEMI, N (%)
				N (%)	N (%)									
Kajiya et al.[96]	STEMI	3M	11	0 (0%)	0 (0%)	0 (0%)	0 (0%)	0 (0%)	-	-	-	-	11	0 (0%)
Diletti et al.[93], BVS STEMI	STEMI	1M	49	0 (0%)	0 (0%)	0 (0%)	0 (0%)	0 (0%)	-	-	-	-	49	0 (0%)
Kocka et al.[67], PRAGUE-19	STEMI	4M	41	0 (0%)	1 (2.4%)	1 (2.4%)	1 (2.4%)	1 (2.4%)	-	-	-	-	41	1 (2.4%)
Wiebe et al.[92]	STEMI	6M	25	0 (0%)	0 (0%)	0 (0%)	0 (0%)	0 (0%)	-	-	-	-	25	0 (0%)
Ielasi et al.[95], RAI registry	STEMI	6M	74	0 (0%)	1 (1.4%)	1 (1.4%)	1 (1.4%)	1 (1.4%)	-	-	-	-	74	1 (1.4%)
Weighted average excluding the GHOST-EU registry	Average F/U: 10.6 Months		3120	0.06%	0.48%	0.54%	0.89%	1171	0.68%	410	1.71%	299	0.67%	
Capodanno et al.[60], GHOST-EU registry	All-comer	6M	1189	5 (0.4%)	11 (0.9%)	16 (1.3%)	23 (2.1%)	626	9 (1.4%)	563	14 (2.5%)	192	4 (2.1%)	
Weighted average including the GHOST-EU registry	Average F/U: 10.3 Months		4309	0.16%	0.60%	0.76%	1.22%	1797	0.94%	973	2.16%	491	1.22%	

Abbreviations: ACS, acute coronary syndrome; F/U, follow-up; N/A, non-available; SAP, stable angina pectoris; ST, stent thrombosis; STEMI, ST-segment elevation myocardial infarction.

CONCLUSIONS

The introduction of bioresorbable scaffold to interventional cardiology heralded the new era of “vascular reparative therapy”. Preclinical animal studies demonstrated the long-term safety of the device as compared to DESs. Although the mechanical strength of Absorb BVS is similar to metallic stents within the range of expansion, the device’s expansile capacity is inherently limited. Accordingly, preprocedural lesion evaluation, implantation techniques and post-dilatation strategy should be optimized for Absorb BVS. Clinical data from the first in man trials mainly based on imaging studies showed the potential benefit of this technology, such as late lumen enlargement, late plaque modification, return of vasomotion, and restoration of pulsatility. The recently published data from the first RCT reported comparable results of Absorb BVS with CoCr-EES in terms of clinical outcomes. However, the clinical utility in complex lesions is yet to be elucidated. Further clinical investigation in a randomized fashion is desirable.

Expert commentary

The current long-term data of Absorb BVS is evidenced in non-complex lesions and it is comparable to the data of DESs, allowing for device use in daily clinical practice. As theoretical advantages of BRS stem from transient support without rigid caging, it may be considered as the first treatment option for lesions which may require “full metal jacket” stenting. The use of a BRS implies no restriction to future percutaneous or surgical revascularization. Implantation of Absorb BVS in complex lesions still needs long-term supporting data. Results of the current ongoing RCTs comparing Absorb BVS and CoCr-EES in complex lesions will validate the initially anticipated benefits of Absorb BVS.

Five-year view

Ongoing randomized controlled trials comparing BRS and DES will confirm the real clinical value of BRS. The results for simple lesions were favorable for BRS, and the results for complex lesions remain to be elucidated. In five years, the current controversial points of the device will be clarified, and clinical use of the device will be more generalized. In addition, the upcoming next generation BRS with thinner struts would be the most promising development to overcome the current limitations.

Key issues

- The advent of fully biodegradable scaffolds heralded the fourth revolution in interventional cardiology as it provides transient scaffolding of the vessel then gradually degrade, permitting the restoration of vascular physiology and integrity.
- The radial strength of Absorb BVS (1.1) has been reported to be comparable with metallic stents when Absorb BVS is deployed within the limits of expansion.
- Absorb BVS demonstrated comparable safety to CoCr-EES in a normal porcine coronary artery model with low-grade inflammation and fibrin deposition.
- The preclinical data showed late lumen and vessel enlargement in Absorb BVS-implanted arteries starting after 12 months and the degradation of Absorb BVS was complete by 36 months.
- Absorb BVS has a limited expansion, the acute gain is lower than CoCr-EES due to the lower pressure during implantation and smaller size of post-dilatation balloon. However, in-stent late lumen loss is equal between Absorb BVS and CoCr-EES.
- There are, currently, limited data supporting the utilization of BVS in complex lesions such as bifurcation lesions requiring two-stent technique, left main lesions, chronic total occlusions and coronary bypass graft and in-stent restenosis.
- RCT comparing Absorb BVS and CoCr-EES (Absorb II trial) revealed that the 1-year composite device orientated endpoint was similar between the Absorb BVS and CoCr-EES groups.
- Implanting Absorb BVS during primary PCI has shown a favorable outcome in selected patients with STEMI as was previously reported in CoCr-EES.
- Concerns remain as for the rate of early and mid-term scaffold thrombosis in the real-world registry, although the rate of scaffold thrombosis was comparable between Absorb BVS and CoCr-EES in the first RCT.

REFERENCES

1. Guiteras-Val P, Varas-Lorenzo C, Garcia-Picart J, Marti-Claramunt V, Auge-Sanpera JM. Clinical and sequential angiographic follow-up six months and 10 years after successful percutaneous transluminal coronary angioplasty. *The American journal of cardiology*, 83(6), 868-874 (1999).
2. Hatrick RI, Ormiston JA, Ruygrok PN *et al*. Very late changes in the dilated lesion following coronary balloon angioplasty: a 17 year serial quantitative angiographic study. *EuroIntervention*, 5(1), 121-126 (2009).
3. Fischman DL, Leon MB, Baim DS *et al*. A randomized comparison of coronary-stent placement and balloon angioplasty in the treatment of coronary artery disease. Stent Restenosis Study Investigators. *N Engl J Med*, 331(8), 496-501 (1994).
4. Serruys PW, de Jaegere P, Kiemeneij F *et al*. A comparison of balloon-expandable-stent implantation with balloon angioplasty in patients with coronary artery disease. Benestent Study Group. *N Engl J Med*, 331(8), 489-495 (1994).
5. Serruys PW, Daemen J. Are drug-eluting stents associated with a higher rate of late thrombosis than bare metal stents? Late stent thrombosis: a nuisance in both bare metal and drug-eluting stents. *Circulation*, 115(11), 1433-1439; discussion 1439 (2007).
6. Ong AT, McFadden EP, Regar E, de Jaegere PP, van Domburg RT, Serruys PW. Late angiographic stent thrombosis (LAST) events with drug-eluting stents. *J Am Coll Cardiol*, 45(12), 2088-2092 (2005).
7. McFadden EP, Stabile E, Regar E *et al*. Late thrombosis in drug-eluting coronary stents after discontinuation of antiplatelet therapy. *Lancet*, 364(9444), 1519-1521 (2004).
8. Camenzind E, Steg PG, Wijns W. Stent thrombosis late after implantation of first-generation drug-eluting stents: a cause for concern. *Circulation*, 115(11), 1440-1455; discussion 1455 (2007).
9. Lagerqvist B, James SK, Stenestrand U, Lindback J, Nilsson T, Wallentin L. Long-term outcomes with drug-eluting stents versus bare-metal stents in Sweden. *N Engl J Med*, 356(10), 1009-1019 (2007).
10. Pfisterer M, Brunner-La Rocca HP, Buser PT *et al*. Late clinical events after clopidogrel discontinuation may limit the benefit of drug-eluting stents: an observational study of drug-eluting versus bare-metal stents. *J Am Coll Cardiol*, 48(12), 2584-2591 (2006).
11. Brodie BR, Pokharel Y, Garg A *et al*. Very late hazard with stenting versus balloon angioplasty for ST-elevation myocardial infarction: a 16-year single-center experience. *Journal of interventional cardiology*, 27(1), 21-28 (2014).
12. Daemen J, Wenaweser P, Tsuchida K *et al*. Early and late coronary stent thrombosis of sirolimus-eluting and paclitaxel-eluting stents in routine clinical practice: data from a large two-institutional cohort study. *Lancet*, 369(9562), 667-678 (2007).
13. Wenaweser P, Daemen J, Zwahlen M *et al*. Incidence and correlates of drug-eluting stent thrombosis in routine clinical practice. 4-year results from a large 2-institutional cohort study. *Journal of the American College of Cardiology*, 52(14), 1134-1140 (2008).
14. Tsuchida K, Daemen J, Tanimoto S *et al*. Two-year outcome of the use of paclitaxel-eluting stents in aorto-ostial lesions. *International journal of cardiology*, 129(3), 348-353 (2008).
15. Finn AV, Nakazawa G, Joner M *et al*. Vascular responses to drug eluting stents: importance of delayed healing. *Arterioscler Thromb Vasc Biol*, 27(7), 1500-1510 (2007).
16. Finn AV, Joner M, Nakazawa G *et al*. Pathological correlates of late drug-eluting stent thrombosis: strut coverage as a marker of endothelialization. *Circulation*, 115(18), 2435-2441 (2007).
17. Joner M, Finn AV, Farb A *et al*. Pathology of drug-eluting stents in humans: delayed healing and late thrombotic risk. *J Am Coll Cardiol*, 48(1), 193-202 (2006).
18. Nebeker JR, Virmani R, Bennett CL *et al*. Hypersensitivity cases associated with drug-eluting coronary stents: a review of available cases from the Research on Adverse Drug Events and Reports (RADAR) project. *J Am Coll Cardiol*, 47(1), 175-181 (2006).
19. Baber U, Mehran R, Sharma SK *et al*. Impact of the everolimus-eluting stent on stent thrombosis: a meta-analysis of 13 randomized trials. *J Am Coll Cardiol*, 58(15), 1569-1577 (2011).
20. Serruys PW, Morice MC, Kappetein AP *et al*. Percutaneous coronary intervention versus coronary-artery bypass grafting for severe coronary artery disease. *N Engl J Med*, 360(10), 961-972

(2009).

21. Spuentrup E, Ruebben A, Mahnken A *et al.* Artifact-free coronary magnetic resonance angiography and coronary vessel wall imaging in the presence of a new, metallic, coronary magnetic resonance imaging stent. *Circulation*, 111(8), 1019-1026 (2005).

22. Onuma Y, Dudek D, Thuesen L *et al.* Five-year clinical and functional multislice computed tomography angiographic results after coronary implantation of the fully resorbable polymeric everolimus-eluting scaffold in patients with de novo coronary artery disease: the ABSORB cohort A trial. *JACC. Cardiovascular interventions*, 6(10), 999-1009 (2013).

23. Serruys PW, Onuma Y, Garcia-Garcia HM *et al.* Dynamics of vessel wall changes following the implantation of the absorb everolimus-eluting bioresorbable vascular scaffold: a multi-imaging modality study at 6, 12, 24 and 36 months. *EuroIntervention*, 9(11), 1271-1284 (2014).

24. Ormiston JA, Serruys PW. Bioabsorbable coronary stents. *Circ Cardiovasc Interv*, 2(3), 255-260 (2009).

25. Castro Rodriguez J, Dessy H, Demanet H. Implantation of an Absorb bioresorbable vascular scaffold in the stenotic aortopulmonary collateral artery of a young child with Alagille syndrome. *Catheterization and cardiovascular interventions*, 86(2), E76-80 (2015).

26. Vorpahl M, Nakano M, Perkins LE *et al.* Vascular healing and integration of a fully bioresorbable everolimus-eluting scaffold in a rabbit iliac arterial model. *EuroIntervention*, 10(7), 833-841 (2014).

27. Onuma Y, Serruys PW, Perkins LE *et al.* Intracoronary optical coherence tomography and histology at 1 month and 2, 3, and 4 years after implantation of everolimus-eluting bioresorbable vascular scaffolds in a porcine coronary artery model: an attempt to decipher the human optical coherence tomography images in the ABSORB trial. *Circulation*, 122(22), 2288-2300 (2010).

***First study described described the bioresorbation process of bioresorbable scaffold.**

28. Otsuka F, Pacheco E, Perkins LE *et al.* Long-term safety of an everolimus-eluting bioresorbable vascular scaffold and the cobalt-chromium XIENCE V stent in a porcine coronary artery model. *Circ Cardiovasc Interv*, 7(3), 330-342 (2014).

29. Farooq V, Serruys PW, Heo JH *et al.* Intracoronary optical coherence tomography and histology of overlapping everolimus-eluting bioresorbable vascular scaffolds in a porcine coronary artery model: the potential implications for clinical practice. *JACC. Cardiovascular interventions*, 6(5), 523-532 (2013).

30. Ormiston JA, Webber B, Ubod B, Darremont O, Webster MW. An independent bench comparison of two bioresorbable drug-eluting coronary scaffolds (Absorb and DESolve) with a durable metallic drug-eluting stent (ML8/Xpedition). *EuroIntervention*, 11(1), 60-67 (2015).

31. Ormiston JA, De Vroey F, Serruys PW, Webster MW. Bioresorbable polymeric vascular scaffolds: a cautionary tale. *Circ Cardiovasc Interv*, 4(5), 535-538 (2011).

32. Foin N, Lee R, Mattesini A *et al.* Bioabsorbable vascular scaffold overexpansion: insights from in vitro post-expansion experiments. *EuroIntervention*, 11(3) (2015).

33. Oberhauser JP, Hossainy S, Rapoza RJ. Design principles and performance of bioresorbable polymeric vascular scaffolds. *EuroIntervention*, 5 Suppl F, F15-22 (2009).

34. Hoffmann R, Mintz GS, Kent KM *et al.* Serial intravascular ultrasound predictors of restenosis at the margins of Palmaz-Schatz stents. *The American journal of cardiology*, 79(7), 951-953 (1997).

35. Gyongyosi M, Yang P, Khorsand A, Glogar D. Longitudinal straightening effect of stents is an additional predictor for major adverse cardiac events. Austrian Wiktor Stent Study Group and European Paragon Stent Investigators. *J Am Coll Cardiol*, 35(6), 1580-1589 (2000).

36. McDaniel MC, Samady H. The sheer stress of straightening the curves: biomechanics of bioabsorbable stents. *JACC. Cardiovascular interventions*, 4(7), 800-802 (2011).

37. Onuma Y, Serruys PW. Bioresorbable scaffold: the advent of a new era in percutaneous coronary and peripheral revascularization? *Circulation*, 123(7), 779-797 (2011).

38. Brown AJ, McCormick LM, Braganza DM, Bennett MR, Hoole SP, West NE. Expansion and malapposition characteristics after bioresorbable vascular scaffold implantation. *Catheterization and cardiovascular interventions*, 84(1), 37-45 (2014).

39. Foin N, Sen S, Allegria E *et al.* Maximal expansion capacity with current DES platforms: a critical factor for stent selection in the treatment of left main bifurcations? *EuroIntervention*, 8(11), 1315-1325 (2013).

40. Everaert B, Felix C, Koolen J *et al.* Appropriate use of bioresorbable vascular scaffolds in percutaneous coronary interventions: a recommendation from experienced users : A position statement on the use of bioresorbable vascular scaffolds in the Netherlands. *Netherlands heart journal : monthly journal of the Netherlands Society of Cardiology and the Netherlands Heart Foundation*, 23(3), 161-165 (2015).
41. Attizzani GF, Ohno Y, Capodanno D *et al.* New insights on acute expansion and longitudinal elongation of bioresorbable vascular scaffolds in vivo and at bench test: a note of caution on reliance to compliance charts and nominal length. *Catheterization and cardiovascular interventions*, 85(4), E99-e107 (2015).
42. Karabulut A, Demirci Y. Cutting balloon use may ease the optimal apposition of bioresorbable vascular scaffold in in-stent stenosis. *Postępy Kardiologii Interwencyjnej*, 11(1), 64-66 (2015).
43. Miyazaki T, Panoulas VF, Sato K *et al.* In-Scaffold Restenosis in a Previous Left Main Bifurcation Lesion Treated With Bioresorbable Scaffold V-Stenting. *JACC: Cardiovascular Interventions*, 8(1_PA), e7-e10 (2015).
44. Naganuma T, Basavarajaiah S, Latib A, Costopoulos C, Colombo A. Use of BVS in a chronic total occlusion with bifurcation lesion. *International journal of cardiology*, 167(5), e129-e131 (2013).
45. Roleder T, Parma Z, Smolka G, Ochała A, Wojakowski W. *Optical coherence tomography imaging of everolimus-eluting bioresorbable vascular scaffold implanted into coronary vein graft at 3-month follow-up* (2014).
46. Ong PJL, Jafary FH, Ho HH. "First-in-man" use of bioresorbable vascular scaffold in saphenous vein graft. *EuroIntervention*, 9(1), 165 (2013).
47. Tamburino C, Latib A, van Geuns R-JM *et al.* Contemporary practice and technical aspects in coronary intervention with bioresorbable scaffolds: a European perspective. *EuroIntervention*, 11(1), 45-52 (2015).
48. Gomez-Lara J, Diletti R, Brugaletta S *et al.* Angiographic maximal luminal diameter and appropriate deployment of the everolimus-eluting bioresorbable vascular scaffold as assessed by optical coherence tomography: an ABSORB cohort B trial sub-study. *EuroIntervention*, 8(2), 214-224 (2012).
49. Onuma Y, Serruys PW, Muramatsu T *et al.* Incidence and imaging outcomes of acute scaffold disruption and late structural discontinuity after implantation of the absorb Everolimus-Eluting fully bioresorbable vascular scaffold: optical coherence tomography assessment in the ABSORB cohort B Trial (A Clinical Evaluation of the Bioabsorbable Everolimus Eluting Coronary Stent System in the Treatment of Patients With De Novo Native Coronary Artery Lesions). *JACC. Cardiovascular interventions*, 7(12), 1400-1411 (2014).
50. Farooq V, Gomez-Lara J, Brugaletta S *et al.* Proximal and distal maximal luminal diameters as a guide to appropriate deployment of the ABSORB everolimus-eluting bioresorbable vascular scaffold: a sub-study of the ABSORB Cohort B and the on-going ABSORB EXTEND Single Arm Study. *Catheterization and cardiovascular interventions*, 79(6), 880-888 (2012).
- **The study described how to measure maximal lumen diameter for Absorb BVS device sizing.**
51. Ishibashi Y, Nakatani S, Sotomi Y *et al.* Relation between bioresorbable scaffold sizing using QCA-Dmax and clinical outcomes at 1 year in 1232 patients from three study cohorts (ABSORB Cohort B, ABSORB EXTEND and ABSORB II). *JACC: Cardiovascular Interventions*, (In Press).
52. Rzeszutko Ł, Depukat R, Dudek D. Biodegradable vascular scaffold ABSORB BVS™ – scientific evidence and methods of implantation. *Postępy w Kardiologii Interwencyjnej = Advances in Interventional Cardiology*, 9(1), 22-30 (2013).
53. Serruys PW, Chevalier B, Dudek D *et al.* A bioresorbable everolimus-eluting scaffold versus a metallic everolimus-eluting stent for ischaemic heart disease caused by de-novo native coronary artery lesions (ABSORB II): an interim 1-year analysis of clinical and procedural secondary outcomes from a randomised controlled trial. *Lancet*, 385(9962), 43-54 (2015).
- *First randomized controlled trial between BVS and second-generation EES**
54. Gomez-Lara J, Brugaletta S, Diletti R *et al.* Agreement and reproducibility of gray-scale intravascular ultrasound and optical coherence tomography for the analysis of the bioresorbable vascular scaffold. *Catheterization and cardiovascular interventions*, 79(6), 890-902 (2012).

55. Brown AJ, McCormick LM, Hoole SP, West NEJ. Coregistered Intravascular Ultrasound and Optical Coherence Tomography Imaging During Implantation of a Bioresorbable Vascular Scaffold. *JACC: Cardiovascular Interventions*, 6(7), e41-e42 (2013).

56. Suwannasom P, Onuma Y, Campos CM *et al.* Fate of Bioresorbable Vascular Scaffold Metallic Radio-Opaque Markers at the Site of Implantation After Bioresorption. *JACC. Cardiovascular interventions*, 8(8), 1130-1132 (2015).

57. Ormiston JA, Serruys PW, Regar E *et al.* A bioabsorbable everolimus-eluting coronary stent system for patients with single de-novo coronary artery lesions (ABSORB): a prospective open-label trial. *Lancet*, 371(9616), 899-907 (2008).

***First in man trial of bioresorbable scaffold**

58. Serruys PW, Onuma Y, Ormiston JA *et al.* Evaluation of the second generation of a bioresorbable everolimus drug-eluting vascular scaffold for treatment of de novo coronary artery stenosis: six-month clinical and imaging outcomes. *Circulation*, 122(22), 2301-2312 (2010).

59. Spertus JA, Winder JA, Dewhurst TA *et al.* Development and evaluation of the Seattle Angina Questionnaire: a new functional status measure for coronary artery disease. *J Am Coll Cardiol*, 25(2), 333-341 (1995).

60. Capodanno D, Gori T, Nef H *et al.* Percutaneous coronary intervention with everolimus-eluting bioresorbable vascular scaffolds in routine clinical practice: early and midterm outcomes from the European multicentre GHOST-EU registry. *EuroIntervention*, 10(10), 1144-1153 (2015).

***The largest multicenter registry in the real-world use of Absorb BVS.**

61. Ishibashi Y, Nakatani S, Onuma Y. Definite and probable bioresorbable scaffold thrombosis in stable and ACS patients. *EuroIntervention*, (2014).

62. Stettler C, Allemann S, Wandel S *et al.* Drug eluting and bare metal stents in people with and without diabetes: collaborative network meta-analysis. *BMJ (Clinical research ed.)*, 337, a1331 (2008).

63. Mathew V, Holmes DR. Outcomes in diabetics undergoing revascularization: the long and the short of it. *J Am Coll Cardiol*, 40(3), 424-427 (2002).

64. Van Belle E, Perie M, Braune D *et al.* Effects of coronary stenting on vessel patency and long-term clinical outcome after percutaneous coronary revascularization in diabetic patients. *J Am Coll Cardiol*, 40(3), 410-417 (2002).

65. Muramatsu T, Onuma Y, van Geuns RJ *et al.* 1-year clinical outcomes of diabetic patients treated with everolimus-eluting bioresorbable vascular scaffolds: a pooled analysis of the ABSORB and the SPIRIT trials. *JACC. Cardiovascular interventions*, 7(5), 482-493 (2014).

66. Brugaletta S, Gori T, Low AF *et al.* Absorb bioresorbable vascular scaffold versus everolimus-eluting metallic stent in ST-segment elevation myocardial infarction: 1-year results of a propensity score matching comparison: the BVS-EXAMINATION Study (bioresorbable vascular scaffold-a clinical evaluation of everolimus eluting coronary stents in the treatment of patients with ST-segment elevation myocardial infarction). *JACC. Cardiovascular interventions*, 8(1 Pt B), 189-197 (2015).

***The largest study comparing Absorb BVS, DES and BMS in STEMI population using propensity score matching.**

67. Kocka V, Maly M, Tousek P *et al.* Bioresorbable vascular scaffolds in acute ST-segment elevation myocardial infarction: a prospective multicentre study 'Prague 19'. *Eur Heart J*, 35(12), 787-794 (2014).

68. Cortese B, Ielasi A, Varricchio A *et al.* Registro Absorb Italiano (BVS-RAI): an investigators-owned and -directed, open, prospective registry of consecutive patients treated with the Absorb BVS: study design. *Cardiovasc Revasc Med*, (2015).

69. Ormiston JA, Webber B, Ubod B, Webster MW, White J. Absorb everolimus-eluting bioresorbable scaffolds in coronary bifurcations: a bench study of deployment, side branch dilatation and post-dilatation strategies. *EuroIntervention*, 10(10), 1169-1177 (2015).

70. Dzavik V, Colombo A. The absorb bioresorbable vascular scaffold in coronary bifurcations: insights from bench testing. *JACC. Cardiovascular interventions*, 7(1), 81-88 (2014).

71. Onuma Y, Serruys PW, Gomez J *et al.* Comparison of in vivo acute stent recoil between the bioresorbable everolimus-eluting coronary scaffolds (revision 1.0 and 1.1) and the metallic everolimus-eluting stent. *Catheterization and cardiovascular interventions*, 78(1), 3-12 (2011).

72. Zhang YJ, Bourantas CV, Muramatsu T *et al.* Comparison of acute gain and late lumen loss after

PCI with bioresorbable vascular scaffolds versus everolimus-eluting stents: an exploratory observational study prior to a randomised trial. *EuroIntervention*, 10(6), 672-680 (2014).

73. Brugaletta S, Heo JH, Garcia-Garcia HM *et al.* Endothelial-dependent vasomotion in a coronary segment treated by ABSORB everolimus-eluting bioresorbable vascular scaffold system is related to plaque composition at the time of bioresorption of the polymer: indirect finding of vascular reparative therapy? *Eur Heart J*, 33(11), 1325-1333 (2012).

74. Gomez-Lara J, Brugaletta S, Farooq V *et al.* Head-to-head comparison of the neointimal response between metallic and bioresorbable everolimus-eluting scaffolds using optical coherence tomography. *JACC. Cardiovascular interventions*, 4(12), 1271-1280 (2011).

75. Mattesini A, Secco GG, Dall'Ara G *et al.* ABSORB biodegradable stents versus second-generation metal stents: a comparison study of 100 complex lesions treated under OCT guidance. *JACC. Cardiovascular interventions*, 7(7), 741-750 (2014).

****First OCT study to compare acute stent performance between a BVS and second-generation DES in complex coronary artery lesion.**

76. Brugaletta S, Gomez-Lara J, Diletti R *et al.* Comparison of in vivo eccentricity and symmetry indices between metallic stents and bioresorbable vascular scaffolds: insights from the ABSORB and SPIRIT trials. *Catheterization and cardiovascular interventions*, 79(2), 219-228 (2012).

77. Abizaid A, Ribamar Costa J, Jr., Bartorelli AL *et al.* The ABSORB EXTEND study: preliminary report of the twelve-month clinical outcomes in the first 512 patients enrolled. *EuroIntervention*, 10(12), 1396-1401 (2015).

78. Kraak RP, Hassell ME, Grundeken MJ *et al.* Initial experience and clinical evaluation of the Absorb bioresorbable vascular scaffold (BVS) in real-world practice: the AMC Single Centre Real World PCI Registry. *EuroIntervention*, 10(10), 1160-1168 (2015).

79. Azzalini L, L'Allier PL. Bioresorbable vascular scaffold thrombosis in an all-comer patient population: single-center experience. *J Invasive Cardiol*, 27(2), 85-92 (2015).

80. Dzavik V, Muramatsu T, Crooks N, Nakatani S, Onuma Y. Complex bifurcation percutaneous coronary intervention with the Absorb bioresorbable vascular scaffold. *EuroIntervention*, 9(7), 888 (2013).

81. Grundeken MJ, Hassell ME, Kraak RP *et al.* Treatment of coronary bifurcation lesions with the Absorb bioresorbable vascular scaffold in combination with the Tryton dedicated coronary bifurcation stent: evaluation using two- and three-dimensional optical coherence tomography. *EuroIntervention*, (2014).

82. Vaquerizo B, Barros A, Pujadas S *et al.* Bioresorbable everolimus-eluting vascular scaffold for the treatment of chronic total occlusions: CTO-ABSORB pilot study. *EuroIntervention*, (2014).

83. Miyazaki T, Panoulas VF, Sato K, Naganuma T, Latib A, Colombo A. Bioresorbable vascular scaffolds for left main lesions; a novel strategy to overcome limitations. *International journal of cardiology*, 175(1), e11-13 (2014).

84. Miyazaki T, Panoulas VF, Sato K *et al.* In-scaffold restenosis in a previous left main bifurcation lesion treated with bioresorbable scaffold v-stenting. *JACC Cardiovasc Interv*, 8(1 Pt A), e7-e10 (2015).

85. Grundeken MJ, Kraak RP, de Bruin DM, Wykrzykowska JJ. Three-dimensional optical coherence tomography evaluation of a left main bifurcation lesion treated with ABSORB(R) bioresorbable vascular scaffold including fenestration and dilatation of the side branch. *International journal of cardiology*, 168(3), e107-108 (2013).

86. Fernandez D, Brugaletta S, Martin-Yuste V *et al.* First experience of a bioresorbable vascular scaffold implantation in left main stenosis. *International journal of cardiology*, 168(2), 1566-1568 (2013).

87. Sato K, Latib A, Panoulas VF, Naganuma T, Miyazaki T, Colombo A. A case of true left main bifurcation treated with bioresorbable everolimus-eluting stent v-stenting. *JACC. Cardiovascular interventions*, 7(8), e103-104 (2014).

88. Diletti R, Farooq V, Girasis C *et al.* Clinical and intravascular imaging outcomes at 1 and 2 years after implantation of absorb everolimus eluting bioresorbable vascular scaffolds in small vessels. Late lumen enlargement: does bioresorption matter with small vessel size? Insight from the ABSORB cohort B trial. *Heart*, 99(2), 98-105 (2013).

89. Dudek D, Rzeszutko L, Zasada W *et al.* Bioresorbable vascular scaffolds in patients with acute coronary syndromes: the POLAR ACS study. *Pol Arch Med Wewn*, 124(12), 669-677 (2014).
90. Gori T, Schulz E, Hink U *et al.* Early outcome after implantation of Absorb bioresorbable drug-eluting scaffolds in patients with acute coronary syndromes. *EuroIntervention*, 9(9), 1036-1041 (2014).
91. Cortese B, Ielasi A, Romagnoli E *et al.* Clinical Comparison With Short-Term Follow-Up of Bioresorbable Vascular Scaffold Versus Everolimus-Eluting Stent in Primary Percutaneous Coronary Interventions. *The American journal of cardiology*, (2015).
92. Wiebe J, Mollmann H, Most A *et al.* Short-term outcome of patients with ST-segment elevation myocardial infarction (STEMI) treated with an everolimus-eluting bioresorbable vascular scaffold. *Clin Res Cardiol*, 103(2), 141-148 (2014).
93. Diletti R, Karanasos A, Muramatsu T *et al.* Everolimus-eluting bioresorbable vascular scaffolds for treatment of patients presenting with ST-segment elevation myocardial infarction: BVS STEMI first study. *Eur Heart J*, 35(12), 777-786 (2014).
94. Yew KL. Novel use of absorb bioresorbable vascular scaffold and STENTYS self-apposing coronary stent for complex saphenous vein grafts intervention. *International journal of cardiology*, 177(3), e184-185 (2014).
95. Ielasi A, Latib A, Naganuma T *et al.* Early results following everolimus-eluting bioresorbable vascular scaffold implantation for the treatment of in-stent restenosis. *International journal of cardiology*, 173(3), 513-514 (2014).
96. Kajiya T, Liang M, Sharma RK *et al.* Everolimus-eluting bioresorbable vascular scaffold (BVS) implantation in patients with ST-segment elevation myocardial infarction (STEMI). *EuroIntervention*, 9(4), 501-504 (2013).

Optimization of percutaneous coronary intervention: Indispensables for bioresorbable scaffolds

Erhan Tenekecioglu, Christos V. Bourantas, Mohammad Abdelghani, Yohei Sotomi, Pannipa Suwannasom, Hiroki Tateishi, Yoshinobu Onuma, Mustafa Yilmaz, Patrick W. Serruys

Expert Rev Cardiovasc Ther. 2016;14(9):1053-70.

ABSTRACT

Introduction: With new developments in percutaneous coronary intervention (PCI), such as the introduction of bioresorbable scaffolds (BRS), percutaneous treatment of coronary artery diseases has entered a new era. Without metallic remnants, BRSs appear able to overcome several limitations of the existing metallic stents and provide a physiologic treatment of coronary artery pathology.

Areas covered: BRS have different mechanical properties compared to the traditional metallic stents that should be taken into account during their implantation. Lesion selection, device sizing and satisfied pre-dilatation should be implemented prudently. Although intravascular imaging is not mandatory for the implantation of BRS, it may have a value in optimizing device deployment assess final results and reduce the risk of device related adverse events such as re-stenosis, or scaffold thrombosis. This review aims to reveal the crucial points about the methods of optimization of BRS implantation.

Expert commentary: The target lesions for BRS should be selected meticulously. Pre-dilatation, post-dilatation and intra-vascular imaging techniques should be implemented appropriately to avoid undesirable events after scaffold implantation.

Key words: Bioresorbable scaffold; optimal stent implantation; intracoronary imaging; optical coherence tomography; intravascular ultrasound.

1. INTRODUCTION

Percutaneous coronary intervention (PCI) has been established as one of the most efficient strategies for the treatment of coronary artery disease. The advent of the metallic drug eluting stents (DES) has enabled the treatment of complex lesions and high-risk patients and improved procedural outcomes. Nevertheless, DES have significant limitations including the risk of neo-atherosclerosis, and late stent thrombosis and restenosis which affects long term prognosis. To overcome this drawbacks bioresorbable scaffolds(BRS) were introduced in PCI[1]. These devices have the ability to resolve after their implantation allowing restoration of vessel wall structural integrity, conformability, physiologic function and reduce the risk of late complications [2,3,4]. On the other hand, these devices have several limitations which should be taken into account during their implantation. First of all, they are bulky which make difficult their deployment in tortuosity and calcified vessels. In addition, they have thick struts that affect the local hemodynamic environment and limited extensibility. These properties of BRSs require appropriate scaffold selection and optimal implantation that can be facilitated with the use of intravascular imaging. The aim of this review article is to present the current evidence about the implantation technique for BRS and the role of intravascular imaging in implantation of BRS [5].

2. OPTIMIZATION OF PERCUTANEOUS CORONARY INTERVENTION –

Lessons learnt from the metallic stents

Although there is no clear definition of optimal PCI, it can be considered the procedure that results in optimal angiographic results in post-implantation acute period (i.e., no evidence of underexpansion, edge dissection, or device malapposition) and in long-term prevention of stent thrombosis and re-intervention.

An optimal PCI requires accurate assessment of lesion dimensions i.e., length of the lesion, diameter stenosis and reference vessel diameter. Intravascular imaging before scaffold/stent deployment enables detailed assessment of lesion characteristics and provide useful prognostic information including the circumferential location of the stenosis, the length of the diseased segment, the composition of the plaque and extent of calcific burden which can be used for optimal procedure planning [6].

2.1. IVUS-guided PCI

Visual assessment and quantitative coronary angiography analysis have significant limitations in assessing the lesion characteristics [7]. Satisfactory stent expansion and strut apposition, effectively reduces in-stent re-stenosis (ISR) and thrombosis and led to substantial reduction of repeat PCIs [8]. Device under-expansion, edge dissection, incomplete apposition and incomplete lesion coverage are the IVUS predictors of adverse events following DES implantation [9-11]. A subgroup analysis from the MAIN-COMPARE registry revealed improved three-year mortality with IVUS-guidance compared to coronary angiography guided PCI after adjustment with propensity-score matching [10,12].

In BMS and DES, IVUS guided PCI was shown to reduce the angiographic re-stenosis and target vessel revascularization (TVR). The results however did not translate into a reduction of long-term mortality and non-fatal MI [13-15]. In a previous meta-analysis, IVUS-guided PCI offered a significant reduction in MACE [16]. In ADAPT-DES, IVUS guidance offered lower 1-year definite/probable thrombosis, MI, MACE, ischemic TLR and TVR rates [17]. In ACC/AHA and ESC guidelines for myocardial revascularization, IVUS is considered as a useful tool for improving stent deployment and guide coronary stent implantation [18,19].

IVUS can provide useful information about lesion length and landing zone that are essential in long and diffuse lesions [20]. By definition, the reference segment should have <40% plaque burden in the cross-section adjacent to the lesion [21]. Pre-PCI IVUS can give information about arterial remodeling, calcium extent, dissection and thrombus [22]. In case of extensive calcification debulking or aggressive pre-dilatation should be considered before device implantation [23]. Virtual Histology-IVUS(VH-IVUS) can also predict no-reflow phenomenon which appears to be more frequent in lesions with an increased necrotic core burden [24] however the way to optimize post-procedural results and reduce the risk of non-reflow remains unclear especially after the results of the recently published Canary study [25-27].

Following stent deployment IVUS can be used to detect device underexpansion and selection of the appropriate size balloon for aggressive post-dilatation with higher pressures [28]. Regarding the impact of IVUS on restenosis and adverse events, in IVUS substudies of TAXUS IV, V, and VI, TAXUS ATLAS Workhorse, Long Lesion and Direct stent trials, post-implantation MLA predicted in-stent restenosis at 9 months [9]. According to the MUSIC trial, adequate expansion is defined as >90% of the mean reference cross-sectional area (CSA) or > 100% of the smaller reference CSA with complete apposition and symmetric expansion of the device

defined by a minimal lumen diameter/ maximal lumen diameter of ≥ 0.7 (**Table-1**) [23]. In AVID trial, stent apposition with stent CSA > 90% of the luminal area in distal reference edge segment optimized the outcome of IVUS-guided PCI [29]. In HOME-DES trial, optimal PCI was depicted as apposition of the stent struts without edge dissection and adequate expansion in which minimal stent area was > 5.0 mm² or > 90% of the luminal area in distal reference segment [30].

Table 1. Intravascular ultrasound criteria for optimal stent deployment (Adapted from de Jaegere et al [23])

MUSIC criteria
Complete apposition of the stent over its entire length against the vessel wall
Minimum lumen area (MLA):
In-stent MLA $\geq 90\%$ of the average reference lumen area or $\geq 100\%$ of the reference segment with the lowest lumen area
In-stent MLA of proximal stent entrance $\geq 90\%$ of proximal reference lumen area
If the in-stent MLA is > 9.0 mm ² :
In-stent MLA $\geq 80\%$ of the average reference lumen area or $\geq 90\%$ of the reference segment with the lowest lumen area
In-stent MLA of proximal stent entrance $\geq 90\%$ of the proximal reference lumen area
Symmetric stent expansion defined by the minimum lumen diameter divided by the maximum lumen diameter ≥ 0.7
AVIO study criteria
Final minimum stent cross sectional area of at least 70% of the hypothetical cross-sectional area of the fully inflated balloon used for post-dilatation
The optimal balloon size that should be used for post-dilatation is the average of the media-to-media diameters of the distal and proximal stent segments, as well as at the sites of maximal narrowing within the stent. The value is rounded to the lowest 0.00 or 0.50 mm. For values ≥ 3.5 mm, the operator could downsize the balloon diameter based on clinical judgment.

2.2. OCT-guided PCI

In ILUMIEN I, treatment strategy changed the selection of stent length in 68% of the cases, the stent diameter in 39% and the number of implanted stents in 13% of study population [31]. Post-PCI OCT evaluation enables detecting the residual edge dissections [32] (**Figure 1**) and

stent under-expansions, optimize final results and improve clinical outcomes – in the ILUMIEN I study the event rate was only 1.5%(patient-oriented MACE) [31] Similarly in the ILUMIEN II trial, the MACE was significantly lower in the OCT guided optimization subgroup and the modifications made according to OCT imaging results culminated in decreased peri-procedural myocardial infarction(MI) rates [33].

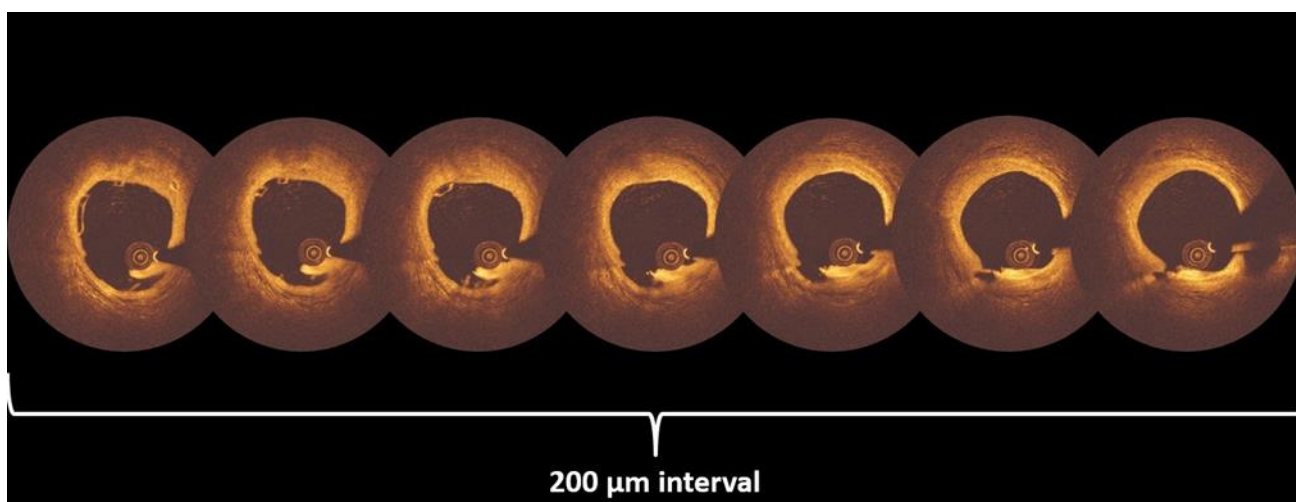


Figure 1. An example of edge dissection proximal to the Absorb BVS within 200 μm OCT interval

The morphology of the plaque derived from OCT can be useful to select best strategy for PCI. OCT has similar accuracy in detection of the calcified plaques as IVUS [34]; with its circumferential extent, it also enables detection of the depth of the calcific tissue. This information can be used to decide the approach for lesion preparation (i.e., balloon pre-dilation vs. debulking) which is essential in BVS. OCT-detected thin-cap fibrous atheroma (TCFA) is a significant predictor of peri-procedural MI and no-reflow after device implantation [35,36]. Microvascular obstruction and no-reflow phenomenon were seen more often in lesions with an increased lipid arc and thin fibrous cap [37]. OCT enables differentiation between plaque rupture and erosion for defining the cause of intravascular thrombus formation. In plaque erosion, without stent implantation, only thrombus retrieval can be enough for establishing adequate coronary flow especially in cases without significant luminal stenosis [38].

In OCT, malapposition is defined in cases that the distance between the abluminal edge of the strut and the vessel wall is more than the thickness of the strut (**Figure 2**). The degree of malapposition is characterized by the arc of the malapposition, length of the malapposition

and the distance between malapposed struts and the vessel wall. Small malappositions can be covered with endothelial layer [39], on the other hand significant malapposition (>200 micron) is a risk factor for stent thrombosis in acute phase [8,40]. Tissue protrusion between the struts can be detected by OCT, and appears as a predictor of peri-procedural MI [36,41]. While tissue protrusion between the struts is characterized by smooth surface and absence of signal attenuation, the protrusion of thrombus is depicted as an irregular surface with signal attenuation [41]. OCT can detect edge dissections after device implantation, better than IVUS [43]. If there is no stenosis in the true lumen, the dissection may not need further intervention [39].

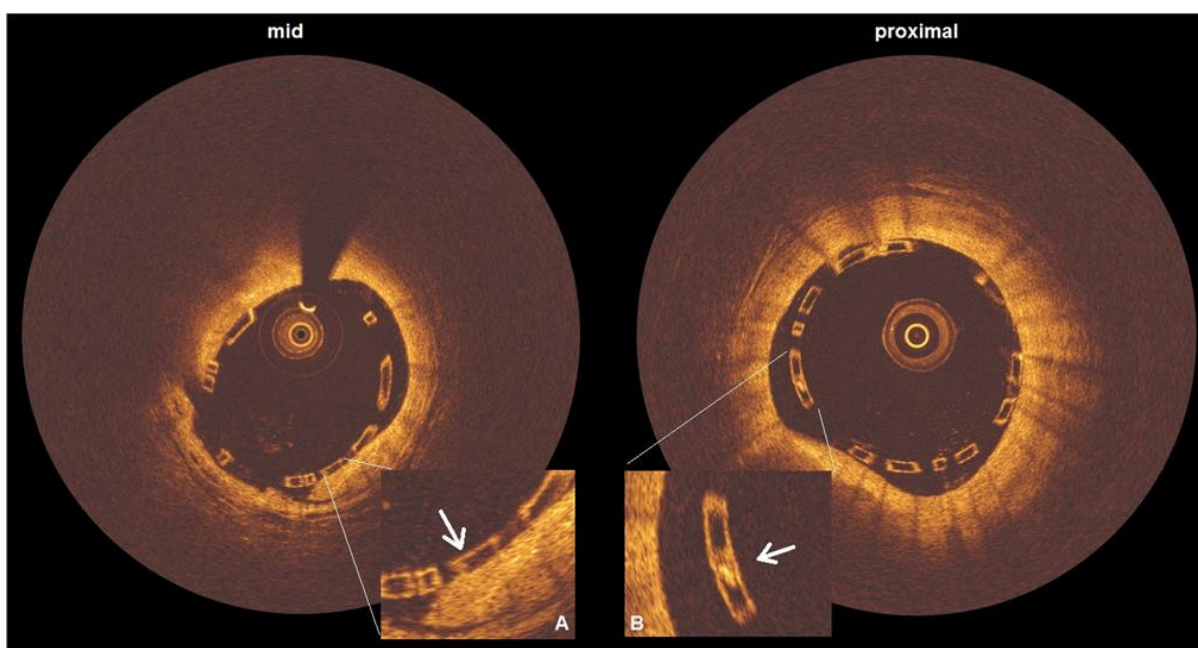


Figure 2. Incomplete strut apposition in mid and proximal segments of the scaffold. There is an example of apposed strut in A (white arrow), and malapposed strut in B (white arrow).

Fourier domain-OCT(FD-OCT) renders precise investigation of the coronary lumen. In OPUS-CLASS trial [42], FD-OCT afforded exact quantification of the vessel lumen with reliable intra-observer reproducibility. In CLI-OPCI study, in comparison to the group with coronary angiography guidance alone, the group with angiography-plus-OCT guidance had less cardiac death, MI and lower rate of the composite of cardiac death, MI, or repeat revascularization at 1-year; adding OCT guidance was independently associated with a significant lower risk of cardiac death or MI (odds ratio =0.49 [0.25-0.96], $p=0.037$) [43].

2.3-Assessment of coronary stent deployment using computer enhanced x-ray images validation

Conventional X-ray coronary angiography systems have significant limitations in visualizing the stents' deployment. Recently some computer enhancement algorithms have been introduced to improve stent visibility in X-ray angiograms [44-46]. StentBoost, IC stent and StentOP are some of the commercialized software [47]. These enhancement systems aim to reduce the radiographic contrast used during stent implantation and detect stent underexpansion. Compared to the IVUS, these digital enhancement systems don't add cost, time and don't increase the risk for any procedural complication [48].

3. PCI WITH BIORESORBABLE SCAFFOLDS

The ABSORB BVS (Abbott Vascular, Santa Clara, CA, USA) and the DeSolve BRS (Elixir Medical, Sunnyvale, CA, USA) are the only BRS that are currently commercially available; in this review we will focus on the ABSORB BVS which has been tested in numerous clinical trials and have recently acquired FDA approval. Absorb BVS is made of PLLA, coated with a layer of a 1:1 mixture of an amorphous matrix of poly-D, L-lactide (PDLLA) and elutes everolimus (8.2 µg/mm). Absorb BVS is manufactured using extrusion and laser machining techniques and has 157 µm strut thickness composed of in-phase zig-zag hoops linked with bridges design [49].

3.1-Target patient population for BRS

Though there is no randomized data, from "real-world" experience, it seems that patients who have long segment disease and need multivessel PCI are suitable for treatment with BRS to reduce the risk of ST and in-stent restenosis (ISR)[50,51]. Another patient subset that could benefit from PCI with BRS is long LAD disease that is not suitable for coronary artery by-pass graft (CABG) or "full metal jacket", since full metal stent implantation of the vessel has increased ST and ISR risks [51]. Younger patients seem to get benefit by BRS implantation as the BRS implanted vessel can be treated with additional PCI or CABG in the future. The lesions/patients that appear suitable for Absorb BVS are summarized in **Table 2**; this table was generated according to the details from ABSORB Cohort A[52], ABSORB Cohort B[53], ABSORB EXTEND[54], ABSORB II trials[55]. Recently published, ABSORB III was a non-inferiority study and recruited 2008 patients with up to 2 de novo lesions. The patients will be followed up for at least 5-years. TLF at 1-year occurred in 7.8% of the patients in the Absorb BVS group and in

6.1% of the patients in the Xience group (difference, 1.7 percentage points; 95% confidence interval, -0.5 to 3.9; P=0.007 for non-inferiority and P=0.16 for superiority) [56]. In ABSORB IV trial, 3000 patients are planned to be included and randomized to ABSORB BVS and Xience V stent implantation at 1:1. Follow-up will be at least 5-years in 160 US and non-US sites. Primary end-point is TLF between 1 and 5 years [57].

Table 2. Ideal patients for Absorb BVS

The lesions/patients included in the previous trials	The lesions/patients excluded from the previous trials	Ideal patients for Absorb BVS	Uncertain or Off-label use
<ul style="list-style-type: none"> -‘De novo’ lesions -Diameter 2.3–3.8 mm -Length max. 28 mm -Stable angina, unstable angina or ^{silent} ischaemia -Maximum 2 lesions 	<ul style="list-style-type: none"> -Left main coronary artery -In-stent restenosis -Ostial lesions -Chronic total occlusions -Bifurcation lesions with side branches \geq 2 mm diameter -Diffuse and excessive calcifications -Severe tortuosity -Thrombotic lesions -STEMI -LVEF<30% -Arterial and venous bypass grafts 	<ul style="list-style-type: none"> -Diffuse disease of LAD that requires long stents -Diffuse disease of the vessel \geq 2.5 mm requires long stents -Young patients -Any patient with good life expectancy (> 5 years) -Age<70 years -Age 70-80 years with one of the following situations; PAD, COPD, CVA, renal failure, DM, BMI > 40 or LVEF < 40 % - ‘De-novo’ lesions with max 28 mm length 	<ul style="list-style-type: none"> -Bifurcation PCI with 2-scaffold approach -Chronic total occlusions -Lesions with extensive calcifications -In-stent restenosis -Arterial/venous bypass grafts -Vessel >4.0 mm diameter

PAD: Peripheral artery disease, COPD: Chronic obstructive pulmonary disease, CVA: cerebrovascular accident, BMI: Body mass index, LVEF: Left ventricle ejection fraction

The ostial lesions seem not to be in favor of BRS implantation due to higher residual stenosis and scaffold thrombosis rates [58,59]. In aorto-ostial lesions, high radial-strength stents are recommended. In GHOST-EU trial, ostial lesions increased the hazard ratio for TLF [58]. Previous case reports and a single-center registry (OCTOPUS) evaluated the feasibility of BRS implantation in saphenous vein grafts (SVG) [59-62] and demonstrated that their implantation in SVG lesions is feasible if the graft has a diameter up to 4 mm. The malapposed strut ratio was comparable to that observed in native coronary arteries while the neointimal coverage ratio was less evident probably because of the morphological features of the SVG. There should be more randomized studies for the evaluation of SVG for the PCI with BRS.

3.2-General implantation rules for the PCI with BRS: *Indispensables for BRS (Table 3)*

3.2.1-Evaluation of the patient and lesion suitability

As a general rule, BRS should not be deployed in lesions that cannot be adequately prepared with balloon pre-dilatation; pre-dilatation should result in <40% residual stenosis and the balloon should be fully expanded. Insufficient pre-dilatation, may result in BVS under-expansion, that is associated with a risk of thrombus formation or restenosis [63]. Lesion location is also important for scaffold implantation. In case of heavy tortuosity and calcifications, it may be challenging to advance the device to the diseased segment. The vessels with >4.0 mm diameter should not be selected for the implantation. The left main lesions need scrutiny owing to its large size [63].

Table 3. Technical facts for Absorb BVS implantation (modified from Rzeszutko Ł, et al [70] and Everaert B et al [109])

Technical implementation	Details
Lesion selection	Excessive calcification or tortuous segments should be abstained to preclude device displacement. Limited clinical data for bifurcation cases, chronic total occlusion, left main disease, in-stent restenosis or coronary bypass graft; no randomized trials for these clinical cases.
Device selection	1-QCA-Dmax [proximal and distal Dmax] Proximal and distal Dmax values in the range: For lesions with 2.0-3.0 mm – Absorb BVS 2.5 mm, For lesions with 2.5-3.3 mm – Absorb BVS 3.0 mm, For lesions with 3.0-3.8 mm – Absorb BVS 3.5 mm should be selected. 2) One of the values outside of these ranges – the selection of the scaffold diameter depends on the operator's decision. 3) IVUS and OCT can be helpful for true reference vessel diameter in case of doubt.
Predilatation	1)Pre-dilatation is sine qua non with a balloon size with a 1:1 balloon / scaffold size ratio 2) NC balloon with equal size to planned scaffold should be considered in case of persistent %DS > 40% following first attempt of pre-dilatation 3)The scaffold should not be implanted unless adequate preparation with pre-dilatation
Device delivery to the target lesion	1) Apply with constant tension on the introductory system and should avoid dotter technique. 2) Repeated introduction of the retracted scaffold may cause damage to the scaffold and a new device should be used after 30 min of the first attempt. 3) In case of any resistance on the guiding catheter, the whole system should be removed together with the guiding catheter.
Device deployment	1)Progressive inflation by 2 atm every 5 s minimal total time of inflation is 30 s, RBP should not be exceeded. 2)In case of overlapping of 2 scaffolds, the first device should be implanted distally and the overlapping segment should be confined to 1-4 mm.
Post-dilatation	Post-dilatation should be performed in cases of residual stenosis≥10% and performed by high pressure using NC balloon whose diameter should not exceed 0.5 mm over the nominal value of Absorb BVS. After scaffold implantation, dual antiplatelet therapy is recommended for a minimum of 12 months and it should be prolonged upon the clinical situation

3.2.2-Target segment preparation and Scaffold size selection

Quantitative coronary angiography (QCA) and intravascular imaging modalities appear to enable more accurate device sizing than visual inspection of coronary angiography which is associated with a high inter- and intra-observer variability. During QCA, the maximal lumen diameters (Dmax) in the proximal and distal vessel segment of interest are extracted using an interpolated diameter line that is produced from the proximal to the distal healthy segments. This interpolated line gives an average of the proximal and distal vessel diameters and renders a reference diameter at the site of minimal lumen diameter within the diseased segment. For a Dmax lower than 2.5 or higher than 3.3 mm, a 3.0 mm Absorb BVS will be too big or too small respectively, for the vessel segment. The tapering of the target segment should also be taken into account; in case of tapering, scaffold size selection is performed upon the proximal vessel diameter or interpolated method [64]. On the other hand, OCT analysis reported that the interpolated method may underestimate the maximal lumen diameter [65] and implantation of the Absorb BVS in a large vessel can result in malapposition which cannot be treated with scaffold overexpansion due to the risk of strut fracture [66]. Conversely, in case of scaffold implantation in vessels smaller than the nominal size of the scaffold, edge dissections can be inevitable. To overcome these limitations Dmax measurement has been suggested where the oversizing of the scaffold is minimized compared to the interpolated reference vessel diameter measurement (**Figure 3**) [64].

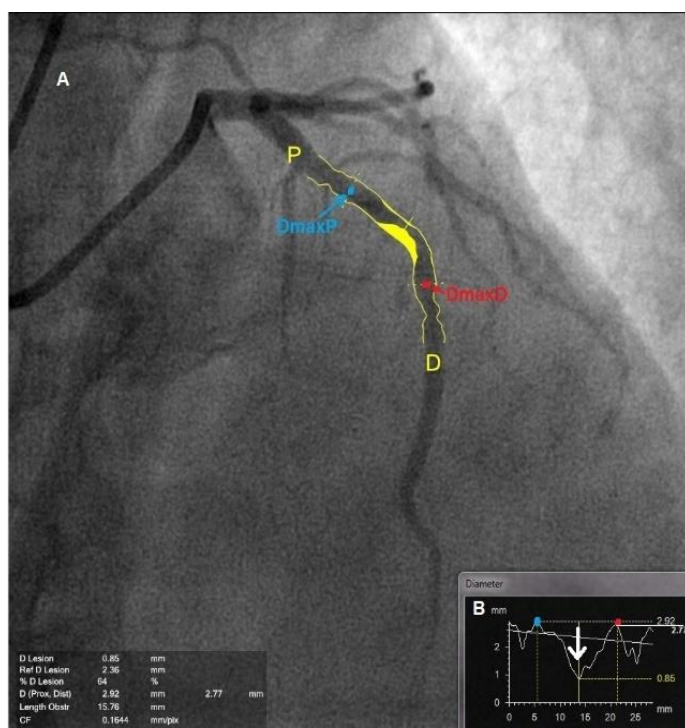


Figure-3: The method used to measure proximal and distal Dmax with QCA is shown. In the pre-procedural angiography (A) the operator should define the landing zone (white arrow) (B) where the scaffold will be implanted. Within the landing zone, the peak of the diameter function curve proximal to the minimal lumen diameter is defined as proximal (P) Dmax, whereas the peak diameter function curve distal (D) to the minimal lumen diameter is defined as distal Dmax (D). In this case, the proximal and distal Dmax of 2.92 and 2.77 mm led to the correct sizing of the Absorb (3.0 mm) with regard to the vessel diameter (E). DMAXD = maximal lumen diameter distal; DMAXP = maximal lumen diameter proximal; MLD = minimal lumen diameter; QCA = quantitative coronary angiography; RVD = reference vessel diameter.

3.2.3-Lesion preparation

Preparing the lesion with balloon inflation before the BRS implantation is a *condicio sine qua non* for a satisfactory implantation. Predilatation should result in residual stenosis less than 40%, otherwise underexpansion instigates intimal hyperplasia or thrombosis [67]. It is recommended that the ratio of balloon reference vessel diameter should be 1:1. Even in heavily calcified lesions, in tortuous lesions or in lesions located in angulated vessel segments, pre-dilatation is essential using balloons with increased diameter. Though, there is no evidence to support the use of non-compliant (NCB) balloons over compliant balloons (CB) we recommend pre-dilatation with NCB as it allows a more controlled and aggressive – if needed – lesion preparation [68]. In case of heavy calcification which hampers expansion, high-pressure balloons, cutting balloons and rotational atherectomy are the choices that can be considered.

3.2.4-Scaffold implantation

The 2.5 mm and 3.0 mm diameter device of the Absorb BVS has a crossing profile of $\leq 0.060''$ and the 3.5mm scaffold a crossing profile of $\leq 0.065''$, therefore optimal lesion preparation is essential for advancing the scaffold to the lesion [69]. During the difficulties in crossing the lesion a supportive guidewire or a guide extension (i.e., GuidLiner®; Vascular Solutions, Inc., Minneapolis, MN, USA, or Guidezilla®; Boston Scientific, Marlborough, MA, USA) should be considered. The 7Fr- GuidLiner provides an adequate inner diameter (0.071'' ID) and this device requires an 8F guiding catheter. The deployment process should be held out in more than 30 seconds by a pressure increase of 2-atm in every 5 seconds till acceptable maximal nominal pressure and complete expansion of the scaffold [70]. The limit for overexpansion should be 0.5 mm plus the nominal diameter of the device. In a successful expansion, the residual luminal diameter stenosis should be $<10\%$. If residual diameter stenosis is $\geq 10\%$, post-dilatation should be undertaken with a NCB at higher pressures. The scaffold should cover at least 2 mm healthy segment at the proximal and distal segment so as to avoid geographical miss. Three important points should be mentioned; 1- BVS implantation should be performed only in case of full expansion of the NCB as demonstrated by coronary angiography in 2 orthogonal planes, 2- Implantation of a BVS should be the same size as the RVD at 10 atm to 12 atm, 3-post-dilatation should be implemented with NCB up to a maximum of 0.5 mm larger at 14-16 atm [71]. For the lesion with Dmax 2.0 mm-3.0 mm, Absorb BVS with 2.5 mm should

be chosen. For the lesions with 2.5-3.3 mm Dmax, 3.0 mm Absorb BVS should be chosen. During post-dilatation, Absorb BVS with 2.5 mm should be post-dilated with 2.75 mm or 3.0 mm balloons not exceeding the 3.0 mm balloon size. Absorb BVS with 3.0 mm diameter should be post-dilated with 3.25 mm or 3.5 mm balloon which should not exceed 3.5 mm. For Absorb BVS with 3.5 mm, post-dilatation with 3.75 mm or 4.0 mm balloon that should not exceed 4.0 mm can be used [70].

3.3-Factors affecting PCI with BRS

3.3.1-Device related factors: Absorb BVS has a crossing profile as 1.43 ± 0.02 mm which is more than its metallic equivalent stent CoCr-EES (1.14 ± 0.01 mm) and thicker struts. These properties often render scaffold delivery and deployment a challenging procedure. Owing to its bulky structure, overlapping of two BRS should be minimized and confined to large vessels (>3.0 mm) (**Figure 4**).

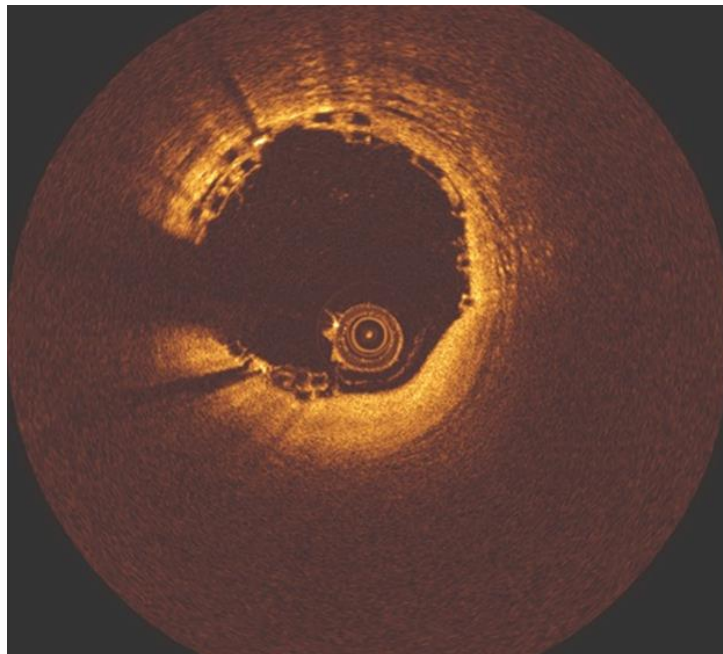


Figure 4. Two overlapped Absorb BVS with radiopaque metallic markers.

Absorb BVS has lower radial strength than its equivalent CoCr platform (Xience V) (1.4 ± 0.2 atm vs. 1.6 ± 0.1 atm, $p=0.02$ in Mercy test, 1.1 ± 0.1 atm vs. 1.3 ± 0.1 atm, $p=0.02$ in Elixir test) [72] and therefore there is a risk of device underexpansion that is associated with an increased risk of acute scaffold thrombosis. On the other hand, overexpansion of the scaffold should also be avoided since BVS can be overexpanded by only 0.5 mm; further post-dilatation is associated with a risk of scaffold fracture [73].

3.3.2-Vessel related factors: Within the vessel related factors, vessel diameter, lesion length, lesion calcification, chronicity of the occlusion, side branches and the bifurcation status should be considered. In ABSORB Cohort A, ABSORB Cohort B, ABSORB EXTEND and ABSORB II trials, de novo lesions with 2.3-3.8 mm diameter and short lesions- to avoid deployment of a 2nd device and scaffold overlapping- were included [52-55]. Within nominal pressure, the largest available Absorb BVS has a nominal diameter of 3.5 mm, hence vessel larger than 4.0 mm in diameter should not be treated with Absorb BVS. Heavily calcified lesions may be adequately prepared with a rotablator before BRS implantation. To date only sporadic cases have been reported for preparing the calcified lesion with cutting balloon and rotational atherectomy [74].

3.4-Optimization after scaffold implantation

The interventionalists with a large experience of BRS implantation are performing high pressure post-dilatation with a NCB size 0.25 or 0.5 mm larger than the nominal size of the device [70]. Despite the bench test showed that Absorb BVS had a larger acute gain [72], the acute gain in RCT (ABSORB-II) was demonstrated to be lower [55]. This should be due to higher dilatation pressure and balloon diameter at the highest-pressure during implantation or post-dilatation in the metallic stent arm in the study. Thus, more aggressive strategy can be promoted during Absorb BVS implantation with respecting the safety limit of size and pressure.[73]

3.4.1-Quantitative Coronary Angiography

Acute luminal gain after implantation and late lumen loss at follow-up predicate scaffold stenosis in earlier and late phases following implantation. For acute recoil estimation, 2 definitive images in QCA should be evaluated in the same angiographic projection; the first image should be acquired during scaffold expansion of the last balloon inflation (i.e., the scaffold delivery balloon or the post-dilatation balloon) at the highest pressure and the second image frame should be obtained after the last balloon deflation and following nitrate administration. Acute scaffold recoil is calculated as $[(\text{mean diameter of the scaffold delivery balloon at the highest pressure}) - (\text{mean luminal diameter of scaffolded segment immediately after implantation}) / (\text{mean diameter of the scaffold delivery balloon at the highest pressure})]$. In two studies the acute recoil was not different between the Absorb BVS and the metallic EES [75] [55]. Late lumen loss and late luminal gain are the difference between the minimal lumen diameter (MLD) immediately after scaffold implantation and the MLD at follow-up. Vasomotor

assessment provides evidence of scaffold dismantlement and restoration of the endothelial function reacting to administered nitroglycerin and acetylcholine. After intracoronary Acetylcholine administration the mean lumen diameters in the scaffolded segment is measured. Vasoconstriction after Ach is characterized as 3% difference in mean lumen diameter. In Absorb BVS, at 24-month, there was an obvious increase in the mean lumen diameter after Ach administration compared with patients at 12 months [+6.16 (-1.07, +13.14) vs. -6.41% (-11.74, -1.17); $p = 0.006$] [2].

3.4.2-Gray-scale Intravascular Ultrasound

Following scaffold implantation, IVUS can be used to assess scaffolded segment and 5-mm edge segments to measure the lumen area, scaffolded area, neointimal area and intra-scaffold luminal stenosis area.

Symmetry and eccentricity are metrics that have been used to evaluate scaffold apposition. Eccentricity is the ratio of the minimum and maximum diameters in the related cross-section. Symmetry index is the ratio of the minimum scaffold diameter to the maximum scaffold diameter (Figure 5A and 5B).

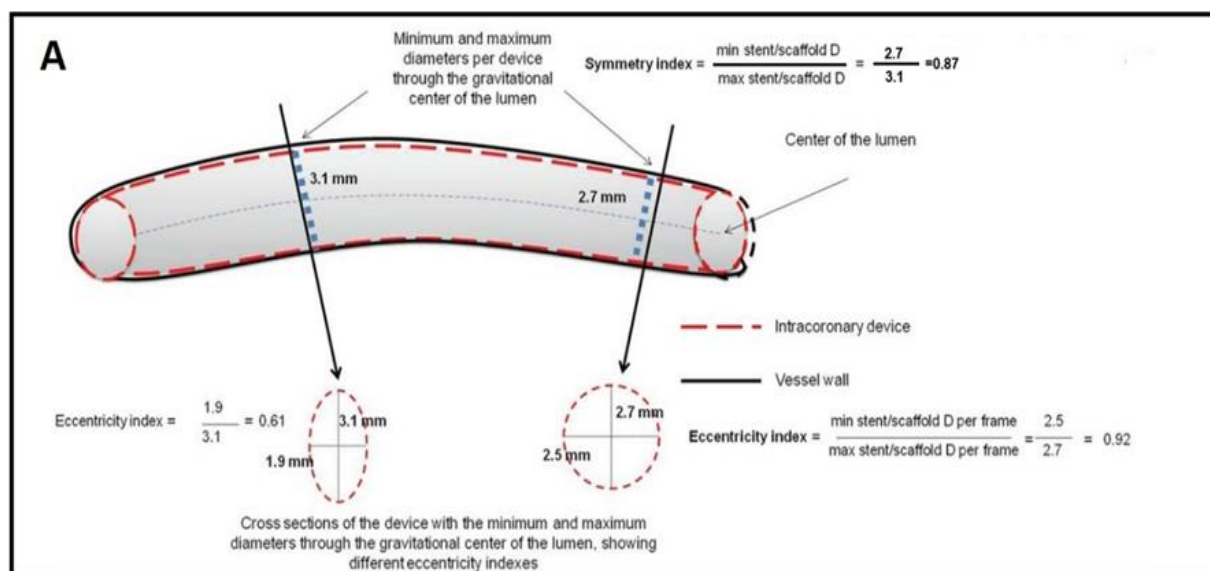


Figure 5A. Relationship between the symmetry and eccentricity indices of an intracoronary device. Minimum and maximum diameters over the length of the device are shown. Two cross-sections with different eccentricity indices are also shown (Adapted from Brugaletta et al. Catheter Cardiovasc Interv. 2012;79(2):219-228)

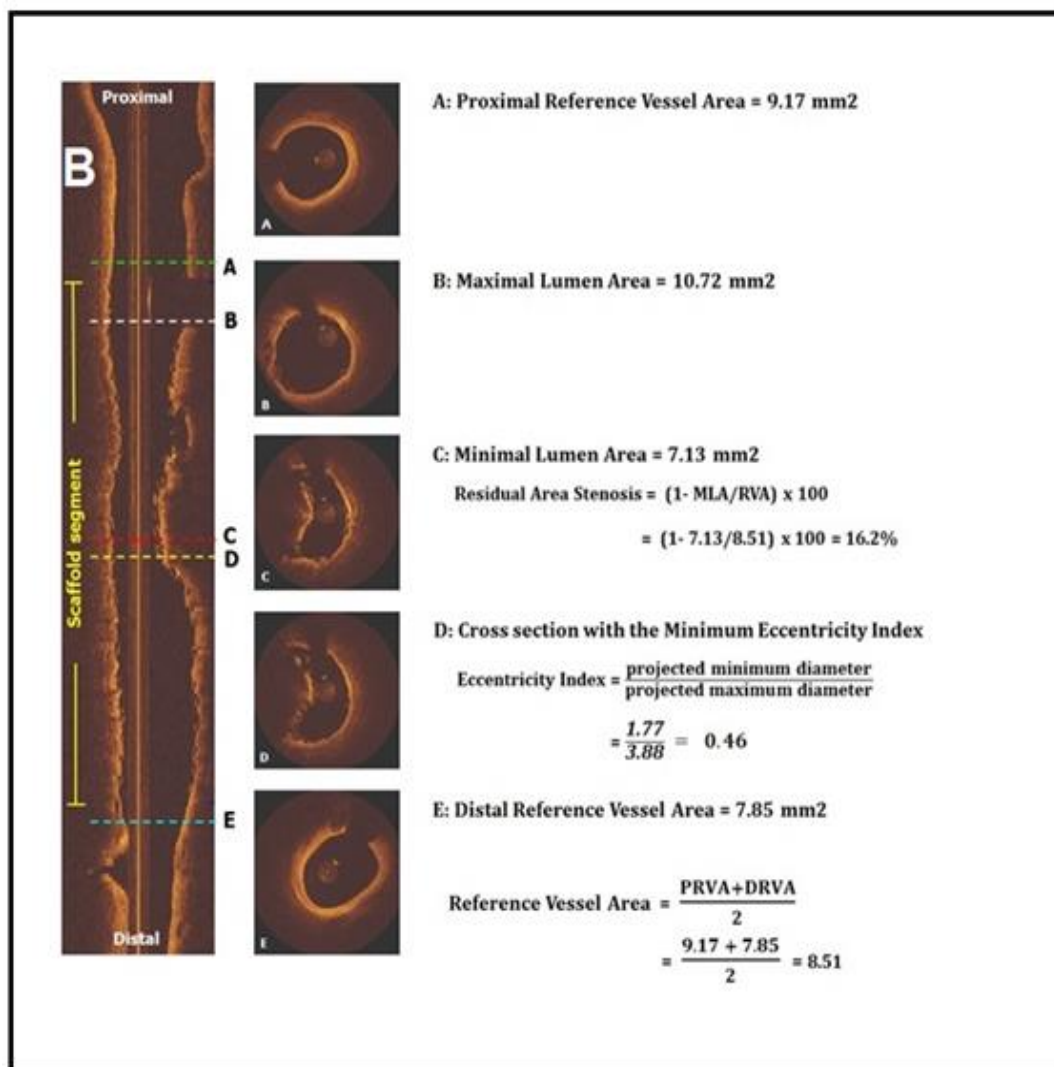


Figure 5B. OCT cross-sectional images illustrating the calculations of reference vessel area (A and E), eccentricity index (D), maximal and minimal lumen area (B and C). Abbreviations: MLA – minimal lumen area; RVA- reference vessel area; DRVA – distal reference vessel area; PRVA – proximal reference vessel area

With IVUS, incomplete apposition is defined as at least 1 strut separation from the vessel wall. In the analyses of Brugaletta et al, lesions treated with the Absorb BVS had higher eccentricity and symmetry index compared to the metallic EES, without significant impact in MACE, at 6 months follow-up [76]. An eccentricity value of 0.7 has previously been shown to be an acceptable cut-off in the evaluation of good stent expansion in the MUSIC trial, with favorable angiographic results seen at 6-month follow-up [23] It should be noted that underexpansion and low eccentricity index may be associated with thrombus formation and scaffold thrombosis after implantation (**Figure 6 and 7**). Late scaffold recoil is the reduction of the scaffolded segment which is the result of the constriction of the external elastic membrane at follow-up. Late recoil is measured as the difference of the scaffold area post-implantation and

scaffold area at follow-up. Of note in the Absorb BVS 1.1, the mean scaffold area increased from baseline to 3 years by IVUS (6.3 to 7.1 mm²) and by OCT (7.8 to 8.6 mm²) [77].

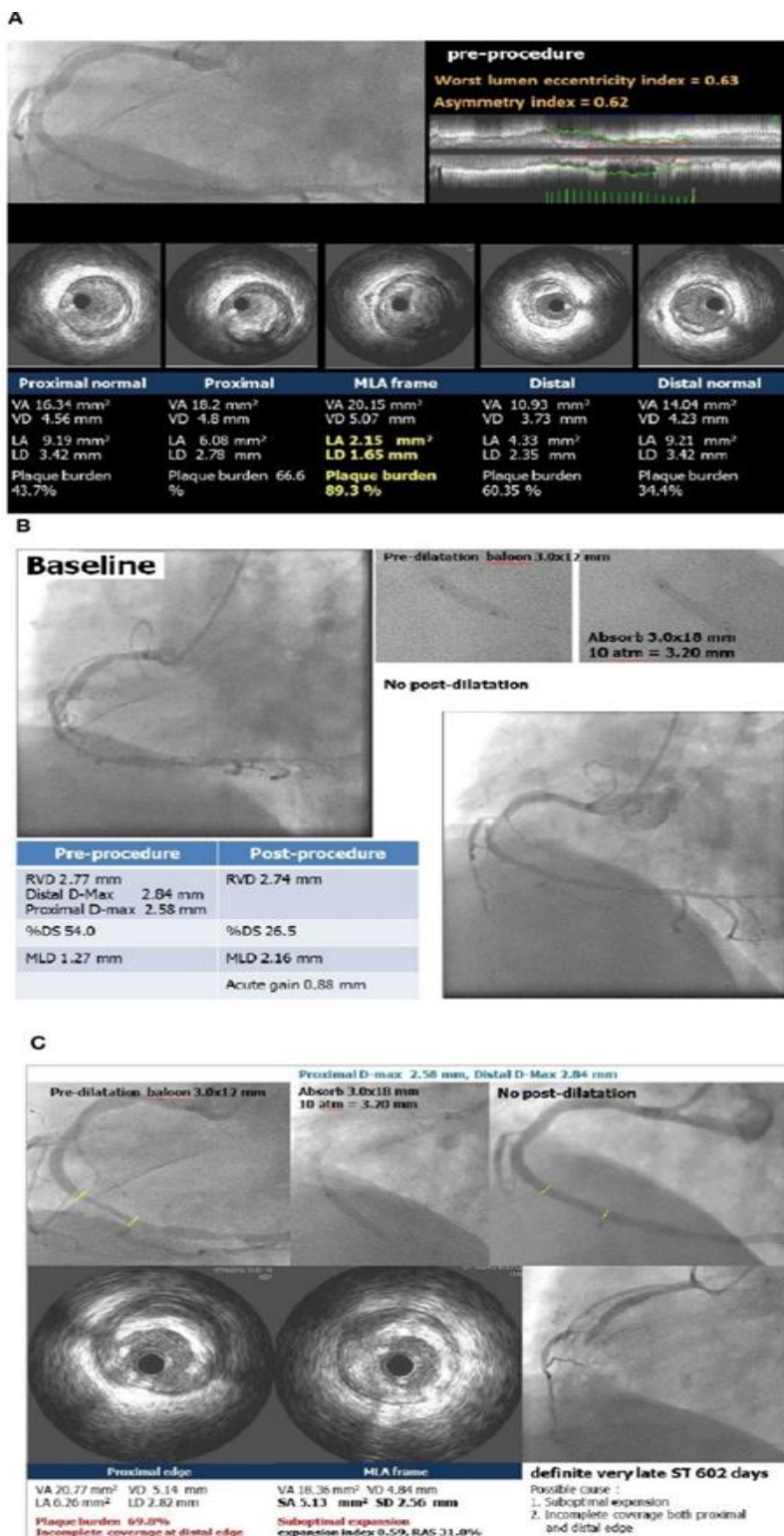


Figure 6. Implantation of Absorb BVS (3.0 x 18 mm). after implantation, the residual diameter stenosis is 26.5%. Acute gain is 0.88 mm (A). In the segment of MLA plaque burden is 89.3%. Note that the worst lumen eccentricity is 0.63 and asymmetry index is 0.62 (B). Due to underexpansion of the scaffold and incomplete coverage of the lesion both at proximal and distal scaffold edges, stent thrombosis occurred at 602 days (C).

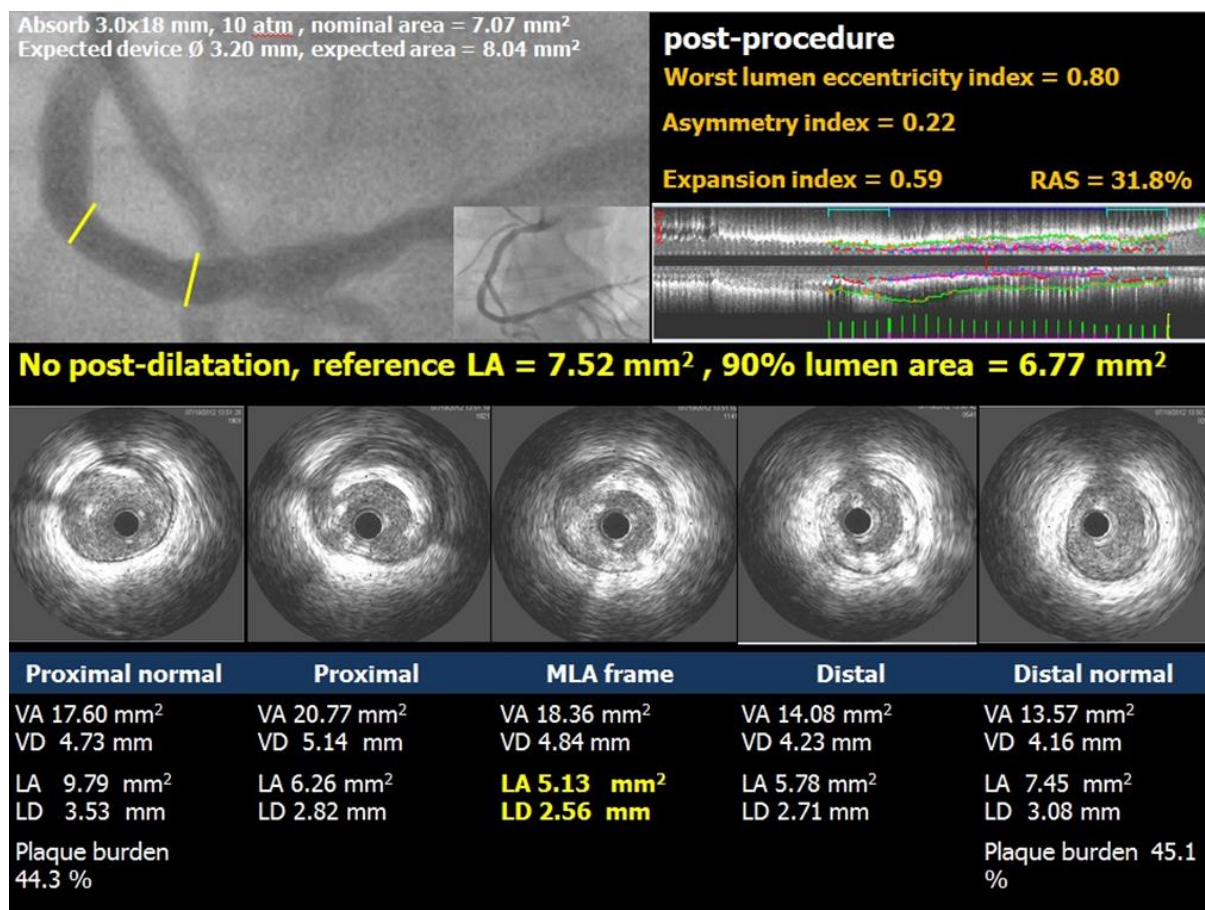


Figure 7. Post-procedural evaluation of the case in Figure 3. After scaffold implantation worst lumen eccentricity index is 0.80, asymmetry index is 0.22, expansion index is 0.59 and residual area stenosis (RAS) is 31.8%. Note that according to MUSIC criteria, the MLA (5.13 mm²) is under the 90% of the mean reference lumen area (7.52 mm²).

3.4.3-Optical Coherence Tomography

Similarly, to IVUS, OCT can be used to assess lesion dimensions and the composition of the plaque. If there is inadequate lesion preparation or calcium bridges after pre-dilatation, metallic stents should be considered instead of BVS, to prevent underexpansion and significant recoil. OCT imaging may also allow assessment of the ostium of the side branches that enables prediction of acute occlusion or plaque shifting at SB area.

Following scaffold implantation, OCT can be used to assess the strut area, strut core area, neointimal area, lumen area, scaffold area, incomplete scaffold apposition area and eccentricity index. The strut area consists of the core black area plus the surrounding light-scattering border (**Figure 8**). However, at follow-up with endothelial coverage and intimal thickening the strut area is defined only by the core-black area due to the absence of the light-scattering frame owing to the surrounding tissue [78]. The scaffold and lumen area can be

extracted by software that incorporates semi-automated detection algorithms. Following scaffold implantation, the lumen area is traced at the back side (abluminal) of the struts.

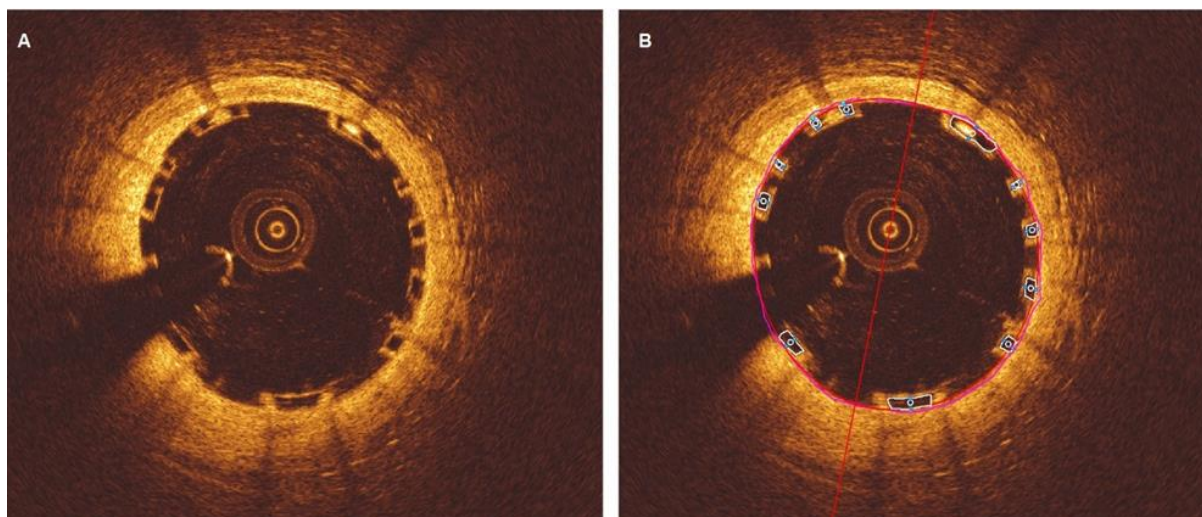


Figure 8. Representation of apposed struts

At follow-up, the endoluminal contour of the neointima defines the luminal area. In case of malapposition, the endoluminal contour should be behind the malapposed struts (**Figure 9**). The scaffold area is delineated by the abluminal edges of the struts.

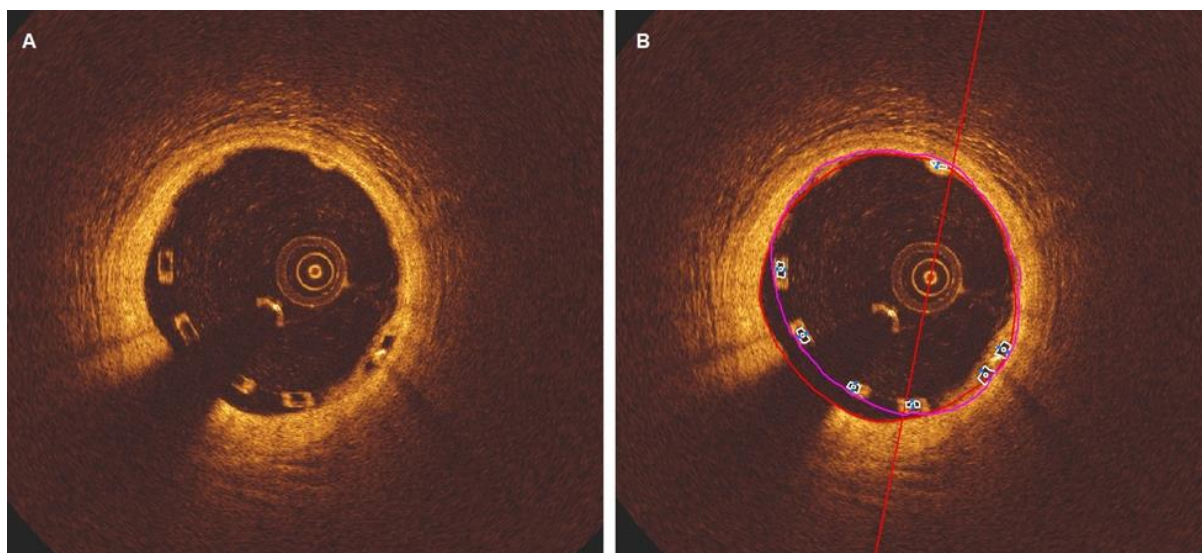


Figure 9. In malapposition, the endoluminal contour should be behind the malapposed struts (red). The scaffold area is delineated with the contour joining the mid-points of the abluminal edge of the frame borders of the struts (pink).

The neointimal coverage is measured between the abluminal side of the strut core and the luminal contour after subtracting 150-micron strut thickness from this measurement.

Neointimal hyperplasia area is the difference between the scaffold area and the of lumen area plus the black box area [78] (**Figure 10 A-H**).

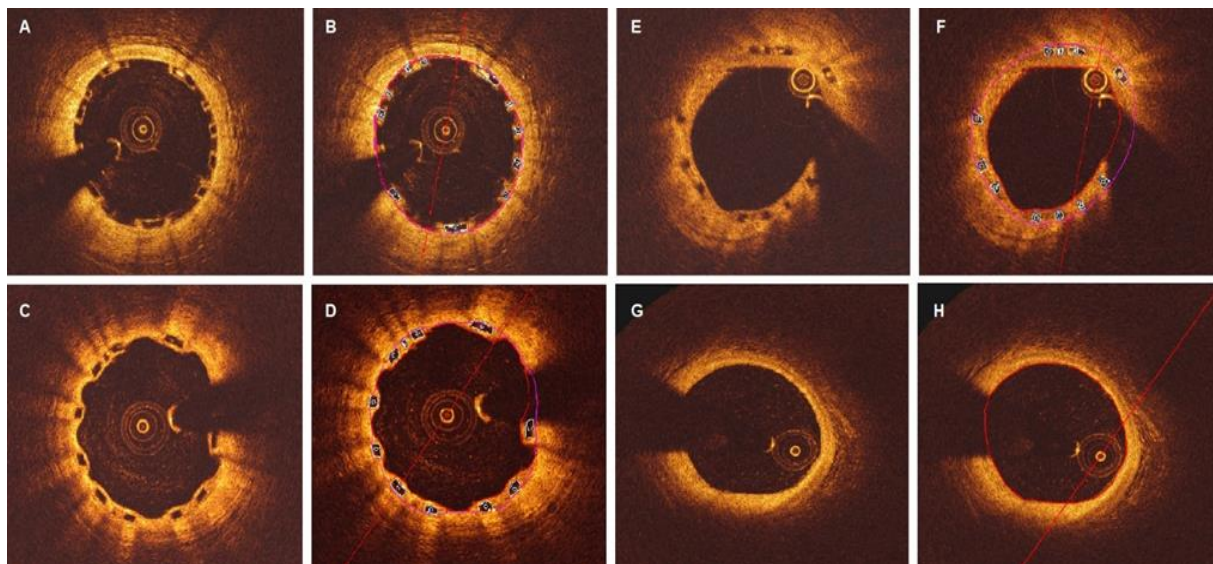


Figure 10. Neointimal hyperplasia area is the difference between the scaffold area (pink contour) and the sum of lumen area (red contour) and black box area(white). Panel A and B show baseline after scaffold implantation, Panel C and D show 1-year follow up after implantation, Pane E and F show 3-year follow up after implantation, Panel G and H show 5-year follow up after implantation. Note that, at 5 year no strut sign detected anymore.

OCT is the prominent method for assessing and treating the strut apposition, edge dissection, thrombus formation or strut disruptions. The reference vessel size determines the treatment of scaffold malapposition or scaffold underexpansion; if the vessel diameter is >4.0 mm and there is significant malapposition, a second metallic DES should be deployed. In case of a thrombus within the scaffolded segment, thrombus aspiration, plain old balloon angioplasty (POBA) and a glycoprotein IIb/IIIa inhibitor [GPIIb/IIIa] can be used. In case of edge dissection, a second BRS or a metallic DES can be deployed. During the assessment of BVS at long-term follow-up, assessing the neointimal coverage of the struts, the neointimal hyperplasia intensity and the recoil patterns can be accomplished by OCT evaluation. [78].

3.5-The effect of Optimization on long-term follow-up

PCI optimization in BRS appear to be associated with better long-term outcomes and reduces the risk of scaffold thrombosis and ISR. Several factors have been associated with scaffold thrombosis and ISR. Advanced age, renal failure, presentation with acute coronary syndromes, diabetes mellitus, smoking, history of CABG, poor left ventricular ejection fraction, early discontinuation of DAPT, resistance to P2Y12 inhibitor are patient-related factors which are

associated with high risk of BRS failure. Bifurcation lesion, heavy calcified lesions, long lesions and CTO are lesion-related factors that can be associated with device failure. Procedure related risk factors are strut malapposition, undersized stents, in-stent and edge dissections, stent overlapping, longer stent lengths, increased strut thickness which engender flow disruptions within the scaffolded segments and geographical miss. To overcome these issues, adequate post-dilatation, prolonged antiplatelet treatment after the implantation (at least 12 months), further dilation with balloons for malapposition and bail-out stenting of dissections are the treatment options that can be implemented. Excessive neointimal hyperplasia should be treated with a drug eluting balloon (DEB) within the 6-month after scaffold implantation. However, after 6-month since the scaffold structure begins to deform due to the PLLA and PLA hydrolysis, the radial strength of the device decreases and thus ISR should be treated with an additional metallic device (BMS or DES) instead of using a DEB [79].

3.6-Specific lesion subsets and technical difficulties

The ongoing multicenter AIDA (Amsterdam Investigator-initiated Absorb strategy All-comers) trial will provide more insights into the use of BVS in complex lesions [80]. Also COMPARE-ABSORB which was presented in EuroPCR 2015 is an ongoing trial investigating the non-inferiority of Absorb BVS to the metallic EES regarding TLF at 1-year and 5-year [81]. The patients who is at high risk for re-stenosis such as known diabetes, multivessel disease, lesion with length >28 mm, small vessels (target lesion reference vessel diameter between 2.25-2.75 mm) and bifurcation lesion with single stent strategy, are the target population for recruitment to the trial.

3.6.1-Bifurcations:

Despite the current recommendation that doesn't indicate BVS implantation across a SB ≥ 2 mm in diameter (Instructions for Use Manual 2012, Abbott Vascular, Santa Clara) there are concerns that the thicker struts of the BVS may cover SB orifice, that rewiring of the SB will be difficult through the thick struts and there can be the risk of scaffold fracture while trying to rewire the SB or in case of bail-out stenting of SB. In bifurcation lesions provisional stenting technique should be preferred if BRS are used. In case of SB intervention, proximal optimization technique (POT) and SB dilatation with a 2.0- or 2.5-mm NCB at low pressures followed by POT is the suggested bail out strategy [68,72]. OCT or IVUS can be used to assess the ostium of the SB. In case of significant stenosis and the risk of acute occlusion, the SB

ostium should be pre-dilated at low pressure with a NC balloon followed by simultaneous inflation of the MB and SB with the SB balloon protruding marginally (not kissing balloon) in the MB. If stenting is needed in SB, a 2.5 mm BVS can be used and forwarded through the struts of the BVS in MB. If there is problem in advancing the second BVS through the struts of the BVS in MB, a low-profile metallic DES can be considered [51,63,83] (**Figure- 11**). In case of the protrusion of the BVS in SB into the scaffold of MB, the crush technique can be used as a salvage approach to restore the disrupted geometry [84,85].

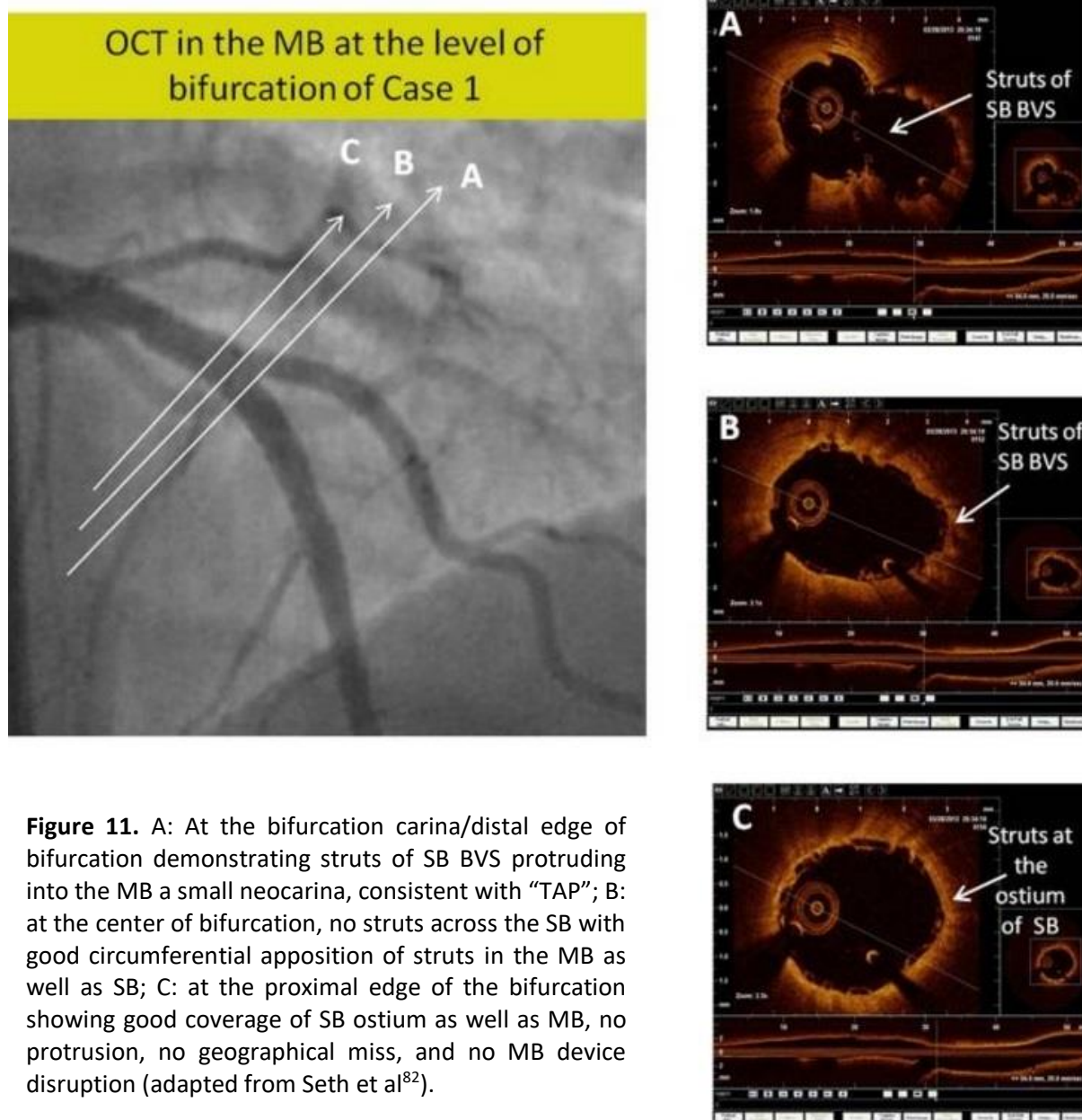


Figure 11. A: At the bifurcation carina/distal edge of bifurcation demonstrating struts of SB BVS protruding into the MB a small neocarina, consistent with “TAP”; B: at the center of bifurcation, no struts across the SB with good circumferential apposition of struts in the MB as well as SB; C: at the proximal edge of the bifurcation showing good coverage of SB ostium as well as MB, no protrusion, no geographical miss, and no MB device disruption (adapted from Seth et al⁸²).

3.6.2-Long Lesions:

The current available longest scaffold has 28 mm length, and in longer lesions, overlapping two or more scaffolds can be utilized. However, because of the thick struts, scaffold overlapping may delay the healing process [86]. To minimize overlap, two techniques are advised; “marker-to-marker” (~1 mm of overlap) and “scaffold-to-scaffold” (no overlap) techniques. In “marker-to-marker” technique, the second scaffold is implanted so as the markers of the first and second scaffolds’ are overlap (**Figure 4**). This strategy prevents gap restenosis. During the implantation of the second scaffold, the size selection for the scaffold and the implantation order, even not proven but at least theoretical, should be considered in which the distal scaffold should be implanted first in order to avoid probable distortions within the device [63].

3.6.3-Chronic total occlusions:

BRS appears as an effective alternative for the treatment of CTO. In CTO-ABSORB pilot study, all the scaffolds were deployed successfully; at one-month follow up no major adverse event recorded and 6.4% SB occlusion was reported [87]. In another study, Ojeda et al reported a high technical success rate of BVS implantation at CTO lesions and at mid-term follow up there was a low rate of adverse events reported [88]. The results from GHOST-CTO registry confirmed the efficacy and safety of BRS implantation in CTO lesions; there were no significant difference between BRS and metallic DES for SB occlusion rates, residual SYNTAX score, periprocedural MI, and the frequency of contrast-induced kidney injury [89].

The calcifications and the under-filled distal coronary bed stemming from the chronic low flow make the treatment of CTO troublesome for BRS implantation. A theoretical advantage of BRS in CTOs treated with dissection/re-entry techniques is the fact that this approach results in aneurysm formation which if treated with DES may result in late stent malapposition stent thrombosis and restenosis; on the other hand, BRS have the ability to resorb and thus there is no risk for late stent malapposition, restenosis and thrombosis [90]. The results of a pilot study reported the feasibility of Absorb BVS in CTO lesions with favorable short- and mid-term outcomes [87]. Despite the limitations of the Absorb BVS (i.e., the thicker struts of the scaffold, the risk of strut fracture due to overexpansion), all the scaffolds in this study were deployed successfully without any major adverse event at 1-month.

3.6.4-In-stent restenosis:

From scant cases to multicenter registries, BRS have been under appraisal in patients with ISR [91,92] BRSs have theoretical advantages over drug-coated balloon (DCB). They enable longer anti-proliferative drug delivery and are coated with everolimus rather than paclitaxel which is a less effective antiproliferative drug. In addition, in contrast to DES, BRS enables temporally scaffolding and doesn't leave a layered metallic structure which makes BRS an effective alternative for the treatment of restenosis. The favorable results were independent from the type of ISR lesion (focal or diffuse, de novo or recurrent, BMS- or DES-ISR) [92-94]. To avoid an on-going inflammatory reaction in the treated segment with DES which brings its own risk of restenosis [95], BRS seems a valuable alternative in ISR.

3.6.5-Acute Coronary Syndromes and Thrombotic Lesions:

In BVS-EXAMINATION study, 3 groups of patients were investigated; patients treated with DES, BMS and Absorb BVS. Although the analysis in BVS EXAMINATION was based on propensity matching, no randomization was performed and the analyzed data were acquired from different institutions at different time points, the study provided opportunity for a historical comparison. At 12 –months follow up, no significant difference in the outcomes were reported; in the Absorb BVS group scaffold thrombosis and TLR rates were 2.4 % and 1.7% [96]. Gori et al. compared outcomes in patients admitted with an ACS treated with an Absorb BVS and an everolimus-DES. The incidence of major adverse cardiac events (MACE: death, non-fatal myocardial infarction, or re-intervention) in hospital before discharge, at one-month and six-month, were similar between the study groups [97]. In an Italian registry (BVS-RAI, n=122 patients), the clinical end-points (cardiac death, myocardial infarction, and target lesion revascularization) were also similar in the patients that were admitted with STEMI treated with Absorb BVS or EES [98]. Diletti and colleagues reported the feasibility of implanting BRS in STEMI patients in a single-center study (n=49 patients); a TIMI-flow III was achieved in 91.7% of the recruited patients and the mean percentage of the malapposed struts per patient was $2.80 \pm 3.90\%$ [99]. In the multicenter prospective PRAGUE-19 study that included 142 STEMI patients, 49 Absorb BVS were used in 41 patients (29% of all consecutive STEMI patients). Absorb BVS device success rate was 98% (40 of 41 patients) without any technical difficulties. Thrombolysis In Myocardial Infarction (TIMI)-III flow was restored in 95% of the patients, and the mean acute scaffold recoil ratio was 9.7%. OCT imaging demonstrated a low rate of strut malapposition of 1.1% [100]. In a small cohort of STEMI patients, Wiebe et

al reported encouraging results of STEMI patients treated by BRS [101]. POLAR-ACS study included, 3 cohorts; 46 patients with unstable angina, 38 patients with non-ST-segment STEMI and 16 patients with STEMI that were treated with Absorb BVS. TIMI-III flow was achieved in 99% of the patients. In 2 patients peri-procedural MI was reported. At 1-year follow-up 1 scaffold thrombosis related MI and 1 TLR was reported [102]. The recently published results of the TROFI-II trial, showed that Absorb BVS was comparable to metallic EES in terms of arterial healing at 6-months. The frequency of malapposed struts and uncovered struts were lower in the Absorb BVS group [111].

Previous trials have confirmed the safety of BVS implantation in thrombotic lesions [97,99,100]. BVS is likely to reduce the risk of distal embolization as it has thicker struts and increased surface that may jail the thrombotic particles between the vessel wall and the scaffold. Moreover, in ACS, vasospasm and thrombus may compel the proper assessment of lumen diameter and thus malapposition has been reported more often in this setting. In contrast to DES, BRS has the ability to resorb and eliminate the risk of late stent malapposition [103].

3.7-Optimal antiplatelet treatment after PCI with BRS

Polymeric materials are less thrombogenic than metallic stents [104]. It has been shown that the bioresorption of the BVS does not cause vessel inflammation at 2, 3, and 4 years [105]. The tissue coverage as assessed by OCT was at 97% at 6-months in Absorb BVS [106]. Currently there is no consensus on the duration of the dual antiplatelet therapy (DAPT) in patients treated with BRS. However, in previous trials, the duration of DAPT has been at least 12-months and additional DAPT left to the physician's discretion. Despite occasional case reports notified very late scaffold thrombosis after discontinuation of DAPT, more data are needed to confirm these findings [107,108]. The current recommendation is DAPT for at least 12 months in all patients. Of note, the new adenosine diphosphate P2Y₁₂ receptor antagonists, prasugrel and ticagrelor, have been only prescribed in a small number of participants in the GHOST-EU registry (26.2%) and the bifurcation subgroup (19%) [85]. However, it seems reasonable to use more potent anti-platelet agents in patients treated with BRS especially in complex procedures and in patients with low bleeding risk. Since there is no data about the patients with oral anticoagulation (OAC) therapy, it is feasible to avoid implanting BRS in such patients [109]. However, in inevitable situations, DAPT should continue with OAC. Despite there is no randomized trial comparing DAPT plus OAC in DES and BRS, previously it has been shown in

patients with DES, triple therapy (DAPT+OAC) was feasible and safe.[110] In a recent observational study(n=377) in patients with indication for OAC that underwent DES implantation, minor and major bleedings were reported more frequently in patients with prasugrel than in patients with clopidogrel therapy [111].

3.8-Treating BRS failure

In a recent multi-center registry report, decreased LVEF, ostial lesions and interruption of DAPT have been shown to be related with ScT. QCA analysis has denoted that BRS implantation in smaller vessels prompted ScT [112,113,56]. OCT analysis has also confirmed that incomplete expansion of BRS can inevitably incite ScT [112,113,56]. Intravascular imaging should always be considered in cases of scaffold failure to assess the underlying etiology and guide further treatment. Scaffold underexpansion and malapposition can be treated with balloon dilatation using NCB respecting the overexpansion limit (0.5 mm) of Absorb BVS. In case of large vessels (> 4 mm) and malapposition, deployment of large metallic stents should be considered to cover the malapposed segment. Underexpansion should be treated by POBA, however, if needed DES should be used to provide adequate radial support. BRS failure after 6-months stemming from mechanical issues will require additional DES implantation (**Figure 12**).

Restenosis due to neointimal hyperplasia within 6-months after initial implantation can be treated with a DEB. After 6-months due to the hydrolysis of the polylactide chains, the radial strength of the BRS decreases and thus ISR should be treated with a new device that will provide radial support. Limited strut fractures might be managed with only balloon inflation and prolonged DAPT, however further disruptions will require new stent/scaffold implantation.

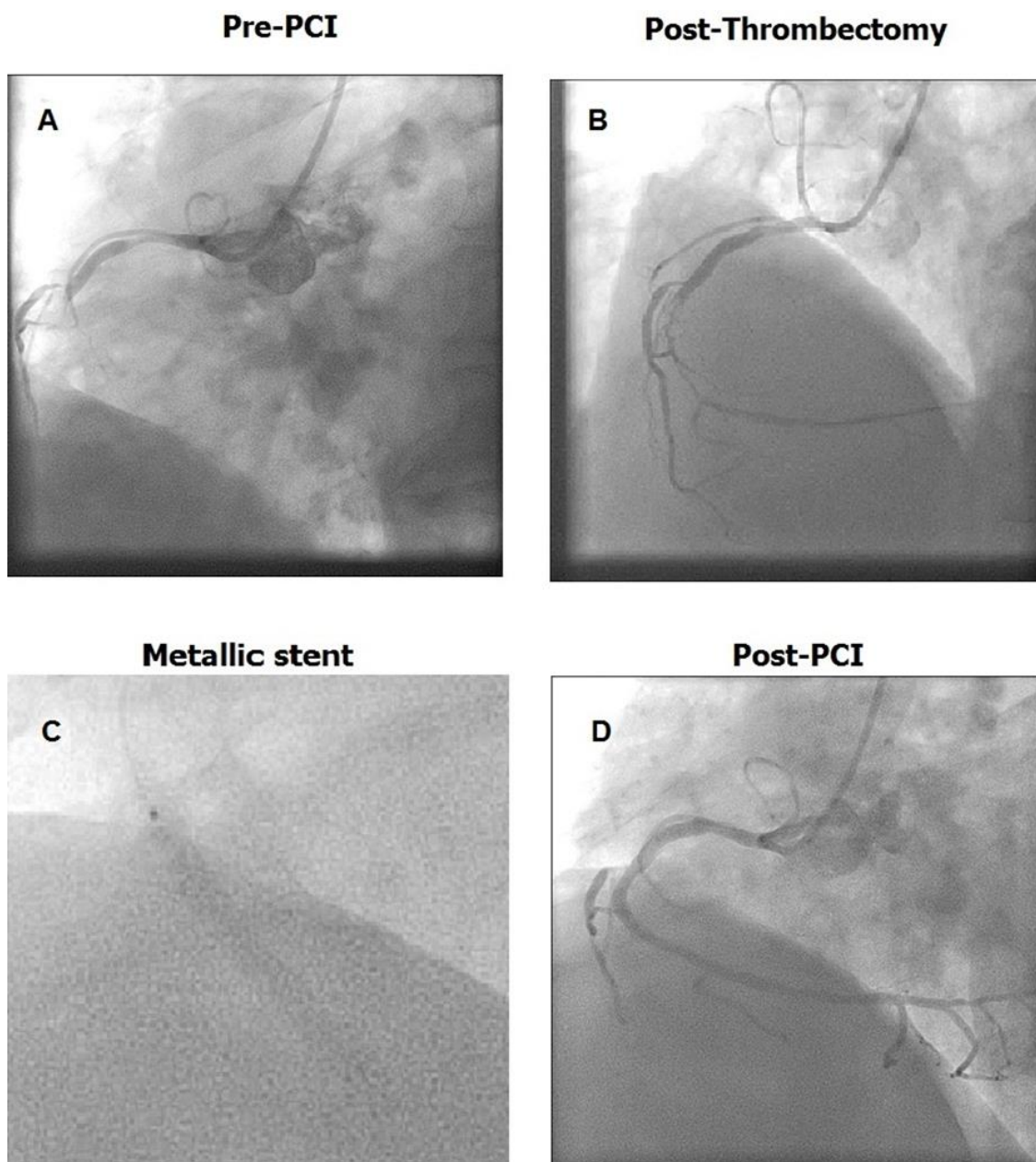


Figure 12. Diagnostic angiogram demonstrating the scaffold thrombosis 602 days after scaffold implantation (A). After thrombectomy, angiogram revealed that TIMI 2 flow in RCA was established (B). After thrombectomy, metallic-stent (C) was implanted and TIMI 3 flow was restored (D).

4. CONCLUSION

BRS implantation requires comprehensive assessment of the target lesion. The intracoronary imaging techniques provide useful information for optimizing BRS implantation. With careful lesion preparation, devoting care during scaffold implantation, performing post-dilatation and intravascular imaging in mandatory cases, BRS provide reasonable opportunities within several lesion scenarios. Optimisation should not be limited to post-implantation intravascular

imaging; adequate anti-platelet treatment should be administered to prevent overwhelming events at post-implantation follow up.

5. EXPERT COMMENTARY

For the optimisation of PCI with BRS, there are several crucial points to be implemented. The lesions suitable for BRS should be selected carefully, the appropriate device size should be selected according to the mentioned techniques, the lesion should be prepared with pre-dilatation, the scaffold implantation procedure should be performed rigorously and patiently. The target segment should be assessed with intracoronary imaging techniques before the implantation and the scaffolded segment should be evaluated for malapposition and disruption after the implantation. If post-dilatation is required, non-compliant balloon should be used and the scaffold should be enlarged not 0.5 mm above its nominal diameter.

6. KEY POINTS

- BRS should not be implanted in coronary lesions not prepared properly with balloon pre-dilatation.
- The lesions for BRS implantation should be assessed carefully; target segment location (proximal versus distal), vessel size (device under-expansion) and plaque morphology (calcification status) should be evaluated comprehensively.
- Detailed review of QCA, IVUS and OCT for scaffold size selection and lumen size assessment is a sine qua non for the PCI with BRS.
- The scaffold should cover at least 2 mm healthy segments at each edge.
- Since the largest available Absorb BVS is 3.5 mm at its nominal pressure, the vessel diameter > 4.0 mm should not be planned for the treatment because of the risk of malapposition.
- To get full expansion, the scaffold should be expanded above the 0.5 mm of its nominal diameter carefully at nominal pressure. Deployment beyond nominal pressure should only be recommended for large vessels, or small scaffold to vessel ratios. Due to the current very semi-compliant aspects of the delivery balloon at high pressure serious bulging develops increasing the risk of proximal and mainly distal edge dissections. For these lesions, high pressure non-compliant post dilatation is the safest option. In case of malapposition or under-expansion, post-dilatation with NCB should be performed.

-Owing to its bulky structure, overlapping of two BRS should be minimized and the overlapping should be confined to the larger vessels (>3.0 mm).

-Measuring the maximal lumen diameters (Dmax) in the proximal and distal vessel segment of interest during QCA should be implemented. Dmax renders a reference diameter at the site of minimal lumen diameter at the diseased segment for the implantation.

-High-pressure post-dilatation with NCB is a *de rigueur* in PCI with BRS.

7. FIVE-YEAR VIEW

For the optimization of the PCI with BRS, in the next a few years we may be able to see OCT systems with faster pullback speeds. For axial deployment optimization, in order to reduce malapposition and underexpansion rates, both OCT and IVUS should be performed frequently, to prevent hazardous results. On the other hand, associated with scaffold geometry, scaffolds with thinner struts will be useful for getting better optimization results at post-implantation in terms of less flow disruption within the scaffolded segment and related less risk of thrombus or neointimal hyperplasia formations. BRSs with thinner streamlined struts will be useful for local hemodynamics within the scaffolded segments. Hybrid intravascular imaging with the combination of OCT and IVUS, may render the potential for detection of high-risk lesions and identification of high-risk patients that can benefit from aggressive treatment of coronary atherosclerosis to get optimal PCI results.

Acknowledgments

We would like to thank to the investigators who have contributed to the progression of the field with their invaluable efforts.

Disclosures

ET has a research grant from TUBITAK (The Scientific and Technological Research Council of Turkey). PWS and YO are the members of Advisory Board of Abbott Vascular.

REFERENCES

1. Gruntzig A. Transluminal dilatation of coronary-artery stenosis. *Lancet* 1978; 1:263.
2. Brugaletta S, Heo JH, Garcia-Garcia HM, et al. Endothelial-dependent vasomotion in a coronary segment treated by ABSORB everolimus-eluting bioresorbable vascular scaffold system is related to plaque composition at the time of bioresorption of the polymer: indirect finding of vascular reparative therapy? *Eur Heart J*. 2012;33(11):1325-33. **** Important article about the degradation process of the Absorb BVS and resumption of vasomotion.**
3. Verheye S, Ormiston JA, Stewart J, et al. A next-generation bioresorbable coronary scaffold system-from bench to first clinical evaluation: 6- and 12-month clinical and multimodality imaging results. *J Am Coll Cardiol Intv* 2014;7: 89–99.
4. Gomez-Lara J, Garcia-Garcia HM, Onuma Y, et al. A comparison of the conformability of everolimus-eluting bioresorbable vascular scaffolds to metal platform coronary stents. *JACC Cardiovasc Interv*. 2010 Nov;3(11):1190-8. doi: 10.1016/j.jcin.2010.07.016.
5. Onuma Y, Dudek D, Thuesen L, et al. Five-year clinical and functional multislice computed tomography angiographic results after coronary implantation of the fully resorbable polymeric everolimus-eluting scaffold in patients with de novo coronary artery disease: the ABSORB cohort A trial. *JACC Cardiovasc Interv*. 2013;6(10):999-1009.
6. Alfonso F, Byrne RA, Rivero F, et al. Current treatment of in-stent restenosis. *J Am Coll Cardiol*. 2014;63(24):2659-2673.
7. Brodie BR, Cooper C, Jones M, et al. Postdilatation Clinical Comparative Study (POSTIT) Investigators. Is adjunctive balloon postdilatation necessary after coronary stent deployment? Final results from the POSTIT trial. *Catheter Cardiovasc Interv* 2003; 59:184-192.
8. Cook S, Wenaweser P, Togni M, et al. Incomplete stent apposition and very late stent thrombosis after drug-eluting stent implantation. *Circulation* 2007; 115:2426-2434.
9. Doi H, Maehara A, Mintz GS, et al. Impact of post-intervention minimal stent area on 9-month follow-up patency of paclitaxel eluting stents: an integrated intravascular ultrasound analysis from the TAXUS IV, V, and VI and TAXUS ATLAS Workhorse, Long Lesion, and Direct Stent Trials. *JACC Cardiovasc Interv* 2009; 2:1269-1275. **** Important article for struggling lesions for DES**
10. Kimura M, Mintz GS, Carlier S, et al. Outcome after acute incomplete sirolimus-eluting stent apposition as assessed by serial intravascular ultrasound. *Am J Cardiol* 2006; 98:436-442. 2006; 98:436-442.
11. Hong MK, Lee CW, Kim JH, et al. Impact of various intravascular ultrasound criteria for stent optimization on the six-month angiographic restenosis. *Catheter Cardiovasc Interv* 2002; 56:178-183.
12. Gil RJ, Pawłowski T, Dudek D, Horszczaruk G, Zmudka K, Lesiak M, Witkowski A, Ochoła A, Kubica J; Investigators of Direct Stenting vs Optimal Angioplasty Trial (DIPOL). Comparison of angiographically guided direct stenting technique with direct stenting and optimal balloon angioplasty guided with intravascular ultrasound: the multicenter, randomized trial results. *Am Heart J* 2007; 154:669 – 675.
13. Casella G, Klaus V, Ottani F, et al. Impact of intravascular ultrasound-guided stenting on long-term clinical outcome: a meta-analysis of available studies comparing intravascular ultrasound-guided and angiographically guided stenting. *Catheter Cardiovasc Interv* 2003; 59: 314-321.
14. Parise H, Maehara A, Stone GW, et al. Metaanalysis of randomized studies comparing intravascular ultrasound versus angiographic guidance of percutaneous coronary intervention in pre-drug-eluting stent era. *Am J Cardiol* 2011; 107: 374-382.

15. Chieffo A, Latib A, Caussin C, et al. A prospective, randomized trial of intravascular-ultrasound guided compared to angiography guided stent implantation in complex coronary lesions: the AVIO trial. *Am Heart J* 2013; 165: 65-72
16. Klersy C, Ferlini M, Raisaro A, et al. Use of IVUS guided coronary stenting with drug eluting stent: A systematic review and meta-analysis of randomized controlled clinical trials and high-quality observational studies. *Int J Cardiol* 2013; 170: 54-63.
17. Witzensbichler B, Maehara A, Weisz G, et al. Relationship Between Intravascular Ultrasound Guidance and Clinical Outcomes After Drug-Eluting Stents: The Assessment of Dual Antiplatelet Therapy With Drug-Eluting Stents (ADAPT-DES) Study. *Circulation* 2014;129(4):463–470.
18. Levine GN, Bates ER, Blankenship JC, et al. 2011 ACCF/AHA/SCAI Guideline for Percutaneous Coronary Intervention. A report of the American College of Cardiology Foundation/American Heart Association Task Force on Practice Guidelines and the Society for Cardiovascular Angiography and Interventions. *J Am Coll Cardiol*. 2011;58(24):e44-122. ** *Guideline for PCI*
19. Authors/Task Force members, Windecker S, Kolh P, et al. 2014 ESC/EACTS Guidelines on myocardial revascularization: The Task Force on Myocardial Revascularization of the European Society of Cardiology (ESC) and the European Association for Cardio-Thoracic Surgery (EACTS) Developed with the special contribution of the European Association of Percutaneous Cardiovascular Interventions (EAPCI). *Eur Heart J*. 2014 Oct 1;35(37):2541-619.
20. Sakurai R, Ako J, Morino Y, et al. Predictors of edge stenosis following sirolimus-eluting stent deployment (a quantitative intravascular ultrasound analysis from the SIRIUS trial). *Am J Cardiol* 2005; 96:1251-1253
21. Leung WH, Alderman EL, Lee TC, Stadius ML. Quantitative arteriography of apparently normal coronary segments with nearby or distant disease suggests presence of occult, nonvisualized atherosclerosis. *J Am Coll Cardiol*. 1995 Feb;25(2):311-7.
22. Lee DY, Eigler N, Luo H, et al. Effect of intracoronary ultrasound imaging on clinical decision making. *Am Heart J* 1995;129: 1084-93. 42. Mintz GS, Pichard AD, Kovach JA, et al. Impact of preintervention intravascular ultrasound imaging on transcatheter treatment strategies in coronary artery disease. *Am J Cardiol* 1994; 73:423-30.
23. de Jaegere P, Mudra H, Figulla H, et al. Intravascular ultrasound- guided optimized stent deployment: Immediate and 6 months clinical and angiographic results from the Multicenter Ultrasound Stenting In Coronaries Study (MUSIC Study). *Eur Heart J* 1998; 19:1214-1223. ** *One of the most important article for IVUS guidance for PCI*
24. Higashikuni Y, Tanabe K, Tanimoto S, et al. Impact of plaque composition on the re-reflow phenomenon in patients with acute coronary syndrome: an intravascular ultrasound radiofrequency analysis. *Circ J* 2008; 72:1235-41.
25. Wachtell K, Lagerqvist B, Olivecrona GK, et al. Novel Trial Designs: Lessons Learned from Thrombus Aspiration During ST-Segment Elevation Myocardial Infarction in Scandinavia (TASTE) Trial. *Curr Cardiol Rep*. 2016 ;18(1):11.
26. Jolly SS, Cairns JA, Yusuf S et al. Outcomes after thrombus aspiration for ST elevation myocardial infarction: 1-year follow-up of the prospective randomized TOTAL trial. *Lancet*. 2016;387(10014):127-135.
27. Stone GW, Maehara A, Muller JE, et al. Plaque Characterization to Inform the Prediction and Prevention of Periprocedural Myocardial Infarction During Percutaneous Coronary Intervention: The CANARY Trial (Coronary Assessment by Near-infrared of Atherosclerotic Rupture-prone Yellow). *JACC Cardiovasc Interv*. 2015;8(7):927-936
28. Fujii K, Carlier SG, Mintz GS, et al. Stent underexpansion and residual reference segment stenosis are related to stent thrombosis after sirolimus-eluting stent implantation: an intravascular ultrasound study. *J Am Coll Cardiol* 2005; 45:995-998.

29. Russo RJ, Silva PD, Teirstein PS, et al. A randomized controlled trial of angiography versus intravascular ultrasound-directed bare-metal coronary stent placement (the AVID Trial). *Circ Cardiovasc Interv*. 2009 ;2(2):113-23.
30. Jakabcin J, Spacek R, Bystron M, et al. Long-term health outcome and mortality evaluation after invasive coronary treatment using drug eluting stents with or without the IVUS guidance. Randomized control trial: HOME DES IVUS. *Catheter Cardiovasc Interv* 2010; 75:578-583.
31. Wijns W, Shite J, Jones MR, et al. Optical coherence tomography imaging during percutaneous coronary intervention impacts physician decision-making: ILUMIEN I study. *Eur Heart J*. 2015 Aug 4. pii: ehv367. [Epub ahead of print]
32. Chamié D, Bezerra HG, Attizzani GF, et al. Incidence, predictors, morphological characteristics, and clinical outcomes of stent edge dissections detected by optical coherence tomography. *JACC Cardiovasc Interv* 2013; 6:800–13.
33. Maehara A, Ben-Yehuda O, Ali Z, et al. Comparison of Stent Expansion Guided by Optical Coherence Tomography vs. Intravascular Ultrasound: The ILUMIEN II Study. *JACC Cardiovasc Interv*. 2015;8(13):1704-14. ** *Information about optimization techniques with OCT*
34. Gomez-Lara J, Brugaletta S, Diletti R, et al. Agreement and reproducibility of gray-scale intravascular ultrasound and optical coherence tomography for the analysis of the bioresorbable vascular scaffold. *Catheter Cardiovasc Interv* 2012; 79: 890-902.
35. Tanaka A, Imanishi T, Kitabata H, et al. Lipid-rich plaque and myocardial perfusion after successful stenting in patients with non-ST-segment elevation acute coronary syndrome: an optical coherence tomography study. *Eur Heart J* 2009; 30: 1348-55.
36. Porto I, Di Vito L, Burzotta F, et al. Predictors of periprocedural (type IVa) myocardial infarction, as assessed by frequency-domain optical coherence tomography. *Circ Cardiovasc Interv* 2012; 5: 89-96, S81-6.
37. Ozaki Y, Tanaka A, Tanimoto T, et al. Thin-cap fibroatheroma as high-risk plaque for microvascular obstruction in patients with acute coronary syndrome. *Circ Cardiovasc Imaging* 2011; 4: 620-7.
38. Prati F, Uemura S, Souteyrand G, et al. OCT-based diagnosis and management of STEMI associated with intact fibrous cap. *JACC Cardiovasc Imaging* 2013; 6: 283-7.
39. Kume T, Okura H, Miyamoto Y, et al. Natural history of stent edge dissection, tissue protrusion and incomplete stent apposition detectable only on optical coherence tomography after stent implantation – preliminary observation. *Circ J* 2012; 76: 698-703.
40. Finn AV, Nakazawa G, Joner M, et al. Vascular responses to drug eluting stents: importance of delayed healing. *Arterioscler Thromb Vasc Biol* 2007; 27: 1500-10.
41. Kubo T, Imanishi T, Kitabata H, et al. Comparison of vascular response after sirolimus-eluting stent implantation between patients with unstable and stable angina pectoris: a serial optical coherence tomography study. *JACC Cardiovasc Imaging* 2008; 1: 475-84.
42. Kubo T, Akasaka T, Shite J, et al. OCT compared with IVUS in a coronary lesion assessment: the OPUS-CLASS study. *JACC Cardiovasc Imaging* 2013; 6: 1095-104.
43. Prati F, Di Vito L, Biondi-Zoccai G, et al. Angiography alone versus angiography plus optical coherence tomography to guide decision-making during percutaneous coronary intervention: the Centro per la Lotta contro l'Infarto-Optimisation of Percutaneous Coronary Intervention (CLI-OPCI) study. *EuroIntervention*. 2012;8(7):823-29.
44. Schoonenberg G, Florent R. Advanced visibility enhancement for stents and other devices: Image processing aspects. *Cardiol Clin* 2009; 27:477–490.
45. Eng MH, Klein AP, Wink O, Hangsen A, Carroll JD, Garcia JA. Enhanced stent visualization: A case series demonstrating practical applications during PCI. *Int J Cardiol* 2010;141: e8–e16.
46. Rogers KR, Michaels AD. Enhanced x-ray visualization of coronary stents: Clinical aspects. *Cardiol Clin* 2009; 27:467–475.

47. Davies AG, Conway D, Reid S, Cowen AR, Sivananthan M. Assessment of coronary stent deployment using computer enhanced x-ray images-validation against intravascular ultrasound and best practice recommendations. *Catheter Cardiovasc Interv.* 2013;81(3):419-27.
48. Orford JL, Lerman A, Holmes DR. Routine intravascular ultrasound guidance of percutaneous coronary intervention: A critical reappraisal. *J Am Coll Cardiol* 2004; 43:1335–1342.
49. Serruys PW, Onuma Y, Ormiston JA, de Bruyne B, Regar E, Dudek D, et al. Evaluation of the second generation of a bioresorbable everolimus drug-eluting vascular scaffold for treatment of de novo coronary artery stenosis: six-month clinical and imaging outcomes. *Circulation.* 2010;122(22):2301-12.
50. Dixon SR, Grines CL, Munir A, et al. Analysis of target lesion length before coronary artery stenting using angiography and near-infrared spectroscopy versus angiography alone. *Am J Cardiol* 2012;109:60-6.
51. Latib A, Costopoulos C, Naganuma T, et al. Which patients could benefit the most from bioresorbable vascular scaffold implant: from clinical trials to clinical practice. *Minerva Cardioangiol.* 2013;61(3):255-62. ** *Gives information about the suitable candidates for BVS implantation*
52. Serruys PW, Ormiston JA, Onuma Y, et al. A bioabsorbable everolimus-eluting coronary stent system (ABSORB): 2-year outcomes and results from multiple imaging methods. *Lancet.* 2009 Mar 14;373(9667):897-910.
53. Serruys PW, Onuma Y, Ormiston JA, et al. Evaluation of the second generation of a bioresorbable everolimus drug-eluting vascular scaffold for treatment of de novo coronary artery stenosis: six-month clinical and imaging outcomes. *Circulation.* 2010 Nov 30;122(22):2301-12.
54. Abizaid A, Ribamar Costa J Jr, Bartorelli AL, et al. The ABSORB EXTEND study: preliminary report of the twelve-month clinical outcomes in the first 512 patients enrolled. *EuroIntervention.* 2015;10(12):1396-401.
55. Serruys PW, Chevalier B, Dudek D, et al. A bioresorbable everolimus-eluting scaffold old versus a metallic everolimus-eluting stent for ischaemic heart disease caused by de-novo native coronary artery lesions (ABSORB II): an interim 1-year analysis of clinical and procedural secondary outcomes from a randomised controlled trial. *Lancet* 2015; 385: 43–54. ** *First randomized trial comparing the metallic DES and bioresorbable scaffold*
56. Ellis SG, Kereiakes DJ, Metzger DC, et al. Everolimus-Eluting Bioresorbable Scaffolds for Coronary Artery Disease. *N Engl J Med.* 2015 Nov 12;373(20):1905-15.
57. ABSORB III and IV. Pivotal Clinical Trial Program. Presented by Greg Stone in TCT 2012 on 23rd Oct 2012. Miami Beach, Florida, USA.
58. T. Gori, G. Guagliumi, T. Münzel. Absorb bioresorbable scaffold implantation for the treatment of an ostial chronic total occlusion *Int J Cardiol*, 172 (2014), pp. e377–e378
59. Ong PJ, Jafary FH, Ho HH. “First-in-man” use of bioresorbable vascular scaffold in saphenous vein graft. *EuroIntervention.*2013;9:165.
60. Roleder T, Parma Z, Smolka G, et al. Optical coherence tomography imaging of everolimus-eluting bioresorbable vascular scaffold implanted into coronary vein graft at 3-month follow-up. *Eur Heart J.* 2014; 35:2207.
61. Roleder T, Ochala A, Smolka G, et al. Implantation of a bioabsorbable vascular scaffold into a coronary vein graft: a two-week angiography follow-up. *Kardiol Pol.* 2014; 72:281.
62. Roleder T, Wanha W, Smolka G, Zimoch J, Ochala A, Wojakowski W. Bioresorbable vascular scaffolds in saphenous vein grafts (data from OCTOPUS registry). *Postepy Kardiol Interwencyjne.* 2015;11(4):323-326.

63. Tamburino C, Latib A, van Geuns RJ, et al. Contemporary practice and technical aspects in coronary intervention with bioresorbable scaffolds: a European perspective. *EuroIntervention*. 2015;11(1):45-52. ** *A guidance source for BRS implantation*
64. Farooq V, Gomez-Lara J, Brugaletta S, et al. Proximal and distal maximal luminal diameters as a guide to appropriate deployment of the ABSORB everolimus-eluting bioresorbable vascular scaffold: a sub-study of the ABSORB Cohort B and the on-going ABSORB EXTEND Single Arm Study. *Catheter Cardiovasc Interv*. 2012 ;79 :880-8.
65. Gomez-Lara J, Diletti R, Brugaletta S, et al. Angiographic maximal luminal diameter and appropriate deployment of the everolimus-eluting bioresorbable vascular scaffold as assessed by optical coherence tomography: an ABSORB cohort B trial sub-study. *EuroIntervention*. 2012; 8:214-24.
66. Onuma Y, Serruys PW, Muramatsu T, et al. Incidence and imaging outcomes of acute scaffold disruption and late structural discontinuity after implantation of the absorb Everolimus-Eluting fully bioresorbable vascular scaffold: optical coherence tomography assessment in the ABSORB cohort B Trial (A Clinical Evaluation of the Bioabsorbable Everolimus Eluting Coronary Stent System in the Treatment of Patients With De Novo Native Coronary Artery Lesions). *JACC Cardiovasc Interv*. 2014 ;7 :1400-11.
67. Brown AJ, McCormick LM, Braganza DM, et al. Expansion and malapposition characteristics after bioresorbable vascular scaffold implantation. *Catheter Cardiovasc Interv*. 2014 ;84(1) :37-45.
68. Ozel E, Tastan A, Ozturk A, et al. What is better for predilatation in bioresorbable vascular scaffold implantation: a non-compliant or a compliant balloon? *Anatol J Cardiol* 2015; 15. DOI:10.5152/AnatolJCardiol.2015.6184. In press.
69. Kolandaivelu K, Swaminathan R, Gibson WJ, et al. Stent thrombogenicity early in high-risk interventional settings is driven by stent design and deployment and protected by polymer-drug coatings. *Circulation*. 2011; 123(13):1400-9.
70. Rzeszutko Ł, Depukat R and Dudek D. Biodegradable vascular scaffold ABSORB BVS™ – scientific evidence and methods of implantation. *Postępy w Kardiologii Interwencyjnej = Advances in Interventional Cardiology*. 2013; 9:22-30. ** *A significant article for guidance for the implantation of Absorb BVS*
71. Puricel S, Cuculi F, Weissner M, et al. Bioresorbable Coronary Scaffold Thrombosis: Multicenter Comprehensive Analysis of Clinical Presentation, Mechanisms, and Predictors. *J Am Coll Cardiol*. 2016;67(8):921-31.
72. Ormiston JA, Webber B, Ubod B, et al. An independent bench comparison of two bioresorbable drug-eluting coronary scaffolds (Absorb and DESolve) with a durable metallic drug-eluting stent (ML8/Xpedition). *EuroIntervention*. 2015;11:60-67.
73. Sotomi Y, Suwannasom P, Tenekecioglu E, et al. Differential aspects between cobalt-chromium everolimus drug-eluting stent and Absorb everolimus bioresorbable vascular scaffold: from bench to clinical use. *Expert Rev Cardiovasc Ther*. 2015;13(10):1127-1145. ** *Substantial information for the comparison of two different stent types*.
74. Basavarajaiah S, Naganuma T, Latib A, et al. Can bioabsorbable scaffolds be used in calcified lesions? *Catheter Cardiovasc Interv*. 2014;84(1):48-52.
75. Onuma Y, Serruys PW, Gomez J, et al. Comparison of in vivo acute stent recoil between the bioresorbable everolimus-eluting coronary scaffolds (revision 1.0 and 1.1) and the metallic everolimus-eluting stent. *Catheter Cardiovasc Interv* 2011; 78:3–12.
76. Brugaletta S, Gomez-Lara J, Diletti R, et al. Comparison of in vivo eccentricity and symmetry indices between metallic stents and bioresorbable vascular scaffolds: insights from the ABSORB and SPIRIT trials. *Catheter Cardiovasc Interv*. 2012;79(2):219-28.
77. Serruys PW, Onuma Y, Garcia-Garcia HM, et al. Dynamics of vessel wall changes following the implantation of the Absorb everolimus-eluting bioresorbable vascular scaffold: a multi-imaging modality study at 6, 12, 24 and 36 months. *EuroIntervention* 2014; 9:1271–84.

78. Nakatani S, Sotomi Y, Ishibashi Y, et al. Comparative analysis method of permanent metallic stents (XIENCE) and bioresorbable poly-L-lactic (PLLA) scaffolds (Absorb) on optical coherence tomography at baseline and follow-up. *EuroIntervention*. 2015;11(6). ** *A substantial article for defining updated methodology in evaluation of Absorb BVS after implantation*
79. Felix C, Everaert B, Jepson N, Tamburino C, van Geuns R. Treatment of bioresorbable scaffold failure. *Eurointervention* 2015; 11: V175-V180
80. Woudstra P, Grundeken MJ, Kraak RP, Hassell ME, Arkenbout EK, Baan J Jr, et al. Amsterdam Investigator-initiated Absorb strategy all-comers trial (AIDA trial): a clinical evaluation comparing the efficacy and performance of ABSORB everolimus-eluting bioresorbable vascular scaffold strategy vs the XIENCE family (XIENCE PRIME or XIENCE Xpedition) everolimus-eluting coronary stent strategy in the treatment of coronary lesions in consecutive all-comers: rationale and study design. *Am Heart J*. 2014;167(2):133-140.
81. COMPARE ABSORB: bioresorbable vascular scaffold versus Xience in complex lesions and patients subsets. Presented by P. Smits at EuroPCR 2015, Paris, France.
82. Seth A, Sengottuvelu G, Ravisekar V. Salvage of side branch by provisional "TAP technique" using Absorb™ bioresorbable vascular scaffolds for bifurcation lesions: first case reports with technical considerations. *Catheter Cardiovasc Interv*. 2014 ;84(1):55-61.
83. Detre KM, Wright E, Murphy ML, et al. Observer agreement in evaluating coronary angiograms. *Circulation* 1975;52: 979–86.
84. Costopoulos C, Naganuma T, Latib A, Colombo A. Optical coherence tomography of a bifurcation lesion treated with bioresorbable vascular scaffolds with the "mini-crush" technique. *JACC Cardiovasc Interv*. 2013; 6:1326-1327.
85. Latib A, Capodanno D, Lesiak M, Tamburino C, Colombo A. Lessons from the GHOST-EU registry. *EuroIntervention*. 2015;11 Suppl V: V170-4. doi: 10.4244/EIJV11SVA41.
86. Farooq V, Serruys PW, Heo JH, et al. Intracoronary optical coherence tomography and histology of overlapping everolimus-eluting bioresorbable vascular scaffolds in a porcine coronary artery model: the potential implications for clinical practice. *JACC Cardiovasc Interv*. 2013; 6:523-32.
87. Vaquerizo B, Barros A, Pujadas S, Bajo E, Estrada D, Miranda-Guardiola F, et al. Bioresorbable everolimus-eluting vascular scaffold for the treatment of chronic total occlusions: CTO-ABSORB pilot study. *EuroIntervention*. 2015;11(5):555-563.
88. Ojeda S, Pan M, Romero M, Suárez de Lezo J, Mazuelos F, Segura J, et al. Outcomes and computed tomography scan follow-up of bioresorbable vascular scaffold for the percutaneous treatment of chronic total coronary artery occlusion. *Am J Cardiol*. 2015;115(11):1487-1493.
89. La Manna A, Chisari A, Giacchi G, Capodanno D, Longo G, Di Silvestro M, et al. Everolimus-eluting bioresorbable vascular scaffolds versus second generation drug-eluting stents for percutaneous treatment of chronic total coronary occlusions: Technical and procedural outcomes from the GHOST-CTO registry. *Catheter Cardiovasc Interv*. 2016 Jan 12. doi: 10.1002/ccd.26397. [Epub ahead of print]
90. Valenti R, Vergara R, Migliorini A, et al. Predictors of reocclusion after successful drug-eluting stent-supported percutaneous coronary intervention of chronic total occlusion. *J Am Coll Cardiol*. 2013;61(5):54
91. Grasso C, Attizzani GF, Patané M, et al. First-in-human description of everolimus-eluting bioabsorbable vascular scaffold implantation for the treatment of drug-eluting stent failure: insights from optical coherence tomography. *Int J Cardiol*. 2013 ;168 :4490-1.
92. Ielasi A, Latib A, Naganuma T, Cortese B, Sato K, Miyazaki T, Panoulas VF, Tespili M, Colombo A. Early results following everolimus-eluting bioresorbable vascular scaffold implantation for the treatment of in-stent restenosis. *Int J Cardiol*. 2014 ;173 :513-4.
93. Moscarella E, Varricchio A, Stabile E, Latib A, Ielasi A, Tespili M, Cortese B, Calabrò P, Granata F, Panoulas VF, Franzone A, Trimarco B, Bonzani G, Esposito G, Colombo A. Bioresorbable vascular scaffold implantation for the treatment of coronary in-stent restenosis: results from multicenter Italian experience. *Int J Cardiol*. 2015; 199:366-72.

94. Rivero F, Bastante T, Cuesta J, Benedicto A, Restrepo JA, Alfonso F. Treatment of in-stent restenosis with bioresorbable vascular scaffolds: optical coherence tomography insights. *Can J Cardiol*. 2015;31(3):255-259.
95. Buchanan GL, Basavarajaiah S, Chieffo A, Stent thrombosis: incidence, predictors and new technologies. *Thrombosis*. 2012 ; 2012 :956962.
96. Brugaletta S, Gori T, Low AF, et al. Absorb bioresorbable vascular scaffold versus everolimus-eluting metallic stent in ST-segment elevation myocardial infarction: 1-year results of a propensity score matching comparison: the BVS-EXAMINATION Study (bioresorbable vascular scaffold-a clinical evaluation of everolimus eluting coronary stents in the treatment of patients with ST segment elevation myocardial infarction). *JACC Cardiovasc Interv* 2015; 8:189–197
97. Gori T, Schulz E, Hink U, et al. Early outcome after implantation of Absorb bioresorbable drug eluting scaffolds in patients with acute coronary syndromes. *EuroIntervention*. 2014; 9:1036-41.
98. Cortese B, Ielasi A, Romagnoli E, et al. Clinical Comparison With Short-Term Follow-Up of Bioresorbable Vascular Scaffold Versus Everolimus-Eluting Stent in Primary Percutaneous Coronary Interventions. *Am J Cardiol*. 2015;116(5):705-10.
99. Diletti R, Karanasos A, Muramatsu T, et al. Everolimus-eluting bioresorbable vascular scaffolds for treatment of patients presenting with ST-segment elevation myocardial infarction: BVS STEMI first study. *Eur Heart J*. 2014; 35:777-86.
100. Kocka V, Maly M, Tousek P, et al. Bioresorbable vascular scaffolds in acute ST-segment elevation myocardial infarction: a prospective multicenter study 'Prague 19'. *Eur Heart J*. 2014;35: 787-94.
101. Wiebe J, Möllmann H, Most A, et al. Short-term outcome of patients with ST-segment elevation myocardial infarction (STEMI) treated with an everolimus-eluting bioresorbable vascular scaffold. *Clin Res Cardiol*. 2014;103(2):141-8.
102. Sabaté M, Windecker S, Iñiguez A, Okkels-Jensen L, Cequier A, Brugaletta S, et al. Everolimus-eluting bioresorbable stent vs. durable polymer everolimus-eluting metallic stent in patients with ST-segment elevation myocardial infarction: results of the randomized ABSORB ST-segment elevation myocardial infarction-TROFI II trial. *Eur Heart J*. 2016 Jan 14;37(3):229-40.
103. Onuma Y, Ormiston J, Serruys PW. Bioresorbable scaffold technologies. *Circ J* 2011; 75:509–520.
104. Seifert B, Romaniuk P, Groth TH. Bioresorbable, heparinized polymers for stent coating: in vitro studies on heparinization efficiency, maintenance of anticoagulant properties and improvement of stent hemocompatibility. *J Mater Sci Mater Med*. 1996; 7:465-9.
105. Onuma Y, Serruys PW, Perkins LE, Okamura T, Gonzalo N, García-García HM, et al. Intracoronary optical coherence tomography and histology at 1 month and 2, 3, and 4 years after implantation of everolimus-eluting bioresorbable vascular scaffolds in a porcine coronary artery model: an attempt to decipher the human optical coherence tomography images in the ABSORB trial. *Circulation*. 2010;122(22):2288-300.
106. Onuma Y, Serruys PW, Ormiston JA, Regar E, Webster M, Thuesen L, Dudek D, Veldhof S, Rapoza R. Three-year results of clinical follow-up after a bioresorbable everolimus-eluting scaffold in patients with de novo coronary artery disease: the ABSORB trial. *EuroIntervention*. 2010; 6:447-53.
107. Karanasos A, van Geuns RJ, Zijlstra F, Regar E. Very late bioresorbable scaffold thrombosis after discontinuation of dual antiplatelet therapy. *Eur Heart J*. 2014;35(27):1781.
108. Sato K, Panoulas VF, Naganuma T, Miyazaki T, Latib A, Colombo A. Optimal duration of dual antiplatelet therapy after implantation of bioresorbable vascular scaffolds: lessons from optical coherence tomography. *Can J Cardiol*. 2014;30(11): 1460.e15-7.
109. Everaert B, Felix C, Koolen J, et al. Appropriate use of bioresorbable vascular scaffolds in percutaneous coronary interventions: a recommendation from experienced users: A position statement on the use of bioresorbable vascular scaffolds in the Netherlands. *Neth Heart J*. 2015;23(3):161-5.

110. Sarafoff N, Drepepa G, Mehilli J et al.: Aspirin and clopidogrel with or without phenprocoumon after drug eluting coronary stent placement in patients on chronic oral anticoagulation. *J. Intern. Med.* 2008; (264): 472–480.\
111. Sarafoff N, Martischnig A, Wealer J, et al. Triple therapy with aspirin, prasugrel, and vitamin K antagonists in patients with drug-eluting stent implantation and an indication for oral anticoagulation. *J Am Coll Cardiol.* 2013; 61:2060–2066.
112. Gori T, Schulz E, Munzel T. Immediate, acute, and subacute thrombosis due to incomplete expansion of bioresorbable scaffolds. *J Am Coll Cardiol Interv* 2014; 7:1194–5
113. Karanasos A, Van Mieghem N, van Ditzhuijzen N, et al. Angiographic and optical coherence tomography insights into bioresorbable scaffold thrombosis: single-center experience. *Circ Cardiovasc Interv* 2015;8: e002369.

Chapter 3

**Intracoronary Optical Coherence
Tomography: Clinical and Research
Applications and Intravascular Imaging
Software Overview**

**Randomized comparison of Absorb
bioresorbable vascular scaffold and
Mirage microfiber sirolimus eluting
scaffold using multi-modality imaging**

Intracoronary Optical Coherence Tomography: Clinical and Research Applications and Intravascular Imaging Software Overview

Erhan Tenekecioglu, Felipe N. Albuquerque, Yohei Sotomi, Yaping Zeng, Pannipa Suwannasom, Hiroki Tateishi, Rafael Cavalcante, Yuki Ishibashi, Shimpei Nakatani, Mohammad Abdelghani, Jouke Dijkstra, Christos Bourantas, Carlos Collet, Antonios Karanasos, Maria Radu, Ancong Wang, Takashi Muramatsu, Ulf Landmesser, Takayuki Okamura, Evelyn Regar, Lorenz Räber, Giulio Guagliumi, Robert T. Pyo, Yoshinobu Onuma, Patrick W. Serruys

Catheter Cardiovasc Interv. 2017;89(4):679-689.

ABSTRACT

By providing valuable information about the coronary artery wall and lumen, intravascular imaging may aid in optimizing interventional procedure results and thereby could improve clinical outcomes following percutaneous coronary intervention (PCI). Intravascular optical coherence tomography (OCT) is a light-based technology with a tissue penetration of approximately 1 to 3 mm and provides near histological resolution. It has emerged as a technological breakthrough in intravascular imaging with multiple clinical and research applications. OCT provides detailed visualization of the vessel following PCI and provides accurate assessment of post-procedural stent performance including detection of edge dissection, stent struts apposition, tissue prolapse, and healing parameters. Additionally, it can provide accurate characterization of plaque morphology and provides key information to optimize post-procedural outcomes. This manuscript aims to review the current clinical and research applications of intracoronary OCT and summarize the analytic OCT imaging software packages currently available.

INTRODUCTION

The increased use of intravascular imaging-guided percutaneous coronary intervention (PCI) requires the interventional cardiologist to have a deep understanding of the current clinical and research applications of different intravascular imaging modalities. Intracoronary optical coherence tomography (OCT) is an intravascular light-based technology with a near histological resolution of 10-20 μ m. It allows characterization of the vessel wall beyond simply the luminal dimensions and has wide applications in interventional cardiology. In this report, we provide a review of the clinical and research applications of intracoronary OCT along with a brief description of the current analytic software packages applied for intravascular imaging analyses.

Plaque composition

OCT is a useful tool in visualization of the plaque composition primarily due to its high resolution. Atherosclerotic plaques and calcification can be well defined by OCT and determined by the presence of a well-delineated, low back scattering region with low alight attenuation and low reflectivity characteristics.¹ The fibrous component of the plaque is recognized as a homogenous tissue with high reflectivity and low attenuation, while the lipid component has diffuse edges with high light reflectivity and attenuation. Therefore, lipid pool is mostly seen as diffusely bordered, signal-poor areas overlaid with signal-rich bands that correspond to fibrous caps.²

Fibrous cap analysis

The large proportion of the coronary events have been attributed to rupture of thin-cap fibroatheromas (TCFA), which are coronary plaques characterized by a large necrotic core covered by a thin fibrous cap infiltrated with macrophages. A thickness of 65 μ m is considered the threshold of plaque instability and one of the major morphological determinants of plaque rupture.³ OCT is widely used and has good sensitivity and specificity for identifying TCFA. Detection of the fibrous cap thickness can be performed semi-automatically using the QCU-CMS software (Medis, Leiden, The Netherlands); which automatically segments and delineates the adluminal and abluminal boundaries of the fibrous cap using dynamic programming on the Cartesian OCT images (**Figure 1**). The semi-automated method was developed to overcome the limited reproducibility of a purely manual approach. It allows a less subjective volumetric assessment of the fibrous cap and is more reproducible compared

to the manual method, providing the minimal, maximal and mean cap thickness as well as the angle of the lipid pool. ⁴ Several factors can induce the appearance of a false thin or thick cap fibroatheroma. The presence of a smooth muscle cells and the lack of connective tissue in the fibrous cap may induce the misdiagnosis of lipid core in the TCFA. ⁵

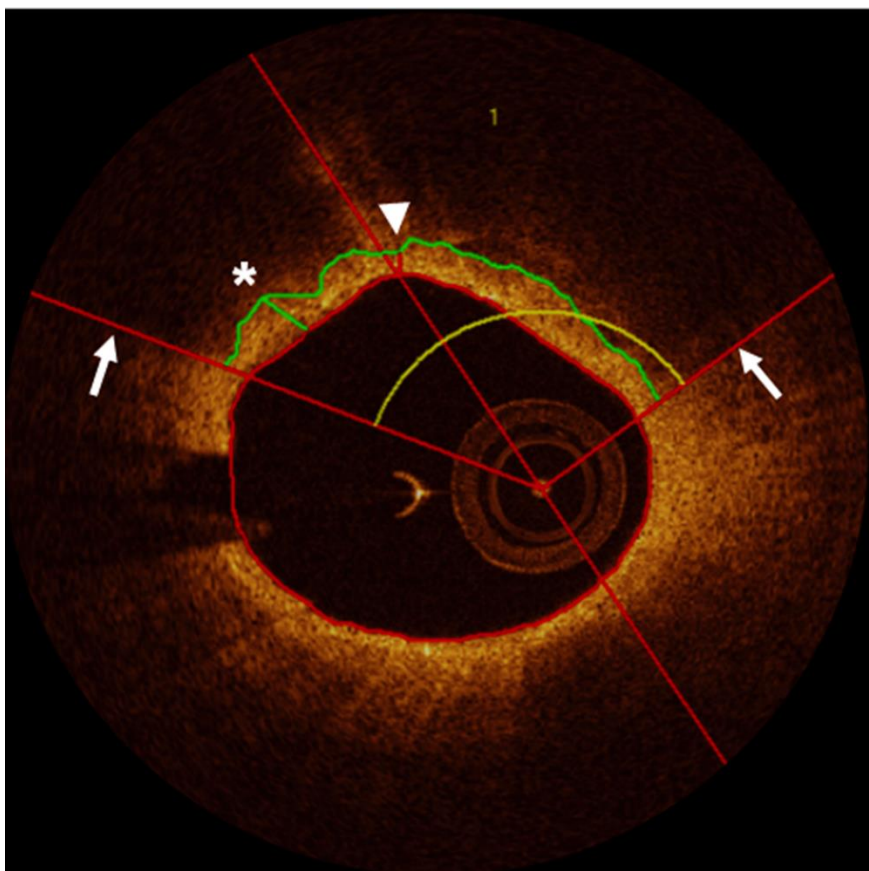


Figure 1. Illustration of the semi-automated fibrous cap thickness detection method. The lateral extremities of the necrotic core are defined by the two angular red lines (arrows). The green contour delineates the abluminal border of the fibrous cap, where the green (*) and the red (arrowhead) lines indicate the maximum and minimum cap thickness.

Accumulation of foam cells can lead to superficial shadowing due to strong light scattering and can also mimic the appearance of false TCFA. Another mechanism for misclassification in the fibrous plaque is tangential signal dropout that induces light attenuation along an oblique line-of-sight. ⁶ Atherosclerotic plaque components play an important role in OCT light backscattering. Calcification, connective tissue and extracellular lipid content of the plaque may also affect the diagnosis of TCFA. The distribution pattern of the foam cells introduces different types of light scattering which induces misdiagnosis for thickness of the fibrous caps and plaque types (**Figure 2**). ⁵ There is no consensus on the how many quadrants of an OCT image

or lipid arc should be dark to be defined as TCFA.^{5,7} In some studies proposed that necrotic core should subtend an arc $>90^\circ$ or encompassed >1 quadrant of OCT image.⁷

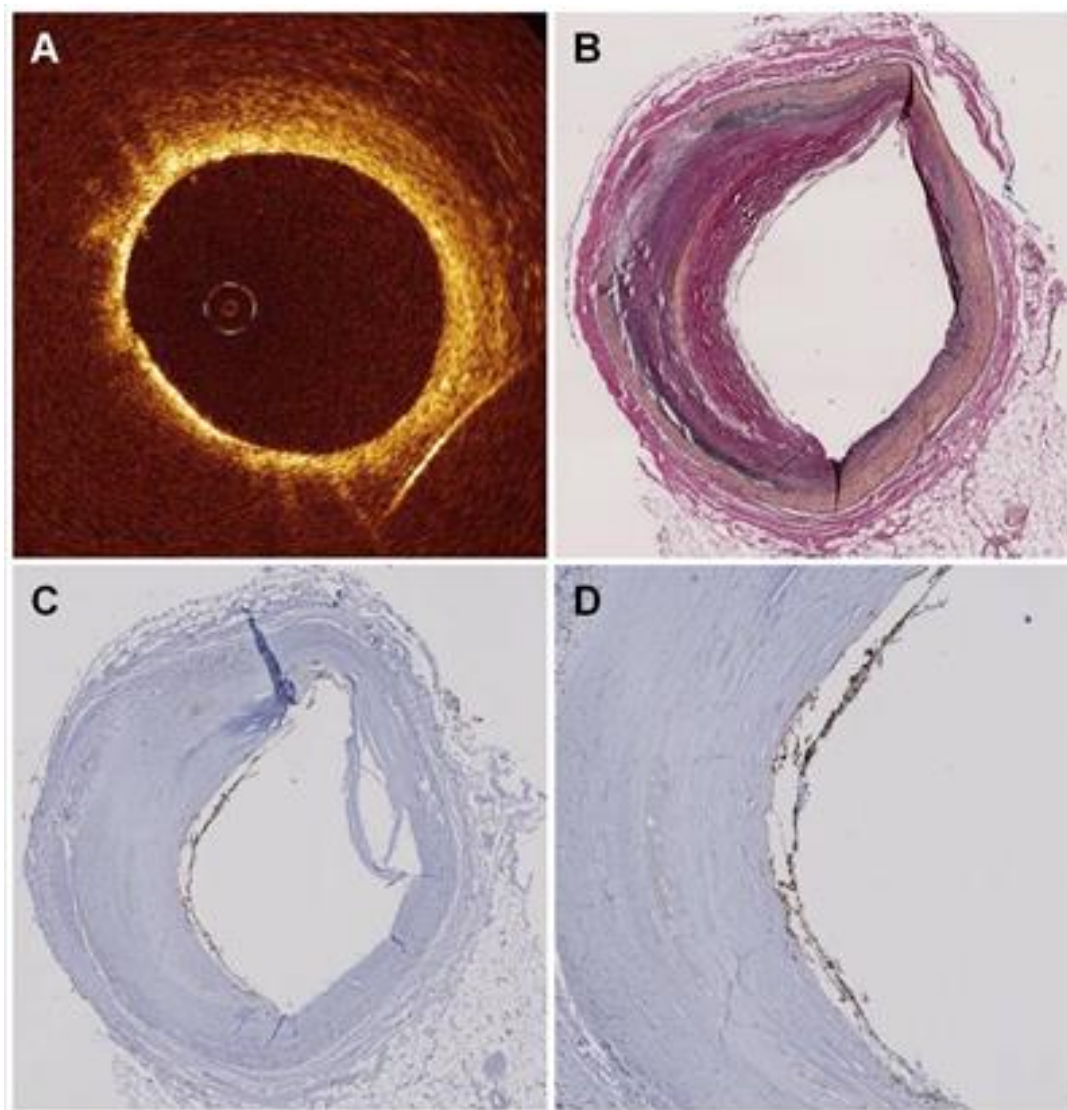


Figure 2. The accumulation of the foam cells induces different types of light scattering which leads to misdiagnosis for thickness of the fibrous caps and plaque types. Macrophage accumulation causes an appearance of pseudo TCFA (A), while elastic van Gieson staining demonstrates a fibrotic lesion (at 9 o'clock) (B). CD68 staining shows the accumulated macrophages in the inner layer of the intima (at 9 o'clock in C and D).

Assessment of stent/scaffold performance and post-implantation optimization

OCT provides excellent image resolution allowing detailed assessment of the implanted stents and coronary arteries. It assists the pre-procedural planning with exact dimensions (lesion length, lesion severity, landing zone, stent sizing), detection of complications and facilitates the operators to achieve optimal PCI results. The common geometric parameters used in stent/scaffold procedures and performance evaluations are readily measurable.

Lumen and stent/scaffold areas- There are two commercially available software packages for the assessment of stent implantation and procedural optimization. The QIvus 3.0 software package (Medis, Leiden, The Netherlands) allows off-line semi-automatic stent and vessel lumen analysis. The ILUMIEN™ PCI Optimization System software (St. Jude Medical, Minnesota, USA) provides automated lumen profile and displays the key stent planning metrics. Highly-accurate on-line measurements of the lumen contour with automatic marking of the minimal lumen area (MLA) after selection of the region of interest, distance between references, percent area stenosis (%AS) and percent diameter stenosis (%DS) are available to the operator. Additionally, the software can automatically detect malapposition. The new features of graphic unit interface are 1) Stent roadmapping on angiography co-registration which provides the ability to visualize the intended stent landing zone on the angiography co-registration and evaluate the stent position prior to the implant; 2) Automatic metallic stent strut detection and apposition, allowing immediate visualization of the stent segment with malapposed struts to evaluate and decide for further post-dilation. A false color scale automatically displays in corresponding cross-section and assess the malapposition distance at each malapposed strut (**Figure 3**).

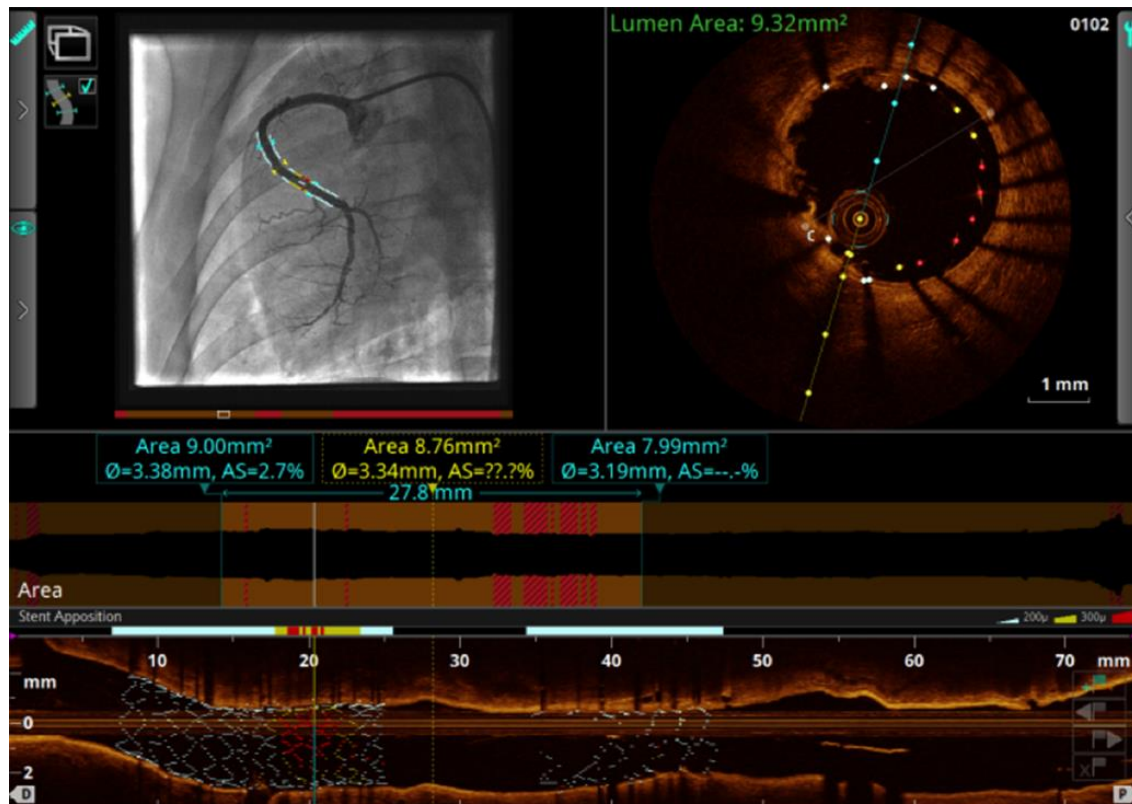


Figure 3. The software provides the intended stent landing zone on the co-registration angiography to evaluate the appropriate stent position prior to the implant.

Misinterpretations of the OCT images can occur due to eccentricity of the image-wire in the vessel lumen. If the OCT catheter is oblique to the vessel axis, the lumen may appear elliptical and distorted, affecting the accuracy of its measurement.⁸ If the imaging catheter is located close the luminal wall, the light beam is emitted parallel to the luminal surface and that specific part of the coronary wall may seem to attenuate the light when in reality light is actually not penetrating in that zone. This imaging artefact can be confused with the appearance of superficial accumulation of macrophages, lipid pool, necrotic core or a TCFA.⁷

Eccentricity and asymmetry- The eccentricity and symmetry of the implanted stent/scaffold can be readily assessed by OCT. The eccentricity index is defined as the ratio between the minimum and maximum diameters of the stent/scaffold in each frame. The asymmetry index is calculated as the difference between the maximum and minimum stent/scaffold diameters, divided by the maximum stent/scaffold diameter (**Figure 4**).

Stent expansion and residual area stenosis - The expansion index is defined as the minimal stent/scaffold area divided by the reference lumen area. The percentage of residual area stenosis is calculated as: $[1 - (\text{minimal lumen area}/\text{reference lumen area}) \times 100]$.

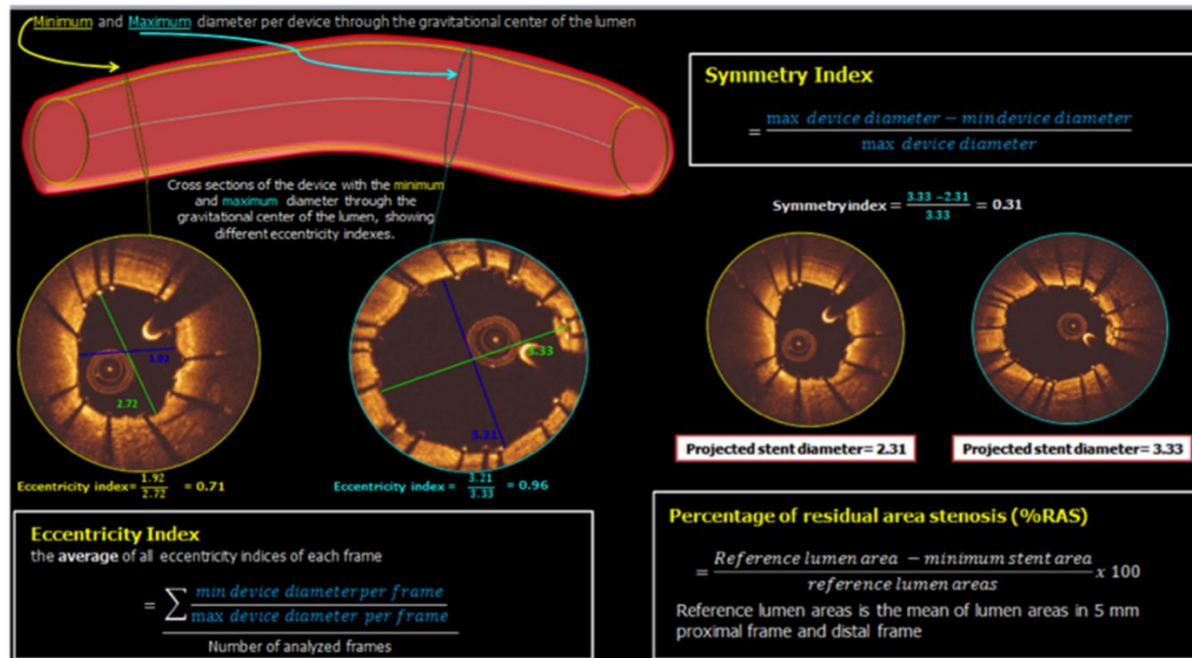


Figure 4. Definitions of eccentricity index, symmetry index and residual artery stenosis.

Metallic stent and bioresorbable scaffold strut detection

Automatic stent strut detection facilitates the quantitative stent strut analysis and provides the basis of rapid creation of a three-dimensional (3-D) stent reconstruction. An automated

metallic stent strut detection method using OCT was developed with the MeVisLab toolbox (MeVis Medical Solutions AG, Bremen, Germany). This method is based on the intensity features and shadow edge detection. The metal stent strut typically appears as a bright spot with a trailing dark shadow behind it since the metal stent strut reflects most of the light, while the normal vessel tissue scatters and attenuates the light (**Figure 5**). The automated method for metallic strut detection uses the local image intensity of every scan-line to detect the candidate pixels of the stent struts in the preprocessed OCT images. The edges of the trailing shadows are detected to assist the candidate pixels clustering for each strut, to reduce the false positives and to find the dark struts with clear shadows. The method is independent of pre-selection, strut status or lumen/vessel wall segmentation and was validated in real clinical studies and shown to be reliable.⁹

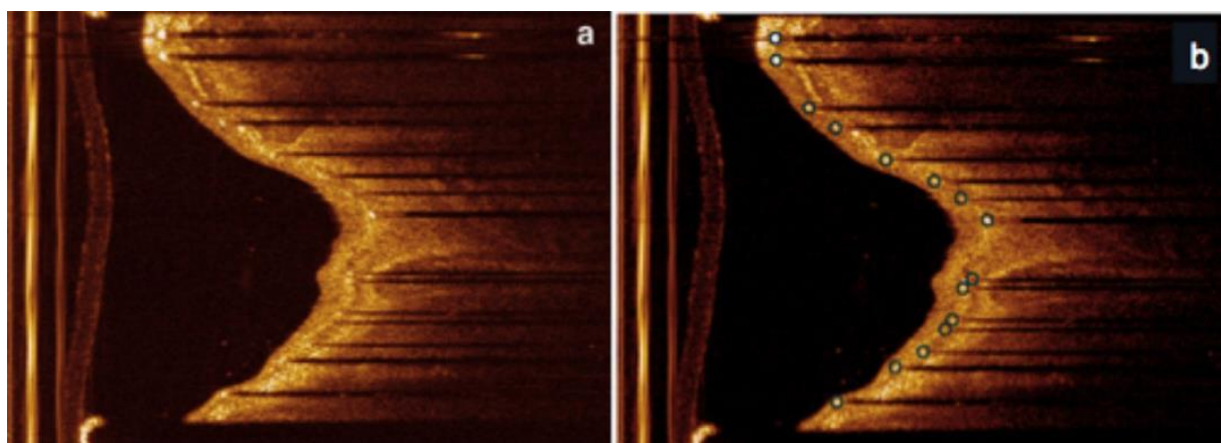


Figure 5. OCT images of the metallic stent struts with dark shadows (a) and the automated metallic stent strut detection results delineated by the white circles (b).⁹

Another automated method was implemented to detect bioresorbable scaffolds struts. The shapes of the bioresorbable struts are corrected by re-opening the Cartesian images from the lumen center. Based on the intensity and gradient features, candidate line segments that constitute possible scaffold struts are detected on each scan-line and these segments are clustered to candidate struts followed by a series of false positive removal filters. Finally, refined contours of all bioresorbable scaffold struts are generated for area measurements (**Figure 6**). The sunflower effect is an OCT image artifact observed during the implantation of metallic coronary stents. It appears as a bending of the stent struts toward the imaging catheter, likely due to an eccentric position of the imaging catheter in the vessel lumen. This artifact appears more noticeable when the catheter is in contact with the luminal wall. Since the light beam rotates over a stent strut, only one part of the strut reflects light back to the

catheter. Due to oblique light reflection, the struts may seem malapposed to the vessel wall and lead to misinterpretation of the apposition measurement and lead to misinterpretations in the apposition measurements and inaccuracy of the measurement (**Figure 7**).^{10,11}

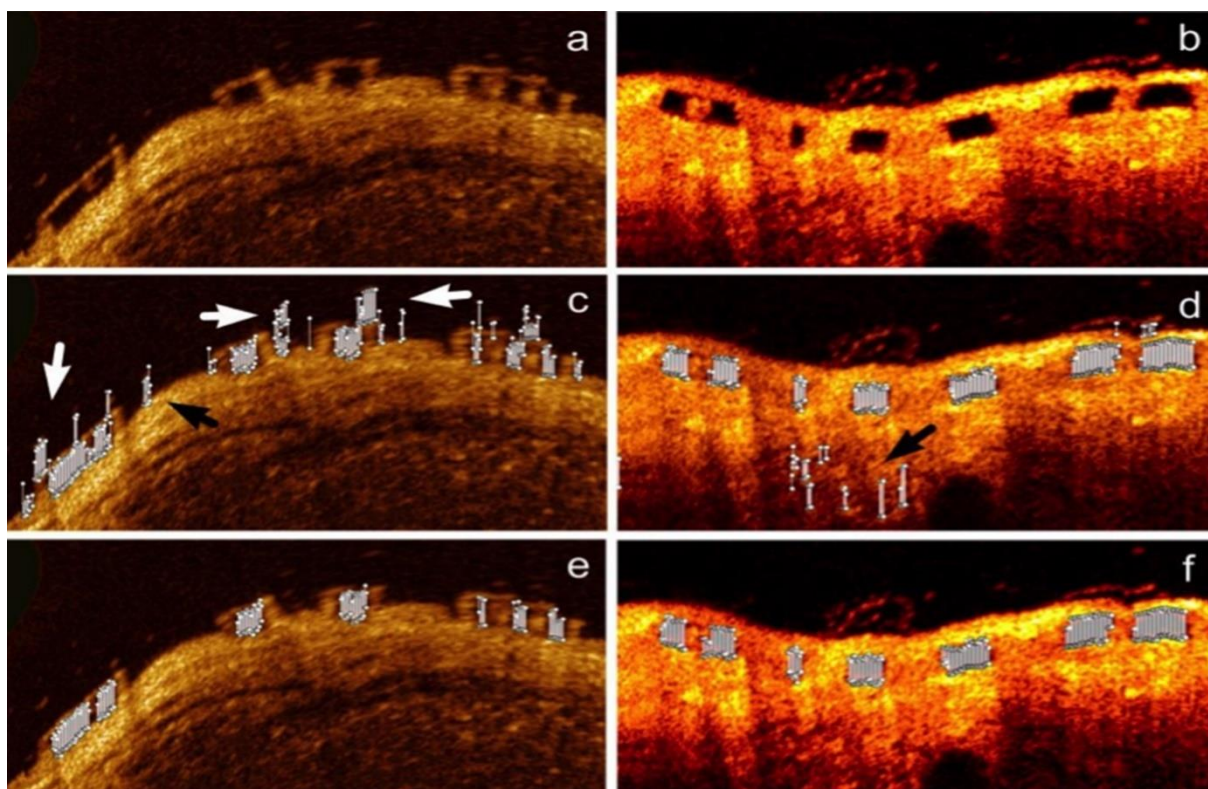


Figure 6. OCT images of the bioresorbable scaffold struts at baseline (A) and at follow-up (B). The black and white arrows (C and D) represent the false line segments caused by residual blood or noise in tissue that were posteriorly removed after clustering (E and F).⁵⁸



Figure 7. Stent struts always face to the catheter (Sunflower effect). This effect is more pronounced when the catheter is located eccentric within the vessel lumen towards the side of the vessel wall.

Stent/scaffold embedment

The assessment of strut-vessel wall interaction can be performed by OCT using the embedment analysis. The interpolated lumen contour should be drawn at the site where the metallic or polymeric struts are embedded (**Figure 8**). This contour interpolates through the protruding metallic or polymeric struts. Using this interpolated lumen contour, malapposition and the degree of embedment are assessed per individual strut. The degree of the embedment can be calculated by the following formula: $1 - (\text{the distance between the midpoint of the endoluminal strut surface to the interpolated lumen contour}) / \text{strut thickness} \times 100 (\%)$. Completely protruding is defined as the abluminal surface of metallic or polymeric struts being aligned with the interpolated lumen contour line (0% embedment). When the degree of embedment is between 0% and 50%, the strut is classified as partially protruding. When the degree is between 50 and 100%, such struts are categorized as partially embedded. Complete embedment is defined as the endoluminal surface of metallic or polymeric struts being aligned with the interpolated lumen contour line (100% embedment). When the tissue is covering the endoluminal surface of struts, they are considered as buried struts. In a recent study¹², using a new dedicated software, embedment status was classified into 6 classes (Embedment Class [EC] 0–5) based on the degree of embedment (percentage). If struts were malapposed (indicated as negative value of percentage in the software), this was classified as EC0. When the strut was partially embedded in the vessel wall, the degree of embedment was categorized by each quartile ($0 \% \leq \text{EC1} < 25 \%$, $25 \% \leq \text{EC2} < 50 \%$, $50 \% \leq \text{EC3} < 75 \%$, $75 \% \leq \text{EC4} < 100 \%$). When the tissue was covering the endoluminal surface of struts, the struts were considered as “buried”, EC5 ($\geq 100 \%$)

Tissue prolapse

OCT is able to distinguish different types of vessel injury during stent implantation. Tissue prolapse is defined as a convex-shaped protrusion of tissue between adjacent stent struts towards the lumen without disruption of the continuity of the luminal vessel surface. Protrusion of tissue between struts are considered tissue prolapse if the distance from the arc that connects adjacent stent struts to the greatest extent of protrusion is $>50 \mu\text{m}$. Lipids rich plaques may demonstrate a higher prevalence of tissue prolapse than fibrous plaques and its clinical impact after stenting is not entirely understood.

Light attenuation

The coherent OCT light beam propagates according to the Lambert-Beer's law, which proposes that high light attenuation coefficients result in a faster and exponential decrement in the irradiance of the light beam in depth. Since the light attenuation coefficient is related to the optical property of the medium, the attenuation coefficient provides information about the medium composition. Total light attenuation is related to absorption by the tissue and light scattering.¹³ The attenuation coefficient can be measured by fitting an exponential curve through the OCT depth profiles.

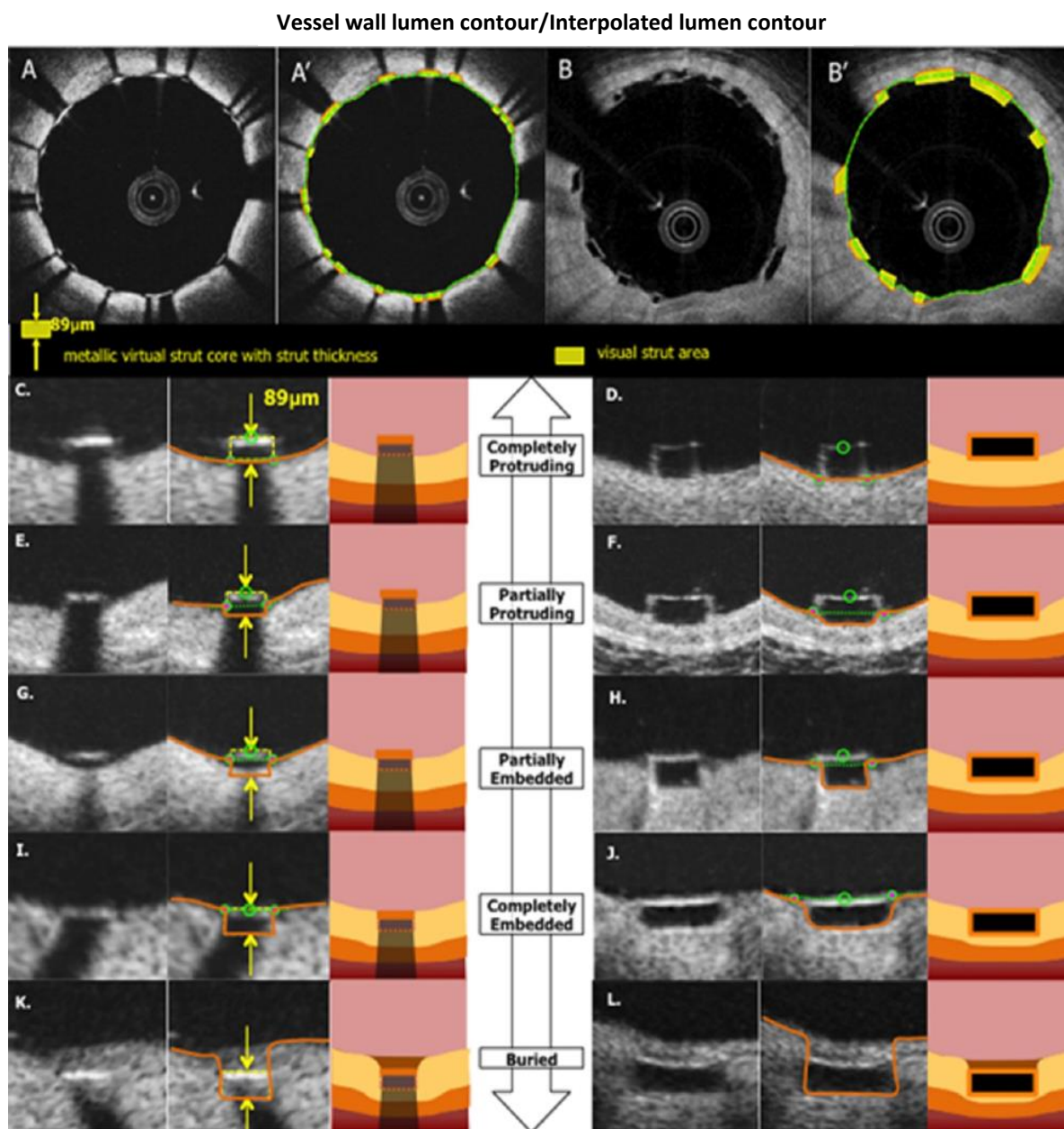


Figure 8. Cross-sections with well-apposed metallic struts and polymeric struts (A and B). Strut area measurement and the interpolated lumen contour (A' and B'). Definitions of embedment based on the distance between strut and interpolated lumen contours (C-L).⁵⁹

A disadvantage of OCT is its lower depth of light penetration compared to IVUS.¹⁴ However, the coronary arteries have low light absorption and the OCT light can penetrate around 2-3 millimeters in the vessel wall.¹⁵ Optical light attenuation analysis is used to identify vessel wall components and facilitate tissue characterization (**Figure 9**). Ex-vivo studies have demonstrated an association of high attenuation (attenuation coefficient $\geq 8\text{mm}^{-1}$) with high-risk plaque components such as necrotic core, while low attenuation ($< 6\text{mm}^{-1}$) was associated with healthy vessel, intimal thickening or calcified plaque.¹⁶ Results from attenuation analysis can be plotted in 2-D maps demonstrating the maximum attenuation values throughout the analyzed segment. Custom-built software created by Matlab Release 2012b (The Mathworks, Inc., Natick, MA, USA) has been used for the assessment of tissue attenuation within a plaque.¹⁶

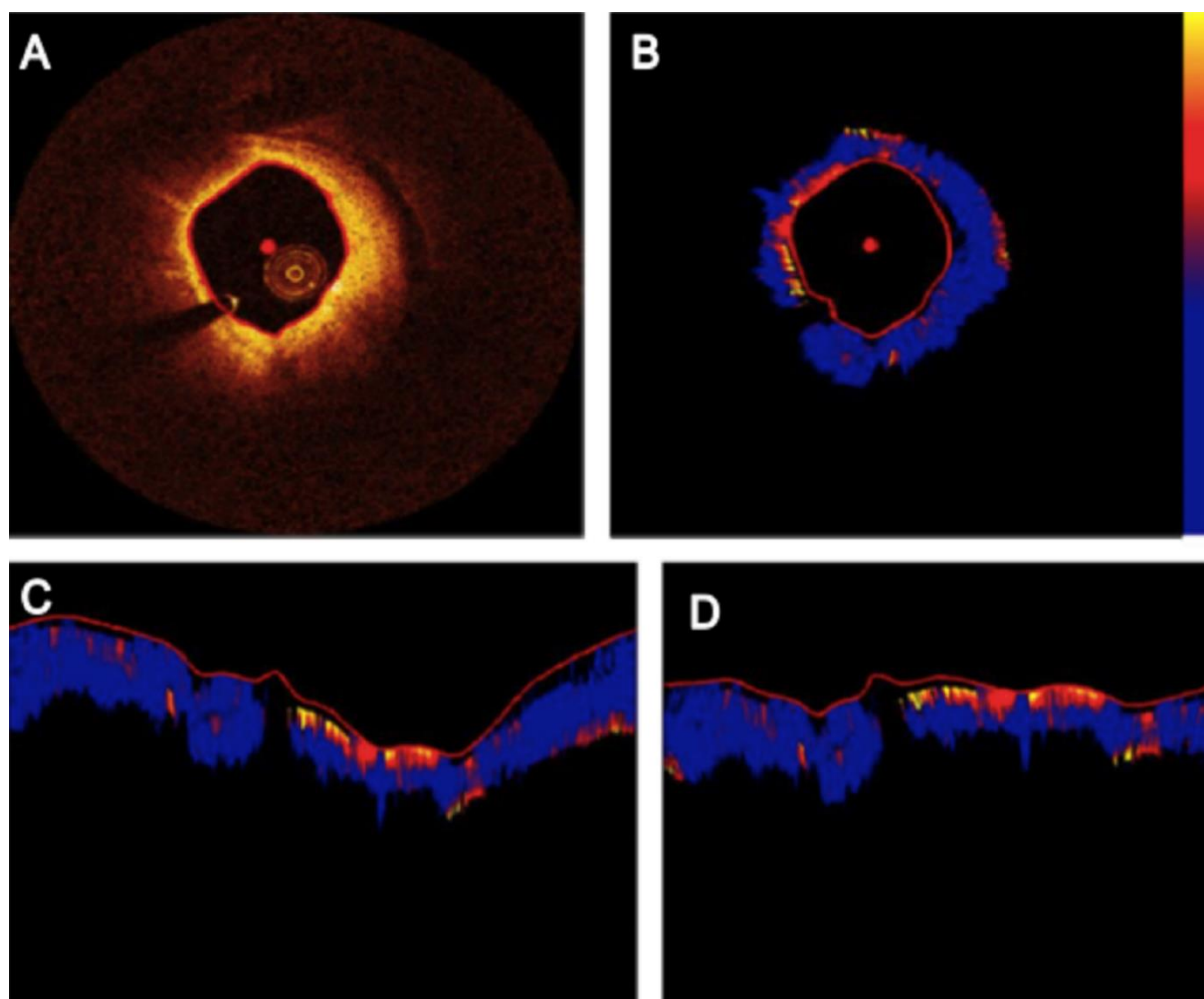


Figure 9. OCT and attenuation images with lumen border and the centroid (A and B). Lower panels illustrate a polar image before (C) and after (D) the shift of origin.¹⁶

Light intensity

OCT can also be applied for quantitative light intensity/density analysis using dedicated software (QCU-CMS, Leiden, The Netherlands) to evaluate the bioresorbable scaffolds strut core.¹⁷ The OCT images consist of a “black core” area surrounded by reflective borders due to differences in the refraction index post-procedure (**Figure 10**). Changes in strut appearance on OCT correspond to the cell proliferation of the provisional matrix and the appearance of connective tissue surrounding the cell nuclei stained in black in a Movat histological preparation. The quantitative light intensity analysis of strut cores on OCT could be used as a surrogate method for monitoring the matrix infiltration and integration of collagen-rich connective tissue within the polymeric struts.

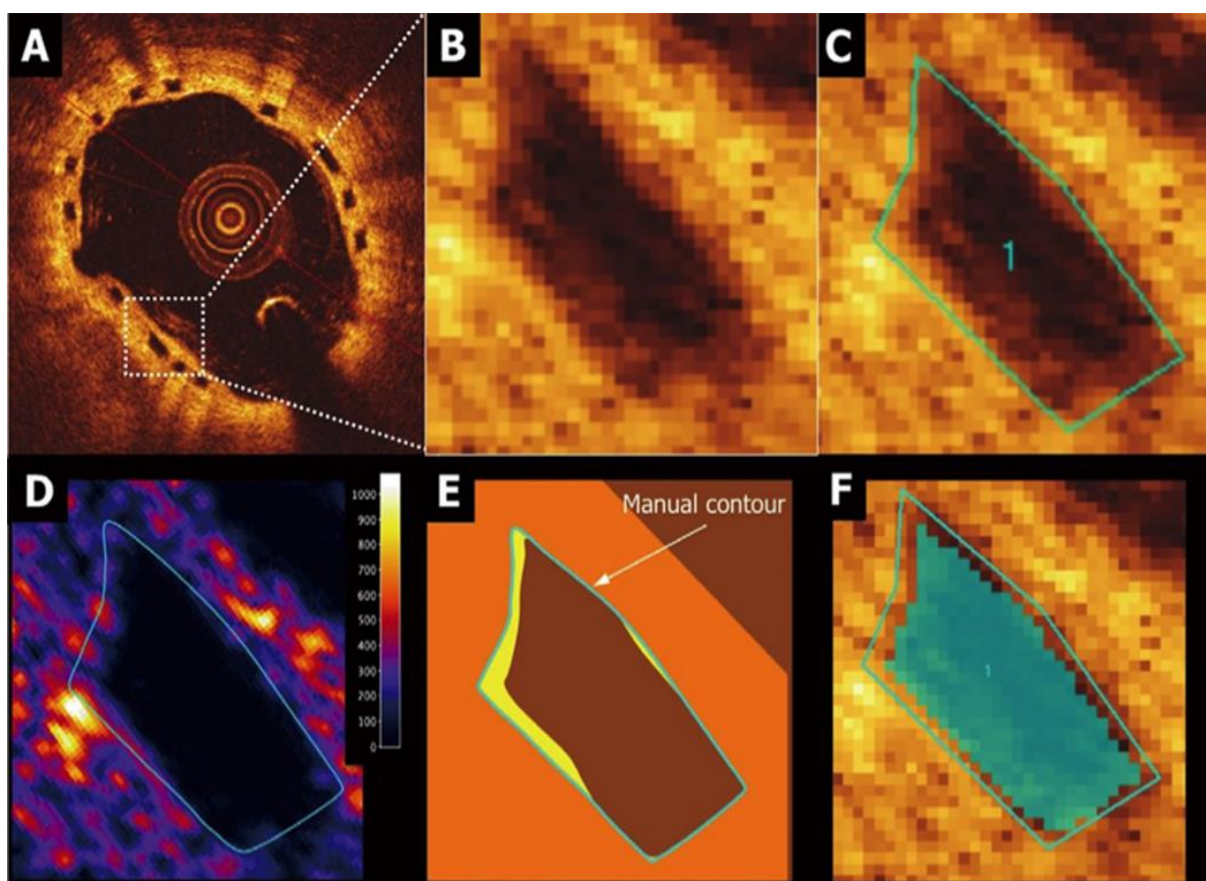


Figure 10. Bioresorbable scaffold strut core for light intensity assessment (A and B). Strut core contours are manually drawn and light intensity mapping around the strut core (C and D). The strut core borders at follow-up often include the reflective strut frame borders, so part of the bright reflective frame can be misclassified as a strut core region (E). The strut core region after automatic subtraction of 2 pixels inside the manual contours (F).¹⁷

Endothelial shear stress

Neointimal formation is modulated by several factors, including the vessel wall trauma post-stent implantation, the underlying plaque burden and the local endothelial shear stress (ESS) patterns. Studies have suggested that ESS promotes neointimal formation in bare-metal stents, whereas in drug-eluting stents, the association between ESS and neointimal proliferation is weak and affected by the type and the release kinetics of the eluted drug.¹⁸ Moreover, silico blood flow simulation studies have underscored the effect of stent design on local hemodynamic patterns and shear rate that appears to affect the risk of stent thrombosis. Several methodologies were developed for the reconstruction of coronary anatomy from OCT data. These approaches include: 1) detection of the lumen/stent/scaffold borders 2) extraction of the luminal centerline from two angiographic projections, 3) placement of the detected OCT contours perpendicularly onto the lumen centerline and 4) estimation of the absolute orientation of the OCT frames using anatomical landmarks seen in both OCT and angiographic images. The obtained models provide geometrically correct and detailed reconstruction of the luminal morphology and enable processing with computational fluid dynamic techniques and assessment of the local hemodynamic forces.

OCT-based reconstruction appears superior to IVUS-based modeling as OCT images have a higher resolution and allows more accurate assessment of luminal pathology and detailed visualization of the protruded strut in stented/scaffolded segments. There is robust evidence showing that OCT-based modeling can be used to evaluate flow disturbances in evaginations, and the effect of the implanted stent/scaffold on the local hemodynamic micro-environment and thus it is expected to have future application in evaluating the hemodynamic implications of different bioresorbable scaffold designs (**Figure 11**)¹⁹.

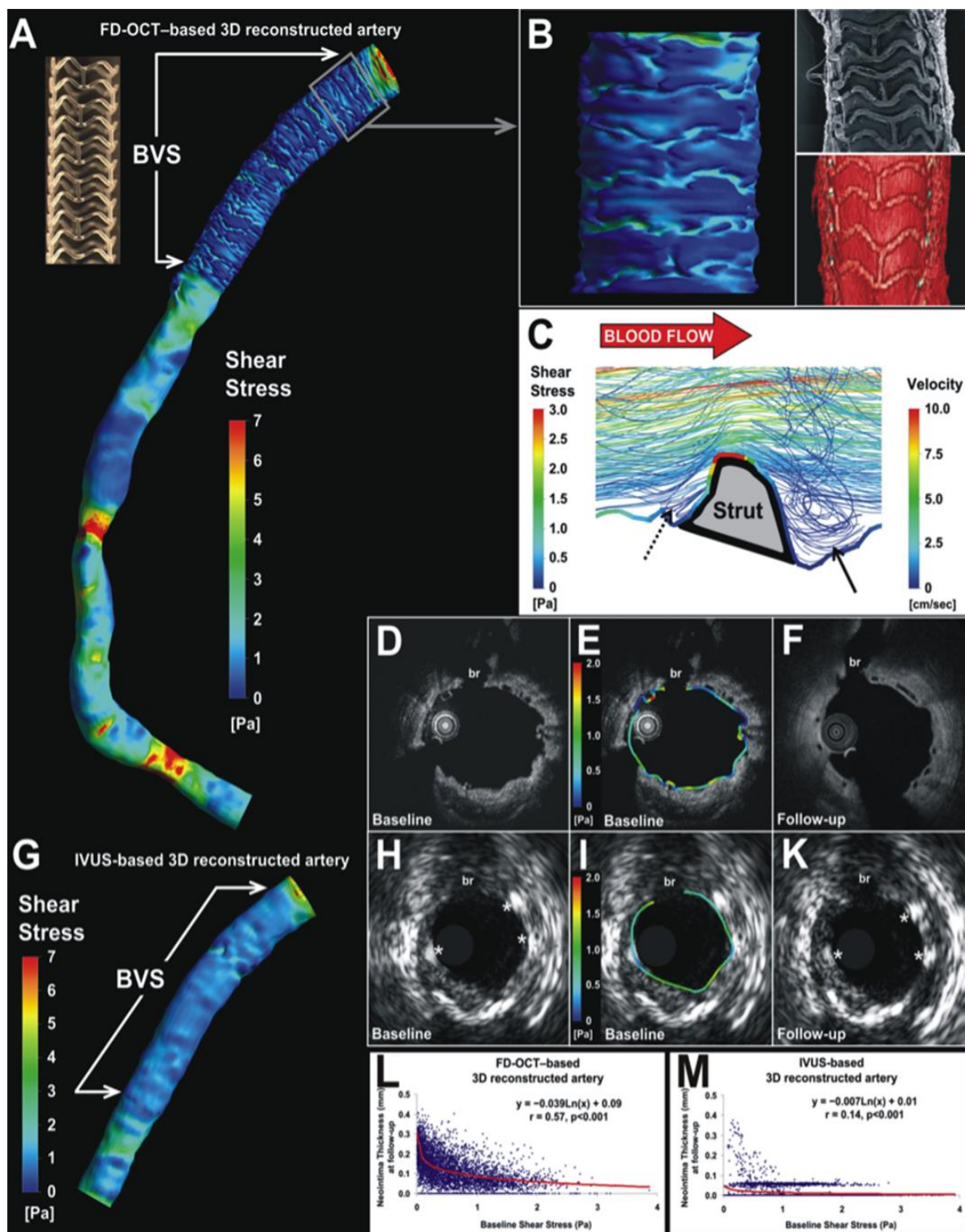


Figure 11. 3-D reconstruction of a scaffolded segment from OCT, angiography and local ESS distribution (color-coded map). Absorb BVS image (A) and a magnified view of the reconstructed surface shown in an electron microscopy image post scaffold deployment and a 3-D image of the patient's artery (B). Flow streamlines around the strut demonstrate flow disturbances and recirculation zones distal (arrow) and proximal to the strut (dotted arrow) that result in low ESS (C). Panels D, E and F portray corresponding OCT cross-sectional images. Fusion of IVUS with angiography images including local ESS distribution (G). Corresponding IVUS and OCT images (H-K). The ESS distribution has homogeneous pattern (I). The association between ESS and neointima thickness is much stronger in the OCT-based ($r=0.57$) versus the IVUS-based ($r=0.14$) reconstruction (L, M).⁶⁰

Edge dissection and coronary evagination

Several studies suggested that OCT has higher accuracy in detecting edge dissections compared to angiography or IVUS.²⁰ Edge dissection is defined as a disruption of the luminal surface in the 5mm native segment that is adjacent to the proximal and distal edge of the stent and most often due to the vessel trauma during stent implantation. Edge dissections are classified as flaps, cavities, double-lumen dissections or fissures (**Figure 12**). Gonzalo and colleagues found that the incidence of non-flow-limiting OCT edge-dissections after stent implantation were approximately 34%, the majority of the cases healed uneventfully, and the edge dissections that were angiographically silent were not associated with acute stent thrombosis or restenosis after one-year follow-up.²⁰ Coronary evaginations are defined as an outward vessel bulging of the luminal contours between the stent struts.²¹ Uncovered struts, late malapposition, positive remodeling, chronic inflammation as well as ecstasies and aneurysms are the features associated with very late ST.^{22,23} In the study by Radu et al, the researchers found nearly all these features to be more common in lesions with major coronary evaginations, suggesting that major evaginations may be part of the same pathophysiological entity commonly determined as inadequate healing following DES implantation, proposing a possible link with late ST. Since patient number was too small for a meaningful evaluation for such a relationship.²¹

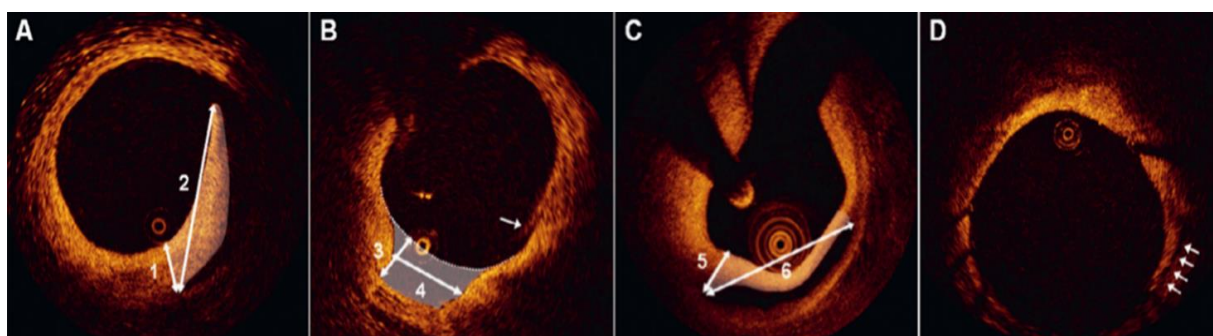


Figure 12. The classification of edge dissections. Panel A-Dissection flap with indication of the flap root thickness (1), flap length (2), and flap area (white shading). Panel B-Dissection cavity with the cavity depth (3), cavity width (4) and cavity area (white shading). Panel C-Double lumen dissection with indication of the largest cap thickness (5), cap width (6), and cap area (white shading). Panel D-Illustration of a fissure.²¹

Larger coronary evaginations are visualized as angiographic contrast staining out of the stent contour, a phenomenon called peri-stent contrast staining (PSS). PSS has been observed in 2% of the sirolimus-eluting stents (SES), but not in bare metal stents. The evaginations with a

depth and length more than 0.3 millimeter remained more frequently in SES compared to other types of DES.¹² Coronary evaginations found within 12-months after SES implantation may be associated with target lesion revascularization and very late stent thrombosis at 3 years.²³

Bifurcation lesions

2-D OCT images cannot always accurately depict the complex 3-D structure of a coronary bifurcation. To overcome this limitation, 3-D reconstructions of OCT images were proposed. Several software packages are used for the generation of 3-D OCT images that can help accurately depict procedural aspects of bifurcation intervention such as wire position and carina shift after intervention. Moreover, measurement of the side branch ostium from a main vessel pullback might lead to significant error to the estimation of the side-branch ostium dimensions.²⁴ Therefore, the cut-plane analysis, an approach based on 3-D rendering of a main vessel pullback and generation of cross-sectional images perpendicular to the side branch centerline, was recently developed and provides reliable measurements of the side-branch ostium from a main vessel pullback, reducing the need for an additional side-branch OCT pullback (**Figure 13**).²⁴

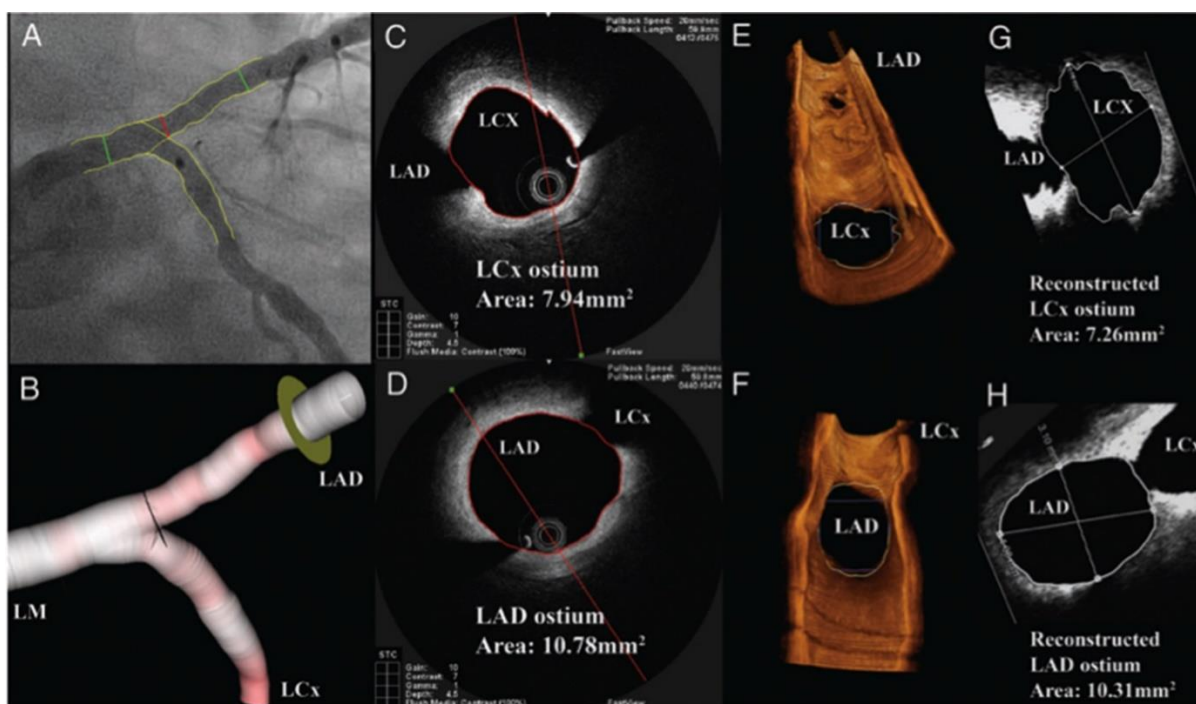


Figure 13. OCT images of left main bifurcation with 2-D and 3-D angiographic views (A and B). OCT pullback showing the ostium of the left circumflex and left anterior descending arteries (C and D). 3-D renderings showing the contralateral branch ostium (E and F). Cut-plane analysis showing reconstructed ostia (G and H).²⁴

Stent healing and healing score

OCT technology using a computer-assisted densitometric analysis (Genetools software, Syngene, Cambridge, UK) has been used to compare the optical intensity of areas of stent struts and shown to aid in the differentiation between fibrin vs. neointima in the stent strut coverage (**Figure 14**).²⁵ The OCT healing score was designed to evaluate the healing process after stent/scaffold implantation and consist of a weighted index based on the stent/scaffold-related post-implantation characteristics: presence of uncovered and/or malapposed stent/scaffold struts and intraluminal filling defects. The TROFI study evaluated serial OCT images in patients with STEMI and the healing score was assessed using customized offline software (Qlvus, Medis, Leiden University, Leiden, The Netherlands).²⁶

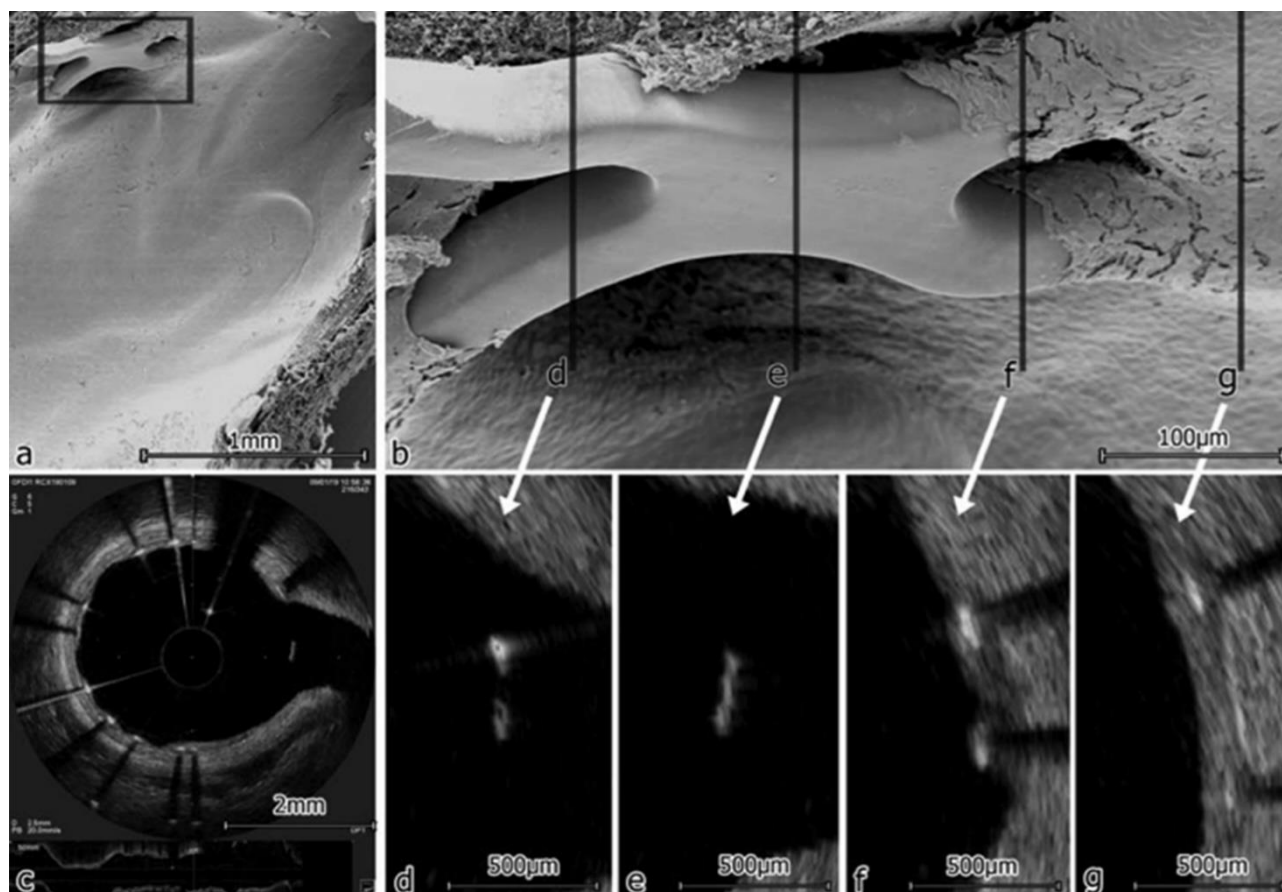


Figure 14. Demonstrate the corresponding images of scanning electron microscopy and OCT imaging analysis of the same stent segment.²⁵

Fusion of intravascular ultrasound-virtual histology and OCT images

IVUS has a penetration depth of approximately 8-10mm and provides cross-sectional images of the entire vessel wall allowing reliable assessment of the plaque burden. IVUS-virtual

histology (IVUS-VH) relies on the processing of the backscattered radio frequency signal to construct tissue maps and classify plaque in four components (fibrous–green; fibro-fatty–greenish-yellow; necrotic core–red; and dense calcium–white).²⁷ However, IVUS-VH has a limited resolution (100 to 200 μ m), cannot visualize the fibrous cap, underestimate the intima layer thickness and has limited ability in visualizing micro-calcifications and the composition of the plaque behind the calcium.

OCT allows a detailed assessment and visualization of structures close to the lumen surface and is a better tool for the evaluation of plaque characteristics related to increased vulnerability. OCT has advantages in assessing the calcific distribution and calcification burden, but has a limited penetration depth, which makes the assessment of plaque burden impossible. Fusion image of co-registered IVUS-VH and OCT has been developed with diagnostic algorithms that take advantage of the individual strengths of both technologies (Figure 15).

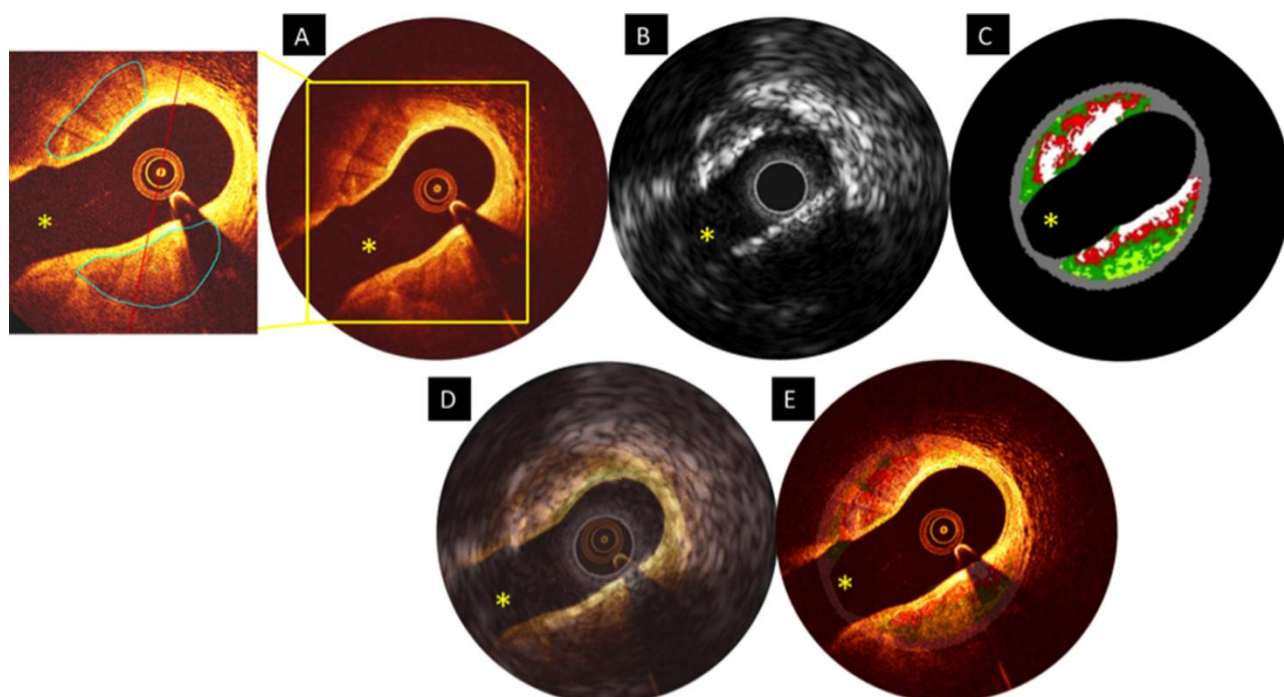


Figure 15. Matched IVUS, OCT and IVUS-VH images (A, B and C). The yellow asterisks indicate the side branch. Two calcifications are shown at both borders of the side branch. Fusion images of OCT + IVUS (D) and OCT + IVUS-VH (E).

The cross-sectional images are uploaded in the software (Adobe Photoshop Elements 12). After matching the calibration line of 1mm, the images are rotated using cross-sectional landmarks. The fusing information of the matched OCT and IVUS images, the contours of all visible tissue compartments and the external elastic membrane are delineated and colored

using the following color codes: white=calcium; green=fibrous tissue; red=necrotic/lipid tissue; grey=media stripe (**Figure 14**).

Assessment of intravascular thrombus

OCT provides high-resolution images that are able to differentiate red and white thrombus. Muramatsu and colleagues suggested that red thrombi were characterized by high backscattering protrusions with signal-free shadowing while the white thrombi were visualized as signal-rich, low-backscattering projections.²⁸ Kume and colleagues suggested that OCT may differentiate types of thrombus with good sensitivity compared to histologic examinations using public domain software (National Institute of Health, Bethesda, Maryland).²⁹ The optical frequency domain imaging technique provides better imaging resolution and can be used to quantitatively evaluate intraluminal masses with specific intravascular imaging software (QCU-CMS, Leiden University, Leiden, The Netherlands) in patients with ST-elevation myocardial infarction after stent implantation.

Assessment of Macrophage content

The infiltration of macrophages may weaken the structural integrity of the fibrous cap and increase the likelihood of rupture. Patients who died of acute coronary syndrome were more likely to have activated macrophages in their coronary artery specimens compared to those with stable angina. The high resolution of OCT can accurately detect the macrophage content in the fibrous cap. Tearney and colleagues suggested a strong and positive correlation between OCT and fibrous cap macrophage density and a negative correlation of between OCT and smooth muscle actin density, suggesting that OCT may be a valuable tool to understand the effect of macrophages to plaque progression and rupture in patients with coronary artery disease.³⁰ Beside the macrophages, there are several types of plaque components that can cause bright spots in OCT. Fibrin accumulations, neoatherosclerosis development after previous stent implantation, elastic lamina, cholesterol crystals and micro calcifications are other possible reasons for bright spots in OCT.^{7,31,32}

OCT-guided PCI

In ILUMIEN I, with OCT, during PCI, treatment strategy changed the selection of stent length in 68% of the cases, the stent diameter in 39% and the number of implanted stents in 13% of study population.³³ Post-PCI OCT assessment provides detection of the residual edge dissections³⁴ and stent under-expansions, optimize final results and improve clinical outcomes; in ILUMIEN I trial the event rate was only 1.5%(patient-oriented MACE).³³ In the

same direction, in ILUMIEN II trial, the MACE was significantly less in OCT guided optimization subgroup and the modifications made according to OCT imaging results concluded in reduced peri-procedural myocardial Infarction(MI) rates.³⁵

OCT derived plaque morphology information can be helpful to determine best strategy during PCI. OCT has similar accuracy to detect calcified plaques as in IVUS³⁶; with its circumferential extent, it also gives information about the depth of the calcific tissue. With this information, it can be decided for the appropriate approach for lesion preparation (i.e., balloon pre-dilation vs. debulking) which is crucial in BRS. OCT-detected thin-cap fibrous atheroma(TCFA) is a predictor of peri-procedural MI and no-reflow following stent implantation.^{37,38} Microvascular obstruction and no-reflow phenomenon were seen more frequently in lesions with an increased lipid arc and thin fibrous cap.³⁹ OCT can discriminate plaque rupture and erosion to depict the underlying cause for intravascular thrombus formation. Coronary plaques with superficial erosions can induce thrombi that develop on the dysfunctional intimal layer. In these cases, the obstruction is developed due to the precipitated thrombi rather than the underlying plaque itself. In autopsy studies, endothelial erosion recognized in 40% of the cases with fatal coronary thrombi.⁴⁰ In the report by Prati et al, in 60% of the patients, total coronary occlusion was detected and after removal of the thrombi, OCT imaging was implemented and revealed non-critical residual obstructions in which the treatment decision was left to the operators. Twelve patient were followed with medical treatment and 19 cases received percutaneous stent implantation. At two-years follow up, none of the cases from medical group and 1 patient from the PCI group received additional revascularization.⁴¹ OCT has crucial importance in treatment decisions in cases with thrombotic occlusions superimposed on a non-critical plaque in STEMI. In case of plaque erosion, without stent implantation, only thrombus retrieval can be sufficient to establish a satisfactory coronary flow particularly in vessels without significant stenosis.^{41,42}

In OCT, malapposition is defined in cases that the distance between the abluminal edge of the strut and the vessel wall is more than the thickness of the strut. The degree of malapposition is determined with the arc of the malapposition, length of the malapposition and the distance between malapposed struts and the vessel wall. Small malappositions are usually covered with endothelium⁴³, however significant malapposition (>200 micron) is a risk for stent thrombosis immediately after stent implantation.^{23,44} OCT can detect the tissue protrusion between the struts which can be a predictor of peri-procedural MI.^{38,45} Tissue protrusion

between the struts is visualized as a smooth surface and absence of signal attenuation. The protrusion of thrombus is seen as an irregular surface with signal attenuation.⁴⁵ OCT can detect edge dissections after device implantation, better than IVUS.⁴⁶ If there is no stenosis in the true lumen and flow disruption, the dissection may not need further intervention.⁴³ Spontaneous coronary dissection is diagnosed a non-traumatic and non-iatrogenic separation of the coronary arterial walls.⁴⁷ With its higher resolution (10-20 μm), OCT can view true lumen, false lumen, intimal tears and allows measuring the depth of the false lumen and thickness of the intimal flaps⁴⁷. However, due to lower penetration depths compared to IVUS, OCT may not visualize the full extent of intramural hematoma (smooth, diffuse, narrowing but otherwise normal vessels) within the vessel wall.⁴⁸

Fourier domain-OCT(FD-OCT) provides rigorous examination of the coronary vessel lumen. In OPUS-CLASS trial⁴⁹, FD-OCT provided precise quantification of the vessel lumen with reliable intra-observer reproducibility. In CLI-OPCI study, in comparison to coronary angiography guidance, angiography-plus-OCT guidance revealed less cardiac death, MI and lower rate of the composite of cardiac death, MI, or repeat revascularization at 1-year follow up; addition of the OCT guidance was independently associated with a significant lower risk of cardiac death or MI (odds ratio =0.49 [0.25-0.96], $p=0.037$).⁴⁶ In several previous studies, OCT derived minimal lumen area(MLA) was found smaller than IVUS-derived MLA.⁵⁰⁻⁵² The measurement differences between two methodologies may lead to suboptimal stent expansion. In case of PCI guided by OCT, using IVUS criteria can result in restenosis and stent thrombosis. The current OCT technology needs contrast injection during the image acquisition in order to get a reliable data. The volume of the contrast media is the point that should be taken into account since the renal failure due to increased contrast volume is one of the major causes of in-hospital and long-term mortality and morbidity after PCI.^{53,54}

In the current ESC/EACT PCI guidelines⁵⁵ OCT and/or IVUS is recommended as Class IIa with level –of-evidence as C. OCT is emphasized as more accurate than IVUS in detecting subtle morphological details including malapposition, residual thrombus, plaque prolapse and residual dissections after stent implantation. During post-implantation follow up, OCT is more accurate than IVUS for assessing neointimal thickness, strut apposition and coverage.^{56,57}

Statistical considerations for OCT data

OCT data at the strut level are not independent within lesions and patients, which are the actual elements of clinical relevance. Crude strut analysis, in which percentages of all pooled

struts are reported, ignores this interdependency and results in misleadingly low p-values and artificially narrow confidence intervals. Different approaches like generalized estimating equation models and non-parametric analyses of aggregated data have been applied in clinical studies and might lead to conflicting results with complex interpretation. Multilevel logistic regression models provide overall percentage estimators centered on lesion-specific percentages and are, therefore, more appropriate for comparing data at the strut level. In addition, graphical representation of the data at the lesion level may help to fully understand the clinical relevance of the study results.

CONCLUSION

Intracoronary OCT provides high-resolution images allowing optimal assessment of the intravascular structures with broad research and clinical applications. Knowledge of the current OCT intravascular imaging software packages and their applications are crucial to better characterize and understand the vascular biology of atherosclerotic disease, to provide a more objective assessment and to guide the decision-making process in modern interventional cardiology.

REFERENCES

1. Kubo T, Imanishi T, Takarada S, et al. Assessment of culprit lesion morphology in acute myocardial infarction: ability of optical coherence tomography compared with intravascular ultrasound and coronary angiography. *J Am Coll Cardiol*. 2007;50(10):933-939.
2. Yabushita H, Bouma BE, Houser SL, et al. Characterization of human atherosclerosis by optical coherence tomography. *Circulation*. 2002;106(13):1640-1645.
3. Radu MD, Yamaji k, Garcia-Garcia HM, et al. Variability in the measurement of minimal fibrous cap thickness and reproducibility of fibroatheroma classification by optical coherence tomography using manual versus semi-automated assessment. *EuroIntervention : journal of EuroPCR in collaboration with the Working Group on Interventional Cardiology of the European Society of Cardiology*. 2015;In press.
4. Wang Z, Chamie D, Bezerra HG, et al. Volumetric quantification of fibrous caps using intravascular optical coherence tomography. *Biomedical optics express*. 2012;3(6):1413-1426.
5. Phipps JE, Hoyt T, Vela D, et al. Diagnosis of Thin-Capped Fibroatheromas in Intravascular Optical Coherence Tomography Images: Effects of Light Scattering. *Circ Cardiovasc Interv*. 2016;9(7).
6. van Soest G, Regar E, Goderie TP, et al. Pitfalls in plaque characterization by OCT: image artifacts in native coronary arteries. *JACC Cardiovasc Imaging*. 2011;4(7):810-813.
7. Tearney GJ, Regar E, Akasaka T, et al. Consensus standards for acquisition, measurement, and reporting of intravascular optical coherence tomography studies: a report from the International Working Group for Intravascular Optical Coherence Tomography Standardization and Validation. *J Am Coll Cardiol*. 2012;59(12):1058-1072.
8. Delachartre P, Cachard C, Finet G, Gerfault FL, Vray D. Modeling geometric artefacts in intravascular ultrasound imaging. *Ultrasound Med Biol*. 1999;25(4):567-575.
9. Wang A, Eggermont J, Dekker N, et al. Automatic stent strut detection in intravascular optical coherence tomographic pullback runs. *The international journal of cardiovascular imaging*. 2013;29(1):29-38.
10. Bezerra HG, Costa MA, Guagliumi G, Rollins AM, Simon DI. Intracoronary optical coherence tomography: a comprehensive review clinical and research applications. *JACC Cardiovasc Interv*. 2009;2(11):1035-1046.
11. Elahi S, Mancuso JJ, Milner TE, Feldman MD. Sunflower artifact in OCT. *JACC Cardiovasc Imaging*. 2011;4(11):1220-1221.
12. Sotomi Y, Tateishi H, Suwannasom P, et al. Quantitative assessment of the stent/scaffold strut embedment analysis by optical coherence tomography. *Int J Cardiovasc Imaging*. 2016;32(6):871-883.
13. Villard JW, Cheruku KK, Feldman MD. Applications of optical coherence tomography in cardiovascular medicine, part 1. *J Nucl Cardiol*. 2009;16(2):287-303.
14. Bouma BE, Tearney GJ. *Handbook of optical coherence tomography*. New York: Marcel Dekker; 2002.
15. Regar E vLT, Serruys PW, . *Optical coherence tomography in cardiovascular research*. 1st ed: Informa Healthcare; 2007.

16. Gnanadesigan M, van Soest G, White S, et al. Effect of temperature and fixation on the optical properties of atherosclerotic tissue: a validation study of an ex-vivo whole heart cadaveric model. *Biomed Opt Express*. 2014;5(4):1038-1049.
17. Nakatani S, Onuma Y, Ishibashi Y, et al. Temporal evolution of strut light intensity after implantation of bioresorbable polymeric intracoronary scaffolds in the ABSORB cohort B trial—an application of a new quantitative method based on optical coherence tomography. *Circ J*. 2014;78(8):1873-1881.
18. Papafaklis MI, Bourantas CV, Theodorakis PE, et al. The effect of shear stress on neointimal response following sirolimus- and paclitaxel-eluting stent implantation compared with bare-metal stents in humans. *JACC Cardiovasc Interv*. 2010;3(11):1181-1189.
19. Papafaklis MI, Bourantas CV, Farooq V, et al. In vivo assessment of the three-dimensional haemodynamic micro-environment following drug-eluting bioresorbable vascular scaffold implantation in a human coronary artery: fusion of frequency domain optical coherence tomography and angiography. *EuroIntervention*. 2013;9(7):890.
20. Gonzalo N SP, Okamura T, Shen ZJ, Garcia-Garcia HM, Onuma Y, van Geuns RJ, Ligthart J, Regar E. Relation between plaque type and dissections at the edges after stent implantation: an optical coherence tomography study. *International Journal of Cardiology*. 2011;150(2):151-155.
21. Radu MD, Raber L, Kalesan B, et al. Coronary evaginations are associated with positive vessel remodelling and are nearly absent following implantation of newer-generation drug-eluting stents: an optical coherence tomography and intravascular ultrasound study. *Eur Heart J*. 2014;35(12):795-807.
22. Cook S WP, Togni M, Billinger M, Morger C, Seiler C, Vogel R, Hess O, Meier B, Windecker S. Incomplete stent apposition and very late stent thrombosis after drug-eluting stent implantation. *Circulation*. 2007;115(18):8.
23. Imai M, Kadota K, Goto T, et al. Incidence, risk factors, and clinical sequelae of angiographic peri-stent contrast staining after sirolimus-eluting stent implantation. *Circulation*. 2011;123(21):2382-2391.
24. Karanasos A, Tu S, van Ditzhuijzen NS, et al. A novel method to assess coronary artery bifurcations by OCT: cut-plane analysis for side-branch ostial assessment from a main-vessel pullback. *Eur Heart J Cardiovasc Imaging*. 2015;16(2):177-189.
25. Templin C, Meyer M, Muller MF, et al. Coronary optical frequency domain imaging (OFDI) for in vivo evaluation of stent healing: comparison with light and electron microscopy. *Eur Heart J*. 2010;31(14):1792-1801.
26. Garcia-Garcia HM, Muramatsu T, Nakatani S, et al. Serial optical frequency domain imaging in STEMI patients: the follow-up report of TROFI study. *Eur Heart J Cardiovasc Imaging*. 2014;15(9):987-995.
27. Nair A, Kuban BD, Tuzcu EM, Schoenhagen P, Nissen SE, Vince DG. Coronary plaque classification with intravascular ultrasound radiofrequency data analysis. *Circulation*. 2002;106(17):2200-2206.
28. Muramatsu T, Garcia-Garcia HM, Lee IS, Bruining N, Onuma Y, Serruys PW. Quantitative optical frequency domain imaging assessment of in-stent structures in patients with ST-segment elevation myocardial infarction: impact of imaging sampling rate. *Circ J*. 2012;76(12):2822-2831.

29. Kume T, Akasaka T, Kawamoto T, et al. Assessment of coronary arterial thrombus by optical coherence tomography. *Am J Cardiol.* 2006;97(12):1713-1717.
30. Tearney GJ, Yabushita H, Houser SL, et al. Quantification of macrophage content in atherosclerotic plaques by optical coherence tomography. *Circulation.* 2003;107(1):113-119.
31. Ali ZA, Roleder T, Narula J, et al. Increased thin-cap neoatheroma and periprocedural myocardial infarction in drug-eluting stent restenosis: multimodality intravascular imaging of drug-eluting and bare-metal stents. *Circ Cardiovasc Interv.* 2013;6(5):507-517.
32. Cilingiroglu M, Oh JH, Sugunan B, et al. Detection of vulnerable plaque in a murine model of atherosclerosis with optical coherence tomography. *Catheter Cardiovasc Interv.* 2006;67(6):915-923.
33. Wijns W, Shite J, Jones MR, et al. Optical coherence tomography imaging during percutaneous coronary intervention impacts physician decision-making: ILUMIEN I study. *Eur Heart J.* 2015;36(47):3346-3355.
34. Chamie D, Bezerra HG, Attizzani GF, et al. Incidence, predictors, morphological characteristics, and clinical outcomes of stent edge dissections detected by optical coherence tomography. *JACC Cardiovasc Interv.* 2013;6(8):800-813.
35. Maehara A, Ben-Yehuda O, Ali Z, et al. Comparison of Stent Expansion Guided by Optical Coherence Tomography Versus Intravascular Ultrasound: The ILUMIEN II Study (Observational Study of Optical Coherence Tomography [OCT] in Patients Undergoing Fractional Flow Reserve [FFR] and Percutaneous Coronary Intervention). *JACC Cardiovasc Interv.* 2015;8(13):1704-1714.
36. Gomez-Lara J, Brugaletta S, Diletti R, et al. Agreement and reproducibility of gray-scale intravascular ultrasound and optical coherence tomography for the analysis of the bioresorbable vascular scaffold. *Catheter Cardiovasc Interv.* 2012;79(6):890-902.
37. Tanaka A, Imanishi T, Kitabata H, et al. Lipid-rich plaque and myocardial perfusion after successful stenting in patients with non-ST-segment elevation acute coronary syndrome: an optical coherence tomography study. *Eur Heart J.* 2009;30(11):1348-1355.
38. Porto I DVL, Burzotta F, Niccoli G, Trani C, Leone AM, Biasucci LM, Vergallo R, Limbruno U, Crea F. Predictors of periprocedural (type IVa) myocardial infarction, as assessed by frequency-domain optical coherence tomography. *Circ Cardiovasc Interv.* 2012;5(1):7.
39. Ozaki Y, Tanaka A, Tanimoto T, et al. Thin-cap fibroatheroma as high-risk plaque for microvascular obstruction in patients with acute coronary syndrome. *Circ Cardiovasc Imaging.* 2011;4(6):620-627.
40. Braunwald E. Coronary plaque erosion: recognition and management. *JACC Cardiovasc Imaging.* 2013;6(3):288-289.
41. Prati F, Uemura S, Souteyrand G, et al. OCT-based diagnosis and management of STEMI associated with intact fibrous cap. *JACC Cardiovasc Imaging.* 2013;6(3):283-287.
42. Jia H, Dai J, Hou J, et al. Effective anti-thrombotic therapy without stenting: intravascular optical coherence tomography-based management in plaque erosion (the EROSION study). *Eur Heart J.* 2016.
43. Kume T, Okura H, Miyamoto Y, et al. Natural history of stent edge dissection, tissue protrusion and incomplete stent apposition detectable only on optical coherence tomography after stent implantation - preliminary observation. *Circ J.* 2012;76(3):698-703.

44. Finn AV, Nakazawa G, Joner M, et al. Vascular responses to drug eluting stents: importance of delayed healing. *Arterioscler Thromb Vasc Biol.* 2007;27(7):1500-1510.
45. Kubo T, Imanishi T, Kitabata H, et al. Comparison of vascular response after sirolimus-eluting stent implantation between patients with unstable and stable angina pectoris: a serial optical coherence tomography study. *JACC Cardiovasc Imaging.* 2008;1(4):475-484.
46. Prati F, Di Vito L, Biondi-Zoccai G, et al. Angiography alone versus angiography plus optical coherence tomography to guide decision-making during percutaneous coronary intervention: the Centro per la Lotta contro l'Infarto-Optimisation of Percutaneous Coronary Intervention (CLI-OPCI) study. *EuroIntervention.* 2012;8(7):823-829.
47. Alfonso F, Bastante T, Garcia-Guimaraes M, et al. Spontaneous coronary artery dissection: new insights into diagnosis and treatment. *Coron Artery Dis.* 2016;27(8):696-706.
48. Alfonso F, Paulo M, Gonzalo N, et al. Diagnosis of spontaneous coronary artery dissection by optical coherence tomography. *J Am Coll Cardiol.* 2012;59(12):1073-1079.
49. Kubo T, Akasaka T, Shite J, et al. OCT compared with IVUS in a coronary lesion assessment: the OPUS-CLASS study. *JACC Cardiovasc Imaging.* 2013;6(10):1095-1104.
50. Yamaguchi T, Terashima M, Akasaka T, et al. Safety and feasibility of an intravascular optical coherence tomography image wire system in the clinical setting. *Am J Cardiol.* 2008;101(5):562-567.
51. Gonzalo N, Serruys PW, Garcia-Garcia HM, et al. Quantitative ex vivo and in vivo comparison of lumen dimensions measured by optical coherence tomography and intravascular ultrasound in human coronary arteries. *Rev Esp Cardiol.* 2009;62(6):615-624.
52. Okamura T, Onuma Y, Garcia-Garcia HM, et al. First-in-man evaluation of intravascular optical frequency domain imaging (OFDI) of Terumo: a comparison with intravascular ultrasound and quantitative coronary angiography. *EuroIntervention.* 2011;6(9):1037-1045.
53. McCullough PA. Contrast-induced acute kidney injury. *J Am Coll Cardiol.* 2008;51(15):1419-1428.
54. Rihal CS, Textor SC, Grill DE, et al. Incidence and prognostic importance of acute renal failure after percutaneous coronary intervention. *Circulation.* 2002;105(19):2259-2264.
55. Authors/Task Force m, Windecker S, Kolh P, et al. 2014 ESC/EACTS Guidelines on myocardial revascularization: The Task Force on Myocardial Revascularization of the European Society of Cardiology (ESC) and the European Association for Cardio-Thoracic Surgery (EACTS) Developed with the special contribution of the European Association of Percutaneous Cardiovascular Interventions (EAPCI). *Eur Heart J.* 2014;35(37):2541-2619.
56. Prati F, Guagliumi G, Mintz GS, et al. Expert review document part 2: methodology, terminology and clinical applications of optical coherence tomography for the assessment of interventional procedures. *Eur Heart J.* 2012;33(20):2513-2520.
57. Radu MD, Raber L, Heo J, et al. Natural history of optical coherence tomography-detected non-flow-limiting edge dissections following drug-eluting stent implantation. *EuroIntervention.* 2014;9(9):1085-1094.
58. Wang A, Nakatani S, Eggermont J, et al. Automatic detection of bioresorbable vascular scaffold struts in intravascular optical coherence tomography pullback runs. *Biomedical optics express.* 2014;5(10):3589-3602.
59. Nakatani S, Sotomi Y, Ishibashi Y, et al. Comparative analysis method of permanent metallic stents (XIENCE) and bioresorbable poly-L-lactic (PLLA) scaffolds (Absorb) on optical coherence

tomography at baseline and follow-up. *EuroIntervention : journal of EuroPCR in collaboration with the Working Group on Interventional Cardiology of the European Society of Cardiology*. 2015;11(6).

60. Papafaklis MI, Bourantas CV, Yonetsu T, et al. Anatomically correct three-dimensional coronary artery reconstruction using frequency domain optical coherence tomographic and angiographic data: head-to-head comparison with intravascular ultrasound for endothelial shear stress assessment in humans. *EuroIntervention*. 2015;11(4):407-415.

Randomized comparison of Absorb bioresorbable vascular scaffold and Mirage microfiber sirolimus eluting scaffold using multi-modality imaging

Erhan Tenekecioglu, Patrick W. Serruys, Yoshinobu Onuma, MD, Ricardo Costa, Daniel Chamié, Yohei Sotomi, Ting-Bin Yu, Alexander Abizaid, Houn-Bang Liew, Teguh Santoso

JACC Cardiovasc Interv. 2017;10(11):1115-1130.

ABSTRACT

Introduction: Current generation of bioresorbable scaffolds (BRS) has several limitations, such as thick square struts with large footprint that precludes their deep embedment into the vessel wall resulting in protrusion into the lumen with micro disturbance of the flow. Mirage Bioresorbable Microfiber sirolimus-eluting Scaffold (Mirage BRMS) is designed to address these concerns.

Methods: In this prospective, single-blinded trial, 60 patients were randomly allocated in a 1:1-ratio to treatment with a Mirage BRMS and Absorb bioresorbable vascular scaffold. The clinical end points were assessed at 30-days, 6-and 12-months. In-device angiographic late loss at 12-months was quantified. Secondary optical coherence tomographic end points were assessed post-scaffold implantation, at 6- and 12-months.

Results: Median angiographic post-procedure in-scaffold minimal lumen diameter (MLD) of Mirage and Absorb were 2.38[2.06-2.62] mm and 2.55[2.26-2.71] mm, respectively [Effect size(d)=-0.29]. At 12-months, median angiographic in-scaffold MLD of Mirage and Absorb were not statistically different (1.90[1.57-2.31] mm versus 2.29[1.74-2.51] mm; d =-0.36). At 12-months follow up, median in-scaffold late lumen loss of Mirage and Absorb were 0.37[0.08-0.72]mm and 0.23[0.15-0.37] mm, respectively (d =0.20). On OCT, post-procedure diameter stenosis (DS) of Mirage was 11.2±7.1%, increased to 27.4±12.4% at 6-months and remained stable (31.8±12.9%) at 1-year, whereas the post-procedure OCT DS of Absorb was 8.4±6.6%, increased to 16.6±8.9% and remained stable (21.2±9.9%) at 1-year follow-up (Mirage vs. Absorb: $d_{\text{post-procedure}}$ =0.41, $d_{6\text{-months}}$ =1.00, $d_{12\text{-months}}$ =0.92). Angiographic median in-scaffold DS were significantly different between study groups at 12-months (28.6[21.0-40.7] for Mirage, 18.2[13.1-31.6] for Absorb; d =0.39). Device- and patient-oriented composite end-points were comparable between the two study groups.

Conclusion: At 12-months, angiographic in-scaffold late loss was not statistically different between Mirage and Absorb, although diameter stenosis on angiography and on OCT was significantly higher in Mirage than in Absorb. The technique of implantation was suboptimal for both devices and future trial should be OCT-guided to allow for optimal implantation and appropriate assessment of the new technology, considering the novel mechanical properties of Mirage.

Key words: Bioresorbable scaffolds; scaffold design; scaffold mechanical properties; clinical results.

INTRODUCTION

Bioresorbable scaffold (BRS) may potentially overcome many pitfalls related to metallic drug eluting stent (DES). If a bioresorbable scaffold is ultimately expected to have the same range of applicability as durable metal stent, the gap in the mechanical properties between the two devices should be minimal.

Currently the existing limitations are: 1-Low tensile and radial strength which require thick struts to prevent acute recoil, 2-Insufficient ductility which impacts on scaffold crimping and retention on delivery balloon and limits the range of scaffold expansion during deployment, 3-Early mechanical disruption or late structural discontinuity of the struts inherent to the polymer used and its elongation at break and resorption decay. In other words, the optimal performance goal and the mechanical dilemma with BRS is to obtain a high tensile strength combined with ductility and high elongation at break (1).

Poly-lactide or poly D, L-lactide have tensile strength ranging between 45 and 70 MPa with an elongation break of 2-6% while cobalt chromium has a tensile strength of 1449 MPa and elongation break of 40% (2). Currently polymer experts test complex composition of polymer mixing poly-lactide, polyglycolide and polycaprolactone to alter the mechanical properties and to achieve radial strength and ductility that could be comparable at least with stainless steel stent. Another way to modify the mechanical properties of the poly-lactide is to intervene on the molecular orientation of the polymer by using proprietary manufacturing processes that involve stretching (melt extrusion, drawing) and temperature alteration (annealing). The Manli Cardiology microfiber technology has explored the concept of molecular orientation of the polylactide in order to create a circular single monofilament (diameter of 125/150 microns) with specific mechanical properties. The scaffold design consists of a helicoidal coil structure in which the monofilament maintains its directional mechanical properties as well as its circular geometry (**Figure 1**). In the final assembly of the scaffold, 3 longitudinal spines are attached at ambient temperature to guarantee the mechanical stability of the helicoidal structures. Mirage sirolimus-eluting bioresorbable microfiber scaffold (Mirage BRMS, Manli Cardiology, Singapore) with strut thickness of 125 micron has a tensile strength of 300 MPa with an elongation at break of 35% and a radial strength of 120 kPa, -very comparable to the radial strength of the Xience V for a strut thickness of 81 micron. In addition, in vitro and in

vivo degradation profile has confirmed that the Mirage polylactide is basically fully biodegraded after 14 months (Figure 1, Figure 2).

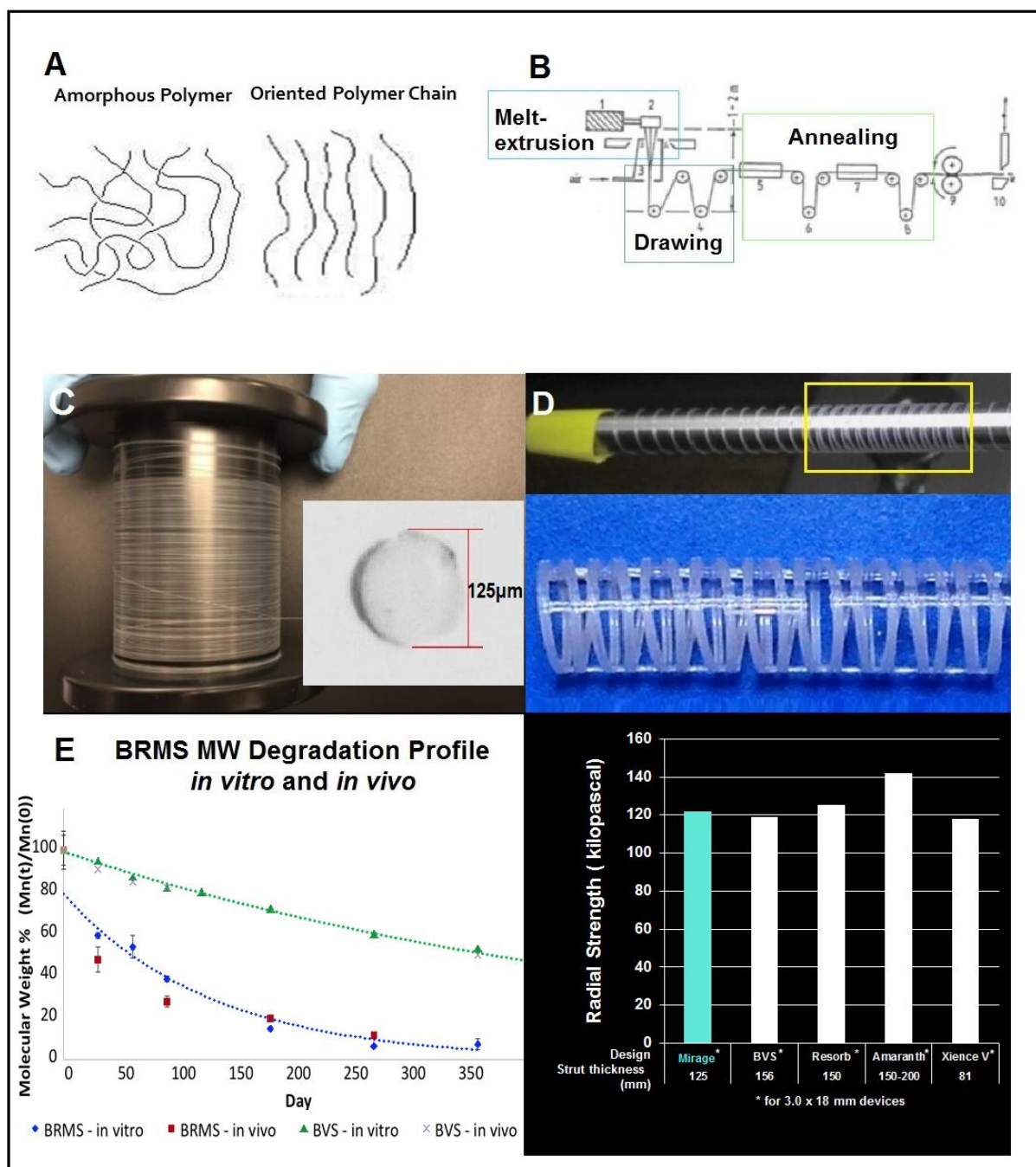


Figure 1. Manli Cardiology's Microfiber Technology

Highly oriented polylactide polymer is extruded and annealed to form a circular monofilament with preferred directional mechanical properties (A, B). Conversion of a circular monofilament into a helicoidal scaffold with circular strut geometry. Coil design enables scaffold to inherit monofilament's directional mechanical properties and monofilament's circular geometry (C, D). Three longitudinal spines are attached at ambient temperature to guarantee the mechanical stability of the helicoidal structures (D). In vitro and in vivo degradation profile in comparison with the BVS confirms that the Mirage polylactide is basically fully biodegraded after 14 months (E). Mirage scaffold with strut thickness of 125 micron has a tensile strength of 300 MPa with an elongation at break of 35% and a radial strength of 120 kPa, -very comparable to the radial strength of the Xience V for a strut thickness of 81 micron (F).

The primary objective of this study was to evaluate the safety and effectiveness of the Mirage BRMS compared to the Absorb BVS (Absorb bioresorbable vascular scaffold) in the treatment of stenotic target lesions located in native coronary arteries, ranging from ≥ 2.25 mm to ≤ 4.0 mm in diameter. The secondary objectives of this study were to establish the medium-term safety, effectiveness and performance of the Mirage BRMS, assessed at multiple time points through assessment of clinical, angiographic and OCT data.

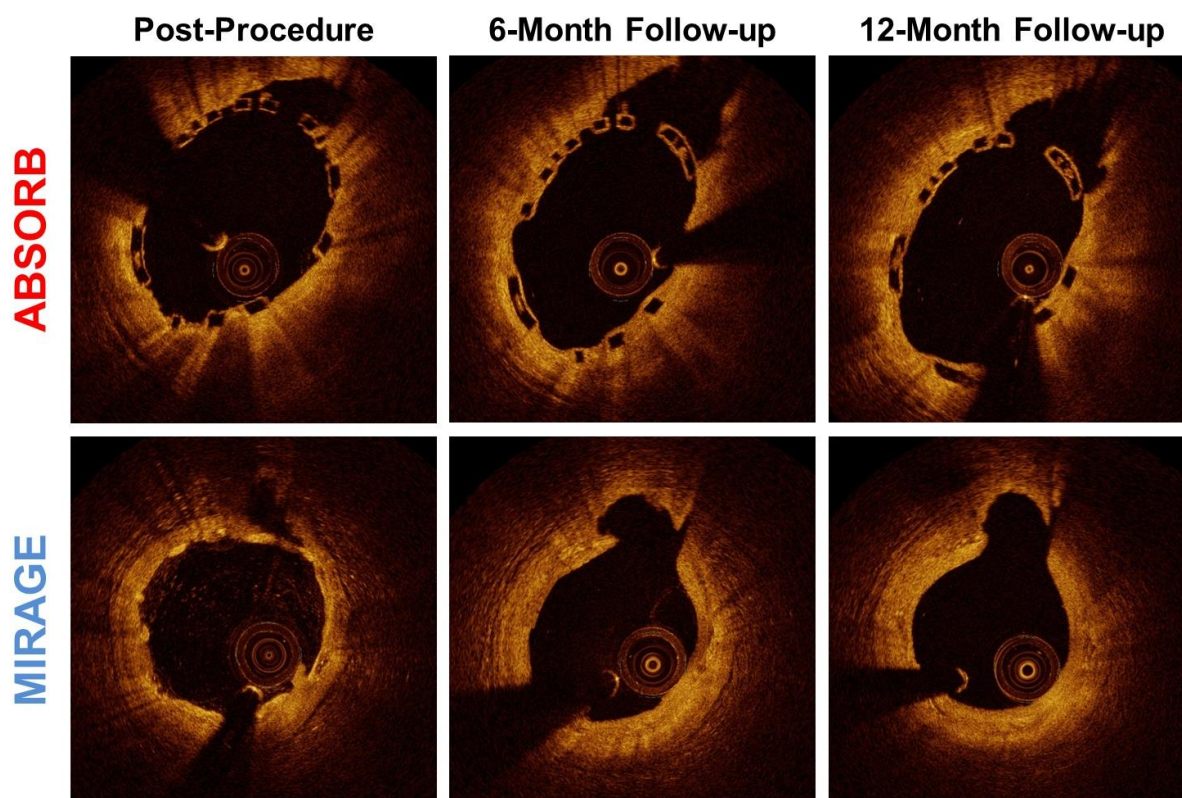


Figure 2. OCT follow up in Absorb and Mirage scaffolds

In vitro and in vivo degradation profile has confirmed that the Mirage polylactide is basically fully biodegraded after 14 months.

METHODS

Description of the device

The Mirage is a poly-L-lactic acid (PLLA) based scaffold with less than 5% of Dextro-rotary isomer of polylactic acid (PLA). As described in the introduction, the device has a helicoidal structure which provides high flexibility. The strut thickness for a scaffold with a diameter ≤ 3 mm is 125 micron, while scaffolds with diameter greater than 3 mm have a strut thickness of

150 micron. The aim of this new technology of device is not only to reduce the strut thickness but also to increase the embedment of the struts. Due to the round shape of struts, it will be easier to embed the strut into the vessel wall, thereby reducing the disturbance of the flow (3). The vessel coverage ratio is high, around 40 to 47% as compared to 27% for the Absorb BVS. The device is available with the following diameters; 2.5, 2.75, 3.0, 3.5 and 4.0 mm with the following lengths of 18, 28 and 38 mm. The crossing profile of the smallest device (2.5 mm) is as low as 1.12 mm while the 4.0 mm scaffold has a profile of 1.47 mm. Three radiopaque markers are incorporated in the device and allow for fluoroscopic assessment. Of note, the helicoidal structure contributes to the flexibility of the device and facilitates the side branch access through the fenestration between the helicoidal rings. The internal scaffold dimensions for the various nominal sizes available as a function of inflation pressure are reported in **Table 1** of the electronic supplement. The limits of scaffold expansion in Mirage is approximately 10% (personal communication). In Mirage, the molecular weight decreases by more than 90% in approximately 1-year, while in Absorb, the depolymerization process is complete within approximately 3.5 years (4).

Table 1. Baseline patient characteristics

	MIRAGE (N=31)	ABSORB (N=29)	Relative rate [95% CI]	P
Age, years, mean \pm SD	59 \pm 5.3	56 \pm 7.6	3.00 [-1.67; 7.61] ³	0.201 ¹
Gender (Female)	25.8% (8/31)	24.1% (7/29)		1 ²
Hypertension	41.9% (13/31)	65.5% (19/29)	1.56 [0.96; 2.55]	0.077 ²
Diabetes	19.4% (6/31)	27.6% (8/29)	1.43 [0.56; 3.61]	0.547 ²
Insulin-dependent	0% (0/31)	3.4% (1/29)	-	1 ²
Hypercholesterolemia	53.3% (16/30)	69.0% (20/29)	1.29 [0.85; 1.96]	0.237 ²
Smoker	41.9% (13/31)	44.8% (13/29)	1.06 [0.64; 1.74]	1 ²
Current	32.2% (10/31)	34.5% (10/29)	1.07 [0.52; 2.19]	1 ²
Previous MI	10.7% (3/28)	10.7% (3/28)	1.00 [0.22; 4.54]	0.773 ²
Previous PCI	19.4% (6/31)	20.1% (6/29)	1.07 [0.39; 2.94]	1 ²
Stable Angina/Silent Ischemia	96.8% (30/31)	96.6% (28/29)	1.00 [0.91; 1.1]	1 ²
Stable Angina	51.6% (16/31)	58.6% (17/29)	1.14 [0.73; 1.78] [*]	0.606 ²
Silent Ischemia	45.2% (14/31)	37.9% (11/29)		
Unstable Angina / STEMI	3.2% (1/31)	3.4% (1/29)		

(1) T-test, (2) Fisher's exact test, (3) Mean difference (Absorb - Mirage)

(*) Ratio Stable Angina / Silent Ischemia. (One case NSTEMI omitted from Absorb Group and one case of Unstable angina from Mirage)

Clinical trial, imaging modalities and study population

The Mirage clinical trial is a randomized trial with a 1:1 allocation between the Mirage BRMS and the Absorb BVS. Prior to the start of the randomization trial, 8 patients were included as a run-in-phase at two sites, one in Indonesia and one in Malaysia. Patients were recruited between August 25th and October 23rd 2014. The enrollment was completed in October 2014. Patients underwent angiography and optical coherence tomography (OCT) pre-and post-procedure, at 6- and 12-months.

The angiographic endpoint is in-scaffold late lumen loss at 12-months. Secondary OCT endpoints include multiple parameters while the secondary clinical end-points are composite of cardiac death target vessel myocardial infarction (MI) and clinically indicated (CI) lesion revascularization (5).

Inclusion and exclusion criteria for the present study are identical to the criteria used for the Absorb Cohort-B trial (2). Patients with a known hypersensitivity or contraindication to aspirin, heparin, bivalirudin, ticlopidine and clopidogrel, poly (L-lactide), poly (D, L-lactide), sirolimus, everolimus, platinum or a sensitivity to contrast media which cannot be adequately pre-medicated, acute MI [ST Segment Elevation MI (STEMI) or Non-ST Segment Elevation MI (NSTEMI)], left ventricular ejection fraction $\leq 30\%$, renal insufficiency (e.g., serum creatinine level of more than 2.0 mg/dL, or subject on dialysis), patient with planned elective surgery within the first 6-months after the coronary procedure that will require discontinuing either aspirin or clopidogrel, concurrent medical condition with a life expectancy of less than 18-months, restenotic lesions, lesions located in the left main coronary artery, lesions involving an epicardial side branch ≥ 2 mm in diameter by visual assessment and/or ostial lesion $> 40\%$ stenosis by visual estimation or side branch requiring pre-dilatation, thrombus or another clinically significant stenosis (including side branch) in the target vessel, total occlusion (TIMI flow 0) prior to wire passing, moderate to severe calcification and tortuosity of the target vessel, were excluded. The ethics committee at each participating institution approved the protocol and each patient gave written informed consent before inclusion.

Procedure

The target lesion was predilated in both groups. A predilatation ratio of 1:1 between the predilatation balloon and the reference vessel with a balloon shorter than the Mirage and Absorb was mandated. After intracoronary nitrate injection, quantitative coronary angiography (QCA) was used for proper vessel sizing before scaffold implantation. Following the scaffold

implantation, post-dilatation was left at the discretion of the operator but when performed it was applied to the entire length of the scaffolded segment using a balloon with a similar matched length. After scaffold implantation procedure, intravascular imaging was performed for documentary purposes (**On-line supplementary Table-2**).

Quantitative Coronary Angiography

Minimum lumen diameter, interpolated reference diameter, diameter stenosis (DS), late loss in device and in the 5-mm proximal and distal to the device were determined by QCA (Pie Medical, Leiden, Netherlands) (6). Balloon artery ratio was evaluated by measuring the average pre-procedure reference diameter of the mean proximal (5 mm) and mean distal (5 mm) edges diameter versus the fully expanded balloon (maximum balloon diameter according to chart of the manufacturer, (during delivery or at the time of the post-dilatation) (7). Acute recoil was quantified by measuring the full expanded balloon during the implantation in comparison with the diameter of the vessel post-scaffolding (8). Reference diameter and percent DS were calculated using interpolation method (9, 10).

Optical Coherence Tomography

All the procedures were done under angiographic guidance. OCT imaging was performed only for documentary purposes. Post-procedure lumen areas (minimal, mean, reference), lumen asymmetry and eccentricity, strut coverage and apposition were assessed by OCT. Scaffold expansion index was specifically defined as the ratio of minimum scaffold area divided by maximum reference lumen area (2).

The population includes patients with de novo lesion 48 mm in length in 2 different epicardial vessels and allows scaffold implantation with overlapping of maximum 2 scaffolds per lesion. The device was available in 2 lengths, 18 and 28 mm and the device diameters in the inventory were 2.5 mm, 3.0 mm, 3.5 mm and 4.0 mm.

Definitions

Clinical device success was defined as successful delivery of the device and attainment of <50% residual stenosis by QCA of the target lesion using Mirage scaffold and delivery system. Clinical procedure success was defined as attainment of 50% residual stenosis of the target lesion and no in-hospital major cardiac events up to seven days after the index procedure. The major adverse cardiac event (MACE) was categorized either as patient-oriented composite end-point (all-cause death, any MI, any revascularization) or Device-oriented composite end-points (cardiac death, target vessel MI, target lesion revascularization). Peri-procedural MI is defined

according to the SCAI definition (5). Spontaneous MI was defined according to the third universal definition.(11)

Target lesion failure is a composite of cardiac death - that cannot be clearly attributed to a non-cardiac event or non-target vessel-, target vessel related MI or clinically indicated target lesion revascularization (CI-TLR). Clinically-indicated revascularizations imply a positive functional study, ischemic ECG changes at rest in a myocardial distribution consistent with the target vessel, or ischemic symptoms. Revascularization of a target lesion with an in-lesion DS $\geq 70\%$ (by QCA) in the absence of the above-mentioned ischemic signs or symptoms is also considered clinically-indicated.

Statistical analysis

This feasibility study was designed to provide preliminary observations and generate hypotheses for future studies. The sample size was not defined on the basis of an endpoint hypothesis but rather to provide some information about the device efficacy and safety. The sample size requirement was established by assessment of the minimum number of patients needed to provide reliable and non-trivial results. The sample size is in the range of the test group in the Absorb Cohort-A trial (n=30) and the Absorb Cohort-B1(n=45) and -B2(n=56) trials (12, 13). The current clinical investigation is essentially a first-in-man study that aims at providing information on safety and effectiveness with a limited number of subjects exposed to the Mirage BRMS device, as compared to the Absorb BVS. Angiographic end-point was in-device late lumen loss assessed by QCA at 12-months follow up.

Continuous variables were tested for normality with Kolmogorov-Smirnov test and are presented as mean \pm SD or median (interquartile range) as appropriate. Most of the angiographic data had a non-Gaussian distribution while the OCT data presented with a Gaussian distribution. Categorical variables are presented as counts and percentages. Continuous variables were compared by the Kruskal-Wallis test or Mann Whitney U test. Categorical variables were compared by the Fisher's exact test. Since the trial was designed as a feasibility study, instead of p-values, the effect sizes(*d*) were used in statistical analysis.

RESULTS

Baseline patient demographics and lesion characteristics

Table 1 shows the baseline patient demographics and lesion characteristics and tabulates either the mean difference(age) or the relative rate of baseline characteristics with their 95%

confidence intervals. The majority of the patients has stable angina and silent ischemia. Two patients (with STEMI or NSTEMI) were protocol violation but included in the intention-to-treat analysis.

The majority of the treated lesions were located in the left anterior descending coronary artery (LAD). Lesions were characterized by moderate or severe calcification in 46% and 35% for the Mirage and Absorb groups, respectively. Small vessels according to the interpolated reference vessel diameter <2.5 mm on QCA of was found in 7/35 (20%) in Mirage versus 9/34 (27%) in Absorb. Bifurcations with side branch visually greater or equal to 2 mm and/or protected by guidewire were involved in the treated lesion in 49% and 41% for the Mirage and the Absorb groups, respectively. In terms of ACC/AHA classification, the majority of the lesions were classified as B2 lesions. The core lab adjudicated the lesions as Type-C in 29% and 38% of the cases treated either with Mirage or Absorb. As far as the technique of implantation is concerned, pre-dilatation was the rule with only 2 exceptions in the Absorb group; the device success was 100% in both groups, 6 patients needed an additional scaffold or stent. Noticeably, balloon post-dilatation was only performed in 57% and 59% of the Mirage and Absorb cases (**Table 2**).

Table 2. Pre-procedure lesion characteristics and Procedural techniques

PRE-PROCEDURE MORPHOLOGY AND TECHNIQUE	MIRAGE (n=35)	ABSORB (n=34)	p ¹
Target vessel:			0.111
LAD	24/35 (68.57%)	15/34 (44.12%)	
LCX	5/35 (14.29%)	7/34 (20.59%)	
RCA	6/35 (17.14%)	12/34 (35.29%)	
Calcium (moderate/severe)	16/35 (45.71%)	12/34 (35.29%)	0.525
Bifurcation	17/35 (48.57%)	14/34 (41.18%)	0.707
Lesion class (ACC/AHA):			0.844
A	1/35 (2.86%)	1/34 (2.94%)	
B1	4/35 (11.43%)	4/34 (11.76%)	
B2	20/35 (57.14%)	16/34 (47.06%)	
C	10/35 (28.57%)	13/34 (38.24%)	
Technique:			
Balloon predilatation	35/35 (100%)	32/34 (94.12%)	0.460
Study scaffold implant	35/35 (100%)	34/34 (100%)	0.904
Additional study scaffold implant	3/35 (8.57%)	1/34 (2.94%)	0.627
Additional metallic stent implanted	1/35 (2.86%)	1/34 (2.94%)	1.000
Balloon postdilatation (other than the delivery balloon)	20/35 (57.14%)	20/34 (58.82%)	1.000

(1) Fisher's exact test

Study course and rates of follow-ups

Sixty patients were randomized, 31 to Mirage BRMS and 29 to Absorb BVS, including 35 and 34 lesions, respectively. One patient in the Mirage group, suffered a scaffold thrombosis at day-3. The angiographic residual DS of this severely calcified lesion, even after post-dilatation was 33%. OCT shows an expansion and eccentricity index of 80.5% and 0.47, respectively. Intra-scaffold dissection and malapposition were also diagnosed on OCT. Patient showed antiplatelet resistance both to clopidogrel and aspirin (576 ARU) and genotype analysis indicated a decreased CYP2C19 activity and a poor metabolizer phenotype. The patient received 2 metallic drug eluting stents and was further treated with ticagrelor. The QCA data of this lesion was not included in the 6- or 12-months angiographic follow up. **Figure 3** is a flow chart that provides the rate of OCT, angiographic and clinical follow-up at 6- and 12-months. In addition, the flow chart reports all the TLR at 6-months and 12-months. In each group, 2 patients were lost-to-follow up. At 1-year, the cumulative rate of all TLR was 20.7% (n=6 patients) in the Mirage group and in 18.5% (n=4 patients [one patient underwent 2 TLR]) in the Absorb group. The values of QCA pre-TLR for these patients were carried forward to 6-months and/or 1-year in the statistical analysis. In Mirage group, three patients had a non-ischemia driven TLR at angiographic follow up.

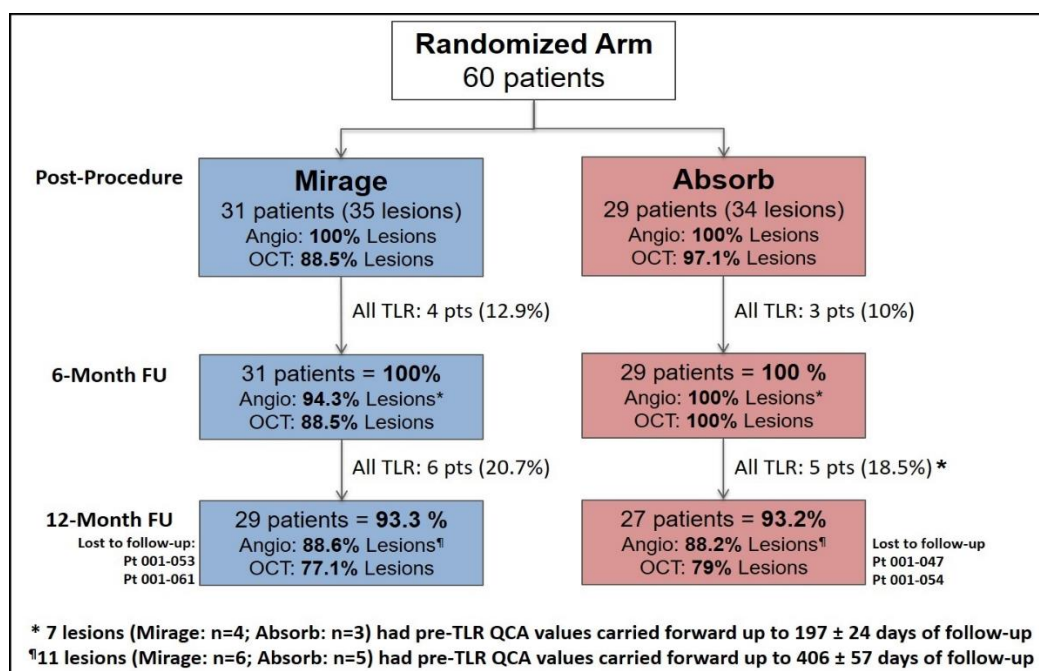


Figure 3. Mirage first-in-man trial flow char

The QCA at baseline shows an obstruction lesion length of about 14 mm with a reference interpolated diameter of 2.85 mm and a MLD of 1.25 mm resulting in a DS of 56% in both

groups. The median DS in Mirage BRMS group was 16.3% and 12.3% in Absorb BVS group with effect size (d) of 0.48. The acute recoil was numerically slightly higher in the Absorb group 7.11% versus 5.97% in Mirage, but that difference failed to be statistically significant ($p=0.285$, $d:-0.40$). Absolute acute recoil was 0.20 (0.14-0.28) mm in Mirage and 0.24 (0.17-0.36) mm in Absorb ($d = -0.23$). Post-procedure there was no significant difference between the Mirage and the Absorb, however there was a borderline p -value ($p=0.058$) ($d=0.48$) for the median DS (16.3% vs. 12.3%). The latter difference in DS became significant at 6-months (28% vs. 16.9%, $p=0.026$, $d=0.36$) and was confirmed at 12-months (28.6% vs. 18.2%, $p=0.046$ $d=0.39$). However, all the differences in mean DS were non-significant and it must be emphasized that there was no statistical difference in the median angiographic late-loss at 6- (0.18 mm vs. 0.13 mm) and 12-months (0.37 mm vs. 0.23 mm) (**Table 3**).

The **Figure 4**, shows the cumulative distribution frequency curves in-device late lumen loss (median) in Mirage and Absorb study groups at 6- and 12-months. The binary restenosis rates at 6-months were 12.1% in the Mirage (4/33 lesions) and 11.8 % in the Absorb (4/34 lesions) while the rates at 12 months were 19.4% (6/31 lesions) in the Mirage group and 16.7% (5/30 lesions) in the Absorb group.

In the scaffolded segments, side branches visually greater or equal to 2 mm and/or protected by guidewire, were documented at the corelab in 49% (17/34) of Mirage lesion and 41% (14/34) of Absorb lesion. However, the rates of side branch occlusion were only one case (1/17) in Mirage and zero case (0/14) in Absorb.”

OCT sub-study at 6-months and 1-year:

Table 4 shows the quantitative OCT results post-procedure at 6- and 12-months follow up. Post-procedure all the quantitative measurements of the Mirage and Absorb did not differ, with the exception of the scaffold eccentricity index. Post-procedure scaffold expansion percentages at baseline were $75.6 \pm 23.4\%$ for Mirage and $84.6 \pm 9.7\%$ for Absorb ($d=-0.50$). The frequency of post-dilatation with a balloon different from the delivery balloon was similar in both scaffold groups (48.6% in Mirage, 40% in Absorb; $d=0.77$). The ratio of the nominal diameter of the post-dilatation balloon to nominal diameter of the scaffold was comparable (1.02 ± 0.04 in Mirage, 1.04 ± 0.06 in Absorb; $d= -0.40$). The post-dilatation balloon nominal diameters were large enough to expand the device in both study groups (Ratio of post-dilatation balloon nominal diameter to mean reference diameter on OCT was 1.13 ± 0.14 for Mirage and 1.09 ± 0.10 for Absorb; $d=0.34$).

Table-3: QCA results (Median) of pre-procedure, post-procedure, 6-months and 12-months follow up

PRE-PROCEDURE	MIRAGE (n=35)	ABSORB (n=34)	MEDIAN Difference* [Bootstrap 95% CI]	p ¹
LESION LENGTH	13.9 [11.4 - 21.3]	14.7 [11.3 - 22.7]	0.8 [-2.4; 7.1]	0.701
REFERENCE DIAMETER	2.84 [2.57 - 3.2]	2.84 [2.44 - 3]	0.00 [-0.25; 0.20]	0.787
MLD	1.26 [1.08 - 1.42]	1.25 [0.86 - 1.43]	-0.01 [-0.30; 0.21]	0.653
% DIAMETER STENOSIS	55.7 [50.7- 60.0]	55.9 [50.8 - 64.6]	0.18 [-4.42; 6.92]	0.728
POST PROCEDURE	MIRAGE (n=35)	ABSORB (n=34)	MEDIAN Difference* [Bootstrap 95% CI]	p ¹
MEAN DIAMETER - IN-SCAFFOLD	2.81 [2.49 - 3.05]	2.88 [2.5 - 2.98]	0.07 [-0.14; 0.25]	0.644
REFERENCE DIAMETER - IN-SCAFFOLD	2.90 [2.6 - 3.19]	2.86 [2.55 - 3.02]	-0.04 [-0.27; 0.26]	0.792
MLD - IN-SCAFFOLD	2.38 [2.06 - 2.62]	2.55 [2.26 - 2.71]	0.17 [-0.14; 0.30]	0.334
% DIAMETER STENOSIS - IN-SCAFFOLD	16.3 [9.14 - 25.01]	12.3 [6.61 - 17.83]	-3.98 [-12.93; 1.51]	0.058
ACUTE GAIN - IN-SCAFFOLD	1.08 [0.88 - 1.44]	1.22 [0.99 - 1.47]	0.14 [-0.13; 0.34]	0.195
ACUTE GAIN - IN-SEGMENT	1.08 [0.84 - 1.37]	1.19 [0.93 - 1.46]	0.11 [-0.14; 0.31]	0.210
% ACUTE RECOIL	5.97 [3.35 - 7.59]	7.11 [1.21 - 12.41]	1.14 [-2.00; 4.00]	0.285
BALLOON-ARTERY RATIO	1.07 [1.04 - 1.12]	1.04 [1.01 - 1.09]	-0.03 [-0.04; 0.01]	0.218
6-MONTH FU	MIRAGE (n=33)	ABSORB (n=34)	Difference [95% CI]	p ¹
MEAN DIAMETER - IN-SCAFFOLD	2.52 [2.13 - 2.74]	2.67 [2.34 - 2.84]	0.15 [-0.14; 0.46]	0.118
REFERENCE DIAMETER - IN-SCAFFOLD	2.88 [2.53 - 3.12]	2.86 [2.46 - 2.99]	-0.02 [-0.25; 0.31]	0.721
MLD - IN-SCAFFOLD	2.11 [1.65 - 2.39]	2.35 [2.06 - 2.56]	0.24 [-0.04; 0.61]	0.114
% DIAMETER STENOSIS - IN-SCAFFOLD	28.0 [19.87 - 38.24]	17.0 [12.18 - 24.16]	-11.02 [-16.91; -3.47]	0.026
LATE LUMEN LOSS - IN-SCAFFOLD	0.23 [0.04 - 0.44]	0.17 [0.05 - 0.23]	-0.06 [-0.20; 0.10]	0.633
LATE LUMEN LOSS - PROXIMAL EDGE	0.15 [0.06 - 0.33]	0.12 [0.03 - 0.16]	-0.03 [-0.19; 0.06]	0.224
LATE LUMEN LOSS - DISTAL EDGE	0.11 [0.04 - 0.32]	0.06 [0.03 - 0.14]	-0.05 [-0.25; 0.02]	0.239
LATE LUMEN LOSS - IN-SEGMENT	0.18 [0.02 - 0.44]	0.13 [0.03 - 0.23]	0.05 [-0.15; 0.25]	0.568
12-MONTH FU	MIRAGE (n=32)	ABSORB (n=30)	Difference [95% CI]	p ¹
MEAN DIAMETER - IN-SCAFFOLD	2.34 [1.98 - 2.65]	2.64 [2.2 - 2.79]	0.30 [-0.14; 0.52]	0.147
REFERENCE DIAMETER - IN-SCAFFOLD	2.87 [2.49 - 3.07]	2.86 [2.43 - 2.99]	-0.01 [-0.31; 0.25]	0.688

(continued)

MLD - IN-SCAFFOLD	1.90 [1.57 - 2.31]	2.29 [1.74 - 2.51]	0.39 [-0.02; 0.69]	0.137
% DIAMETER STENOSIS – IN-SCAFFOLD	28.6 [21.0 - 40.7]	18.2 [13.1 - 31.6]	-10.4 [-20.3; -1.4]	0.046
LATE LUMEN LOSS - IN-SCAFFOLD	0.37 [0.08 - 0.72]	0.23 [0.15 - 0.37]	-0.14 [-0.32; 0.11]	0.521
LATE LUMEN LOSS - PROXIMAL EDGE	0.32 [0.18 - 0.47]	0.18 [0.1 - 0.32]	-0.14 [-0.28; 0.05]	0.181
LATE LUMEN LOSS - DISTAL EDGE	0.23 [0.11 - 0.44]	0.15 [0.08 - 0.27]	-0.08 [-0.32; 0.05]	0.211
LATE LUMEN LOSS - IN-SEGMENT	0.36 [0.08 - 0.72]	0.22 [0.13 - 0.36]	-0.14 [-0.42; 0.08]	0.414
(1) Mann-Whitney's test				

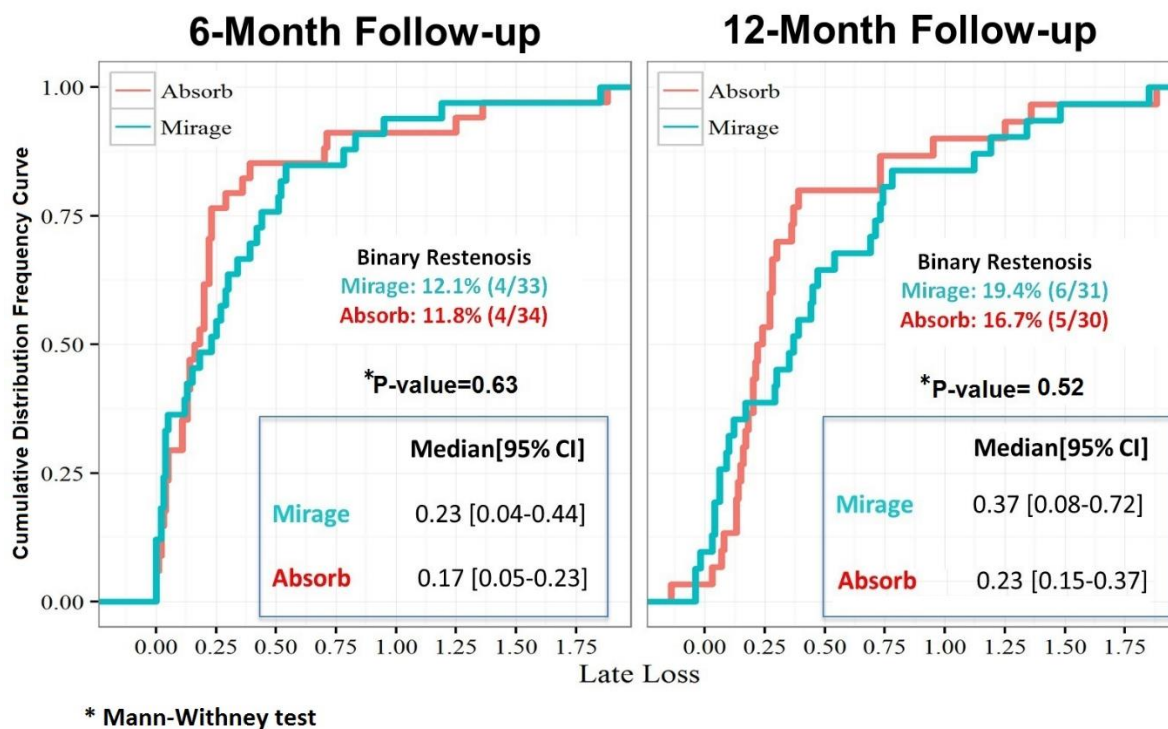


Figure 4. Cumulative distribution frequency curves for in-device lumen loss in Mirage and Absorb study groups at 6- and 12-months and binary restenosis rates at 6-months

The difference in the ratio of nominal scaffold diameter to mean reference diameter on OCT between Mirage and Absorb group and in the ratio of expected scaffold diameter according to dilatation pressure to mean reference diameter on OCT in Mirage and Absorb group were not statistically different ($p=0.070$, $d=0.74$ and $p=0.430$, $d=0.19$) (Table 5).

In particular, the in-scaffold minimum lumen area (MLA) post-procedure was identical in both groups. At 6-months follow up, the percentage of LA stenosis and DS calculated according to 2 different methods were significantly higher in the Mirage group compared to the Absorb group. In particular, MLA was significantly lower in the Mirage when compared to the Absorb ($2.91 \pm 1.57 \text{ mm}^2$ vs. $3.98 \pm 1.73 \text{ mm}^2$; $p=0.011$, $d= -0.66$). These statistically significant differences were maintained at 12-months. The MLA in the Mirage was then $2.85 \pm 1.50 \text{ mm}^2$ vs. $3.95 \pm 1.91 \text{ mm}^2$ ($p=0.036$, $d=-0.65$). Of note, no malapposition was documented in both groups. Strict serial assessments of OCT in the Mirage group show for all quantitative measurements significant change between post-procedure and 6-months with decrease of the absolute parameters (mean in-scaffold LA, MLA) and increase in relative changes (lumen and diameter percentage stenosis).

Table 4: Quantitative OCT Results

	Post-Procedure			6-Month FU			12-Months FU		
	Mirage (N = 32)	Absorb (N = 33)	P*	Mirage (N = 31)	Absorb (N = 34)	P*	Mirage (N = 27)	Absorb (N = 27)	P*
Analysed Scaffold Length, mm	24.3±10.7	21.4 ±5.1	0.089	23.2 ± 9.4	21.6 ± 4.9	0.777	24.7 ± 10.5	20.9 ± 4.9	0.222
Mean Reference Lumen Area, mm²	6.95 ± 2.67 (n=31)	6.45 ± 2.13	0.586	6.19 ± 2.82	5.88 ± 2.04	0.907	6.10 ± 2.26	6.06 ± 2.47	0.936
Maximum Reference Lumen Area, mm²	7.68 ± 2.86 (n=31)	7.16 ± 2.27	0.638	7.19 ± 3.75 (n=29)	6.59 ± 2.25	0.869	6.87 ± 2.52 (n=26)	6.77 ± 2.83	0.972
Minimum In-Scaffold Lumen Area, mm²	5.32 ± 1.65	5.30 ± 1.50	0.808	2.91 ± 1.57	3.98 ± 1.73	0.011	2.85 ± 1.50	3.95 ± 1.91	0.036
Lumen Area Stenosis, % [method 1] †	20.8 ± 14.4 (n=31)	16.1 ± 11.4	0.148	47.9 ± 19.8 (n=29)	33.1 ± 18.6	0.001	51.9 ± 17.9 (n=26)	36.3 ± 15.8	0.001
Lumen Area Stenosis, % [method 2] ‡	28.9 ± 10.7 (n=31)	25.0 ± 8.8	0.223	53.5 ± 18.8 (n=29)	40.4 ± 16.3	0.001	57.4 ± 15.2 (n=26)	42.8 ± 14.1	0.001
Lumen Diameter Stenosis, % [method 1] †	11.0 ± 8.1 (n=31)	8.4 ± 6.2	0.145	28.8 ± 14.1 (n=29)	18.1 ± 13.1	0.001	31.5 ± 12.8 (n=26)	20.6 ± 10.2	0.001

(continued)

Lumen Diameter Stenosis, % [method 2] ¶	15.8 ± 6.3 (n=31)	13.5 ± 5.0	0.239	33.1 ± 14.4 (n=29)	22.9 ± 12.1	<0.001	35.6 ± 11.8 (n=26)	24.9 ± 9.6	0.001
ISA Area, mm²	0.19 ± 0.19 (n=29)	0.18 ± 0.13 (n=26)	0.526	N/A	N/A
LEI	0.21 ± 0.03	0.20 ± 0.03	0.147	0.20 ± 0.03	0.19 ± 0.03	0.782	0.16 ± 0.03	0.19 ± 0.04	0.039
SEI	0.17 ± 0.03	0.12 ± 0.03	<0.001	...	0.13 ± 0.03	N/A	...	0.13 ± 0.03	N/A

N/A: not applicable; SEI: scaffold eccentricity index [(maximum scaffold diameter – minimum scaffold diameter) / maximum scaffold diameter]; LEI: lumen eccentricity index [(maximum in-scaffold lumen diameter – minimum in-scaffold lumen diameter) / maximum in-scaffold lumen diameter]

* Scaffold expansion: minimum scaffold area / maximum reference lumen area

‡ Lumen Area Stenosis [method 1]: (Mean Reference Lumen Area – In-Scaffold MLA / Mean Reference Lumen Area)

§ Lumen Area Stenosis [method 2]: (Maximum Reference Lumen Area – In-Scaffold MLA / Maximum Reference Lumen Area)

† Lumen Diameter Stenosis [method 1]: (Mean Reference Lumen Diameter – In-Scaffold Lumen Diameter at MLA / Mean Reference Lumen Area)

¶ Lumen Diameter Stenosis [method 2]: (Maximum Reference Lumen Diameter – In-Scaffold Lumen Diameter at MLA / Maximum Reference Lumen Area)

For lumen diameter stenosis calculations, diameters were estimated as the diameter of a circle that has an equivalent area to the cross-section areas analyzed

Table 5. Procedural characteristics at the lesion level in patients with post-procedure OCT

	Mirage BRMS	Absorb BVS	P value
Nominal scaffold diameter (mm)*	3.12 ± 0.45 (n=37)	2.94 ± 0.35 (n=35)	0.094 ^a
Mean reference diameter on OCT (mm) [‡]	2.88 ± 0.52 (n=32)	2.83 ± 0.47 (n=34)	0.827
Frequency of post-dilatation with a balloon different from the delivery balloon, n (%)	18/37 (48.6%)	14/35 (40%)	0.460 ^b
Post-dilatation balloon nominal diameter (mm) [‡]	3.19 ± 0.41 (n=37)	3.06 ± 0.38 (n=35)	0.181 ^a
Ratio of post-dilatation balloon nominal diameter to nominal scaffold diameter	1.02 ± 0.04 (n=37)	1.04 ± 0.06 (n=35)	0.264 ^a
Ratio of nominal scaffold diameter to mean reference diameter on OCT	1.09 ± 0.13 (n=32)	1.04 ± 0.08 (n=34)	0.070 ^a
Ratio of post-dilatation balloon nominal diameter to mean reference diameter on OCT	1.13 ± 0.14 (n=32)	1.09 ± 0.10 (n=34)	0.188 ^a
Ratio of expected scaffold diameter according to dilatation pressure to mean reference diameter on OCT	1.16 ± 0.12 (n=32)	1.18 ± 0.09 (n=34)	0.430 ^a

^a Mann-Whitney U test; ^b Chi-square

* A total of 34 lesions were included in the Mirage group. Three of these were treated with two overlapping scaffolds each. For the sake of this comparison, the scaffolds were computed separately adding to 37 scaffolds.

[‡] Mean reference diameter is the average of the mean distal and proximal reference lumen diameter.

[‡] In cases that post-dilatation was not performed, the nominal diameter of the delivery balloon was used.

Between 6- and 12-months, there was an additional significant decrease in MLA (Difference and 95% CI: -0.36 [-0.57 to -1.59]) (p=0.003, d=0.25). The other relative measurements (LA and DS percentage) also indicated an additional increase in stenosis albeit of borderline significance (**Table 6**).

Table 6. Serial OCT Results in the Mirage Group

	29 pairs			26 pairs			26 pairs					
	0M	6M	Diff. [95% CI]	P*	6M	12M	Diff [95% CI]	P*	0M	12M	Diff. [95% CI]	P*
Mean In-Scaffold LA, mm ²	6.53±1.90	4.46 ± 1.66	-2.06 [-2.51 to -1.61]	<0.001	4.61±1.67	4.49±1.73	-0.11 [-0.32 to 0.08]	0.509	6.33±1.96	4.52±1.74	-1.81 [-2.28 to -1.35]	<0.001
Mean In-Scaffold MLA, mm ²	5.33±1.71	2.98 ± 1.57	-2.35 [-2.91 to -1.79]	<0.001	3.17±1.50	2.80±1.51	-0.36 [-0.57 to -1.59]	0.003	5.15±1.75	2.82±1.52	-2.32 [-2.88 to -1.75]	<0.001
Lumen Area Stenosis, % [method 1]*	20.7±13.2 (n=27)	47.5 ± 20.4 (n=27)	26.8 [19.2 to 34.4]	<0.001	46.9±18.7 (n=25)	52.8±17.6 (n=25)	5.9 [0.1 to 11.6]	0.048	22.7±10.8 (n=25)	52.4±18.0 (n=25)	29.8 [22.6 to 37.0]	<0.001
Lumen Area Stenosis, % [method 2]§	28.3±10.6 (n=27)	53.1 ± 19.4 (n=27)	24.7 [17.6 to 31.9]	<0.001	52.6±17.8 (n=25)	58.2±14.9 (n=25)	5.7 [-0.3 to 11.6]	0.069	29.2±9.3 (n=25)	58.0±15.2 (n=25)	28.7 [22.2 to 35.3]	<0.001
Lumen Diameter Stenosis, % [method 1]*	10.9±7.2 (n=27)	28.6 ± 14.6 (n=27)	17.7 [12.3 to 23.1]	<0.001	27.8±12.6 (n=25)	32.1±12.6 (n=25)	4.3 [0.5 to 8.1]	0.040	11.9±6.1 (n=25)	31.9±12.9 (n=25)	20.0 [14.8 to 25.1]	<0.001
Lumen Diameter Stenosis, % [method 2]¶	15.4±6.2 (n=27)	32.8 ± 14.8 (n=27)	17.4 [12.0 to 22.9]	<0.001	32.0±12.6 (n=25)	36.2±11.6 (n=25)	4.2 [0.1 to 8.3]	0.061	15.9±5.6 (n=25)	36.0±11.8 (n=25)	20.2 [15.3 to 25.0]	<0.001

*Related-samples Wilcoxon Signed Rank test

† Lumen Area Stenosis [method 1]: (Mean Reference Lumen Area – In-Scaffold MLA / Mean Reference Lumen Area)

§ Lumen Area Stenosis [method 2]: (Maximum Reference Lumen Area – In-Scaffold MLA / Maximum Reference Lumen Area)

* Lumen Diameter Stenosis [method 1]: (Mean Reference Lumen Diameter – In-Scaffold Lumen Diameter at MLA / Mean Reference Lumen Area)

¶ Lumen Diameter Stenosis [method 2]: (Maximum Reference Lumen Diameter – In-Scaffold Lumen Diameter at MLA / Maximum Reference Lumen Area)

For lumen diameter stenosis calculations, diameters were estimated as the diameter of a circle that has an equivalent area to the cross-section areas analyzed

Serial OCT measurements in the Absorb group showed a similar pattern of change although the quantitative differences were numerically lower (**Table 7**). In patients without TLR, serial OCT measurements demonstrated comparable luminal DS in Absorb and Mirage groups (**Figure 5**).

Table 7. Serial OCT Results in the Absorb Group

	0M	6M	Diff. [95% CI]	P*	6M	12M	Diff [95% CI]	P*	0M	12M	Diff. [95% CI]	P*
	33 pairs				26 pairs				26 pairs			
Mean In-Scaffold LA, mm ²	6.58±1.84	5.32±1.86	-1.26 [-1.46 to -1.06]	<0.001	5.53 ± 1.92	5.47 ± 2.16	-0.06 [-0.23 to 0.10]	0.589	6.76 ± 1.86	5.37 ± 2.13	-1.38 [-1.71 to -1.05]	<0.001
Mean In-Scaffold MLA, mm ²	5.29 ± 1.50	3.89 ± 1.68	-1.40 [-1.70 to -1.09]	<0.001	4.17 ± 1.64	3.94 ± 1.90	-0.23 [-0.51 to 0.05]	0.216	5.42 ± 1.54	3.85 ± 1.87	-1.57 [-2.01 to -1.13]	<0.001
Lumen Area Stenosis, % [method 1] [†]	16.1 ± 11.4	33.9 ± 18.3	17.7 [11.3 to 24.2]	<0.001	31.2 ± 13.9	36.3 ± 15.8	5.1 [-0.7 to 10.9]	0.124	16.0 ± 12.2	37.3 ± 15.2	21.3 [14.9 to 27.7]	<0.001
Lumen Area Stenosis, % [method 2] [§]	25.0 ± 8.8	41.1 ± 16.1	16.1 [10.9 to 21.2]	<0.001	38.9 ± 12.0	42.8 ± 14.1	4.0 [-1.0 to 8.9]	0.200	24.9 ± 9.3	43.6 ± 13.8	18.7 [13.3 to 24.1]	<0.001
Lumen Diameter Stenosis, % [method 1] [†]	8.4 ± 6.2	18.5 ± 13.0	10.2 [5.5 to 14.8]	<0.001	16.2 ± 9.1	20.6 ± 10.2	4.4 [0.1 to 8.7]	0.075	8.4 ± 6.6	21.2 ± 9.9	12.8 [8.8 to 16.9]	<0.001
Lumen Diameter Stenosis, % [method 2] [§]	13.5 ± 5.0	23.3 ± 12.0	9.8 [5.8 to 13.9]	<0.001	21.2 ± 8.0	24.9 ± 9.6	3.7 [-0.2 to 7.6]	0.136	13.4 ± 5.3	25.4 ± 9.4	12.0 [8.3 to 15.7]	<0.001

***Related-samples Wilcoxon Signed Rank test**

[†] Lumen Area Stenosis [method 1]: (Mean Reference Lumen Area – In-Scaffold MLA / Mean Reference Lumen Area)

[§] Lumen Area Stenosis [method 2]: (Maximum Reference Lumen Area – In-Scaffold MLA / Maximum Reference Lumen Area)

[†] Lumen Diameter Stenosis [method 1]: (Mean Reference Lumen Diameter – In-Scaffold Lumen Diameter at MLA / Mean Reference Lumen Area)

[§] Lumen Diameter Stenosis [method 2]: (Maximum Reference Lumen Diameter – In-Scaffold Lumen Diameter at MLA / Maximum Reference Lumen Area)

For lumen diameter stenosis calculations, diameters were estimated as the diameter of a circle that has an equivalent area to the cross-section areas analyzed

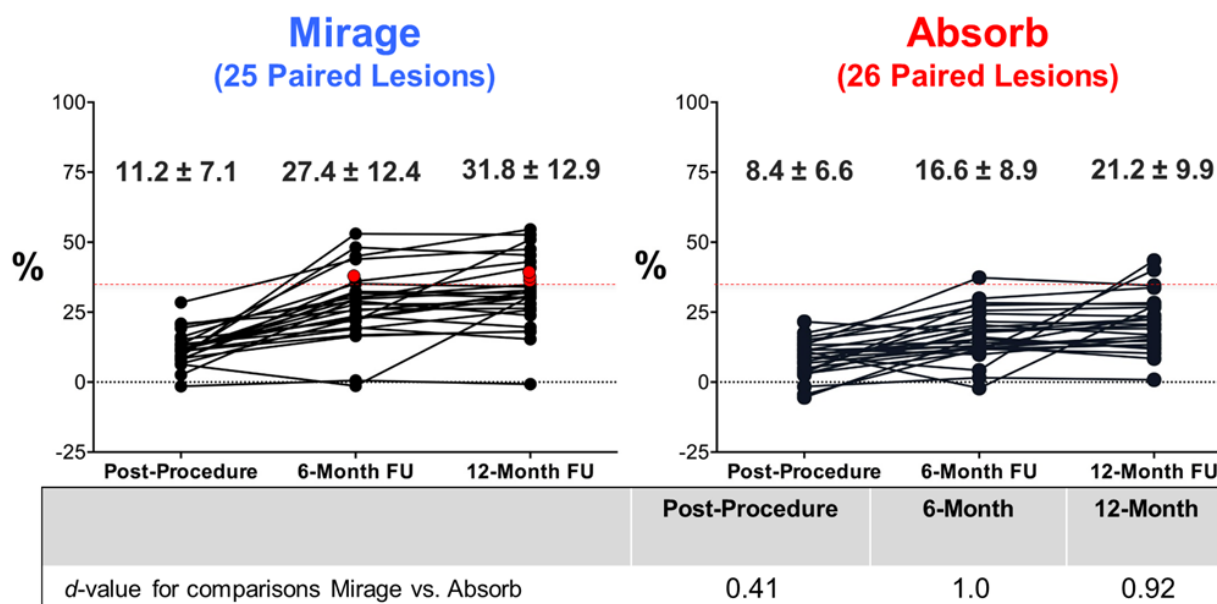


Figure 5. Serial OCT-derived lumen diameter stenosis

Diameter was calculated as the diameter of a circle that has an equivalent area to the cross-section areas analyzed by OCT. Lumen diameter stenosis was calculated as (Mean Ref lumen diameter – In-scaffold lumen diameter at minimum lumen area) / Mean Reference lumen diameter. In Mirage arm, one patient had a percent DS of $\geq 50\%$ at 6-months and three patients had a percent DS of $\geq 50\%$ at 1-year (red filled circles). Mann-Whitney test was used for all comparisons.

Clinical events in study groups are listed in **Table 8**. In 6-months and 12-months follow up, there was no statistical difference for MI, TLF, CI-TLR between the scaffold groups.

Figure 6a shows the device-oriented composite end-point. In the Mirage group, one patient experienced a peri-procedural MI according to the SCAI definition and another a definite scaffold thrombosis at day-3, resulting in STEMI and TLR. Subsequently, 3 patients underwent a CI-TLR, so that the cumulative incidence of event was 16.9% at 360 days. In the Absorb, 4 CI-TLR were observed up to 360 days resulting in a composite end point of 11.0%.

Figure 6b shows the patient-oriented composite end points including all death, MI or revascularization. The cumulative event up to 540-days amount to 31.7% in Absorb BVS and 25.8% in Mirage BRMS.

Table 8. Clinical events in scaffold groups

	Mirage	Absorb	p value
Non-hierarchical analysis	N=31*	N=29*	
All deaths	0/29 (0.0%)	0/27 (0.0%)	-
Cardiac deaths	0/29 (0.0%)	0/27 (0.0%)	-
Myocardial infarction per protocol	2/29 (6.9%)	0/27 (0.0%)	0.492
Q-wave	2/29 (6.9%)	0/27 (0.0%)	0.492
Non-Q-wave	0/29 (0.0%)	0/27 (0.0%)	-
Target vessel myocardial infarction	2/29 (6.9%)	0/27 (0.0%)	0.492
Q wave myocardial infarction	2/29 (6.9%)	0/27 (0.0%)	0.492
Non-Q wave myocardial infarction	0/29 (0.0%)	0/27 (0.0%)	-
Non-target vessel myocardial infarction	0/29 (0.0%)	0/27 (0.0%)	-
Q wave myocardial infarction	0/29 (0.0%)	0/27 (0.0%)	-
Non-Q wave myocardial infarction	0/29 (0.0%)	0/27 (0.0%)	-
All target-lesion revascularisation	7/29 (24.1%)	5/27 (18.5%)	0.748
Clinically indicated target-lesion revascularisation	5/29 (17.2%)	4/27 (14.8%)	1.000
Non-clinically indicated target-lesion revascularisation	2/29 (6.9%)	1/27 (3.7%)	1.000
All target-vessel revascularisation	7/29 (24.1%)	6/27 (22.2%)	1.000
Clinically indicated target-vessel revascularisation	5/29 (17.2%)	5/27 (18.5%)	1.000
Non-clinically indicated target-vessel revascularisation	2/29 (6.9%)	1/27 (3.7%)	1.000
Non-target-vessel revascularisation	0/29 (0.0%)	4/27 (14.8%)	0.048
Clinically indicated non-target-vessel revascularisation	0/29 (0.0%)	0/27 (0.0%)	-
Non-clinically indicated non-target-vessel revascularisation	0/29 (0.0%)	4/27 (14.8%)	0.048
All revascularisation	7/29 (24.1%)	8/27 (29.6%)	0.765
Clinically indicated revascularisation	5/29 (17.2%)	5/27 (18.5%) #	1.000
Non-clinically indicated revascularisation	2/29 (6.9%)	5/27 (18.5%) #	0.244
Composite secondary endpoints (Hierarchical analysis)			
Cardiac death, target-vessel myocardial infarction, and clinically indicated target-lesion revascularisation (target-lesion failure; device-oriented composite endpoint)	5/29 (17.2%)	4/27 (14.8%)	0.731
Cardiac deaths	0/29 (0.0%)	0/27 (0.0%)	-
Target vessel myocardial infarction	1/29 (3.4%)	0/27 (0.0%)	0.492

(continued)

Clinically indicated target-lesion revascularisation	4/29 (13.8%)	4/27 (14.8%)	1.000
All death, all myocardial infarction, and all revascularisation (patient-oriented composite endpoint)	8/29 (27.6%)	8/27 (29.6%)	1.000
All deaths	0/29 (0.0%)	0/27 (0.0%)	-
Any myocardial infarction	2/29 (6.9%)	0/27 (0.0%)	0.492
Any revascularization	6/29 (20.7%)	8/27 (29.6%)	0.542
Thrombosis endpoints			
Definite scaffold or stent thrombosis	1/29 (3.4%)	0/27 (0.0%)	1.000
Acute (0–1 day)	0/29 (0.0%)	0/27 (0.0%)	-
Sub-acute (2–30 days)	1/29 (3.4%)	0/27 (0.0%)	1.000
Late (31–365 days)	0/29 (0.0%)	0/27 (0.0%)	-
Very late (>365 days)	0/29 (0.0%)	0/27 (0.0%)	-
Definite or probable scaffold or stent thrombosis	1/29 (3.4%)	0/27 (0.0%)	1.000
Acute (0–1 day)	0/29 (0.0%)	0/27 (0.0%)	-
Sub-acute (2–30 days)	1/29 (3.4%)	0/27 (0.0%)	1.000
Late (31–365 days)	0/29 (0.0%)	0/27 (0.0%)	-
Very late (>365 days)	0/29 (0.0%)	0/27 (0.0%)	-

Data are expressed as number (percentage). P values were calculated from Fisher's exact test.

*In Mirage arm, 2 patients were lost to follow-up without events (001-047, 001-054). In Absorb arm, 2 patients were lost to follow-up without events (001-053, 001-061). #02-008 and 01-028 had both CI-TLR/TVR and non-CI non TVR.

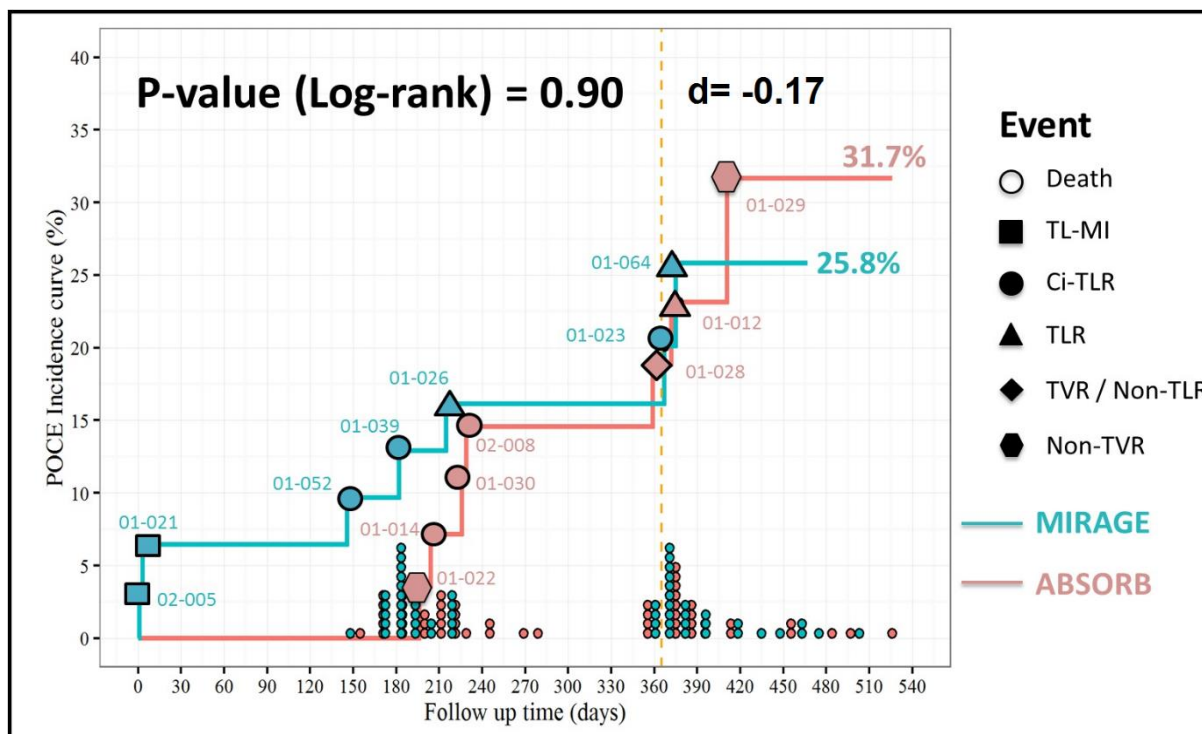


Figure 6a. Cumulative Curves for Patient-Oriented Cardiac Events

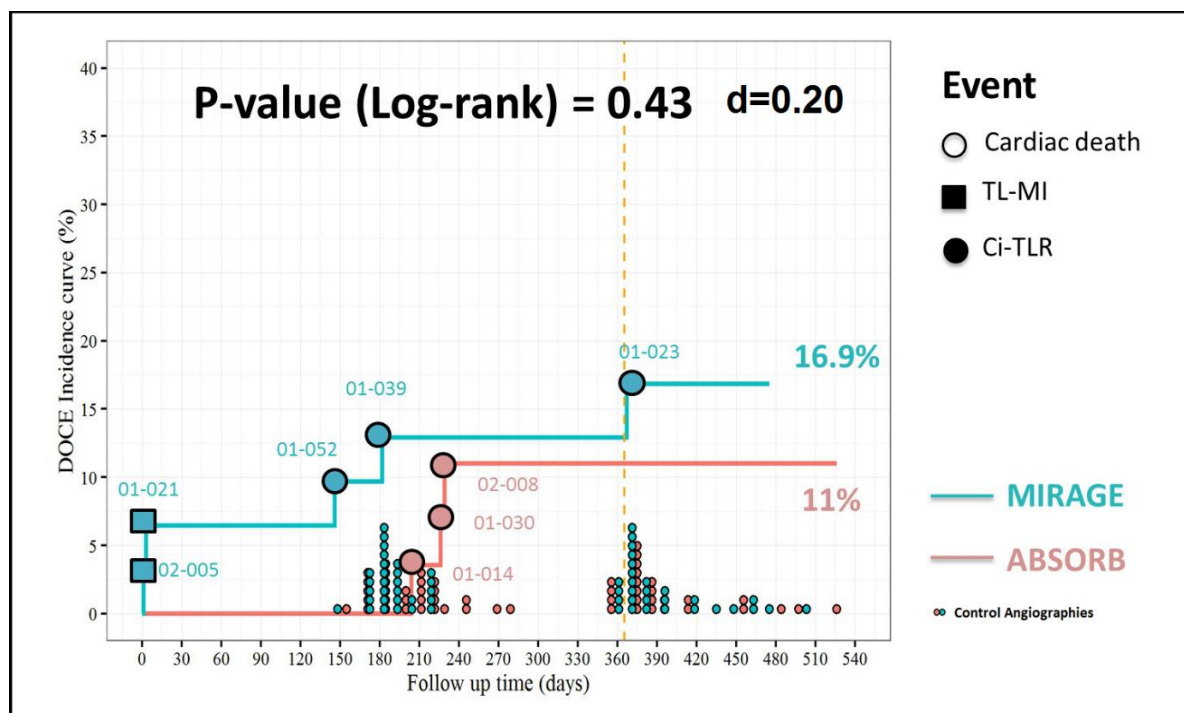


Figure 6b. Cumulative Curves for Device-Oriented Cardiac Events

DISCUSSION

The findings of the present study can be summarized as follows: **1-**At 12-months follow up, median angiographic in scaffold late lumen loss of Mirage and Absorb were not statistically different, although, -in absence of a prospective and proper statistical hypothesis-, no formal conclusion can be stated on equivalence and/or non-inferiority of the new BRS-Mirage, as compared to the Absorb. **2-**Secondary angiographic and optical coherence tomographic endpoint indicated less satisfactory performance of the Mirage as compared to the Absorb, although the technique of implantation was suboptimal considering the novel mechanical properties of the Mirage that were not fully exploited in this trial.

The Manli technology originated from research conducted in Singapore and the first-in-man trial has been conducted in the same geographical area, namely Indonesia and Malaysia. Considering the complexity of the patients and lesions in this region of the far-east, it was decided to conduct up-front a randomized trial comparing the new technology with the CE-mark and FDA approved Absorb technology so that the performance of the new technology could be better assessed with its comparator among patients recruited exclusively in Indonesia and Malaysia. The study population and the morphological type of lesions treated are characterized by a high incidence of silent ischemia, frequent involvement of bifurcation and Type-B and -C lesions.

In this small randomized trial comparing Mirage BRMS and Absorb BVS, there were no major difference in acute mechanical behavior between the 2 devices in terms of recoil, balloon-artery ratio, expansion index and resulting MLD.

At 12-months the binary restenosis rates were comparable. These binary restenosis rates were somewhat higher than previously reported for the BVS device and presumably attributed to the more complex morphology of the lesions attempted (B2/C lesions in 90%) (14). At the time of the patient enrollment, the technique of implantation did not incorporate current knowledge stemming from more contemporary studies on BRS, such as oversized pre-dilatation, mandatory post-dilatation, systematic use of non-compliant balloon and use of intravascular imaging for guidance (7). In the present trial, only half of the lesions were post-dilated and the scaffold expansion was 75.6 ± 23.4 % for Mirage and 84.6 ± 9.7 % for Absorb. The technical criteria of appropriate implantation (ratio of post-dilatation balloon nominal diameter to nominal scaffold diameter, etc.) were fulfilled in both arms. The scaffolds used

were adequately sized and precluded “small size device problems” immediately post-implantation at follow up (9).

In Absorb Cohort B trial, in-scaffold late lumen loss was 0.19 ± 0.18 mm at 6-month and 0.27 ± 0.32 mm at 12-month (15). In first-in-man trial of Elixir (DESolve trial), the angiographic late lumen loss at 180 day was 0.19 ± 0.19 mm (16). In absence of QCA at 12-months in the DESolve, the 12-months MSCT can be interpreted as a surrogate of conventional angiography and documented a lumen diameter stenosis of $15.9 \pm 10.0\%$. The results of Absorb and DESolve have demonstrated comparable follow up pattern in terms of late lumen loss. In the Absorb arm of the current trial, the median in-scaffold late lumen loss at 6-months was 0.17 [0.05-0.23] mm and 0.23 [0.15-0.37] mm at 12-months and seem comparable with the performance of the Absorb Cohort-B trial. In Mirage arm, the median late-lumen loss at 6-months follow up was 0.23 [0.04-0.44] mm and 0.37 [0.08-0.72] mm at 12-months, -values higher than the late losses in Absorb Cohort B and DESolve trials.

The scaffold manufacturing process of wrapping a monocircular filament around a metallic rod allows for a large variety of nominal sizes of device (2.5 mm, 2.75 mm, 3.0 mm, etc.). Therefore, selection of precisely sized device should be implemented to treat vessel of which dimensions have been thoroughly investigated and sized with OCT.

OCT, a more sensitive and accurate measurement of lumen dimension, clearly indicated some significantly larger reduction of the lumen area at follow up in the Mirage group than in the Absorb group. The fact that the Mirage strut is not translucent on OCT renders the assessment of the scaffold area at baseline difficult and makes the evaluation of the scaffold expansion or shrinking at follow up problematic. It is therefore difficult to attribute the lumen area reduction at 6- or 12-months to either an early shrinking (too fast bioresorption of the scaffold) or to an excess of neointimal growth (insufficient cytostatic cell inhibition) or to a combination of both phenomena.

In other words, future trials should be OCT-guided to allow for optimal implantation taking advantage of quarter-sized device and non-compliant balloon. Today it is still unclear what would be the optimal condition of implantation. Since the ductility of this device -in other words its capability of expansion- is rather limited, sizing is of-paramount importance, if the operator wants to use adequately the tensile strength of the device and its ability to resist elongation-at-break. In other words, the operator should be aware of the unique mechanical

feature of this novel technology and accordingly should adjust the sizing technique to take the advantage of the mechanical feature of the Mirage BRMS.

Limitations

This study has the following limitations; first, in absence of formal statistical hypothesis, the sample size was not based on statistical power. The number of lesions and patients tested were insufficient to draw statistically sound conclusions. Secondly, despite the fact that it's a first-in-man trial, relatively complex lesions were included in both arms and the complexity of the lesion may have affected the angiographic late-loss. Strict inclusion-exclusion criteria were not respected in 45% of the patient and more complex lesions were included in the study compared to the protocol-mandated inclusion and exclusion criteria in the protocol. In a first-in-man study, the investigators should follow exactly the inclusion and exclusion criteria and extremely complex lesions should not be included in this kind of feasibility and safety trial.

CONCLUSION

The current first-in-man study comparing two bioresorbable scaffolds demonstrated that, at 12-months, angiographic late lumen loss in device was similar between the Mirage BRMS and Absorb BVS. The other angiographic or OCT parameters (diameter stenosis) suggested a slightly, but significantly higher degree of percentage lumen obstruction in Mirage compared to the Absorb, although this was not translated into either angiography binary restenosis or clinical outcomes. The relatively high degree of late loss in both arms could be due to the inclusion of complex lesions and suboptimal technique of implantation. Since the technology is new with struts having different mechanical and optical properties compared to the other bioresorbable scaffold, the guidance on OCT is of paramount importance to establish the optimal implantation technique with this particular device.

WHAT IS KNOWN: Pre-dilatation, sizing and post-dilatation have paramount importance during the implantation of BRS. Smooth lesions provide acceptable results with Absorb BVS, which has wide clinical experience.

WHAT IS NEW: Different technologies in BRS are under development. With its high tensile strength, Mirage BRMS promises treatment of tough lesions. With the current trial, the indispensable role of post-dilatation of the scaffold and OCT imaging during implantation have been recognized.

WHAT IS NEXT: Introducing the new technologies into the field will shed light on the treatment opportunities for more complex lesions. Adequate lesion preparation with OCT imaging during implantation process appears to fill the “gap” in treatment of complex diseases with BRS.

Disclosures

PW Serruys and Y Onuma are members of International Advisory Board of Abbott Vascular.

REFERENCES

1. Serruys PW. Effects of polymer manufacturing processes on the mechanical properties of BRS. TCT 2015 – Transcatheter Cardiovascular Therapeutics 2015 Congress; 14th October 2015; San Francisco, CA, USA2015.
2. Serruys PW, Onuma Y, Ormiston JA, de Bruyne B, Regar E, Dudek D, et al. Evaluation of the second generation of a bioresorbable everolimus drug-eluting vascular scaffold for treatment of de novo coronary artery stenosis: six-month clinical and imaging outcomes. *Circulation*. 2010;122(22):2301-12.
3. Jiménez JM, Davies PF. Hemodynamically driven stent strut design. *Ann Biomed Eng*. 2009 Aug;37(8):1483-94.
4. Otsuka F, Pacheco E, Perkins LE, Lane JP, Wang Q, Kamberi M, et al. Long-term safety of an everolimus-eluting bioresorbable vascular scaffold and the cobalt-chromium XIENCE V stent in a porcine coronary artery model. *Circ Cardiovasc Interv*. 2014;7(3):330-42.
5. Cutlip DE, Windecker S, Mehran R, Boam A, Cohen DJ, van Es GA, et al. Clinical end points in coronary stent trials: a case for standardized definitions. *Circulation*. 2007;115(17):2344-51.
6. Ishibashi Y, Nakatani S, Sotomi Y, Suwannasom P, Grundeken MJ, Garcia-Garcia HM, et al. Relation Between Bioresorbable Scaffold Sizing Using QCA-Dmax and Clinical Outcomes at 1 Year in 1,232 Patients From 3 Study Cohorts (ABSORB Cohort B, ABSORB EXTEND, and ABSORB II). *JACC Cardiovasc Interv*. 2015;8(13):1715-26.
7. Mattesini A, Secco GG, Dall'Ara G, Ghione M, Rama-Merchan JC, Lupi A, et al. ABSORB biodegradable stents versus second-generation metal stents: a comparison study of 100 complex lesions treated under OCT guidance. *JACC Cardiovasc Interv*. 2014;7(7):741-50.
8. Onuma Y, Serruys PW, Gomez J, de Bruyne B, Dudek D, Thuesen L, et al. Comparison of in vivo acute stent recoil between the bioresorbable everolimus-eluting coronary scaffolds (revision 1.0 and 1.1) and the metallic everolimus-eluting stent. *Catheter Cardiovasc Interv*. 2011;78(1):3-12.
9. Tateishi H, Suwannasom P, Sotomi Y, Nakatani S, Ishibashi Y, Tenekecioglu E, et al. Edge Vascular Response After Resorption of the Everolimus-Eluting Bioresorbable Vascular Scaffold- A 5-Year Serial Optical Coherence Tomography Study. *Circ J*. 2016;80(5):1131-41.
10. Serruys PW, Chevalier B, Sotomi Y, Cequier A, Carrie D, Piek JJ, et al. Comparison of an everolimus-eluting bioresorbable scaffold with an everolimus-eluting metallic stent for the treatment of coronary artery stenosis (ABSORB II): a 3 year, randomised, controlled, single-blind, multicentre clinical trial. *Lancet*. 2016.
11. Thygesen K, Alpert JS, Jaffe AS, Simoons ML, Chaitman BR, White HD, et al. Third universal definition of myocardial infarction. *Circulation*. 2012;126(16):2020-35.
12. Onuma Y, Dudek D, Thuesen L, Webster M, Nieman K, Garcia-Garcia HM, et al. Five-year clinical and functional multislice computed tomography angiographic results after coronary implantation of the fully resorbable polymeric everolimus-eluting scaffold in patients with de novo coronary artery disease: the ABSORB cohort A trial. *JACC Cardiovasc Interv*. 2013;6(10):999-1009.
13. Onuma Y, Serruys PW, Muramatsu T, Nakatani S, van Geuns RJ, de Bruyne B, et al. Incidence and imaging outcomes of acute scaffold disruption and late structural discontinuity after implantation of the absorb Everolimus-Eluting fully bioresorbable vascular scaffold: optical coherence tomography assessment in the ABSORB cohort B Trial (A Clinical Evaluation of the Bioabsorbable Everolimus Eluting Coronary Stent System in the Treatment of Patients With De Novo Native Coronary Artery Lesions). *JACC Cardiovasc Interv*. 2014;7(12):1400-11.
14. Serruys PW, Onuma Y, Dudek D, Smits PC, Koolen J, Chevalier B, et al. Evaluation of the second generation of a bioresorbable everolimus-eluting vascular scaffold for the treatment of de

- novo coronary artery stenosis: 12-month clinical and imaging outcomes. *J Am Coll Cardiol.* 2011;58(15):1578-88.
15. Serruys PW, Onuma Y, Garcia-Garcia HM, Muramatsu T, van Geuns RJ, de Bruyne B, et al. Dynamics of vessel wall changes following the implantation of the absorb everolimus-eluting bioresorbable vascular scaffold: a multi-imaging modality study at 6, 12, 24 and 36 months. *EuroIntervention.* 2014;9(11):1271-84.
 16. Verheye S, Ormiston JA, Stewart J, Webster M, Sanidas E, Costa R, et al. A next-generation bioresorbable coronary scaffold system: from bench to first clinical evaluation: 6- and 12-month clinical and multimodality imaging results. *JACC Cardiovasc Interv.* 2014;7(1):89-99.

Supplement Table 1. Scaffold diameters at nominal and burst pressures

Inflation Pressure (atm)	Scaffold ID (mm)				
	Nominal balloon diameter \pm 10% These values are for reference only				
	2.5	2.75	3.0	3.5	4.0
*8 nominal	*2.52	*2.75	*3.01	3.39	4.00
10	2.57	2.82	3.06	*3.46	*4.05
12	2.64	2.86	3.10	3.52	4.08
14	2.66	2.90	3.14	3.56	4.14
16	2.69	2.93	3.17	3.62	4.18
18	2.72	2.96	3.21	3.66	4.23
20** RBP	**2.75	**3.00	**3.25	3.70	4.27
22**	2.75	3.02	3.25	**3.73	**4.30
24			3.27	3.77	4.33

Supplement Table 2. Procedural details for scaffold groups

	Absorb	Mirage
Pre-dilatation	Mandatory	Mandatory
Intravascular imaging during lesion preparation (additional to QCA)	Not mandatory but highly recommended	Not mandatory but highly recommended
Scaffolding	Balloon inflation performed increasing 5 atm per 2 sec.	Slow balloon inflation
Post-dilatation	At the operator's discretion	Mandatory, but in 31 patients post-dilatation was not performed.
Overlapping	Allowed for maximum 2 scaffolds	Allowed for maximum 2 scaffolds
OCT imaging after implantation	Mandatory	Mandatory
Bailout procedure	Mirage, Biomatrix Flex / Nobori stent	Absorb BVS, Xience V, Xience Prime

Chapter 4

Assessment of the hemodynamic characteristics of Absorb BVS in a porcine coronary artery model

Hemodynamic analysis of a novel bioresorbable scaffold in porcine coronary artery model

Non-Newtonian pulsatile shear stress assessment: a method to differentiate bioresorbable scaffold platforms

Assessment of the hemodynamic characteristics of Absorb BVS in a porcine coronary artery model

Erhan Tenekecioglu, Ryo Torii, Christos Bourantas, Mohammad Abdelghani, Rafael Cavalcante, Yohei Sotomi, Tom Crake, Solomon Su, Teguh Santoso, Yoshinobu Onuma, Patrick W. Serruys

Int J Cardiol. 2017; 227: 467-473.

ABSTRACT

Background and aim: Local hemodynamic changes are one of the main factors determines the vessel wall biological response after stent/scaffold implantation. Computational fluid dynamic studies provide opportunity to investigate *in silico* the rheological effects of implanted stent/scaffold. The aim of this study was to assess the local flow hemodynamics in scaffolded vessel segments in porcine coronary models.

Methods: In the epicardial coronary arteries of 6 healthy mini-pigs, 6 Absorb bioresorbable vascular scaffolds (Absorb BVS) were implanted. Optical coherence tomography (OCT) was performed after scaffold implantation and the images were fused with the angiographic data to reconstruct the 3D coronary artery anatomy. Blood flow simulations were performed and Endothelial Shear Stress (ESS) distribution was estimated for each scaffold. In a linear mixed-effect model, the contributing factors for low (<1.0 Pa) ESS levels were assessed. At 30-day post-implantation, histopathological assessment was performed at 2 scaffolded segments.

Results: In scaffolded segments, the median ESS was 0.57(IQR: 0.29-0.99) Pa. In linear mixed-effect analysis, cross-section area was associated with low shear stress levels. In scaffolded segments, the percentage of the recirculation zones per scaffolded luminal surface was $3.26 \pm 2.07\%$. At 30-day histopathological assessment of implanted vessel segments revealed minimal injury score, minimal neointimal inflammation and minimal adventitial inflammation scores with moderate endothelial coverage. Fibrin accumulation were seen at $95.69 \pm 2.47\%$ of the struts.

Conclusion: The thicker rectangular strut design of the Absorb BVS incited flow disruptions within the scaffolded vessel segments inducing fibrin accumulation. CFD assessment can be used to improve the scaffold design for a more “hemo-compatible” geometry.

Key words: Endothelial shear stress; bioresorbable scaffold; computational fluid dynamic

INTRODUCTION

Bioresorbable scaffold (BRS) has been introduced to overcome the drawbacks of metallic drug-eluting stents such as late stent thrombosis-due to delayed/incomplete healing-, neoatherosclerotic lesion development, and permanent metallic caging engenders abnormal vessel wall physiology (1). Stent/scaffold implantation induces crucial changes in local hemodynamic microenvironment in the treated vessel segment that greatly influences the reaction of the vessel wall (2). Restenosis in coronaries implanted with variety of stent types was proved to depend on the vessel size and stent design (3).

Endothelial shear stress (ESS) is the main conducive factor for the vessel wall response after stent/scaffold implantation (3). With its high resolution, optical coherence tomography (OCT) based *in silico* fluid dynamic models provide unique opportunity to study the effects of intracoronary stent/scaffold on the hemorheological changes (4). Following stent/scaffold implantation, computational fluid dynamic (CFD) studies have revealed disruptions in laminar flow and local alterations in ESS that can predispose the treated segments to platelet activation, intimal hyperplasia and as a consequence, thrombosis and in-stent re-stenosis (4).

Absorb bioresorbable vascular scaffold (Absorb BVS, Abbott Vascular, Santa. Clara, California, USA) is the first commercially-available BRS and has a long list of investigations. Following the Absorb scaffold implantation in diseased coronaries, lower ESS was shown to induce neointimal thickening during follow up (4). In the present exploratory study, we aimed at revealing the effect of device geometry and strut design on ESS distribution in implanted vessel segments without any atherosclerotic disease in porcine coronary models.

METHODS

Six Yucatan mini-swine pigs with healthy coronaries underwent percutaneous coronary intervention (PCI) via femoral access through a standard procedure (5). Overall, six Absorb BVS were implanted in 6 coronary arteries. The treated coronary arteries were studied by OCT imaging following the scaffold implantation. The animal study protocol was approved by the Institutional Animal Care and Use Committee and the study was conducted in accordance with the American Heart Association guidelines for preclinical research and the Guide for the Care and Use of Laboratory Animals (6).

Device description:

Absorb BVS is made of poly L-lactic acid (PLLA), coated with a layer of a 1:1 mixture of an amorphous matrix of poly D, L-lactic acid (PDLLA) and elutes everolimus ($8.2 \mu\text{g}/\text{mm}$). Absorb BVS, which is manufactured using extrusion and laser machining techniques, has $157\mu\text{m}$ strut thickness and a design of in-phase zig-zag hoops linked with bridges (**Figure 1**).

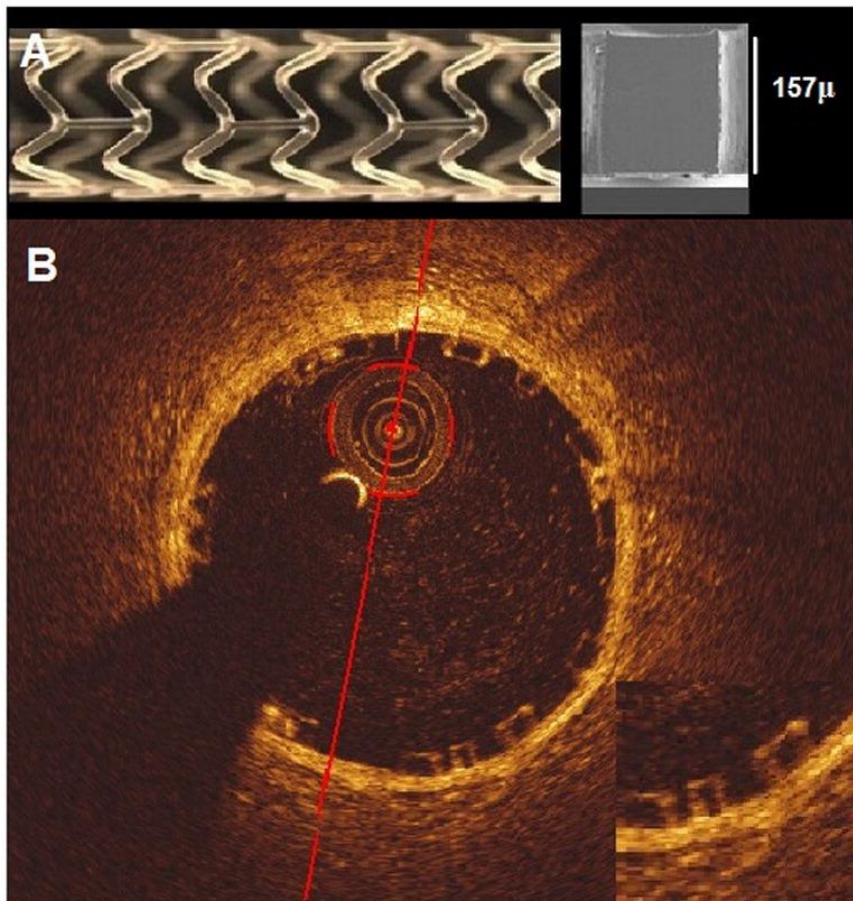


Figure 1. Absorb BVS 1.1 and the cross-section of Absorb BVS strut (A). OCT cross-section image of Absorb BVS. The strut of the Absorb BVS is rectangular and translucent (B).

Data acquisition

Coronary angiography was performed using Siemens HiCor cardiac angiography system (Siemens, Erlangen, Germany). The treated vessel segments were scrutinized using a frequency-domain OCT system (C8-XR OCT Intravascular Imaging System; St. Jude Medical, St. Paul, MN, USA) that was pulled-back at a speed of $18 \text{ mm}/\text{sec}$. A non-occlusive flushing technique was used for blood clearance by injection of contrast media. The acquired data were stored in DICOM format and transferred to a workstation for further analysis.

Coronary artery reconstruction

Coronary artery reconstruction was implemented using a well-established and validated methodology (7). In x-ray angiographic and OCT images, the radiopaque markers and the anatomical landmarks (i.e. side branches), identified both on angiography and OCT, were used to define the scaffolded segment and proximal-distal native vessel segments.

In the segment of interest, the OCT images portraying the scaffolded and the native vessel were identified and analyzed at a 0.1 mm interval in the scaffolded segment and a 0.2 mm interval in the native vessel segment. The flow area -defined in the native segment by the lumen border and in the scaffolded segment by the adluminal side of the scaffold struts and by the luminal surface in the inter-strut areas (8)- was then delineated.

Two post-procedure end-diastolic angiographic images with at least 30°-angle difference illustrating the segment of interest with minimal foreshortening were selected with the table in the isocenter. In these images, the luminal borders were detected for the segment of interest and used to extract the luminal centerline which was then used to define the 3D luminal centerline of the segment of interest (7). The flow area borders detected on OCT images were then superimposed perpendicularly onto the luminal centerline and anatomical landmarks, that is side-branches seen in both OCT and angiographic images were used to define the absolute orientation of the OCT frames (7).

Blood flow simulation

The reconstructed 3D geometries were processed with CFD techniques. After finite volume mesh generation, blood flow was simulated and the ESS was estimated by solving the 3D Navier-Stokes equations (ANSYS Fluent, Canonsburg, Pennsylvania) (9). In order to evaluate the impact of the scaffold design on the local hemodynamic micro-environment, the mesh density around the scaffold struts and within the boundary layer of the flow field at inter-strut area was increased to have an average element edge of 30 μm (equal to 0.25 of the thickness of the scaffold strut). Blood was assumed to be a homogeneous, Newtonian fluid with a viscosity of 0.0035 Pa.s and a density of 1,050 kg/m³. At the inflow of the 3D CFD model, a steady flow profile was simulated. As shown in previous publications, no significant differences exist between the ESS estimated in pulsatile and steady flow simulation (10,11). For each reconstruction, blood flow was estimated by measuring, in the 2 angiographic projections, the number of frames required for the contrast agent to pass from the inlet to

the outlet of the reconstructed segment, the volume of the reconstructed segment and the cine frame rate (3, 12). The arterial wall was considered to be rigid, consistent with what is expected post-implantation. No-slip conditions were applied to the scaffold surface. At the outlet of the model, zero pressure conditions were applied. ESS at the luminal surface was calculated as the product of blood viscosity and the gradient of blood velocity at the wall (13). The ESS was measured in the native and the scaffolded segments around the circumference of the lumen at a 5° interval (sector) and along the axial direction at a 0.2 mm interval with the use of an in-house algorithm (4) (**Figure 2**). The recirculation zones in the vicinity of the struts were quantified based on the direction of the ESS vector and the centerline vector. Areas where the ESS vector had opposite direction to the centerline vector were considered to be exposed to recirculation.

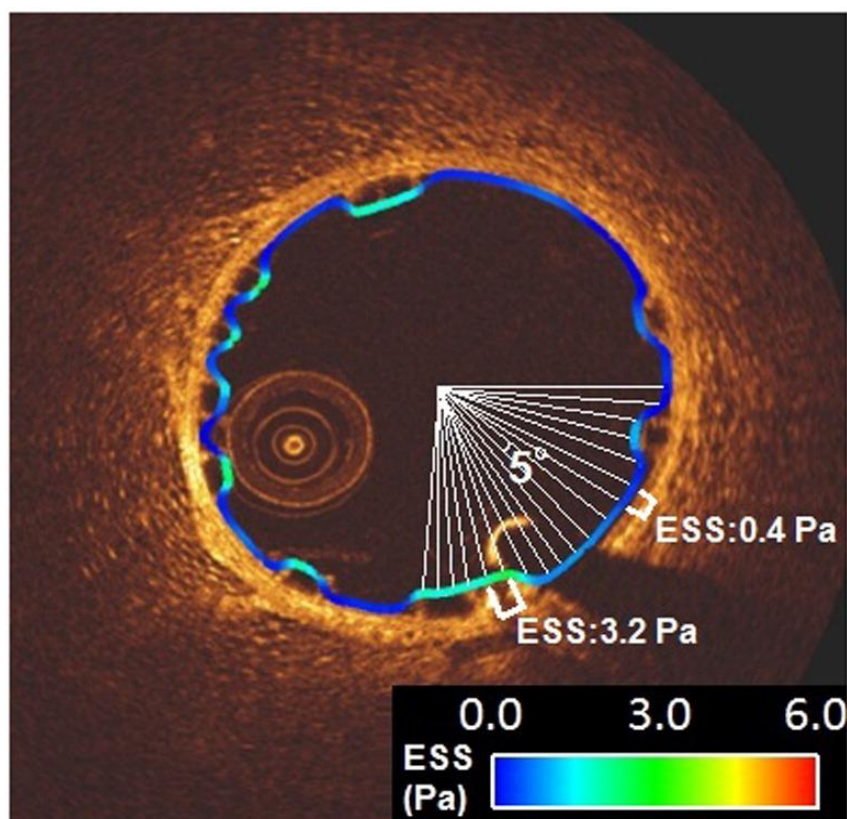


Figure 2. Circumferential ESS values (median, maximum and minimum) over the luminal perimeter at 5°-subunits (sectors) counted from 3 o'clock.

Histopathological analysis

Two animals from the study population were humanely euthanized for histopathological assessment at 30-day post-implantation. Other animals left for histological analysis at 180 days, 360 days and 720 days post-implantation. Each of sacrificed animal had 1 implanted Absorb BVS. One Absorb BVS (Absorb BVS-6, 3.0x 18 mm) was implanted in the RCA of the

first animal, and the other one (Absorb BVS-2, 3.0x18mm) was implanted in the LCx of the second animal. Sections from the proximal, mid and distal portions of each scaffolded segments were cut on a rotary microtome at six microns, mounted and stained with hematoxylin and eosin (H&E) and Movat pentachrome stains. All sections (n=6) were examined by light microscopy for the presence of inflammation, thrombus, and vessel wall injury. The cross-sectional areas (external elastic lamina [EEL], internal elastic lamina [IEL], and lumen) of each scaffolded section were measured. Neointimal thickness was measured as the distance from the inner surface of each scaffold strut to the luminal border. Area measurements were used to calculate vessel layer areas with the following formulas: Medial Area = EEL Area- IEL Area, Neointimal Area = IEL Area- Lumen Area, % Stenosis = $[1 - (\text{Lumen Area} / \text{IEL Area})] \times 100$. To compare neointimal organization and healing, data were collected on each scaffold section including, strut apposition to the vessel wall, fibrin deposition, calcification, granuloma and giant cell reactions and hemorrhage around the scaffold struts and was expressed as a percentage of the total number of struts in each section. A vessel injury score was calculated according to the Schwartz method (14). An overall neointimal inflammation (score 0-4) and adventitial inflammation (score 0-3) and fibrin value (score 0-3) were scored for each section. Scaffolded vessels with two or more granulomatous reactions around the scaffold struts in any section were assigned a neointimal inflammation “grade 4”. A description of these scores is demonstrated in **Table 1**. Endothelial coverage was estimated and expressed as the percentage of the lumen circumference covered by endothelium.

Statistical analysis

Continuous variables were tested for normality of distribution with Kolmogorov-Smirnov test and are presented as mean \pm SD or median (interquartile range) as appropriate. Categorical variables are presented as frequencies and percentages. Continuous variables were compared by the Kruskal-Wallis test or Mann Whitney U test. Categorical variables were compared by the Pearson Chi-square test.

There were several layers of grouping within the data of the study; six animals (level 4) received scaffold implants in up to three different arteries (level 3), where only one scaffold was implanted in each artery. Each scaffolded segment has several cross-sections (level 2) and each circumferential contour was divided into 72 sectors (5°-subunits) (level 1) in which ESS was measured. As the data in the study have multi-level structure and unbalanced design,

mixed effects models were used to analyze the data. Since the ESS data have a skewed distribution, square root transformations of the ESS data were performed to get a normal distribution for ESS data. The multi-level model was built with fixed effects on cross-sectional area, vessel type and the 5-degree subunits and random effects on animal ID, vessel type and cross-section ID. All computations were done using the statistical analysis program SPSS V.22, R V. 3.2.3(15) and the R package lme4(16).

Table 1. Description of Semi-Quantitative Histology Scores

Attribute	Score	Description of Assigned Weight
Injury Score (Using the method described by Schwartz et al ¹⁴)	0	Internal elastic lamina (IEL) intact, endothelium typically denuded, media may be compressed but not lacerated
	1	IEL lacerated, media typically compressed but not lacerated
	2	IEL lacerated, media visibly lacerated, external elastic lamina (EEL) intact but may be compressed
	3	EEL lacerated, typically large lacerations of media extending through EEL, coil wires sometimes residing in adventitia
Neointimal Inflammation Score	0	<25% struts with fewer than 10 inflammatory cells
	1	Up to 25% struts with greater than 10 inflammatory cells
	2	25-50% struts with greater than 10 inflammatory cells
	3	>50% struts with greater than 10 inflammatory cells
	4	2 or more struts with associated granulomatous inflammatory reactions
Fibrin Score	0	No fibrin is appreciated (or only small strands)
	1	At least 25% of struts involving confluent fibrin that surrounds up to 25% of the strut circumference
	2	At least 50% of struts involving confluent fibrin that surrounds >25% of strut Fibrin Score circumference
	3	All struts with confluent fibrin surrounding >50% of strut circumference or 25-50% of struts with confluent fibrin involving >25% of strut circumference with extension or bridging between struts
Adventitial Inflammation Score	0	No inflammation to minimal interspersed inflammatory cells anywhere in the adventitia
	1	Mild peripheral inflammatory infiltration or focally moderated in <25% of adventitial area
	2	Moderate peripheral inflammatory infiltration or focally marked in 25-50% of adventitial area
	3	Heavy peripheral inflammatory infiltration or focally marked in >50% of adventitial area

RESULTS

In the study animals (n=6), one left anterior descending artery (LAD), 3 left circumflex arteries (LCx) and 2 right coronary arteries (RCA) were treated. All scaffolds were well-apposed to the vessel wall and there were no malapposed struts. The list of scaffold diameters, lengths, deployment pressures, post-implantation dilatation balloon pressures, post-implantation

scaffold diameters and the implantation locations in the treated coronaries are shown in **Table 2**. The median ESS values and dimensions of the proximal non-scaffolded segment, scaffolded segment and the distal non-scaffolded segment are shown in **Table 3**.

Table 2. Inventory of scaffolds with implantation parameters.

Scaffold	Animal	Vessel	Scaffolded vessel segment	Scaffold size (mm)	Deployment balloon pressure (atm)	Post-dilatation balloon inflation pressure (atm)	The diameter of the scaffold after implantation (in vitro) (mm)
ABSORB BVS-1	Animal-A	LCx	Prox	3.0 x 18	7	7	3.0
ABSORB BVS-2	Animal-B	LCx	Mid	3.0 x 18	7	8	3.0
ABSORB BVS-3	Animal-C	LCx	Prox	3.0 x 18	7	8	3.0
ABSORB BVS-4	Animal-D	RCA	Mid	3.0 x 15	7	14	3.3
ABSORB BVS-5	Animal-E	LAD	Mid	3.0 x 18	7	7	3.0
ABSORB BVS-6	Animal-F	RCA	Mid	3.0 x 18	7	7	3.0

Table 3. The median ESS and lumen area in OCT in scaffolded and non-scaffolded segment in OCT for each scaffold. The data are tabulated according to the ranking of ESS

Scaffold	Animal	Median ESS (Q1-Q3)- Scaffolded segment (Pa)	Median Lumen Area (Q1-Q3)- Scaffolded segment (mm ²)	Median Lumen area (Q1-Q3)- Dist non-scaffolded segment (mm ²)	Median Lumen area (Q1-Q3)- Prox non-scaffolded segment (mm ²)
ABSORB BVS-1	A	0.22 (0.12-0.39)	8.0 (6.94-8.36)	3.48 (3.38-3.61)	5.62 (5.17-6.68)
ABSORB BVS-2	B	0.48 (0.27-0.82)	8.38 (7.93-8.71)	4.11 (3.94-4.41)	6.17 (5.32-6.38)
ABSORB BVS-3	C	0.56 (0.33-0.87)	6.92 (6.81-7.14)	5.04 (4.11-5.15)	6.04 (4.89-7.05)
ABSORB BVS-4	D	0.75 (0.51-1.10)	8.69 (8.55-8.93)	4.78 (4.52-5.10)	7.75 (7.57-8.09)
ABSORB BVS-5	E	0.75 (0.40-1.35)	7.96 (7.70-8.36)	7.37 (6.72-7.89)	12.63 (11.1-14.2)
ABSORB BVS-6	F	0.79 (0.43-1.29)	7.42 (7.24-7.51)	5.01 (4.21-7.23)	6.11 (5.7-6.4)

In scaffolded segments, the median ESS was 0.57 (interquartile range [IQR]: 0.29-0.99) Pa. The histogram of ESS for the Absorb BVS (**Figure 3**) showed that, 75% of the scaffolded surface was exposed to a low (<1 Pa), athero-promoting ESS environment (**Figure 4**). The mean percentage of recirculation area per scaffolded vessel segment surface area was 3.26±2.07%

(Figure 5). After setting the model with random and fixed effects variables, multi-level linear regression analysis revealed that an increase in the cross-sectional area was associated with a significant decrease in ESS ($p < 0.00001$).

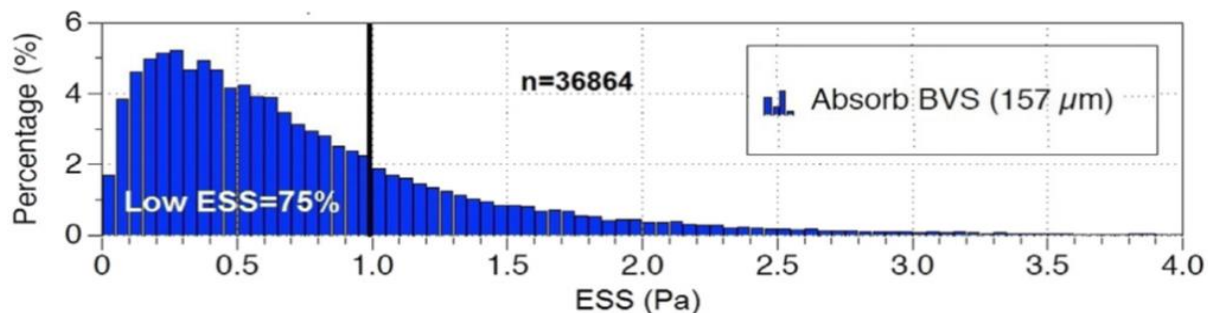


Figure 3. Histograms of ESS in scaffolded segments in Absorb BVS. “n” denotes the number of total ESS estimations at 5°-sectorial level.

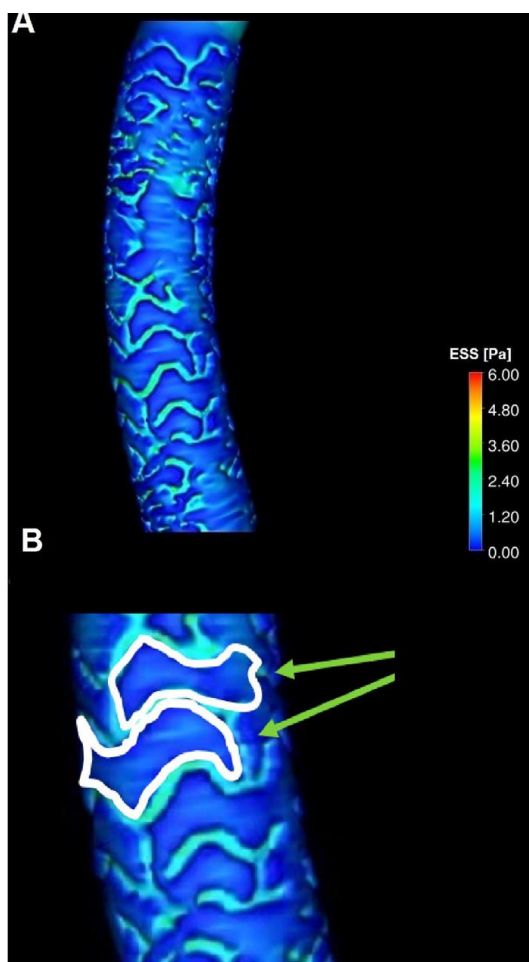


Figure 4. Three-dimensional reconstruction of scaffolded coronary anatomy from the fusion of coronary angiograms and OCT data with the local ESS being portrayed in a color-coded map (dark blue indicates low ESS < 1.0 Pa and aquamarine an ESS \geq 1.0 Pa) for Absorb BVS (A and B).

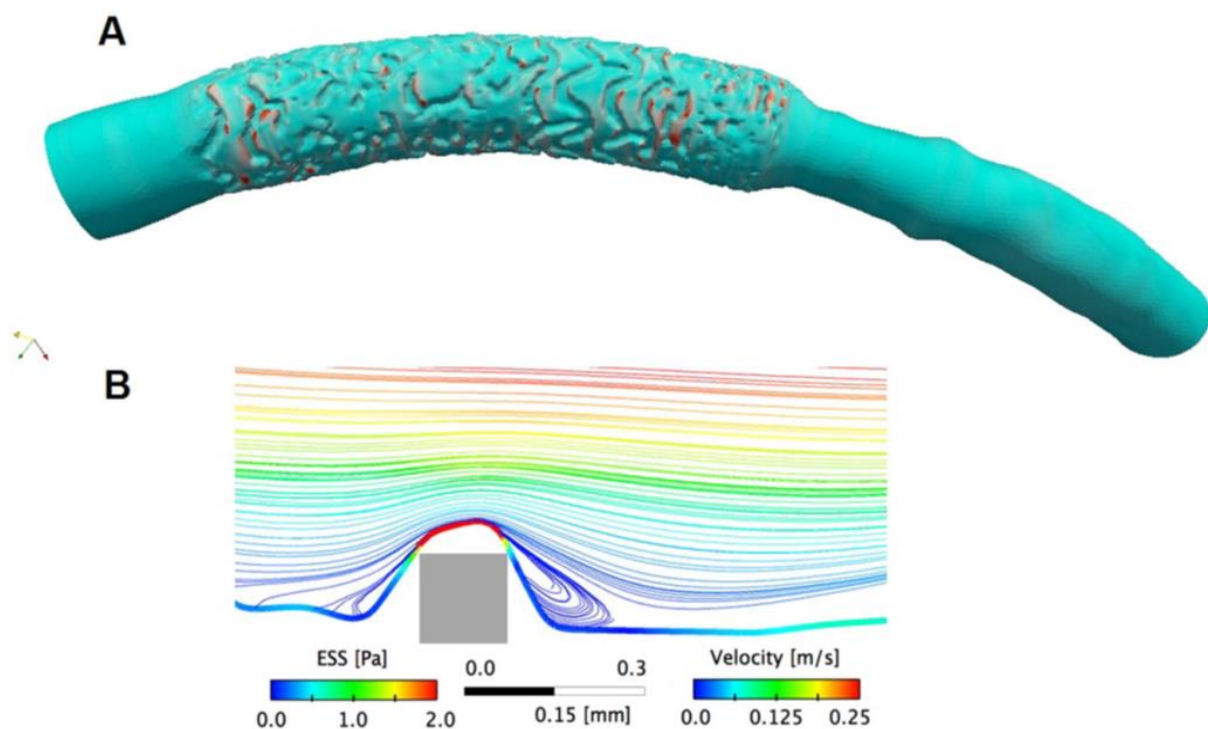


Figure 5. Recirculation zones (red) were quantified based on the ESS and the centerline direction (proximal \rightarrow distal). The red areas in the luminal surface are where the vectors of the ESS are pointing opposite (more than 90-degrees away from) the proximal-to-distal direction along the centerline **(A)**. Rectangular cross-section induces recirculations upstream and downstream of the struts **(B)**.

The results of the histopathological analysis are shown in section level **(Table 4)** and device level **(Table 5)**. At 30-day histopathological assessment, the micro-sections from the scaffolded segments demonstrated minimal neointimal inflammation and minimal adventitial inflammation scores **(Figure 6)**. From all prepared histological sections ($n=6$), totally 72 struts were analysed. Around strut fibrin deposition is moderate to severe (mean score = 2.50 ± 0.24) and seen at $95.69 \pm 2.47\%$ of the evaluated struts. Calcification is seen at the majority (mean = $53.28 \pm 15.14\%$) of strut borders in all sections. The luminal surface showed incomplete endothelialization with frequent adherent luminal inflammatory cells. There was no luminal thrombus in the scaffolded vessels.

Table 4. Histo-pathological analysis of 2 scaffolded vessel segments.

Histological findings from the proximal, mid and distal segments of the scaffolded segments.

Scaffold	Ves.	Sec.	EEL Area	IEL Area	LA	NA	MA	Ste. (%)	NT (Mn)	Inj. Sc	Mal. (%)	Fib (%)	Fib Sc	Gran (%)	N. inf Sc	Giant cell (%)	RBC (%)	End. Cov. (%)	Adv Inf Sc
D30-2	LCx	Prox	8.39	6.87	4.52	2.35	1.52	34.2	0.102	0.45	0.00	81.82	3	0	0	27.27	54.55	10	0
D30-2	LCx	Mid	8.32	7.01	4.58	2.43	1.31	34.7	0.126	0.92	0.00	100.0	3	0	0	8.33	75.00	20	0
D30-2	LCx	Dist	7.83	6.99	4.53	2.46	0.84	35.2	0.105	0.62	0.00	100.0	2	0	1	23.08	61.54	40	0
D30-6	RCA	Prox	7.96	6.97	4.29	2.68	0.99	38.5	0.130	0.00	0.00	100.0	2	0	0	41.67	41.70	99	0
D30-6	RCA	Mid	8.06	6.89	4.31	2.58	1.17	37.5	0.138	0.08	0.00	92.31	2	0	0	30.77	30.80	80	0
D30-6	RCA	Dist	8.87	7.53	4.28	3.25	1.34	43.2	0.217	0.45	0.00	90.00	3	0	0	63.64	45.45	90	0

Ves: Vessel, Sec: Section, EEL: External elastic lamina, IEL: internal elastic lamina, NA: Neointimal area, MA: Medial area, Ste:

Stenosis, NT(Mn): Neointimal thickness (Mean), Inj Sc: Injury score, Mal: Malapposition, Fib: Fibrin, Gran: Granulocyte, N.inf Sc:

Neointimal inflammation score, RBC: Red blood cell, End. Cov.: Endothelial Coverage, Adv. Inf. Sc: Adventitial Inflammation

score

Table 5a. Morphometric analysis results from all sections (proximal, mid, distal) (mean \pm SD) at light microscopy.

EEL Area (mm ²)	IEL Area (mm ²)	Lumen Area (mm ²)	Medial Area (mm ²)	Neointimal Area (mm ²)	Stenosis (%)	Neointimal Thickness (mm)
8.24 \pm 0.082	7.04 \pm 0.12	4.42 \pm 0.18	1.20 \pm 0.040	2.62 \pm 0.30	37.19 \pm 3.53	0.14 \pm 0.036

Table 5b. Histologic analysis results from all sections (mean \pm SD) at light microscopy.

Strut Malapposition (%)	Struts with Fibrin (%)	Struts with Granuloma (%)	Struts with Giant Cells (%)	Struts with RBCs (%)	Struts with Calcification (%)	Endothelialization (%)
8.24 \pm 0.082	7.04 \pm 0.12	4.42 \pm 0.18	1.20 \pm 0.040	2.62 \pm 0.30	37.19 \pm 3.53	0.14 \pm 0.036
						6

Table 5c. Histologic analysis of non-parametric scores from all sections (mean \pm SD) at light microscopy.

Mean Injury Score	Mean Fibrin Score	Neointimal Inflammation Score	Adventitial Inflammation Score
8.24 \pm 0.082	7.04 \pm 0.12	4.42 \pm 0.18	1.20 \pm 0.040

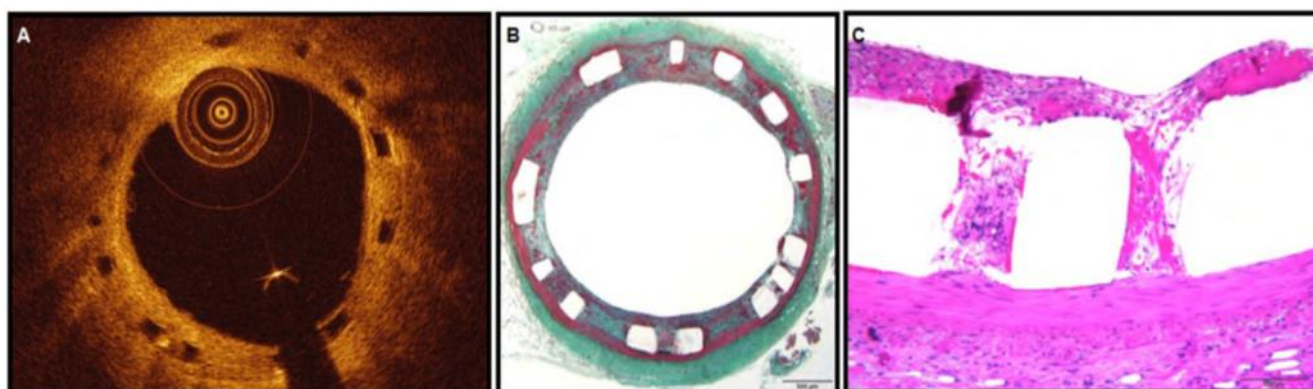


Figure 6: Low (2x) (A) and High (20x) (B) power representative image of Absorb BVS. Images shown are stained by Movat (2x) (A) and Hematoxylin and eosin (20x) (B). All struts were morphologically identical as open acellular regions with well-defined borders. Neointimal hyperplasia was thicker at inter-strut zones than top of the struts (A, B)

DISCUSSION

In this exploratory study, we investigated the effect of scaffold design and strut profile of Absorb BVS on local hemodynamic microenvironment in healthy coronary arteries of porcine model. The main findings were as follows: 1) Thick rectangular non-streamlined struts of Absorb BVS caused recirculations and related low shear stress zones within the scaffolded luminal surface 2) The histopathological analysis showed minimal injury, minimal neointimal and adventitial inflammation at scaffolded segments 3) There was moderate to severe fibrin accumulation around the struts.

The relation between stent/scaffold design and disrupted flow hemodynamics inducing neointimal tissue response and in-stent restenosis has been demonstrated previously (17). It's obvious that it's strenuous to evaluate this relationship through *in vivo* studies. Several *in silico* studies have demonstrated the impact of stent design on local hemodynamics after stent implantation (2). The zig-zag hoop designed rings and thicker rectangular struts induced flow separations, stagnation zones and related lower shear stress zones in the vicinity of the struts in Absorb BVS in this study.

After constitution of a new luminal surface with implanted scaffold struts, shifted shear stress induces several patho-biological mechanisms within the vessel wall (18). The luminal surface coverage ratio, the curvature status of the implanted vessel segment, the design of the stent/scaffold, the strut geometry, the implantation process itself (implantation pressure, post-dilatation pressure, etc.), embedment status of the stent struts are the factors for altered shear stress levels in scaffolded segment (18). Twenty-six percent luminal coverage ratio of Absorb BVS which is higher than its metallic equivalent, leads to higher endothelial denudation. This increased endothelial denudation with lower shear stress zones sets a susceptible environment for increased neointimal thickening through a continuous inflammation within the vessel wall (19 20). However, adequate inter-strut distance (1.0 mm for Absorb BVS) enables the flow streamlines to recover their laminarity after the disruption around the rectangular thicker struts (21 22). This recovery should reduce the detrimental effect of low shear stress levels on the vessel wall. While the lower shear stress levels at besides the struts and at inter-strut zones induce neointimal hyperplasia, the top of the struts induce less tissue hyperplasia due to increased shear stress levels at top of the struts (4). The histopathological analysis confirmed the variety of neointimal response at top of the struts and inter-strut zones due to the different levels of shear stress at top of struts and inter-strut

areas. Both those mechanisms, adequate inter-strut distance and higher shear stress levels at top of the struts, with the anti-proliferative drug have counteracting effect for increased neointimal hyperplasia at follow up post implantation in Absorb BVS (4,23).

Inadequate re-endothelialization of the scaffold struts at 30-day histological analysis might be the result of several factors. The flow disruption in the scaffolded segment impairs nitric oxide production which has influence on endothelial homeostasis (24). Another factor might be the increased anti-proliferative drug uptake by the vessel tissue due to the stagnation zones in the lower shear zones beside the struts. These stagnation zones can induce clotting process which affects the anti-proliferative drug kinetics. Increased fibrin accumulation around the struts within the histological specimens supports this pathomechanism in our study. *In silico* models approved the drug recycle between the thrombus and the lumen that prohibits the drug to pass from clot around the strut to the vessel wall which can prevent the endothelial regeneration at strut zones (25). In the absence of a laminar shear stress, endothelial differentiation of several types of stem cells is deteriorated which also may help to explain the defective re-endothelialization of the struts at 30-day in our study (26,27).

Limitations

There are some limitations in this research study. First, scaffold implantation was performed in healthy coronary vessels. Therefore, it was not possible to assess the impact of scaffold under-expansion or of the composition of the underlying plaque on strut embedment which can influence the flow hemodynamics in scaffolded segments. Second, there was no comparator which would enable to make a hypothesis for the hemo-rheologic properties of Absorb BVS. Third, in this exploratory study, at 30-day post-implantation, only two animals were sacrificed for histological analyses that was very limited for making a generalized comment for the histological analysis. Other animals will be euthanized at 180-day, 360-day and 720-day post-implantation for histological assessment.

CONCLUSION

With its current design and strut profile, Absorb BVS induces fluctuations at ESS and related pathologic findings in scaffolded segments. The CFD examination should be handled delicately in order to improve the design characteristics of Absorb BVS in such a “hemo-compatible” way with reducing its strut thickness, converting the struts profile into a more streamlined form.

Disclosures

E. Tenekecioglu has a research grant from TUBITAK (The Scientific Council of Turkey). P.W. Serruys is a member of the International Advisory Board of Abbott Vascular. Y. Onuma is a member of the International Advisory Board of Abbott Vascular.

REFERENCES

- 1) Mukete BN, van der Heijden LC, Tandjung K, Baydoun H, Yadav K, Saleh QA, Doggen CJ, Rafah NA, Le Jemtel TH, von Birgelen C. Safety and efficacy of everolimus-eluting bioresorbable vascular scaffolds versus durable polymer everolimus-eluting metallic stents assessed at 1-year follow-up: A systematic review and meta-analysis of studies. *Int J Cardiol.* 2016;221:1087-1094
- 2) Jimenez JM, Davies PF. Hemodynamically driven stent strut design. *Annals of biomedical engineering* 2009;37:1483-94.
- 3) Kastrati, A. J., Mehilli, J., Dirschinger, J., Pache, J., Ulm, K., Schuhlen, H., et al., , "Restenosis After Coronary Placement of Various Stent Types," *Am J Cardiol.* 2001;87(1):34-9.
- 4) Bourantas CV, Papafaklis MI, Kotsia A, Farooq V1, Muramatsu T, Gomez-Lara J, Zhang YJ, Iqbal J, Kalatzis FG, Naka KK, Fotiadis DI, Dorange C, Wang J, Rapoza R, Garcia-Garcia HM, Onuma Y, Michalis LK, Serruys PW. Effect of the endothelial shear stress patterns on neointimal proliferation following drug-eluting bioresorbable vascular scaffold implantation: an optical coherence tomography study. *JACC Cardiovascular interventions* 2014; 7: 315-24.
- 5) Williams PD, Malik N, Kingston PA. Coronary angiography and percutaneous coronary intervention in the porcine model: a practical guide to the procedure. *Animal.* 2012;6(2):311-320.
- 6) National Research Council (U.S.). Committee for the Update of the Guide for the Care and Use of Laboratory Animals (2011). *Guide for the Care and Use of Laboratory Animals.* Washington, DC: National Academies Press.
- 7) Bourantas CV, Papafaklis MI, Lakkas L, Sakellarios A, Onuma Y, Zhang YJ, Muramatsu T, Diletti R, Bizopoulos P, Kalatzis F, Naka KK, Fotiadis DI, Wang J, Garcia Garcia HM, Kimura T, Michalis LK, Serruys PW. Fusion of optical coherence tomographic and angiographic data for more accurate evaluation of the endothelial shear stress patterns and neointimal distribution after bioresorbable scaffold implantation: comparison with intravascular ultrasound-derived reconstructions. *Int J Cardiovasc Imaging.* 2014;30(3):485-94.
- 8) Nakatani S, Sotomi Y, Ishibashi Y, Grundeken MJ, Tateishi H, Tenekecioglu E, Zeng Y, Suwannasom P, Regar E, Radu MD, Räber L, Bezerra H, Costa MA, Fitzgerald P, Prati F, Costa RA, Dijkstra J, Kimura T, Kozuma K, Tanabe K, Akasaka T, Di Mario C, Serruys PW, Onuma Y. Comparative analysis method of permanent metallic stents (XIENCE) and bioresorbable poly-L-lactic (PLLA) scaffolds (Absorb) on optical coherence tomography at baseline and follow-up. *EuroIntervention.* 2015;11(6).
- 9) Papafaklis MI, Bourantas CV, Theodorakis PE, Katsouras CS, Fotiadis DI, Michalis LK. Relationship of shear stress with in-stent restenosis: bare metal stenting and the effect of brachytherapy. *International journal of cardiology* 2009;134:25-32.
- 10) Feldman CL, Ilegbusi OJ, Hu Z, Nesto R, Waxman S, Stone PH. Determination of in vivo velocity and endothelial shear stress patterns with phasic flow in human coronary arteries: a methodology to predict progression of coronary atherosclerosis. *Am Heart J.* 2002;143(6):931-9.
- 11) Tenekecioglu E, Torii R, Bourantas C, Crake T, Zeng Y, Sotomi Y, Onuma Y, Yilmaz M, Santoso T, Serruys PW. Preclinical assessment of the endothelial shear stress in porcine-based models following implantation of two different bioresorbable scaffolds: effect of scaffold design on the local haemodynamic micro-environment. *EuroIntervention.* 2015;12(1). doi: 10.4244/EIJY16M05_01. [Epub ahead of print]
- 12) Sakamoto S, Takahashi S, Coskun AU, Papafaklis MI, Takahashi A, Saito S, Stone PH, Feldman CL. Relation of Distribution of Coronary Blood Flow Volume to Coronary Artery Dominance. *Am J Cardiol* 2013.
- 13) Stone PH, Saito S, Takahashi S, Makita Y, Nakamura S, Kawasaki T, Takahashi A, Katsuki T, Nakamura S, Namiki A, Hirohata A, Matsumura T, Yamazaki S, Yokoi H, Tanaka S, Otsuji S, Yoshimachi F, Honye J, Harwood D, Reitman M, Coskun AU, Papafaklis MI, Feldman CL;

- PREDICTION Investigators. Prediction of progression of coronary artery disease and clinical outcomes using vascular profiling of endothelial shear stress and arterial plaque characteristics: the PREDICTION Study. *Circulation*. 2012 Jul 10;126(2):172-81.
- 14) Schwartz RS, Huber KC, Murphy JG, Edwards WD, Camrud AR, Vlietstra RE, Holmes DR. Restenosis and the proportional neointimal response to coronary artery injury: results in a porcine model. *J Am Coll Cardiol*. 1992;19(2):267-274.
 - 15) R Core Team. R: A Language and Environment for Statistical Computing. R Foundation for Statistical Computing, Vienna, Austria, 2015.
 - 16) Bates D, Maechler M, Bolker B, and Walker S. lme4: Linear Mixed-Effects Models using 'Eigen' and S4, 2015. R package version 1.1-10.
 - 17) Garasic JM, Edelman ER, Squire JC, Seifert P, Williams MS, Rogers C. Stent and artery geometry determine intimal thickening independent of arterial injury. *Circulation* 2000;101: 812–8.
 - 18) Koskinas KC, Chatzizisis YS, Antoniadis AP, Giannoglou GD Role of endothelial shear stress in stent restenosis and thrombosis: pathophysiologic mechanisms and implications for clinical translation. *J Am Coll Cardiol*. 2012 Apr 10;59(15):1337-49.
 - 19) Liehn EA, Schober A, Weber C Blockade of keratinocyte-derived chemokine inhibits endothelial recovery and enhances plaque formation after arterial injury in ApoE-deficient mice. *Arterioscler Thromb Vasc Biol*. 2004; 24(10):1891-6.
 - 20) Gijzen FJ, Oortman RM, Wentzel JJ et al. Usefulness of shear stress pattern in predicting neointima distribution in sirolimus-eluting stents in coronary arteries. *Am J Cardiol*. 2003;92(11):1325-8.
 - 21) Berry JL, Santamarina A, Moore Jr JE, Roychowdhury S, Routh WD, Experimental and computational flow evaluation of coronary stents, *Ann. Biomed. Eng.* 28 (2000), 386–398.
 - 22) Akagawa E, Ookawa K, Ohshima N. Endovascular stent configuration affects intraluminal flow dynamics and in vitro endothelialization. *Biorheology*. 2004;41(6):665-80.
 - 23) Serruys PW, Onuma Y, Garcia-Garcia HM, et al. Dynamics of vessel wall changes following the implantation of the absorb everolimus-eluting bioresorbable vascular scaffold: a multi-imaging modality study at 6, 12, 24 and 36 months. *EuroIntervention*. 2014 20;9(11):1271-1284.
 - 24) Liu X, Wang M, Zhang N, Fan Z, Fan Y, Deng X. Effects of endothelium, stent design and deployment on the nitric oxide transport in stented artery: a potential role in stent restenosis and thrombosis. *Med Biol Eng Comput*. 2015;53(5):427-439.
 - 25) Hwang CW, Levin AD, Jonas M, Li PH, Edelman ER. Thrombosis modulates arterial drug distribution for drug-eluting stents. *Circulation*. 2005;111(13):1619-26
 - 26) Potter CM, Lao KH, Zeng L, Xu Q. Role of biomechanical forces in stem cell vascular lineage differentiation. *Arterioscler Thromb Vasc Biol*. 2014;34(10):2184-90.
 - 27) Fang F, Wasserman SM, Torres-Vazquez J, Weinstein B, Cao F, Li Z, Wilson KD, Yue W, Wu JC, Xie X, Pei X. The role of Hath6, a newly identified shear-stress-responsive transcription factor, in endothelial cell differentiation and function. *J Cell Sci*. 2014;127(Pt 7):1428–1440.

Corrigendum

Corrigendum to “Assessment of the hemodynamic characteristics of Absorb BVS in a porcine coronary artery model.” [Int J Cardiol. 2017 Jan 15;227: 467-473]

Erhan Tenekecioglu, Ryo Torii, Christos Bourantas, Mohammad Abdelghani, Rafael Cavalcante, Yohei Sotomi, Tom Crake, Solomon Su, Teguh Santoso, Yoshinobu Onuma, Patrick W. Serruys

Int J Cardiol. 2017; 235:206.

Dear Editorial office of International Journal of Cardiology;

We realized that during the proof of our published article entitled “Assessment of the hemodynamic characteristics of Absorb BVS in a porcine coronary artery model” we made a mistake probably because of copy-paste process of the table sketch for Table 5b and Table-5c. We sincerely apologize for that mistake and kindly request from the journal to amend it. We incorporated the update for Table-5b and Table-5c as follows:

Table 5b. Histologic analysis results from all sections (mean \pm SD) at light microscopy.

Strut malapposition (%)	Struts with fibrin (%)	Struts with granuloma (%)	Struts with giant cells (%)	Struts with RBCs (%)	Endothelialization (%)
0.0 \pm 0.0	94.02 \pm 7.41	0.0	32.46 \pm 18.75	51.51 \pm 15.64	56.5 \pm 38.07

Table-5c: Histologic analysis of non-parametric scores from all sections (mean \pm SD) at light microscopy.

Mean injury score	Mean fibrin score	Neointimal inflammation score	Adventitial inflammation score
0.42 \pm 0.34	2.5 \pm 0.55	0.17 \pm 0.41	0.0 \pm 0.0

The authors would like to apologise for any inconvenience caused.

DOI of original article: 10.1016/j.ijcard.2016.11.005.

Hemodynamic analysis of a novel bioresorbable scaffold in porcine coronary artery model

Erhan Tenekecioglu, Ryo Torii, Christos Bourantas, Carlos Collet, Rafael Cavalcante, Yohei Sotomi, Yaping Zeng, Tom Crake, Alexandre Abizaid, Yoshinobu Onuma, Solomon Su, Teguh Santoso, Patrick W. Serruys

Catheter Cardiovasc Interv. 2018;91(6):1084-1091.

ABSTRACT

Background: *In-silico* studies have provided evidence that stent/scaffold design affects the local hemodynamics, major determinant of clinical outcomes following stent implantation. The shear stress distribution assessment can provide useful insights for the hemodynamic performance of the implanted stent/scaffold. Our aim was to investigate the effect of a novel bioresorbable scaffold, Mirage on local hemodynamics.

Method: The main epicardial coronary arteries of 7 healthy mini-pigs were implanted with 11 Mirage Microfiber sirolimus-eluting Bioresorbable Scaffolds (MMSES). Optical coherence tomography (OCT) was performed post scaffold implantation and the obtained images were fused with angiographic data to reconstruct the coronary artery anatomy. Blood flow simulation was performed and Endothelial Shear Stress (ESS) distribution was estimated for each of the 11 scaffolds. ESS data were extracted in each circumferential 5-degree subunit of each cross-section in the scaffolded segment. The generalized linear mixed-effect analysis was implemented for the ESS data in 2 groups; 150 μ m strut thickness MMSES and 125 μ m strut thickness MMSES.

Results: The median of ESS per scaffold group is as follows; MMSES (150 μ m): 0.85(0.49-1.40) Pa, MMSES (125 μ m): 0.68(0.35-1.18) Pa. ESS was significantly higher in MMSES (150 μ m) compared to MMSES (125 μ m). Both MMSES (150 μ m) and MMSES (125 μ m) revealed low recirculation zone per luminal surface area [3.17 \pm 1.97% per luminal surface area in MMSES (150 μ m), 2.71 \pm 1.32% per luminal surface area in MMSES (125 μ m)].

Conclusion: Local hemodynamic micro-environment seems to be favorable in MMSES considering the limited area of recirculation. This pilot study warrants comparative assessment with commercially available bioresorbable scaffold.

INTRODUCTION

Metallic drug eluting stents have significant limitations including the risks of neoatherosclerosis, late stent thrombosis and restenosis which affect long term prognosis. Bioresorbable scaffolds (BRS) have been introduced to overcome these issues with potential benefits of allowing future treatments, non-invasive imaging procedures and recovering vessel physiology during bioresorption process of the scaffold. Despite its supreme benefits, recent reports of neoatherosclerosis and scaffold thrombosis have emerged concerns about the designs of BRS¹. Thicker struts, bulky structure, non-streamlined strut geometry and early mechanical disruption have been charged for underlying pathological mechanisms. Local coronary hemodynamics, particularly endothelial shear stress (ESS) seems to drive these mechanisms². Following stent/scaffold implantation, the device geometry, strut profile and curvature status of the implanted vessel segment influence the rheological behavior of the scaffolded segment³. The *in-vivo* evaluation of the impact of protruding struts on local hemodynamic patterns in the current available BRS has revealed the interaction between shifted ESS and the intimal tissue response⁴.

Mirage Microfiber Sirolimus-Eluting bioresorbable Scaffold (MMSES, Manli Cardiology, Singapore) is a novel coronary stent that has substantial differences in geometrical design, strut profile, strut thickness, and strut connector alignments. The objective of this preclinical study was to determine the flow characteristics and ESS distribution in MMSES implanted coronary artery segments.

METHODS

We analyzed data from Yucatan mini-pigs implanted with MMSES. Seven mini-pigs with healthy coronaries underwent percutaneous coronary intervention (PCI) in the three epicardial coronary arteries via the femoral access according to standard procedures. Six coronaries were implanted with a single MMSES with 150 μ m strut thickness [MMSES (150 μ m)] and 5 coronaries with a MMSES with 125 μ m strut thickness [MMSES (125 μ m)]. The treated coronary arteries were imaged by OCT immediately after the scaffold implantation. The protocol approval for the animal study was received from the Institutional Animal Care and Use Committee and the study was conducted in accordance to the American Heart

Association guidelines for preclinical research and the Guide for the Care and Use of Laboratory Animals ⁵.

Scaffold design

Mirage scaffold is produced from poly-D-L-Lactide (PDLLA) of which D(dextro-rotary)-isomer constitutes <5% of the total Polylactic acid (PLA), coated with a biodegradable PLA eluting sirolimus. MMSES is manufactured by winding the polylactide monofilaments into helix-coiled structure. The struts have circular profile with thickness of 125 μ m in scaffolds with diameter \leq 3mm, and 150 μ m in scaffolds with diameter \geq 3.5mm (**Figure 1**).

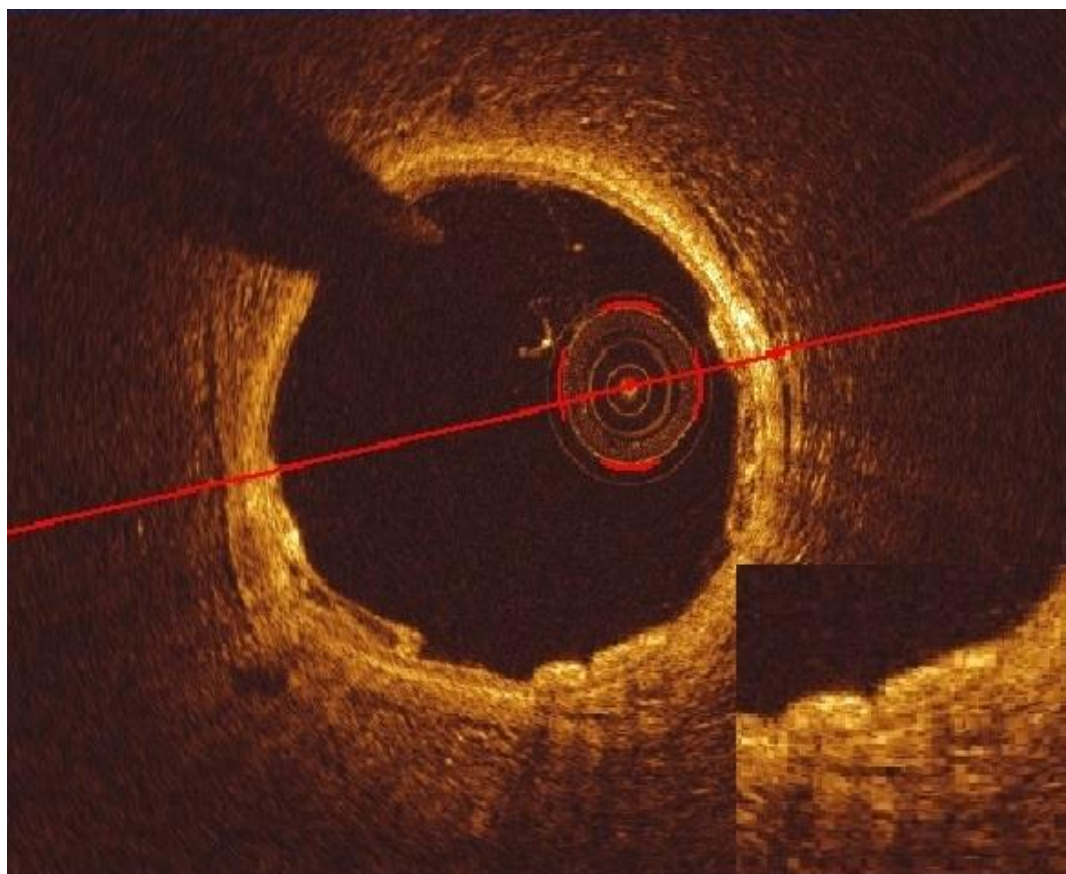


Figure 1. OCT cross-section image of Mirage scaffold. The strut of the Mirage scaffold is circular and non-translucent.

The scaffold design consists of a helicoidal coil structure in which the monofilament maintains its directional mechanical properties as well as its circular geometry (**Figure-2a**). The helical-coil design is fastened by longitudinal spine microfibers providing radial strength for the MMSES (150 μ m) (148.54 kPa) and MMSES (125 μ m) (120.54 kPa) comparable to the current

available BRS ⁶. MMSES (125 μ m) and MMSES (150 μ m) have a tensile strength of 300 MPa with an elongation at break of 35% (information from the manufacturer).

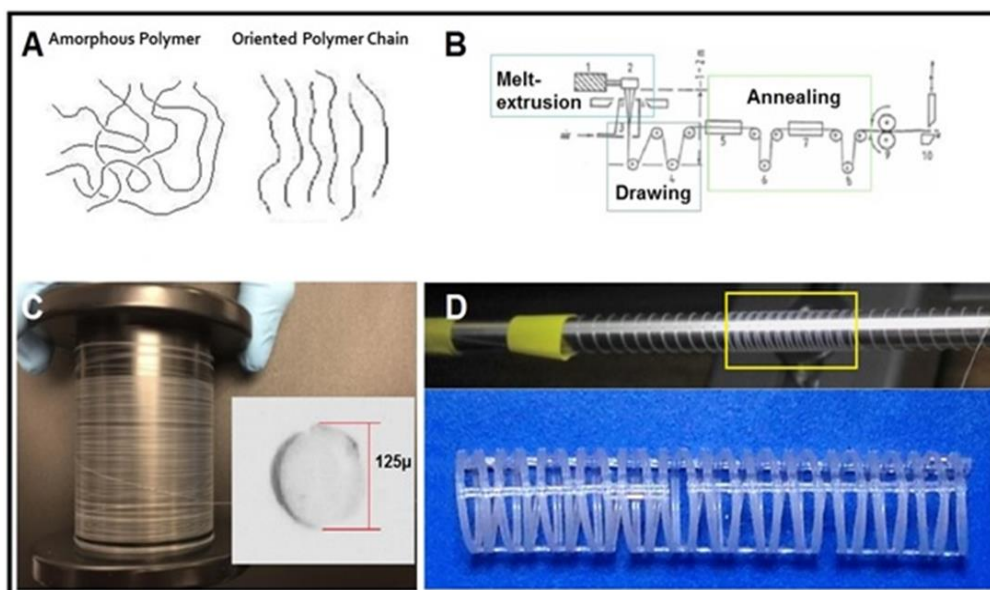


Figure 2a. Manli Cardiology's Microfiber Technology. Highly oriented polylactide polymer is extruded and annealed to form a circular monofilament with preferred directional mechanical properties (A, B). Conversion of a circular monofilament into a helicoidal scaffold with circular strut geometry. Coil design enables scaffold to inherit monofilament's directional mechanical properties and monofilament's circular geometry (C, D). Three longitudinal spines are attached at ambient temperature to guarantee the mechanical stability of the helicoidal structures (D).

In addition, *in vitro* and *in vivo* degradation profile has confirmed that the Mirage polylactide is basically fully biodegraded after 14 months (**Figure 2b**).

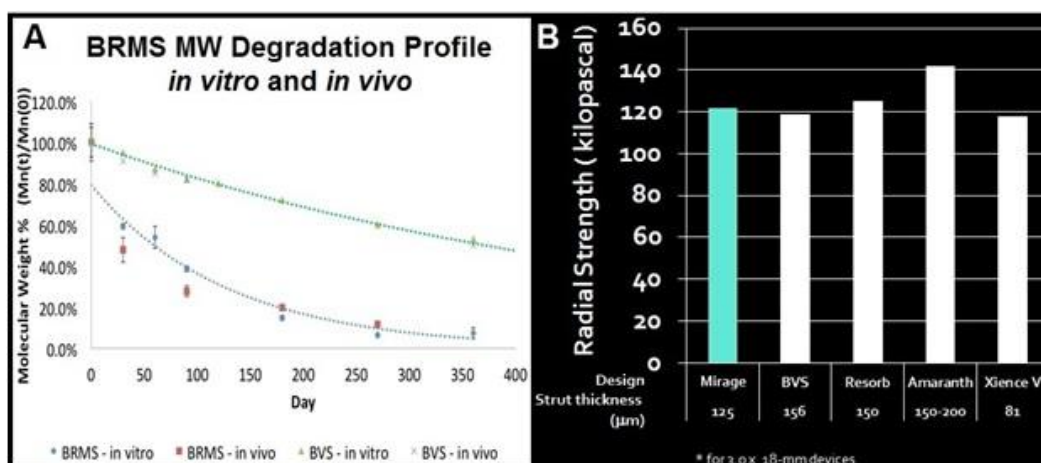


Figure 2b. Mirage scaffold degradation and radial strength profile

In vitro and *in vivo* degradation profile in comparison with the BVS has confirmed that the Mirage polylactide is basically fully biodegraded after 14 months (A). Mirage scaffold with strut thickness of 125 micron has a tensile strength of 300 MPa with an elongation at break of 35% and a radial strength of 120 kPa, -very comparable to the radial strength of the Xience V for a strut thickness of 81 micron (B).

Data acquisition

X-ray angiography was performed using Siemens HiCor cardiac angiography system (Siemens, Erlangen, Germany). OCT was performed following scaffold implantation in all the coronary arteries implanted with bioresorbable scaffolds. The treated segments were studied using a frequency-domain OCT system (C8-XR OCT Intravascular Imaging System; St. Jude Medical, St. Paul, MN, USA) that was pulled-back at a speed of 18mm/sec. A non-occlusive flushing technique was used for blood clearance by injection of contrast media. The acquired data were stored in DICOM format and transferred to a workstation for further analysis.

Coronary artery reconstruction

Coronary artery reconstruction was performed using a well-established and validated methodology ⁷. In brief the angiographic and OCT data were reviewed to identify the scaffolded segment and the most proximal and distal anatomical landmarks (i.e., side branches) to the scaffolded segment, that were visible in both coronary angiography and OCT. These landmarks were used to define the segment of interest, that was reconstructed from OCT and X-ray angiographic data for Computational Fluid Dynamic (CFD) model ⁷.

In the segment of interest, an observer identified the OCT images portraying the scaffolded and the native coronary artery and analyzed the OCT frames at every 0.1 mm interval in the scaffolded segment and at every 0.2 mm interval in the native vessel. In the native and the scaffolded segment, the observer delineated the flow area – defined in the native segment by the lumen border and in the scaffolded segment by the adluminal side of the struts and by the lumen surface in the areas between the struts ⁸.

Two post-procedure end-diastolic X-ray angiographic images with at least >30° angle difference portraying the segment of interest with minimal foreshortening were selected with the table in the isocenter. In these images the lumen borders were detected for the segment of interest and used to extract the luminal centerline that was then used to define the 3D luminal centerline of the segment of interest ⁷. The borders detected in the OCT images were then placed perpendicularly onto the luminal centerline and anatomical landmarks, that were side-branches seen in both OCT and X-ray images were used to define the absolute orientation of the OCT frames ⁷.

Blood flow simulation

The reconstructed images were processed with CFD techniques. A finite volume mesh was generated and then blood flow simulation was performed and the ESS was estimated by

solving the 3D Navier-Stokes equations (ANSYS Fluent, Canonsburg, Pennsylvania) ⁹. To assess the effect of the scaffold designs on the local hemodynamic micro-environment, the mesh density around the scaffold struts and within the boundary layer of the flow field between the struts was increased to have an average element edge of 30 μ m (equal to $\frac{1}{4}$ of the strut thickness of the scaffold strut). Blood was assumed to be a homogeneous, Newtonian fluid with a viscosity of 0.0035 Pa.s and a density of 1,050 kg/m³. A steady flow profile was simulated at the inflow of the 3D models. Previously, publications showed that there are no significant differences between the ESS estimated in pulsatile and steady flow simulations ^{10,11}. Blood flow for each reconstruction was estimated by measuring, in the 2 angiographic projections, the number of frames required for the contrast agent to pass from the inlet to the outlet of the reconstructed segment, the volume of the reconstructed segment and the cine frame rate ^{2,12}. The arterial wall was considered to be rigid. No-slip conditions were imposed at the scaffold surface. At the outlet of the model zero pressure conditions were imposed. ESS at the baseline luminal surface was calculated as the product of blood viscosity and the gradient of blood velocity at the wall ¹³. The ESS was measured in the native and the scaffolded segment around the circumference of the lumen per 5 $^{\circ}$ interval(sector) and along the axial direction per 0.2mm interval with the use of an in-house algorithm ⁴ (**Figure 3**).

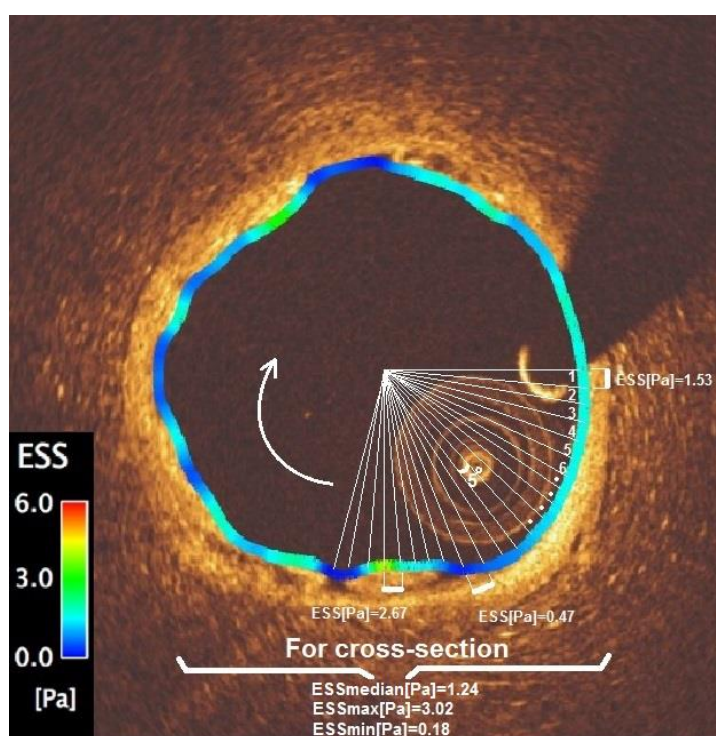


Figure 3. Circumferential ESS values (median, maximum and minimum) over the luminal perimeter at 5 $^{\circ}$ -subunits (sectors) counted from 3 o'clock.

The recirculation zones in the vicinity of the struts were quantified based on the direction of the ESS vector and the centerline vector. Areas where the ESS vector had opposite direction to the centerline vector were considered to be exposed to recirculation zones (**Figure 4**).

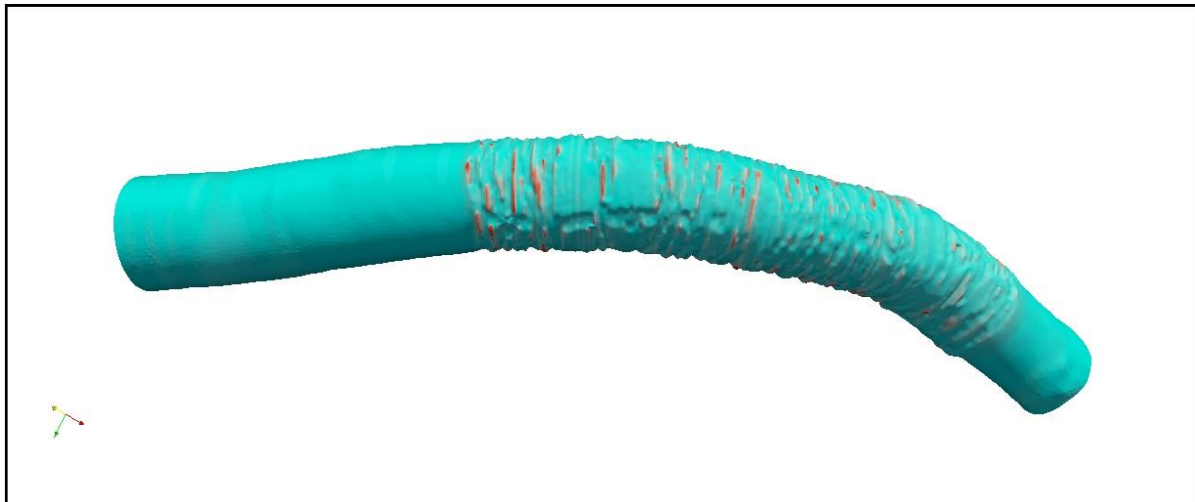


Figure 4. Recirculation zones (red) were quantified based on the ESS and the centerline direction (proximal → distal). The red areas in the luminal surface are where the vectors of the ESS are pointing opposite (more than 90-degrees away from) the proximal-to-distal direction along the centerline.

Statistical analysis

Continuous variables were tested for normality with Kolmogorov-Smirnov test and are presented as mean \pm SD or median (interquartile range) as appropriate. Categorical variables are presented as counts and percentages. Mixed linear model with an assumed Gaussian distribution was used for the comparisons of continuous variables to take into account the clustered nature of >1 scaffolds analysed from the same animals and >1 cross-sections from the same scaffold and >1 5°-sectors from the same cross-sections, that should be in correlations within the clusters. Pearson correlation coefficient were used to evaluate the strength and direction of the linear relationship between the strut thickness, cross-section area and ESS. Statistical significance was assumed at a probability (P) value of <0.05. All statistical analyses were performed with SPSS (version 22.0.0, IBM, New York).

RESULTS

In MMSES (150 μ m) group (n=6 arteries), 2 LAD, 1 LCX and 3 RCA, in MMSES (125 μ m) group (n=5 arteries) 2 LAD, 1 LCX and 2 RCA were treated. The list of scaffolds with diameters, lengths, deployment pressures, post-implantation dilatation balloon pressures, post-

implantation scaffolded vessel segment diameters and the treated coronaries with the implantation locations are shown in **Table 1**.

Table 1. Inventory of scaffolds with strut thicknesses and implantation parameters.

Scaffold	Animal	Vessel	Scaffolded vessel segment	Scaffold size (mm)	Deployment balloon pressure (atm)	Post-dilatation balloon inflation pressure (atm)	The scaffolded vessel segment diameter after implantation (mm)
MMSES-1(125 μm)	Animal-E	LCx	Mid	2.75 x 13	6	16	3.0
MMSES-2(125 μm)	Animal-F	LAD	Prox	2.75 x 13	16	18	3.0
MMSES-3(150 μm)	Animal-D	LCx	Mid	3.50 x 15	6	14	3.7
MMSES-4(150 μm)	Animal-D	RCA	Mid	3.50 x 15	6	16	3.7
MMSES-5(125 μm)	Animal-E	LAD	Mid	2.50 x 15	6	16	2.6
MMSES-6(150 μm)	Animal-C	LAD	Prox	3.50 x 15	6	16	3.7
MMSES-7(150 μm)	Animal-G	RCA	Mid	3.50 x 15	6	14	3.8
MMSES-8(125 μm)	Animal-A	RCA	Mid	3.00 x 15	12	20	3.3
MMSES-9(125 μm)	Animal-F	RCA	Mid	3.00 x 15	10	18	3.3
MMSES-10(150 μm)	Animal-B	RCA	Mid	3.50 x 15	18	18	3.8
MMSES-11(150 μm)	Animal-A	LAD	Prox	3.50 x 15	16	18	3.8

The dimensions of the proximal segment, scaffolded segment and the distal segment are shown in **Table 2** and **supplementary Table 1**.

Table 2. The OCT analyzes of scaffolded and non-scaffolded segments according to the scaffold type (Device level)

	MMSES (150 μm) (n=6)	MMSES (125 μm) (n=5)
Scaffolded segment lumen area (mm ²)	8.65 (4.50-12.80)	6.35 (3.49-9.21)
Distal non-scaffolded segment lumen area (mm ²)	7.67 (5.85-9.42)	5.14 (2.01-8.27)
Proximal non-scaffolded segment lumen area (mm ²)	7.67 (5.85-9.49)	5.58 (4.69-6.47)
Strut area (mm ²)	0.88 (0.60-1.16)	0.63 (0.22-1.04)

The results are as Median (Quartile 1-Quartile 3)

The median ESS of MMSES (150 μm) and MMSES (125 μm) are 0.85(IQ:0.49-1.39) and 0.68(IQ:0.35-1.18), respectively. The histograms of ESS for the MMSES (150 μm) and MMSES (125 μm) (**Figure 5**) show that, 58% of the scaffolded vessel luminal surface in the MMSES (150 μm) and 66% MMSES (125 μm) was exposed to a low (<1 Pa) athero-promoting ESS environment (**Figure 6**) (**Table 3**).

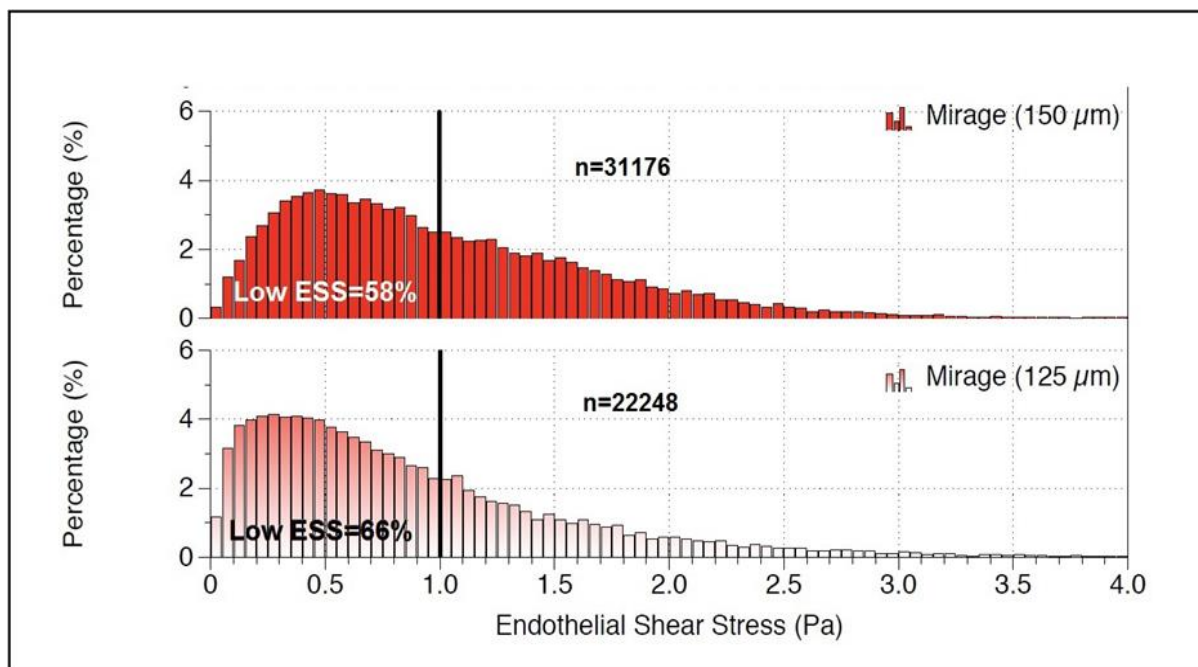


Figure 5. Histograms of ESS in scaffolded segments in scaffold groups. “n” denotes the number of total ESS estimations at 5°-sectorial level.

These paradoxical results should stem from the fact that the MMSES (125 μ m) was implanted in small size (<3.0 mm) vessels while the MMSES (150 μ m) was implanted in bigger size (>3.5 mm) vessels; when the strut thickness was divided to final lumen diameter after the implantation the mean ratio in MMSES (125 μ m) was 0.020 and in MMSES (150 μ m) was 0.017. The percentages of recirculation area per scaffolded vessel segment surface area were 3.17 \pm 1.97% in MMSES (150 μ m) and 2.71 \pm 1.32 % in MMSES (125 μ m). At device level, there was no statistical difference between the scaffold groups for recirculation area ($p=0.91$) (**Table 4**). ESS had a negative correlation with strut thickness ($r=-0.17$, $p<0.0001$). The strut thickness had significant correlation with the recirculation zone area per luminal surface area ($r=0.555$, $p<0.0001$).

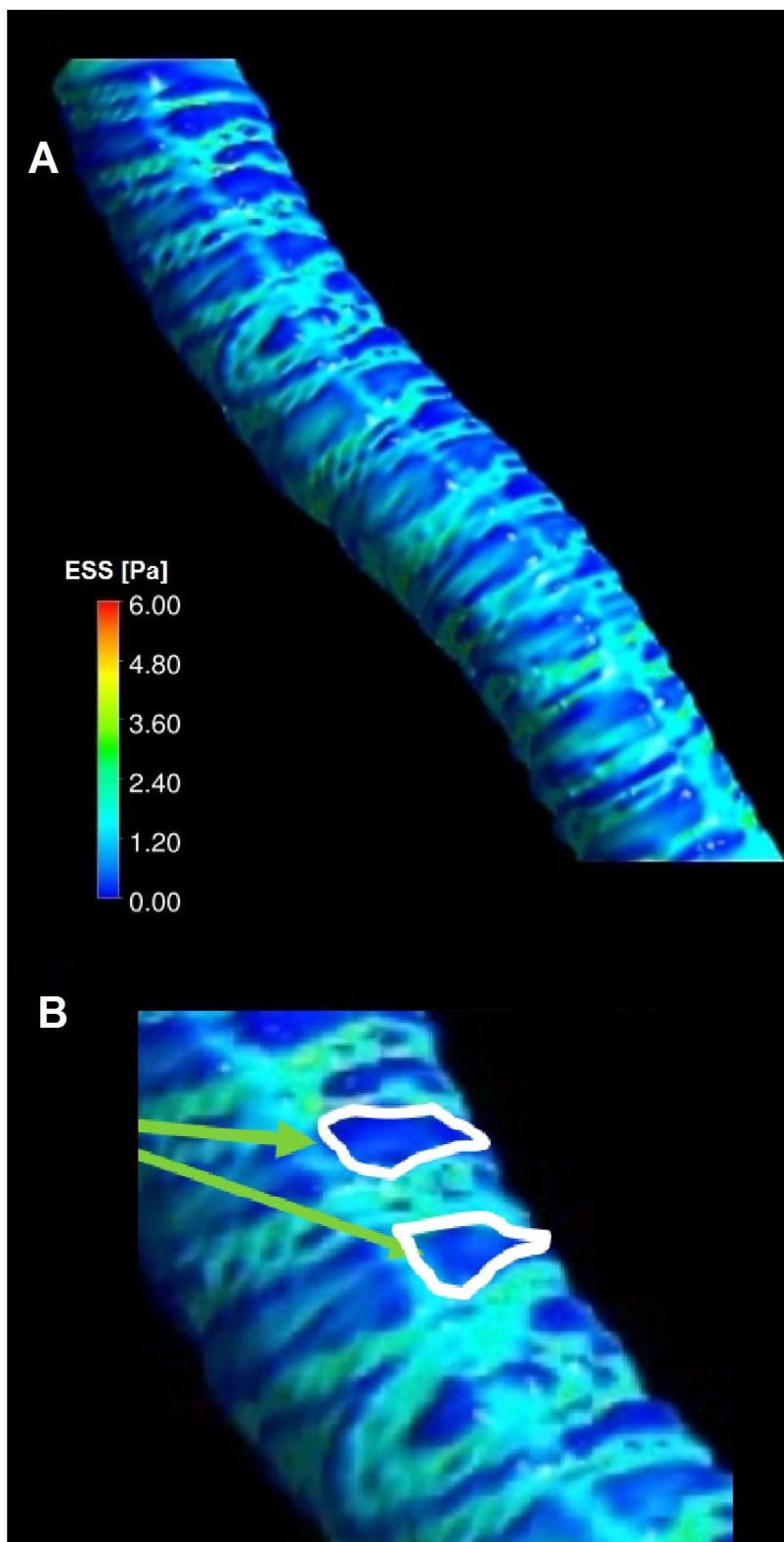


Figure 6. Three-dimensional reconstruction of scaffolded coronary anatomy from the fusion of coronary angiograms and OCT data with the local ESS being portrayed in a color-coded map (dark blue indicates low ESS < 1.0 Pa and aquamarine an ESS ≥ 1.0 Pa) for Mirage scaffold (A and B).

Table 3. The median ESS of the scaffold groups in 5°-sectorial subunit level.

	MMSES (150 μ) (n=31176) Median (Q1-Q3)	MMSES (125 μ) (n=22248) Median (Q1-Q3)
ESS [Pa] (5°-sectorial subunit level)	0.85 (0.49-1.39)	0.68(0.35-1.18) [§]
ESS ≤ 1.0 Pa (%)	57.7	66.4 [¶]

[[§] significant difference between MMSES (150μm) and MMSES (125μm); p<0.00001, [¶] significant difference between MMSES (150μm) and MMSESBRMS (125μm); p<0.00001. p-values derived from a multilevel linear regression model that adjusted ESS values for vessel type and scaffold cross-sectional area, given the clustered nature of the data]

Table 4. Recirculation area per scaffolded vessel surface area percentages in scaffold groups

Scaffold	Recirculation area per scaffolded vessel surface area (%)	Mean ± SD
MMSES-3 (150 μm)	5.81	3.17±1.97
MMSES-4 (150 μm)	1.35	
MMSES-6 (150 μm)	1.60	
MMSES-7 (150 μm)	3.98	
MMSES-10 (150 μm)	1.40	
MMSES-11 (150 μm)	4.88	
MMSES-1 (125 μm)	2.00	2.71±1.32 [‡]
MMSES-2 (125 μm)	2.81	
MMSES-5 (125 μm)	0.87	
MMSES-8 (125 μm)	3.93	
MMSES-9 (125 μm)	3.98	

[‡] Comparison between MMSES (150μm) and MMSES (125μm), p=0.91

DISCUSSION

In this exploratory study, we evaluated Mirage scaffold with two types of strut thicknesses in porcine coronary artery models. The findings were as follows; 1-The thinner strut version Mirage scaffold [MMSES (125 μ m)] was implanted in smaller vessels (<3.0 mm) while thick strut version Mirage [MMSES (150 μ m)] was implanted in bigger size (>3.5 mm) vessels which induced lower ESS in MMSES (125 μ m) than in MMSES (150 μ m) and due to the same fact, 2-The percent luminal surface exposed to lower-ESS (<1.0 Pa) was higher in MMSES (125 μ m) as compared to MMSES (150 μ m). 3- Scaffolded segments revealed minimal recirculation zones per scaffolded luminal surface. However, due to device level comparison, there was no significant difference for recirculation area percentages between MMSES (150 μ m) and MMSES (125 μ m).

Several *in-silico* studies have mentioned the effect of stent design on local hemodynamics after device implantation. Mirage scaffold has a unique helicoidal design with thinner strut thicknesses. The circular strut profile gives an advantage to Mirage scaffold inducing potentially less flow disruption³. The streamlined strut profile exhibited minimal recirculation areas and less shifted ESS distributions in this novel scaffold¹⁴. The helicoidal design provides less flow disruption and recirculation areas compared to the corrugated ring design^{14 15}. Mirage scaffold has 45% vessel luminal coverage ratio which can also help to explain low percentage of recirculation areas per luminal surface in scaffolded segments. The high coverage ratio with streamlined strut profile should have enabled the flow streamlines be in an aligned structure within the scaffolded segments. The increased luminal surface coverage decreases the risk of the interaction between disrupted flow and denuded endothelial layer that prevents the activation of pathological cellular mechanisms for tissue response and thrombus formation. In Mirage scaffold, the maximal coil pitch between the helicoidal rings is 0.8 mm which is enough for an inter-strut space to recover a smooth flow after disruption in the vicinity of the struts^{16,17}. Helicoidal design, thinner circular strut, increased luminal surface coverage and an adequate maximal coil pitch are the contributing factors for relatively low flow disruption in the scaffolded vessel segments.¹⁴ *In-vitro* experimental studies have demonstrated that the different strut designs have different influences on the local flow behavior. Strut thickness, strut shape and material properties have impact on the local flow. While strut thickness increases, the flow disruption gets increase¹⁸. Not only the strut thickness, but also the strut cross-profile has impact on flow disruption. The effect of strut

thickness on the flow disruption in streamlined and non-streamlined strut profiles is not the same; as the thickness increases in a non-streamlined strut design, the flow disturbance demonstrates a non-linear increment. Regarding the increase in flow disruption, experiments have demonstrated a rise in the fibrin accumulation around the struts. In the same line with these experimental studies, we have reported the effect of square-shaped struts on the local flow dynamics using similar porcine model and similar methodology for the flow simulation and shear stress analysis. In our previous study^{14,19}, in Absorb implanted segments median shear stress level was 0.57 ([IQR]: 0.29-0.99) Pa. In Absorb implanted segments, 75% of the scaffolded surface was exposed to a low (< 1 Pa) athero-promoting ESS and the percentage of recirculation area was 3.26±2.07%. Using similar animal model and CFD methodology, in the present study, median ESS of MMSES(150µm) and MMSES(125µm) were 0.85(IQ:0.49-1.39) Pa and 0.68(IQ:0.35-1.18) Pa which were quite higher than Absorb in our previous study.¹⁴ Regarding low ESS, 58% of the scaffolded vessel luminal surface in MMSES(150µm) and 66% in MMSES(125µm) were exposed to low (<1 Pa) ESS those were quite lower than in Absorb (75%). The percentages of recirculation area per scaffolded vessel surface area were 3.17±1.97% in MMSES (150µm) and 2.71±1.32 % in MMSES (125µm) which were lower than in Absorb (3.26±2.07%).

In many experimental CFD analyses, thinner streamlined struts were in favor of flow hemodynamics, inducing less flow separation and less recirculation zones in the vicinity of the struts (3). In our exploratory study, the ESS values were paradoxically lower in MMSES (125µm) than in MMSES (150µm). The main factor to explain this paradoxical result is the fact that as realized in Table-2 the final diameter of the vessels in Mirage(150µm) was higher (mean 3.75 mm) than in Mirage (125 µm) (mean 3.04 mm) following the implantation. When the strut thickness is divided to the final luminal diameters in scaffolded vessel segments after implantation, it will be realized that the ratio of strut thickness/final lumen size is lower (strut thickness/final lumen diameter=0.017) in Mirage(150µm) than in Mirage(125µm) (strut thickness/final lumen diameter=0.020). It's obvious that the scaffolds with thinner struts [Mirage (125µm)] were implanted in smaller vessels (<3.0 mm) whereas thick strut version of Mirage [Mirage (150µm)] was implanted in bigger size vessels (>3.5 mm). However, in smaller vessels, even thinner struts induced lower ESS which denotes the fact that in small vessels the deteriorating effect of the struts are not avoidable despite thinner design. Because of this point, in correlation with mean ESS values, we found lower surface area exposed to <1 Pa ESS

in Mirage (150 μm) rather than in Mirage (125 μm). These results showed that during planning stage of the PCI, scaffold strut thickness/vessel size diameter ratio should be taken into account to decrease fluctuations in ESS post-implantation. Another contributing factor for paradoxical result might be due to the Coanda effect; the flow is accelerating over the convex surfaces and in thicker circular struts this effect increases along with the elevated shear stress levels on the top surface of the struts.²⁰ As the thicker struts get in touch with the faster flowing flow zones in the radial direction within the vessel lumen, it results in higher shear stress levels at the top surface of the struts which also contributed higher levels of ESS in Mirage(150 μm) compared to Mirage (125 μm) (**Supplement Figure**).”

Limitations

The current results require interpretation within the constraints of some limitations. First, scaffold implantation was performed in healthy coronary arteries. Therefore, it was not possible to examine the implications of scaffold under-expansion or the composition of the underlying plaque on strut embedment which potentially influence the local flow hemodynamics. Second, there was no comparator which would enable to make a hypothesis for the “*hemo-compatible*” properties of Mirage bioresorbable scaffold. Another point is that, since our study was a preclinical study, there was no any clinical implication to demonstrate. However, the clinical implications of the difference in endothelial shear stress can be extrapolated from the literature.

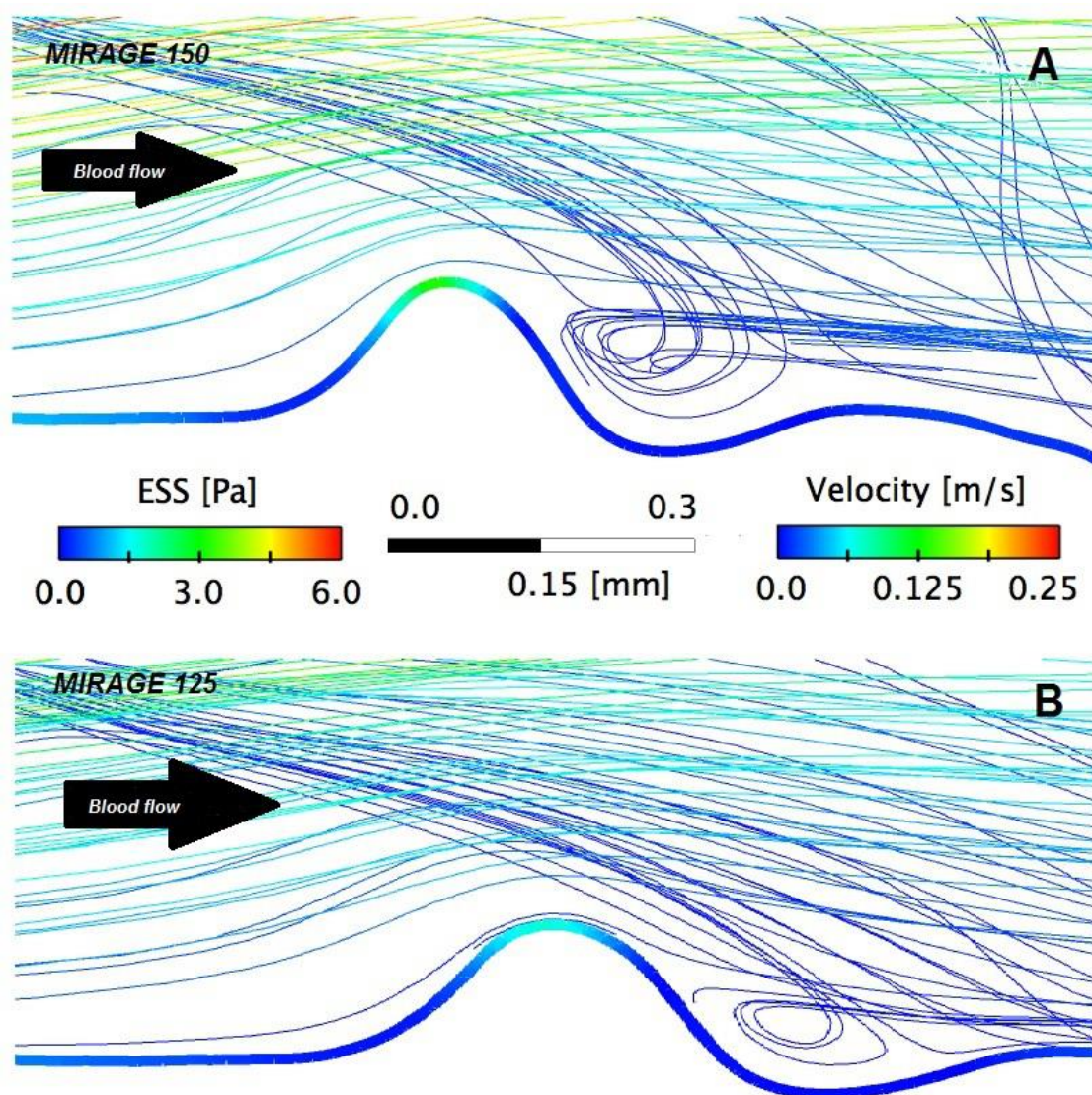
CONCLUSION

Mirage scaffold has unique properties of helicoidal design, thinner struts -compared to current commercially available scaffolds- and streamlined strut profile. Thinner strut version of Mirage induced lower ESS than thicker strut version of Mirage due to the higher ratio of strut thickness/lumen area in Mirage (125 μm). The size of the target vessel segment should be assessed before the implantation of Mirage scaffold and small vessels should not be implanted with Mirage. The CFD study can be used to increase the *hemo-compatibility* of the bioresorbable scaffolds. The results should prompt further comparative study with the commercially available scaffolds in animal and human models.

Disclosures

E. Tenekecioglu has a research grant from TUBITAK (The Scientific Council of Turkey). P.W. Serruys is a member of the International Advisory Board of Abbott Vascular. Y. Onuma is a member of the International Advisory Board of Abbott Vascular.

ONLINE SUPPLEMENT



Supplement Figure 1. Demonstration of the different level peak shear stress over the struts with the similar cross-section profile with different thicknesses. MMSES with 150 μ m strut thickness induces higher peak shear stress at the top of the strut (A). MMSES with 125 μ m strut thickness reveals lower peak shear stress at the top of the strut as compared to the MMSES with 150 μ m strut (B).

Supplementary Table 1. The median ESS and lumen area in OCT in scaffolded and non-scaffolded segment in OCT for each scaffold. The data are tabulated according to the ranking of ESS in Mirage bioresorbable scaffold.

Scaffold	Animal	Median ESS (Q1-Q3)- Scaffolded segment (Pa)	Median Lumen Area (Q1-Q3)- Scaffolded segment (mm ²)	Median Lumen area (Q1-Q3)- Distal non-scaffolded segment (mm ²)	Median Lumen area (Q1-Q3)- Proximal non-scaffolded segment (mm ²)
MMSES-1 (125 μm)	E	0.48 (0.27-0.76)	7.02 (6.88-7.11)	4.37 (4.26-4.47)	4.58 (4.21-4.72)
MMSES-2 (125 μm)	F	0.48 (0.24-0.87)	8.98 (8.29-9.81)	7.40 (4.59-7.95)	5.75 (5.59-6.12)
MMSES-3 (150 μm)	D	0.56 (0.35-0.86)	10.94 (10.56-11.45)	6.90 (6.21-7.46)	7.67 (6.38-8.77)
MMSES-4 (150 μm)	D	0.62 (0.29-1.04)	5.78 (5.66-5.92)	5.14 (4.50-5.69)	5.79 (3.94-8.52)
MMSES-5 (125 μm)	E	0.63 (0.35-1.04)	11.21 (10.92-11.40)	8.71 (8.25-9.14)	6.14 (5.06-7.91)
MMSES-6 (150 μm)	C	0.92 (0.56-1.35)	12.59 (12.49-12.74)	10.94 (10.33-11.48)	9.84 (9.49-10.81)
MMSES-7 (150 μm)	G	0.94 (0.52-1.51)	7.13 (7.08-7.35)	7.80 (7.42-7.95)	5.58 (5.45-5.81)
MMSES-8 (125 μm)	A	0.94 (0.53-1.56)	7.25 (7.04-7.78)	4.57 (4.39-7.05)	5.18 (4.74-5.44)
MMSES-9 (125 μm)	F	0.96 (0.50-1.60)	10.87 (10.68-11.21)	7.25 (7.02-7.50)	7.67 (7.42-9.09)
MMSES-10 (150 μm)	B	1.00 (0.67-1.39)	9.74 (9.44-10.18)	6.34 (6.18-6.98)	7.59 (7.22-7.52)
MMSES-11 (150 μm)	A	1.44 (0.86-1.86)	10.47 (10.13-10.95)	6.29 (4.60-7.85)	8.78 (8.56-9.20)

REFERENCES

1. Mukete BN, van der Heijden LC, Tandjung K, et al. Safety and efficacy of everolimus-eluting bioresorbable vascular scaffolds versus durable polymer everolimus-eluting metallic stents assessed at 1-year follow-up: A systematic review and meta-analysis of studies. *International journal of cardiology*. 2016;221:1087-1094.
2. Papafaklis MI, Bourantas CV, Theodorakis PE, et al. The effect of shear stress on neointimal response following sirolimus- and paclitaxel-eluting stent implantation compared with bare-metal stents in humans. *JACC Cardiovascular interventions*. 2010;3(11):1181-1189.
3. Jimenez JM, Davies PF. Hemodynamically driven stent strut design. *Annals of biomedical engineering*. 2009;37(8):1483-1494.
4. Bourantas CV, Papafaklis MI, Kotsia A, et al. Effect of the endothelial shear stress patterns on neointimal proliferation following drug-eluting bioresorbable vascular scaffold implantation: an optical coherence tomography study. *JACC Cardiovascular interventions*. 2014;7(3):315-324.
5. The Guide for the Care and Use of Laboratory Animals. *ILAR Journal*. 2016;57(2):NP-NP.
6. Ormiston JA, Webber B, Ubod B, Darremont O, Webster MW. An independent bench comparison of two bioresorbable drug-eluting coronary scaffolds (Absorb and DESolve) with a durable metallic drug-eluting stent (ML8/Xpedition). *EuroIntervention : journal of EuroPCR in collaboration with the Working Group on Interventional Cardiology of the European Society of Cardiology*. 2015;11(1):60-67.
7. Bourantas CV, Papafaklis MI, Lakkas L, et al. Fusion of optical coherence tomographic and angiographic data for more accurate evaluation of the endothelial shear stress patterns and neointimal distribution after bioresorbable scaffold implantation: comparison with intravascular ultrasound-derived reconstructions. *The international journal of cardiovascular imaging*. 2014;30(3):485-494.
8. Nakatani S, Sotomi Y, Ishibashi Y, et al. Comparative analysis method of permanent metallic stents (XIENCE) and bioresorbable poly-L-lactic (PLLA) scaffolds (Absorb) on optical coherence tomography at baseline and follow-up. *EuroIntervention : journal of EuroPCR in collaboration with the Working Group on Interventional Cardiology of the European Society of Cardiology*. 2016;12(12):1498-1509.
9. Papafaklis MI, Bourantas CV, Theodorakis PE, Katsouras CS, Fotiadis DI, Michalis LK. Relationship of shear stress with in-stent restenosis: bare metal stenting and the effect of brachytherapy. *International journal of cardiology*. 2009;134(1):25-32.
10. Feldman CL, Ilegbusi OJ, Hu Z, Nesto R, Waxman S, Stone PH. Determination of in vivo velocity and endothelial shear stress patterns with phasic flow in human coronary arteries: a methodology to predict progression of coronary atherosclerosis. *American heart journal*. 2002;143(6):931-939.
11. Tenekecioglu E, Torii R, Bourantas C, et al. Preclinical assessment of the endothelial shear stress in porcine-based models following implantation of two different bioresorbable scaffolds: effect of scaffold design on the local haemodynamic micro-environment. *EuroIntervention : journal of EuroPCR in collaboration with the Working Group on Interventional Cardiology of the European Society of Cardiology*. 2016;12(10):1296.
12. Sakamoto S, Takahashi S, Coskun AU, et al. Relation of distribution of coronary blood flow volume to coronary artery dominance. *The American journal of cardiology*. 2013;111(10):1420-1424.
13. Stone PH, Saito S, Takahashi S, et al. Prediction of progression of coronary artery disease and clinical outcomes using vascular profiling of endothelial shear stress and arterial plaque characteristics: the PREDICTION Study. *Circulation*. 2012;126(2):172-181.

14. Tenekecioglu E, Torii R, Bourantas C, et al. Assessment of the hemodynamic characteristics of Absorb BVS in a porcine coronary artery model. *International journal of cardiology*. 2017;227:467-473.
15. Seo T, Schachter LG, Barakat AI. Computational study of fluid mechanical disturbance induced by endovascular stents. *Annals of biomedical engineering*. 2005;33(4):444-456.
16. Berry JL, Santamarina A, Moore JE, Jr., Roychowdhury S, Routh WD. Experimental and computational flow evaluation of coronary stents. *Annals of biomedical engineering*. 2000;28(4):386-398.
17. Akagawa E, Ookawa K, Ohshima N. Endovascular stent configuration affects intraluminal flow dynamics and in vitro endothelialization. *Biorheology*. 2004;41(6):665-680.
18. Jimenez JM, Prasad V, Yu MD, et al. Macro- and microscale variables regulate stent haemodynamics, fibrin deposition and thrombomodulin expression. *Journal of the Royal Society, Interface*. 2014;11(94):20131079.
19. Tenekecioglu E, Torii R, Bourantas C, et al. Corrigendum to "Assessment of the hemodynamic characteristics of Absorb BVS in a porcine coronary artery model" [Int. J. Cardiol. 227 (2017) 467-473]. *International journal of cardiology*. 2017;235:206.
20. Subhash M, Dumas A. Computational Study of Coanda Adhesion Over Curved Surface. *SAE Int J Aerosp*. 2013;6(1):260-272.

Non-Newtonian pulsatile shear stress assessment: a method to differentiate bioresorbable scaffold platforms

Erhan Tenekecioglu, Ryo Torii, Christos Bourantas, Carlos Collet, Yosuke Miyazaki, Taku Asano, Yuki Katagiri, Rasha Al-Lamee, Yoshinobu Onuma, Patrick W. Serruys

Eur Heart J. 2017;38(33):2570.

CASE REPORTS IN INTERVENTIONAL CARDIOLOGY

In-vitro and in-silico studies have shown that stent/scaffold implantation induces changes in local hemodynamic microenvironment.^{1,2} Coronary angiography and optical coherence tomography data were used to reconstruct three-dimensional (3D) geometry of the right coronary of two healthy mini-swine implanted with 3.0x18 mm Absorb BVS (Abbott Vascular, Santa Clara, CA, USA) and 3.0x14 mm ArterioSorb (Arterius, Bradford, UK) (Figure). The angiographic data were utilized to estimate the coronary flow velocity.³ Computational fluid dynamics (CFD) techniques were implemented to simulate pulsatile coronary blood flow through 3-dimensional patient-specific finite volume mesh by solving Navier-Stokes equations. Blood was considered a non-Newtonian fluid, and a pulsatile flow profile was imposed at inflow of the model. Quemada equation was used for shear-thinning blood rheology which scrutinizes hematocrit and shear rate.⁴ Endothelial shear stress (ESS) at the lumen and scaffold surfaces was calculated as the product of local blood viscosity and near wall velocity gradient.² Embedment/protrusion analysis was implemented using a dedicated software (QCU-CMS v 16.9, Medis, Leiden, Netherlands)⁵

ESS was measured in the scaffolded segment around the circumference of the lumen per 5° interval (sector) and along the axial direction per 0.2 mm interval (cross-section). In ArterioSorb mean embedment depth was 39±14µm and protrusion distance was 89±7µm whereas in Absorb embedment depth was 33±12µm and protrusion distance was 150±9µm. Thinner struts of ArterioSorb (n=4824) rendered higher ESS than in Absorb BVS (n=5328) at all coronary flow periods (Minimum, maximum, end-diastolic, cyclic average) (Figure). ESS was noted higher at top-of-the struts (red color areas) whereas inter-strut zones demonstrate lower ESS (dark blue areas) (Figure, panel-B, -C and -D). Pulsatile simulation unraveled that even at maximal coronary flow, there are some low ESS areas which potentiate thrombus formation (Video). However, in ArterioSorb such kind of low ESS areas were noted much less than in Absorb which can introduce less risk of thrombosis at follow up.

The thickness and the embedment/protrusion distances have impact on shear stress distribution around the struts. Thinner and deeper embedded struts of ArterioSorb induce much less low-ESS in the vicinity of the struts. Pulsatile non-Newtonian ESS analysis provide opportunity to assess local ESS in different phase of coronary flow. CFD studies can provide development of more *hemocompatible* coronary scaffolds.

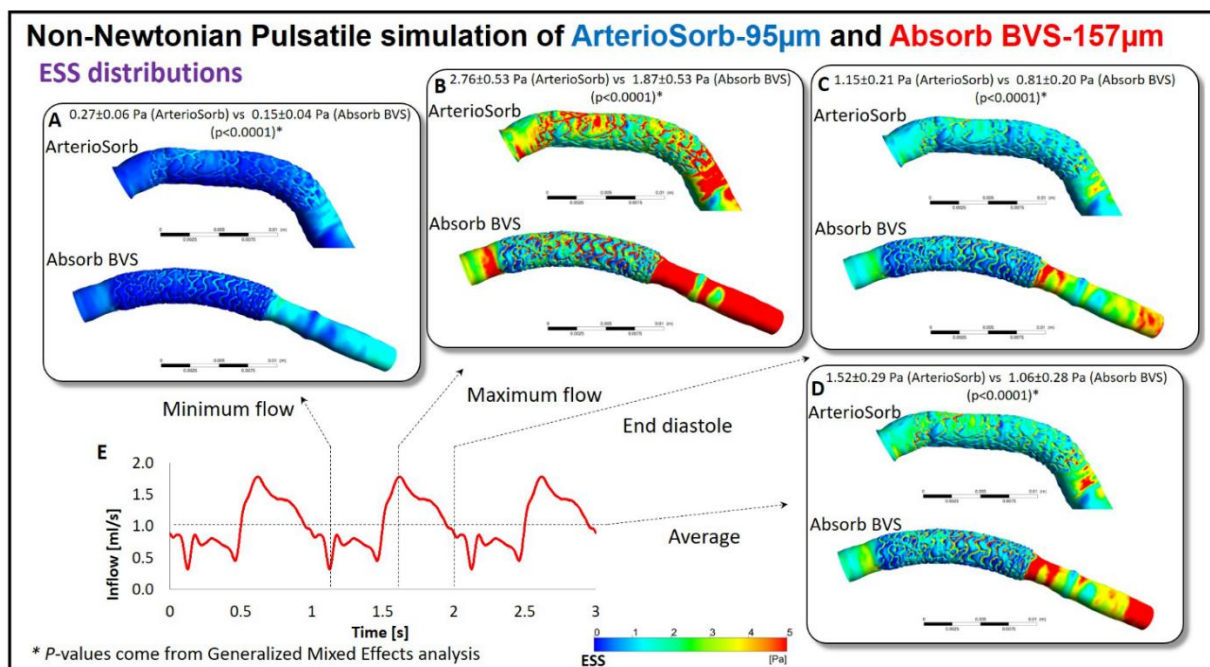
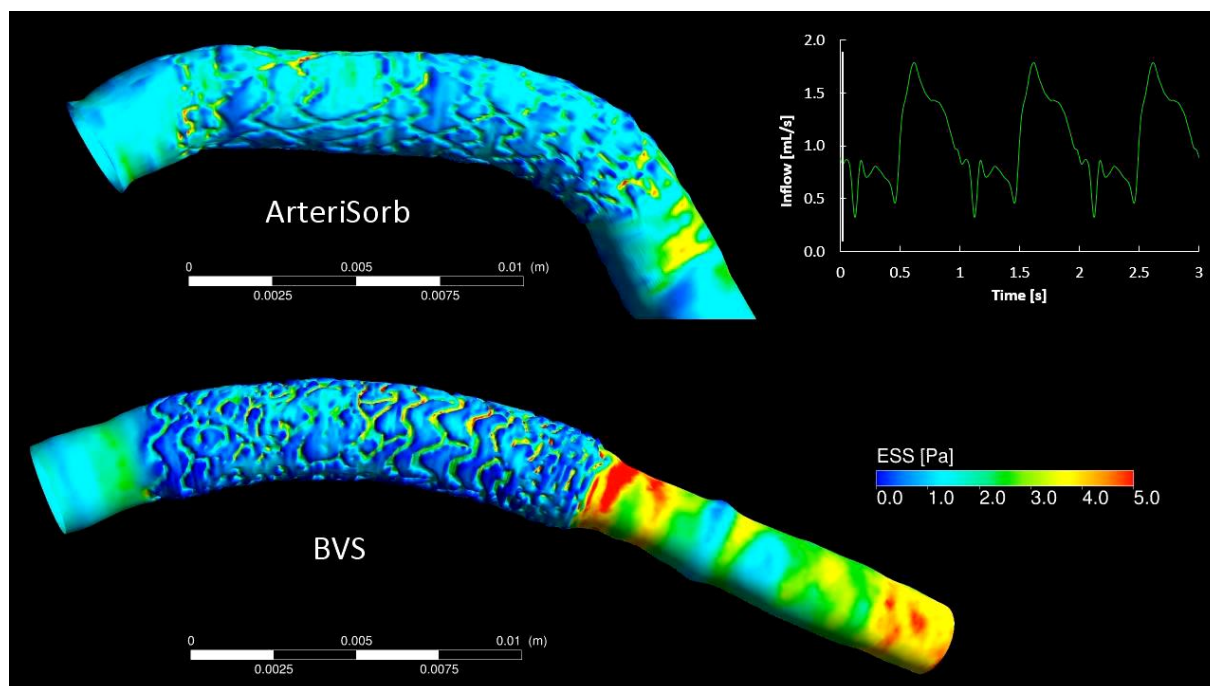


Figure. ESS distributions in ArterioSorb and Absorb BVS in different phase of coronary flow (Panels A, B, C and D). In each flow phase, mean ESS (upper part in panel) is significantly higher in ArterioSorb than in Absorb BVS.



Video. The movie demonstrated phasic changes in ESS distribution according to the coronary flow in ArterioSorb and Absorb BVS. At maximal coronary flow, ArterioSorb reveals less low-ESS areas compared to the Absorb.

REFERENCES

1. Jimenez JM, Davies PF. Hemodynamically driven stent strut design. *Annals of biomedical engineering*. 2009;37(8):1483-1494.
2. Tenekecioglu E, Poon EK, Collet C, et al. The Nidus for Possible Thrombus Formation: Insight From the Microenvironment of Bioresorbable Vascular Scaffold. *JACC Cardiovascular interventions*. 2016;9(20):2167-2168.
3. Bourantas CV, Papafaklis MI, Lakkas L, et al. Fusion of optical coherence tomographic and angiographic data for more accurate evaluation of the endothelial shear stress patterns and neointimal distribution after bioresorbable scaffold implantation: comparison with intravascular ultrasound-derived reconstructions. *The international journal of cardiovascular imaging*. 2014;30(3):485-494.
4. Quemada D. Rheology of concentrated disperse systems III. General features of the proposed non-newtonian model. Comparison with experimental data. *Rheologica Acta*. 1978;17(6):643-653.
5. Sotomi Y, Tateishi H, Suwannasom P, et al. Quantitative assessment of the stent/scaffold strut embedment analysis by optical coherence tomography. *The international journal of cardiovascular imaging*. 2016;32(6):871-883.

Chapter 5

Preclinical assessment of the endothelial shear stress in porcine-based models following implantation of two different bioresorbable scaffolds: effect of scaffold design on the local hemodynamic micro-environment

Difference in hemodynamic microenvironment in vessels scaffolded with Absorb BVS and Mirage BRMS: insights from a preclinical endothelial shear stress study

Post-implantation shear stress assessment: an emerging tool for differentiation of bioresorbable scaffolds

Preclinical assessment of the endothelial shear stress in porcine-based models following implantation of two different bioresorbable scaffolds: effect of scaffold design on the local hemodynamic micro-environment

Erhan Tenekecioglu, Ryo Torii, Christos Bourantas, Tom Crake, Yaping Zeng, Yohei Sotomi, Yoshinobu Onuma, Mustafa Yilmaz, Teguh Santoso, Patrick W. Serruys

EuroIntervention. 2016;12(10):1296.

IMAGES IN INTERVENTIONAL CARDIOLOGY

In vitro studies have demonstrated that stent implantation changes local hemodynamics as the protruding struts disturb the flow resulting in recirculation zones and low endothelial shear stress (ESS)¹⁻³. Angiographic and OCT data were used to reconstruct 3D geometry of the right coronary artery of two healthy mini-swine implanted with 3.0×18 mm Absorb BVS (Abbott Vascular, Santa Clara, CA, USA) and 3.0×15 mm Mirage BRMS (Manli Cardiology Ltd., Singapore) (**Online Figure 1**). The angiographic data were used to estimate flow velocity⁴.

During the computational flow dynamic study, ESS was measured in the scaffolded segment around the circumference of the lumen per 5° interval and along the axial direction per 0.2 mm interval (cross-section). Mean ESS was lower in Absorb BVS compared to Mirage BRMS in steady flow simulation (0.60 ± 0.51 Pa [n=5,256] vs. 1.09 ± 0.76 Pa [n=6,336], respectively; $p<0.001$); 70% of the scaffolded surface in Absorb BVS and 53% in Mirage BRMS was exposed to a low (<1 Pa) athero-promoting ESS (**Online Figure 1**). The presented p-value is for hypothesis generation based on 5° subunit analysis (n=11,592) and needs cautious interpretation.

The difference in ESS may have arisen from strut geometry, strut thickness (**Online Figure 2**), alignment of the strut connectors, luminal diameter, vessel curvature and boundary conditions. In our case, after excluding other factors, lower ESS in Absorb BVS is potentially attributed to the flow disturbances caused by thicker rectangular struts (**Panel A, Panel B, Panel C, Panel D, Online Figure 2**). Longitudinal images (**Panel A, Panel B**) portray the flow patterns and ESS distribution during steady (**Panel C, Panel D**) and pulsatile (**Panel E, Panel F**) models; flow streamlines were taken at the highest velocity point in diastole. While recirculation zones were noted in proximal/distal regions of Absorb BVS (**Panel C, Panel E**), there was no recirculation in Mirage BRMS (**Panel D, Panel F, Moving image 1, Moving image 2**).

OCT-based reconstruction provides *in vivo* assessment of the effect of different scaffold designs on local hemodynamics and can be useful in optimizing scaffold design.

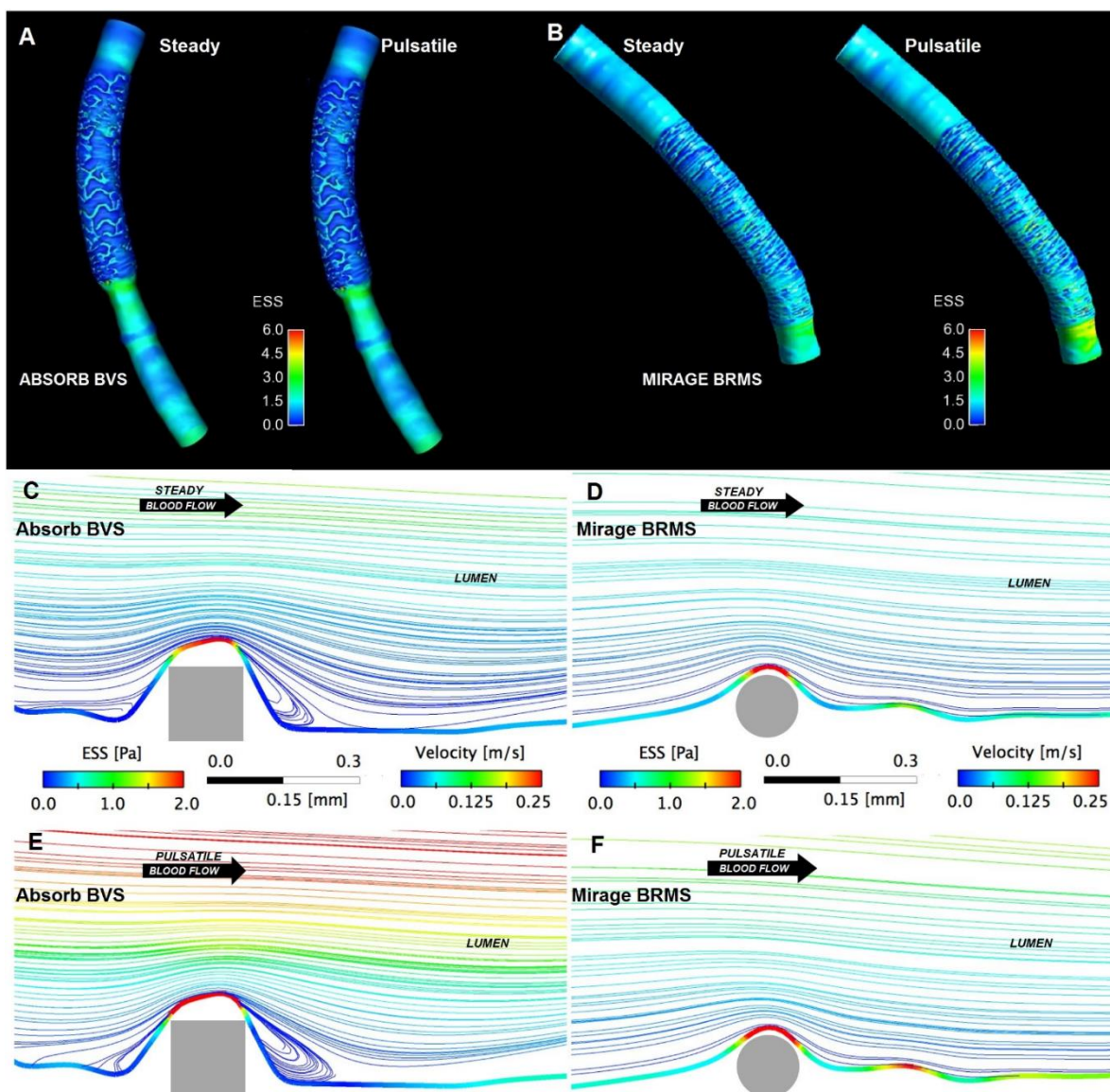
Funding

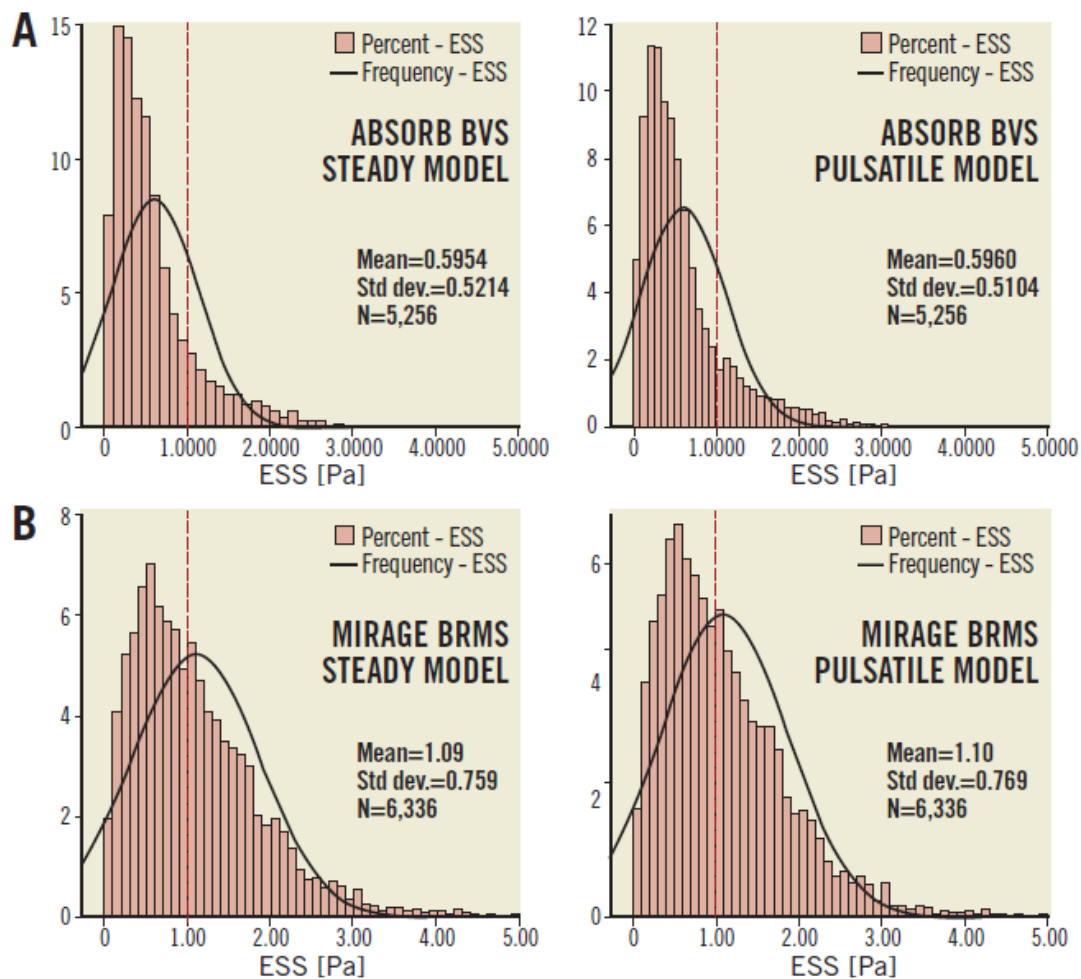
E. Tenekecioglu has received a research grant from TUBITAK (The Scientific and Technological Research Council of Turkey).

Conflict of interest statement

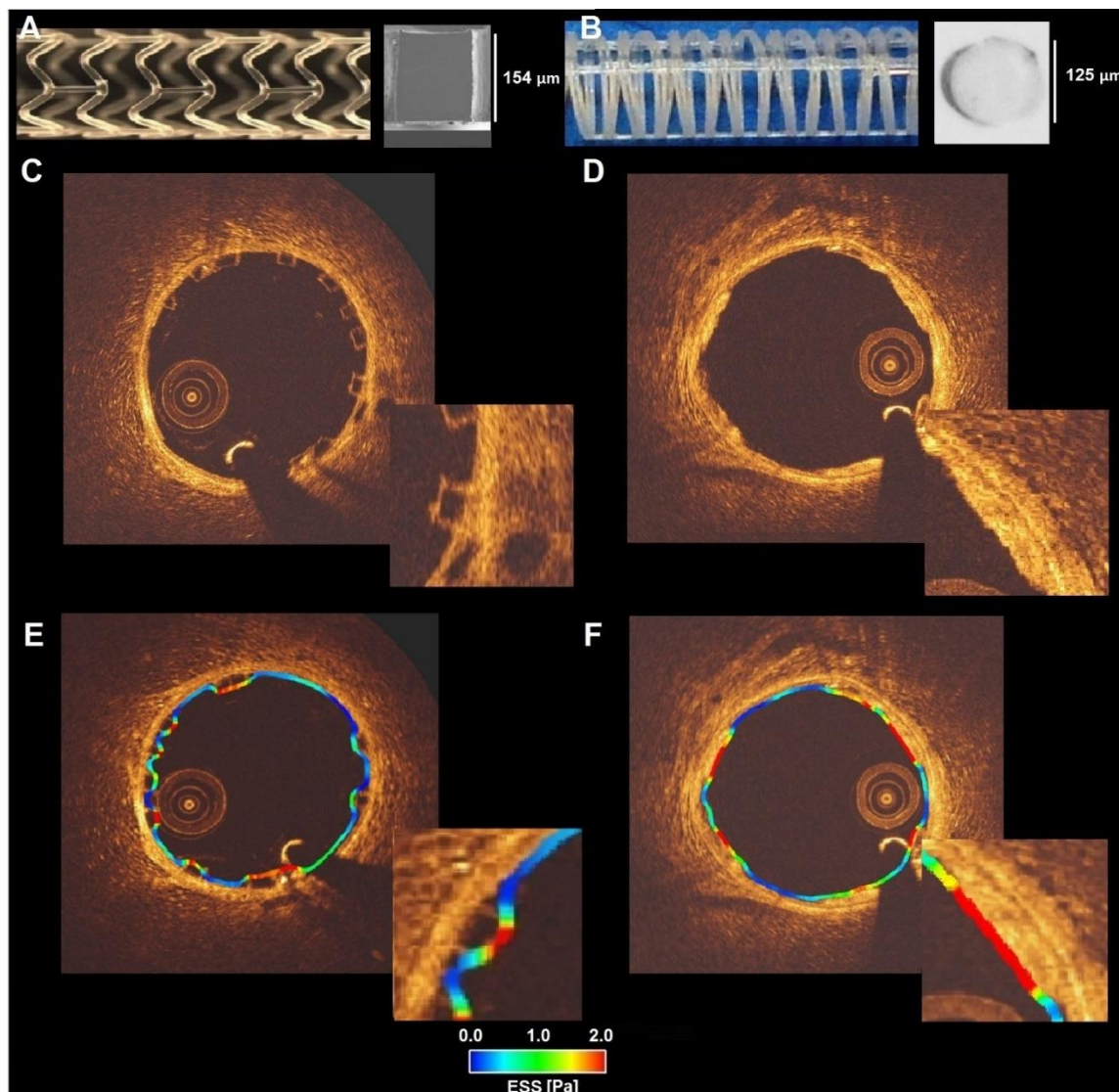
P.W. Serruys and Y. Onuma are members of the International Advisory Board of Abbott Vascular. The other authors have no conflicts of interest to report.

Figure





Online Figure 1. ESS distribution in Absorb BVS and Mirage BRMS in steady and pulsatile flow models. ESS distribution in Absorb BVS (A) and Mirage BRMS (B) in steady (left) and pulsatile (right) flow models. There was no significant difference in ESS distribution between steady and pulsatile flow simulation in both devices (0.60 ± 0.51 Pa vs. 0.60 ± 0.52 Pa; $p=0.95$ in Absorb BVS and 1.09 ± 0.76 Pa vs. 1.10 ± 0.76 Pa; $p=0.89$ in Mirage BRMS). The observed differences in ESS between Absorb BVS and Mirage BRMS were maintained even if the pulsatile conditions were applied for the flow simulation. ESS results were skewed towards lower ESS in Absorb BVS compared to Mirage BRMS as shown in the histograms of ESS distributions.



Online Figure 2. Differences in scaffold design, strut geometry and related ESS distribution at both scaffolds. Absorb BVS 1.1 and cross-section of Absorb BVS strut (A). Mirage BRMS and cross-section of Mirage BRMS strut (B). OCT cross-sectional image of Absorb BVS 1.1 with magnified view of a rectangular strut (C). OCT cross-sectional image of Mirage BRMS with magnified view of an ovoid strut (D). ESS distribution in the cross-sections (C & D). Low ESS noted in the areas between the struts and high ESS on the top of the struts in Absorb BVS (E) and Mirage BRMS (F).

Moving images

Moving image 1. Pulsatile flow simulation in Absorb BVS.

Moving image 2. Mirage BRMS. It is obvious that the different strut design has an impact on the flow velocity which is reduced in the surface of the Absorb BVS.

REFERENCES

1. Jiménez JM, Davies PF. Hemodynamically driven stent strut design. *Ann Biomed Eng.* 2009; 37:1483-94.
2. Kolandaivelu K, Swaminathan R, Gibson WJ, Kolachalama VB, Nguyen-Ehrenreich KL, Giddings VL, Coleman L, Wong GK, Edelman ER. Stent thrombogenicity early in high-risk interventional settings is driven by stent design and deployment and protected by polymer-drug coatings. *Circulation.* 2011; 123:1400-9.
3. LaDisa JF Jr, Olson LE, Douglas HA, Warltier DC, Kersten JR, Pagel PS. Alterations in regional vascular geometry produced by theoretical stent implantation influence distributions of wall shear stress: analysis of a curved coronary artery using 3D computational fluid dynamics modeling. *Biomed Eng Online.* 2006; 5:40.
4. Bourantas CV, Papafaklis MI, Lakkas L, Sakellarios A, Onuma Y, Zhang YJ, Muramatsu T, Diletti R, Bizopoulos P, Kalatzis F, Naka KK, Fotiadis DI, Wang J, Garcia-Garcia HM, Kimura T, Michalis LK, Serruys PW. Fusion of optical coherence tomographic and angiographic data for more accurate evaluation of the endothelial shear stress patterns and neointimal distribution after bioresorbable scaffold implantation: comparison with intravascular ultrasound-derived reconstructions. *Int J Cardiovasc Imaging* 2014; 30:485-94.

**Difference in hemodynamic
microenvironment in vessels scaffolded with
Absorb BVS and Mirage BRMS: insights from
a preclinical endothelial shear stress study**

Erhan Tenekecioglu, Ryo Torii, Christos Bourantas, Yohei Sotomi, Rafael Cavalcante, Yaping Zeng, Carlos Collet, Tom Crake, Pannipa Suwannasom, Yoshinobu Onuma, Patrick W. Serruys

EuroIntervention. 2017;13(11):1327-1335.

ABSTRACT

Background: *In silico* studies have provided robust evidence that stent design affects local hemodynamic forces, which appear as a major determinant of clinical outcomes following stent implantation. However, implications of different stent/scaffold configurations on local hemodynamic forces have not yet been investigated *in vivo* in a comparative fashion.

Method and Results: Eight healthy mini pigs were implanted with six Absorb everolimus-eluting Bioresorbable Vascular Scaffolds (Absorb BVS) and five Mirage sirolimus-eluting Bioresorbable Microfiber Scaffolds (Mirage BRMS). Optical coherence tomography (OCT) was performed and strut protrusion was assessed post scaffold implantation. Following the reconstruction of coronary anatomy blood flow simulation was performed and endothelial shear stress (ESS) was estimated on top of the struts and at luminal surface between the struts in each scaffold. The thicker struts in Absorb ($152\pm 140\mu\text{m}$) resulted in an increased protruded distance compared to Mirage ($117\pm 123\mu\text{m}$) ($p=0.003$). This had an effect in the local hemodynamic microenvironment. ESS at top-of-the struts were higher in Absorb (1.69 ± 1.20 Pa) than in Mirage (1.53 ± 0.91 Pa), ($p<0.001$) but lower at inter-strut zones (0.60 ± 0.51 Pa vs 0.63 ± 0.50 Pa; $p<0.01$) compared to Mirage. Both scaffold types revealed comparable percentages of vessel luminal surface exposed to recirculation.

Conclusion: Absorb demonstrated higher shear stress on top of the struts compared to Mirage. However, in the inter-struts zones shear stress was higher in Mirage than in Absorb. Further research is required to examine potential value of *in vivo* computational modeling in optimizing scaffold configuration and clinical outcomes.

Key words: Bioresorbable scaffold; endothelial shear stress; scaffold design; strut geometry; hemodynamic microenvironment.

INTRODUCTION

Local coronary hemodynamic forces, particularly endothelial shear stress (ESS) appear to regulate vessel wall response following implantation of metallic stents or bioresorbable scaffolds (BRS). Numerous *in vivo* studies implemented intravascular ultrasound (IVUS) based-modeling to examine the association between neointimal hyperplasia and ESS and demonstrated an inverse association between ESS and neointimal growth in bare metal stents¹ while in drug eluting stents this association appears to be regulated by the anti-proliferative drug.² Traditionally coronary reconstruction performed with IVUS has limited resolution and does not allow detailed assessment of lumen morphology especially in stented segments. Recent reports implementing optical coherence tomography-based modeling have provided further insights about the implications of scaffold implantation on the local hemodynamic microenvironment enabling for the first-time *in vivo* evaluation of the effect of the protruded struts on the local hemodynamic patterns.^{3, 4}

Absorb everolimus-eluting Bioresorbable Vascular Scaffolds (Absorb BVS, Abbott Vascular, Santa Clara, CA, USA) and Mirage sirolimus-eluting Bioresorbable Microfiber Scaffolds (Mirage BRMS, Manli Cardiology, Singapore) have substantial differences in strut thickness, geometrical features and strut connector alignment which, as it has been shown in *in silico* studies, determine flow characteristics and ESS distribution. The aim of this study is to compare the ESS distribution in two differently shaped scaffolds using OCT-based modeling.

METHODS

We analyzed data from Yucatan mini pigs implanted with Absorb and Mirage scaffolds (Figure-1). Eight Yucatan mini pigs with healthy coronaries underwent percutaneous coronary intervention (PCI) in the three epicardial coronary arteries via the femoral access according to standard procedures.⁵ Six coronary arteries were implanted with a single Absorb and five with a Mirage. The treated coronary arteries were studied by OCT imaging immediately after scaffold implantation. The protocol approval for the animal study was received from the Institutional Animal Care and Use Committee and the study was conducted in accordance to the American Heart Association guidelines for preclinical research and the Guide for the Care and Use of Laboratory Animals.⁶

Scaffold design

Absorb is made of poly L-lactic acid (PLLA), coated with a layer of a 1:1 mixture of an amorphous matrix of poly D, L-lactic acid (PDLLA) and elutes everolimus ($8.2 \mu\text{g}/\text{mm}^2$). Absorb is manufactured using extrusion and laser machining techniques, has $157\mu\text{m}$ strut thickness and in-phase zig-zag hoops linked with bridges design.

Mirage is made of PDLLA of which D (dextro-rotary)-isomer constitutes <5% of the total polylactic acid (PLA), is coated with a biodegradable PLA and is eluting sirolimus. Mirage is manufactured by winding the polylactide monofilaments into helix-coiled structure attached by longitudinal spine microfibers. The struts have circular shape and a thickness of $125\mu\text{m}$ (Figure-1). The helical-coil design is fastened by longitudinal spine microfibers which provide a radial strength to the device (148.54 kPa) that is similar to the Absorb (148.00 kPa).⁷

Data acquisition

X-ray angiography was performed using Siemens HiCor cardiac angiography system (Siemens, Erlangen, Germany). OCT was performed following scaffold implantation in all treated coronary arteries. The scaffolded segments were assessed using a C8-XR OCT System (St. Jude Medical, St. Paul, MN, USA) that was pulled-back at a speed of $18 \text{ mm}/\text{sec}$. A non-occlusive flushing technique was used for blood clearance by injection of contrast media. The acquired data were stored in DICOM format and transferred to a workstation for further analysis.

Protrusion analyses

The protrusion analyses in OCT, was performed using a special version of QCU-CMS software (version 4.69, Leiden University Medical Center, Leiden, The Netherlands). The analysis in OCT was performed in the scaffolded segment at every $100\mu\text{m}$ using a methodology presented previously⁸ (Figure-1). The details of protrusion analysis can be found in **Appendix**.

Coronary artery reconstruction

Coronary artery reconstruction was performed using a well-established and validated methodology.⁹ Two reconstructions were performed for each scaffold and proximal/distal non-scaffolded segments: one from the flow area borders (flow model) in both scaffolded and non-scaffolded segments and the other from the flow area in the non-scaffolded segment and the lumen area in the scaffolded segment (reference model) (Figure 2A and 2B). The details of 3D coronary artery reconstruction can be found in **Appendix**.

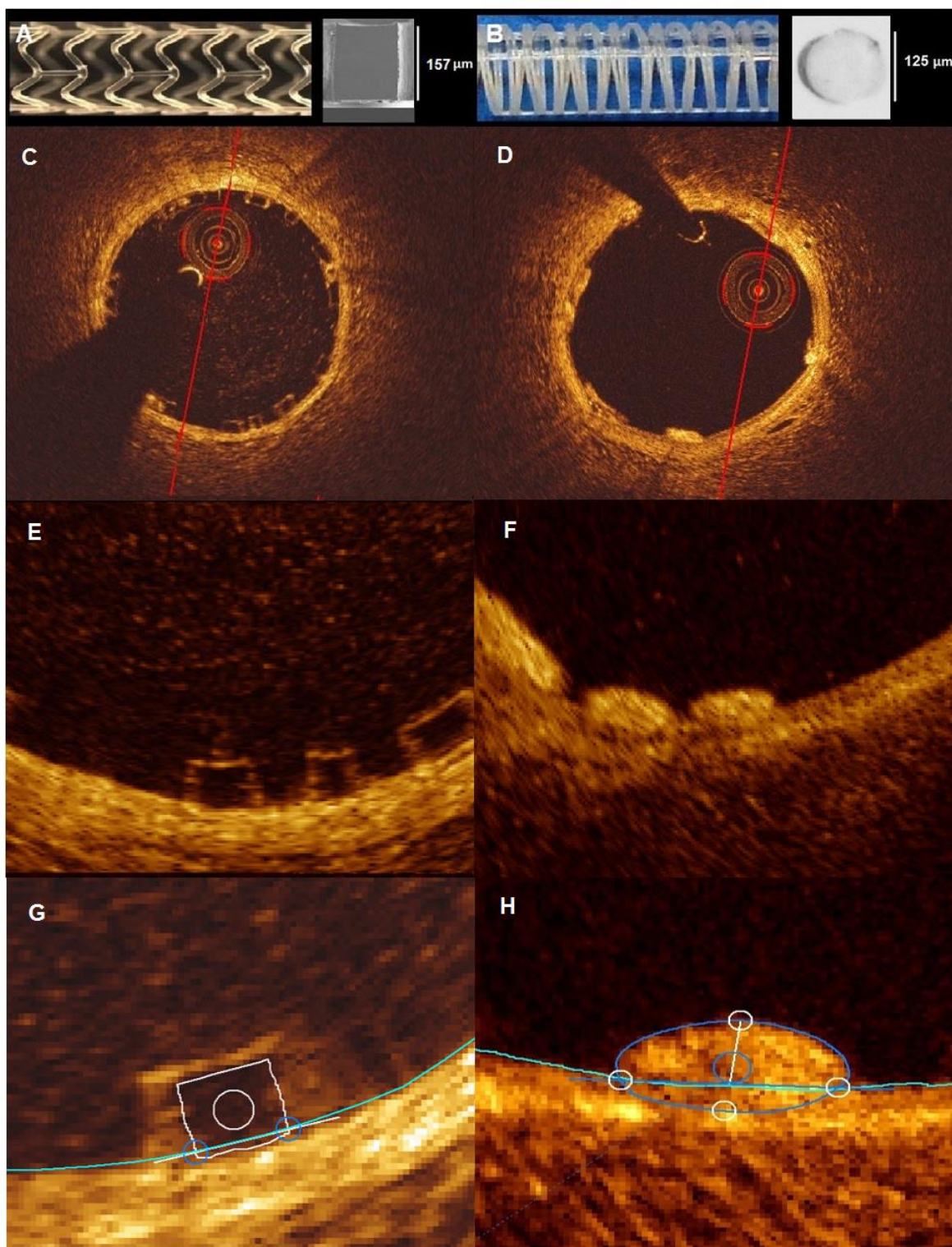


Figure 1. Absorb BVS 1.1 and the cross-section of Absorb BVS strut(A). Mirage BRMS and the cross-section of Mirage BRMS strut(B). The strut of Absorb has a translucent rectangular shape (C, E) whereas the strut of the Mirage is circular, non-translucent (D, F) and protrudes less in the lumen of the vessel. Representation of the protrusion analysis in Absorb(G) and Mirage (H).

Figure 2A

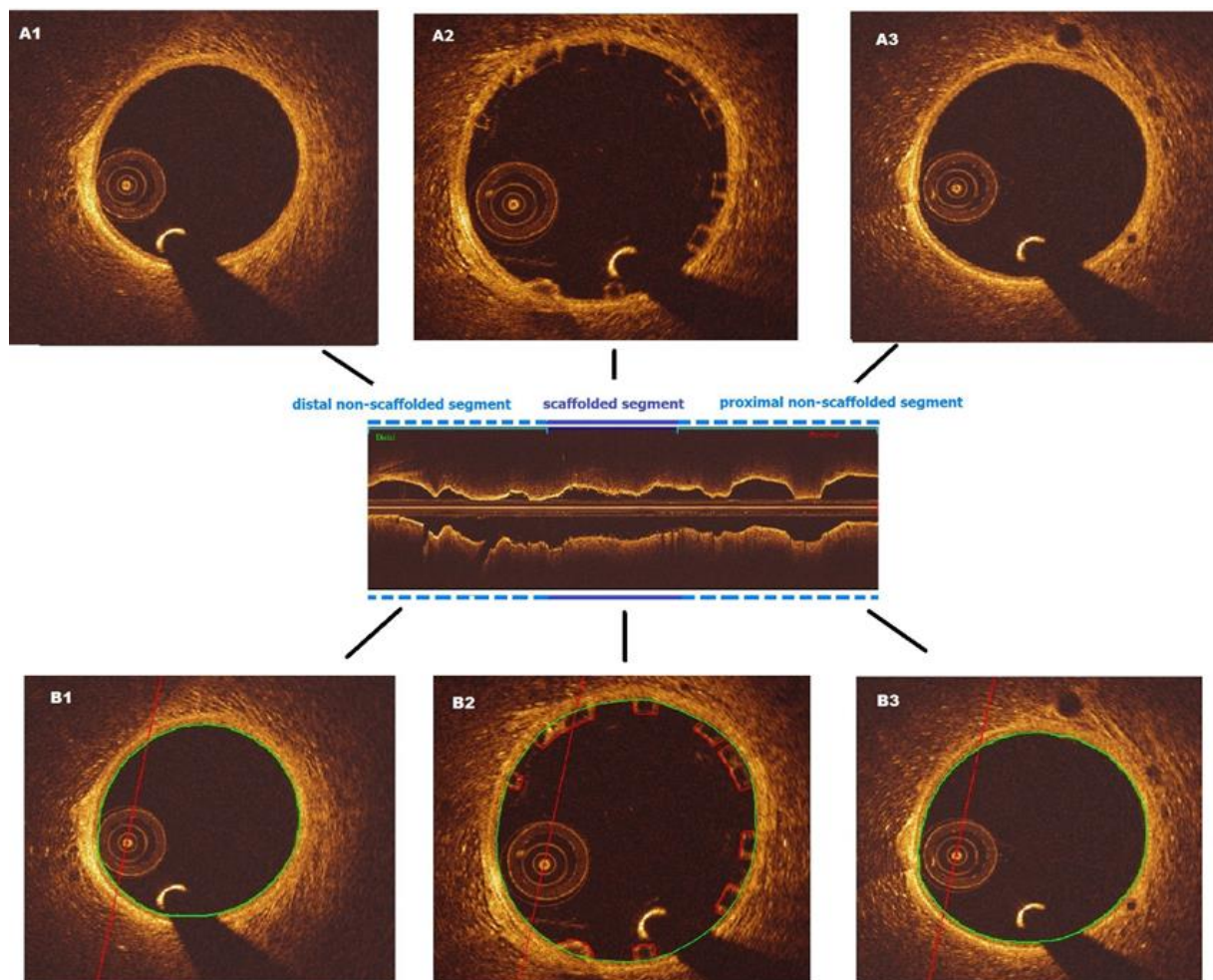


Figure 2B

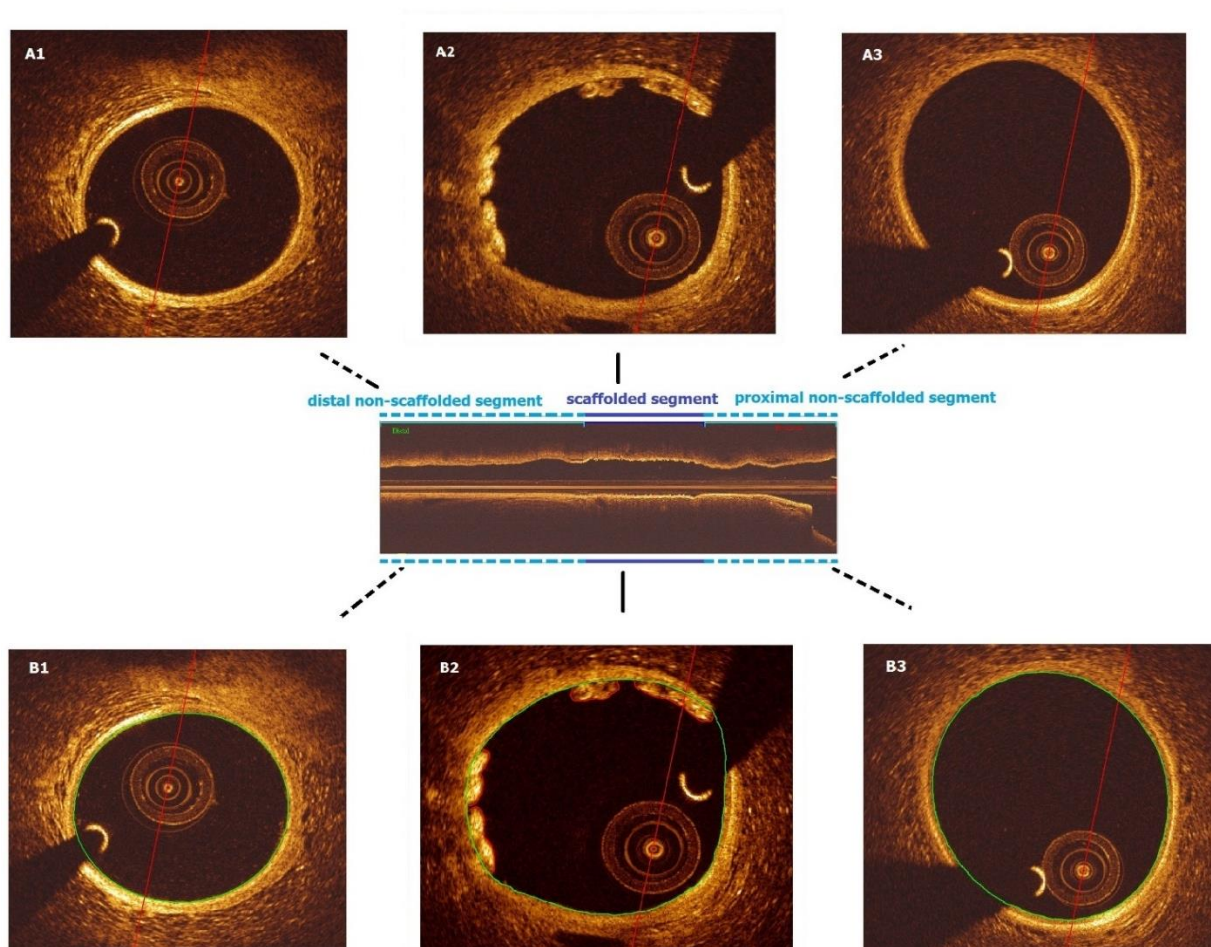


Figure 2. In the non-scaffolded and scaffolded segments, the observer delineated the flow area – defined in the non-scaffolded segment by the lumen border (**Figure 2A panel-B1 and B3, Figure 2B panel-B1 and B3**) and in the scaffolded segment by the adluminal side of the struts and by the lumen border in the areas between the struts (**Figure-2A panel-B2, Figure-2B panel-B2**).

Blood flow simulation

The flow models were processed with Computational Flow Dynamic techniques. A finite volume mesh was generated and then blood flow simulation was performed and the ESS was estimated by solving the 3D Navier-Stokes equations (ANSYS Fluent, Canonsburg, Pennsylvania).¹⁰ The ESS was measured at top of the strut and at the luminal surface between the struts in the scaffolded segment and along the axial direction per 0.2mm interval with the

use of an in-house algorithm (**Figure-3**). The details of 3D coronary artery reconstruction can be found in **Appendix**.

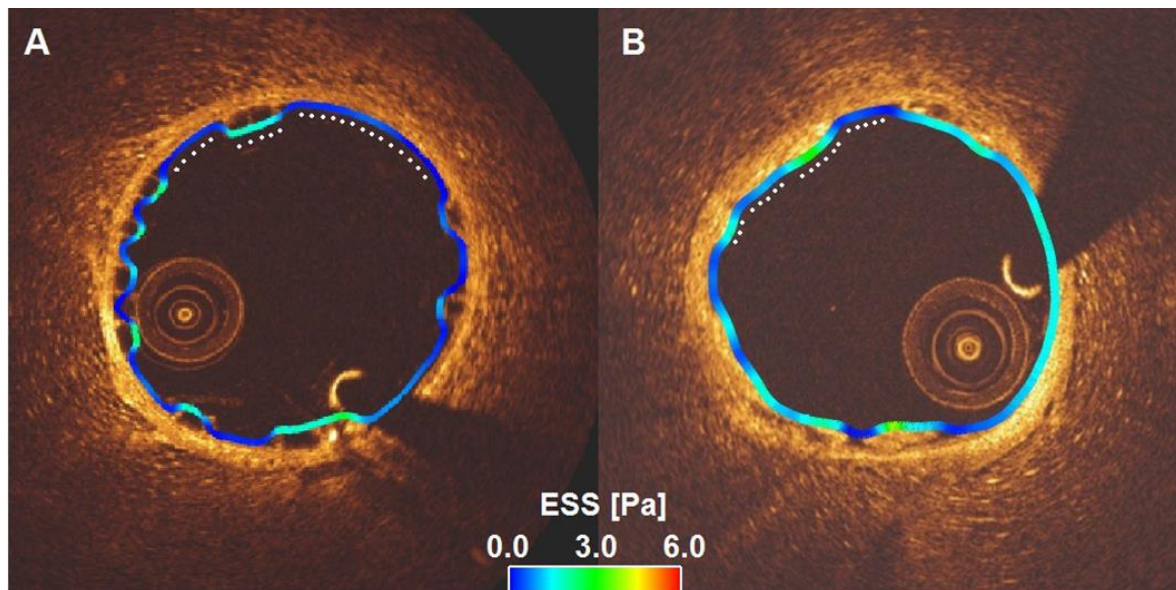


Figure 3. Shear stress is analyzed at-top of the struts and in the inter-strut areas separately at each circumferential 1°-angle in each cross-section. The white dots depict circumferential 1°-angle location.

Statistical analysis

Continuous variables were tested for normality with Kolmogorov-Smirnov test and are presented as mean \pm SD or median (interquartile range) as appropriate. Categorical variables are presented as counts and percentages. Continuous variables were compared by the Kruskal-Wallis test or Mann Whitney-U test. Categorical variables were compared by the Pearson Chi-square test. A $p < 0.05$ was considered statistically significant.

As the data in the study have multi-level structure and unbalanced design, mixed effects models were used for statistical analysis. To compare the ESS values in different scaffold groups, the multi-level model was initially built with fixed effects on scaffold type, cross-sectional area and interaction of the scaffold type with cross-sectional area and random effects on animal ID, scaffold type and cross-section ID. After comparing different models using maximum likelihood, best fitted model was selected.

In the protrusion analysis, animal and device types were implemented as random effect, while post-dilatation pressure was input as fixed effect into the model.

Reproducibility of protrusion analysis for Absorb was previously reported by Sotomi et al⁸. In the present study, reproducibility of the protrusion analysis for Mirage was assessed with the

interclass correlation coefficient (ICC) for absolute agreement (ICCa) with its 95 % confidence intervals (CI) using randomly selected 100 Mirage struts. ⁸ Analyses were done using the statistical analysis program SPSS V.21, R V. 3.2.3 and the R package lme4.¹¹

RESULTS

One left anterior descending coronary artery (LAD), 3 left circumflex (LCx) and 2 right coronary arteries (RCA) were implanted with an Absorb and 2 LAD, 1 LCx and 2 RCA with a Mirage. Scaffold dimensions and procedural parameters are shown in **Supplementary Table 1** in Appendix. The dimensions of the proximal edge segment, of the scaffolded segment and of the distal edge segment are shown in **Table1**.

Table 1a. OCT analysis of scaffolded and non-scaffolded segments according to the scaffold type (device level)

	ABSORB BVS (n=6)	MIRAGE BRMS (n=5)	P
Scaffolded segment lumen area (mm ²)	7.57 (7.11-7.78)	6.35 (3.49-9.21)	0.22
Distal non-scaffolded segment lumen area (mm ²)	4.97 (4.25-5.81)	5.14 (2.01-8.27)	0.26
Proximal non-scaffolded segment lumen area (mm ²)	6.34 (6.06-9.74)	5.58 (4.69-6.47)	0.49
Strut area (mm ²)	0.22 (0.20-0.23)	0.63 (0.22-1.04)	<0.001

The results are as Median (Quartile1-Quartile3)

Table 1b. OCT lumen area in scaffolded and non-scaffolded segment for each scaffold.

Scaffold	Animal	Median LA (Q1-Q3)- Scaffolded segment (mm ²)	Median LA (Q1-Q3)- Distal non-scaffolded segment (mm ²)	Median LA (Q1-Q3)- Proximal non-scaffolded segment (mm ²)
ABSORB BVS-1	A	8.0 (6.94-8.36)	3.48 (3.38-3.61)	5.62 (5.17-6.68)
ABSORB BVS -2	B	8.38 (7.93-8.71)	4.11 (3.94-4.41)	6.17 (5.32-6.38)
ABSORB BVS-3	C	6.92 (6.81-7.14)	5.04 (4.11-5.15)	6.04 (4.89-7.05)
ABSORB BVS-4	D	8.69 (8.55-8.93)	4.78 (4.52-5.10)	7.75 (7.57-8.09)
ABSORB BVS-5	E	7.96 (7.70-8.36)	7.37 (6.72-7.89)	12.63 (11.14-14.24)
ABSORB BVS-6	F	7.42 (7.24-7.51)	5.01 (4.21-7.23)	6.11 (5.68-6.41)
MIRAGE BRMS-1	F	7.02 (6.88-7.11)	4.37 (4.26-4.47)	4.58 (4.21-4.72)
MIRAGE BRMS-2	F	5.78 (5.66-5.92)	5.14 (4.50-5.69)	5.79 (3.94-8.52)
MIRAGE BRMS-3	G	8.98 (8.29-9.81)	7.40 (4.59-7.95)	5.75 (5.59-6.12)
MIRAGE BRMS-4	A	7.25 (7.04-7.78)	4.57 (4.39-7.05)	5.18 (4.74-5.44)
MIRAGE BRMS-5	H	7.13 (7.08-7.35)	7.80 (7.42-7.95)	5.58 (5.45-5.81)

Protrusion analysis

The protrusion analyses were performed in cross-section and in device level. In cross-section level analysis, there was a significant difference between the scaffolds in the protrusion

distances ($152 \pm 140 \mu\text{m}$ for Absorb, $117 \pm 123 \mu\text{m}$ for Mirage; $p=0.003$) fact that should be attributed to different strut thicknesses. Similar were the results in the device level analysis. The protrusion distances were significantly increased in the Absorb comparing to Mirage ($152 \pm 12.2 \mu\text{m}$ vs $116 \pm 11.1 \mu\text{m}$; $p < 0.0001$). The inter-observer reproducibility [ICC_a:0.884 CI (0.827-0.922)] and the intra-observer reproducibility [(ICC_a:0.782 CI (0.675-0.854))] for the protrusion distances indicated good agreement in Mirage.

Endothelial shear stress analysis

There were several layers of grouping within the data of the study; eight animals (level 3) received scaffold implants in their coronary arteries, and different types of scaffolds were used in different vessels within the same animal. Each scaffolded segment had several cross-sections (level 2) and in each cross-section (level 1) the ESS was measured on the top of the struts and at the luminal surface between the struts. After setting the model with random and fixed effects variables, multi-level linear regression analysis revealed that, Absorb had significantly higher ESS at top of the struts compared to the Mirage. In the luminal surface in the areas between the struts, Mirage revealed higher ESS compared to the Absorb. On top of the struts the ESS in Absorb were 1.69 ± 1.20 Pa and 1.53 ± 0.91 Pa in the Mirage, respectively ($p < 0.001$) while in the areas between struts, the mean ESS values were 0.60 ± 0.51 Pa and 0.63 ± 0.50 Pa respectively ($p < 0.001$) (**Table 2**); 52% of the scaffolded surface in the Absorb and 47% in the Mirage ($125 \mu\text{m}$) was exposed to a low (< 1 Pa) athero-promoting ESS environment ($p < 0.0001$) (**Figure 4**).

Table 2. The endothelial shear stress (ESS) values at the top of the struts and between the struts in the scaffold groups.

Scaffold	ABSORB BVS	Mirage BRMS	p-value*
Strut-top ESS (Pa)	1.69 ± 1.20	1.53 ± 0.91	< 0.001
Inter-strut ESS (Pa)	0.60 ± 0.51	0.63 ± 0.50	< 0.001

*p-values comes from linear mixed effects analysis.

Lumen cross sectional area had also an effect on the ESS. Increase in the cross-sectional area resulted in a significant decrease in ESS both at top of the struts and at inter-strut zones ($p < 0.001$ for the ESS on top of the strut, $p < 0.001$ for inter-strut ESS). The maximum and mean shear rates and the

percentage volumes of the scaffolded segments exposed to shear rates $>500 \text{ s}^{-1}$ and $>1000 \text{ s}^{-1}$ were numerically higher in Absorb than in Mirage nevertheless these differences didn't reach a statistical significance, (Table 3) (Figure 5).

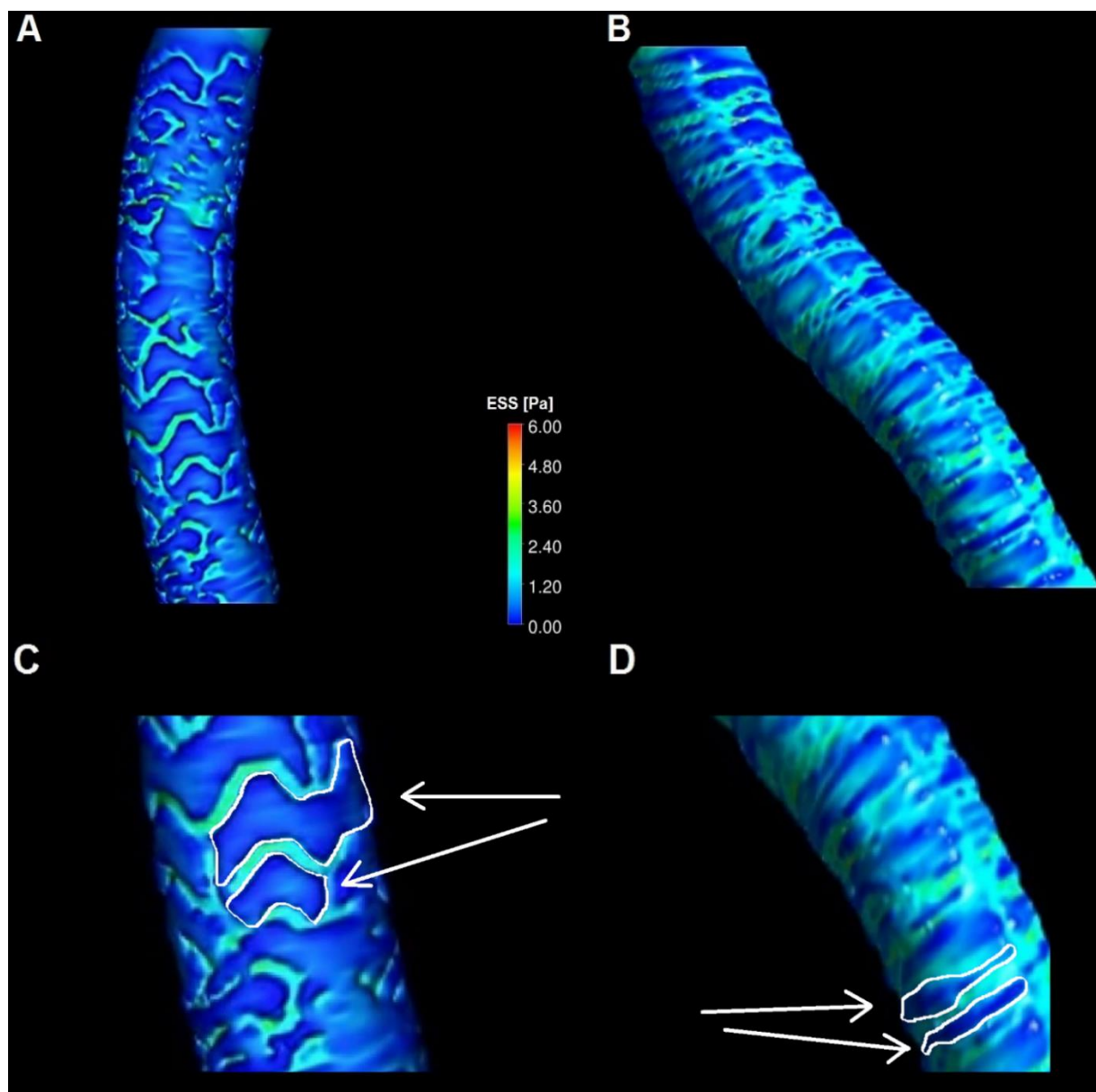
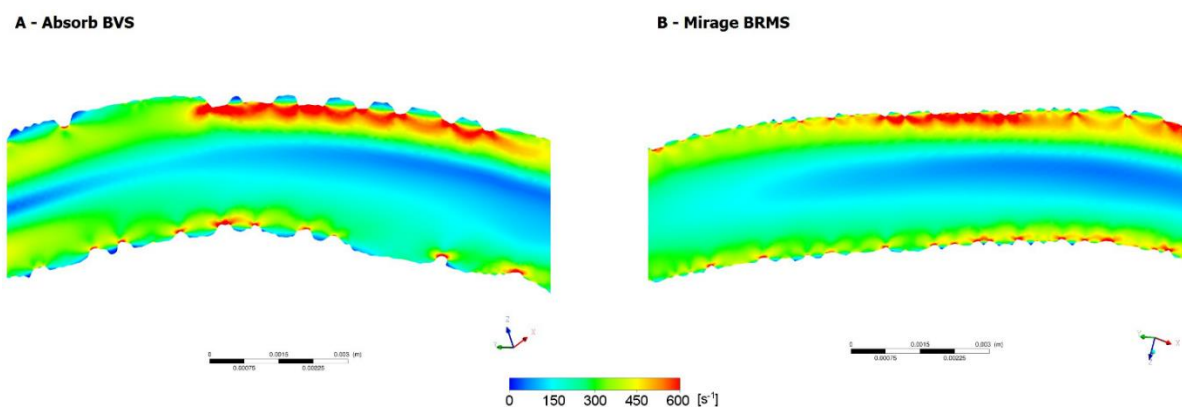


Figure 4. Three-dimensional reconstruction of scaffolded coronary anatomy from the fusion of coronary angiograms and OCT data with the local ESS being portrayed in a color-coded map (dark blue indicates low ESS $<1.0 \text{ Pa}$ and aquamarine demonstrates ESS $\geq 1.0 \text{ Pa}$) for Absorb (A and C) and Mirage (B and D). Note the larger dark blue area in Absorb (C).

Table 3. Shear rate analysis results in the scaffolded segments in both types of scaffolds

	Absorb BVS	Mirage BRMS	P value
Maximum shear rate (s^{-1})	2060 \pm 1778	1621 \pm 755	0.58
Mean shear rate (s^{-1})	238 \pm 133	234 \pm 67	0.95
Percentage volume exposed to shear rate > 500 s^{-1} (%)	7.6 \pm 16	1.1 \pm 2.7	0.59
Percentage volume exposed to shear rate > 1000 s^{-1} (%)	3.7 \pm 5.7	0.09 \pm 0.25	0.39

**Figure 5.** Shear rate is increased at top of the struts in Absorb(panel-A) and in Mirage(panel-B) scaffolds

Similarly, the percentage of the recirculation areas was numerically higher in the Absorb, but again this difference did not reach a statistical significance (3.26 ± 2.07 vs 2.71 ± 1.32 ; $p = 0.87$) (**Supplementary Table 2**) (**Figure 6**).

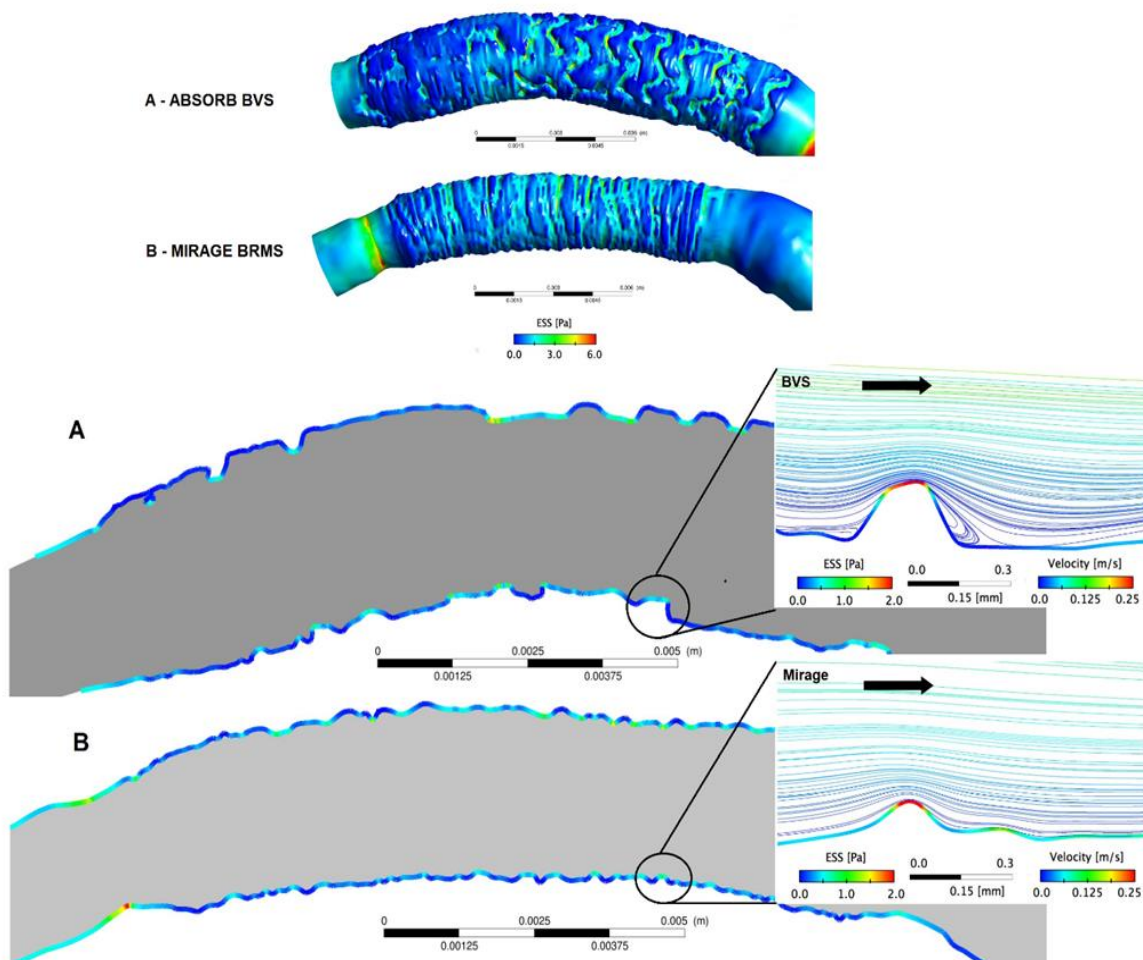


Figure 6. The blood flow streamlines are shown with velocity and ESS color coded bars for the Absorb and Mirage. ESS values are high on top of the strut. Low ESS is noted between the Absorb struts (thick rectangular) (A) and Mirage struts (thinner circular) (B). While recirculation zones were noted in the distal regions of the Absorb(A), there was no reversed flow in the distal region of the Mirage(B).

DISCUSSION

In this study, we evaluated two different types of BRS with different strut geometries, thicknesses and strut connector alignment in a porcine coronary artery model. The findings can be summarized as follows: 1) The protrusion distances were higher in Absorb, fact that should be attributed to the increased strut thickness of this scaffold, this difference resulted in 2) increased ESS at top of the strut in this device and 3) lower ESS in the areas between the struts compared to the Mirage, 4) in a numerically higher percentage volumes exposed to high

shear rates and 5) increased recirculation areas in Absorb; differences however that did not reach statistical significance for recirculation area and shear rate.

Numerous *in silico* studies have demonstrated that stent/scaffold design affects the local hemodynamic forces following its implantation.^{12, 13} The strut shape, strut thickness, maximal coil pitch distance and the struts alignment with regards to coronary flow as well as the alignment of the strut connectors appear to determine the local flow patterns.¹³ More importantly, the differences in the local hemodynamic profile following stent/scaffold configuration appears to determine clinical outcomes after PCI. In bare metal stent era, it has been shown that stents with thinner struts are associated with a lower incidence of in-stent restenosis and better clinical outcomes, while in DES the implications of stent configuration on clinical outcomes has been suppressed by the anti-proliferative drug.¹⁴⁻¹⁶ In BRS era however there is a shift in the paradigm. Recent registry and meta-analysis studies have revealed in increased incidence of stent thrombosis following BRS implantation.^{17, 18} These alarming findings have been attributed to the suboptimal local hemodynamics induced by the thick rectangular shaped struts and scaffold under-expansion, and efforts are currently made to optimize scaffold designs.

In silico studies may be helpful in assessing the effect of stent/scaffold design on ESS in treated segments, but they have significant limitations. First, they assume that the stent struts are well apposed. Reports have shown that this is not the case in the clinical setting where up to 30% of the struts are embedded into the vessel wall.¹⁹ In addition, they assume that the stent/scaffold is fully deployed in the treated vessel and thus they are unable to assess the implications of stent/scaffold underexpansion, or early recoil on the ESS distribution.²⁰ Finally, they don't take into account the vessel curvature and the changes induced during device implantation on vessel geometry, which depend on vessel curvature and on the mechanical properties of the deployed device, and appear to affect the local hemodynamic forces.²¹

Taking into account these limitations, we examined for the first time *in vivo*, in an animal model, the implications of two different scaffold designs with different configuration on the local flow patterns. We found higher ESS on the top of the struts in Absorb compared to the Mirage. Absorb has thicker rectangular shaped struts which as it has been shown in previous experimental and *in silico* studies, they protrude in the lumen and obstruct flow resulting in higher ESS at the top of the struts and flow disturbances, recirculation zones, and low ESS in

the areas between the struts. On the other hand, Mirage has configuration with a thinner circular shaped strut engender lower ESS values at top of the struts, compared to the Absorb scaffold, and cause less flow disruption, resulting in relatively higher ESS in the areas between the struts (Figure-6).¹⁵

In addition to strut geometry, luminal surface coverage ratio and maximal coil pitch distances between the coil rings influence the hemodynamic microenvironment in scaffolded segments. Mirage (45%) has significantly higher vessel coverage ratio than Absorb (27%). The smaller pitch distance (distance between the helical rings) in Mirage (0.8 mm vs 1.0 mm in Absorb) is likely to increase flow stagnation areas and decrease the ESS in these segments.^{22, 23} However as it was shown in this analysis strut thickness was the most important determinant of ESS and thus the ESS were higher in Mirage in the areas between the struts.

Apart from the differences in the ESS, we have noticed differences in the shear rate in the two scaffold designs. Although the mean shear rate values were similar in Absorb and Mirage, the maximum shear rate values and the percentage of the volume of the scaffolded segment exposed to high shear rate was numerically higher in the Absorb comparing to Mirage indicating a larger variability of the shear rate values in the Absorb. In addition, we found that the recirculation areas were numerically lower in the thinner strut Mirage(125 μ m). This finding is consistent with the results of CFD models which indicate that thinner circular struts lead to a more streamlined flow pattern with less disruptions and flow recirculations.¹⁴ Nevertheless, due to small sample size of the device level analysis, the difference in shear rate and recirculation areas did not reach statistical significance.

The differences in the hemodynamic profile of Absorb and Mirage may have significant clinical implications. The flow disruption noted in Absorb resulted in low ESS that is associated with increased neointima formation³ and scaffold restenosis, while the flow stagnation and recirculation zones noted in the areas between the struts may promote thrombus formation as it has been shown in histology studies.^{22, 24} Finally, high shear rate can trigger activation of platelet and Von-Willebrand factor that can promote thrombus formation.²⁴ This study demonstrated for the first time *in vivo* computational modeling is able to identify and quantify hemodynamic indices which may account for the increased incidence of early scaffold thrombosis and cardiovascular events reported in the early Absorb studies, and thus it can be used to test and improve the hemodynamic profile of future bioresorbable scaffold designs.

Limitations

A significant limitation of the current analysis is that scaffold implantation was performed in healthy coronary arteries. Therefore, it was not possible to examine the implications of scaffold under-expansion²⁰ or the composition of the underlying plaque on strut embedment which potentially influence the local flow hemodynamics. It would be instructive to assess the stent/scaffold behavior in atherosclerotic vessels to approximate its actual use. Second, the small number of the studied scaffolds did not allow us to assess the impact of scaffold design on shear rate and recirculation zones. Moreover, there were differences in the balloon inflation and post-dilatation pressures between groups. Nevertheless, this did not have an impact on strut protrusion a paradox that should be attributed to the fact that the scaffolds were implanted in healthy vessels. Finally, there were differences in the lumen areas in the two groups which are likely to affect the ESS values. Nevertheless, these differences were not statistically significant; in addition, in the linear mixed effect analysis scaffold type was independently associated with the ESS distribution.

CONCLUSIONS

In vivo computational modeling enables assessment of the effect of different scaffolds implantation on the local hemodynamic patterns. Mirage with circular thinner struts, with a helicoids alignment result in a superior ESS patterns compared to the thick rectangular shaped struts of the Absorb with a zig-zag hoops alignment. This preclinical study is the preamble of the randomized clinical trial comparing Mirage and Absorb in a first-in-man study. Further research is required to examine the potential value of the *in vivo* computational modeling in optimizing scaffold configuration and clinical outcomes.

Impact on daily practice

Mirage scaffold is a novel BRS and its unique design could provide better local hemodynamic microenvironment in treated vessels.

Funding

This study was sponsored by Manli Cardiology, Singapore, Singapore.

Disclosure

E. Tenekecioglu has a research grant from TUBITAK (The Scientific Council of Turkey). P.W. Serruys and Y. Onuma are members of the International Advisory Board of Abbott Vascular. All other authors have no conflicts of interest to declare.

REFERENCES

1. Wentzel JJ, Krams R, Schuurbiers JC, Oomen JA, Kloet J, van Der Giessen WJ, Serruys PW, Slager CJ. Relationship between neointimal thickness and shear stress after Wallstent implantation in human coronary arteries. *Circulation* 2001;103(13):1740-5.
2. Papafaklis MI, Bourantas CV, Theodorakis PE, Katsouras CS, Naka KK, Fotiadis DI, Michalis LK. The effect of shear stress on neointimal response following sirolimus- and paclitaxel-eluting stent implantation compared with bare-metal stents in humans. *JACC Cardiovascular interventions* 2010;3(11):1181-9.
3. Bourantas CV, Papafaklis MI, Kotsia A, Farooq V, Muramatsu T, Gomez-Lara J, Zhang YJ, Iqbal J, Kalatzis FG, Naka KK, Fotiadis DI, Dorange C, Wang J, Rapoza R, Garcia-Garcia HM, Onuma Y, Michalis LK, Serruys PW. Effect of the endothelial shear stress patterns on neointimal proliferation following drug-eluting bioresorbable vascular scaffold implantation: an optical coherence tomography study. *JACC Cardiovascular interventions* 2014;7(3):315-24.
4. Papafaklis MI, Bourantas CV, Farooq V, Diletti R, Muramatsu T, Zhang Y, Fotiadis DI, Onuma Y, Garcia Garcia HM, Michalis LK, Serruys PW. In vivo assessment of the three-dimensional haemodynamic micro-environment following drug-eluting bioresorbable vascular scaffold implantation in a human coronary artery: fusion of frequency domain optical coherence tomography and angiography. *EuroIntervention : journal of EuroPCR in collaboration with the Working Group on Interventional Cardiology of the European Society of Cardiology* 2013;9(7):890.
5. Williams PD, Malik N, Kingston PA. Coronary angiography and percutaneous coronary intervention in the porcine model: a practical guide to the procedure. *Animal* 2012;6(2):311-20.
6. National Research Council (U.S.). Committee for the Update of the Guide for the Care and Use of Laboratory Animals., Institute for Laboratory Animal Research (U.S.), National Academies Press (U.S.). *Guide for the care and use of laboratory animals*. In. 8th ed. Washington, D.C.: National Academies Press,; 2011, xxv, 220 p.
7. Ormiston JA, Webber B, Ubod B, Darremont O, Webster MW. An independent bench comparison of two bioresorbable drug-eluting coronary scaffolds (Absorb and DESolve) with a durable metallic drug-eluting stent (ML8/Xpedition). *EuroIntervention : journal of EuroPCR in collaboration with the Working Group on Interventional Cardiology of the European Society of Cardiology* 2015;11(1):60-7.
8. Sotomi Y, Tateishi H, Suwannasom P, Dijkstra J, Eggermont J, Liu S, Tenekecioglu E, Zheng Y, Abdelghani M, Cavalcante R, de Winter RJ, Wykrzykowska JJ, Onuma Y, Serruys PW, Kimura T. Quantitative assessment of the stent/scaffold strut embedment analysis by optical coherence tomography. *The international journal of cardiovascular imaging* 2016;32(6):871-83.
9. Bourantas CV, Papafaklis MI, Lakkas L, Sakellarios A, Onuma Y, Zhang YJ, Muramatsu T, Diletti R, Bizopoulos P, Kalatzis F, Naka KK, Fotiadis DI, Wang J, Garcia Garcia HM, Kimura T, Michalis LK, Serruys PW. Fusion of optical coherence tomographic and angiographic data for more accurate evaluation of the endothelial shear stress patterns and neointimal distribution after bioresorbable scaffold implantation: comparison with intravascular ultrasound-derived reconstructions. *Int J Cardiovasc Imaging* 2014;30(3):485-94.
10. Papafaklis MI, Bourantas CV, Theodorakis PE, Katsouras CS, Fotiadis DI, Michalis LK. Relationship of shear stress with in-stent restenosis: bare metal stenting and the effect of brachytherapy. *International journal of cardiology* 2009;134(1):25-32.
11. Bates D, Mächler M, Bolker B, Walker S. Fitting Linear Mixed-Effects Models Using lme4. 2015 2015;67(1):48.
12. Stone PH, Saito S, Takahashi S, Makita Y, Nakamura S, Kawasaki T, Takahashi A, Katsuki T, Nakamura S, Namiki A, Hirohata A, Matsumura T, Yamazaki S, Yokoi H, Tanaka S, Otsuji S, Yoshimachi F, Honye J, Harwood D, Reitman M, Coskun AU, Papafaklis MI, Feldman CL, Investigators P. Prediction of progression of coronary artery disease and clinical outcomes using vascular profiling of endothelial shear stress and arterial plaque characteristics: the PREDICTION Study. *Circulation* 2012;126(2):172-81.

13. Jimenez JM, Davies PF. Hemodynamically driven stent strut design. *Annals of biomedical engineering* 2009;37(8):1483-94.
14. Pache J, Kastrati A, Mehilli J, Schuhlen H, Dotzer F, Hausleiter J, Fleckenstein M, Neumann FJ, Sattelberger U, Schmitt C, Muller M, Dirschinger J, Schomig A. Intracoronary stenting and angiographic results: strut thickness effect on restenosis outcome (ISAR-STEREO-2) trial. *J Am Coll Cardiol* 2003;41(8):1283-8.
15. Joner M, Nakazawa G, Finn AV, Quee SC, Coleman L, Acampado E, Wilson PS, Skorija K, Cheng Q, Xu X, Gold HK, Kolodgie FD, Virmani R. Endothelial cell recovery between comparator polymer-based drug-eluting stents. *J Am Coll Cardiol* 2008;52(5):333-42.
16. Pache J, Dibra A, Mehilli J, Dirschinger J, Schomig A, Kastrati A. Drug-eluting stents compared with thin-strut bare stents for the reduction of restenosis: a prospective, randomized trial. *Eur Heart J* 2005;26(13):1262-8.
17. Capodanno D, Gori T, Nef H, Latib A, Mehilli J, Lesiak M, Caramanno G, Naber C, Di Mario C, Colombo A, Capranzano P, Wiebe J, Araszkievicz A, Geraci S, Pyxaras S, Mattesini A, Naganuma T, Munzel T, Tamburino C. Percutaneous coronary intervention with everolimus-eluting bioresorbable vascular scaffolds in routine clinical practice: early and midterm outcomes from the European multicentre GHOST-EU registry. *EuroIntervention* 2015;10(10):1144-53.
18. Ishibashi Y, Onuma Y, Muramatsu T, Nakatani S, Iqbal J, Garcia-Garcia HM, Bartorelli AL, Whitbourn R, Abizaid A, Serruys PW, Investigators AE. Lessons learned from acute and late scaffold failures in the ABSORB EXTEND trial. *EuroIntervention* 2014;10(4):449-57.
19. Gomez-Lara J, Radu M, Brugaletta S, Farooq V, Diletti R, Onuma Y, Windecker S, Thuesen L, McClean D, Koolen J, Whitbourn R, Dudek D, Smits PC, Regar E, Veldhof S, Rapoza R, Ormiston JA, Garcia-Garcia HM, Serruys PW. Serial analysis of the malapposed and uncovered struts of the new generation of everolimus-eluting bioresorbable scaffold with optical coherence tomography. *JACC Cardiovasc Interv* 2011;4(9):992-1001.
20. Foin N, Lee R, Bourantas C, Mattesini A, Soh N, Lim JE, Torii R, Ng J, Liang LH, Caiazzo G, Fabris E, Kilic D, Onuma Y, Low AF, Nijjer S, Sen S, Petraco R, Al Lamee R, Davies JE, Di Mario C, Wong P, Serruys PW. Bioresorbable vascular scaffold radial expansion and conformation compared to a metallic platform: insights from in vitro expansion in a coronary artery lesion model. *EuroIntervention* 2016;12(7):834-44.
21. Wentzel JJ, Whelan DM, van der Giessen WJ, van Beusekom HM, Andhyiswara I, Serruys PW, Slager CJ, Krams R. Coronary stent implantation changes 3-D vessel geometry and 3-D shear stress distribution. *Journal of biomechanics* 2000;33(10):1287-95.
22. Berry JL, Santamarina A, Moore JE, Jr., Roychowdhury S, Routh WD. Experimental and computational flow evaluation of coronary stents. *Ann Biomed Eng* 2000;28(4):386-98.
23. Seo T, Schachter LG, Barakat AI. Computational study of fluid mechanical disturbance induced by endovascular stents. *Annals of biomedical engineering* 2005;33(4):444-56.
24. Kolandaivelu K, Swaminathan R, Gibson WJ, Kolachalama VB, Nguyen-Ehrenreich KL, Giddings VL, Coleman L, Wong GK, Edelman ER. Stent thrombogenicity early in high-risk interventional settings is driven by stent design and deployment and protected by polymer-drug coatings. *Circulation* 2011;123(13):1400-9.

Supplementary Table 1. Inventory of scaffolds and implantation parameters.

Scaffold	Animal	Vessel	Scaffolded vessel segment	Scaffold size (mm)	Deployment balloon pressure (atm)	Post-dilatation balloon inflation pressure (atm)	Expected maximal diameter of post-dilatation balloon at maximum inflation pressure (mm)	Post-dilatation balloon diameter at its maximum Inflation pressure during the procedure (mm)	The diameter of the scaffold after implantation (in vitro) (mm)
ABSORB BVS -1	B	RCA	Mid vessel	3.0 x 18	7	7	3.5	3.32	3.0
ABSORB BVS -2	A	LCx	Mid vessel	3.0 x 18	7	8	3.5	3.36	3.0
ABSORB BVS -3	C	LCx	Proximal vessel	3.0 x 18	7	8	3.5	3.32	3.0
ABSORB BVS -4	D	LAD	Mid vessel	3.0 x 18	7	10	3.5	3.36	3.0
ABSORB BVS -5	F	RCA	Mid vessel	3.0 x 15	7	14	3.5	3.56	3.3
ABSORB BVS -6	E	LCx	Mid vessel	3.0 x 18	7	7	3.5	3.32	3.0
MIRAGE BRMS-1	B	LCx	Mid vessel	2.75 x 13	6	16	3.0	3.08	3.0
MIRAGE BRMS-2	B	LAD	Proximal vessel	2.75 x 13	6	12	2.75	2.74	2.6
MIRAGE BRMS-3	E	RCA	Mid vessel	3.0 x 15	10	18	3.5	3.63	3.3
MIRAGE BRMS-4	G	LAD	Proximal vessel	2.75 x 13	16	18	3.0	3.08	3.0
MIRAGE BRMS-5	H	RCA	Mid vessel	3.0 x 15	6	10	3.0	2.84	3.0

Supplementary Table 2. Percentage of recirculation area per scaffolded surface in each scaffold and in the two scaffold groups.

Scaffold	Recirculation area per scaffolded vessel surface area (%)	Mean \pm SD
Absorb BVS-1	3.50	3.26 \pm 2.07
Absorb BVS-2	2.72	
Absorb BVS-3	0.43	
Absorb BVS-4	6.03	
Absorb BVS-5	1.80	
Absorb BVS-6	5.10	
Mirage BRMS-1	2.00	2.71 \pm 1.32 [†]
Mirage BRMS-2	2.81	
Mirage BRMS-3	0.87	
Mirage BRMS-4	3.93	
Mirage BRMS-5	3.98	

[†]Comparison between Absorb BVS and Mirage BRMS($p=0.87$).

APPENDIX

METHOD

Protrusion analyses

Since the struts of Mirage scaffolds are not translucent, the delineation of the abluminal strut border in Mirage cannot be performed unequivocally. Due to this fact, only protrusion analyses were implemented and we used the inter-struts automatic detection of lumen contours as an interpolated boundary to quantify the amount of struts protruding into the lumen. The luminal borders of both scaffold types and each Absorb BVS strut was automatically detected by the software. In Absorb and Mirage scaffolds, struts located at a side branch ostium were excluded from the protrusion analysis. Totally 6207 struts were studied in both types of scaffolds. The analyses were performed at cross-section level (n=1075) and at device level (n=11). Protrusion percentages and protrusion distances were estimated.

Coronary artery reconstruction

In brief, the angiographic and OCT data were reviewed to identify the scaffolded segment and the anatomical landmarks (i.e., side branches) most proximal and distal to the scaffolded segment, that were visible in both coronary angiography and OCT examination. The proximal and distal anatomical landmarks were used to define the segment of interest. In this segment, an observer analyzed the OCT frames at every 100 μ m interval in the scaffolded segment and at every 400 μ m interval in the non-scaffolded segments. In the scaffolded segment an observer delineated the lumen area defined by the lumen border and the flow area defined by the adluminal side of the struts and by the lumen border in the areas between the struts. Moreover, in the non-scaffolded segment the observer annotated the lumen area (which is also the flow area) and was defined by the lumen border (Figure-2A and 2B).¹ Two post-procedural end-diastolic angiographic images with at least >30° angle difference that were acquired with the table in the isocenter and portrayed the segment of interest with minimal foreshortening were selected. In these images the lumen borders were detected in the segment of interest and used to extract the luminal centerline that was then used to define the 3D luminal centerline.² The borders detected in the OCT images² were then placed perpendicularly onto the luminal centerline. Side-branches seen in both OCT and X-ray angiography images were used to define the absolute orientation of the OCT frames.² Two reconstructions were performed for each scaffold and proximal/distal non-scaffolded segments: one from the flow area borders(flow model) in both scaffolded and non-scaffolded segments and the other from the flow area in the non-scaffolded

segment and the lumen area in the scaffolded segment(reference model) (Figure 2A and 2B). For each point detected in the flow model, a corresponding point was identified in the reference model – defined as the closest point from the reference model– and their distance was estimated. Based on this distance, the points of the flow model in the scaffolded segment were classified in two groups; 1) points corresponding to apposed struts (points with Euclidian distance $>2/3$ of the strut thickness i.e., 104 μm for Absorb and 83 μm for Mirage) 2) points corresponding to areas between struts (points with Euclidian distance $<1/3$ of the strut thickness i.e., 52 μm for Absorb and 42 μm for Mirage) and 3) unclassified points (points with Euclidian distance $>1/3$ and $<2/3$ of the strut thickness i.e., 52-104 μm for Absorb and 42-83 μm for Mirage) which correspond to the edges of apposed struts or to embedded struts. After the classification of the points, the points were described as “Top” which corresponds to the top of the struts, “Base” which refers to the luminal surface between the struts and “Intermediate” which refers to the edges of the struts.

To assess the effect of different scaffold designs on the local hemodynamic micro-environment, the mesh density around the scaffold struts and within the boundary layer of the flow field between the struts was increased to have an average element edge of 30 μm (equal to $1/4$ of the strut thickness of the scaffold strut). Blood was assumed to be a homogeneous, Newtonian fluid with a viscosity of 0.0035 Pa.s and a density of 1,050 kg/m³. A steady flow profile was simulated at the inflow of the 3D models, as it has been shown that there are no significant differences between the ESS estimated in pulsatile and steady flow simulation.^{3, 4} Blood flow for each reconstruction was estimated by measuring, in the 2 angiographic projections, the number of frames required for the contrast agent to pass from the inlet to the outlet of the reconstructed segment, the volume of the reconstructed segment and the cine frame rate.^{5, 6} To avoid the effect of the boundary conditions on the ESS distribution in the scaffolded segments(i.e., an increased blood velocity at the inflow would result in higher ESS distribution in the scaffolded segment) and thus have more accurate evaluation of the implications of scaffold design on the local hemodynamic forces, we normalize the ESS values so as in the native vessel the mean ESS to be 1.35Pa which corresponds to the average moderate ESS reported in the *Prediction* study.⁷ This normalization allowed us to compare the effect of the two scaffold types on the ESS as in both types the proximal and distal to the scaffolds native segments were exposed to the same hemodynamic environment. The arterial wall was considered to be rigid. No-slip conditions were imposed at the scaffold surface. At the outlet of the model, zero pressure conditions were imposed. ESS at the baseline luminal surface was calculated as the product of blood viscosity and the gradient of blood velocity at the wall. The ESS was measured at top of the strut and at the luminal surface between the struts in the scaffolded segment and along the axial direction per 0.2mm interval with the use of an in-house algorithm (Figure-3). In addition, the shear rate in the scaffolded segment was calculated and the maximum shear rate, mean shear rate, percentage of the volume of the

scaffolded vessel segment exposed to shear rate $>500 \text{ s}^{-1}$ and percentage of the volume of the scaffolded vessel segment exposed to shear rate $>1000 \text{ s}^{-1}$ were measured in Absorb and Mirage. The recirculation zones in the vicinity of the struts were quantified based on the direction of the ESS vector and the centerline vector. Areas where the ESS vector had opposite direction to the centerline vector were considered to be exposed to recirculation zones.

REFERENCES FOR APPENDIX

1. Serruys PW, Onuma Y, Ormiston JA, de Bruyne B, Regar E, Dudek D, Thuesen L, Smits PC, Chevalier B, McClean D, Koolen J, Windecker S, Whitbourn R, Meredith I, Dorange C, Veldhof S, Miquel-Hebert K, Rapoza R, Garcia-Garcia HM. Evaluation of the second generation of a bioresorbable everolimus drug-eluting vascular scaffold for treatment of de novo coronary artery stenosis: six-month clinical and imaging outcomes. *Circulation* 2010;122(22):2301-12.
2. Bourantas CV, Papafaklis MI, Lakkas L, Sakellarios A, Onuma Y, Zhang YJ, Muramatsu T, Diletti R, Bizopoulos P, Kalatzis F, Naka KK, Fotiadis DI, Wang J, Garcia Garcia HM, Kimura T, Michalis LK, Serruys PW. Fusion of optical coherence tomographic and angiographic data for more accurate evaluation of the endothelial shear stress patterns and neointimal distribution after bioresorbable scaffold implantation: comparison with intravascular ultrasound-derived reconstructions. *Int J Cardiovasc Imaging* 2014;30(3):485-94.
3. Feldman CL, Ilegbusi OJ, Hu Z, Nesto R, Waxman S, Stone PH. Determination of in vivo velocity and endothelial shear stress patterns with phasic flow in human coronary arteries: a methodology to predict progression of coronary atherosclerosis. *American heart journal* 2002;143(6):931-9.
4. Tenekecioglu E, Torii R, Bourantas C, Crake T, Zeng Y, Sotomi Y, Onuma Y, Yilmaz M, Santoso T, Serruys PW. Preclinical assessment of the endothelial shear stress in porcine-based models following implantation of two different bioresorbable scaffolds: effect of scaffold design on the local haemodynamic micro-environment. *EuroIntervention : journal of EuroPCR in collaboration with the Working Group on Interventional Cardiology of the European Society of Cardiology* 2016;12(10):1296.
5. Wentzel JJ, Krams R, Schuurbiers JC, Oomen JA, Kloet J, van Der Giessen WJ, Serruys PW, Slager CJ. Relationship between neointimal thickness and shear stress after Wallstent implantation in human coronary arteries. *Circulation* 2001;103(13):1740-5.
6. Sakamoto S, Takahashi S, Coskun AU, Papafaklis MI, Takahashi A, Saito S, Stone PH, Feldman CL. Relation of distribution of coronary blood flow volume to coronary artery dominance. *The American journal of cardiology* 2013;111(10):1420-4.
7. Stone PH, Saito S, Takahashi S, Makita Y, Nakamura S, Kawasaki T, Takahashi A, Katsuki T, Nakamura S, Namiki A, Hirohata A, Matsumura T, Yamazaki S, Yokoi H, Tanaka S, Otsuji S, Yoshimachi F, Honye J, Harwood D, Reitman M, Coskun AU, Papafaklis MI, Feldman CL. Prediction of progression of coronary artery disease and clinical outcomes using vascular profiling of endothelial shear stress and arterial plaque characteristics: the PREDICTION Study. *Circulation* 2012;126(2):172-81.

Chapter 6

Strut protrusion and shape impact on endothelial shear stress: insights from pre-clinical study comparing Mirage and Absorb bioresorbable scaffolds

The effect of strut thickness on shear stress distribution in a preclinical model

Strut protrusion and shape impact on endothelial shear stress: insights from pre-clinical study comparing Mirage and Absorb bioresorbable scaffolds

Erhan Tenekecioglu, Yohei Sotomi, Ryo Torii, Christos Bourantas, Yosuke Miyazaki, Carlos Collet, Tom Crake, Solomon Su, Yoshinobu Onuma, Patrick W. Serruys

Int J Cardiovasc Imaging. 2017;33(9):1313-1322.

ABSTRACT

Purpose: Protrusion of scaffold struts is related with local coronary flow dynamics that can promote scaffold restenosis and thrombosis. That fact has prompted us to investigate *in vivo* the protrusion status of different types of scaffolds and their relationship with endothelial shear stress (ESS) distributions.

Method: Six Absorb everolimus-eluting Bioresorbable Vascular Scaffolds (Absorb, Abbott Vascular) and 11 Mirage sirolimus-eluting Bioresorbable Microfiber Scaffolds (Mirage, Manli Cardiology) were implanted in coronaries of eight mini pigs. Optical coherence tomography (OCT) was performed post-scaffold implantation and obtained images were fused with angiographic data to reconstruct the 3-dimensional coronary anatomy. Blood flow simulation was performed and ESS distribution was estimated for each scaffold. Protrusion distance was estimated using a dedicated software. Correlation between OCT-derived protrusion and ESS distribution was assessed for both scaffold groups.

Results: A significant difference was observed in the protrusion distances ($156\pm 137\mu\text{m}$ for Absorb, $139\pm 153\mu\text{m}$ for Mirage; $p=0.035$), whereas difference remained after adjusting the protrusion distances according to the luminal areas. Strut protrusion of Absorb is inversely correlated with ESS ($r=-0.369$, $p<0.0001$), whereas in Mirage protrusion was positively correlated with EES ($r=0.192$, $p<0.0001$).

Conclusion: Protrusion distance was higher in Absorb than in Mirage. The protrusion of the thick quadratic struts of Absorb has a tendency to lower shear stress in the close vicinity of struts. However, circular shape of the less thick struts of Mirage didn't show this trend in creating zone of recirculation around the struts. Strut geometry has different effect on the relationship between protrusion and shear stress in Absorb and Mirage scaffolds.

Key words: Protrusion; strut geometry; shear stress; bioresorbable scaffold

INTRODUCTION

A permanent metallic stent constitutes a foreign structure in the vessel wall that induces inflammatory reactions increasing the thrombosis risk at post-implantation follow up [1]. Bioresorbable scaffolds (BRS) have been introduced to address the disadvantages of metallic drug-eluting stents (DES) [2]. Despite its potential long term superiorities, BRS implantation requires some indispensable rules for the attention of good stent result at short and long term follow up[3]. Embedment of the stent / scaffold is one of the surrogate factor affecting the vessel wall reaction after implantation [4]. In metallic stents, the vessel wall stretch and injury have been shown to be related with the embedment status of the device [5, 6]. Not only the embedment, but also the strut protrusion and related local coronary flow hemodynamics, particularly endothelial shear stress (ESS) influence biological response of the vessel wall [7, 8]. Observational atherosclerosis studies have proposed that low ESS promotes atherosclerotic plaque growth in native vessel segments [9, 10] and neointimal hyperplasia in scaffolded segments after percutaneous coronary intervention (PCI) [8].

Optical coherence tomography (OCT) provides high resolution data and detailed insights compared to the intravascular ultrasound [11]. OCT-based computational fluid dynamic (CFD) studies enable to unravel the effects of stent / scaffold design on the local coronary flow behaviors at the strut levels [12]. We investigated the relationship between struts protrusion and local shear stress distributions in the vessel segments implanted with Absorb and Mirage.

METHOD

Study population

Eight Yucatan mini pigs with healthy coronaries underwent PCI in the three epicardial coronary arteries through the femoral access according to the standard procedures [13]. Six coronary arteries were implanted with a single Absorb everolimus-eluting Bioresorbable Vascular Scaffolds (Absorb BVS, Abbott Vascular), six coronaries with a Mirage sirolimus-eluting Bioresorbable Microfiber Scaffold (Mirage BRMS, Manli Cardiology) with 150-micron (μm) strut thickness (Mirage-150) and five coronary arteries with a Mirage BRMS with 125 μm strut thickness (Mirage-125). The protocol approval for the animal study was received from the Institutional Animal Care and Use Committee. The study was conducted in accordance to the

American Heart Association guidelines for preclinical research and the Guide for the Care and Use of Laboratory Animals [14].

Device description

Absorb BVS is composed of polymer backbone of poly L-lactic acid (PLLA), coated with a layer of a 1:1 mixture of poly D, L-lactic acid (PDLLA) eluting an anti-proliferative drug, everolimus ($100 \mu\text{.cm}^{-2}$). Polymer tubes are extruded into thick-walled, small diameter tubes followed by laser cutting [15]. Absorb BVS has $157 \mu\text{m}$ strut thickness and design of in-phase zig-zag hoops linked with bridges (**Figure1**).

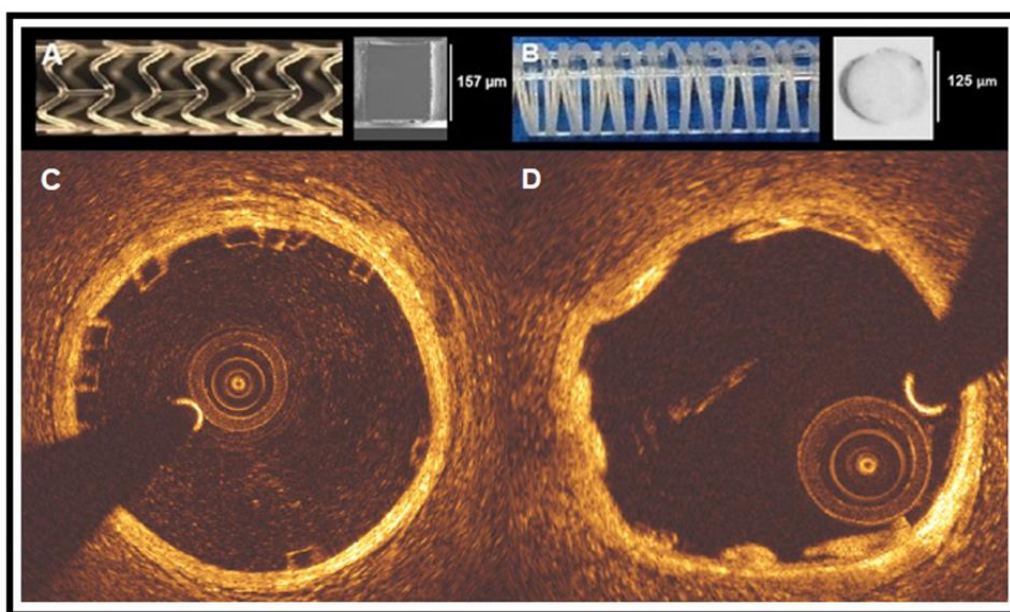


Figure 1. Absorb BVS 1.1 and the cross-section of Absorb BVS strut (A). Mirage BRMS and the cross-section of Mirage BRMS strut (B). While the struts of Absorb are translucent (C), in Mirage the struts are opaque (D) in OCT.

Mirage BRMS is made of PDLLA of which D (dextro-rotary)-isomer constitutes <5% of the total polylactic acid (PLA), coated with a biodegradable PLA delivering sirolimus. In the manufacturing process of Mirage scaffold, the polylactide monofilaments are winded and the helix-coiled structures are attached by longitudinal spine microfibers (**Figure 1**). The struts of Mirage have circular shape with thickness of $125 \mu\text{m}$ in scaffolds with diameter $\leq 3 \text{ mm}$ (Mirage-125), and $150 \mu\text{m}$ in scaffolds with diameter $\geq 3.5 \text{ mm}$ (Mirage-150). The helicoidal design is tightened by longitudinal spine microfibers providing radial strength for the Mirage (148.54 kPa) comparable to the Absorb (148.00 kPa) [16].

Data acquisition

Beside coronary angiography, OCT imaging was implemented after scaffold implantations in all the treated coronary arteries. The treated coronary arteries were evaluated with a frequency-domain OCT system (C8-XR OCT Intravascular Imaging System; St. Jude Medical, St. Paul, MN, USA) with a pull-back speed of 18 mm/sec. A non-occlusive flushing technique was utilized by injection of the contrast media for blood clearance. The OCT analysis was performed in the scaffolded segment at every 100 μm and in the non-scaffolded segments at every 400 μm longitudinal intervals. Coronary angiograms were analyzed with a semi-automated edge contour detection computer analysis system (CAAS QCA-2D system, Pie Medical Imaging BV, Maastricht, the Netherlands) with the dye-filled catheter used for calibration following the procedure. In each scaffold, the largest balloon diameter and maximal inflation pressure during post-dilatation were recorded and used to calculate the balloon/artery ratio (mean inflated balloon diameter/mean reference vessel diameter).

Protrusion analysis by optical coherence tomography

For protrusion analysis, the protrusion distances were estimated semi-automatically using a special version of QCU-CMS software (version 4.69, Leiden University Medical Center, Leiden, The Netherlands) [17] (**Figure 2**).

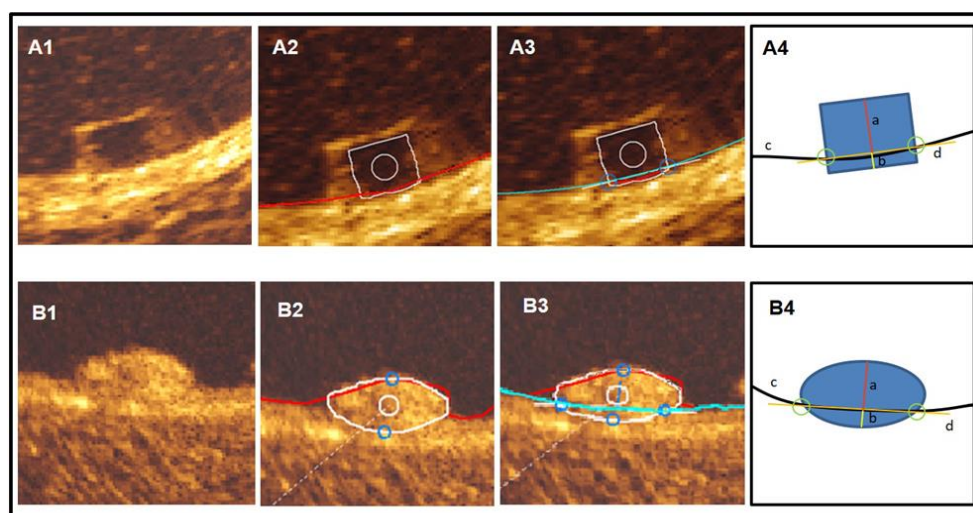


Figure 2. Rectangular shaped struts of Absorb BVS (A1) was automatically detected by QCU-CMS (v.14.9) after automatic detection of luminal contour (red contour) (A2) and interpolated luminal contour (blue contour) (A3), protrusion/embedment distances were detected using the methodology described by Sotomi et al (20) (A3). The illustration (A4) demonstrates the protrusion distance(a), embedment depth(b), interpolated luminal contour (c)and embedment line(d). The adluminal surface of the circular struts of Mirage BRMS (B1) were detected during automatic detection of luminal contour (red) (B2). After automatic detection of interpolated luminal contour (blue contour) (B3) protrusion distances were measured automatically by the software. (B3). The illustration (B4) demonstrates the protrusion distance(a), embedment depth(b), interpolated luminal contour (c)and embedment line(d).

The protrusion analysis in OCT was performed in the scaffolded segment at every 200 μm longitudinal interval using a methodology presented previously [17]. The luminal borders of both scaffold types and each Absorb BVS strut was automatically detected by the software. Since the QCU-CMS has no automatic detection function for the circular struts of Mirage BRMS, the struts of the Mirage were depicted as part of the lumen contours. Secondly, the interpolation of the true lumen contour allows an interpolation that detects the protrusion of the Mirage struts. In Absorb and Mirage groups, struts located at a side branch ostium were excluded from the protrusion analysis. Since, at hinge points the maximum width of the strut in Absorb is 800 μm , the struts with $>800 \mu\text{m}$ in Mirage were excluded from the protrusion analysis [4].

For the assessment of the intra- and inter-observer reproducibility, two analysts (Observer-A, ET, and observer-B, YM) performed OCT protrusion analysis. For the intra-observer reproducibility, observer-A repeated the measurements on the same pullback for 100 struts after an interval of 4-weeks. For the inter-observer reproducibility, the analysis was repeated in 100 struts by observer-B.

Coronary artery reconstruction

Coronary artery reconstruction was implemented using a validated methodology [18]. In x-ray angiographic and OCT images, the radiopaque markers and the anatomical landmarks (i.e., side branches), identified both on angiography and on OCT, were used to define the scaffolded segment and proximal-distal native vessel segments. In the region of interest (ROI), the OCT images depicting the scaffolded and the proximal-distal native vessel segments were identified and analyzed at a 0.1 mm interval in the scaffolded segment and 0.4 mm interval in the native vessel segments. The flow area was delineated and defined in the native segments by the luminal border and in the scaffolded segments by the adluminal side of the struts and by the luminal surface borders between the struts.

Two post-procedure end-diastolic angiographic images with at least 30°-angle difference illustrating the ROI with minimal foreshortening were selected with the table in the isocenter. In these images, the luminal borders were portrayed for the ROI and used to extract the luminal centerline which was then used for the three-dimensional (3D) luminal centerline of the ROI [18]. The borders of flow area identified on OCT images were then mounted perpendicularly onto the luminal centerline and side-branches seen in both OCT and

angiographic images were utilized to establish the absolute orientation of the OCT frames [18].

Computational flow dynamic study

The reconstructed images were processed with CFD techniques. A finite volume mesh was generated and then blood flow simulation was performed. ESS was estimated by solving the 3D Navier-Stokes equations (ANSYS Fluent, Canonsburg, Pennsylvania) [7]. To assess the effect of scaffold designs on the local hemodynamic micro-environment, the mesh density around the struts and within the boundary layer of the flow field between the struts was increased to have an average element edge of 30 μm (equal to $\frac{1}{4}$ of the strut thickness). Blood was assumed to be a homogeneous, Newtonian fluid with a viscosity of 0.0035 Pa.s and a density of 1,050 kg/m³. A steady flow profile was simulated at the inflow of the 3D models. Blood flow for each reconstruction was estimated by measuring, in the 2 angiographic projections, the number of frames required for the contrast agent to pass from the inlet to the outlet of the reconstructed segment, the volume of the reconstructed segment and the cine frame rate [7]. The arterial wall was considered to be rigid. No-slip conditions were imposed at the scaffold surface. At the outlet of the model zero pressure conditions were imposed. ESS at luminal surface was calculated as the product of blood viscosity and the gradient of blood velocity at the wall [9]. The ESS was measured in the native and the scaffolded segment around the circumference of the lumen per 5° interval (sector) and along the axial direction per 0.2 mm interval with the use of an in-house algorithm [9]. The recirculation zones in the vicinity of the struts were quantified based on the direction of the ESS vector and the centerline vector. Areas where the ESS vector had opposite direction to the centerline vector were considered to be exposed to recirculation zones. Recirculation zone percentage was calculated as the vessel luminal surface exposed to recirculation divided by in-device vessel luminal surface area.

Statistical analysis

Data are expressed as mean \pm standard deviation or median and inter-quartile range. Normality of distribution was tested by the Kolmogorov-Smirnov test. Group means for continuous variables with normal and non-normal distributions were compared using Student's t-tests and Mann-Whitney U tests, respectively. Categorical variables were compared using the Pearson's chi-square test or Fischer's exact test, as appropriate. Mixed linear model was used for the comparisons of continuous variables to take into account the

clustered nature of >1 scaffolds analyzed from the same animals, >1 cross-sections from the same scaffolds and >1 struts from the same cross-sections, which might result in unknown correlations among measurements within the clusters. The protrusion heights were analysed at cross-section level and device level for each scaffold type.

Reproducibility of protrusion/embedment analysis for Absorb was previously reported by Sotomi et al [17]. In the present study, reproducibility of the protrusion analysis for Mirage and Absorb were assessed with the interclass correlation coefficient (ICC) for absolute agreement (ICCa) with its 95 % confidence intervals (CI) using randomly selected 100 Mirage and 100 Absorb struts. An ICC<0.4 indicates bad agreement, an ICC between 0.4 and 0.75 indicates moderate agreement, and ICC values >0.75 indicates good agreement [17]. Analyses were performed using the statistical analysis program SPSS V.23 (SPSS Inc., Chicago, IL).

RESULTS

One left anterior descending coronary artery (LAD), three left circumflex coronary arteries (LCx) and two right coronary arteries (RCA) were implanted with an Absorb. In Mirage-150 group, 2 LAD, 1 LCX and 3 RCA, in Mirage-125 group, 2 LAD, 1 LCX and 2 RCA were treated. Procedural characteristics are shown in **Table 1**. Device length was shorter and expected maximum device diameter was larger in Mirage than in Absorb. Although maximum post-dilatation balloon pressure was significantly higher in Mirage, the expected diameter of post-dilatation balloon was comparable in both arms. In QCA, balloon/artery ratio (1.09 ± 0.048 for Absorb vs 1.13 ± 0.10 for Mirage; $p=0.32$) and acute percent recoil ($3.15 \pm 1.15\%$ for Absorb vs $2.56 \pm 2.92\%$ for Mirage; $p=0.65$) were comparable between the scaffold groups.

Table 1. Procedural details

Scaffold	Absorb BVS (n=6)	Mirage BRMS (n=11)	p
Implanted vessel			
LAD / LCx / RCA (n)	1 / 3 / 2	4 / 2 / 5	
Device			
Device nominal size (mm)	3.0 ± 0	3.18 ± 0.37	0.12
Device length(mm)	17.5±1.22	14.63±0.81	<0.001
Expected maximum device diameter (mm)	3.05 ± 0.12	3.43 ± 0.42	0.01
Maximum deployment pressure (atm)	7.0 ± 0	9.82 ± 4.85	0.28
Pre-dilatation			
Pre dilatation performed, n (%)	0(0%)	0(0%)	1.00
Post-dilatation			
Post dilatation performed, n (%)	6 (100%)	11 (100%)	1.00
Post dilatation balloon type			
Semi-compliant balloon, n (%)	0(0%)	0(0%)	
Non-compliant balloon, n (%)	6(100%)	11(100%)	1.00
Balloon nominal size (mm)	3.5 ± 0.0	3.57 ± 0.53	0.34
Maximum post-dilatation balloon pressure (atm)	8.5 ± 2.74	16.36 ± 2.34	0.001
Maximum expected post-dilatation balloon size (mm)	3.37 ± 0.093	3.65 ± 0.59	0.08

OCT results are summarized in **Table 2**. The analyses were performed at cross-section level (n=1306) and device level (n=17). In cross-section level analysis, in-device mean luminal area was significantly larger in Mirage than in Absorb [$9.07 \pm 2.26 \text{ mm}^2$ vs. $7.62 \pm 1.10 \text{ mm}^2$; $p=0.032$). The mean scaffold area was not significantly different between the study arms ($8.00 \pm 0.59 \text{ mm}^2$ for Absorb BVS vs. $9.17 \pm 2.00 \text{ mm}^2$ for Mirage BRMS; $p=0.063$). The mean ESS values were comparable between Absorb and Mirage at cross-section-level analyses [$0.73 \pm 2.19 \text{ Pa}$ vs. $0.93 \pm 1.83 \text{ Pa}$, respectively; $p=0.142$].

Table -2: OCT analyses results in scaffold groups.

Scaffold	Absorb BVS	Mirage BRMS	p
Device level	(n= 6)	(n=11)	
In-device mean lumen area (mm ²)	7.77 ± 0.70	9.34 ± 2.12	0.081
Distal reference mean lumen area (mm ²)	5.08 ± 1.31	6.81 ± 1.75	0.038
Proximal reference mean lumen area (mm ²)	7.46 ± 2.63	6.92 ± 1.71	0.588
Mean scaffold area (mm ²)	8.09 ± 0.63	9.40 ± 2.07	0.129
Mean ESS (Pa)	0.73 ± 0.25	0.93 ± 0.24	0.145
Embedment distance (µm)	22.4 ± 12.8	17.2 ± 13.1	0.43
Protrusion distance (µm)	156 ± 19	139 ± 21	0.035
Protrusion distance / mean lumen diameter	0.05 ± 0.40	0.04 ± 0.47	<0.0001
Cross-section level	(n= 636)	(n=670)	
In-device mean lumen area (mm ²)	7.62 ± 1.10	9.07 ± 2.26	0.032
Distal reference mean lumen area (mm ²)	4.74 ± 1.42	6.69 ± 1.95	0.028
Proximal reference mean lumen area (mm ²)	6.85 ± 2.20	6.77 ± 1.93	0.67
Mean scaffold area (mm ²)	8.00 ± 0.59	9.17 ± 2.0	0.063
Mean ESS (Pa)	0.73 ± 2.19	0.93 ± 1.83	0.142
Embedment distance (µm)	22 ± 37	17 ± 33	0.45
Protrusion distance (µm)	156 ± 137	139 ± 153	0.035
Protrusion distance / mean lumen diameter	0.05 ± 0.0038	0.04 ± 0.0034	<0.0001

Data are expressed as n (%) and mean ± standard deviation.

In the device level analysis, in-device mean lumen area was comparable between the scaffolds (7.77±0.70 mm² for Absorb vs 9.34±2.12 mm² for Mirage; p=0.081). Mean ESS was found comparable between Absorb (0.73±0.25 Pa) and Mirage (0.93±0.24 Pa) (p=0.145). In Absorb (n=6), 75.8±13.0 % and in Mirage (n=11), 62.7±17.6 % of the scaffolded surface was exposed to a low (<1 Pa) athero-promoting ESS environment (p=0.11).

Although numerically less percentage of recirculation area was estimated in Mirage ($2.84 \pm 1.61\%$) than in Absorb ($3.26 \pm 2.07\%$), the difference didn't reach to statistical significance ($p=0.65$).

Protrusion analyses

There were 4591 struts in 477 cross-sections from Absorb and 3314 struts in 593 cross-sections from Mirage recruited into the protrusion analysis. There were 128 and 97 malapposed struts in Absorb and Mirage, respectively. In cross-section level analysis, mean protrusion distances were significantly different between the scaffold groups [$156 \pm 137 \mu\text{m}$ for Absorb, $98.97 \pm 16.47\%$ of the strut thickness in Absorb, $139 \pm 153 \mu\text{m}$ for Mirage ($95.63 \pm 14.48\%$ of the strut thickness in Mirage-150, $89.52 \pm 17.09\%$ of the strut thickness in Mirage-125); $p=0.035$]. After adjusting the protrusion distances according to the luminal cross-section area, the difference in protrusion distances remained significant (0.050 ± 0.038 for Absorb vs 0.041 ± 0.034 for Mirage; $p < 0.0001$). Mean shear stress levels were inversely correlated with protrusion distances in Absorb ($r = -0.369$, $p < 0.0001$), whereas in Mirage, the correlation was in positive direction ($r = 0.192$, $p < 0.0001$) (**Figure 3**).

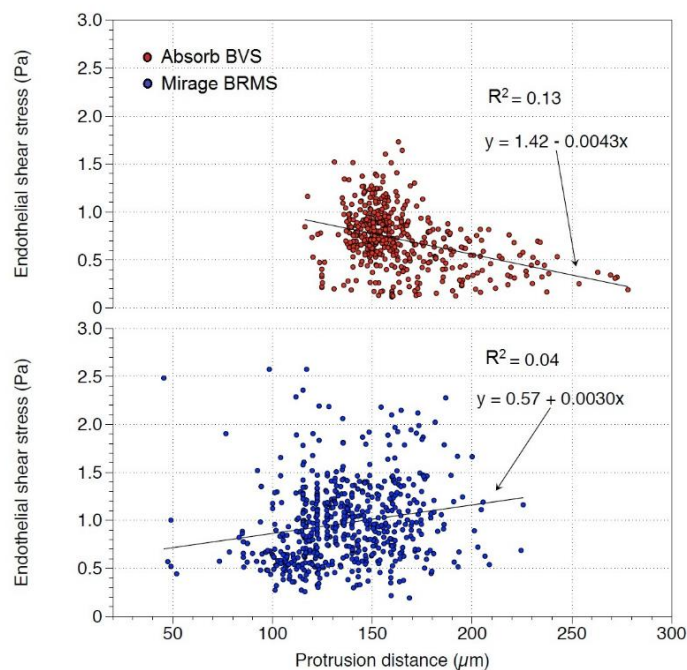
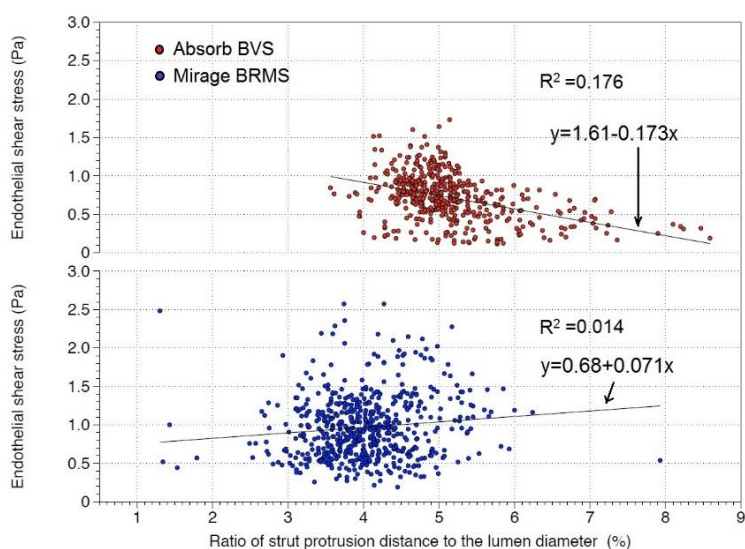
A**B**

Figure 3. Mean shear stress values were inversely correlated with protrusion distances in Absorb BVS. However, in Mirage BRMS, shear stress values were positively correlated with protrusion distances (A). Mean shear stress values were in negative correlation with the adjusted strut protrusion distances in Absorb BVS. In Mirage BRMS, mean shear stress was positively correlated with adjusted protrusion distances (B).

The same trend was observed with the adjusted protrusion distances; mean shear stress values were in negative correlation with the adjusted protrusion distances in Absorb ($r = -0.420$, $p < 0.0001$) and positively correlated with the adjusted protrusion distances in Mirage ($r = 0.116$, $p = 0.005$) (Figure 3).

The inter-observer [ICCa:0.884 CI (0.827-0.922)] and the intra-observer reproducibility [(ICCa:0.782 CI (0.675-0.854))] for the protrusion distances indicated good agreements in Mirage. In Absorb, the protrusion distances demonstrated well inter-observer [ICCa:0.942 CI (0.927-0.957)] and intra-observer [ICCa:0.968 CI (0.964-0.972)] reproducibility.

DISCUSSION

In the present study, we investigated the protrusion status of two different types of BRS and the effects of protrusion on the local hemodynamic microenvironment. The findings can be summarized as follows; 1- The strut protrusion distance was lower in Mirage compared to the Absorb; 2-Mean ESS was comparable between Absorb and Mirage scaffolds, 3- In Mirage, ESS had a positive correlation with strut protrusion, while in Absorb, ESS was inversely correlated with strut protrusion distance.

Scaffold implantation process represents a “double-edged sword”; the struts should be embedded well enough to prevent flow separation due to the protruded obstacles in the new constituted vessel surface. There is however an increased risk of vessel wall stretch and injury in case of deep embedment [4]. The balance should be respected meticulously during the implantation process to avoid from both vessel wall injury and increment in flow disruption.

Relationship between ESS and protrusion

Absorb appears to disrupt the coronary flow due to its thicker rectangular struts and high protrusion distances in the coronary lumen. Mirage, albeit lack of statistical significance, with its circular thinner struts, induced less flow separations which could be explained with the thinner streamlined strut cross-profile and the helicoidal design of the scaffold [19, 20]. Mean shear stress levels were found comparable between the scaffold groups. Despite weak correlation coefficients, ESS has a tendency to decrease with the protrusion distance in Absorb, while in Mirage shear stress is inversely proportional to the protrusion distance. This discrepancy in the relation between the protrusion and ESS in the scaffolds can be explained with the confounding factor of different strut shapes in the scaffolds. In Absorb, the non-streamlined thicker strut profile disrupts the laminar flow inducing lower shear stress around the rectangular struts due to the recirculation and stagnation zones [20]. The shear stress on top of the rectangular struts in Absorb is higher than the shear stress at upstream and downstream sides of the struts (**Figure 4**). But the non-linear increase in flow disruption

around the rectangular struts and related lower ESS levels should have dominated for the relation between ESS and protrusion distance in Absorb [20].

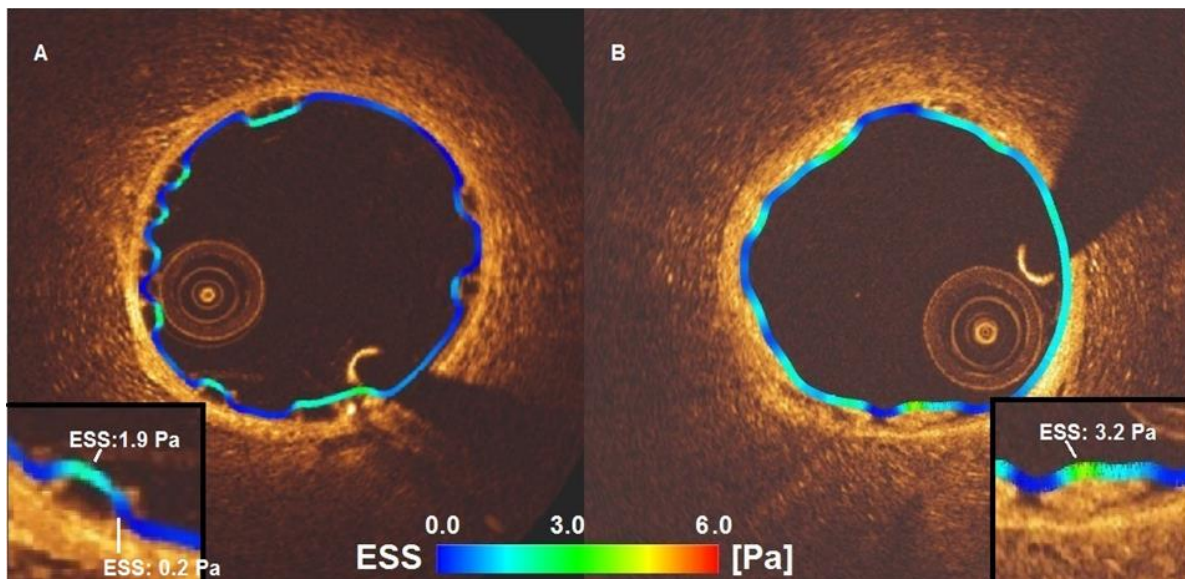


Figure 4. The shear stress distribution in a cross-section from Absorb (A) and Mirage (B). In Absorb, low shear stress zones can be seen between the struts wider than in Mirage. Despite comparable strut thicknesses in Absorb (157 μm) and Mirage (150 μm) the low shear stress zones (dark blue areas) are much less in Mirage scaffolds than in Absorb.

In Mirage, ESS was in positive relation with the strut protrusion which seems to be a paradox. However, reduced flow disruption due to the circular strut geometry and the gradual changes in the slope over the strut surface reversed the relation of ESS with strut protrusion [19, 20]. With the same protruded distances, circular geometries induce less flow disruptions and lower flow separation distances which provide less low shear values around the circular struts [20, 21]. Additionally, according to the Bernoulli principle, the flow accelerates over a streamlined geometry which may also help to explain the positive relation of shear stress with protrusion distance in Mirage. Accelerated flow velocity over the circular struts increases shear stress not only at the top surface but also at the upstream and downstream sides of the circular struts as the protrusion rises [22] [23] (**Figure 4**). In similar strut thicknesses, circular designs demonstrate better performance in terms of shear stress levels [24]. The shear stress distribution from the present study confirms this point. In scaffolds with comparable strut thicknesses, the shear stress distributions unraveled more physiologic shear stress levels in Mirage-150 group than in Absorb (**Figure 5**).

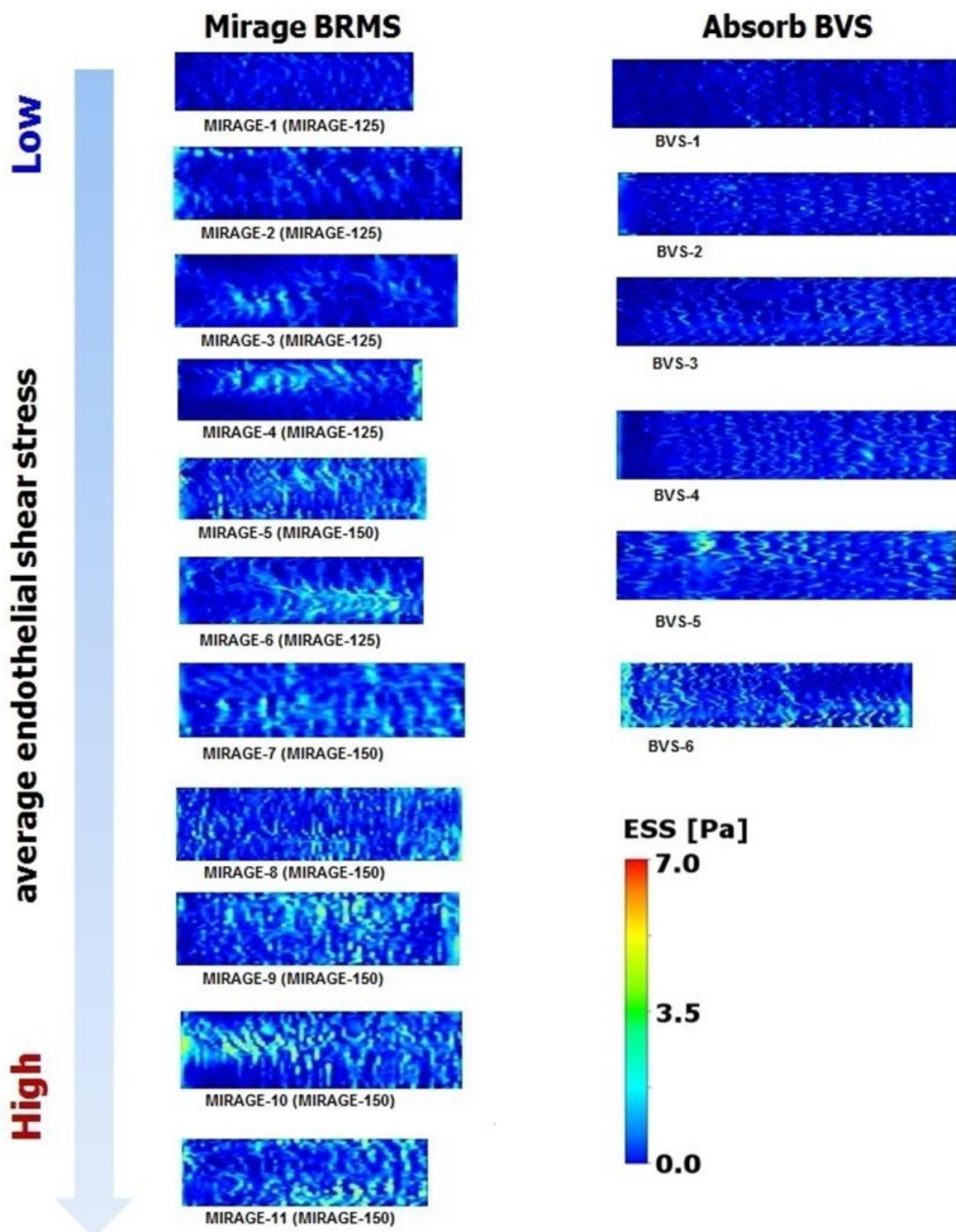


Figure 5. The shear stress distributions of each scaffold in carpet view. Circular struts demonstrate better performance than quadratic geometries in terms of shear stress distribution. The zones of shear stress within physiologic ranges seen more frequently in Mirage-150 than in Absorb BVS, despite comparable strut thicknesses.

The scaffolds with similar strut profile with Absorb BVS such as DREAMS 2G and DESolve, have comparable strut thicknesses (DREAMS 2G: 150 μm [25], DESolve: 150 μm [16]). Besides the strut thickness, the width of the strut is also another factor in penetration of the strut into the vessel wall during the implantation process [26][27]. While the width of the struts in Absorb is around 191 μm in the hoops, the struts of DREAMS and DESolve scaffolds have widths of 140 μm and 165 μm , which means that narrower struts can penetrate into the vessel wall deeper that corresponds to less protrusion and less flow disturbance. CFD modelings can be used to modify the strut design to reach more hemocompatible geometries.

Flow-disruption and decreased shear stress levels in the vicinity of the struts increase a tendency to thrombus formation which was demonstrated in bench studies [21]. Low shear stress has been incriminated for restenosis and stent/scaffold thrombosis at post-implantation follow up [28]. The flow separations beside the rectangular struts promote stagnation zones that create well-suited environment for thrombus formation. However, even with comparable aspect ratios with the quadratic geometries, the flow streamlines slipping over circular struts with less disruption decrease the risk of fibrin aggregation [21].

The fibrin accumulation and thrombus formation may affect the anti-proliferative drug kinetics. Drug diffusion from the polymer to the vessel wall can be interrupted by cumulated fibrin which may impoverish the endothelial lining through the accrued drug around the struts. Impaired endothelial sealing of the struts can increase re-stenosis risk at follow up [29]. At 30-day follow up, 2 animals from the present study sacrificed and underwent histopathological analysis. From Absorb (n=2) and Mirage (n=2), sections (n=12) from proximal, middle and distal portions of each scaffold were assessed by histopathologists. The fibrin score in Absorb (2.5 ± 0.55) was higher than in Mirage (2.17 ± 0.41) ($p = 0.26$) and endothelial coverage rate was lower in Absorb ($56.5 \pm 38.07\%$) than in Mirage ($82.33 \pm 18.99\%$) ($p = 0.18$). However, due to low case number there were no statistical differences between the scaffold groups (**Figure 6**).

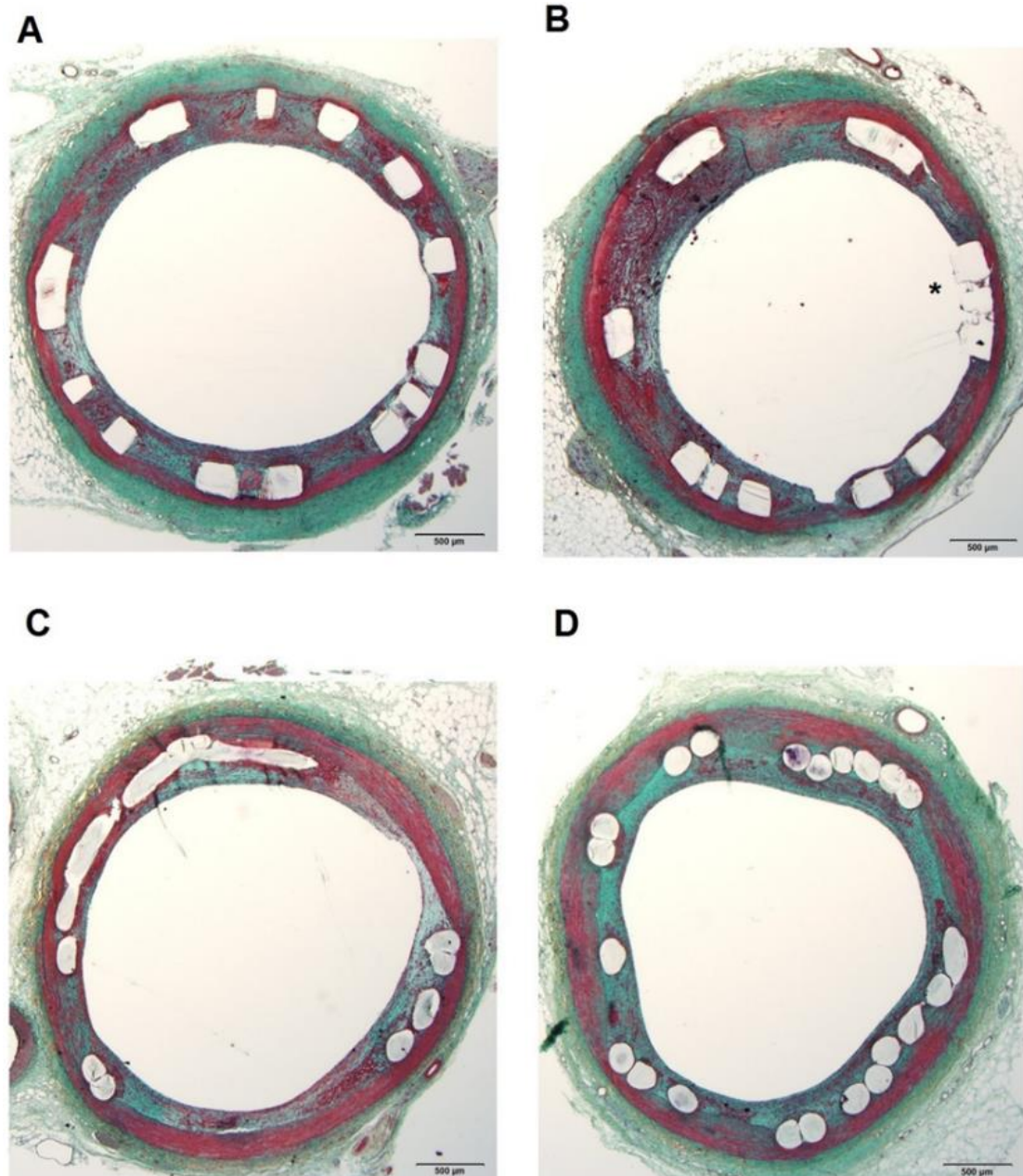


Figure 6. The histology sections from Absorb (A and B) revealed struts with insufficient endothelial coverage (*) whereas in Mirage (C and D), struts were detected fully covered by neointimal tissue.

Limitations

A significant limitation of the current analysis is that scaffold implantation was performed in healthy coronary arteries. Therefore, it was not possible to examine the implications of scaffold under-expansion or the composition of the underlying plaque on strut embedment which potentially influence the local flow hemodynamics. There were differences in the lumen areas in the two groups which are likely to affect the ESS values. Nevertheless, the difference in ESS was not statistically significant; in addition, in linear mixed effect analysis scaffold type

was independently associated with the ESS distribution. There was no clinical result for protrusion-ESS relationship in the current study. Due to low number of cases (totally 12 histology specimens from 4 scaffolds), we didn't present histopathology results at 30-day post-implantation in detail. However, clinical inferences can be exemplified from the literature. Finally, the protrusion software used for the analysis has been established for quadratic struts of Absorb. A well-designed software for circular struts may overcome the constrain of reproducibility in Mirage scaffolds.

CONCLUSION

Protrusion has impact on the local hemodynamics in bioresorbable scaffolds. Strut geometry has diverse effects on the relationship between protrusion distance and shear stress in Absorb and Mirage scaffolds. Protrusion analysis may contribute to figure out hemodynamic performance of the bioresorbable scaffolds.

Compliance with Ethical Standards

All applicable international and institutional guidelines for the care and use of animals were followed.

Disclosures

E. Tenekecioglu has a research grant from TUBITAK (The Scientific Council of Turkey). P.W. Serruys is a member of the International Advisory Board of Abbott Vascular. Y. Onuma is a member of the International Advisory Board of Abbott Vascular.

REFERENCES

1. Buchanan GL, Basavarajaiah S, Chieffo A: Stent thrombosis: incidence, predictors and new technologies. *Thrombosis* 2012, 2012:956962.
2. Serruys PW, Garcia-Garcia HM, Onuma Y: From metallic cages to transient bioresorbable scaffolds: change in paradigm of coronary revascularization in the upcoming decade? *Eur Heart J* 2012, 33(1):16-25b.
3. Sotomi Y, Onuma Y, Dijkstra J, Eggermont J, Liu S, Tenekecioglu E, Zeng Y, Asano T, de Winter RJ, Popma JJ *et al*: Impact of Implantation Technique and Plaque Morphology on Strut Embedment and Scaffold Expansion of Polylactide Bioresorbable Scaffold- Insights From ABSORB Japan Trial. *Circ J* 2016, 80(11):2317-2326.
4. Serruys PW, Suwannasom P, Nakatani S, Onuma Y: Snowshoe Versus Ice Skate for Scaffolding of Disrupted Vessel Wall. *JACC Cardiovasc Interv* 2015, 8(7):910-913.
5. Gunn J, Arnold N, Chan KH, Shepherd L, Cumberland DC, Crossman DC: Coronary artery stretch versus deep injury in the development of in-stent neointima. *Heart* 2002, 88(4):401-405.
6. Schwartz RS, Chronos NA, Virmani R: Preclinical restenosis models and drug-eluting stents: still important, still much to learn. *J Am Coll Cardiol* 2004, 44(7):1373-1385.
7. Papafaklis MI, Bourantas CV, Theodorakis PE, Katsouras CS, Naka KK, Fotiadis DI, Michalis LK: The effect of shear stress on neointimal response following sirolimus- and paclitaxel-eluting stent implantation compared with bare-metal stents in humans. *JACC Cardiovasc Interv* 2010, 3(11):1181-1189.
8. Bourantas CV, Papafaklis MI, Kotsia A, Farooq V, Muramatsu T, Gomez-Lara J, Zhang YJ, Iqbal J, Kalatzis FG, Naka KK *et al*: Effect of the endothelial shear stress patterns on neointimal proliferation following drug-eluting bioresorbable vascular scaffold implantation: an optical coherence tomography study. *JACC Cardiovascular interventions* 2014, 7(3):315-324.
9. Stone PH, Saito S, Takahashi S, Makita Y, Nakamura S, Kawasaki T, Takahashi A, Katsuki T, Nakamura S, Namiki A *et al*: Prediction of progression of coronary artery disease and clinical outcomes using vascular profiling of endothelial shear stress and arterial plaque characteristics: the PREDICTION Study. *Circulation* 2012, 126(2):172-181.
10. Samady H, Eshtehardi P, McDaniel MC, Suo J, Dhawan SS, Maynard C, Timmins LH, Quyyumi AA, Giddens DP: Coronary artery wall shear stress is associated with progression and transformation of atherosclerotic plaque and arterial remodeling in patients with coronary artery disease. *Circulation* 2011, 124(7):779-788.
11. Waksman R, Kitabata H, Prati F, Albertucci M, Mintz GS: Intravascular ultrasound versus optical coherence tomography guidance. *J Am Coll Cardiol* 2013, 62(17 Suppl):S32-40.
12. Tenekecioglu E, Torii R, Bourantas C, Crake T, Zeng Y, Sotomi Y, Onuma Y, Yilmaz M, Santoso T, Serruys PW: Preclinical assessment of the endothelial shear stress in porcine-based models following implantation of two different bioresorbable scaffolds: effect of scaffold design on the local haemodynamic micro-environment. *EuroIntervention* 2016, 12(1).
13. Williams PD, Malik N, Kingston PA: Coronary angiography and percutaneous coronary intervention in the porcine model: a practical guide to the procedure. *Animal* 2012, 6(2):311-320.
14. . In: *Guide for the Care and Use of Laboratory Animals*. 8th edn. Washington (DC); 2011.

15. Alexy RD, Levi DS: Materials and manufacturing technologies available for production of a pediatric bioabsorbable stent. *Biomed Res Int* 2013, 2013:137985.
16. Ormiston JA, Webber B, Ubod B, Darremont O, Webster MW: An independent bench comparison of two bioresorbable drug-eluting coronary scaffolds (Absorb and DESolve) with a durable metallic drug-eluting stent (ML8/Xpedition). *EuroIntervention : journal of EuroPCR in collaboration with the Working Group on Interventional Cardiology of the European Society of Cardiology* 2015, 11(1):60-67.
17. Sotomi Y, Tateishi H, Suwannasom P, Dijkstra J, Eggermont J, Liu S, Tenekecioglu E, Zheng Y, Abdelghani M, Cavalcante R *et al*: Quantitative assessment of the stent/scaffold strut embedment analysis by optical coherence tomography. *The international journal of cardiovascular imaging* 2016, 32(6):871-883.
18. Bourantas CV, Papafaklis MI, Lakkas L, Sakellarios A, Onuma Y, Zhang YJ, Muramatsu T, Diletti R, Bizopoulos P, Kalatzis F *et al*: Fusion of optical coherence tomographic and angiographic data for more accurate evaluation of the endothelial shear stress patterns and neointimal distribution after bioresorbable scaffold implantation: comparison with intravascular ultrasound-derived reconstructions. *The international journal of cardiovascular imaging* 2014, 30(3):485-494.
19. Seo T, Schachter LG, Barakat AI: Computational study of fluid mechanical disturbance induced by endovascular stents. *Ann Biomed Eng* 2005, 33(4):444-456.
20. Jimenez JM, Davies PF: Hemodynamically driven stent strut design. *Annals of biomedical engineering* 2009, 37(8):1483-1494.
21. Jimenez JM, Prasad V, Yu MD, Kampmeyer CP, Kaakour AH, Wang PJ, Maloney SF, Wright N, Johnston I, Jiang YZ *et al*: Macro- and microscale variables regulate stent haemodynamics, fibrin deposition and thrombomodulin expression. *Journal of the Royal Society, Interface* 2014, 11(94):20131079.
22. Schlichting H, Gersten K: Boundary-layer theory, 8th rev. and enl. edn. Berlin ; New York: Springer; 2000.
23. Anderson JD: Fundamentals of Aerodynamics, 4 edn: McGrawHill; 2007.
24. Mejia J, Ruzzeh B, Mongrain R, Leask R, Bertrand OF: Evaluation of the effect of stent strut profile on shear stress distribution using statistical moments. *Biomed Eng Online* 2009, 8:8.
25. Campos CM, Muramatsu T, Iqbal J, Zhang YJ, Onuma Y, Garcia-Garcia HM, Haude M, Lemos PA, Warnack B, Serruys PW: Bioresorbable drug-eluting magnesium-alloy scaffold for treatment of coronary artery disease. *International journal of molecular sciences* 2013, 14(12):24492-24500.
26. Selvadurai APS, Atluri SN: Contact mechanics in the engineering sciences. Duluth, GA: Tech Science Press; 2010.
27. Johnson KL, Johnson KL: Contact Mechanics: Cambridge University Press; 1987.
28. Koskinas KC, Chatzizisis YS, Antoniadis AP, Giannoglou GD: Role of endothelial shear stress in stent restenosis and thrombosis: pathophysiologic mechanisms and implications for clinical translation. *Journal of the American College of Cardiology* 2012, 59(15):1337-1349.
29. Joner M, Finn AV, Farb A, Mont EK, Kolodgie FD, Ladich E, Kutys R, Skorija K, Gold HK, Virmani R: Pathology of drug-eluting stents in humans: delayed healing and late thrombotic risk. *J Am Coll Cardiol* 2006, 48(1):193-202.

The effect of strut thickness on shear stress distribution in a preclinical model

Erhan Tenekecioglu, Ryo Torii, Christos Bourantas, Yosuke Miyazaki, Carlos Collet, Rasha Al-Lameé, Kadem Al-Lameé, Yoshinobu Onuma, Patrick W. Serruys

Int J Cardiovasc Imaging 2017;33(11):1675-1676.

CASE REPORT

In-vitro and *in-silico* studies have shown that stent design and struts thickness introduce significant changes in local hemodynamics. The protruding struts disrupt the laminar flow with the impacts of strut thickness and strut shape. Angiographic and optical coherence tomography (OCT) data were implemented to reconstruct three-dimensional (3D) geometry of the right coronary artery (RCA) of a healthy mini-swine implanted with 3.0x14 mm ArterioSorb (Arterius, UK) with 95micron (μm) strut thickness in proximal segment (final post-dilatation mean lumen diameter:2.78 mm) and 3.0x14 mm ArterioSorb with 120 μm strut thickness in mid-segment (final post-dilatation mean lumen diameter :2.80 mm) of the vessel.

During computational fluid dynamic (CFD) study, endothelial shear stress (ESS) was quantified in the scaffolded segment around the circumference of the lumen per 5°-subunit and along the axial direction per 200 μm interval.¹ Median ESS was lower in the distal scaffold (ArterioSorb-120 μm) (1.17 [0.78-1.55] Pa) than in the proximal scaffold (ArterioSorb-95 μm) (1.25 [0.92-1.88] Pa) in Newtonian steady flow simulation($p<0.0001$). 37.4% of the scaffolded surface in ArterioSorb-120 μm and 32.6% in ArterioSorb-95 μm was exposed to a low (<1 Pa) athero-promoting ESS (Figure). The p-value is based on 5°-subunit (n=15984) analysis using mixed effects regression model.

The difference in ESS may stem from strut thickness, luminal diameter, vessel curvature and flow boundary conditions. In the present case, after excluding other factors, lower ESS in ArterioSorb-120 μm is presumably ascribed to the thicker struts (Figure). However, even in ArterioSorb-120 μm , the shear stress was not as low as reported in Absorb BVS (Median ESS:0.57 Pa)² which should be attributed to the thinner struts of ArterioSorb.

Compliance with Ethical Standards

All applicable international and institutional guidelines for the care and use of animals were followed.

Disclosures:

E. Tenekecioglu has a research grant from TUBITAK (The Scientific Council of Turkey). P.W. Serruys is a member of the International Advisory Board of Abbott Vascular. Y. Onuma is a member of the International Advisory Board of Abbott Vascular.

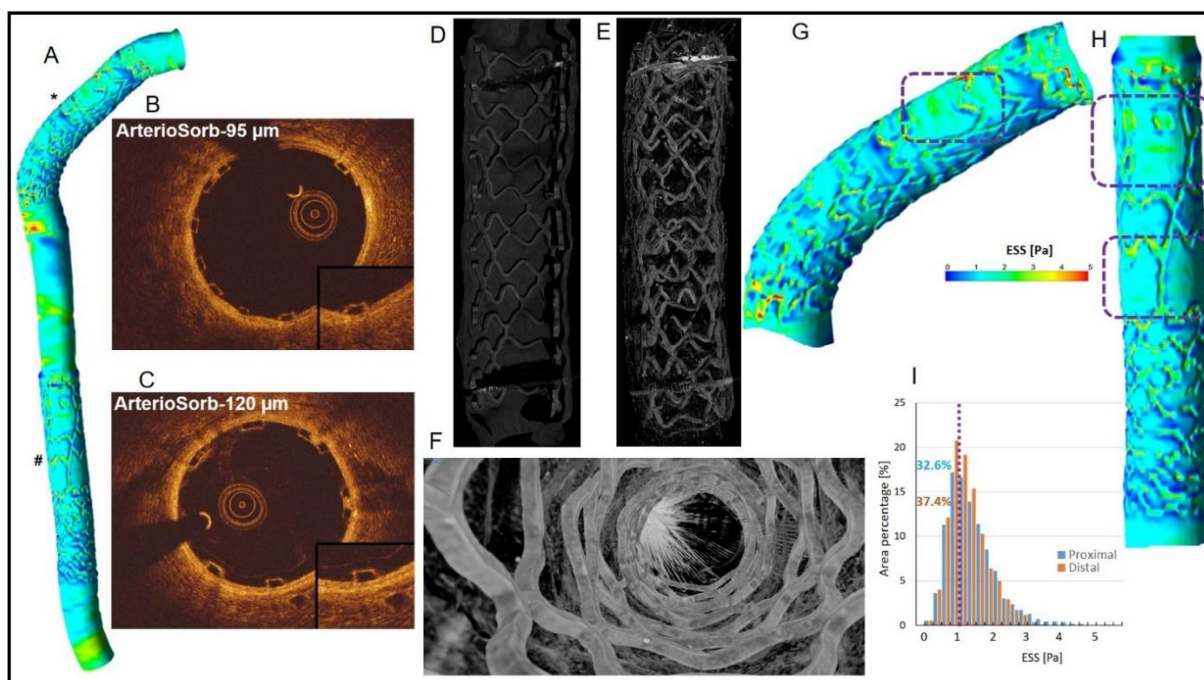


Figure. The CFD model of the two ArterioSorb scaffolds (* ArterioSorb-95 μm , # ArterioSorb-120 μm) with different strut thicknesses in RCA (Panel A). OCT demonstrates well apposed struts in ArterioSorb-95 μm (Panel B) and in ArterioSorb-120 μm (Panel C). Micro-computed tomography shows the scaffold architectures without any discontinuity in ArterioSorb-95 μm (Panel D) and in ArterioSorb-120 μm (Panel E and F). In proximal (Panel G) and the distal scaffolds (Panel H), there are wide zones with smooth surfaces (dotted zones) which are considered to be the result of cardiac motion during the OCT pullback. The histograms (Panel I) demonstrate the percentages of the vessel surface exposed to low-ESS (<1 Pa) in scaffolded vessel segments.

REFERENCES

1. Tenekecioglu E, Torii R, Bourantas C, et al. Preclinical assessment of the endothelial shear stress in porcine-based models following implantation of two different bioresorbable scaffolds: effect of scaffold design on the local haemodynamic micro-environment. *EuroIntervention : journal of EuroPCR in collaboration with the Working Group on Interventional Cardiology of the European Society of Cardiology*. 2016;12(10):1296.
2. Tenekecioglu E, Torii R, Bourantas C, et al. Assessment of the hemodynamic characteristics of Absorb BVS in a porcine coronary artery model. *International journal of cardiology*. 2017;227:467-473.

Post-implantation shear stress assessment: an emerging tool for differentiation of bioresorbable scaffolds

Erhan Tenekecioglu, Ryo Torii, Yuki Katagiri, Ply Chichareon, Taku Asano, Yosuke Miyazaki, Kuniaki Takahashi, Rodrigo Modolo, Rasha Al-Lamee, Kadem Al-Lamee, Carlos Collet, Johan H.C. Reiber, Kerem Pekkan, Robert van Geuns, Christos V. Bourantas, Yoshinobu Onuma, Patrick W. Serruys

Int J Cardiovasc Imaging. 2019;35(3):409-418.

ABSTRACT

Objective: Optical coherence tomography based computational flow dynamic (CFD) modeling provides detailed information about the local flow behavior in stented/scaffolded vessel segments. Our aim is to investigate the *in-vivo* effect of strut thickness and strut protrusion on endothelial wall shear stress (ESS) distribution in ArterioSorb Absorbable Drug-Eluting Scaffold (ArterioSorb) and Absorb everolimus-eluting Bioresorbable Vascular Scaffold (Absorb) devices that struts with similar morphology (quadratic structure) but different thickness.

Methods: In three animals, six coronary arteries were treated with ArterioSorb. At different six animals, six coronary arteries were treated with Absorb. Following three-dimensional(3D) reconstruction of the coronary arteries, Newtonian steady flow simulation was performed and the ESS were estimated. Mixed effects models were used to compare ESS distribution in the two devices.

Results: There were 4591 struts in the analyzed 477 cross-sections in Absorb (strut thickness=157 μ m) and 3105 struts in 429 cross-sections in ArterioSorb (strut thickness=95 μ m) for the protrusion analysis. In cross-section level analysis, there was significant difference between the scaffolds in the protrusion distances. The protrusion was higher in Absorb (97% of the strut thickness) than in ArterioSorb (88% of the strut thickness). ESS was significantly higher in ArterioSorb (1.52 \pm 0.34Pa) than in Absorb (0.73 \pm 2.19Pa) (p=0.001). Low- and very-low ESS data were seen more often in Absorb than in ArterioSorb.

Conclusions: ArterioSorb is associated with a more favorable ESS distribution compared to the Absorb. These differences should be attributed to different strut thickness/strut protrusion that has significant effect on shear stress distribution.

Keywords: Bioresorbable scaffolds; shear stress; computational fluid dynamics; scaffold design

INTRODUCTION

As a promising technology, bioresorbable scaffolds (BRS) introduced new terms such as *degradation, disappearance* and *recovery in vasomotricity*, into the interventionalists' jargon. However, relatively high thrombosis events have been a serious setback in the development of this technology and jeopardized the *change in the paradigm* in percutaneous coronary revascularization [1, 2]. In the era of metallic DES, beside the implantation techniques, the stent design and strut thickness were deemed responsible for the adverse events [3, 4].

Stent/scaffold implantation creates a new endoluminal surface with near-wall blood flow interference that have major mechano-transduction impact [5]. Compared to pre-implantation, in instrumented vessel segments disturb the blood flow in relation to the scaffold design, particularly strut geometry and strut thickness [6, 7]. The blood rheology, local hemodynamic factors, prominently shear stress, play an important role in the vessel wall biology [5]. While laminar and relatively high shear stress is *athero-protective* and holds the platelets and endothelium *quiescent*, low and oscillatory shear stress upregulates inflammatory oxidative reactions, can induce thrombus formation, promote reactive neointima and subject the vessel wall to atherosclerotic changes [8, 9].

Optical coherence tomography (OCT) based computational flow dynamic model provides detail information on the local flow environment in stented/scaffolded vessel segments [10]. Our aim was to investigate *in-vivo* the effect of quadratic strut designs and strut protrusion on shear stress distribution in the vessel segments treated with BRS.

METHODS

Study design and animal models

We analyzed data from Yucatan mini pigs implanted with Arteriosorb™ Absorbable Drug-Eluting Scaffold (ArterioSorb, Arterius Ltd., Leeds, UK) and Absorb everolimus-eluting Bioresorbable Vascular Scaffold (Absorb BVS, Abbott Vascular, Santa Clara, CA, USA). In three animals, six coronary arteries were treated with ArterioSorb and in other six animals, six coronary arteries were treated with Absorb." Study protocol was approved by the Institutional Animal Care and Use Committee of the testing facility (AccelLAB Inc., Boisbriand, Quebec, Canada) and were in compliance with the Canadian Council on Animal Care regulations. Animal husbandry, medication administration, and stent implantation were performed according to standards. The Testing Facility is accredited by the Association for

Assessment and Accreditation of Laboratory Animal Care (AAALAC) and the Canadian Council on Animal Care (CCAC) [11].

Scaffold design

ArterioSorb is made up of poly L-lactic acid (PLLA), coated with a layer of poly D, L-lactic acid (PDLLA) eluting rapamycin ($1.45 \mu\text{g}/\text{mm}^2$). ArterioSorb is manufactured using melt processing (extrusion) and die-drawing (solid-phase orientation) techniques with strut thicknesses of $95 \mu\text{m}$ and $120 \mu\text{m}$. The strut width is $170 \mu\text{m}$. ArterioSorb is composed of an 8-cell open-cell design with smaller cells at the center to improve the radial strength and cell connectors distributed in a spiral design (**Figure 1**). The vessel coverage ratio in ArterioSorb is 29%. ArterioSorb has two pairs of radiopaque markers at distal and proximal edge of the scaffold. Absorb is produced from PLLA, coated with a layer of a 1:1 mixture of an amorphous matrix of PDLLA and elutes everolimus ($8.2 \mu\text{g}/\text{mm}^2$). Absorb is manufactured using extrusion and laser machining techniques, has $157\mu\text{m}$ strut thickness and design of in-phase zig-zag hoops linked with bridges (**Figure1**). The strut width is $176 \mu\text{m}$. The vessel coverage ratio of Absorb is 27%. Absorb has two pairs of radiopaque markers at distal and proximal edge of the scaffold.

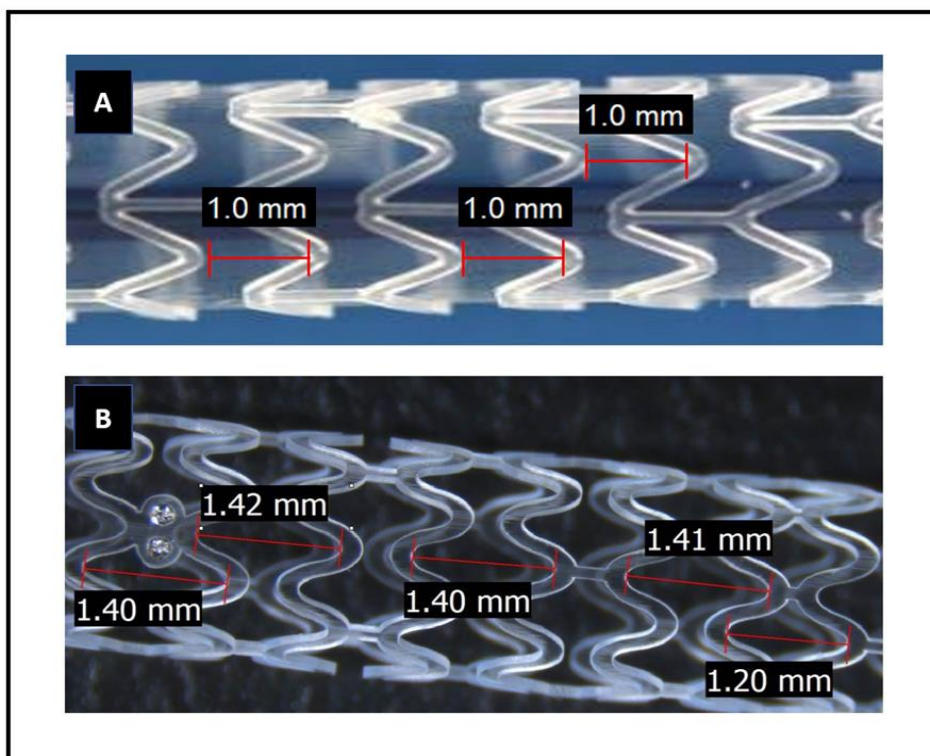


Figure 1. The design of the Absorb bioresorbable vascular scaffold (Absorb) (A) and ArterioSorb bioresorbable scaffold (ArterioSorb) (B). In Absorb, the length of the cells is the same where as in ArterioSorb, the cells in the middle of the device are smaller than the cells in the proximal and distal of the scaffold.

Scaffold implantation

To prevent any effect of swirling-flow due to vessel curvature, on the scaffolded segment ESS distribution, we didn't include the cases with increased curvature. After pre-implant angiography was obtained, the target scaffold diameter was calculated from the reference vessel diameter which was 1.1 x (with a range of 1.05 x to 1.15 x) the reference vessel diameter. Then the device was introduced into the selected artery by advancing the balloon catheter through the guide catheter and over the guidewire to the deployment site. The scaffolds were deployed according to the Interventionalist's judgment using the product compliance charts and target vessel size as a guide, to achieve a targeted balloon-to-artery ratio of 1.1:1 with a range of 1.05:1 to 1.15:1. The balloon was not deployed below nominal pressure or higher than Rated Burst Pressure. The balloon was inflated slowly, at a 1 atm increment every 2 seconds until the scaffold is expanded. The final pressure should be maintained for at least 30 seconds. An angiogram of the balloon at full inflation was recorded and the maximal inflation pressure was noted. Post-dilatation was performed in all cases using a non-compliant balloon or by a semi-compliant balloon to ensure good apposition of the scaffold, and the target balloon to artery ratio met the requirements, for vessel diameters up to 3.20mm at the discretion of the operator.

Data acquisition

X-ray angiography was performed using Siemens Axiom cardiac angiography system (Siemens, Erlangen, Germany). For the post-implantation and post-dilatation angiographies, two projections with at least 25 degrees apart from each other were selected. When multiple balloon inflations were performed, the image with the highest pressure was used for analysis. Quantitative coronary angiography (QCA) measurements were obtained from these images using the QAngio® XA 7.3 system and Medis QCA-CMS 6.0 software (Medis, Leiden, The Netherlands).

OCT was performed before and after scaffold implantation in all treated coronary arteries, using a frequency-domain (FD) OCT system (Illumien OCT Intravascular Imaging System; St. Jude Medical, St. Paul, MN, USA). When post-dilatation was performed, OCT was performed following each post-dilatation and at the end of the procedure to document OCT parameters at each successive stage. A non-occlusive flushing technique was used for blood clearance by injection of contrast media. After administration of nitrates (0.2 mg NTG intracoronary), the

FD-OCT imaging catheter was advanced into the coronary artery in rapid exchange technique. The OCT catheter was advanced beyond the device, into the distal vessel, and pulled back to a point proximal to the device frequently to the ostium of the treated vessel. After FD-OCT catheter placement, blood was cleared by injection of iso-osmolar contrast. The FD-OCT pull-back was started as soon as the artery was cleared from blood and stopped when the imaging core reached the guiding catheter. Qualitative analysis of the captured images was then performed (such as strut malapposition) off line. The acquired data were stored in DICOM format and transferred to a workstation for further analysis. The OCT analysis was performed using QCU-CMS software (version 4.69, Leiden University Medical Center, Leiden, The Netherlands) [12].

Protrusion analysis by optical coherence tomography

For protrusion analysis, the protrusion distances were estimated semi-automatically using a special version of QCU-CMS software (version 4.69, Leiden University Medical Center, Leiden, The Netherlands) [12]. The protrusion analysis in OCT was performed in the scaffolded segment at every 200 μm longitudinal interval using a methodology presented previously [12]. Interobserver reproducibility analysis in protrusion in quadratic struts has been published previously [12].

Coronary artery reconstruction

Coronary artery reconstruction was conducted implementing a validated methodology [13]. In x-ray angiographic and OCT images, anatomical landmarks (i.e., side branches) and the radiopaque markers were identified and used to define the scaffolded segment and proximal-distal native vessel segments. After matching, the OCT images portraying the scaffolded and the proximal-distal non-scaffolded native vessel segments were analyzed at a 100-micron (μm) interval in the scaffolded segment and 400 μm interval in the native vessel segments. The flow area was traced and defined in the native segments by the luminal border and in the scaffolded segments by the adluminal side of the struts and by the vessel luminal surface borders between the struts.[14]

Two post-procedure end-diastolic angiographic images with at least 25°-angle difference showing the analyzed OCT frames (region of interest, ROI) with minimal foreshortening were selected. In these images, the luminal borders were delineated for the ROI and processed to

extract the luminal centerline which was then used for the three-dimensional (3D) luminal centerline of the ROI [13]. The borders of flow area identified on OCT images were then mounted perpendicularly onto the luminal centerline and side-branches seen in both OCT and angiographic images were utilized to establish the absolute orientation of the OCT frames [13].

Computational flow dynamic study

The reconstructed models were processed with CFD techniques. A finite volume mesh was generated and then blood flow simulation was performed. ESS was estimated by solving the 3D Navier-Stokes equations (ANSYS Fluent, Canonsburg, Pennsylvania) [15]. To assess the effect of scaffold designs on the local flow patterns, the mesh density around the struts and within the boundary layer of the flow between the struts was increased to have an average element edge equal to 1/5 of the strut thickness. Blood was assumed to be a homogeneous, Newtonian fluid with a viscosity of 0.0035 Pa.s and a density of 1,050 kg/m³. A steady flow profile was simulated at the inflow of the 3D models. Blood flow for each reconstruction was estimated by measuring, in the 2 angiographic projections, the number of frames required for the contrast agent to pass from the inlet to the outlet of the reconstructed segment, the volume of the reconstructed segment and the cine frame rate [15]. The arterial wall was considered to be rigid and no-slip conditions were implemented at the scaffold surface. At the outlet of the model zero pressure conditions were imposed. ESS at vessel luminal surface was calculated as the product of blood viscosity and the gradient of blood velocity at the wall [16]. The ESS was measured in the native and the scaffolded segment around the circumference of the lumen per 5° interval (sector) and along the axial direction per 200 µm interval with the use of an in-house algorithm [16].

Statistical analysis

Continuous variables were tested for normality distribution with Kolmogorov-Smirnov test and are presented as mean ± SD or median (interquartile range) as appropriate. Categorical variables are presented as counts and percentages. Continuous variables were compared by the Kruskal-Wallis test or Mann Whitney-U test. Categorical variables were compared by the Pearson Chi-square test. Since the data have multi-level structure and unbalanced design, mixed effects model was used for statistical analysis. To compare the ESS values in different scaffold groups, the multi-level model was initially built with fixed effects on scaffold type,

cross-sectional area and interaction of the scaffold type with cross-sectional area and random effects on animal ID, scaffold ID and cross-section ID. After comparing different models using maximum likelihood, best fitted model was selected. A $p < 0.05$ was considered statistically significant. Analyses were done using the statistical analysis program SPSS V.21, R V. 3.2.3 and the R package lme4.[17]

RESULTS

Three left anterior descending coronary artery (LAD) and 3 right coronary arteries (RCA) were implanted with an ArterioSorb and 1 LAD, 3 left circumflex (LCx) and 2 RCA with an Absorb. Scaffold dimensions, the flow velocities for each investigated vessel and procedural parameters are shown in **Table 1 and Table 2**. In QCA, the dimensions of scaffolded segment and non-scaffolded segments are shown in **Table 3**. Mean lumen diameters and areas are comparable between the two scaffold groups.

In OCT, in the device level analysis in-scaffold mean lumen area were comparable in the two scaffold groups. In the cross-section level analysis, in-scaffold mean lumen area was slightly higher in Absorb ($7.62 \pm 1.10 \text{ mm}^2$) compared with the ArterioSorb ($7.35 \pm 0.86 \text{ mm}^2$) ($p=0.052$) (**Table 4**).

Table 1. Scaffold dimensions and flow velocities for ArterioSorb and Absorb

Scaffold	Animal	Vessel	Scaffolded vessel segment	Scaffold size (mm)	Mean lumen diameter after post-dilatation (mm)	Flow velocities (m/s)
ArterioSorb-1	A	LAD	Distal	3.0 x 14	3.28	0.181
ArterioSorb-1	A	RCA	Mid	3.0 x 14	3.37	0.098
ArterioSorb-1	B	LAD	Mid	3.0 x 14	3.32	0.138
ArterioSorb-1	B	RCA	Proximal	3.0 x 14	3.00	0.135
ArterioSorb-1	C	LAD	Mid	3.0 x 14	3.16	0.155
ArterioSorb-1	C	RCA	Distal	3.0 x 14	3.20	0.147
Absorb BVS -1	E	RCA	Mid	3.0 x 18	3.32	0.104
Absorb BVS -2	D	LCx	Mid	3.0 x 18	3.06	0.103
Absorb BVS -3	F	LCx	Proximal	3.0 x 18	3.32	0.091
Absorb BVS -4	G	LAD	Mid	3.0 x 18	3.16	0.172
Absorb BVS -5	I	RCA	Mid	3.0 x 15	3.16	0.108
Absorb BVS -6	H	LCx	Mid	3.0 x 18	3.32	0.104

Table 2. Procedural details

Scaffold	Absorb (n=6)	ArterioSorb (n=6)	p
Implanted vessel			
LAD / LCx / RCA (n)	1 / 3 / 2	4 / 2 / 5	
Device			
Device nominal size (mm)	3.0 ± 0	3.0 ± 0	0.12
Device length(mm)	17.5±1.22	14.00±0	<0.001
Maximum deployment pressure (atm)	7.0 ± 0	14.71 ± 2.94	
Pre-dilatation			
Pre-dilatation performed, n (%)	0(0%)	0(0%)	1.00
Post-dilatation			
Post dilatation performed, n (%)	6 (100%)	6 (100%)	1.00
Post dilatation balloon type			
Semi-compliant balloon, n (%)	0(0%)	0(0%)	
Non-compliant balloon, n (%)	6(100%)	6(100%)	1.00
Maximum post-dilatation balloon pressure (atm)	8.5 ± 2.7	16.2 ± 3.0	0.001
Maximum expected post-dilatation balloon size(mm)	3.37 ± 0.093	3.65 ± 0.59	0.08

Table 3. QCA variables in scaffold groups

	Absorb (157µm) n=6	ArterioSorb (95µm) n=6	p
Mean Lumen Diameter Pre-implantation (scaffolded segment) (mm)	2.84±0.15	2.83±0.16	0.11
Mean Lumen Area Pre-implantation (scaffolded segment) (mm ²)	6.74±0.45	6.58±0.77	0.67
Mean Lumen Diameter Post-implantation (scaffolded segment) (mm)	3.22±0.11	3.03±0.25	0.07
Mean Lumen Area Post-implantation (scaffolded segment) (mm ²)	7.49±0.63	7.21±1.58	0.69
Mean Lumen Diameter Post-implantation (non-scaffolded segment) (mm)	3.19±0.12	2.95±0.19	0.045
Mean Lumen Area Post-implantation (non-scaffolded segment) (mm ²)	7.36±0.85	6.83±1.25	0.038

Table 4. OCT analyses results in scaffold groups.

	Absorb	ArterioSorb	p
Device level	(n= 6)	(n=6)	
In-scaffold mean lumen area (mm²)	7.77 ± 0.70	7.33±0.69	0.074
Distal reference mean lumen area (mm²)	5.08 ± 1.31	6.19 ± 1.45	0.194
Proximal reference mean lumen area (mm²)	7.46 ± 2.63	7.81 ± 0.49	0.751
Mean scaffold area (mm²)	8.10 ± 0.61	7.76 ± 0.70	0.190
Cross-section level	(n= 478)	(n=429)	
In-scaffold mean lumen area (mm²)	7.62 ± 1.10	7.35 ± 0.86	0.052
Distal reference mean lumen area (mm²)	5.07 ± 1.42	6.20 ± 1.41	0.465
Proximal reference mean lumen area (mm²)	6.85± 2.20	7.74 ± 0.93	0.843
Mean scaffold area (mm²)	8.00 ± 0.59	7.77 ± 0.87	<0.0001

Data are expressed as n (%) and mean ± standard deviation.

Protrusion analysis

There were 4591 struts in 477 cross-sections from Absorb and 3105 struts in 429 cross-sections from ArterioSorb in the protrusion analysis. There were 128 and 25 malapposed struts in Absorb and ArterioSorb, respectively. The protrusion analyses were performed in device and cross-section levels (**Table 5**). In device level analysis, ArterioSorb struts protruded ($84 \pm 6\mu\text{m}$) in the vessel wall less than in Absorb ($153 \pm 18\mu\text{m}$) ($p=0.004$). In cross-section level analysis, there was significant difference between the two scaffolds in strut protrusion ($153 \pm 137\mu\text{m}$ for Absorb, $84 \pm 12\mu\text{m}$ for ArterioSorb; $p < 0.0001$), that can be attributed to difference in strut thicknesses. The protrusion was higher in Absorb (97% of the strut thickness) than in ArterioSorb (88% of the strut thickness). When the protrusion distance was adjusted according to the lumen diameters, the ratio of protrusion distance / mean lumen diameter was higher in Absorb BVS (0.052 ± 0.0038) compared with the ArterioSorb (0.028 ± 0.0045) (<0.0001).

Table 5. Protrusion and ESS results

	Absorb	ArterioSorb	p
Device level	(n=6)	(n=6)	
Protrusion distance (μm)	153 \pm 18	84 \pm 6	0.004
Protrusion distance / mean lumen diameter	0.019 \pm 0.002	0.012 \pm 0.002	<0.0001
In-scaffold mean ESS (Pa)	0.73 \pm 0.25	1.51 \pm 0.22	0.03
Proximal non-scaffolded segment mean ESS (Pa)	1.40 \pm 0.06	1.08 \pm 0.30	0.04
Distal non-scaffolded segment mean ESS (Pa)	1.31 \pm 0.07	1.39 \pm 0.25	0.26
Cross-section level	(n=478)	(n=429)	
Protrusion distance (μm)	153 \pm 137	84 \pm 12	<0.0001
Protrusion distance / mean lumen diameter	0.052 \pm 0.0038	0.028 \pm 0.0045	<0.0001
In-scaffold mean ESS (Pa)	0.73 \pm 2.19	1.52 \pm 0.34	0.001
Proximal non-scaffolded segment mean ESS (Pa)	n=124 1.41 \pm 0.36	n=170 1.00 \pm 0.47	0.355
Distal non-scaffolded segment mean ESS (Pa)	n=147 1.29 \pm 0.46	n=260 1.39 \pm 0.69	0.647

Endothelial shear stress analysis

There were several layers of grouping within study data; nine animals (level 3) received scaffold implants in their coronary arteries, and similar types of the scaffolds were used in different vessels within the same animal. Each scaffolded segment had several cross-sections (level 2) and in each cross-section the ESS was quantified circumferentially in 5-degree sectorial subunits (level 1). ESS was significantly higher in ArterioSorb (1.52 \pm 0.34 Pa) than in Absorb (0.73 \pm 2.19 Pa) (p=0.001) (Table 5). In both types of scaffolds, there were inverse correlations between strut protrusion and ESS. Low- (<1.0 Pa) and very-low (<0.5 Pa) ESS estimations were seen more often in Absorb implanted vessel segments as compare to the ArterioSorb (Figure 2).

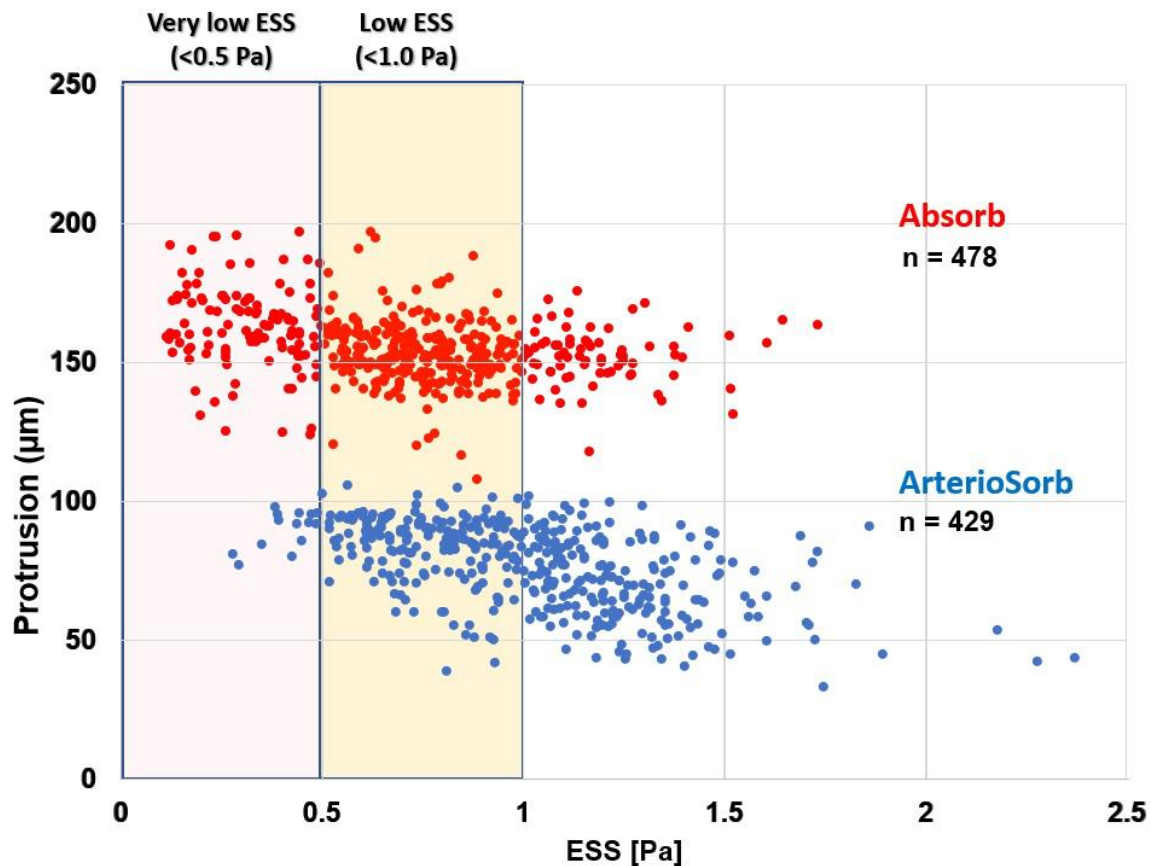


Figure 2. The low- and very-low ESS (median ESS per-cross-section) were recorded much more in Absorb than ArterioSorb.

DISCUSSION

In this study, we investigated two different types of BRS with similar strut geometry but different strut thicknesses in porcine coronary artery models. The findings can be summarized as follows; 1-Strut protrusion was higher in Absorb (97% of the strut thickness) than in ArterioSorb (88% of the strut thickness). 2) The decreased protrusion resulted noted in ArterioSorb in higher ESS in these scaffolds compared to the Absorb. 3) Due to less strut protrusion in ArterioSorb, low and very low ESS were seen less in ArterioSorb than Absorb. Stent/scaffold induced hemodynamic changes are one of the decisive determinants of PCI outcomes [13, 15, 18-20]. Several factors, such as vessel curvature in the treated segment, residual stenosis following device implantation, local deformation at the edges of the implanted device, tissue protrusion between the struts, scaffold design properties are factors responsible for the hemodynamic repercussion following stent/scaffold implantation. Among these factors, stent/scaffold design and strut apposition status are of utmost importance due to a relationship between new established luminal surface and local flow behaviors. Shear

stress has been demonstrated to be inversely related with neointimal healing process following stent/scaffold implantation [21]. In this relationship, strut thickness and protrusion emerge as cornerstone factors for the flow behaviors post-PCI [22]. Besides the micro level changes around the struts, fluid shear stress at a macro level is influenced by the vessel luminal dimensions after stent/scaffold implantation.

In the present report, two types of scaffolds were implanted in straight vessels. Both scaffolds have square-shaped strut designs, however ArterioSorb has thinner strut thickness of 95 micron which obviously induces less flow separations compared to thicker struts of Absorb (Figure 3) [6, 23].

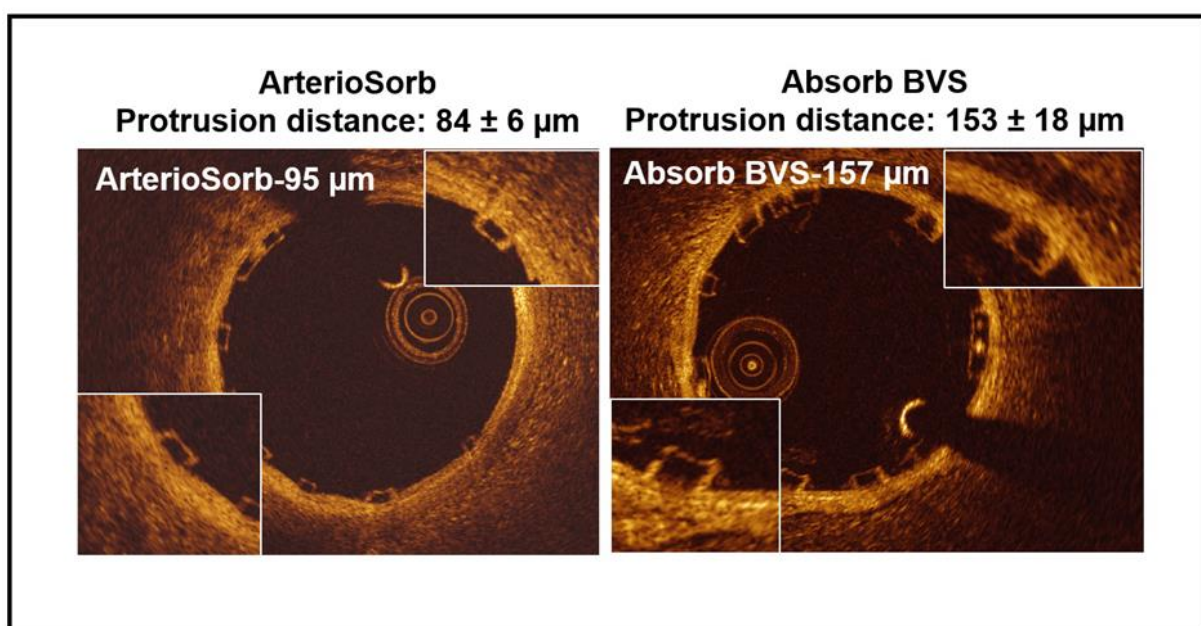


Figure 3. The protrusion in ArterioSorb was less than Absorb, due to the thinner struts of ArterioSorb.

Less flow separation will subject the newly set vessel surface to relatively higher endothelial wall shear stress (Figure 4). In ArterioSorb, the final luminal area post-implantation was slightly smaller than the Absorb and there was an obvious difference in the strut protrusion between the scaffolds. After adjusting the protrusion distances according to the final luminal dimensions, ArterioSorb had lower ratio of protrusion distance/luminal diameter as compared to the Absorb.

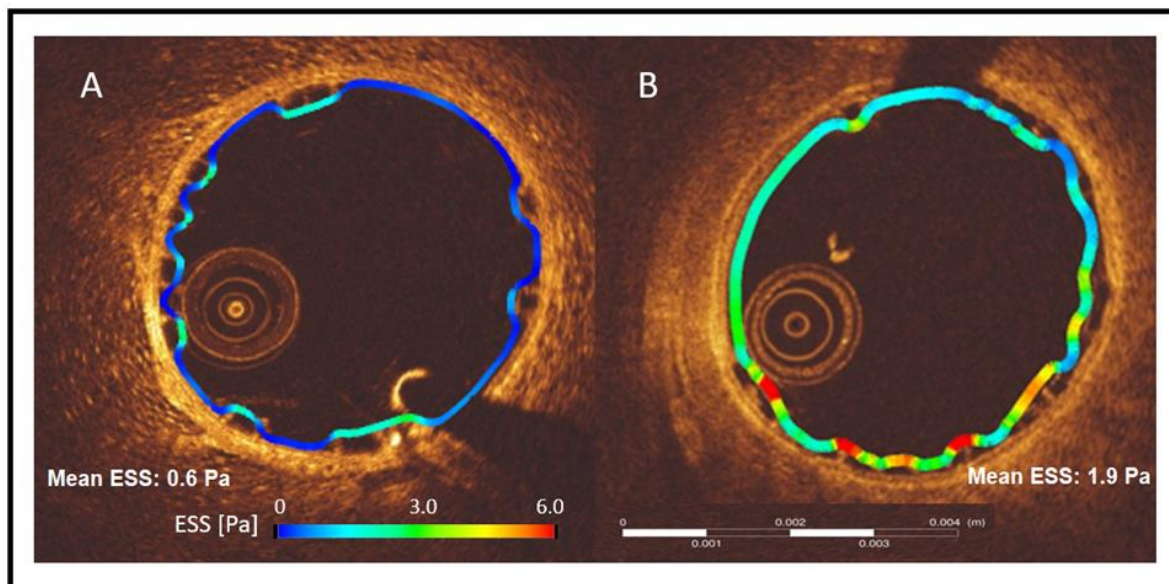


Figure 4. Due to thinner struts in ArterioSorb (A), the shear stress magnitudes were relatively higher than in Absorb (B). In the cross-sections from Absorb and ArterioSorb, mean ESS were 0.6 Pa and 1.9 Pa, respectively.

The inter-strut distance has impact on the recovery of the laminar flow between the struts [24]. The inter-strut distance should be at least six times the strut thickness [24]. ArterioSorb has maximum inter-strut distance of 1.4 mm which is longer than in Absorb (1.0 mm) and provides a significant advantage for the recovery of laminar flow resulting in more physiological ESS between the struts (**Figure 5**).

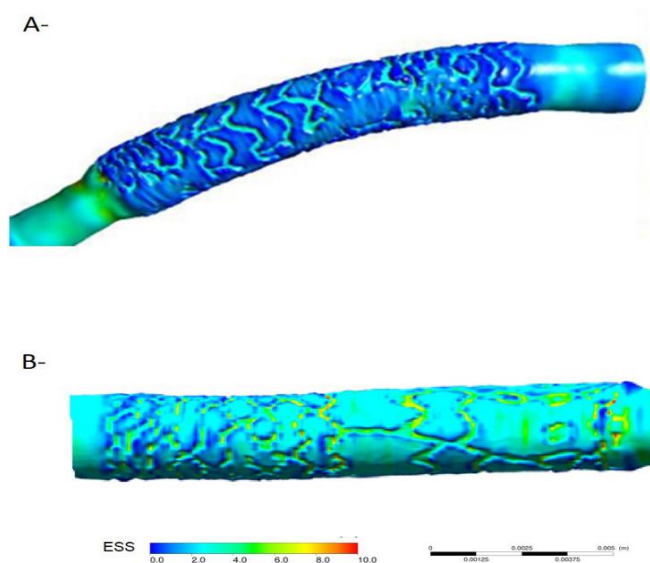


Figure 5. The inter-strut distance is 1.0 mm in Absorb (A) whereas 1.4 mm in ArterioSorb (B). The wider inter-strut distance provides more space to ArterioSorb to regain laminar flow and more physiological ESS over the wall boundary.

Bare metal stent (BMS) studies have emphasized that stent design influences clinical outcomes [3, 25]. Anti-proliferative drugs have changed the paradigm in drug-eluting metallic stents as the drug reduced the vessel wall proliferative reaction and prolonged vessel wall healing process. In BRS, the findings of the recently reported clinical studies raised concerns

about the potential risk of scaffold thrombosis that have been at least partially attributed to BRS design [26]. The non-streamlined strut design has significant effects on local flow patterns even in highest coronary flow that cannot be omitted [26, 27]. To address this limitation, industry has focused on more “*hemocompatible*” scaffold designs with different strut thicknesses, alignment and geometry. The present study has shown that *in vivo* OCT based CFD modeling can be used to investigate the hemodynamic performance of different scaffolds. CFD may have a significant role in the optimization of the scaffold design in favor of coronary flow [28]. In addition to high-tech CFD studies, protrusion analysis on OCT appears to contribute to optimized implantation which is critical for satisfactory results at follow-up after PCI [29, 30].

Limitations

A major limitation of the present study is the fact that scaffold implantation was performed in healthy coronary arteries. Therefore, it was not possible to investigate the implications of scaffold under-expansion or the effect of the underlying treated plaque on strut protrusion which is likely to determine the local hemodynamic features.

Secondly, one of the main limitations was the small sample size. Several criteria were implemented for filtering suitable cases. To prevent any effect of swirling-flow due to vessel curvature, on the scaffolded segment ESS distribution, we didn't include the cases with curvature. Also, the cases without two angiographic projections at least with >25-degree difference couldn't be reconstructed. However, total strut and cross-section numbers provided well-fitted statistical models for getting reliable conclusions.

Thirdly, the treated vessels (LAD, LCx and RCA) were different and there was an uneven distribution for the vessels treated between the study groups. Moreover, vessel diameters, the deployment pressures and the balloon pressures during post-dilation were different which might induce potential differences in the flow between the treated segments.

It's well known that side-branches can impact on the flow and shear stress distribution in the scaffolded segment[7]. One of the limitations of this study was that we did not include in the reconstructions of the side branches. However, there was no side branches bigger than 1.5 mm in the scaffolded segments in our data which could dissipate the concerns about that point.

CONCLUSION

In vivo OCT based CFD modeling can be used to evaluate the implications of scaffold configuration on the local hemodynamic forces. The thinner strut of ArterioSorb has less effect on the ESS patterns compared to the thicker struts of the Absorb. Further research is required to examine the potential value of the *in vivo* CFD modeling in optimizing scaffold configuration and clinical outcomes.

Disclosures

E. Tenekecioglu has a research grant from TUBITAK (The Research and Scientific Council of Turkey). P.W. Serruys is a member of the International Advisory Board of Abbott Vascular. Y. Onuma is a member of the International Advisory Board of Abbott Vascular.

Conflict of Interest

The authors declare that they have no conflict of interest.

REFERENCES

1. Serruys PW, Chevalier B, Sotomi Y, Cequier A, Carrie D, Piek JJ, Van Boven AJ, Dominici M, Dudek D, McClean D *et al*: Comparison of an everolimus-eluting bioresorbable scaffold with an everolimus-eluting metallic stent for the treatment of coronary artery stenosis (ABSORB II): a 3 year, randomised, controlled, single-blind, multicentre clinical trial. *Lancet (London, England)* 2016, 388(10059):2479-2491.
2. Serruys PW, Garcia-Garcia HM, Onuma Y: From metallic cages to transient bioresorbable scaffolds: change in paradigm of coronary revascularization in the upcoming decade? *European heart journal* 2012, 33(1):16-25b.
3. Pache J, Kastrati A, Mehilli J, Schuhlen H, Dotzer F, Hausleiter J, Fleckenstein M, Neumann FJ, Sattelberger U, Schmitt C *et al*: Intracoronary stenting and angiographic results: strut thickness effect on restenosis outcome (ISAR-STEREO-2) trial. *Journal of the American College of Cardiology* 2003, 41(8):1283-1288.
4. Kastrati A, Mehilli J, Dirschinger J, Dotzer F, Schuhlen H, Neumann FJ, Fleckenstein M, Pfaffert C, Seyfarth M, Schomig A: Intracoronary stenting and angiographic results: strut thickness effect on restenosis outcome (ISAR-STEREO) trial. *Circulation* 2001, 103(23):2816-2821.
5. Slager CJ, Wentzel JJ, Gijzen FJ, Schuurbiers JC, van der Wal AC, van der Steen AF, Serruys PW: The role of shear stress in the generation of rupture-prone vulnerable plaques. *Nature clinical practice Cardiovascular medicine* 2005, 2(8):401-407.
6. Jimenez JM, Davies PF: Hemodynamically driven stent strut design. *Annals of biomedical engineering* 2009, 37(8):1483-1494.
7. Li Y, Gutierrez-Chico JL, Holm NR, Yang W, Hebsgaard L, Christiansen EH, Maeng M, Lassen JF, Yan F, Reiber JH *et al*: Impact of Side Branch Modeling on Computation of Endothelial Shear Stress in Coronary Artery Disease: Coronary Tree Reconstruction by Fusion of 3D Angiography and OCT. *Journal of the American College of Cardiology* 2015, 66(2):125-135.
8. ZENG L, ZAMPETAKI A, XU Q: ENDOTHELIAL CELL PROLIFERATION AND DIFFERENTIATION IN RESPONSE TO SHEAR STRESS. In: *Hemodynamics and Mechanobiology of Endothelium*. edn.: WORLD SCIENTIFIC; 2012: 213-246.
9. JIMÉNEZ JM, DAVIES PF: DESIGN IMPLICATIONS FOR ENDOVASCULAR STENTS AND THE ENDOTHELIUM. In: *Hemodynamics and Mechanobiology of Endothelium*. edn.: WORLD SCIENTIFIC; 2012: 291-312.
10. Tenekecioglu E, Sotomi Y, Torii R, Bourantas C, Miyazaki Y, Collet C, Crake T, Su S, Onuma Y, Serruys PW: Strut protrusion and shape impact on endothelial shear stress: insights from pre-clinical study comparing Mirage and Absorb bioresorbable scaffolds. *The international journal of cardiovascular imaging* 2017.
11. National Research Council (U.S.). Committee for the Update of the Guide for the Care and Use of Laboratory Animals., Institute for Laboratory Animal Research (U.S.), National Academies Press (U.S.): Guide for the care and use of laboratory animals. In., 8th edn. Washington, D.C.: National Academies Press,; 2011: xxv, 220 p.
12. Sotomi Y, Tateishi H, Suwannasom P, Dijkstra J, Eggermont J, Liu S, Tenekecioglu E, Zheng Y, Abdelghani M, Cavalcanti R *et al*: Quantitative assessment of the stent/scaffold strut embedment analysis by optical coherence tomography. *Int J Cardiovasc Imaging* 2016, 32(6):871-883.
13. Bourantas CV, Papafaklis MI, Lakkas L, Sakellarios A, Onuma Y, Zhang YJ, Muramatsu T, Diletti R, Bizopoulos P, Kalatzis F *et al*: Fusion of optical coherence tomographic and angiographic data for more accurate evaluation of the endothelial shear stress patterns and neointimal distribution after bioresorbable scaffold implantation: comparison with intravascular ultrasound-derived reconstructions. *The international journal of cardiovascular imaging* 2014, 30(3):485-494.

14. Serruys PW, Onuma Y, Ormiston JA, de Bruyne B, Regar E, Dudek D, Thuesen L, Smits PC, Chevalier B, McClean D *et al*: Evaluation of the second generation of a bioresorbable everolimus drug-eluting vascular scaffold for treatment of de novo coronary artery stenosis: six-month clinical and imaging outcomes. *Circulation* 2010, 122(22):2301-2312.
15. Papafaklis MI, Bourantas CV, Theodorakis PE, Katsouras CS, Naka KK, Fotiadis DI, Michalis LK: The effect of shear stress on neointimal response following sirolimus- and paclitaxel-eluting stent implantation compared with bare-metal stents in humans. *JACC Cardiovasc Interv* 2010, 3(11):1181-1189.
16. Stone PH, Saito S, Takahashi S, Makita Y, Nakamura S, Kawasaki T, Takahashi A, Katsuki T, Nakamura S, Namiki A *et al*: Prediction of progression of coronary artery disease and clinical outcomes using vascular profiling of endothelial shear stress and arterial plaque characteristics: the PREDICTION Study. *Circulation* 2012, 126(2):172-181.
17. Bates D, Mächler M, Bolker B, Walker S: Fitting Linear Mixed-Effects Models Using lme4. 2015 2015, 67(1):48.
18. Bourantas CV, Papafaklis MI, Kotsia A, Farooq V, Muramatsu T, Gomez-Lara J, Zhang YJ, Iqbal J, Kalatzis FG, Naka KK *et al*: Effect of the endothelial shear stress patterns on neointimal proliferation following drug-eluting bioresorbable vascular scaffold implantation: an optical coherence tomography study. *JACC Cardiovascular interventions* 2014, 7(3):315-324.
19. Bourantas CV, Raber L, Zaugg S, Sakellarios A, Taniwaki M, Heg D, Moschovitis A, Radu M, Papafaklis MI, Kalatzis F *et al*: Impact of local endothelial shear stress on neointima and plaque following stent implantation in patients with ST-elevation myocardial infarction: A subgroup-analysis of the COMFORTABLE AMI-IBIS 4 trial. *International journal of cardiology* 2015, 186:178-185.
20. Shishido K, Antoniadis AP, Takahashi S, Tsuda M, Mizuno S, Andreou I, Papafaklis MI, Coskun AU, O'Brien C, Feldman CL *et al*: Effects of Low Endothelial Shear Stress After Stent Implantation on Subsequent Neointimal Hyperplasia and Clinical Outcomes in Humans. *Journal of the American Heart Association* 2016, 5(9).
21. Foin N, Gutierrez-Chico JL, Nakatani S, Torii R, Bourantas CV, Sen S, Nijjer S, Petraco R, Kouser C, Ghione M *et al*: Incomplete stent apposition causes high shear flow disturbances and delay in neointimal coverage as a function of strut to wall detachment distance: implications for the management of incomplete stent apposition. *Circulation Cardiovascular interventions* 2014, 7(2):180-189.
22. Beier S, Ormiston J, Webster M, Cater J, Norris S, Medrano-Gracia P, Young A, Cowan B: Hemodynamics in Idealized Stented Coronary Arteries: Important Stent Design Considerations. *Annals of biomedical engineering* 2016, 44(2):315-329.
23. Jimenez JM, Prasad V, Yu MD, Kampmeyer CP, Kaakour AH, Wang PJ, Maloney SF, Wright N, Johnston I, Jiang YZ *et al*: Macro- and microscale variables regulate stent haemodynamics, fibrin deposition and thrombomodulin expression. *Journal of the Royal Society, Interface* 2014, 11(94):20131079.
24. Berry JL, Santamarina A, Moore JE, Jr., Roychowdhury S, Routh WD: Experimental and computational flow evaluation of coronary stents. *Annals of biomedical engineering* 2000, 28(4):386-398.
25. Dibra A, Kastrati A, Mehilli J, Pache J, von Oepen R, Dirschinger J, Schomig A: Influence of stent surface topography on the outcomes of patients undergoing coronary stenting: a randomized double-blind controlled trial. *Catheterization and cardiovascular interventions : official journal of the Society for Cardiac Angiography & Interventions* 2005, 65(3):374-380.
26. Tenekecioglu E, Poon EK, Collet C, Thondapu V, Torii R, Bourantas CV, Zeng Y, Onuma Y, Ooi AS, Serruys PW *et al*: The Nidus for Possible Thrombus Formation: Insight From the Microenvironment of Bioresorbable Vascular Scaffold. *JACC Cardiovascular interventions* 2016, 9(20):2167-2168.
27. Thondapu V, Tenekecioglu E, Poon EK, Collet C, Torii R, Bourantas CV, Chin C, Sotomi Y, Jonker H, Dijkstra J *et al*: Endothelial shear stress 5 years after implantation of a coronary bioresorbable scaffold. *Eur Heart J* 2018.

28. Capodanno D, Gori T, Nef H, Latib A, Mehilli J, Lesiak M, Caramanno G, Naber C, Di Mario C, Colombo A *et al*: Percutaneous coronary intervention with everolimus-eluting bioresorbable vascular scaffolds in routine clinical practice: early and midterm outcomes from the European multicentre GHOST-EU registry. *EuroIntervention : journal of EuroPCR in collaboration with the Working Group on Interventional Cardiology of the European Society of Cardiology* 2015, 10(10):1144-1153.
29. Serruys PW, Onuma Y: Dmax for sizing, PSP-1, PSP-2, PSP-3 or OCT guidance: interventionalist's jargon or indispensable implantation techniques for short- and long-term outcomes of Absorb BRS? *EuroIntervention* 2017, 12(17):2047-2056.
30. Sotomi Y, Onuma Y, Dijkstra J, Eggermont J, Liu S, Tenekecioglu E, Zeng Y, Asano T, de Winter RJ, Popma JJ *et al*: Impact of Implantation Technique and Plaque Morphology on Strut Embedment and Scaffold Expansion of Polylactide Bioresorbable Scaffold- Insights From ABSORB Japan Trial. *Circ J* 2016, 80(11):2317-2326.

Chapter 7

Expert Recommendations on the assessment of wall shear stress in human coronary arteries: existing methodologies, technical considerations, and clinical applications

Expert Recommendations on the assessment of wall shear stress in human coronary arteries: existing methodologies, technical considerations, and clinical applications

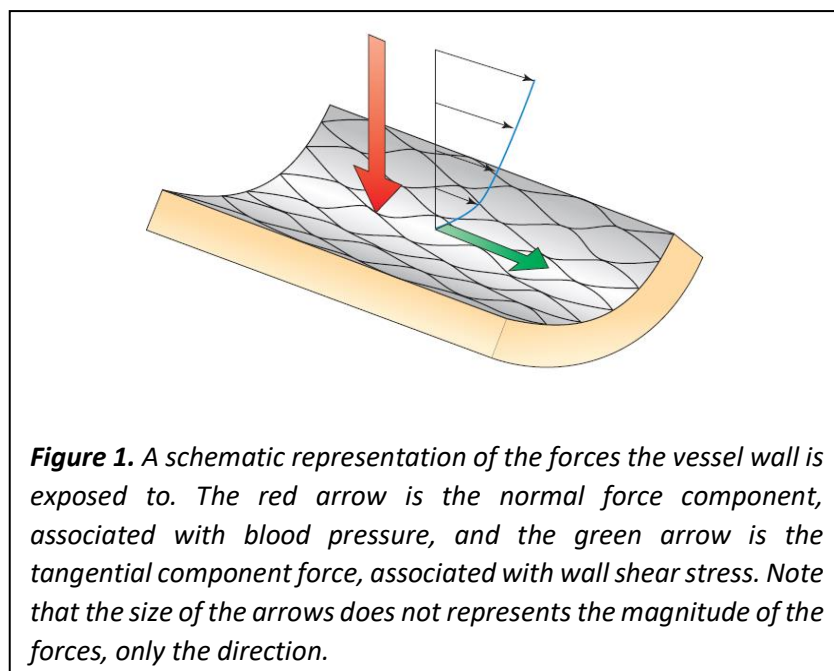
Frank Gijzen, Yuki Katagiri, Peter Barlis, Christos Bourantas, Carlos Collet, Umit Coskun, Joost Daemen, Jouke Dijkstra, Elazer Edelman, Paul Evans, Kim van der Heiden, Rod Hose, Bon-Kwon Koo, Rob Krams, Alison Marsden, Francesco Migliavacca, Yoshinobu Onuma, Andrew Ooi, Eric Poon, Habib Samady, Peter Stone, Kuniaki Takahashi, Dalin Tang, Vikas Thondapu, Erhan Tenekecioglu, Lucas Timmins, Ryo Torii, Jolanda Wentzel, Patrick Serruys

Eur Heart J. 2019; 40(41):3421-3433.

1. INTRODUCTION

1.1 What is wall shear stress?

When blood flows through an artery, it exerts forces on the vessel wall (**Figure 1**). The perpendicular component of that force vector is associated with blood pressure, leading to deformation of the cells in the vessel wall. The tangential component of that force vector is much smaller and can be sensed by the endothelium through a shearing deformation ('shearing force'). Each force has a magnitude and direction, and for the shear force, they both change during the cardiac cycle. If we normalize this tangential force vector by the area, we obtain the wall shear stress (unit: $1 \text{ Pa} = 10 \text{ dynes/cm}^2$). Wall shear stress has a major impact on endothelial function and therefore plays a key role in atherosclerotic disease development and in long term evolution and healing of vessels treated by intravascular devices. Wall shear stress is orders of magnitude smaller than other mechanical stresses affecting the coronary arteries, such as tensile stress or compressive stress and exerts its powerful vascular effects not by a mechanical impact on vascular structure per se, but uniquely by triggering biologic signaling. The biological impact of wall shear stress will be reviewed briefly in section 2.



1.2 How do we calculate wall shear stress?

Since wall shear stress in coronary arteries cannot be measured directly, we need to compute through solving the equations that describe the motion of fluids: the Navier-Stokes equations. The most widely used method to solve these complex equations is called Computational Fluid Dynamics (CFD). Given the appropriate input data, the velocity and pressure distribution can be computed with CFD and the local wall shear stress distribution in coronary arteries can be derived. CFD in the coronary arteries has recently gained increased clinical interest with the advent of computed tomography coronary angiography-derived fractional flow reserve (FFR_{CT}) technology for non-invasive assessment of coronary stenosis severity.

The solution of the full Navier-Stokes equations provides complete velocity and pressure information at *any* location in the coronary artery at *any* point in time. Solving these equations can be time consuming and computationally expensive and therefore many studies make use of simplified equations, many of them building on the seminal work of Young and Tsai and Gould¹⁻³. Reductional approaches can be useful for specialized applications, but they often rely on assumptions that do not hold for coronary artery flow. A recent series of applications produce predictions of bulk pressure drops in stenosed arteries under hyperemia to determine the fractional flow reserve (FFR). Especially under elevated flow conditions, the non-linear nature of the Navier-Stokes equations becomes dominant, often leading to an underestimation of the pressure drop when applying reduced models.

1.3 Aim and outline

The aim of this manuscript is to provide guidelines for appropriate use of CFD to obtain reproducible and reliable wall shear stress maps in native and instrumented human coronary arteries. The outcome of CFD heavily depends on the quality of the input data, which include vessel geometrical data, proper boundary conditions and material models. Available methodologies to reconstruct coronary artery anatomy are discussed in Section 3. Computational procedures implemented to simulate blood flow in native coronary arteries are presented in Section 4. The effect of including different geometrical scales due to the presence of stent struts in instrumented arteries is highlighted in Section 5. The clinical implications are discussed in section 6, and concluding remarks are presented in section 7.

2. THE BIOLOGICAL RELEVANCE OF WALL SHEAR STRESS

2.1 Wall shear stress and the endothelium

Wall shear stress is sensed by endothelial cells via multiple wall shear stress-responsive cell components, which (de)activate intra-cellular pathways leading to regulation of gene and protein expression. This force-induced regulatory process plays a continuous role in the development, growth, remodeling and maintenance of the vascular system (**Table 1 and Figure 2**).

Table 1. In cultured endothelium, 0 ± 0.5 Pa is often used to mimic athero-prone shear stress, whereas 1.2 – 1.5 Pa is the most frequently used value to simulate normal, often termed high, arterial shear stress. Consistent with this, a low, oscillatory shear stress of 0.05 ± 0.5 Pa was measured in the disease prone region of the internal carotid artery^{106,146} and in healthy human coronary arteries, time-averaged wall shear stress was found to be approximately 1.4 Pa¹⁴⁷. In atherosclerotic human arteries, shear stress can vary with changes in geometry. It is elevated at the stenosis of plaques reaching >7 Pa in some instances¹⁴⁸. In cultured endothelium, 7.5 Pa is used to mimic elevated shear stress in vitro¹⁴⁹. However, it should be noted that low shear stress is associated with plaque progression in diseased human coronary arteries¹²⁰. The effect of shear stress profiles on early and late atherosclerosis are reviewed in⁴, and their effect on neoatherosclerosis in stented vessels are reviewed in^{31,137}.

label	range (Pa) ^{106, 146-149}	effects in:		
		early atherosclerosis ⁴	advanced atherosclerosis ⁴	stented segments ^{31, 137}
oscillatory	0 ± 0.5	athero-prone	athero-prone	neoathero-prone
Low	0-1			
normal/high	1-7	athero-protective	no consensus*	neoathero-protective
elevated	>7	NA	erosion	NA

NA: Not Applicable; *: see Appendix B, table B1

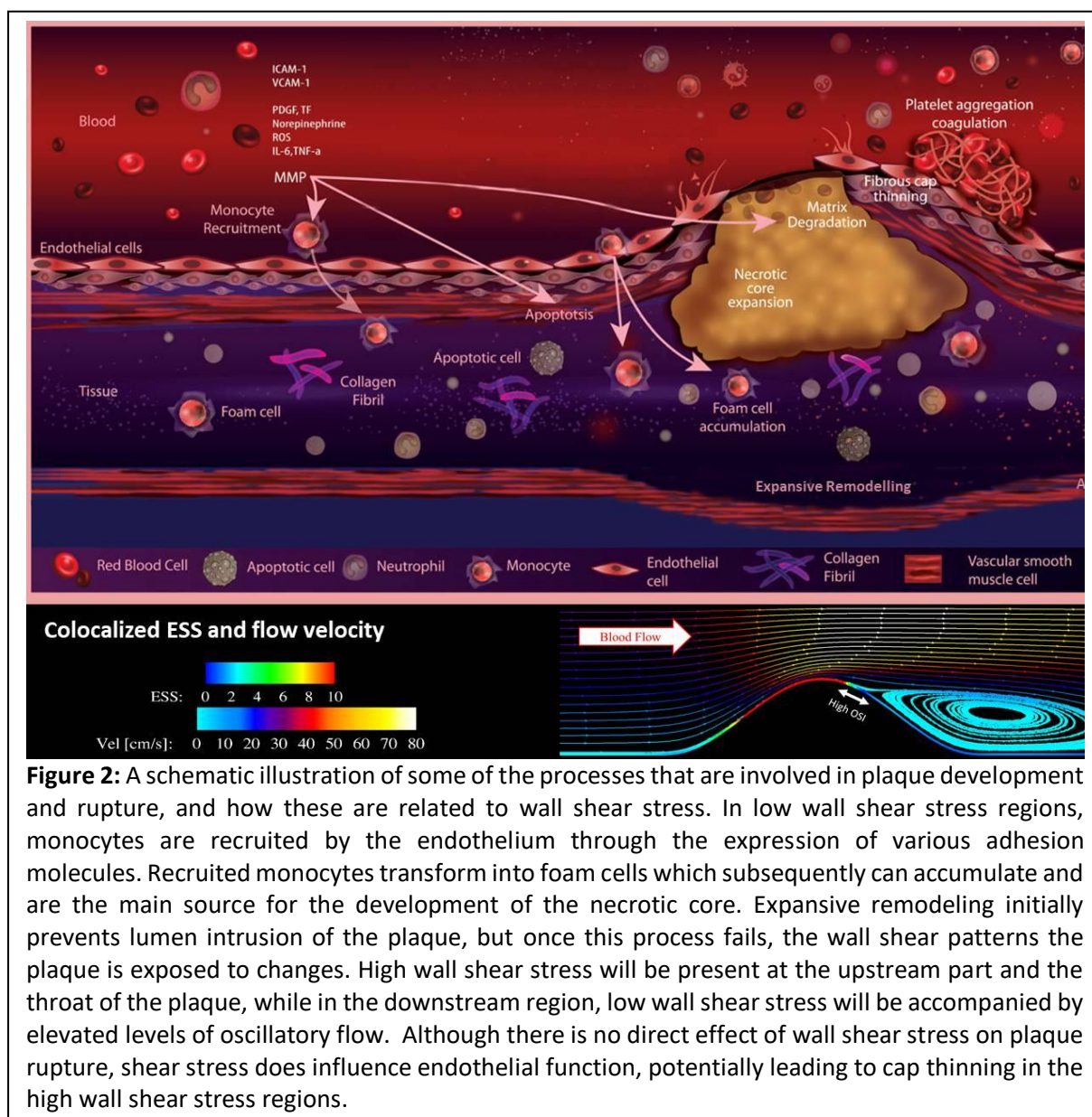


Figure 2: A schematic illustration of some of the processes that are involved in plaque development and rupture, and how these are related to wall shear stress. In low wall shear stress regions, monocytes are recruited by the endothelium through the expression of various adhesion molecules. Recruited monocytes transform into foam cells which subsequently can accumulate and are the main source for the development of the necrotic core. Expansive remodeling initially prevents lumen intrusion of the plaque, but once this process fails, the wall shear patterns the plaque is exposed to changes. High wall shear stress will be present at the upstream part and the throat of the plaque, while in the downstream region, low wall shear stress will be accompanied by elevated levels of oscillatory flow. Although there is no direct effect of wall shear stress on plaque rupture, shear stress does influence endothelial function, potentially leading to cap thinning in the high wall shear stress regions.

Generally, endothelial cells exposed to high, unidirectional wall shear stress assume a quiescent state, while endothelial cells exposed to low and/or directional varying wall shear stress are activated, displaying a pro-inflammatory state⁴. There is also an important interplay between wall shear stress and pro-inflammatory cytokines such as TNF and IL-1 β . These cytokines function as central drivers of arterial inflammation by inducing endothelial expression of adhesion protein and chemokines that co-operate to capture leukocytes from the blood stream to the vessel wall. High shear stress reduces the ability of TNF or IL-1 β to activate EC whereas low shear stress primes them for proinflammatory responsiveness⁵⁻⁸. Recently, the Canakinumab Anti-inflammatory Thrombosis Outcomes Study (CANTOS)

revealed that targeting of IL-1 β led to reduced cardiovascular events in patients with a previous myocardial infarction, thereby highlighted the importance of IL-1 β in atheroprotection⁹. The molecular mechanisms underlying the pro- or anti-inflammatory effects of wall shear stress are governed by wall shear stress-responsive transcription factors. The anti-inflammatory transcription factors KLF2 and Nrf2 are activated by high wall shear stress and have been shown to be involved in the regulation of 70% of high wall shear stress-induced genes. In contrast, the transcription factors AP-1 and NF- κ B are activated by low and/or oscillatory wall shear stress and positively regulate pro-inflammatory genes¹⁰⁻¹⁵. The wall shear stress responsive pathways also regulate endothelial function and vessel integrity. This includes short term regulation of vascular tone, via release of potent vasodilators and vasoconstrictors like nitric oxide (NO) and endothelin-1 (ET-1), respectively, but also long-term processes including vascular remodeling (e.g., outward/inward remodeling, angiogenesis and collateral formation) to meet tissue perfusion demand. This section provides a brief overview of some of the most important mechanisms and pathways that relate wall shear stress to atherosclerosis and restenosis. For a more detailed description of these and other pathways, and their role in priming of endothelial cells, the reader is referred to other review articles^{16, 17}.

2.2 Wall shear stress and early atherosclerosis

Many of the same signaling pathways that regulate developmental, homeostatic and adaptive mechanisms in arteries play a key role in the development of coronary artery disease initiation and progression, partly explaining site specific susceptibility to atherosclerosis¹⁸. The low and/or oscillatory wall shear stress-induced inflammatory activation of the endothelium typically occurs at the inner bend of curved arteries, ostia of branches, lateral walls of bifurcations, at surgical junctions such as end-to-side anastomoses, and up or downstream from luminal obstructions. At these sites, circulating inflammatory cells, primarily monocytes, interact with adhesion molecules like VCAM-1 and MCP-1 (transcriptional targets of AP-1 and NF- κ B), expressed on the activated endothelial cells. The monocytes then enter the sub-endothelial layer where they become macrophages that engulf lipoproteins and subsequently transdifferentiate into foam cells, trapping them inside the arterial wall and leading to atherosclerotic plaque initiation: the fatty streak. During progression of atherosclerosis, the plaque grows. Initially the artery will remodel outward to preserve lumen area and tissue perfusion, thereby maintaining the wall shear stress profile before lesion onset and promoting

the pro-inflammatory activation of the endothelium now overlying the plaque. In this way, low wall shear stress continues to contribute to early plaque growth. In contrast to branches and bifurcations, regions of arteries with uniform geometry are generally exposed to laminar flow and undisturbed wall shear stress which induces anti-inflammatory and atheroprotective processes, in part, via activation of KLF2 and Nrf2 which suppress inflammatory and pro-apoptotic signaling pathways ¹¹.

2.3 Wall shear stress and advanced atherosclerosis

In the advanced stages of the disease, both high and low wall shear stress have been suggested to play a detrimental role. Plaques vary in terms of geometry and composition. Some have a preserved lumen that is continuously exposed to their original wall shear stress, either low in curved segments or oscillating in bifurcations, while others have a narrowed lumen that is mainly exposed to increased spatial and temporal variations in wall shear stress¹⁸. In both cases, wall shear stress may influence plaque composition, leading to varied risk of plaque vulnerability. In coronary plaques with a preserved lumen, low wall shear stress has been correlated to a reduction in smooth muscle cells, reduced collagen production, and increased metalloproteinase (MMP) activity¹⁹.

Two thirds of acute coronary syndromes are caused by plaque rupture. One third demonstrates a thrombus overlying a non-ruptured plaque, in which the event appears to be caused by endothelial erosion²⁰. Less is known about the mechanisms regulating plaque erosion than those for plaque rupture. It has been suggested that both high and low wall shear stress can be causative of erosion^{21, 22}. Unlike plaque rupture, endothelial erosion tends to occur on stable, thick-capped atherosclerotic plaques²³. On these stable, inward remodeled plaques, endothelial apoptosis and loss of endothelial contact with the underlying extracellular matrix are processes believed to be involved in endothelial erosion and have been shown to be induced by high wall shear stress (reviewed in²³). However, endothelial detachment was observed to be twice as frequent on the downstream side of lumen narrowing plaques²⁴, suggesting a role for low and/or oscillatory wall shear stress ²⁵. These apparently conflicting observations suggest that biological mechanism, in concert to wall shear stress, may play a role in this process.

2.4 Wall shear stress and in-stent restenosis

It has been proposed that wall shear stress also plays an important role in stented arteries²⁶. Stents alter local artery geometry and concomitantly wall shear stress patterns. If the

deployed stent is patent and without luminal irregularities, the local wall shear stress pattern will be primarily physiologic or vasculoprotective. If the artery geometry is curved or tortuous, however, then by restoring the three-dimensional (3D) geometry present before lumen intrusion, the wall shear stress profile that caused the disease may be reinstated. In addition, the presence of stent struts, depending on their height and width, can lead to the generation of disturbed wall shear stress in between the struts²⁷⁻³⁰. Furthermore, stent implantation may increase the local curvature at the entrance and exit of the stent, further enhancing disturbed shear-stress regions³¹. Higher wall shear stress on the abluminal surface of the struts induces platelet activation and modifies their morphology³². The activated platelets resume their discoid geometry as they enter the lower wall shear stress zones within the recirculation zone behind the struts, causing conformational changes in von Willebrand receptors and platelet aggregation^{33, 34}. Furthermore, low, disturbed wall shear stress zones beside the struts can induce the platelets to release platelet-derived growth factor that stimulates endothelial proliferation in these stagnation zones^{35, 36}. The higher wall shear stress on top of the struts results in poor endothelialization³⁷, while the low, disturbed wall shear stress in the vicinity of the struts reduces endothelial migration³⁰ and initiates smooth muscle cell migration into the subintimal layer³⁸. Through all these mechanisms presented above, wall shear stress has been associated with neo-intima development and neoatherosclerosis (neo-atherosclerosis biological mechanisms are reviewed in^{30,31}) in human coronary arteries which can ultimately result in the need for repeat interventions³⁰.

3. IMAGING CORONARY ARTERIES: A BRIEF REVIEW

3.1 Why is 3D luminal data so important?

Assessment of hemodynamic parameters requires a precise imaging and 3D reconstruction of the lumen geometry. In general, coronary arteries are imaged using traditional X-ray angiography, multi-slice computed tomography angiography (CTCA), magnetic resonance imaging (MRI) and various intravascular imaging techniques including intravascular ultrasound (IVUS), optical coherence tomography (OCT) and near-infrared spectroscopy (NIRS) - IVUS. In addition, several other invasive imaging modalities are under development and may have future applications in coronary reconstruction and overcome limitations of the existing techniques enabling detailed assessment of plaque morphology³⁹.

3.2 Geometry assessment with invasive and non-invasive coronary angiography

With traditional X-ray angiography, the contrast filled lumen of the coronary arteries is visualized using x-rays, generating a 2D projection of the arterial lumen, with a pixel size of 150-250 μm . Combining information from two or more x-ray images selected at the same moment during the cardiac cycle, a 3D reconstruction of the coronary artery lumen can be generated⁴⁰⁻⁴³. Due to their ease of application, and the widespread availability of angiography, these 3D reconstruction techniques have been incorporated in commercially available software⁴⁴. However, the accuracy of coronary angiography-based wall shear stress computations remains controversial, as some studies have demonstrated a moderate association between the wall shear stress estimated in angiographic-based models and those reconstructed from intravascular imaging, while others have shown a strong correlation⁴⁵⁻⁴⁸. On the other hand, there is robust evidence on its efficacy in calculating hemodynamic parameters which are less sensitive to the exact lumen shape, such as FFR, which is defined as the ratio of pressure distal to the lesion to the proximal pressure⁴⁹. The efficacy of CFD analysis in models reconstructed from multiple angiographic projections or rotational angiography in predicting the FFR has been validated against in vivo measurements with promising initial results⁵⁰⁻⁵³.

CTCA enables reconstruction of the entire coronary tree and it can be used to study plaque distribution in coronary bifurcations and the effect of the local hemodynamic forces in these vulnerable segments⁵⁴. These advantages however come at a cost of a lower imaging resolution (240-500 μm) and less reliable characterization of the composition of the plaque; limitations that are likely to have an impact on the estimated wall shear stress and affect the association between local hemodynamic forces and plaque characteristics^{55,56}. Several recent studies however, have used CTCA-based models to evaluate wall shear stress and two reports have shown that computational modelling in CTCA-based reconstruction can provide useful information and predict segments that will exhibit atherosclerotic disease progression highlighting its value in the study of atherosclerosis⁵⁷⁻⁵⁹.

MRI has also been utilized to reconstruct 3D anatomical models for CFD analyses but its image resolution is limited for coronary arteries (resolution 1000-1340 μm); therefore, this modality is currently not recommended for coronary artery lumen reconstruction.

3.3 Imaging approaches based on fusion with intravascular techniques

To overcome the limitations of angiography and CTCA, and to reconstruct high-resolution models of the coronary arteries fusion of angiography or CTCA and intravascular imaging has been proposed⁶⁰⁻⁶⁵. These methods benefit from the high spatial resolution of the non-X ray-based imaging modalities in each cross section and allows imaging of the vessel wall and its components⁶⁶⁻⁶⁸. Coronary reconstruction based on fusion of IVUS or OCT and angiography or CTCA includes the following steps: 1) the extraction of the IVUS catheter path or the lumen centerline from two end-diastolic angiographic projections, 2) the segmentation of the end-diastolic IVUS or OCT frames, 3) the placement of the contours perpendicularly onto the catheter path or the lumen centerline and the estimation of their relative twist using the Frenet-Serret formula or the sequential triangulation algorithm and 4) the comparison of the silhouette of the back-projected lumen model with the lumen silhouette on the angiographic projections^{60, 61} or the use of anatomical landmarks visible in both IVUS or OCT and X-ray imaging or CTCA⁶²⁻⁶⁴ to estimate the absolute orientation of the IVUS or OCT frames (**Figure3**)⁶⁴.

IVUS was the first invasive imaging modality that was used to reconstruct coronary anatomy. This modality with its high penetration depth enables assessment of luminal morphology and plaque burden and has provided unique insights about the role of wall shear stress on atherosclerotic evolution^{18, 66}. A limitation of IVUS is its limited efficacy to assess plaque composition and its low resolution (65-150 μm) that do not allow microscopic evaluation of plaque pathology. NIRS-IVUS imaging appears able to assess more accurately plaque tissue characteristics and today several studies are ongoing that use this modality to examine the effect of the local hemodynamic forces on plaque composition.⁶⁹

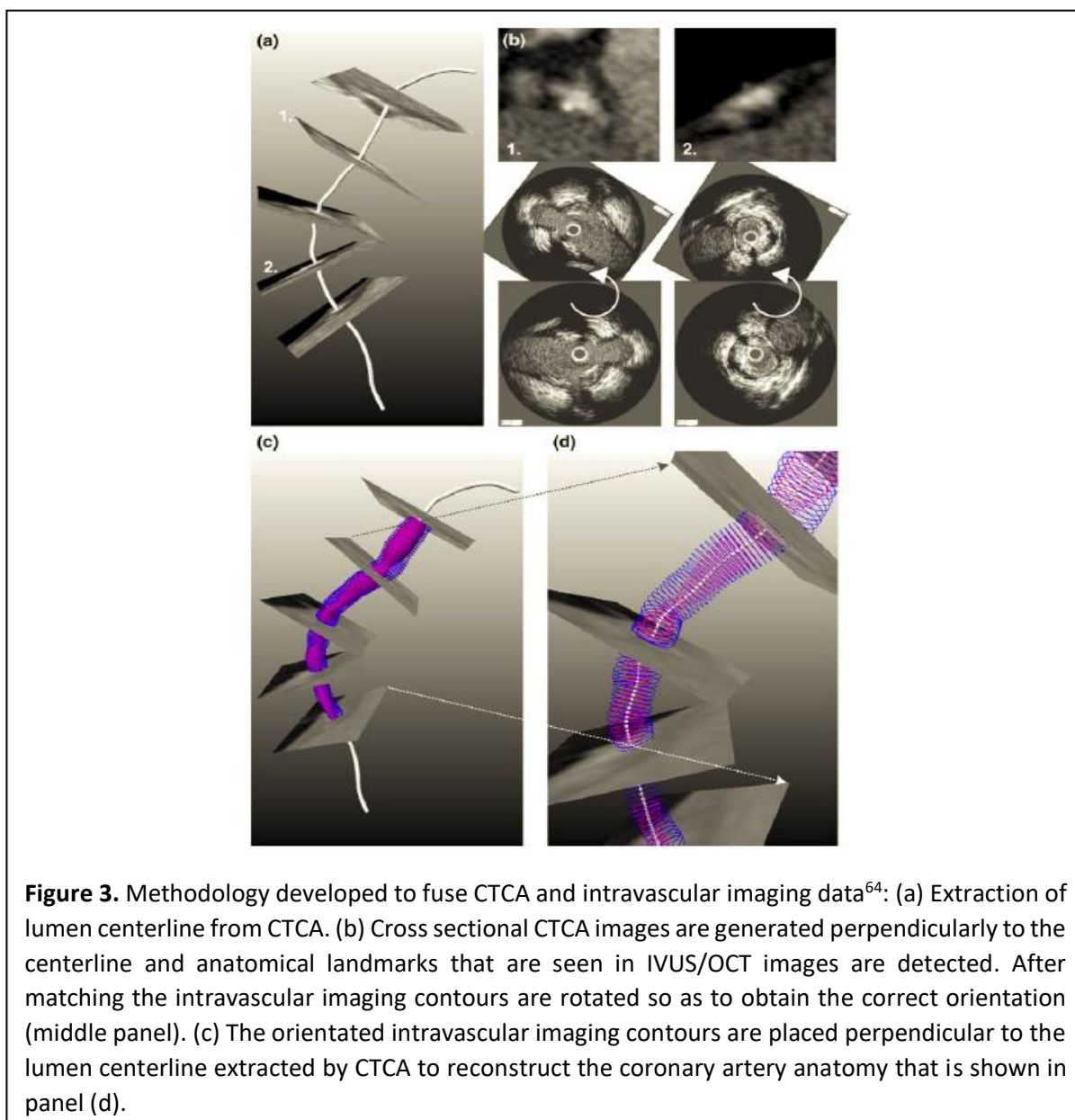


Figure 3. Methodology developed to fuse CTCA and intravascular imaging data⁶⁴: (a) Extraction of lumen centerline from CTCA. (b) Cross sectional CTCA images are generated perpendicularly to the centerline and anatomical landmarks that are seen in IVUS/OCT images are detected. After matching the intravascular imaging contours are rotated so as to obtain the correct orientation (middle panel). (c) The orientated intravascular imaging contours are placed perpendicular to the lumen centerline extracted by CTCA to reconstruct the coronary artery anatomy that is shown in panel (d).

Another modality that enables accurate evaluation of the superficial plaque is high-resolution OCT (12-18 μm) that is able to assess plaque micro-characteristics associated with plaque vulnerability that are unseen by IVUS such as the fibrous cap thickness, neovessels, cholesterol crystals and macrophages accumulation⁷⁰. Moreover, OCT, in contrast to IVUS, allows visualization of the lumen protruded struts in stented and scaffolded segments that, as it has been shown in *in silico* studies, can create micro flow disturbances and recirculation zones in the areas between the struts^{31, 71}. Therefore, OCT-based 3D reconstruction of stented segments is currently considered superior to IVUS-based strategies⁷², and the available strategies are discussed in more detail in section 5.1

Preferred imaging modality for assessing wall shear stress in different clinical scenarios

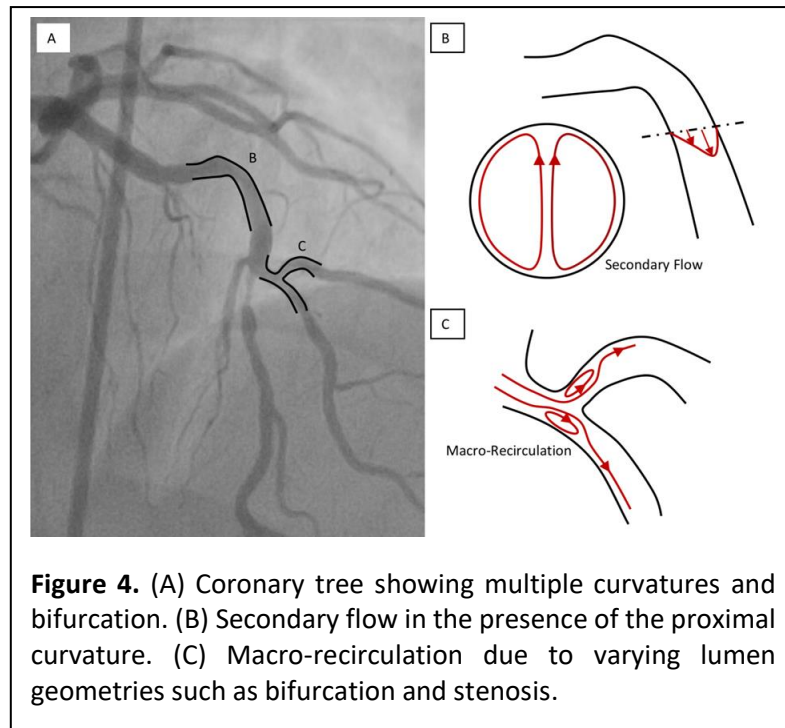
- Studies aiming to investigate the effect of wall shear stress on plaque progression and changes in plaque composition should preferably create coronary artery models using fusion of IVUS/NIRS-IVUS and coronary angiography or CTCA
- Studies aiming to investigate the influence of the local wall shear stress on plaque micro-characteristics should preferably create the 3D lumen using fusion of OCT and biplane angiography or CTCA
- Studies aiming to investigate the influence of the local wall shear stress distribution in a stented regions should preferably create the 3D lumen using fusion of OCT and biplane angiography or CTCA
- 3D QCA and CTCA have limited accuracy in evaluating lumen and vessel wall anatomy but it can be considered to assess the wall shear stress and FFR on plaque evolution in low risk patients where intravascular imaging is not an option.
- MRI-based lumen reconstructions are currently not accurate enough for assessment of the wall shear stress distribution.

4. WALL SHEAR STRESS IN NATIVE ARTERIES

Wall shear stress inside the coronary artery lumen can be simulated by numerically solving the mathematical equations governing the motion of the arteries and blood flow with relevant boundary conditions⁷³. The system as a whole represents a complex fluid-solid interaction (FSI) problem. However, it was demonstrated that full FSI analysis (i.e., including the motion of the walls of the heart) of the right coronary artery only accounts for ~5 % difference in the most widely used metric, the time-averaged wall shear stress in a recent study⁷⁴. For detailed information, the reader is referred to ⁷⁵. In this section, we will focus on wall shear stress computations in coronary arteries with rigid, non-deforming walls. Recommendations will be provided for 3D geometry reconstruction of the artery lumen; the boundary conditions and material properties of blood needed to conduct the CFD simulations, the available software platforms (CFD solvers), and post-processing techniques for wall shear stress analysis. Technical details for section 4 and 5 are provided in **Appendix A**.

4.1 Geometrical model construction

The characteristics of blood flow in the coronary arteries are strongly dependent on the 3D curvature, the presence of bifurcations, and lumen intruding plaques as well as the pulsatile nature of the flow (**Figure 4**).



These geometrical and physical parameters will introduce haemodynamic features such as secondary flow and/or recirculation⁷⁶, which will play a critical role in determining the wall shear stress dynamics at the region of interest (ROI). The inclusion of the proximal segment of the coronary arteries allows for a natural development of the secondary flow, which is essential for an accurate representation of the distal wall shear stress pattern⁷⁷. Therefore, segmentation and 3D reconstructions, whether it is from CTCA, 3D-QCA, IVUS or OCT⁷⁸⁻⁸¹, should be extended to the ostium of both right and left coronary artery whenever possible. In addition, the presence of arterial bifurcations has a major impact on wall shear stress patterns⁸². Firstly, there is a global effect of bifurcations on wall shear stress. At each bifurcation, coronary flow is distributed between the main vessel and side branch, mainly depending on their diameters^{83,90}. This leads to a reduction of blood flow in the main vessel, which is typically accompanied by tapering of the lumen of the mother vessel. Secondly, coronary bifurcations also have a local effect of wall shear stress patterns, inducing local regions of disturbed flow, potentially containing reversal of flow due to the presence of macro-recirculation (**Figure 4C**). Selection criteria to determine what side branch should be included can be found in **Appendix A.1**.

4.2 Meshing procedure

The reconstructed 3D geometries will be filled with grid points which represent the volume of the blood within the ROI. These grid points form the basis for the mesh elements, which are

required to compute velocity and pressure from the governing equations for blood flow. In this meshing procedure, the individual grid spacing, or mesh size, is determined by the complexity of the arteries of interest. Generally, a finer grid spacing is required in the regions where large changes in the velocity profiles (see also **Figure 1**) are anticipated. This implies that a smaller elements are often used at the vessel wall, while larger elements are admissible in the central part of the artery, where the smaller changes in the velocity profiles are present (see also **Appendix A, Figure A2**). The optimal grid spacing needs to be determined by a mesh convergence analysis to demonstrate that further mesh refinement will not result in significant changes to the wall shear stress estimations. This is an essential step for each CFD analysis (see also **Appendix A.3**).

4.3 Boundary conditions

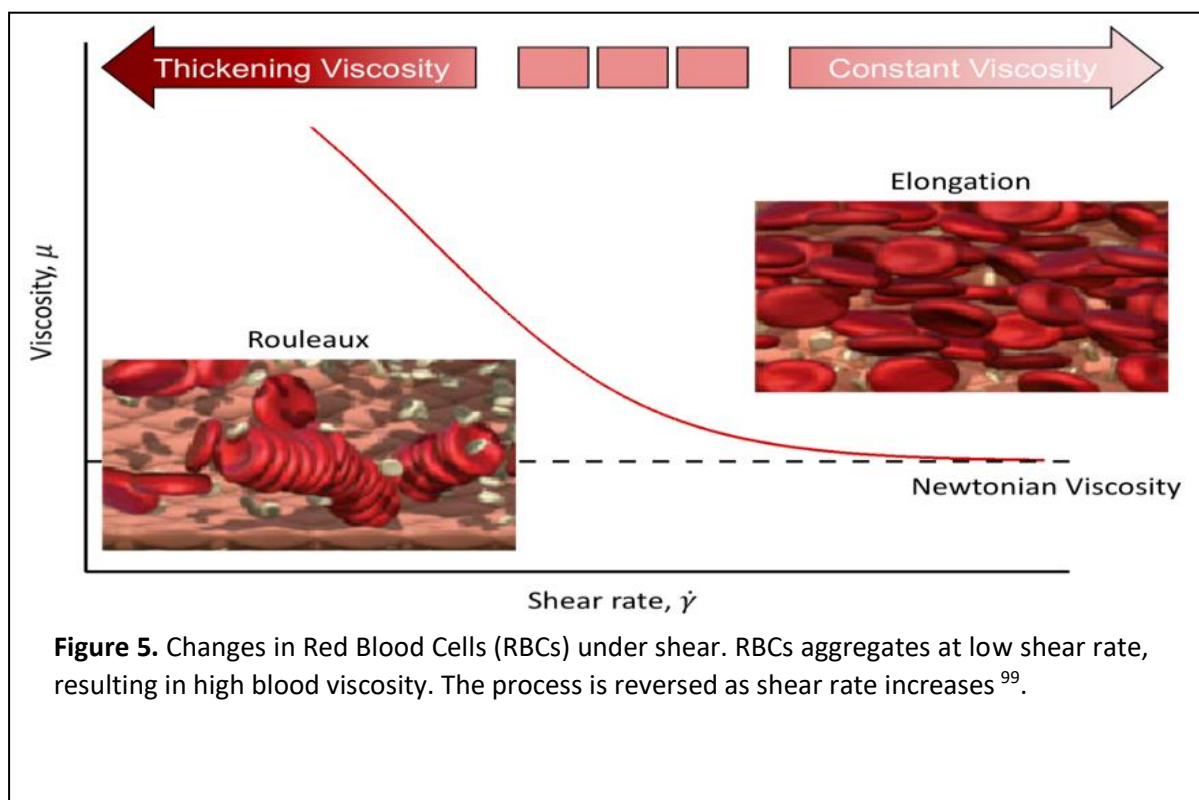
For CFD in coronary arteries in a rigid geometry, boundary conditions need to be described for the inlet, the outlet(s) and the arterial wall. In steady flow simulations, the inflow velocity used is a time-averaged value over a cardiac cycle and time variation of the velocity at the inlet is neglected. The value for the time-averaged inlet can be obtained using either TIMI (Thrombolysis In Myocardial Infarction) frame count⁸³, including a modified TIMI frame count through the calculated true 3D reconstructed volume of the lumen segment of interest⁸⁴, or a more sophisticated –but less widely available– intracoronary Doppler ultrasound blood flow velocity measurement⁸⁵. If patient-specified flow measurements are not available, scaling laws can be applied. Various scaling laws are available that relate the local diameter of the artery to the average velocity⁸⁶⁻⁸⁸. In a coronary artery bifurcation study, the redistribution of coronary flow between the main vessel and side branch should be considered carefully. Ideally, patient-specific data should be used to determine the flow redistribution. These data can be obtained during clinical procedures, e.g. based on computed tomography perfusion⁸⁹ or myocardial volume⁹⁰. If these are not available, one can use a diameter-based scaling laws^{91, 92}. A constant pressure boundary at the model outlets can be applied to regulate the flow redistribution. Lastly, a no-slip and no-penetration boundary condition is prescribed at the arterial wall.

In recent years, interest in faithfully recreating the pulsating coronary fluid environments has become more common due to the additional information that can be obtained from analysing the temporal variation of wall shear stress^{76, 93}. The pulsatile nature of coronary flow can only be fully revealed with transient or unsteady CFD simulations. Suitable modifications to the

boundary conditions at both inlet and outlet are needed to capture the coronary flow phasic behaviour (**Appendix A.4**). In particular, the difference between phasic coronary flow in the left and right coronaries should be accounted for. With velocity-derived inlet boundary condition, the time-varying inflow velocity can be derived from patient-specific measurements^{84,85}, or the time-averaged velocity values can be combined with a generic velocity waveform^{83,94,95}. At the outlet, the implementation of specialized coronary boundary condition model is needed if the phasic change in coronary pressure in pulsatile CFD analyses are studied.^{96,97} Another commonly used boundary condition method is to couple the inlets and outlets to lumped parameter circuit models representing cardiac and coronary physiology via an analogy to electrical circuits and is described in details in **Appendix A.4**.

4.4 Blood rheology

Blood comprises a mixture of red blood cells (RBC), white blood cells, platelet and plasma. Herein, we focus on one of the predominant features of blood, namely the ability of RBC to aggregate and elongate under different flow conditions, and the resulting effect on blood viscosity and subsequent impact on the wall shear stress calculation. It has been shown that at low shear rate⁹⁸, RBCs aggregate and eventually form “rouleaux” which in turns increases the viscosity of the blood (**Figure 5**)⁹⁹. However, RBC aggregation is a reversible process. That is, rouleaux begin to break up with increasing shear rate and return to single individual RBCs. The separation of RBCs from rouleaux results in an initial decrease in local blood viscosity that ultimately asymptotes to a constant value at higher shear rate¹⁰⁰. This fluid behaviour of viscosity being inversely proportional to the shear rate is often referred to as a shear-thinning behaviour, making blood a non-Newtonian fluid. Most CFD simulations have simplified the shear-thinning fluid behaviour of blood to a Newtonian fluid using a constant blood viscosity of 3.5~4.0 mPa·s¹⁰¹. However, it is advised to implement suitable shear-thinning model (e.g. Carreau–Yasuda model¹⁰², and Quemada model¹⁰³) in coronary flow CFD studies.



4.5 Solution strategies

The solution procedure in CFD simulations involves various steps, each with their own settings that determine the solution accuracy. These settings are extremely important and depend on many factors, including the solution method used, and on the flow regime. The appropriate choice of these settings requires engineering skills and in-depth knowledge about computational methods^{104 105}. A key concept in the solution procedure is convergence. In CFD simulations, the Navier-Stokes equations are solved in an iterative manner. For each iteration, the error in solving the equations should reduce and the solution is said to be “converged” when residual (error) values of velocity and pressure are below a certain threshold (see also Appendix A.5). Only converged solutions provide reliable wall shear stress maps. A list of CFD software platforms that are available and used in the community is provided in **Table 2**.

Table 2. Commonly used CFD software platforms. #SimVascular¹²⁴ provides various plug-ins that allow implementation of appropriate lumped parameter models, and tutorials on how to run coronary simulations

Commercial/open source		Remarks
ANSYS Fluent	Commercial	excellent user-interfaces and more technical support, but offer less control over the process
STAR-CMM+		
COMSOL		
OpenFoam	Open Source	require a high level of expertise to ensure appropriate implementation, but provide the necessary tools to customize the computational procedure.#
SimVascular		
Crimson		

4.6 Post processing

Several metrics can be derived from the computed wall shear stress distribution. Wall shear stress values up to about one to two vessel diameters after the inlet and about half or one vessel diameter length before the outlet side of geometry may have artificial values related to the boundary conditions and should be excluded from analyses. Wall shear stress metrics including temporal components include the oscillatory shear index ¹⁰⁶, relative residence time ¹⁰⁷ and a recently introduced metric call the transverse wall shear stress ¹⁰⁸. For a visualization of these quantities, the reader is referred to **Appendix A (figure A4)**. Statistical analysis of the above quantities often requires mapping (in both circumferential and axial directions) of the CFD results to the cross-section contours in the ROI. It is important to emphasize that both mapping should be performed based on the resolution of the mesh, and the resolution of the medical imaging data, especially in case of IVUS and OCT-based CFD analyses. Further recommendations can be found in **Appendix A.6**.

Main recommendations for 'wall shear stress in native arteries'

- Arterial lumen reconstructions from ostium of both right and left coronary artery proximal to ROI need to be included for physiological blood flow development.
- Bifurcation reconstructions, especially immediately proximal to the ROI, are essential for accurate computation of the local wall shear stress distributions.
- The arterial lumen containing the blood is represented by thousands or even millions of mesh elements and individual element size can only be determined by a mesh-refinement study.
- Simulation results with 3% discrepancy or less at each mesh refinement step are considered mesh independent.
- Non-Newtonian blood properties should be accounted for by implementing suitable shear-thinning model.
- Each CFD simulation should be carefully checked on convergence, and convergence criteria depend on the problem at hand and the solution strategy.
- Wall shear stress and its variants are related to various pathological processes, and appropriate processing of the data depends on what process is studied.

5. WALL SHEAR STRESS IN STENTS

Simulation of blood flow in stented arteries adds another layer of complexity compared to flows in native arteries – flow around the stent struts creates small vortices on the order of the size of struts (**Figure 6**). Such small-scale flow characteristics can be labelled as the micro flow environment whereas the flow patterns in the scale of the whole vessel, primarily determined by vessel curvature and narrowing, can be called the macro environment. The flow around a strut is characterised as a region with accelerated flow, causing high wall shear stress on the abluminal strut surface and a recirculation zone at the downstream side of the strut, depending on the flow speed and strut shape. Due to the small size of the stent struts, and the flow features associated with them, special care needs to be paid when performing CFD in stented segments.

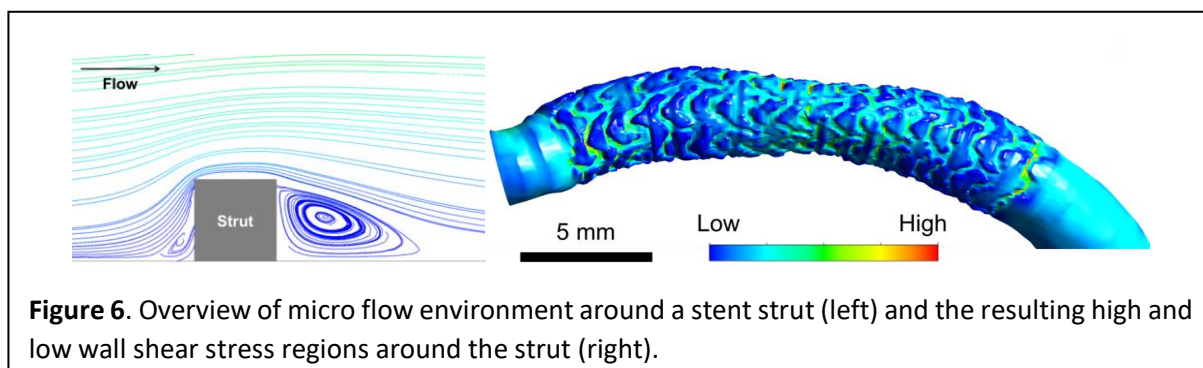


Figure 6. Overview of micro flow environment around a stent strut (left) and the resulting high and low wall shear stress regions around the strut (right).

5.1 Geometrical model construction and meshing procedure

Reconstruction of a stented artery is challenging and requires reconstruction of the vessel lumen with struts protruding inward, as if the pattern of strut is imprinted on the native vessel border (**Figure 6**). The geometry reconstruction is even more complex when the strut is mal-apposed since there are small gaps between the struts and the vessel wall. In order to capture the flow features around a strut, a very high mesh resolution is required (see **Appendix A.2** for technical details). At the same time, use of a 2D approximation and/or localised model around a strut (or a series of struts) is still an option depending on the research question such as comparison of hypothetical stent implantation scenarios using different strategies²⁸.

5.2 Blood rheology

Blood properties may require an additional consideration when dealing with micro flow environment as the size of RBCs (6-8 μm) is roughly in the same order of magnitude as the struts (tens of μm), which can potentially affect flow patterns. Around the top of the strut, the difference between Newtonian approximation and non-Newtonian model may not be substantial because shear rates are high¹⁰⁹. On the contrary, shear rate in the flow recirculation behind the strut is low and the impact of the blood viscosity model in determining the patterns of the flow is expected to be higher. Blood particles can be considered in a multiscale approach by allowing them to aggregate, forming rouleaux and interact with flow. The importance of including blood particles in flow simulations on this scale is an open question: the presence of a cell-free layer near the arterial wall is well documented¹¹⁰ in small arteries and arterioles but not adequately described in medium sized arteries (diameter > 1 mm) like coronaries, especially with stents.

5.3 Solution strategy and post-processing

When blood is modelled as a homogenous fluid without particles, the solution procedure is generally the same as that for native arteries. However, additional attention is needed to the temporal resolution of the simulations (**Appendix A.5**). Additional models for the cellular volume and membrane for the blood cells are required in case these particles are accounted for. This is typically achieved by treating the volume occupied by RBCs as another fluid or phase with the cellular membrane as an interface¹¹¹⁻¹¹³. Such models require much higher computing power and specialized solvers, particularly when the ROI is a whole vessel that should contain millions of RBCs. This type of computation in 3D has only been realised up to relatively short segment of vessels so far and supercomputers are typically required^{114 115}. Post-processing methods should be selected in accordance with the research question as outlined in **Appendix A.6**. When wall shear stress values are compared against plaque characteristics, the accuracy to co-register the two types of information needs to be considered to judge whether point-to-point comparison can be more reliable than comparison per segment. The amount of wall shear stress data from CFD is typically large, especially when comparing profiles changing over the time. Selecting an effective method to present the data such as the use of a histogram^{93, 116}, which can also be in a form of a cumulative curve, is important (**Appendix A, Figure A5**).

Main recommendations for 'wall shear stress in stents'

- Macroscopic flow patterns are determined by global vessel geometry, and microscopic flow pattern governed by stent struts. Both play important roles in determining wall shear stress distribution in stented vessels.
- High-resolution computational mesh generation is a key element to adequately capture the flow pattern, especially the micro-scale features. Depending on the type of elements used, approximately ten elements are needed to discretize the height of a stent strut.
- The macroscopic effect of blood particles may be considered by incorporating non-Newtonian blood models. More physiologically realistic models of blood particles are needed to study the effect of individual particles, but such simulations still require unrealistically high computational demand.

6. CLINICAL APPLICATIONS

In vitro and *in vivo* animal studies demonstrate that wall shear stress is a potent modulator of endothelial function and influences the development of atherosclerosis¹¹⁷. As such, the major clinical interest in wall shear stress arises from its ability to identify patients at risk for future cardiovascular events or complications after stent placement. Many investigators have tackled this complex problem using various simulation techniques described above. Although several clinical CFD studies seem to reflect the observations of *in vitro* and animal experiments, findings in human patients are far from unanimous or clear-cut. This section summarizes clinical literature and steps that may be undertaken to propel CFD analysis into clinical application in the future. **Appendix B** contains tables that synopsise the clinical studies in native arteries (**Table B1**) and stented arteries (**Table B2**).

6.1 Wall shear stress in human native coronaries

A large body of studies has investigated wall shear stress in relation to coronary plaque morphology in native coronary arteries. IVUS-based CFD studies have associated low wall shear stress with enlargement of plaque area and necrotic core^{66, 118}, increased plaque eccentricity¹¹⁹ and reduction in lumen and vessel area^{120, 121}. Studies have also correlated high wall shear stress with progression of necrotic core and dense calcium in addition to regression of fibro-fatty and fibrous tissues^{66, 122}. The co-existence of high plaque burden both with low and high wall shear stress values improves prediction of plaque progression and vulnerability, respectively^{120, 123}. OCT-based CFD studies have similarly shown that low wall shear stress is

correlated with a higher prevalence of lipid, with thinner fibrous caps^{124, 125} along with higher macrophage density and more superficial calcification¹²⁵.

The largest trial examining wall shear stress in relation to clinical events was an IVUS-based analysis of 506 Japanese patients showing that low wall shear stress was able to predict lesions progressing to require percutaneous coronary intervention (PCI) during the 6-10 month follow up period¹²⁰. Notably, however, most of these interventions (n=39/53, 74%) occurred in asymptomatic patients treated for angiographic progression during protocol-mandated follow up coronary imaging. Despite the relatively large number of patients studied, the number of symptomatic clinical events was too low to infer relationships with wall shear stress.

An alternative approach has been to retrospectively study patients with symptomatic clinical events. A recent post-hoc CFD analysis of patients from the Providing Regional Observations to Study Predictors of Events in the Coronary Tree (PROSPECT) study compared baseline wall shear stress in patients with non-culprit plaques leading to major adverse cardiovascular events (MACE) with patients that did not develop MACE during 3.4 years of clinical follow-up.¹²⁶ The investigators demonstrated that the presence of low wall shear stress was significantly associated with the development of non-culprit MACE. In the presence of ≥ 2 anatomic risk factors such as high plaque burden, smaller minimal lumen area, or thin cap fibroatheroma morphology, lesions with low wall shear stress had a 3-year MACE rate of 52.1% compared to lesions with < 2 anatomic risk factors and low wall shear stress (14.4%), versus 0% in lesions with physiologic or high wall shear stress regardless of anatomic risk factors. These results suggest that low wall shear stress is important for clinically significant plaque progression, and that low wall shear stress incrementally improves the positive predictive value to identify patients at risk for future clinical events. However, the investigators were careful to point out that not all plaques with low wall shear stress developed MACE, and that it remains unclear which individual lesions will progress to cause clinical events.

The role of high wall shear stress is also gaining more interest in recent years. IVUS-based CFD studies of ruptured culprit plaques have demonstrated a strong correlation between focal elevation in wall shear stress and the site of plaque rupture^{127, 128}. An OCT-based CFD analysis of a single case demonstrated similar results¹²⁹. Spatial co-localization cannot serve as evidence of causality; however, these studies suggest that identifying high wall shear stress

over vulnerable atheroma may improve detection of plaques prior to rupture. A CTCA-based CFD study also showed that high wall shear stress had an incremental value over luminal narrowing in discriminating high-risk plaques⁵⁷. The probability of high-risk plaques increased at both extremes of wall shear stress with the lowest at the physiological range of wall shear stress (≈ 40 dyne/cm²). The Exploring the Mechanism of Plaque Rupture in Acute Coronary Syndrome Using Coronary CT Angiography and Computational Fluid Dynamics (EMERALD) study analyzed 72 patients with clearly documented acute coronary syndrome (ACS) and available CTCA acquired between 1 month and 2 years before the development of ACS and showed that the noninvasive hemodynamic assessment including wall shear stress enhanced the identification of high-risk plaques that subsequently caused ACS. In that study, the average wall shear stress of 66 culprit lesions were significantly higher than that of 150 non-culprit lesions¹³⁰. These findings were recently corroborated in a small cohort of the FAMEII trial, in which it was shown that high wall shear stress in the upstream part of a plaque contributed to the prognostic value of FFR to predict MI¹³¹. Despite evidence correlating wall shear stress with atherosclerosis, advances on several fronts will be necessary if wall shear stress is to be used for identification of future culprit lesions. The most obvious and important one is the need for large, prospective, image-based clinical CFD studies evaluating hard clinical endpoints along with plaque morphology. However, since wall shear stress as it is currently determined does not contribute with sufficiently high sensitivity or specificity to accurately predict clinically significant progression of atherosclerotic plaques, additional methodological advances will also be necessary.

The use of high-resolution and multiple hybrid imaging modalities may provide additional information about how fluid dynamic measures relate to vascular pathophysiology. Improved imaging may also aid arterial reconstructions through more detailed lumen/vessel geometry and facilitate the incorporation of side branches. In terms of CFD methodology, advances may include routine use of pulsatile flow conditions, non-Newtonian rheological models of blood, and complementary or novel fluid dynamic parameters. Naturally, ongoing improvements in computing power and streamlining of workflows are also expected to improve the on-line clinical application of these techniques.

Ultimately, with further advances it is anticipated that clinical CFD analyses will emerge as one of many diagnostic and prognostic tools in clinical practice. Regulatory bodies around the world have also increasingly acknowledged the importance of streamlining the approval

process for new technologies, evidenced, for example, by the UK's Accelerated Access Review pathway. The development and approval of FFR_{CT} illustrates how wall shear stress analyses may similarly navigate the regulatory approval process as sufficient clinical data supporting their use emerges. In terms of CFD simulation to calculate wall shear stress, another question remains how to use this data: clinicians must be prepared with the appropriate treatments. If future culprit lesions can be reliably identified, prospective treatment strategies theoretically include a combination of risk stratification, lifestyle management, systemic and/or targeted drug therapy, "preventative" PCI, or any number of other interim developments. Work in this area is underway, but optimal strategies have yet to be defined. Given the small but non-trivial risk associated with PCI and stent/scaffold placement, pre-emptive interventional treatment has been difficult to justify thus far. However, prospective studies randomizing patients to various non-invasive pre-emptive treatments based on their CFD profile should be considered to identify the ideal treatment of future culprit lesions.

Main findings from clinical trials: wall shear stress in native arteries

- Both low and high wall shear stress have been associated with aspects of plaque progression and vulnerability by clinical imaging studies, but the precise relationships remain unclear and studies are sometimes contradictory.
- Low wall shear stress has been associated with future angiographically-driven revascularization and non-culprit MACE.
- High wall shear stress has been associated with future myocardial infarctions.

6.2 Wall shear stress in stents

Treatment of coronary stenosis by PCI through the implantation of metallic or polymeric devices by definition induces flow alterations²⁸. Patient, device, and procedural factors all play a role in the final macro and micro-environmental flow profile¹³². The advent of patient-specific blood flow simulations has been instrumental in characterizing local hemodynamics of stented regions to better understand device healing and complications such as restenosis and thrombosis¹³³. At the macroenvironment, several geometric modifications occur after PCI that have a direct implication for the wall shear stress pattern. A step-up phenomenon in lumen area, frequently observed at the inflow of the treated region, alters the flow and has been associated with areas of low wall shear stress. In contrast, at the distal segment of the stented region a decrease in lumen area or step-down increases shear stress¹³⁴. The clinical consequence of this kind of shear stress pattern has not been completely understood;

however, several studies have linked low wall shear stress to neointimal hyperplasia formation after bare metal stent (BMS) implantation¹³⁵. Low wall shear stress might trigger vascular smooth muscle migration, proliferation and matrix formation which may lead to in-stent restenosis¹³⁶. Stent under-expansion has been shown to be associated with in-stent restenosis and thrombosis and also influence wall shear stress distribution¹³⁷, with areas of high wall shear stress at the upstream and low wall shear stress at the downstream of the under-expanded region. Stent mal-apposition, another consequence of a sub-optimal implantation, was found to impact wall shear stress and arterial healing. Strut detachment from the vessel wall greater than 100 μm induces flow disturbances affecting strut coverage at mid-term follow-up¹⁰⁹.

At the microenvironment level, the interaction among stent struts, a denudated vessel wall and blood components may play a role as a substrate for stent thrombosis¹³⁸. Refinements of the 3D reconstruction techniques for CFD simulations, using high-definition images from OCT made possible to investigate the impact of stent design and strut thickness in-vivo. The wall shear stress distribution was found to fluctuate amongst the different region of the stent struts^{31, 139}. In front or at the inflow of the strut, areas of moderate to high wall shear stress have been described. At the top of the struts, high wall shear stress values have been correlated with shear-mediated activation of platelets and activation of von Willebrand factor¹⁴⁰. Behind the struts, low wall shear stress with areas of recirculation promotes platelet aggregation which may predispose to thrombus formation and stent thrombosis in an endothelium activated by injury^{31, 139}. The magnitude of the blood flow alterations has been shown to be dependent on the height and thickness of the device struts^{138, 141}. A sub-optimal wall shear stress immediately after stenting may serve for risk stratification based on CFD. It has been shown that, in wide range of follow-up period (n=36, median 8.0 years, 0.4-16.7 years), the low wall shear stress immediately after stent implantation can be a predictor of neoatherosclerosis¹⁴². Here, the wall shear stress was quantified on vessel wall without reconstructing the actual stent strut structure and averaged wall shear stress over vessel wall segment was used in the analysis. This implies that wall shear stress on a smoothed lumen geometry after initial endothelialization post stent implantation can serve as a predictor, in cases of adequate stent expansion and strut apposition.

Several meta-analyses have demonstrated that first-generation metallic stents made from stainless steel and with thick-strut (>140 μm) are associated with worse clinical outcomes as

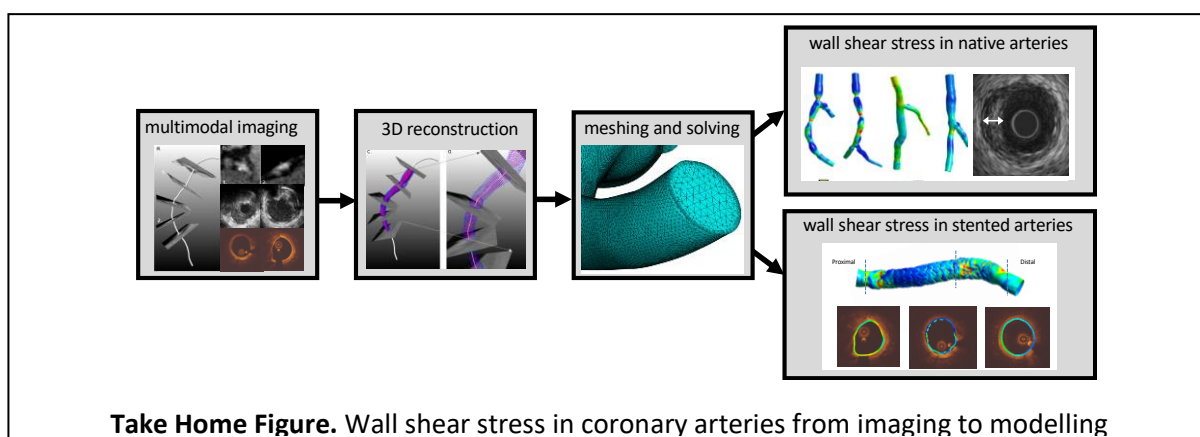
compared to newer thinner strut DES (<100 μm)^{143, 144}. Moreover, the advent of new-generation stents with reduced strut thickness has decreased the rates of in-stent restenosis and thrombosis¹⁴⁴. Although, newer and thinner platforms exhibit enhanced hemodynamic profile and reduced blood flow alteration, the improvement in clinical outcomes cannot be attributed solely to the strut thickness but rather to a combination of improved polymer biocompatibility, new metallic alloys and better stent design. The field of CFD has allowed us to better understand the impact of coronary devices on blood flow disturbances and their consequences on arterial healing after PCI¹³³. In the 2016 report, the Federal and Drug Administration (FDA) recommended computational modelling of coronary stents as a tool to guide developments in the field¹⁴⁵. The increasing amount of evidence correlating wall shear stress with arterial healing, neointimal formation and thrombotic risk may translate CFD to clinical practice. The exponential growth of computer technology and expertise of bioengineers and clinicians have the potential not only to improve stent designs but also to guide stent deployment and ultimately PCI. OCT 3D lumen reconstruction after stenting with automatic evaluation of mal-apposition can be performed online. The combination with CFD for online wall shear stress assessment in stented regions to optimize stent deployment may be feasible in the near future. Nevertheless, clinical studies addressing the incremental value of the integration of computational fluid dynamics and wall shear stress are warranted. A number of clinical studies are ongoing to investigate the focal and potentially more global effects of adverse wall shear stress after stenting on device healing. These include the Shear Stent study (NCT02098876), Absorb III Imaging Sub-study (NCT01751906), and the ISR Flow study.

Main findings from clinical trials: wall shear stress in stents

- Neointimal thickness has been shown to be inversely correlated to wall shear stress.
- Low wall shear stress after BMS implantation was associated with neointimal hyperplasia formation. However, after DES low wall shear stress does not correlate with in-stent hyperplasia.
- After bioresorbable scaffold implantation low wall shear stress promotes neointimal hyperplasia and contribute to scaffold healing with normalisation of wall shear stress
- There is an inverse association between baseline wall shear stress and the incidence of neoatherosclerosis in both BMS and DES

7. CONCLUDING REMARKS

Wall shear stress affects endothelial function, plaque progression, vascular remodeling, and arterial healing after PCI. Since wall shear stress cannot be measured directly in human coronary arteries, we utilize the Navier-Stokes equations describing the motion of a fluid, using CFD. The results of CFD are greatly affected by the quality of the input data, especially the 3D geometrical data of the coronary artery lumen. In this paper, we reviewed critically the proposed methodologies applied to obtain reproducible and reliable wall shear stress maps. Advances in methodologies integrating angiography or CTCA with intravascular imaging and improvements in computing power have enabled us to simulate wall shear stress in both native and stented coronary arteries. Currently, CFD is already applied in various clinical applications, mainly to compute pressure drop and determine FFR. The increasing amount of evidence correlating wall shear stress with e.g., neointimal formation and thrombosis can translate wall shear stress analyses into clinical practice. For example, we can evaluate the impact of the scaffold design, in particular of the strut thickness and shape and the alignment of strut connectors on the local hemodynamic forces with these techniques. Apart from application in stented arteries, we also envision application of wall shear stress metrics in native arteries. One could for instance generate wall shear stress maps of all the coronary vessels, much like currently is done for FFR_{CT} , subdivide these maps into regions labeled according to the levels given in table 1, and use these maps to predict location of plaque progression and plaque rupture. Although we acknowledge that additional clinical research is needed to identify the predictive strength of wall shear stress in atherosclerosis and stented segments, we expect that with further advances in imaging and computational power CFD analyses will be available as one of the major diagnostic and prognostic tools in routine clinical practice.



REFERENCES

1. Young DF, Tsai FY. Flow characteristics in models of arterial stenoses. I. Steady flow. *Journal of biomechanics* 1973;6(4):395-410.
2. Young DF, Tsai FY. Flow characteristics in models of arterial stenoses. II. Unsteady flow. *Journal of biomechanics* 1973;6(5):547-59.
3. Gould KL, Kelley KO, Bolson EL. Experimental validation of quantitative coronary arteriography for determining pressure-flow characteristics of coronary stenosis. *Circulation* 1982;66(5):930-7.
4. Kwak BR, Back M, Bochaton-Piallat ML, Caligiuri G, Daemen MJ, Davies PF, Hoefer IE, Holvoet P, Jo H, Krams R, Lehoux S, Monaco C, Steffens S, Virmani R, Weber C, Wentzel JJ, Evans PC. Biomechanical factors in atherosclerosis: mechanisms and clinical implications. *Eur Heart J* 2014;35(43):3013-20, 3020a-3020d.
5. Passerini AG, Polacek DC, Shi C, Francesco NM, Manduchi E, Grant GR, Pritchard WF, Powell S, Chang GY, Stoeckert CJ, Davies PF. Coexisting proinflammatory and antioxidative endothelial transcription profiles in a disturbed flow region of the adult porcine aorta. *Proceedings of the National Academy of Sciences* 2004;101(8):2482-2487.
6. Dai G, Kaazempur-Mofrad MR, Natarajan S, Zhang Y, Vaughn S, Blackman BR, Kamm RD, Garcia-Cardena G, Gimbrone MA, Jr. Distinct endothelial phenotypes evoked by arterial waveforms derived from atherosclerosis-susceptible and -resistant regions of human vasculature. *Proc Natl Acad Sci U S A* 2004;101(41):14871-6.
7. Chiu JJ, Lee PL, Chen CN, Lee CI, Chang SF, Chen LJ, Lien SC, Ko YC, Usami S, Chien S. Shear stress increases ICAM-1 and decreases VCAM-1 and E-selectin expressions induced by tumor necrosis factor-alpha in endothelial cells. *Arteriosclerosis Thrombosis and Vascular Biology* 2004;24(1):73-79.
8. Partridge J, Carlsen H, Enesa K, Chaudhury H, Zakkar M, Luong L, Kinderlerer A, Johns M, Blomhoff R, Mason JC, Haskard DO, Evans PC. Laminar shear stress acts as a switch to regulate divergent functions of NF-kappa B in endothelial cells. *Faseb Journal* 2007;21(13):3553-3561.
9. Ridker PM, Everett BM, Thuren T, MacFadyen JG, Chang WH, Ballantyne C, Fonseca F, Nicolau J, Koenig W, Anker SD, Kastelein JJP, Cornel JH, Pais P, Pella D, Genest J, Cifkova R, Lorenzatti A, Forster T, Kobalava Z, Vida-Simiti L, Flather M, Shimokawa H, Ogawa H, Dellborg M, Rossi PRF, Troquay RPT, Libby P, Glynn RJ. Antiinflammatory Therapy with Canakinumab for Atherosclerotic Disease. *The New England journal of medicine* 2017;377(12):1119-1131.
10. Bryan MT, Duckles H, Feng S, Hsiao ST, Kim HR, Serbanovic-Canic J, Evans PC. Mechanoresponsive networks controlling vascular inflammation. *Arteriosclerosis, thrombosis, and vascular biology* 2014;34(10):2199-205.
11. Fledderus JO, Boon RA, Volger OL, Hurttala H, Yla-Herttuala S, Pannekoek H, Levonen AL, Horrevoets AJ. KLF2 primes the antioxidant transcription factor Nrf2 for activation in endothelial cells. *Arteriosclerosis, thrombosis, and vascular biology* 2008;28(7):1339-46.
12. Zakkar M, Van der Heiden K, Luong le A, Chaudhury H, Cuhlmann S, Hamdulay SS, Krams R, Edirisinghe I, Rahman I, Carlsen H, Haskard DO, Mason JC, Evans PC. Activation of Nrf2 in endothelial cells protects arteries from exhibiting a proinflammatory state. *Arteriosclerosis, thrombosis, and vascular biology* 2009;29(11):1851-7.
13. Van der Heiden K, Cuhlmann S, Luong le A, Zakkar M, Evans PC. Role of nuclear factor kappaB in cardiovascular health and disease. *Clinical science (London, England : 1979)* 2010;118(10):593-605.

14. Cuhlmann S, Van der Heiden K, Saliba D, Tremoleda JL, Khalil M, Zakkar M, Chaudhury H, Luong le A, Mason JC, Udalova I, Gsell W, Jones H, Haskard DO, Krams R, Evans PC. Disturbed blood flow induces RelA expression via c-Jun N-terminal kinase 1: a novel mode of NF-kappaB regulation that promotes arterial inflammation. *Circulation research* 2011;108(8):950-9.
15. Hajra L, Evans AI, Chen M, Hyduk SJ, Collins T, Cybulsky MI. The NF-kappa B signal transduction pathway in aortic endothelial cells is primed for activation in regions predisposed to atherosclerotic lesion formation. *Proceedings of the National Academy of Sciences of the United States of America* 2000;97(16):9052-9057.
16. Baeyens N, Bandyopadhyay C, Coon BG, Yun S, Schwartz MA. Endothelial fluid shear stress sensing in vascular health and disease. *The Journal of clinical investigation* 2016;126(3):821-8.
17. Chatzizisis YS, Coskun AU, Jonas M, Edelman ER, Feldman CL, Stone PH. Role of endothelial shear stress in the natural history of coronary atherosclerosis and vascular remodeling: molecular, cellular, and vascular behavior. *Journal of the American College of Cardiology* 2007;49(25):2379-93.
18. Wentzel JJ, Chatzizisis YS, Gijsen FJ, Giannoglou GD, Feldman CL, Stone PH. Endothelial shear stress in the evolution of coronary atherosclerotic plaque and vascular remodelling: current understanding and remaining questions. *Cardiovascular research* 2012;96(2):234-43.
19. Koskinas KC, Sukhova GK, Baker AB, Papafaklis MI, Chatzizisis YS, Coskun AU, Quillard T, Jonas M, Maynard C, Antoniades AP, Shi GP, Libby P, Edelman ER, Feldman CL, Stone PH. Thin-capped atheromata with reduced collagen content in pigs develop in coronary arterial regions exposed to persistently low endothelial shear stress. *Arteriosclerosis, thrombosis, and vascular biology* 2013;33(7):1494-504.
20. Kubo T, Imanishi T, Takarada S, Kuroi A, Ueno S, Yamano T, Tanimoto T, Matsuo Y, Masho T, Kitabata H, Tsuda K, Tomobuchi Y, Akasaka T. Assessment of culprit lesion morphology in acute myocardial infarction: ability of optical coherence tomography compared with intravascular ultrasound and coronary angiography. *Journal of the American College of Cardiology* 2007;50(10):933-9.
21. Dolan JM, Meng H, Singh S, Paluch R, Kolega J. High fluid shear stress and spatial shear stress gradients affect endothelial proliferation, survival, and alignment. *Annals of biomedical engineering* 2011;39(6):1620-31.
22. Giannopoulos AA, Antoniades AP, Croce K, Chatzizisis YS. Erosion of Thin-Cap Fibroatheroma in an Area of Low Endothelial Shear Stress: Anatomy and Local Hemodynamic Environment Dictate Outcomes. *JACC Cardiovascular interventions* 2016;9(8):e77-e78.
23. White SJ, Newby AC, Johnson TW. Endothelial erosion of plaques as a substrate for coronary thrombosis. *Thrombosis and haemostasis* 2016;115(3):509-19.
24. Cicha I, Worner A, Urschel K, Beronov K, Goppelt-Struebe M, Verhoeven E, Daniel WG, Garlich CD. Carotid plaque vulnerability: a positive feedback between hemodynamic and biochemical mechanisms. *Stroke* 2011;42(12):3502-10.
25. Peiffer V, Sherwin SJ, Weinberg PD. Does low and oscillatory wall shear stress correlate spatially with early atherosclerosis? A systematic review. *Cardiovascular research* 2013;99(2):242-50.
26. Stone PH, Coskun AU, Kinlay S, Clark ME, Sonka M, Wahle A, Ilegbusi OJ, Yeghiazarians Y, Popma JJ, Orav J, Kuntz RE, Feldman CL. Effect of endothelial shear stress on the progression of coronary artery disease, vascular remodeling, and in-stent restenosis in humans: in vivo 6-month follow-up study. *Circulation* 2003;108(4):438-44.
27. Gijsen FJ, Oortman RM, Wentzel JJ, Schuurbiers JC, Tanabe K, Degertekin M, Ligthart JM, Thury A, de Feyter PJ, Serruys PW, Slager CJ. Usefulness of shear stress pattern in predicting neointima

distribution in sirolimus-eluting stents in coronary arteries. *The American journal of cardiology* 2003;92(11):1325-8.

28. Kolandaivelu K, Swaminathan R, Gibson WJ, Kolachalama VB, Nguyen-Ehrenreich KL, Giddings VL, Coleman L, Wong GK, Edelman ER. Stent thrombogenicity early in high-risk interventional settings is driven by stent design and deployment and protected by polymer-drug coatings. *Circulation* 2011;123(13):1400-9.

29. Rogers C, Tseng DY, Squire JC, Edelman ER. Balloon-artery interactions during stent placement: a finite element analysis approach to pressure, compliance, and stent design as contributors to vascular injury. *Circulation research* 1999;84(4):378-83.

30. Ng J, Bourantas CV, Torii R, Ang HY, Tenekecioglu E, Serruys PW, Foin N. Local Hemodynamic Forces After Stenting: Implications on Restenosis and Thrombosis. *Arteriosclerosis, thrombosis, and vascular biology* 2017;37(12):2231-2242.

31. Van der Heiden K, Gijzen FJ, Narracott A, Hsiao S, Halliday I, Gunn J, Wentzel JJ, Evans PC. The effects of stenting on shear stress: relevance to endothelial injury and repair. *Cardiovasc Res* 2013;99(2):269-75.

32. Ruggeri ZM. Platelet Adhesion under Flow. *Microcirculation (New York, NY : 1994)* 2009;16(1):58-83.

33. Nesbitt WS, Westein E, Tovar-Lopez FJ, Tolouei E, Mitchell A, Fu J, Carberry J, Fouras A, Jackson SP. A shear gradient-dependent platelet aggregation mechanism drives thrombus formation. *Nature medicine* 2009;15(6):665-73.

34. Shankaran H, Alexandridis P, Neelamegham S. Aspects of hydrodynamic shear regulating shear-induced platelet activation and self-association of von Willebrand factor in suspension. *Blood* 2003;101(7):2637-45.

35. Resnick N, Gimbrone MA, Jr. Hemodynamic forces are complex regulators of endothelial gene expression. *FASEB journal : official publication of the Federation of American Societies for Experimental Biology* 1995;9(10):874-82.

36. Skorczewski T, Erickson LC, Fogelson AL. Platelet motion near a vessel wall or thrombus surface in two-dimensional whole blood simulations. *Biophysical journal* 2013;104(8):1764-72.

37. Malek AM, Gibbons GH, Dzau VJ, Izumo S. Fluid shear stress differentially modulates expression of genes encoding basic fibroblast growth factor and platelet-derived growth factor B chain in vascular endothelium. *The Journal of clinical investigation* 1993;92(4):2013-21.

38. Chiu J-J, Chien S. Effects of Disturbed Flow on Vascular Endothelium: Pathophysiological Basis and Clinical Perspectives. *Physiological Reviews* 2011;91(1):327-387.

39. Bourantas CV, Jaffer FA, Gijzen FJ, van Soest G, Madden SP, Courtney BK, Fard AM, Tenekecioglu E, Zeng Y, van der Steen AFW, Emelianov S, Muller J, Stone PH, Marcu L, Tearney GJ, Serruys PW. Hybrid intravascular imaging: recent advances, technical considerations, and current applications in the study of plaque pathophysiology. *European heart journal* 2017;38(6):400-412.

40. Tu S, Huang Z, Koning G, Cui K, Reiber JH. A novel three-dimensional quantitative coronary angiography system: In-vivo comparison with intravascular ultrasound for assessing arterial segment length. *Catheterization and cardiovascular interventions : official journal of the Society for Cardiac Angiography & Interventions* 2010;76(2):291-8.

41. Guggenheim N, Dorsaz PA, Doriot PA, Suilen C, Chappuis F, Rutishauser W. 3D determination of the intravascular volume and flow of coronary arteries. *Int J Biomed Comput* 1994;35(1):13-23.

42. Wahle A, Wellnhofer E, Mugaragu I, Saner HU, Oswald H, Fleck E. Assessment of diffuse coronary artery disease by quantitative analysis of coronary morphology based upon 3-D reconstruction from biplane angiograms. *IEEE Trans Med Imaging* 1995;14(2):230-41.
43. Schuurbiens JC, Lopez NG, Ligthart J, Gijsen FJ, Dijkstra J, Serruys PW, Van der Steen AF, Wentzel JJ. In vivo validation of CAAS QCA-3D coronary reconstruction using fusion of angiography and intravascular ultrasound (ANGUS). *Catheter Cardiovasc Interv* 2009;73(5):620-6.
44. Ramcharitar S, Daeman J, Patterson M, van Guens RJ, Boersma E, Serruys PW, van der Giessen WJ. First direct in vivo comparison of two commercially available three-dimensional quantitative coronary angiography systems. *Catheterization and cardiovascular interventions : official journal of the Society for Cardiac Angiography & Interventions* 2008;71(1):44-50.
45. Toutouzas K, Chatzizisis YS, Riga M, Giannopoulos A, Antoniadis AP, Tu S, Fujino Y, Mitsouras D, Doulaverakis C, Tsampoulatidis I, Koutkias VG, Bouki K, Li Y, Chouvarda I, Cheimariotis G, Maglaveras N, Kompatsiaris I, Nakamura S, Reiber JH, Rybicki F, Karvounis H, Stefanadis C, Tousoulis D, Giannoglou GD. Accurate and reproducible reconstruction of coronary arteries and endothelial shear stress calculation using 3D OCT: comparative study to 3D IVUS and 3D QCA. *Atherosclerosis* 2015;240(2):510-9.
46. Schrauwen JT, Karanasos A, van Ditzhuijzen NS, Aben JP, van der Steen AF, Wentzel JJ, Gijsen FJ. Influence of the Accuracy of Angiography-Based Reconstructions on Velocity and Wall Shear Stress Computations in Coronary Bifurcations: A Phantom Study. *PloS one* 2015;10(12):e0145114.
47. Timmins LH, Suo J, Eshtehardi P, Molony DS, McDaniel MC, Oshinski JN, Giddens DP, Samady H. Comparison of angiographic and IVUS derived coronary geometric reconstructions for evaluation of the association of hemodynamics with coronary artery disease progression. *The international journal of cardiovascular imaging* 2016;32(9):1327-1336.
48. Bourantas CV, Ramasamy A, Karagiannis A, Sakellarios A, Zanchin T, Yamaji K, Ueki Y, Shen X, Fotiadis DI, Michalis LK, Mathur A, Serruys PW, Garcia-Garcia HM, Koskinas K, Torii R, Windecker S, Raber L. Angiographic derived endothelial shear stress: a new predictor of atherosclerotic disease progression. *Eur Heart J Cardiovasc Imaging* 2018.
49. Collet C, Onuma Y, Sonck J, Asano T, Vandeloo B, Kornowski R, Tu S, Westra J, Holm NR, Xu B, de Winter RJ, Tijssen JG, Miyazaki Y, Katagiri Y, Tenekecioglu E, Modolo R, Chichareon P, Cosyns B, Schoors D, Roosens B, Lochy S, Argacha JF, van Rosendaal A, Bax J, Reiber JHC, Escaned J, De Bruyne B, Wijns W, Serruys PW. Diagnostic performance of angiography-derived fractional flow reserve: a systematic review and Bayesian meta-analysis. *Eur Heart J* 2018;39(35):3314-3321.
50. Morris PD, Ryan D, Morton AC, Lycett R, Lawford PV, Hose DR, Gunn JP. Virtual fractional flow reserve from coronary angiography: modeling the significance of coronary lesions: results from the VIRTU-1 (VIRTUal Fractional Flow Reserve From Coronary Angiography) study. *JACC Cardiovascular interventions* 2013;6(2):149-57.
51. Papafaklis MI, Muramatsu T, Ishibashi Y, Lakkas LS, Nakatani S, Bourantas CV, Ligthart J, Onuma Y, Echavarría-Pinto M, Tsirka G, Kotsia A, Nikas DN, Mogabgab O, van Geuns RJ, Naka KK, Fotiadis DI, Brilakis ES, Garcia-Garcia HM, Escaned J, Zijlstra F, Michalis LK, Serruys PW. Fast virtual functional assessment of intermediate coronary lesions using routine angiographic data and blood flow simulation in humans: comparison with pressure wire - fractional flow reserve. *EuroIntervention : journal of EuroPCR in collaboration with the Working Group on Interventional Cardiology of the European Society of Cardiology* 2014;10(5):574-83.
52. Tu S, Westra J, Yang J, von Birgelen C, Ferrara A, Pellicano M, Nef H, Tebaldi M, Murasato Y, Lansky A, Barbato E, van der Heijden LC, Reiber JH, Holm NR, Wijns W, Group FPTS. Diagnostic Accuracy of Fast Computational Approaches to Derive Fractional Flow Reserve From Diagnostic Coronary

Angiography: The International Multicenter FAVOR Pilot Study. *JACC Cardiovasc Interv* 2016;9(19):2024-2035.

53. Xu B, Tu S, Qiao S, Qu X, Chen Y, Yang J, Guo L, Sun Z, Li Z, Tian F, Fang W, Chen J, Li W, Guan C, Holm NR, Wijns W, Hu S. Diagnostic Accuracy of Angiography-Based Quantitative Flow Ratio Measurements for Online Assessment of Coronary Stenosis. *J Am Coll Cardiol* 2017;70(25):3077-3087.

54. van der Giessen AG, Wentzel JJ, Meijboom WB, Mollet NR, van der Steen AF, van de Vosse FN, de Feyter PJ, Gijssen FJ. Plaque and shear stress distribution in human coronary bifurcations: a multislice computed tomography study. *EuroIntervention* 2009;4(5):654-61.

55. Voros S, Rinehart S, Qian Z, Vazquez G, Anderson H, Murrieta L, Wilmer C, Carlson H, Taylor K, Ballard W, Karpaliotis D, Kalynych A, Brown C, 3rd. Prospective validation of standardized, 3-dimensional, quantitative coronary computed tomographic plaque measurements using radiofrequency backscatter intravascular ultrasound as reference standard in intermediate coronary arterial lesions: results from the ATLANTA (assessment of tissue characteristics, lesion morphology, and hemodynamics by angiography with fractional flow reserve, intravascular ultrasound and virtual histology, and noninvasive computed tomography in atherosclerotic plaques) I study. *JACC Cardiovascular interventions* 2011;4(2):198-208.

56. Maurovich-Horvat P, Schlett CL, Alkadhi H, Nakano M, Stolzmann P, Vorpahl M, Scheffel H, Tanaka A, Warger WC, 2nd, Maehara A, Ma S, Kriegel MF, Kaple RK, Seifarth H, Bamberg F, Mintz GS, Tearney GJ, Virmani R, Hoffmann U. Differentiation of early from advanced coronary atherosclerotic lesions: systematic comparison of CT, intravascular US, and optical frequency domain imaging with histopathologic examination in ex vivo human hearts. *Radiology* 2012;265(2):393-401.

57. Park JB, Choi G, Chun EJ, Kim HJ, Park J, Jung JH, Lee MH, Otake H, Doh JH, Nam CW, Shin ES, De Bruyne B, Taylor CA, Koo BK. Computational fluid dynamic measures of wall shear stress are related to coronary lesion characteristics. *Heart* 2016;102(20):1655-61.

58. Sakellarios A, Bourantas CV, Papadopoulou SL, Tsirka Z, de Vries T, Kitslaar PH, Girasis C, Naka KK, Fotiadis DI, Veldhof S, Stone GW, Reiber JH, Michalis LK, Serruys PW, de Feyter PJ, Garcia-Garcia HM. Prediction of atherosclerotic disease progression using LDL transport modelling: a serial computed tomographic coronary angiographic study. *Eur Heart J Cardiovasc Imaging* 2017;18(1):11-18.

59. Bourantas CV, Papadopoulou SL, Serruys PW, Sakellarios A, Kitslaar PH, Bizopoulos P, Girasis C, Zhang YJ, de Vries T, Boersma E, Papafaklis MI, Naka KK, Fotiadis DI, Stone GW, Reiber JH, Michalis LK, de Feyter PJ, Garcia-Garcia HM. Noninvasive Prediction of Atherosclerotic Progression: The PROSPECT-MSCT Study. *JACC Cardiovasc Imaging* 2016;9(8):1009-11.

60. Slager CJ, Wentzel JJ, Schuurbijs JC, Oomen JA, Kloet J, Krams R, von Birgelen C, van der Giessen WJ, Serruys PW, de Feyter PJ. True 3-dimensional reconstruction of coronary arteries in patients by fusion of angiography and IVUS (ANGUS) and its quantitative validation. *Circulation* 2000;102(5):511-6.

61. Wahle A, Prause PM, DeJong SC, Sonka M. Geometrically correct 3-D reconstruction of intravascular ultrasound images by fusion with biplane angiography--methods and validation. *IEEE Trans Med Imaging* 1999;18(8):686-99.

62. Bourantas CV, Papafaklis MI, Athanasiou L, Kalatzis FG, Naka KK, Siogkas PK, Takahashi S, Saito S, Fotiadis DI, Feldman CL, Stone PH, Michalis LK. A new methodology for accurate 3-dimensional coronary artery reconstruction using routine intravascular ultrasound and angiographic data: implications for widespread assessment of endothelial shear stress in humans. *EuroIntervention* 2013;9(5):582-93.

63. Papafaklis MI, Bourantas CV, Yonetsu T, Vergallo R, Kotsia A, Nakatani S, Lakkas LS, Athanasiou LS, Naka KK, Fotiadis DI, Feldman CL, Stone PH, Serruys PW, Jang IK, Michalis LK. Anatomically correct

three-dimensional coronary artery reconstruction using frequency domain optical coherence tomographic and angiographic data: head-to-head comparison with intravascular ultrasound for endothelial shear stress assessment in humans. *EuroIntervention* 2015;11(4):407-15.

64. van der Giessen AG, Schaap M, Gijsen FJ, Groen HC, van Walsum T, Mollet NR, Dijkstra J, van de Vosse FN, Niessen WJ, de Feyter PJ, van der Steen AF, Wentzel JJ. 3D fusion of intravascular ultrasound and coronary computed tomography for in-vivo wall shear stress analysis: a feasibility study. *Int J Cardiovasc Imaging* 2010;26(7):781-96.

65. Bourantas CV, Kourtis IC, Plissiti ME, Fotiadis DI, Katsouras CS, Papafaklis MI, Michalis LK. A method for 3D reconstruction of coronary arteries using biplane angiography and intravascular ultrasound images. *Comput Med Imaging Graph* 2005;29(8):597-606.

66. Samady H, Eshtehardi P, McDaniel MC, Suo J, Dhawan SS, Maynard C, Timmins LH, Quyyumi AA, Giddens DP. Coronary artery wall shear stress is associated with progression and transformation of atherosclerotic plaque and arterial remodeling in patients with coronary artery disease. *Circulation* 2011;124(7):779-88.

67. Guo X, Giddens DP, Molony D, Yang C, Samady H, Zheng J, Mintz GS, Maehara A, Wang L, Pei X, Li ZY, Tang D. Combining IVUS and Optical Coherence Tomography for More Accurate Coronary Cap Thickness Quantification and Stress/Strain Calculations: A Patient-Specific Three-Dimensional Fluid-Structure Interaction Modeling Approach. *J Biomech Eng* 2018;140(4).

68. Wentzel JJ, van der Giessen AG, Garg S, Schultz C, Mastik F, Gijsen FJ, Serruys PW, van der Steen AF, Regar E. In vivo 3D distribution of lipid-core plaque in human coronary artery as assessed by fusion of near infrared spectroscopy-intravascular ultrasound and multislice computed tomography scan. *Circ Cardiovasc Imaging* 2010;3(6):e6-7.

69. Puri R, Madder RD, Madden SP, Sum ST, Wolski K, Muller JE, Andrews J, King KL, Kataoka Y, Uno K, Kapadia SR, Tuzcu EM, Nissen SE, Virmani R, Maehara A, Mintz GS, Nicholls SJ. Near-Infrared Spectroscopy Enhances Intravascular Ultrasound Assessment of Vulnerable Coronary Plaque: A Combined Pathological and In Vivo Study. *Arterioscler Thromb Vasc Biol* 2015;35(11):2423-31.

70. Tearney GJ, Regar E, Akasaka T, Adriaenssens T, Barlis P, Bezerra HG, Bouma B, Bruining N, Cho JM, Chowdhary S, Costa MA, de Silva R, Dijkstra J, Di Mario C, Dudek D, Falk E, Feldman MD, Fitzgerald P, Garcia-Garcia HM, Gonzalo N, Granada JF, Guagliumi G, Holm NR, Honda Y, Ikeno F, Kawasaki M, Kochman J, Koltowski L, Kubo T, Kume T, Kyono H, Lam CC, Lamouche G, Lee DP, Leon MB, Maehara A, Manfrini O, Mintz GS, Mizuno K, Morel MA, Nadkarni S, Okura H, Otake H, Pietrasik A, Prati F, Raber L, Radu MD, Rieber J, Riga M, Rollins A, Rosenberg M, Sirbu V, Serruys PW, Shimada K, Shinke T, Shite J, Siegel E, Sonoda S, Suter M, Takarada S, Tanaka A, Terashima M, Thim T, Uemura S, Ughi GJ, van Beusekom HM, van der Steen AF, van Es GA, van Soest G, Virmani R, Waxman S, Weissman NJ, Weisz G. Consensus standards for acquisition, measurement, and reporting of intravascular optical coherence tomography studies: a report from the International Working Group for Intravascular Optical Coherence Tomography Standardization and Validation. *Journal of the American College of Cardiology* 2012;59(12):1058-72.

71. Koskinas KC, Chatzizisis YS, Antoniadis AP, Giannoglou GD. Role of endothelial shear stress in stent restenosis and thrombosis: pathophysiologic mechanisms and implications for clinical translation. *J Am Coll Cardiol* 2012;59(15):1337-49.

72. Bourantas CV, Papafaklis MI, Lakkas L, Sakellarios A, Onuma Y, Zhang YJ, Muramatsu T, Diletti R, Bizopoulos P, Kalatzis F, Naka KK, Fotiadis DI, Wang J, Garcia Garcia HM, Kimura T, Michalis LK, Serruys PW. Fusion of optical coherence tomographic and angiographic data for more accurate evaluation of the endothelial shear stress patterns and neointimal distribution after bioresorbable scaffold implantation: comparison with intravascular ultrasound-derived reconstructions. *The international journal of cardiovascular imaging* 2014;30(3):485-94.

73. Thondapu V, Bourantas CV, Foin N, Jang IK, Serruys PW, Barlis P. Biomechanical stress in coronary atherosclerosis: emerging insights from computational modelling. *European heart journal* 2017;38(2):81-92.
74. Torii R, Wood NB, Hadjiloizou N, Dowsey AW, Wright AR, Hughes AD, Davies J, Francis DP, Mayet J, Yang GZ, Thom SAM, Xu XY. Fluid-structure interaction analysis of a patient-specific right coronary artery with physiological velocity and pressure waveforms. *Commun Numer Meth En* 2009;25(5):565-580.
75. Yang C, Bach RG, Zheng J, Naqa IE, Woodard PK, Teng Z, Billiar K, Tang D. In vivo IVUS-based 3-D fluid-structure interaction models with cyclic bending and anisotropic vessel properties for human atherosclerotic coronary plaque mechanical analysis. *IEEE transactions on bio-medical engineering* 2009;56(10):2420-8.
76. Barlis P, Poon EK, Thondapu V, Grundeken MJ, Tu S, Hayat U, Ooi A, Moore S, Tenekecioglu E, Wykrzykowska JJ, Serruys PW. Reversal of flow between serial bifurcation lesions: insights from computational fluid dynamic analysis in a population-based phantom model. *EuroIntervention* 2015;11(5):e1-3.
77. Manbachi A, Hoi Y, Wasserman BA, Lakatta EG, Steinman DA. On the shape of the common carotid artery with implications for blood velocity profiles. *Physiological measurement* 2011;32(12):1885-97.
78. Boutsianis E, Dave H, Frauenfelder T, Poulikakos D, Wildermuth S, Turina M, Ventikos Y, Zund G. Computational simulation of intracoronary flow based on real coronary geometry. *European journal of cardio-thoracic surgery : official journal of the European Association for Cardio-thoracic Surgery* 2004;26(2):248-56.
79. Tu S, Holm NR, Koning G, Maeng M, Reiber JH. The impact of acquisition angle differences on three-dimensional quantitative coronary angiography. *Catheterization and cardiovascular interventions : official journal of the Society for Cardiac Angiography & Interventions* 2011;78(2):214-22.
80. Vani A, Underberg JA. Lowering LDL-Cholesterol and CV Benefits: Is There a Limit to How Low LDL-C Needs to be for Optimal Health Benefits? *Clin Pharmacol Ther* 2018;104(2):290-296.
81. Karanasos A, van der Sijde JN, Ligthart J, Witberg K, Regar E. Utility of Optical Coherence Tomography Imaging with Angiographic Co-registration for the Guidance of Percutaneous Coronary Intervention. *Radcliffe Cardiology* 2015:1-7.
82. Li Y, Gutierrez-Chico JL, Holm NR, Yang W, Hebsgaard L, Christiansen EH, Maeng M, Lassen JF, Yan F, Reiber JH, Tu S. Impact of Side Branch Modeling on Computation of Endothelial Shear Stress in Coronary Artery Disease: Coronary Tree Reconstruction by Fusion of 3D Angiography and OCT. *Journal of the American College of Cardiology* 2015;66(2):125-35.
83. Dodge JT, Jr., Rizzo M, Nykiel M, Altmann J, Hobkirk K, Brennan M, Gibson CM. Impact of injection rate on the Thrombolysis in Myocardial Infarction (TIMI) trial frame count. *Am J Cardiol* 1998;81(10):1268-70.
84. Coskun AU, Yeghiazarians Y, Kinlay S, Clark ME, Ilegbusi OJ, Wahle A, Sonka M, Popma JJ, Kuntz RE, Feldman CL, Stone PH. Reproducibility of coronary lumen, plaque, and vessel wall reconstruction and of endothelial shear stress measurements in vivo in humans. *Catheterization and cardiovascular interventions : official journal of the Society for Cardiac Angiography & Interventions* 2003;60(1):67-78.

85. Tanedo JS, Kelly RF, Marquez M, Burns DE, Klein LW, Costanzo MR, Parrillo JE, Hollenberg SM. Assessing coronary blood flow dynamics with the TIMI frame count method: Comparison with simultaneous intracoronary Doppler and ultrasound. *Catheter Cardio Inte* 2001;53(4):459-463.
86. Murray CD. The Physiological Principle of Minimum Work: I. The Vascular System and the Cost of Blood Volume. *Proceedings of the National Academy of Sciences of the United States of America* 1926;12(3):207-14.
87. Zhou Y, Kassab GS, Molloy S. In vivo validation of the design rules of the coronary arteries and their application in the assessment of diffuse disease. *Physics in medicine and biology* 2002;47(6):977-93.
88. Kassab GS. Scaling laws of vascular trees: of form and function. *Am J Physiol Heart Circ Physiol* 2006;290(2):H894-903.
89. Rossi A, Merkus D, Klotz E, Mollet N, de Feyter PJ, Krestin GP. Stress Myocardial Perfusion Imaging with Multidetector CT. *Radiology* 2014;270(1):24-45.
90. Kurata A, Kono A, Sakamoto T, Kido T, Mochizuki T, Higashino H, Abe M, Coenen A, Saru-Chelu RG, de Feyter PJ, Krestin GP, Nieman K. Quantification of the myocardial area at risk using coronary CT angiography and Voronoi algorithm-based myocardial segmentation. *Eur Radiol* 2015;25(1):49-57.
91. Schrauwen JTC, Coenen A, Kurata A, Wentzel JJ, van der Steen AFW, Nieman K, Gijzen FJH. Functional and anatomical measures for outflow boundary conditions in atherosclerotic coronary bifurcations. *Journal of biomechanics* 2016;49(11):2127-2134.
92. Schrauwen JTC, Schwarz JCV, Wentzel JJ, van der Steen AFW, Siebes M, Gijzen FJH. The impact of scaled boundary conditions on wall shear stress computations in atherosclerotic human coronary bifurcations. *Am J Physiol-Heart C* 2016;310(10):H1304-H1312.
93. Tenekecioglu E, Poon EKW, Collet C, Thondapu V, Torii R, Bourantas CV, Zeng YP, Onuma Y, Ooi ASH, Serruys PW, Barlis P. The Nidus for Possible Thrombus Formation Insight From the Microenvironment of Bioresorbable Vascular Scaffold. *Jacc-Cardiovasc Inte* 2016;9(20):2167-2168.
94. Davies JE, Whinnett ZI, Francis DP, Manisty CH, Aguado-Sierra J, Willson K, Foale RA, Malik IS, Hughes AD, Parker KH, Mayet J. Evidence of a dominant backward-propagating "suction" wave responsible for diastolic coronary filling in humans, attenuated in left ventricular hypertrophy. *Circulation* 2006;113(14):1768-78.
95. Hadjiloizou N, Davies JE, Malik IS, Aguado-Sierra J, Willson K, Foale RA, Parker KH, Hughes AD, Francis DP, Mayet J. Differences in cardiac microcirculatory wave patterns between the proximal left mainstem and proximal right coronary artery. *Am J Physiol Heart Circ Physiol* 2008;295(3):H1198-H1205.
96. Westerhof N, Lankhaar JW, Westerhof BE. The arterial Windkessel. *Med Biol Eng Comput* 2009;47(2):131-141.
97. Kim HJ, Vignon-Clementel IE, Figueroa CA, LaDisa JF, Jansen KE, Feinstein JA, Taylor CA. On coupling a lumped parameter heart model and a three-dimensional finite element aorta model. *Annals of biomedical engineering* 2009;37(11):2153-69.
98. Chien S, Usami S, Dellenback RJ, Gregersen MI. Shear-dependent deformation of erythrocytes in rheology of human blood. *The American journal of physiology* 1970;219(1):136-42.
99. Du VX, Huskens D, Maas C, Al Dieri R, de Groot PG, de Laat B. New insights into the role of erythrocytes in thrombus formation. *Semin Thromb Hemost* 2014;40(1):72-80.

100. Sherwood JM, Kaliviotis E, Dusing J, Balabani S. Hematocrit, viscosity and velocity distributions of aggregating and non-aggregating blood in a bifurcating microchannel. *Biomech Model Mechan* 2014;13(2):259-273.
101. Ku DN. Blood flow in arteries. *Annu Rev Fluid Mech* 1997;29:399-434.
102. Boyd J, Buick JM, Green S. Analysis of the Casson and Carreau-Yasuda non-Newtonian blood models in steady and oscillatory flows using the lattice Boltzmann method. *Phys Fluids* 2007;19(9).
103. Quemada D. Rheology of Concentrated Disperse Systems .3. General Features of the Proposed Non-Newtonian Model - Comparison with Experimental-Data. *Rheol Acta* 1978;17(6):643-653.
104. Hughes TJR. *The Finite Element Method: Linear Static and Dynamic Finite Element Analysis (Dover Civil and Mechanical Engineering)*: Dover Publications; 2000.
105. Anderson JD. *Computational Fluid Dynamics: the Basics with Applications*. McGraw-Hill Education 1995.
106. Ku DN, Giddens DP, Zarins CK, Glagov S. Pulsatile flow and atherosclerosis in the human carotid bifurcation. Positive correlation between plaque location and low oscillating shear stress. *Arteriosclerosis* 1985;5(3):293-302.
107. Himburg HA, Grzybowski DM, Hazel AL, LaMack JA, Li XM, Friedman MH. Spatial comparison between wall shear stress measures and porcine arterial endothelial permeability. *Am J Physiol Heart Circ Physiol* 2004;286(5):H1916-22.
108. Peiffer V, Sherwin SJ, Weinberg PD. Computation in the rabbit aorta of a new metric - the transverse wall shear stress - to quantify the multidirectional character of disturbed blood flow. *J Biomech* 2013;46(15):2651-8.
109. Foin N, Gutierrez-Chico JL, Nakatani S, Torii R, Bourantas CV, Sen S, Nijjer S, Petraco R, Kouser C, Ghione M, Onuma Y, Garcia-Garcia HM, Francis DP, Wong P, Di Mario C, Davies JE, Serruys PW. Incomplete stent apposition causes high shear flow disturbances and delay in neointimal coverage as a function of strut to wall detachment distance: implications for the management of incomplete stent apposition. *Circ Cardiovasc Interv* 2014;7(2):180-9.
110. Sriram K, Salazar Vazquez BY, Tsai AG, Cabrales P, Intaglietta M, Tartakovsky DM. Autoregulation and mechanotransduction control the arteriolar response to small changes in hematocrit. *Am J Physiol Heart Circ Physiol* 2012;303(9):H1096-106.
111. Dupin MM, Halliday I, Care CM. A multi-component lattice Boltzmann scheme: towards the mesoscale simulation of blood flow. *Med Eng Phys* 2006;28(1):13-8.
112. Kruger T, Holmes D, Coveney PV. Deformability-based red blood cell separation in deterministic lateral displacement devices-A simulation study. *Biomicrofluidics* 2014;8(5):054114.
113. Lee TR, Choi M, Kopacz AM, Yun SH, Liu WK, Decuzzi P. On the near-wall accumulation of injectable particles in the microcirculation: smaller is not better. *Sci Rep* 2013;3:2079.
114. Li S, Sugiyama K, Takagi S, Matsumoto Y. A Computational Blood Flow Analysis in a Capillary Vessel including Multiple Red Blood Cells and Platelets. *Journal of Biomechanical Science and Engineering* 2012;7(1):72-83.
115. Zavodszky G, van Rooij B, Azizi V, Hoekstra A. Cellular Level In-silico Modeling of Blood Rheology with An Improved Material Model for Red Blood Cells. *Front Physiol* 2017;8:563.
116. Thondapu V, Tenekecioglu E, Poon EKW, Collet C, Torii R, Bourantas CV, Chin C, Sotomi Y, Jonker H, Dijkstra J, Revalor E, Gijsen F, Onuma Y, Ooi A, Barlis P, Serruys PW. Endothelial shear stress 5 years after implantation of a coronary bioresorbable scaffold. *Eur Heart J* 2018;39(18):1602-1609.

117. Doddaballapur A, Michalik KM, Manavski Y, Lucas T, Houtkooper RH, You X, Chen W, Zeiher AM, Potente M, Dimmeler S, Boon RA. Laminar shear stress inhibits endothelial cell metabolism via KLF2-mediated repression of PFKFB3. *Arterioscler Thromb Vasc Biol* 2015;35(1):137-45.
118. Eshtehardi P, McDaniel MC, Suo J, Dhawan SS, Timmins LH, Binongo JN, Golub LJ, Corban MT, Finn AV, Oshinski JN, Quyyumi AA, Giddens DP, Samady H. Association of coronary wall shear stress with atherosclerotic plaque burden, composition, and distribution in patients with coronary artery disease. *Journal of the American Heart Association* 2012;1(4):e002543.
119. Papafaklis MI, Takahashi S, Antoniadis AP, Coskun AU, Tsuda M, Mizuno S, Andreou I, Nakamura S, Makita Y, Hirohata A, Saito S, Feldman CL, Stone PH. Effect of the local hemodynamic environment on the de novo development and progression of eccentric coronary atherosclerosis in humans: insights from PREDICTION. *Atherosclerosis* 2015;240(1):205-11.
120. Stone PH, Saito S, Takahashi S, Makita Y, Nakamura S, Kawasaki T, Takahashi A, Katsuki T, Nakamura S, Namiki A, Hirohata A, Matsumura T, Yamazaki S, Yokoi H, Tanaka S, Otsuji S, Yoshimachi F, Honye J, Harwood D, Reitman M, Coskun AU, Papafaklis MI, Feldman CL, Investigators P. Prediction of progression of coronary artery disease and clinical outcomes using vascular profiling of endothelial shear stress and arterial plaque characteristics: the PREDICTION Study. *Circulation* 2012;126(2):172-81.
121. Costopoulos C, Timmins LH, Huang Y, Hung OY, Molony DS, Brown AJ, Davis EL, Teng Z, Gillard JH, Samady H, Bennett MR. Impact of combined plaque structural stress and wall shear stress on coronary plaque progression, regression, and changes in composition. *Eur Heart J* 2019.
122. Gijzen FJH, Wentzel JJ, Thury A, Mastik F, Schaar JA, Schuurbiers JCH, Slager CJ, van der Giessen W, de Feyter PJ, van der Steen AFW, Serruys PW. Strain distribution over plaques in human coronary arteries relates to shear stress. *Am J Physiol Heart Circ Physiol* 2008;295:H1608-H1614.
123. Corban MT, Eshtehardi P, Suo J, McDaniel MC, Timmins LH, Rassoul-Arzrumly E, Maynard C, Mekonnen G, King S, 3rd, Quyyumi AA, Giddens DP, Samady H. Combination of plaque burden, wall shear stress, and plaque phenotype has incremental value for prediction of coronary atherosclerotic plaque progression and vulnerability. *Atherosclerosis* 2014;232(2):271-6.
124. Chatzizisis YS, Toutouzas K, Giannopoulos AA, Riga M, Antoniadis AP, Fujinom Y, Mitsouras D, Koutkias VG, Cheimariotis G, Doulaverakis C, Tsampoulatidis I, Chouvarda I, Kompatsiaris I, Nakamura S, Rybicki FJ, Maglaveras N, Tousoulis D, Giannoglou GD. Association of global and local low endothelial shear stress with high-risk plaque using intracoronary 3D optical coherence tomography: Introduction of 'shear stress score'. *Eur Heart J Cardiovasc Imaging* 2016.
125. Vergallo R, Papafaklis MI, Yonetsu T, Bourantas CV, Andreou I, Wang Z, Fujimoto JG, McNulty I, Lee H, Biasucci LM, Crea F, Feldman CL, Michalis LK, Stone PH, Jang IK. Endothelial shear stress and coronary plaque characteristics in humans: combined frequency-domain optical coherence tomography and computational fluid dynamics study. *Circ Cardiovasc Imaging* 2014;7(6):905-11.
126. Stone PH, Maehara A, Coskun AU, Maynard CC, Zaromytidou M, Siasos G, Andreou I, Fotiadis D, Stefanou K, Papafaklis M, Michalis L, Lansky AJ, Mintz GS, Serruys PW, Feldman CL, Stone GW. Role of Low Endothelial Shear Stress and Plaque Characteristics in the Prediction of Nonculprit Major Adverse Cardiac Events: The PROSPECT Study. *JACC Cardiovasc Imaging* 2018;11(3):462-471.
127. Fukumoto Y, Hiro T, Fujii T, Hashimoto G, Fujimura T, Yamada J, Okamura T, Matsuzaki M. Localized elevation of shear stress is related to coronary plaque rupture: a 3-dimensional intravascular ultrasound study with in-vivo color mapping of shear stress distribution. *Journal of the American College of Cardiology* 2008;51(6):645-50.
128. Gijzen F, van der Giessen A, van der Steen A, Wentzel J. Shear stress and advanced atherosclerosis in human coronary arteries. *J Biomechanics* 2013;46(2):240-7.

129. Bourantas CV, Papafaklis MI, Naka KK, Tsakanikas VD, Lysitsas DN, Alamgir FM, Fotiadis DI, Michalis LK. Fusion of optical coherence tomography and coronary angiography - in vivo assessment of shear stress in plaque rupture. *Int J Cardiol* 2012;155(2):e24-6.
130. Lee JM, Choi G, Koo BK, Hwang D, Park J, Zhang J, Kim KJ, Tong Y, Kim HJ, Grady L, Doh JH, Nam CW, Shin ES, Cho YS, Choi SY, Chun EJ, Choi JH, Norgaard BL, Christiansen EH, Niemen K, Otake H, Penicka M, de Bruyne B, Kubo T, Akasaka T, Narula J, Douglas PS, Taylor CA, Kim HS. Identification of High-Risk Plaques Destined to Cause Acute Coronary Syndrome Using Coronary Computed Tomographic Angiography and Computational Fluid Dynamics. *JACC Cardiovasc Imaging* 2018.
131. Kumar A, Thompson EW, Lefieux A, Molony DS, Davis EL, Chand N, Fournier S, Lee HS, Suh J, Sato K, Ko YA, Molloy D, Chandran K, Hosseini H, Gupta S, Milkas A, Gogas B, Chang HJ, Min JK, Fearon WF, Veneziani A, Giddens DP, King SB, 3rd, De Bruyne B, Samady H. High Coronary Shear Stress in Patients With Coronary Artery Disease Predicts Myocardial Infarction. *J Am Coll Cardiol* 2018;72(16):1926-1935.
132. Koppa T, Cheng Q, Yahagi K, Mori H, Sanchez OD, Feygin J, Wittchow E, Kolodgie FD, Virmani R, Joner M. Thrombogenicity and early vascular healing response in metallic biodegradable polymer-based and fully bioabsorbable drug-eluting stents. *Circ Cardiovasc Interv* 2015;8(6):e002427.
133. Wentzel JJ, Gijzen FJ, Schuurbijs JC, van der Steen AF, Serruys PW. The influence of shear stress on in-stent restenosis and thrombosis. *EuroIntervention : journal of EuroPCR in collaboration with the Working Group on Interventional Cardiology of the European Society of Cardiology* 2008;4 Suppl C:C27-32.
134. Thury A, Wentzel JJ, Vinke RV, Gijzen FJ, Schuurbijs JC, Krams R, de Feyter PJ, Serruys PW, Slager CJ. Images in cardiovascular medicine. Focal in-stent restenosis near step-up: roles of low and oscillating shear stress? *Circulation* 2002;105(23):e185-7.
135. Wentzel JJ, Krams R, Schuurbijs JC, Oomen JA, Kloet J, van Der Giessen WJ, Serruys PW, Slager CJ. Relationship between neointimal thickness and shear stress after Wallstent implantation in human coronary arteries. *Circulation* 2001;103(13):1740-5.
136. Ueba H, Kawakami M, Yaginuma T. Shear stress as an inhibitor of vascular smooth muscle cell proliferation. Role of transforming growth factor-beta 1 and tissue-type plasminogen activator. *Arteriosclerosis, thrombosis, and vascular biology* 1997;17(8):1512-6.
137. Torii R, Tenekecioglu E, Bourantas C, Poon E, Thondapu V, Gijzen F, Sotomi Y, Onuma Y, Barlis P, Ooi ASH, Serruys PW. Five-year follow-up of underexpanded and overexpanded bioresorbable scaffolds: self-correction and impact on shear stress. *EuroIntervention* 2017;12(17):2158-2159.
138. Jimenez JM, Davies PF. Hemodynamically driven stent strut design. *Annals of biomedical engineering* 2009;37(8):1483-94.
139. Gogas BD, Yang B, Piccinelli M, Giddens DP, King SB, 3rd, Kereiakes DJ, Ellis SG, Stone GW, Veneziani A, Samady H. Novel 3-Dimensional Vessel and Scaffold Reconstruction Methodology for the Assessment of Strut-Level Wall Shear Stress After Deployment of Bioresorbable Vascular Scaffolds From the ABSORB III Imaging Substudy. *JACC Cardiovascular interventions* 2016;9(5):501-3.
140. Chan CH, Pieper IL, Fleming S, Friedmann Y, Foster G, Hawkins K, Thornton CA, Kanamarlapudi V. The effect of shear stress on the size, structure, and function of human von Willebrand factor. *Artificial organs* 2014;38(9):741-50.
141. Tenekecioglu E, Sotomi Y, Torii R, Bourantas C, Miyazaki Y, Collet C, Crake T, Su S, Onuma Y, Serruys PW. Strut protrusion and shape impact on endothelial shear stress: insights from pre-clinical study comparing Mirage and Absorb bioresorbable scaffolds. *Int J Cardiovasc Imaging* 2017;33(9):1313-1322.

142. Torii R, Stettler R, Raber L, Zhang YJ, Karanasos A, Dijkstra J, Patel K, Crake T, Hamshere S, Garcia-Garcia HM, Tenekecioglu E, Ozkor M, Baumbach A, Windecker S, Serruys PW, Regar E, Mathur A, Bourantas CV. Implications of the local hemodynamic forces on the formation and destabilization of neoatherosclerotic lesions. *Int J Cardiol* 2018;272:7-12.
143. Palmerini T, Biondi-Zoccai G, Della Riva D, Mariani A, Sabate M, Smits PC, Kaiser C, D'Ascenzo F, Frati G, Mancone M, Genereux P, Stone GW. Clinical outcomes with bioabsorbable polymer- versus durable polymer-based drug-eluting and bare-metal stents: evidence from a comprehensive network meta-analysis. *Journal of the American College of Cardiology* 2014;63(4):299-307.
144. Palmerini T, Benedetto U, Biondi-Zoccai G, Della Riva D, Bacchi-Reggiani L, Smits PC, Vlachojannis GJ, Jensen LO, Christiansen EH, Berencsi K, Valgimigli M, Orlandi C, Petrou M, Rapezzi C, Stone GW. Long-Term Safety of Drug-Eluting and Bare-Metal Stents: Evidence From a Comprehensive Network Meta-Analysis. *Journal of the American College of Cardiology* 2015;65(23):2496-507.
145. Morrison TM. Reporting of Computational Modeling Studies in Medical Device Submission—Guidance for Industry and FDA Staff. FDA Regulatory Information; Silver Spring, MD 2016.
146. Zarins CK, Giddens DP, Bharadvaj BK, Sottiurai VS, Mabon RF, Glagov S. Carotid bifurcation atherosclerosis. Quantitative correlation of plaque localization with flow velocity profiles and wall shear stress. *Circ Res* 1983;53(4):502-14.
147. Wentzel JJ, Janssen E, Vos J, Schuurbiers JC, Krams R, Serruys PW, de Feyter PJ, Slager CJ. Extension of increased atherosclerotic wall thickness into high shear stress regions is associated with loss of compensatory remodeling. *Circulation* 2003;108(1):17-23.
148. Malek AM, Alper SL, Izumo S. Hemodynamic shear stress and its role in atherosclerosis. *JAMA* 1999;282(21):2035-42.
149. White SJ, Hayes EM, Lehoux S, Jeremy JY, Horrevoets AJ, Newby AC. Characterization of the differential response of endothelial cells exposed to normal and elevated laminar shear stress. *J Cell Physiol* 2011;226(11):2841-8.

APPENDIX A: TECHNICAL RECOMMENDATIONS

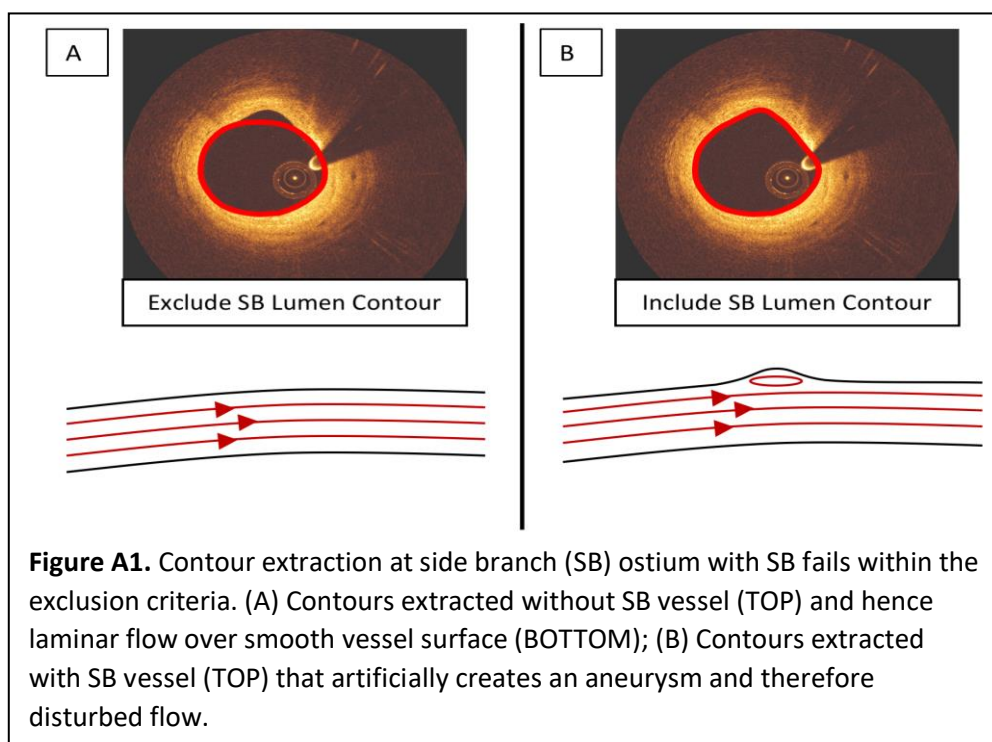
We will provide the reader with guidelines how to generate computational meshes, generate an appropriate set of input conditions, and solve and post-process the CFD simulations. We would want to stress that these recommendations cannot be used as a ‘recipe’: each computational problem is unique, and requires careful considerations regarding all matters discussed below. In case of doubt, one is strongly advised to seek assistance of an expert in CFD. This is not a disclaimer, but an expression of a worry deeply shared within the CFD-community: performing adequate, reliable and meaningful results from CFD is not trivial, and in most cases, requires in-depth knowledge of the procedure.

A.1 Side branch reconstruction

At coronary artery bifurcation, side branch diverts coronary flow from the main vessel and helps transport oxygen-rich blood to different part of heart. Accurate coronary flow distribution into main vessel and side branch is critical to WSS prediction. For that, it is recommended that side branch falls within the following criteria are included in 3D reconstruction:

- 1) side branch is >1 mm in diameter¹;
- 2) $>1/3$ of the main vessel diameter²; and
- 3) a bifurcation located immediately proximal and distal, and within a distance of 1 diameter of the ROI³.

Furthermore, rigorous strategies should be employed to extract lumen contour proximal, at and distal to side branch ostium. In particular, when a side branch fails to meet the inclusion criteria, methods that lead to smooth extraction of contours that exclude side branch opening should be employed such that there exists no artificial bulge, and hence no flow disturbances (**Figure A1**).



A.2 Stented arterial segment

In a stented artery, OCT is currently the only imaging modality able to capture the geometrical features of stent struts *in vivo*⁴. Methods aimed at 3D model reconstruction that feature the stent struts include:

- 1) longitudinal interpolation of the segmented IVUS/OCT cross-sectional contours⁵;
- 2) superimposition of known stent geometry in the OCT-based vessel model^{6, 7};
- 3) virtual deployment of a stent in 3D vessel model^{8, 9}.

Option 1 is the easiest approach, but it is only suitable for stents with large stent struts with the struts being well apposed to the wall, and the interval between the OCT images should be sufficiently small. Options 2 and 3 are much more complicated, but the only available option if mal-apposed struts need to be included.

A.3 Meshing requirements

Lumen contours in both CTCA and 3D-QCA are approximated as either circles or ellipses¹⁰, such that lumen geometry and important flow features (e.g., secondary flow, flow reversal) can generally be represented with approximately 70 grid points circumferentially. On the other hand, fusion of IVUS and OCT-angiography reconstructions include lumen boundaries that might have irregular lumen surface features in the presence of atherosclerosis or thrombus. As such, local mesh refinement (LMF), an option that is often available in most CFD meshing programs, should be employed to ensure that the grid conforms to the patient-specific lumen surface. Mesh convergence check remains essential with LMF. Within stented arterial segment, a cell element whose size is approximately 1/10 of the strut thickness was found to capture the recirculation zone behind the strut⁵. In such high-resolution mesh, the total size of mesh ends up with > 10M cells in 3D for a vessel of several cm, resulting in significant computational costs. The LMF approach can be taken to mitigate this, placing very small cells in the stented segment only and not in the native part of the vessel. For the radial direction near the lumen surface (also known as the boundary layer), the mesh elements need to be closely packed for a good numerical approximation of the steep change in velocity profile (and hence wall shear stress) close to the wall (**Figure A2**). As we move away from the lumen surface, there is a more gradual change in the velocity profile. **Table A1** summarises the initial mesh requirements for various different geometric model reconstructions.

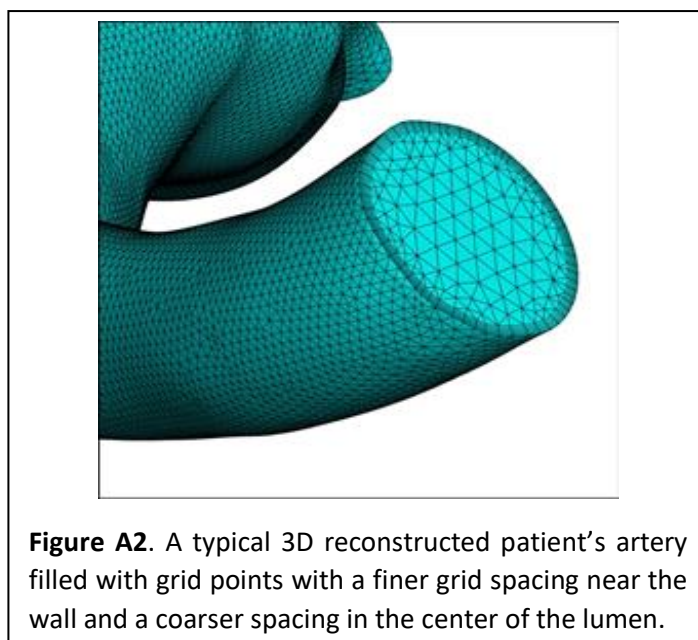


Figure A2. A typical 3D reconstructed patient's artery filled with grid points with a finer grid spacing near the wall and a coarser spacing in the center of the lumen.

Table A1. Spatial solution criteria for different coronary reconstruction methods. LMF stands for local mesh refinement.

	MSCT/3D-QCA	IVUS/OCT-based
Native Artery Surface mesh [μm]	100	100-200 with LMF
Stented Artery Surface mesh [μm]	20	20
Internal Edge mesh [μm]	500	500
Boundary layer mesh thickness [μm]	100	100
Boundary layer mesh number	3-5	3-5
Boundary layer mesh growth rate	1.1-1.3	1.1-1.3

A.4 Boundary Conditions

For velocity inlet boundary condition, it is important to note that the application of this velocity differs based on the location of the inlet. In theory, complex model including the full aortic root and both right and left coronary arteries in a single simulation allows natural flow development into the coronary arteries emergent from the aorta¹¹, but can be extremely expensive to carry out. In the absence of the aortic root, a uniform velocity profile should be prescribed with the inlet of ROI near the ostium and a parabolic profile with the inlet away from the ostium. The velocity inlet is often coupled with a fixed pressure boundary condition at the outlet.

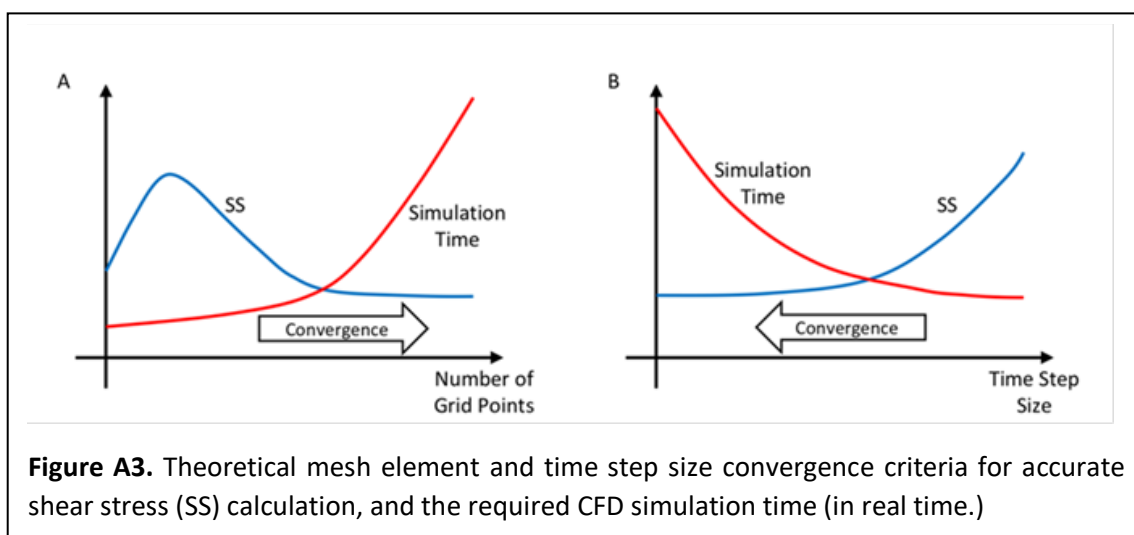
If no patient-specific data are available, the inlet velocity can be estimated using various scaling laws. The most famous scaling law, Murrays law, dates from the early 20th century¹² and is based on physical principles describing minimization of the energy required to transport fluids through networks. This law prescribes a cubed relationship between the diameter and the average velocity. Various more recently developed scaling laws based on empirical data are available as well, and for coronary artery flow the exponent relating diameter to average velocity ranges between 2 and 3^{13, 14, 15}. Setting flow split through branches of the coronary tree, based on such a scaling law, as the outlet boundary condition is also a common and effective approach¹⁶.

In pulsatile simulations, a coupled boundary condition is often an effective way to handle the phasic change in coronary pressure and velocity. One of the simplest approaches would be prescribing, potentially patient-specific, pressure at the inlet combined with a lumped parameter model for the outlet¹⁷, often referred as Windkessel model consisting of peripheral resistance and compliance. Some of the complex models include the full aortic root and both right and left coronary models in a single simulation¹¹. In models where the aortic inlet is linked to a heart model or the aortic inflow is prescribed based on cardiac output, flow into the coronary arteries is emergent from the model, and determined by the prescribed coronary resistances at the model outlets. In these models, specialized coronary lumped parameter boundary conditions are applied at the coronary outlets. These boundary conditions have been shown to produce realistic flow and pressure waveforms that capture the out-of-phase behaviour of coronary physiology, which is crucial for FSI simulations. In these models, variable coronary resistances are included at the outlets, which link to cardiac contraction via a lumped parameter heart model. Resistances are typically distributed via scaling laws based on the outlet diameters. Recent work¹⁸ has demonstrated automated tuning procedures to determine lumped parameter values that are tuned to match a set of non-invasively obtained

patient data, thus allowing one to capture realistic patient specific coronary physiology and flow.

A.5 Solution Strategies

Accurate approximations for both velocity and pressure is a computationally intensive process that requires solving the governing Navier–Stokes equations on each mesh element of the coronary artery over many (from tens to thousands) of iterations (and time steps for pulsatile simulations). With each iteration, the error in solving the equations is reduced and the solution is said to “converged” when residual (error) values of velocity and pressure are below a certain threshold. The value of this threshold is typically between 10^{-3} and 10^{-6} , depending on the problem addressed and the methods chosen to solve the problem.



Further, the solutions are checked for both mesh element and time step size convergence. In general, the greater the number of mesh elements, the better the mesh resolution and hence a more accurate solution. However, it should be realised that the solution time increases exponentially with total number of grid points (see *Figure A3*). Additionally, increasing mesh resolution requires a smaller time step size in order to maintain solution stability and hence further increases simulation time (see *Figure A3*).

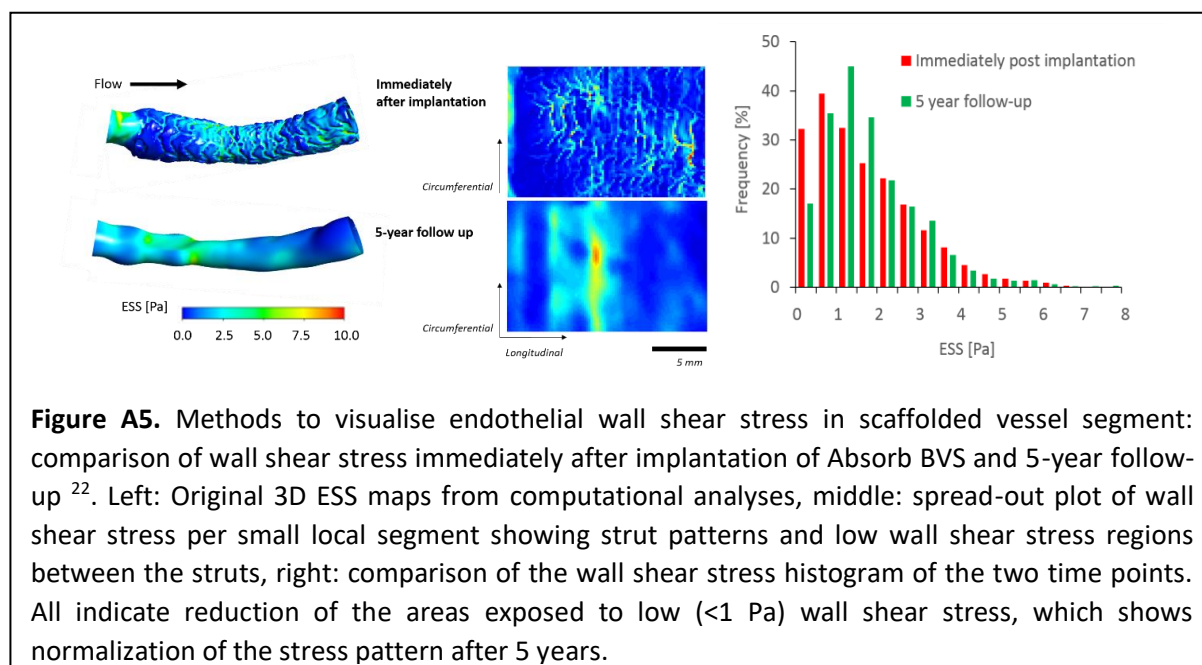
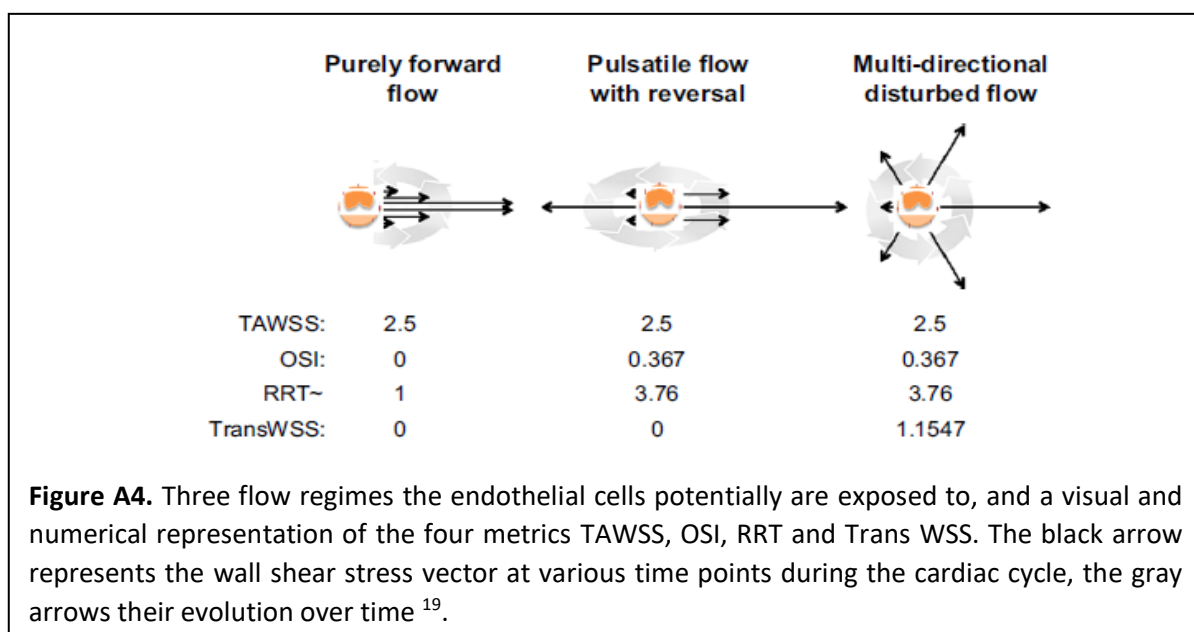
Another factor that could influence the time step size are the “time-scale” of the blood flow. For example, in a stented artery over a single stent strut, a blood particle can pass over the strut in 1 ms, if the strut width is assumed to be 100 μm and blood velocity to be 0.1 m/s. Therefore, clear depiction of microcirculation requires simulations with time a resolution of much less than 1 ms.

A.6 Post-processing

The data obtained from the CFD process are primarily flow velocity and blood pressure. The focus of this paper is wall shear stress that is calculated from the spatial variation of the velocity near the luminal wall but other parameters such as fractional flow reserve can be calculated based on the pressure data. Once luminal maps of the wall shear stress distribution are obtained, and other relevant metrics can be derived for further analysis (see *Figure A4*)¹⁹. These luminal wall shear stress maps generally are down-sampled from the CFD mesh, and several approaches can be followed. For example, a 5° circumferential mapping may be sufficient for CTCA and 3D-QCA reconstruction, but may filter out substantial spatial variation in wall shear stress for IVUS and OCT-based CFD due to the much more detailed patient-specific contours. In the axial direction, 3 mm segmentation is a widely chosen down-sampling

technique as it demonstrated good correlation between wall shear stress and plaque development²⁰. However, depending on IVUS/OCT frame rate and pullback speed, a 3 mm segment can include anywhere between 12–30 frames and may conceal a highly localised abnormal or asymmetric wall shear stress patterns and early disease formation²¹. It is also very important to characterize the wall shear stress distribution around the circumference of the artery lumen, typically in a moving 90° or 45° sector, to identify the highly focal heterogeneity of wall shear stress patterns within areas of artery curvature, bifurcation, or luminal obstruction.

For stented segments, the high-resolution wall shear stress maps are required to depict the micro haemodynamic environment of the stented vessel, with which the effect of the stent strut on areas of elevated or low wall shear stresses can be studied. The amount of wall shear stress data from CFD is typically large, especially when comparing profiles changing over the time. Selecting an effective method to present the data such as the use of a histogram^{5, 22}, which can also be in a form of a cumulative curve, is important (**Figure A5**).



REFERENCES FOR APPENDIX A

1. Li Y, Gutierrez-Chico JL, Holm NR, Yang W, Hebsgaard L, Christiansen EH, Maeng M, Lassen JF, Yan F, Reiber JH, Tu S. Impact of Side Branch Modeling on Computation of Endothelial Shear Stress in Coronary Artery Disease: Coronary Tree Reconstruction by Fusion of 3D Angiography and OCT. *Journal of the American College of Cardiology* 2015;**66**(2):125-35.
2. Tu S, Barbato E, Koszegi Z, Yang J, Sun Z, Holm NR, Tar B, Li Y, Rusinaru D, Wijns W, Reiber JH. Fractional flow reserve calculation from 3-dimensional quantitative coronary angiography and TIMI frame count: a fast computer model to quantify the functional significance of moderately obstructed coronary arteries. *JACC Cardiovasc Interv* 2014;**7**(7):768-77.
3. Gijssen FJ, Wentzel JJ, Thury A, Lamers B, Schuurbiens JC, Serruys PW, van der Steen AF. A new imaging technique to study 3-D plaque and shear stress distribution in human coronary artery bifurcations in vivo. *J Biomech* 2007;**40**(11):2349-57.
4. Chiastra C, Migliori S, Burzotta F, Dubini G, Migliavacca F. Patient-Specific Modeling of Stented Coronary Arteries Reconstructed from Optical Coherence Tomography: Towards a Widespread Clinical Use of Fluid Dynamics Analyses. *Journal of cardiovascular translational research* 2018;**11**(2):156-172.
5. Tenekecioglu E, Poon EKW, Collet C, Thondapu V, Torii R, Bourantas CV, Zeng YP, Onuma Y, Ooi ASH, Serruys PW, Barlis P. The Nidus for Possible Thrombus Formation Insight From the Microenvironment of Bioresorbable Vascular Scaffold. *Jacc-Cardiovasc Inte* 2016;**9**(20):2167-2168.
6. Gogas BD, Yang B, Piccinelli M, Giddens DP, King SB, 3rd, Kereiakes DJ, Ellis SG, Stone GW, Veneziani A, Samady H. Novel 3-Dimensional Vessel and Scaffold Reconstruction Methodology for the Assessment of Strut-Level Wall Shear Stress After Deployment of Bioresorbable Vascular Scaffolds From the ABSORB III Imaging Substudy. *JACC Cardiovascular interventions* 2016;**9**(5):501-3.
7. O'Brien CC, Kolandaivelu K, Brown J, Lopes AC, Kunio M, Kolachalama VB, Edelman ER. Constraining OCT with Knowledge of Device Design Enables High Accuracy Hemodynamic Assessment of Endovascular Implants. *PloS one* 2016;**11**(2):e0149178.
8. Gundert TJ, Shadden SC, Williams AR, Koo BK, Feinstein JA, Ladisa JF, Jr. A rapid and computationally inexpensive method to virtually implant current and next-generation stents into subject-specific computational fluid dynamics models. *Annals of biomedical engineering* 2011;**39**(5):1423-37.
9. Chiastra C, Morlacchi S, Gallo D, Morbiducci U, Cardenes R, Larrabide I, Migliavacca F. Computational fluid dynamic simulations of image-based stented coronary bifurcation models. *J R Soc Interface* 2013;**10**(84):20130193.
10. Tu S, Jing J, Holm NR, Onsea K, Zhang T, Adriaenssens T, Dubois C, Desmet W, Thuesen L, Chen Y, Reiber JH. In vivo assessment of bifurcation optimal viewing angles and bifurcation angles by three-dimensional (3D) quantitative coronary angiography. *The international journal of cardiovascular imaging* 2012;**28**(7):1617-25.
11. Taylor CA, Fonte TA, Min JK. Computational fluid dynamics applied to cardiac computed tomography for noninvasive quantification of fractional flow reserve: scientific basis. *J Am Coll Cardiol* 2013;**61**(22):2233-41.
12. Murray CD. The Physiological Principle of Minimum Work: I. The Vascular System and the Cost of Blood Volume. *Proceedings of the National Academy of Sciences of the United States of America* 1926;**12**(3):207-14.

13. Zhou Y, Kassab GS, Molloy S. In vivo validation of the design rules of the coronary arteries and their application in the assessment of diffuse disease. *Physics in medicine and biology* 2002;**47**(6):977-93.
14. Kassab GS. Scaling laws of vascular trees: of form and function. *Am J Physiol Heart Circ Physiol* 2006;**290**(2):H894-903.
15. Kim HJ, Vignon-Clementel IE, Coogan JS, Figueroa CA, Jansen KE, Taylor CA. Patient-specific modeling of blood flow and pressure in human coronary arteries. *Ann Biomed Eng* 2010;**38**(10):3195-209.
16. van der Giessen AG, Groen HC, Doriot PA, de Feyter PJ, van der Steen AF, van de Vosse FN, Wentzel JJ, Gijzen FJ. The influence of boundary conditions on wall shear stress distribution in patient-specific coronary trees. *J Biomech* 2011;**44**(6):1089-95.
17. Kim HJ, Vignon-Clementel IE, Coogan JS, Figueroa CA, Jansen KE, Taylor CA. Patient-Specific Modeling of Blood Flow and Pressure in Human Coronary Arteries. *Annals of biomedical engineering* 2010;**38**(10):3195-3209.
18. Tran JS, Schiavazzi DE, Ramachandra AB, Kahn AM, Marsden AL. Automated Tuning for Parameter Identification and Uncertainty Quantification in Multi-scale Coronary Simulations. *Computers & fluids* 2017;**142**:128-138.
19. Peiffer V, Sherwin SJ, Weinberg PD. Computation in the rabbit aorta of a new metric - the transverse wall shear stress - to quantify the multidirectional character of disturbed blood flow. *J Biomech* 2013;**46**(15):2651-8.
20. Stone PH, Saito S, Takahashi S, Makita Y, Nakamura S, Kawasaki T, Takahashi A, Katsuki T, Nakamura S, Namiki A, Hirohata A, Matsumura T, Yamazaki S, Yokoi H, Tanaka S, Otsuji S, Yoshimachi F, Honye J, Harwood D, Reitman M, Coskun AU, Papafaklis MI, Feldman CL, Investigators P. Prediction of progression of coronary artery disease and clinical outcomes using vascular profiling of endothelial shear stress and arterial plaque characteristics: the PREDICTION Study. *Circulation* 2012;**126**(2):172-81.
21. Timmins LH, Molony DS, Eshtehardi P, McDaniel MC, Oshinski JN, Samady H, Giddens DP. Focal association between wall shear stress and clinical coronary artery disease progression. *Annals of biomedical engineering* 2015;**43**(1):94-106.
22. Thondapu V, Tenekecioglu E, Poon EKW, Collet C, Torii R, Bourantas CV, Chin C, Sotomi Y, Jonker H, Dijkstra J, Revalor E, Gijzen F, Onuma Y, Ooi A, Barlis P, Serruys PW. Endothelial shear stress 5 years after implantation of a coronary bioresorbable scaffold. *Eur Heart J* 2018;**39**(18):1602-1609.

APPENDIX B: CLINICAL STUDIES

Table B1: Wall shear stress in native arteries

Author	Number of patients	Imaging Modalities	Follow-up	Primary Findings
Stone 2003 ¹	6 ¹	IVUS, angiography	IVUS; 6 months	- Low ESS areas show plaque thickening, expanded EEM radius, preserved lumen radius with increased ESS at follow-up; - High ESS areas show expansive remodeling and increased lumen radius with decreased ESS at follow-up
Stone 2007 ²	13	IVUS, angiography	IVUS; 8 ± 2 months	- Low ESS associated with plaque progression and constrictive remodeling; - Similar incidence of expansive remodeling between low and moderate/higher ESS segments
Gijssen 2008	12	IVUS, angiography palpography	n/a	- Low ESS associated with decrease in tissue strain; - High ESS associated with increase in tissue strain
Samady 2011	20	IVUS angiography	IVUS; 6 months	- Low ESS areas show increased plaque and necrotic core area, reduced EEM and lumen area; - High ESS areas show increased necrotic core and dense calcium, regression of fibrous and fibrofatty areas, increase in EEM and lumen areas
Gijssen 2011	7	IVUS angiography palpography	IVUS + palpography; 6 months	- High ESS associated with interval increase in tissue strain
Stone 2012	374	IVUS angiography	IVUS; 6-10 months	- Large plaque burden and low ESS associated with revascularization
Eshtehardi 2012	27	IVUS angiography	n/a	- Low ESS associated with necrotic core and dense calcium
Wentzel 2013	10	IVUS angiography	n/a	- High ESS is associated with necrotic core
Corban 2014	20	IVUS angiography	IVUS; 6 months	- Combination of plaque burden >40% and low ESS show increased plaque area; - Segments with combination of PIT, plaque burden >60%, and high

¹ In this study, 6 native (unstented) and 6 stented arteries from 8 patients were included. However, only results from native arteries are presented here.

(continued)

				ESS develop increase necrotic core and dense calcium but decreased fibrous and fibrofatty tissue
Vergallo 2014	21	OCT angiography	n/a	- Low ESS areas associated with presence of lipid rich plaque and TCFA, more lipid, higher lipid arc, thinner fibrous caps, higher macrophage density, more superficial calcification; - Most TCFAs found in low ESS areas but most low ESS areas do not contain TCFAs
Stone 2017	23 ²	IVUS angiography	Clinical; 3.4 years	- Low ESS associated with non-culprit MACE
Yamamoto 2017³	20	OCT angiography	OCT; median 205 days	- In segments with low ESS at baseline, fibrous caps are thinner and do not thicken; - Only segments with low ESS showed interval increase in lipid arc; - Segments with high ESS at baseline had thicker fibrous caps which further thickened; - In segments with persistently low ESS, higher prevalence of TCFA and thinner fibrous caps
Kumar 2018	44	Angiography + endothelial function measurement	n/a	- Low ESS associated with endothelial dysfunction
Yamamoto 2019⁴	18	OCT angiography	n/a	- High ESS, ESS gradient, and oscillatory shear index associated with acute plaque erosion and thrombus
Costopoulos 2019⁵	40	IVUS angiography	IVUS; 6-12 months	- Low ESS associated with smaller decrease in PB in areas of plaque regression and greater increases in areas of progression than high ESS areas. - Low ESS areas undergo negative remodeling; high ESS areas show positive remodeling.

EEM = external elastic membrane

ESS = endothelial shear stress

MACE = major adverse cardiovascular event

TCFA = thin-cap fibroatheroma

² 23 patients with non-culprit MACE were compared to 122 matched control patients without MACE during the clinical follow-up period

Table B2: Wall shear stress in stented arteries

Author	Number of patients	Device	Follow-up	Primary Findings
Wentzel 2001 ⁶	14	14 bare metal stents (Wall stent)	IVUS 6 months	- Neointimal thickness was inversely related to WSS.
Papafaklis 2010 ⁷	30	10 bare metal stents (BMS), 10 sirolimus eluting stents, 10 paclitaxel eluting stents	6months	- WSS was inversely correlated with neointima distribution in BMS, and paclitaxel eluting stents but not in sirolimus eluting stents
Bourantas 2015 ⁸	43	18 BMS, 25 biolimus eluting stent	13 months	- WSS was inversely associated with neointima formation in both BMS and biolimus eluting stents In BMS there was an inverse correlation between WSS and necrotic core component detected in the neointima
Shishido 2016 ⁹	374	40.7% bare-metal stents (BMS) and 59.3% 1 st generation DES	6-10 months	-Low WSS after BMS implantation was associated with subsequent in-stent hyperplasia but not after DES implantation. -Post-PCI WSS was not associated with in-stent restenosis.
Tenekecioglu 2016 ¹⁰	17	6 BVS (Absorb, Abbott Vascular) and 11 Mirage Bioresorbable Microfiber Scaffolds (Mirage, Manli Cardiology)		- protrusion distances were higher for the Absorb compared to Mirage scaffold. - Strut protrusion of Absorb was inversely correlated with WSS ($r=-0.369$, $p<0.0001$), whereas in Mirage protrusion was positively correlated with EES ($r=0.192$, $p<0.0001$).
Torii 2017 ¹¹	2	BVS (Absorb, Abbott Vascular)	OCT 5 years	- overexpansion and underexpansion at baseline resulted acutely in two different shear stress distributions; - At 5 years, WSS levels normalized to values close to the physiological ranges.

Torii 2018 ¹²	36	11 BMS, 12 1st generation DES and 13 2nd generation DES	Mean 12.2 ± 2.9 months BMS 7.6 ± 3.0 1 st DES 2.4 ± 2.6 2 nd DES	- inverse association between baseline WSS and the incidence and the burden of neoatherosclerosis and lipid-rich neoatherosclerotic tissue
Thondapu 2018 ¹³	7	Absorb BVS (Absorb, Abbott Vascular)	OCT 5 years	- Immediately after scaffold implantation, coronary arteries demonstrate an alternans of extremely low and high WSS values and localized areas of high blood viscosity. - low WSS promotes neointimal hyperplasia and contribute to scaffold healing with normalisation of WSS and reduction in peak blood viscosity by 5 years.
Li 2018 ¹⁴	10	10 bifurcations with BVS (Absorb, Abbott Vascular)	none	- Inclusion of scaffolds in WSS computation in bifurcations resulted in lower WSS which was most pronounced at side branch ostia.
Tenekecioglu 2018 ¹⁵	8	Eight Absorb BVS (Absorb, Abbott Vascular)	OCT 1 and 5 years	- Strut protrusion disturbs laminar flow, creates regions of low WSS that are associated with neointimal growth and lumen-area reduction

EEM = external elastic membrane

WSS = endothelial shear stress

MACE = major adverse cardiovascular event

TCFA = thin-cap fibroatheroma

PIT = pathological intimal thickening

BVS = bioresorbable vascular scaffold

REFERENCES FOR APPENDIX B

1. Stone PH, Coskun AU, Kinlay S, Clark ME, Sonka M, Wahle A, Ilegbusi OJ, Yeghiazarians Y, Popma JJ, Orav J, Kuntz RE, Feldman CL. Effect of endothelial shear stress on the progression of coronary artery disease, vascular remodeling, and in-stent restenosis in humans: in vivo 6-month follow-up study. *Circulation* 2003;108(4):438-44.
2. Stone PH, Coskun AU, Kinlay S, Popma JJ, Sonka M, Wahle A, Yeghiazarians Y, Maynard C, Kuntz RE, Feldman CL. Regions of low endothelial shear stress are the sites where coronary plaque progresses and vascular remodelling occurs in humans: an in vivo serial study. *Eur Heart J* 2007;28(6):705-10.
3. Yamamoto E, Siasos G, Zaromytidou M, Coskun AU, Xing L, Bryniarski K, Zanchin T, Sugiyama T, Lee H, Stone PH, Jang IK. Low Endothelial Shear Stress Predicts Evolution to High-Risk Coronary Plaque Phenotype in the Future: A Serial Optical Coherence Tomography and Computational Fluid Dynamics Study. *Circ Cardiovasc Interv* 2017;10(8).
4. Yamamoto E, Thondapu V, Poon E, Sugiyama T, Fracassi F, Dijkstra J, Lee H, Ooi A, Barlis P, Jang IK. Endothelial Shear Stress and Plaque Erosion: A Computational Fluid Dynamics and Optical Coherence Tomography Study. *JACC Cardiovasc Imaging* 2019;12(2):374-375.
5. Costopoulos C, Timmins LH, Huang Y, Hung OY, Molony DS, Brown AJ, Davis EL, Teng Z, Gillard JH, Samady H, Bennett MR. Impact of combined plaque structural stress and wall shear stress on coronary plaque progression, regression, and changes in composition. *Eur Heart J* 2019.
6. Wentzel JJ, Krams R, Schuurbiers JC, Oomen JA, Kloet J, van Der Giessen WJ, Serruys PW, Slager CJ. Relationship between neointimal thickness and shear stress after Wallstent implantation in human coronary arteries. *Circulation* 2001;103(13):1740-5.
7. Papafaklis MI, Bourantas CV, Theodorakis PE, Katsouras CS, Naka KK, Fotiadis DI, Michalis LK. The effect of shear stress on neointimal response following sirolimus- and paclitaxel-eluting stent implantation compared with bare-metal stents in humans. *JACC Cardiovasc Interv* 2010;3(11):1181-9.
8. Bourantas CV, Raber L, Zaugg S, Sakellarios A, Taniwaki M, Heg D, Moschovitis A, Radu M, Papafaklis MI, Kalatzis F, Naka KK, Fotiadis DI, Michalis LK, Serruys PW, Garcia Garcia HM, Windecker S. Impact of local endothelial shear stress on neointima and plaque following stent implantation in patients with ST-elevation myocardial infarction: A subgroup-analysis of the COMFORTABLE AMI-IBIS 4 trial. *Int J Cardiol* 2015;186:178-85.
9. Shishido K, Antoniadis AP, Takahashi S, Tsuda M, Mizuno S, Andreou I, Papafaklis MI, Coskun AU, O'Brien C, Feldman CL, Saito S, Edelman ER, Stone PH. Effects of Low Endothelial Shear Stress After Stent Implantation on Subsequent Neointimal Hyperplasia and Clinical Outcomes in Humans. *J Am Heart Assoc* 2016;5(9).
10. Tenekecioglu E, Sotomi Y, Torii R, Bourantas C, Miyazaki Y, Collet C, Crake T, Su S, Onuma Y, Serruys PW. Strut protrusion and shape impact on endothelial shear stress: insights from pre-clinical study comparing Mirage and Absorb bioresorbable scaffolds. *Int J Cardiovasc Imaging* 2017;33(9):1313-1322.
11. Torii R, Tenekecioglu E, Bourantas C, Poon E, Thondapu V, Gijzen F, Sotomi Y, Onuma Y, Barlis P, Ooi ASH, Serruys PW. Five-year follow-up of underexpanded and overexpanded bioresorbable scaffolds: self-correction and impact on shear stress. *EuroIntervention* 2017;12(17):2158-2159.
12. Torii R, Stettler R, Raber L, Zhang YJ, Karanasos A, Dijkstra J, Patel K, Crake T, Hamshere S, Garcia-Garcia HM, Tenekecioglu E, Ozkor M, Baumbach A, Windecker S, Serruys PW, Regar E, Mathur A, Bourantas CV. Implications of the local hemodynamic forces on the formation and destabilization of neoatherosclerotic lesions. *Int J Cardiol* 2018;272:7-12.

13. Thondapu V, Tenekecioglu E, Poon EKW, Collet C, Torii R, Bourantas CV, Chin C, Sotomi Y, Jonker H, Dijkstra J, Revalor E, Gijssen F, Onuma Y, Ooi A, Barlis P, Serruys PW. Endothelial shear stress 5 years after implantation of a coronary bioresorbable scaffold. *Eur Heart J* 2018;39(18):1602-1609.
14. Li Y, Li Z, Holck EN, Xu B, Karanasos A, Fei Z, Chang Y, Chu M, Dijkstra J, Christiansen EH, Reiber JHC, Holm NR, Tu S. Local Flow Patterns After Implantation of Bioresorbable Vascular Scaffold in Coronary Bifurcations- Novel Findings by Computational Fluid Dynamics. *Circ J* 2018;82(6):1575-1583.
15. Tenekecioglu E, Torii R, Katagiri Y, Asano T, Modolo R, Miyazaki Y, Chichareon P, Poon EKW, Gijssen F, Thondapu V, van Klaveren D, Jonker H, Ooi A, Barlis P, Collet C, Onuma Y, Bourantas CV, Serruys PW. Early strut protrusion and late neointima thickness in Absorb bioresorbable scaffold: A serial wall shear stress analysis up to five years. *EuroIntervention* 2018.

Chapter 8

The Nidus for Possible Thrombus Formation: Insight from the Micro Environment of Bioabsorbable Vascular

The Effect of Strut Protrusion on Shear Stress Distribution: Hemodynamic Insights From a Prospective Clinical Trial

The impact of plaque type on strut embedment/protrusion and shear stress distribution in bioresorbable scaffold

The Nidus for Possible Thrombus Formation: Insight from the Micro-Environment of Bioabsorbable Vascular Scaffold

Erhan Tenekecioglu, Eric K. W. Poon, Carlos Collet, Vikas Thondapu, Ryo Torii, Christos V. Bourantas, Yaping Zeng, Yoshinobu Onuma, Andrew S. H. Ooi, Patrick W. Serruys, Peter Barlis

JACC Cardiovasc Interv. 2016; 9(20): 2167-2168.

An Absorb bioresorbable vascular scaffold (Absorb BVS, Abbott Vascular, Santa Clara, California; 3.0x18mm) was implanted in the mid-segment of the left anterior descending (LAD) coronary artery of a patient with stable angina pectoris. Optical coherence tomography (OCT) was performed following scaffold implantation (Pull-back speed 18mm/s acquisition rate 180 frames/s). OCT images demonstrated well-expanded and apposed scaffold. Patient-specific 3D-geometry of scaffolded lumen was generated using OCT and coronary angiography. Computational fluid dynamics (CFD) techniques were used to simulate pulsatile blood flow through 3D patient-specific finite volume mesh by solving Navier–Stokes equations. Blood was considered non-Newtonian fluid and pulsatile flow profile was imposed in the inflow of the model. Shear-thinning blood rheology was simulated using Quemada constitutive equation that takes hematocrit and shear rate into account (1). Endothelial shear stress (ESS) at the lumen and scaffold surfaces was calculated as the product of local blood viscosity and near-wall velocity gradient (2).

Increased ESS was noted at strut surface and outer curve of the bend; low ESS (<0.5 Pa) was noted between successive stent hoops and inner curve of the bend (Figure, Panel-I, -II and -III). An internal view of the scaffold segment, across grey line in Figure, panel-I reveals micro-recirculations (red arrows in Figure, panel-IV) between stent hoops. Arterial curvature created a spiral velocity component (streamlines flowing from top-to-bottom of the vessel in Figure, panel-IV), also termed secondary flow (3).

As a result of skewed velocity profile along the bend (Figure, panel-III), micro-recirculations are less pronounced at outer curve but relatively larger at the inner curve of the bend. It is hypothesized that such micro-recirculations in the vicinity of struts are associated with lower shear rate zones that may become nidus for thrombus formation (4). *In vivo* 3D OCT-based CFD modeling can be used to evaluate the implications of scaffold implantation on the local hemodynamics that may shed light on possible pathophysiological responses such as thrombus formation and neointimal hyperplasia.

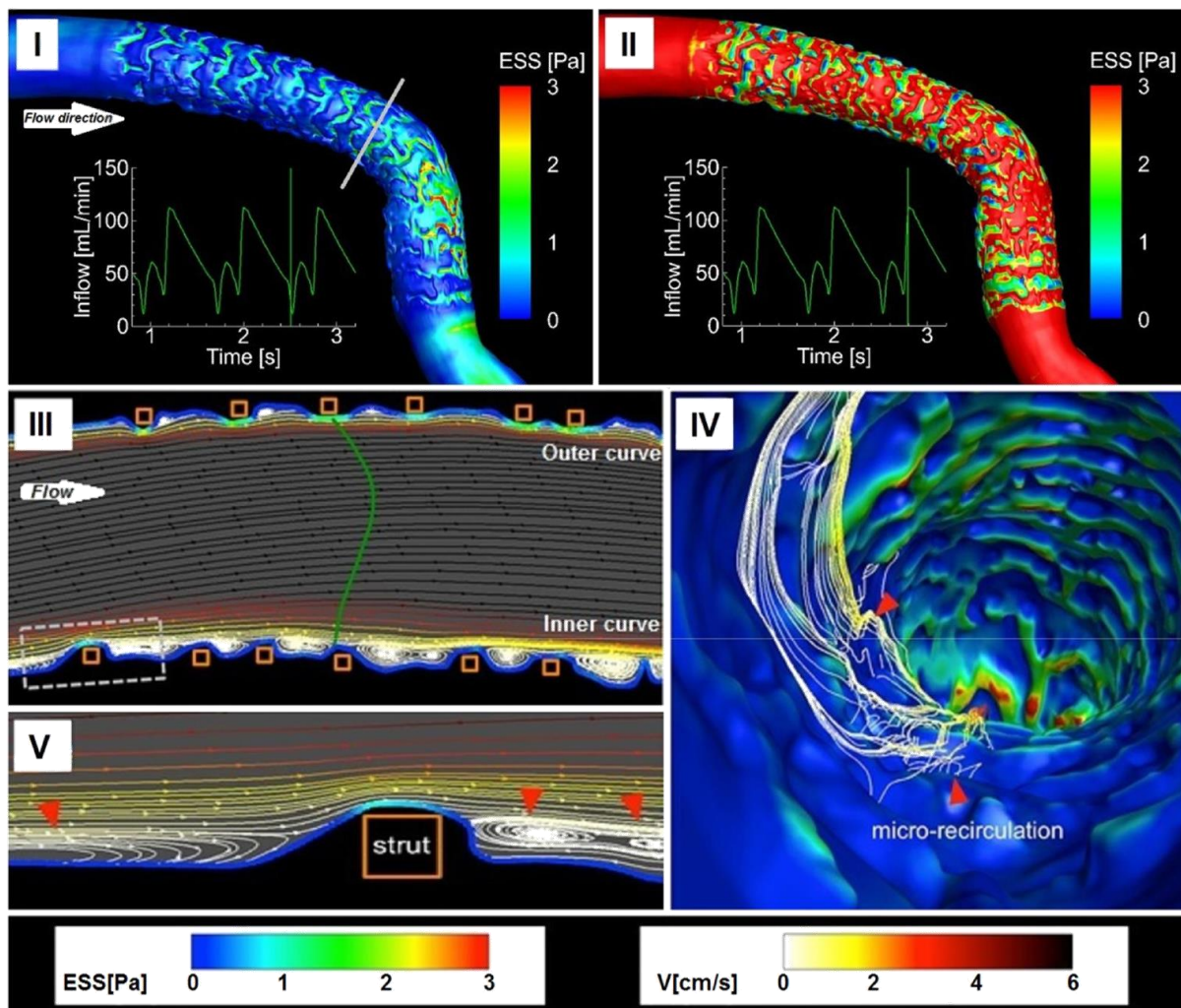


Figure: Shear stress distribution in scaffolded segment in systole and diastole

Panel-I represents flow at peak systole and ESS, panel-II represents the flow at peak diastole and related ESS. Panel-III demonstrates the longitudinal view of the 3D patient specific geometry. The corresponding surface integrated streamlines clearly indicate that the longitudinal velocity component is skewed towards the outer curve of the bend (green velocity profile in panel-III) in the presence of the secondary flow. Panel-IV reveals the streamlines exhibit a spiral velocity component, termed as secondary flow. The micro-recirculations (red arrows in panel-IV and -V) are responsible for the reduction in local shear rate and thus lower local ESS distribution. Conversely, the smaller micro-recirculation zones at the outer curve of the artery correlate with higher local ESS.

REFERENCES

1. Quemada D, Rheology of concentrated disperse systems III. General features of the proposed non-Newtonian model. Comparison with experimental data. *Rheol. Acta* 1978; 17:643–653.
2. Feldman CL, Ilegbusi OJ, Hu Z, Nesto R, Waxman S, Stone PH Determination of in vivo velocity and endothelial shear stress patterns with phasic flow in human coronary arteries: a methodology to predict progression of coronary atherosclerosis. *Am Heart J.* 2002;143(6):931-9.
3. Ku D. Blood flow in arteries. *Ann. Rev. Fluid. Mech* 1997; 29:399-434.
4. Jimenez JM, Davies PF. Hemodynamically driven stent strut design. *Annals of biomedical engineering* 2009; 37:1483-94.

Movie. The coronary flow in scaffolded vessel

The shear stress closely follows the imposed volumetric pulsatile flow rate profile. As demonstrated in left lower panel, pulsatile coronary flow generates streamlines inducing micro-recirculations in the vicinity of the struts. Note that, in the longitudinal 3D model, lower ESS areas -figured out as dark blue areas behind the struts- remain both at diastole and systole.

The Effect of Strut Protrusion on Shear Stress Distribution: Hemodynamic Insights From a Prospective Clinical Trial

Erhan Tenekecioglu, Ryo Torii, Yohei Sotomi, Carlos Collet, Jouke Dijkstra, Yosuke Miyazaki, Tom Crake, Solomon Su, Ricardo Costa, Daniel Chamié, Houn-Bang Liew, Teguh Santoso, Yoshinobu Onuma, Alexander Abizaid, Christos Bourantas, Patrick W. Serruys

JACC Cardiovasc Interv;10(17):1803-1805.

RESEARCH CORRESPONDENCE

After scaffold implantation, local flow dynamics, particularly endothelial shear stress (ESS) is restored by newly constituted luminal surface. Scaffold design and strut embedment/protrusion-which is related to the underlying atherosclerotic plaque type, have impact on the local flow behaviors(1). Disrupted coronary flow in the vicinity of struts induces recirculations and stagnation zones with lower shear stress that triggers biological mechanisms of platelet aggregation and neointimal hyperplasia(1). In the present study, we investigated strut protrusion in two different bioresorbable scaffolds (BRS) and its implication on ESS distribution.

The present analysis processed data from the patients enrolled in the Mirage first-in-man trial. During implantation, all lesions were predilated, post-dilatation was left at the operator's discretion. Nine patients treated with Absorb and 11 patients treated with Mirage scaffolds were selected for computational fluid dynamic (CFD) study. Case selections were based on the orthogonal ($\geq 30^\circ$) angiographic projections with minimal foreshortening and clearly documented lumen on OCT. Scaffold designs are described elsewhere(2). The struts of Absorb were automatically detected by OCT software, QCU-CMS (Leiden University Medical Center, Netherlands). Since QCU-CMS has no automatic detection for circular struts of Mirage, the struts of Mirage were depicted as part of the lumen contours and interpolation of the true lumen contour allows the assessment of the protrusion of the Mirage struts(2, 3). In OCT, plaque composition was characterized and predominant plaque type was determined when several plaque types were identified in one cross-section. The eccentricity index (EI) and expansion index were calculated in OCT. Three-dimensional(3D) reconstruction was performed using a validated methodology(2). CFD techniques were employed to process 3D-models. ESS was estimated around the circumference of the lumen per 5° -interval and along the axial-direction per 0.2mm-interval. As the data have multilevel structure, mixed linear model was used for comparisons of continuous variables in cross-section level analysis.

All scaffolds were 3.0x18mm in both groups. Mean luminal area ($7.12 \pm 1.24 \text{ mm}^2$ vs. $7.10 \pm 1.31 \text{ mm}^2$, $p=0.98$) and mean scaffold area ($7.48 \pm 0.94 \text{ mm}^2$ vs. $7.16 \pm 1.14 \text{ mm}^2$, $p=0.87$) were comparable between Absorb and Mirage. Mean strut area per cross-section was significantly higher in Mirage ($0.31 \pm 0.03 \text{ mm}^2$) compared to Absorb ($0.18 \pm 0.06 \text{ mm}^2$) ($p < 0.0001$). EI was higher in Absorb (0.90 ± 0.06) compared to Mirage (0.86 ± 0.08) ($p < 0.001$). In

Absorb, EI for fibro-calcific plaques, fibroatheromas, fibrous plaques and normal vessel segments were 0.87 ± 0.05 , 0.87 ± 0.06 , 0.91 ± 0.05 and 0.89 ± 0.04 , respectively ($p_{\text{overall}} < 0.0001$). In Mirage, EI for fibro-calcific plaques, fibroatheromas, fibrous plaques and normal segments were 0.80 ± 0.08 , 0.82 ± 0.08 , 0.86 ± 0.08 and 0.93 ± 0.02 , respectively ($p_{\text{overall}} < 0.0001$). Strut protrusion was significantly less in Mirage ($77\pm 23\mu\text{m}$)($62\pm 19\%$ of strut thickness) compared to Absorb($145\pm 31\mu\text{m}$)($92\pm 20\%$ of strut thickness)($p < 0.0001$). Lowest strut protrusion was noted in fibro-atheromas (**Figure**). At cross-section-level analysis, mean ESS was significantly higher in Mirage($2.46\pm 2.17\text{Pa}$) than in Absorb($1.39\pm 0.66\text{Pa}$) ($p < 0.0001$). In 5°-level analysis, 49.30% of the luminal surface in Absorb and 24.48% in Mirage was exposed to low-ESS ($< 1.0\text{ Pa}$) ($p < 0.0001$). CFD results demonstrated higher ESS in fibroatheromas in both scaffolds. Lowest ESS levels were documented in fibrous and fibro-calcific plaques (**Figure**).

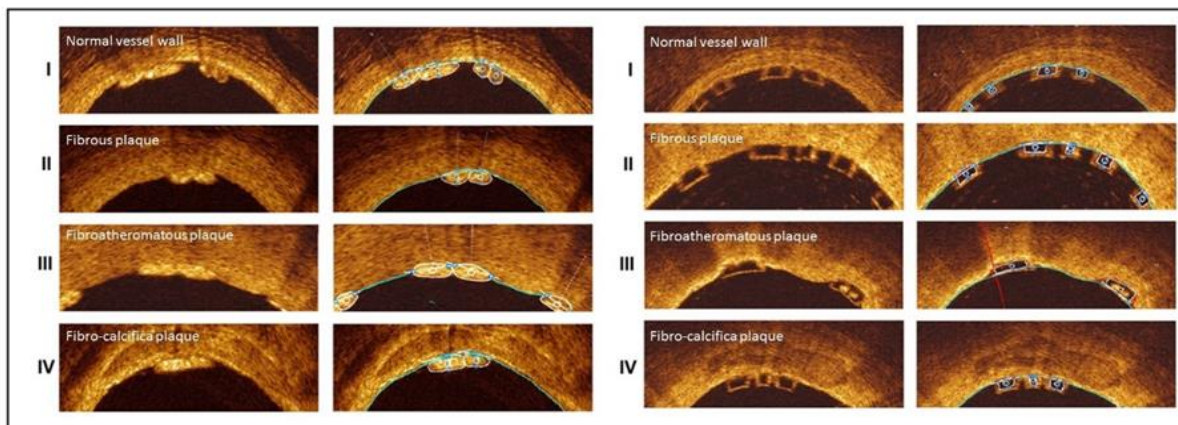
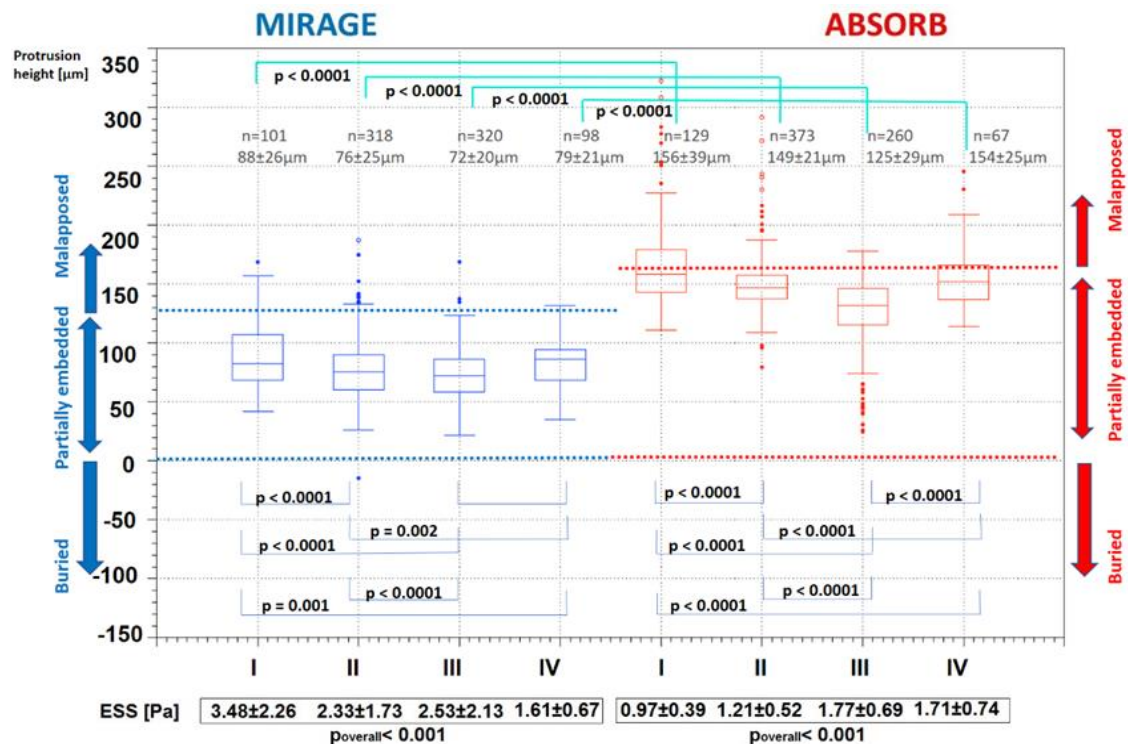


Figure. In both scaffold groups, due to higher strut penetration, fibro-atheromatous plaques demonstrated less protrusion distances compared to other plaque types.

In the present analysis; 1- Strut protrusion was lower in Mirage compared to Absorb; 2- In both scaffold types, lower protrusion was noted in fibroatheromas compared to other plaque types; 3- Differences in protrusion affected local hemodynamics with higher ESS in Mirage than in Absorb; 4- ESS is higher in fibroatheromas when compared to other plaque types. Fibroatheromas are more compliant than fibrous and fibro-calcific plaques and provide deeper penetration resulting in less protrusion. In the present study, fibroatheromas revealed higher strut penetration than fibrous and fibro-calcific plaques in both scaffolds. Mirage struts embedded deeper than Absorb in all plaque types. The factor for higher embedment in Mirage should be sought in the principles of *contact mechanics*(4). The penetration distance (embedment depth) is in an inverse relation with strut contact-radius in which circular

surface of strut in Mirage has shorter contact-radius than square-shaped struts of Absorb(4). When the same force is applied, device with a higher foot-print area would generate a lower pressure on the vessel wall according to the simple principle: $\text{Pressure} = \text{Force} / \text{Area}$. Circular geometries have also the advantage of enabling the flow acceleration crossing over convex strut surface with less disruption, that might also contribute to the improvement in shear stress not only on top-of-the struts but also in the inter-strut zones in Mirage(5). Absorb has lower vessel coverage ratio than Mirage (25% vs 46%). Due to this fact, higher vessel coverage in Mirage requires higher implantation pressures. With the advantage of higher tensile strength (300MPa Mirage vs 60-70MPa Absorb) and higher elongation-at-break in Mirage than Absorb, higher deployment pressures can be applied to embed circular struts of Mirage, deeper than Absorb with low disruption risk. Shear stress distribution seems to be related with scaffold design and strut penetration. Protrusion analysis may help to improve implantation process and hemodynamic performance of bioresorbable scaffolds. Poorly embedded scaffolds can create area with disturbed atheroprone low shear stress zones that may contribute the risk of acute scaffold thrombosis to late neo-atherosclerosis formation adjacent to the struts and later plaque rupture.

REFERENCES

1. Jimenez JM, Davies PF. Hemodynamically driven stent strut design. *Annals of biomedical engineering*. 2009;37(8):1483-94.
2. Tenekecioglu E, Sotomi Y, Torii R, Bourantas C, Miyazaki Y, Collet C, et al. Strut protrusion and shape impact on endothelial shear stress: insights from pre-clinical study comparing Mirage and Absorb bioresorbable scaffolds. *The international journal of cardiovascular imaging*. 2017.
3. Sotomi Y, Tateishi H, Suwannasom P, Dijkstra J, Eggermont J, Liu S, et al. Quantitative assessment of the stent/scaffold strut embedment analysis by optical coherence tomography. *The international journal of cardiovascular imaging*. 2016;32(6):871-83.
4. Johnson KL, Johnson KL. *Contact Mechanics*: Cambridge University Press; 1987.
5. Anderson JD. *Fundamentals of aerodynamics*. Sixth edition. ed. New York, NY: McGraw-Hill Education; 2017. pages cm. p.

The impact of plaque type on strut embedment / protrusion and shear stress distribution in bioresorbable scaffold

Ryo Torii*, Erhan Tenekecioglu*, Yuki Katagiri, Ply Chichareon, Yohei Sotomi, Jouke Dijkstra, Taku Asano, Rodrigo Modolo, Kuniaki Takahashi, Hans Jonker, Robert van Geuns, Yoshinobu Onuma, Kerem Pekkan, Christos V. Bourantas, Patrick W. Serruys

* These authors equally contributed to this work

Eur Heart J Cardiovasc Imaging. 2020; 21(4):454-462.

ABSTRACT

Background and aim: Scaffold design and plaque characteristics influence implantation outcomes and local flow dynamics in treated coronary segments. Our aim is to assess the impact of strut embedment/protrusion of bioresorbable scaffold on local shear stress distribution in different atherosclerotic plaque types.

Method: Fifteen Absorb everolimus-eluting Bioresorbable Vascular Scaffolds were implanted in human epicardial coronary arteries. Optical coherence tomography (OCT) was performed post-scaffold implantation and strut embedment/protrusion were analyzed using a dedicated software. OCT data was fused with angiography to reconstruct three-dimensional coronary anatomy. Blood flow simulation was performed and wall shear stress (WSS) was estimated in each scaffolded surface and the relationship between strut embedment/protrusion and WSS was evaluated.

Results: There were 9083 struts analysed. Ninety-seven percent of the struts($n=8840$) were well apposed and 243(3%) were malapposed. At cross-section level($n=1289$), strut embedment was significantly increased in fibroatheromatous plaques($76\pm 48\mu\text{m}$) and decreased in fibro-calcific plaques ($35\pm 52\mu\text{m}$). Compatible with strut embedment, WSS was significantly higher in lipid-rich fibroatheromatous plaques ($1.50\pm 0.81\text{Pa}$), whereas significantly decreased in fibro-calcified plaques($1.05\pm 0.91\text{Pa}$). After categorization of WSS as low ($<1.0\text{ Pa}$) and normal/high WSS ($\geq 1.0\text{ Pa}$), the percent of low-WSS in the plaque subgroups were 30.1%, 31.1%, 25.4% and 36.2% for non-diseased vessel wall, fibrous plaque, fibro-atheromatous plaque and fibro-calcific plaque, respectively($p\text{-overall}<0.001$).

Conclusion: The composition of the underlying plaque influences strut embedment which seems to have effect on WSS. The struts deeply embedded in lipid-rich fibroatheromas plaques resulted in higher WSS compared to the other plaque types.

Key words: Atherosclerotic plaque; bioresorbable scaffold; strut embedment; strut protrusion; shear stress

INTRODUCTION

Temporary scaffolding of diseased vessels by bioresorbable scaffolds (BRS) were introduced to overcome the limitations of the metallic stents. However, unprecedented relatively high thrombosis rates have raised significant concerns about the efficacy of this technology(1). Late loss in the Absorb BRS was significantly larger than in the metallic everolimus-eluting stent (EES) and device-oriented composite endpoint (cardiac death, target vessel myocardial infarction and clinically-indicated target lesion revascularization [TLR]) at 3 years follow up was higher in Absorb than in metallic Xience (10% vs 5%, $p=0.043$) (1). In the meta-analysis of five randomized clinical trials(2) comparing the Absorb and the EES has shown that post-procedural minimal lumen diameter was a predictive factor for device thrombosis which emphasizes the role of aggressive implantation strategy with high-pressure post-dilatation using intracoronary imaging techniques to optimize scaffold expansion.(3) Intracoronary imaging guided BRS implantation assists in sizing the diseased vessel segment and reference vessel to avoid any mismatch between the diseased and healthy reference vessel segments. To achieve strut embedment without scaffold disruption and for accurate measurement of minimal scaffold area and scaffold asymmetry, intra-coronary imaging guiding is indispensable (4).

Stent/scaffold design has impact on the local flow dynamics in treated vessel segment. This effect depends not only on the device design but also the embedment/protrusion of the scaffold struts within the vessel wall. Well embedded struts induce less flow disruptions with shorter flow separations, whereas increased strut protrusion may cause flow turbulence and recirculation zones around the struts. These disrupted flow areas yield low wall shear stress (WSS) triggering various patho-biological reactions in platelets and endothelial layer of the vessel wall that may result in excessive neointimal hyperplasia(5). The histomorphometric properties of the treated vessel segments, in particularly the underlying atherosclerotic plaque properties determine strut apposition and penetration status(6).

In the present study, we investigated the strut embedment/protrusion patterns in different plaque types treated with BRS and its effect on the local WSS distribution in treated segments.

METHODS

Patient population and Study Device

Fifteen patients implanted with an Absorb bioresorbable vascular scaffold (Absorb, Abbott Vascular, USA), from the Absorb Cohort B2 first-in-man study, were included in the present analysis. The selection criteria for the cases were as follows; the OCT pullback should provide clear imaging of the vessel lumen with scaffold struts, the treated segments were relatively straight vessel segments to prevent any effect of curvatures on the shear stress alterations and the cases should have two separate coronary angiograms with $>25^\circ$ angle between each other for a three-dimensional(3D) centerline extraction to be used in vessel reconstruction for computational fluid dynamic(CFD) simulations. The Absorb is a poly-lactide scaffold eluting an anti-proliferative drug everolimus, with two pairs of radiopaque markers at both ends of the scaffold.

OCT image acquisition and data analysis:

OCT imaging was performed post-procedure in the treated coronary arteries using a frequency-domain (FD) OCT system (C7-XR OCT Intravascular Imaging System; St. Jude Medical, St. Paul, MN, USA) that was pull-backed at a speed of 20 mm/sec. A non-occlusive flushing technique was implemented during the pullback by injection of angiographic contrast medium for blood clearance.

The OCT data were analyzed off-line using QCU-CMS software (Medis Medical Imaging systems, Leiden, The Netherlands) at every 200 μ m interval in the scaffolded segment and at every 400 μ m in the non-scaffolded segments. In scaffolded segment, in each OCT frame, the plaque composition was defined as following: Lipid tissue was delineated as a signal-poor region with poorly depicted borders and a fast drop-off in OCT signal, whereas calcium was defined as a signal-poor zone with sharply delineated borders and a gradual drop-off in OCT signal. OCT frames illustrating the segments with no or little intimal thickening and the typical 3-layered structure of the intima, media and adventitia were considered as normal vessel wall. Fibrous plaque was characterized as the tissue with a high backscattering and a relatively homogeneous OCT signal. Fibroatheroma was specified as a lipid-rich pool with circumferential extent $>90^\circ$ and fibro-calcific plaque, as a plaque that included calcific tissue and no lipid or lipid tissue with a circumferential extent $<90^\circ$. At *strut-level* analysis, for each strut, the underlying tissue type was defined. At *cross-section level*, the predominant plaque

type was determined when several plaque types were identified in one cross-section on OCT(7-9). The eccentricity index was calculated as the ratio between the minimal and the maximal diameter of each cross-section on OCT(10). Expansion index was defined in *device-level* as minimum scaffold area divided by mean reference area (9).

Coronary angiograms were analyzed using a semi-automated edge detection system (CAAS QCA-2D system, Pie Medical Imaging BV, Maastricht, the Netherlands) with the dye-filled catheter used for calibration purposes. In each scaffold, the largest balloon diameter at maximal inflation pressure during deployment or post-dilatation were recorded and used to calculate the balloon/artery ratio (defined as: mean inflated balloon diameter/mean reference vessel diameter). Acute absolute scaffold recoil was calculated as the difference between the mean diameter of the deployment/post-dilatation balloon in its highest pressure(A) and the mean luminal diameter in the scaffolded segment at the end of the procedure(B). Acute percent scaffold recoil was defined as: $A-B/A$ and expressed as percentage(11, 12). Acute luminal gain was defined as the difference between pre- and post-procedural minimum lumen diameter, as assessed by Quantitative Coronary Angiography(QCA)(13).

Embedment/protrusion analysis by optical coherence tomography

For strut embedment/protrusion analysis, the embedment depths and protrusion distances were measured semi-automatically implementing a dedicated version of the QCU-CMS software (version4.69, Leiden University Medical Center, Leiden, The Netherlands). The embedment analysis in OCT was performed in the scaffolded segment at every 200 μ m longitudinal interval using the methodology described previously(8). Frames were excluded from stent strut measurement if >30% of vessel wall was not visible, in which case the next frame was selected for analysis. Struts located at the ostium of a side-branch were excluded from the embedment analysis. Distances were adjusted based on the known thickness of the strut including the polymer coating. A scaffold strut was considered malapposed if the axial distance between strut surface and luminal surface was greater than the strut thickness including its polymer coating. The reproducibility of embedment analysis for Absorb was previously reported by Sotomi et al(8).

Reconstruction of coronary artery anatomy

Three-dimensional(3D) reconstruction of the treated coronary artery was performed using a validated methodology(14). The radiopaque markers and the anatomical landmarks (i.e. Side branches), identified both on angiography and OCT, were used to define the segment of interest which included the scaffolded segment and 5mm proximal and distal non-scaffolded edge segments. The OCT images demonstrating the segment of interest, were analyzed at a 200 μ m interval in the scaffolded segment and 400 μ m interval in the remaining segment of interest. The flow area was defined by the luminal borders in native vessel segments. In the scaffolded segments, the adluminal side of the struts and the lumen borders in the inter-strut areas delineated the flow area(15, 16). In two orthogonal(>25 $^{\circ}$ -angle) angiograms, the luminal borders and lumen centerline were extracted and the lumen centerlines were used to generate 3D luminal centerline to be the backbone of the segments of interest(14). The flow area contours detected in OCT were mounted perpendicularly onto the luminal centerline and anatomical landmarks(side-branches) were used to estimate their orientation(14).

Blood flow simulation

CFD techniques were implemented to process 3D models. A finite volume mesh was generated and numerical blood flow simulation was performed. The WSS was estimated by solving the 3D Navier-Stokes equations (ANSYS Fluent, Canonsburg, Pennsylvania)(17). To examine the influence of scaffold design on the local hemodynamic forces, the mesh density around the struts and at flow boundary near the vessel wall between the struts was increased so as to have average element edge of 30 μ m(equals to 1/5 of the strut thickness).Blood was treated as a homogeneous, Newtonian fluid with a viscosity of 0.0035 Pa.s and a density of 1,050kg/m³. A steady flow profile was implemented at the inflow of the 3D-models. Blood flow for each reconstruction was estimated by measuring, in 2 angiographic projections, the number of frames required for the contrast agent to pass from inlet to the outlet of the reconstructed segment, the volume of the reconstructed segment and the cine frame-rate(17). The arterial wall was considered to be rigid and no-slip conditions were imposed at the scaffold surface and the reconstructed luminal surface. At the outlet of the model, zero pressure condition was implemented. WSS was calculated as the product of blood viscosity and the gradient of blood velocity at the wall and strut surface. WSS was measured in the native and the scaffolded segment around the circumference of the lumen per 5 $^{\circ}$ -

interval(sector) and along the axial direction per 200 μ m interval with the use of an in-house algorithm(18, 19).

Statistical analysis

Numerical data are expressed as mean \pm standard deviation or median and inter-quartile range depending on their distribution which was tested by Kolmogorov-Smirnov test. Continuous variables with normal and non-normal distributions were compared using Student's t-tests and Mann-Whitney U tests, respectively. Categorical variables were compared using the Pearson's chi-square test or Fischer's exact test, as appropriate. As the data in the study have multilevel structure and unbalanced design, mixed linear model was used for the comparisons of continuous variables in the cross-section level analysis; the model took into account the clustered nature of >1 cross-sections from the same scaffold and >1 struts from the same cross-section, which might result in unknown correlations among measurements within the clusters. For WSS comparison between the plaque types, the multi-level model was built with fixed-effects on cross-sectional lumen area, embedment and protrusion distances with random-effects on patient-ID and cross-section ID. All statistical tests were 2-tailed, and an α -level of 0.05 was used to determine statistical significance. Analyses were performed using the statistical analysis program SPSS V.23(SPSS Inc., Chicago, IL)

RESULTS

Fourteen patients (15 lesions:9 left anterior descending coronary arteries,2 left circumflex and 4 right coronary arteries) were investigated in the present study. All the study patients were treated with a 3.0x18 mm Absorb scaffold. Pre-dilatation was mandatory in Absorb Cohort-B trial and performed in all cases. Post-dilatation was left to operator's discretion in the study protocol(16). Patient characteristics are shown in **Table 1**.

Table 1. Baseline Characteristics of the Studied Population (N = 14, Lesion=15)

Age, yrs	61 ± 5
Male	9 (64)
Hypertension	9 (64)
Hypercholesterolemia	11 (79)
Diabetes mellitus	0 (0)
Current smoking	5 (36)
Prior percutaneous coronary intervention	2 (14)
Prior myocardial infarction	2 (14)
Stable angina	11 (79)
Unstable angina	1 (7)
Silent ischemia	0 (0)
Treated vessel	
Left anterior descending artery	9 (60)
Left circumflex artery	2 (13)
Right coronary artery	4 (27)
Ramus intermedius	0 (0)

Values are mean ± SD or n (%).

Procedural characteristics are demonstrated in **Table 2**. QCA analysis post-implantation showed an acute gain of 1.19 ± 0.33 mm and acute percent recoil (using mean lumen diameter) of $7.6 \pm 6.5\%$. Pre-implantation and post-implantation QCA data are shown in **Table 3**.

Table 2. Procedural Characteristics

		N =14, L=15
ACC/AHA lesion class	A	0% (0)
	B1	67% (10)
	B2	33% (5)
	C	0% (0)
Pre-dilatation		100% (15/15)
Pre-dilatation pressure, atm		11.67 ± 2.51
Diameter of scaffolds, mm		3.00 ± 0.0
Expected scaffold diameter, mm		3.30 ± 0.11
Total length of study devices, mm		18.0 ± 0.0
Nominal Scaffold area, mm ²		7.07 ± 0.0
Expected scaffold area, mm ²		8.54 ± 0.58
Deployment pressure, atm		13.00 ± 3.01
Post-dilatation		60% (9)
Post-dilatation pressure, atm		18.29 ± 5.06
Procedure complication		13% (2)
Clinical device success		100% (15/15)
Clinical procedure success		100% (15/15)

Table 3. Results of QCA analysis pre-procedural, post-procedural and at 5- year follow up

Pre-procedure	
Lesion length, mm	9.81 ± 3.87
Pre-procedure reference vessel diameter, mm	2.56 ± 0.31
Pre-procedure minimum lumen diameter, mm	1.04 ± 0.24
Pre-procedure percent diameter stenosis, %DS	58.91 ± 10.19
Dmax-Proximal, mm	2.84 ± 0.30
Dmax-Distal, mm	2.69 ± 0.29
Post-procedure	
Mean lumen diameter, in-scaffold, mm	2.63 ± 0.22
Reference lumen diameter, mm	2.62 ± 0.23
Minimum lumen diameter, in-scaffold, mm	2.23 ± 0.19
In- scaffold percent diameter stenosis, %DS	15.09 ± 5.31
In- scaffold acute absolute gain, mm	1.18 ± 0.31
In- scaffold acute percent gain, %	43.71 ± 11.49
In- scaffold acute absolute recoil, (using mean lumen diameter), mm	0.21±0.18
In- scaffold acute percent recoil, (using mean lumen diameter) %	7.64±6.49
In- scaffold acute absolute recoil (using minimum lumen diameter), mm	0.24±0.17
In- scaffold acute percent recoil, (using minimum lumen diameter), %	9.69±6.88
Ratio of post-dilatation balloon nominal diameter to mean reference diameter	1.14±0.08
Pre-dilatation balloon diameter-RVD ratio	1.04 ± 0.15

OCT analysis results

OCT results are summarized in **Table-4**. Ninety-seven percent of the struts were well apposed (n=8840) to the vessel wall. There were 243 malapposed struts(3%). Post-implantation expansion-index was 0.98±0.21. Post-implantation mean scaffold area was 7.54±0.93mm² and in-scaffold mean lumen area was 7.43±0.88mm² whereas mean lumen area in proximal non-scaffolded edge segment was 7.50±1.84 mm² and mean luminal area in distal non-scaffolded edge segment was 5.39±1.62mm². Mean eccentricity index was 0.67±0.053. Cross-section level analysis(n=1289) showed that in scaffolded segment there is an inverse correlation between the median-WSS and the eccentricity index (*r*: -0.363, *p*<0.0001).

Table 4. Results of post-procedural OCT analysis

Post-procedural	
In-scaffold mean lumen diameter, mm	3.06 ± 0.21
In-scaffold minimum lumen diameter, mm	2.75 ± 0.22
In-scaffold mean lumen area, mm ²	7.43 ± 0.88
In-scaffold minimum lumen area, mm ²	5.98 ± 0.96
Mean scaffold diameter, mm	3.09 ± 0.19
Minimum scaffold diameter, mm	2.80 ± 0.21
Mean scaffold area, mm ²	7.54 ± 0.93
Minimum scaffold area	6.19 ± 0.93
Post-procedure in-scaffold percent diameter stenosis, %DS	15.09 ± 5.31
Mean strut area, mm ²	0.20 ± 0.03
Mean lumen diameter in proximal edge segment, mm	4.68 ± 0.32
Mean lumen area in proximal edge segment, mm ²	7.50 ± 1.84
Mean lumen diameter in distal edge segment, mm	4.03 ± 1.23
Mean lumen area in distal edge segment, mm ²	5.39 ± 1.62
Eccentricity index	0.67 ± 0.05
Asymmetry index	0.23 ± 0.09
Expansion index	0.98 ± 0.21

Embedment/protrusion results

At device level analysis, the strut protrusion distance was 113±14µm. At cross-section level analysis, the protrusion distance was 115±42µm. There was a significant relationship between the embedment depths and plaque types (**Table 5**) (**Figure 1**). Struts over the fibro-atheromatous plaques, were significantly deeper embedded than in other plaque types (**Figure 2**). Deployment/post-dilatation balloon pressures were found to have a modest effect on embedment depths ($r=0.28$, $p=0.048$). Similar to the embedment analysis, the protrusion distances were also significantly related to the underlying plaque types. Lowest strut protrusion was noted in lipid-rich fibroatheromas, whereas in fibrous and fibro-calcific plaques, the strut protrusion was relatively higher (**Table 5**). The majority of the malapposed struts, (75%, $n=149$) were detected in the fibro-calcific group and the rest ($n=94$) were in fibrous plaque group. All of the malapposed struts were detected in one case including totally 26 cross-sections. The newly developed thrombus post-implantation attached to the BVS struts without

limiting the embedment analysis on OCT. Balloon sizing and inflation pressure had no direct effect on strut embedment, although high-pressure post-dilatation (≥ 20 atm) resulted in numerically deeper embedment than low-pressure post-dilatation. Balloon type did not present any significant effect on strut embedment at predilatation ($P=0.49$) or post-dilatation ($P=0.25$).

Table 5. Cross-section level Embedment / Protrusion and WSS according to the plaque type

Plaque type	Embedment depth (μm)	Protrusion distance (μm)	WSS (Pa)
Non-atherosclerotic intimal thickening / normal vessel wall (n=2275)	47 ± 34 * Δ Υ	123 ± 34 ¶ ¶ ¶ ¶	1.44 ± 0.9 ¶ ¶ ¶
Fibrous (n=4191)	53 ± 40 * $\#$ $\&$	118 ± 38 ¶ ¶ ¶ ¶	1.24 ± 0.78 α θ ∞
Fibroatheromatous (n=2027)	76 ± 48 $\#$ ϕ Δ	94.6 ± 46 Ω ¶ ¶ ¶	1.50 ± 0.81 Σ ¶ ¶
Fibro-calcific (n=590)	35 ± 52 $\&$ ϕ Υ	139 ± 50 ¶ ¶ ¶ ¶	1.05 ± 0.91 ∞ ¶ ¶

For embedment: * $p = 0.09$, # $p < 0.001$, & $p < 0.001$, ϕ $p < 0.0001$, Δ $p < 0.0001$, Υ $p < 0.0001$

For protrusion: ¶ $p = 0.74$, ¶ $p < 0.0001$, ¶ $p < 0.0001$, ¶ $p < 0.0001$, ¶ $p < 0.0001$, ¶ $p < 0.0001$

For WSS: θ $p < 0.001$, ∞ $p = 0.06$, ¶ $p < 0.0001$, ¶ $p < 0.0001$, ¶ $p < 0.0001$, Σ $p < 0.0001$

N = total strut number in each plaque type, p-values come from mixed-effects regression analysis

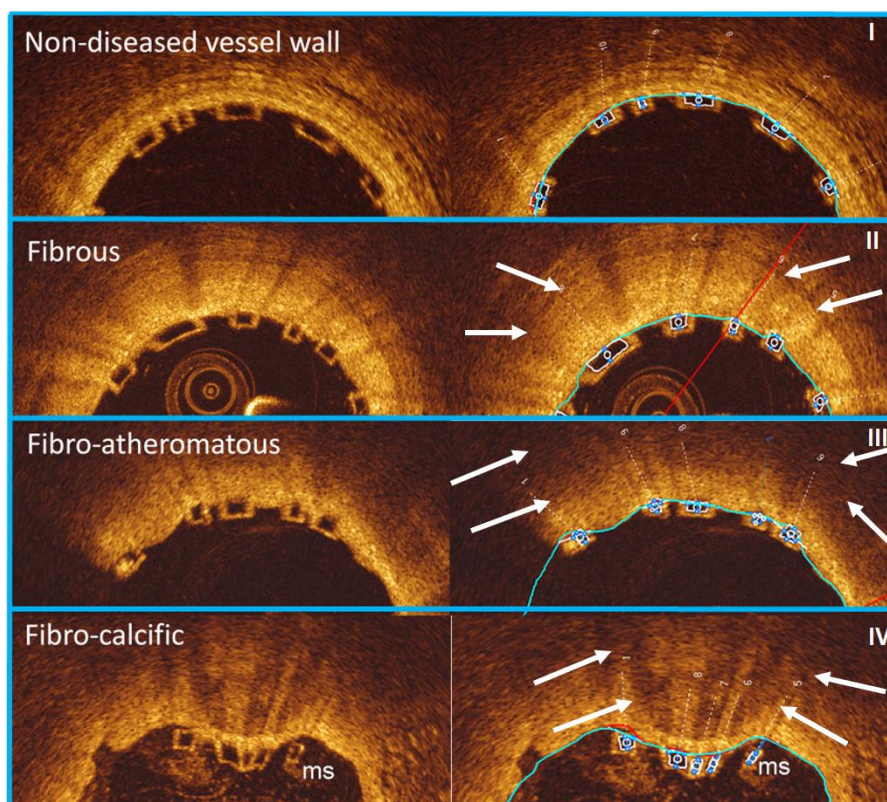


Figure 1. Rectangular shaped struts of Absorb BVS were automatically detected by QCU-CMS (v.14.9) after automatic detection of interpolated luminal contour (blue contour represents embedment contour), protrusion/embedment distances were analyzed semi-automatically using the methodology described by Sotomi et al(8). The white arrows show the fibrous tissue in panel-I, the lipid pool in panel-II and the calcified plaque in panel-IV. The struts were well embedded in fibroatheromatous plaques, whereas fibro-calcific plaque prevents deep penetration of the struts. Most of the malapposed struts (ms) were detected in vessel segments with calcified plaques.

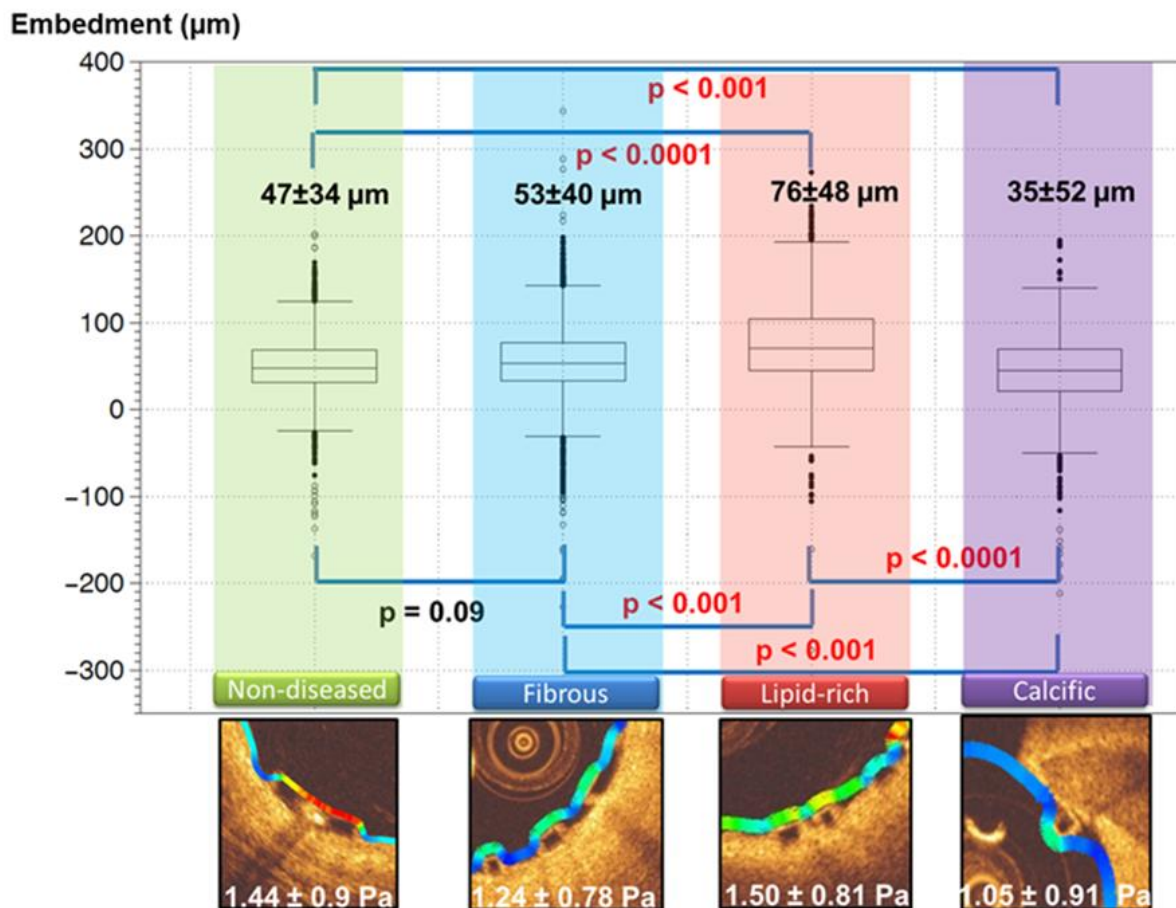


Figure 2. In lipid-rich plaques, the struts embedment was deeper than in other plaque types. In the illustration, embedment distances were demonstrated for each group. Mean WSS for each group was shown in the lower OCT cross-section panels. *P*-values come from mixed effects analysis for the comparison of embedment distances between plaque types.

Wall Shear Stress results

CFD results demonstrated higher WSS in fibro-atheromas in Absorb (**Figure 3**). The lowest WSS values were documented in fibrous and fibro-calcific plaques (**Table 5**). After classifying the WSS as low (<1.0Pa) and normal/high WSS (≥1.0Pa), the percentages of low-WSS in different plaque groups were 30.1%, 31.1%, 25.4% and 36.2% for the healthy vessel wall, the fibrous plaque, the fibro-atheromatous plaque and the fibro-calcific plaque, respectively (*p*-overall <0.001). Overall, there was an inverse linear relationship between strut protrusion distance and WSS (**Figure 4**). In all plaque types, there was a negative correlation between strut protrusion and WSS, which was pronounced in calcified plaques ($r=-0.240$, $p<0.01$ in fibrous; $r=-0.218$, $p<0.01$ in fibroatheroma and $r=-0.261$, $p<0.01$ in fibrocalcific plaques).

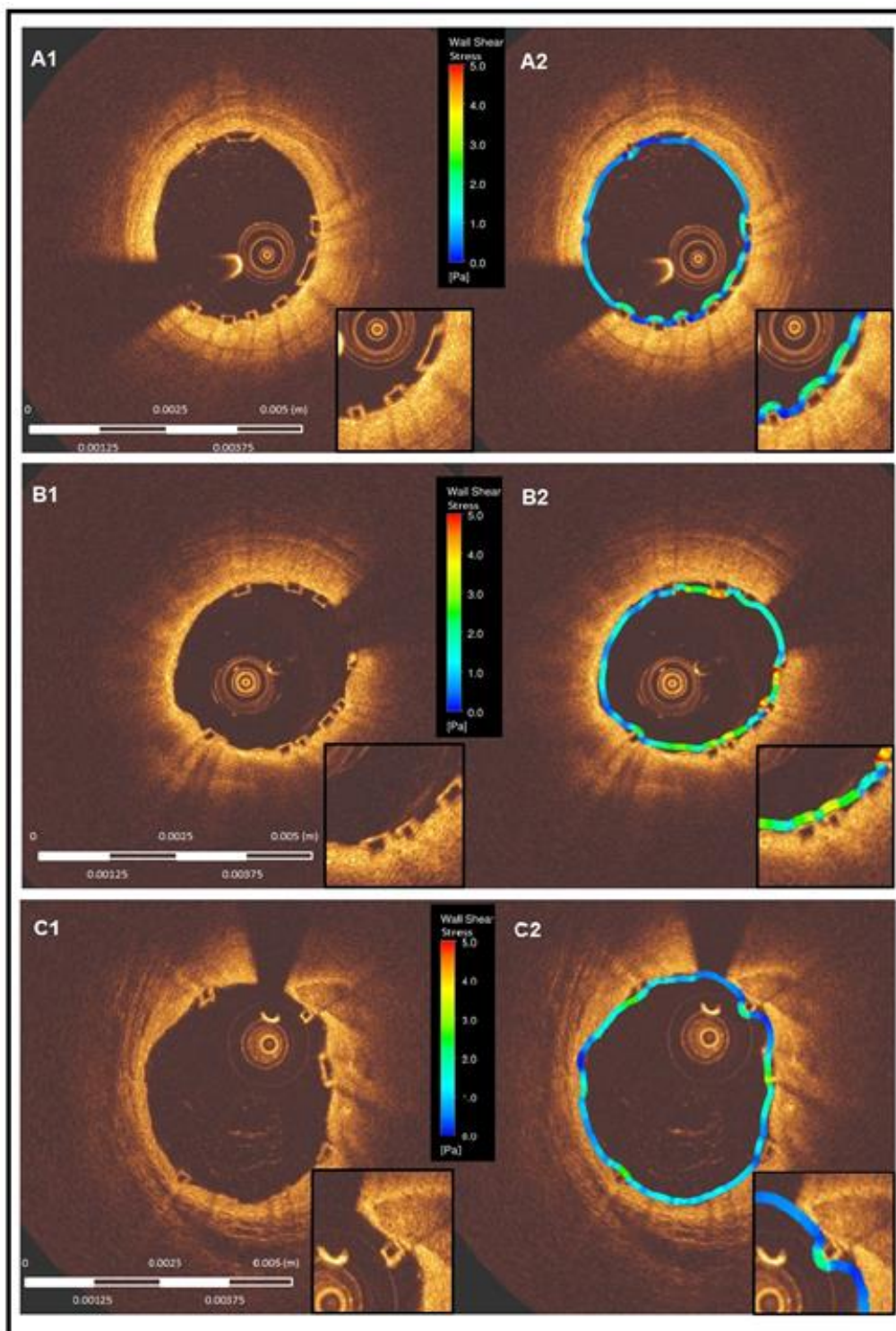


Figure 3. Fibrous plaques were associated with higher strut protrusion distances that induced very low WSS due to flow obstruction and the formation of recirculation zones (A1, A2). Lipid-rich fibro-atheromatous plaques allowed deeper strut embedment which induced less flow disruption in the vicinity of the struts resulting in low WSS gradient between top of the struts and interstrut zones (B1, B2). Due to poor penetration in non-compliant calcified plaques, flow disruption induced higher gradients between the top of the struts and inter-strut zones (Bottom small panel).

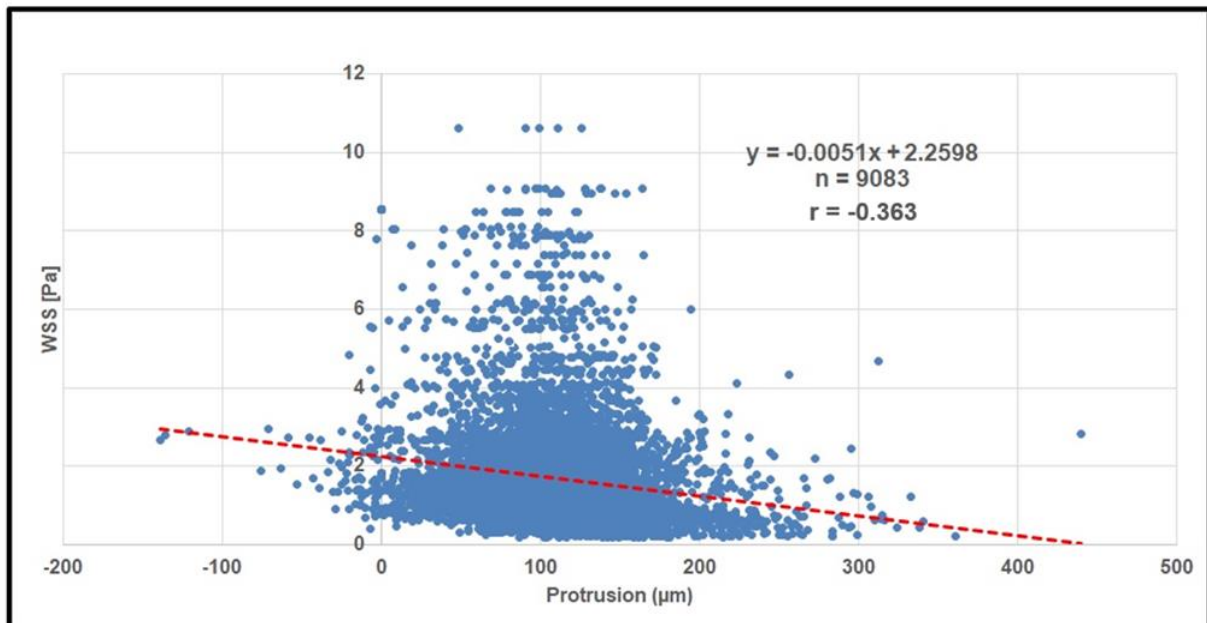


Figure 4. There was an inverse linear correlation between the median WSS and strut protrusion distances.

DISCUSSION

The main results of our study can be summarized as follows; 1-Strut embedment/protrusion differed according to the underlying plaque type with an increased strut embedment in fibro-atheromatous plaques; 2-The strut embedment/protrusion pattern had an evident impact on WSS distribution: in fibro-atheromas, where the struts were deeply embedded, there were less flow disruptions resulting in relatively higher WSS values compared to other plaque types; 3-There was an inverse linear relationship between strut protrusion and WSS which was prominent in calcified plaques compared to the other plaque types.

Despite breathtaking advances in stent/scaffold designs over the last decades, restenosis and stent/scaffold thrombosis continue to be the *Achilles heel* of the PCI(5). PCI outcomes depend on several factors including implantation techniques, treated vessel segment features - particularly plaque characteristics and the design properties of the stent/scaffold. While the normal vessel wall is incompressible, the diseased vessel wall -including atherosclerotic plaque, is compressible and exhibits viscoelasticity while subjected to a pressure load(20, 21). Based on this fact, stent/scaffold strut design and plaque type seem to be the main factors for

strut penetration which determines local flow patterns, regulates neointimal hyperplasia and may be coupled with thrombus formation(5).

Plaque type and strut embedment/protrusion impact on local shear stress

The composition and morphology of the plaque determine its mechanical behaviors. The cellularity level and the tissue composition are the main determinants of the stiffness of the atherosclerotic plaques. Hypocellular plaques, such as fibrous and fibro-calcific plaques, are 1-2 times stiffer than the cellular lipid-rich fibroatheromatous plaques. Lipid-rich fibroatheromatous plaque is the most compliant and least stiff plaque type(22, 23). Mechanical testing of the human atherosclerotic plaques unraveled that during compression-relaxation cycles, fibrous and calcified plaques behave similarly and are stiffer than the lipid-rich atheromatous plaques(24). Young's modulus (elastic modulus), -indicates the resistance of a material to elastic deformation- of fibrotic plaques are two-times higher than lipid-rich fibroatheromas(25).

Stent/scaffold implantation imperils the vessel wall to higher stresses that may injure the internal elastic lamina, induces smooth muscle cell proliferation and neointimal tissue growth which may conclude with in-stent/scaffold restenosis. The level of vessel wall injury depends on stent/scaffold design, vessel geometry, curvature, implantation pressures during the procedure and biomechanical properties of the treated plaque. Under compressive load, particularly lipid-rich plaques demonstrate viscoelastic behavior that reflects their relatively higher compliance. Furthermore, lipid-rich fibroatheromatous plaques are less stiffer than non-diseased healthy vessel wall(26). The stiffness of the vessel wall increases from lipid-rich atheromas to fibrotic and fibro-calcific lesions(27, 28). In the present study, as expected, the polymeric struts penetrated deeper in lipid-rich atheromatous plaques than fibrous and fibro-calcific plaques, due to the viscoelastic properties of these plaque types.

Vessel wall stiffness, determined by plaque phenotype, influences scaffold expansion which has a potential impact on PCI outcomes(9). In calcified lesions, vessel expansion is less than non-calcified lesions(29). During implantation, in calcified, stiff lesions, the presence of calcium reduces the applied stress within the vessel wall that behaves as an *absorber* protecting the vessel wall confronting high pressures(30). Implementing high pressures on cellular and compliant plaques may cause immense injury in the vessel wall whereas the protective role of calcified plaque allows vessel dilatation at higher balloon pressures more

safely(31). Therefore, the same device with the same applied pressures in different types of plaques will result in different levels of tissue injury and luminal gain(23). In the present study, after adjusting according to the plaque type, embedment/protrusion was slightly related with deployment pressures(9).

The endothelization of the denuded artery wall and strut surfaces are related with local WSS.(32). Low WSS induces neointimal growth that covers the struts and inter-strut vessel wall area(18, 33). Low shear stress at the bottom beside the struts induces platelets and endothelium aggregation in the disrupted flow zones and trigger several biological pathways for neointimal regeneration and thrombus formation in the inter-strut zones(34). Flow separation and flow stagnation zones induce confluent endothelial cells migration away from the flow re-attachment points demonstrated in flow chamber experiments(35). Higher embedment with less protrusion provides less flow disruption, yielded by non-low WSS in the vicinity of the struts that protects the vessel wall biology(36). Lipid-rich fibroatheromas with deeper embedded struts demonstrated more *favorable* WSS magnitudes, whereas stiffer fibrous and fibro-calcific plaques unraveled relatively lower WSS due to the flow disturbances related to less strut embedment. Well embedded struts may reduce area with disturbed *athero-prone* low WSS which might have favorable effects on vessel wall healing at follow up post-implantation.

Practical Implications

The idea of designing lesion specific stent and implantation techniques using intravascular imaging modalities has been a research subject. Due to its higher strut thickness, Absorb potentially induces flow disruptions more than the stents/scaffolds with thinner strut designs(37, 38). However, in case of well-embedment, as in lipid-rich plaques, Absorb may provide more "*favorable*" shear stress distribution due to deeper strut penetration which may potentially promote a strategy of BRS implantation according to the underlying plaque type and may mitigate the negative aspects of thicker strut and non-streamline strut geometry (39).

Limitations

The main limitation of the present study was low case number. Several criteria were implemented for filtering suitable cases. To prevent any effect of swirling-flow due to vessel curvature, on the scaffolded segment WSS distribution, we didn't include the cases with curvature and the cases without two angiographic projections at least with >25-degree

difference couldn't be reconstructed. However, total strut and cross-section numbers provided well-fitted statistical models for getting reliable conclusions. The effect of low WSS at follow up was not evaluated in the present study, whereas such clinical inferences can be exemplified from the literature.

CONCLUSION

Treated plaque type influences strut embedment/protrusion in the vessel wall. OCT has high accuracy to detect calcified plaques with its circumferential extent and depth which are crucial information for lesion preparation such as balloon pre-dilatation, debulking etc.). Shear stress distribution is related with strut penetration in the vessel wall. Following bioresorbable scaffold implantation, embedment/protrusion analysis may help to improve implantation process and local hemodynamic forces, that may potentially influence neointimal hyperplasia and thrombus formation.

Disclosures:

P.W. Serruys is a member of the International Advisory Board of Abbott Vascular. Y. Onuma is a member of the International Advisory Board of Abbott Vascular. E. Tenekecioglu has a research grant from TUBITAK (The Research and Scientific Council of Turkey).

REFERENCES

1. Serruys PW, Chevalier B, Sotomi Y, Cequier A, Carrie D, Piek JJ, et al. Comparison of an everolimus-eluting bioresorbable scaffold with an everolimus-eluting metallic stent for the treatment of coronary artery stenosis (ABSORB II): a 3 year, randomised, controlled, single-blind, multicentre clinical trial. *Lancet*. 2016;388(10059):2479-91.
2. Collet C, Asano T, Miyazaki Y, Tenekecioglu E, Katagiri Y, Sotomi Y, et al. Late thrombotic events after bioresorbable scaffold implantation: a systematic review and meta-analysis of randomized clinical trials. *European heart journal*. 2017;38(33):2559-66.
3. Suwannasom P, Sotomi Y, Ishibashi Y, Cavalcante R, Albuquerque FN, Macaya C, et al. The Impact of Post-Procedural Asymmetry, Expansion, and Eccentricity of Bioresorbable Everolimus-Eluting Scaffold and Metallic Everolimus-Eluting Stent on Clinical Outcomes in the ABSORB II Trial. *JACC Cardiovascular interventions*. 2016;9(12):1231-42.
4. Sotomi Y, Suwannasom P, Tenekecioglu E, Collet C, Nakatani S, Okamura T, et al. Imaging assessment of bioresorbable vascular scaffolds. *Cardiovascular intervention and therapeutics*. 2018;33(1):11-22.
5. Ng J, Bourantas CV, Torii R, Ang HY, Tenekecioglu E, Serruys PW, et al. Local Hemodynamic Forces After Stenting: Implications on Restenosis and Thrombosis. *Arteriosclerosis, thrombosis, and vascular biology*. 2017;37(12):2231-42.
6. Tenekecioglu E, Torii R, Sotomi Y, Collet C, Dijkstra J, Miyazaki Y, et al. The Effect of Strut Protrusion on Shear Stress Distribution: Hemodynamic Insights From a Prospective Clinical Trial. *JACC Cardiovascular interventions*. 2017;10(17):1803-5.
7. Kini AS, Vengrenyuk Y, Pena J, Motoyama S, Feig JE, Meelu OA, et al. Optical coherence tomography assessment of the mechanistic effects of rotational and orbital atherectomy in severely calcified coronary lesions. *Catheterization and cardiovascular interventions : official journal of the Society for Cardiac Angiography & Interventions*. 2015;86(6):1024-32.
8. Sotomi Y, Tateishi H, Suwannasom P, Dijkstra J, Eggermont J, Liu S, et al. Quantitative assessment of the stent/scaffold strut embedment analysis by optical coherence tomography. *The international journal of cardiovascular imaging*. 2016;32(6):871-83.
9. Sotomi Y, Onuma Y, Dijkstra J, Eggermont J, Liu S, Tenekecioglu E, et al. Impact of Implantation Technique and Plaque Morphology on Strut Embedment and Scaffold Expansion of Polylactide Bioresorbable Scaffold- Insights From ABSORB Japan Trial. *Circulation journal : official journal of the Japanese Circulation Society*. 2016;80(11):2317-26.
10. Mattesini A, Secco GG, Dall'Ara G, Ghione M, Rama-Merchan JC, Lupi A, et al. ABSORB biodegradable stents versus second-generation metal stents: a comparison study of 100 complex lesions treated under OCT guidance. *JACC Cardiovasc Interv*. 2014;7(7):741-50.
11. Serruys P, De Jaegere P, Bertrand M, Kober G, Marquis JF, Piessens J, et al. Morphologic change in coronary artery stenosis with the Medtronic Wiktor stent: initial results from the core laboratory for quantitative angiography. *Cathet Cardiovasc Diagn*. 1991;24(4):237-45.
12. de Jaegere P, Serruys PW, van Es GA, Bertrand M, Wiegand V, Marquis JF, et al. Recoil following Wiktor stent implantation for restenotic lesions of coronary arteries. *Cathet Cardiovasc Diagn*. 1994;32(2):147-56.
13. Sotomi Y, Onuma Y, Suwannasom P, Tateishi H, Tenekecioglu E, Zeng Y, et al. Is quantitative coronary angiography reliable in assessing the lumen gain after treatment with the everolimus-eluting bioresorbable polylactide scaffold? *EuroIntervention*. 2016;12(8):e998-e1008.
14. Bourantas CV, Papafaklis MI, Lakkas L, Sakellarios A, Onuma Y, Zhang YJ, et al. Fusion of optical coherence tomographic and angiographic data for more accurate evaluation of the endothelial shear stress patterns and neointimal distribution after bioresorbable scaffold implantation: comparison with intravascular ultrasound-derived reconstructions. *Int J Cardiovasc Imaging*. 2014;30(3):485-94.
15. Nakatani S, Sotomi Y, Ishibashi Y, Grundeken MJ, Tateishi H, Tenekecioglu E, et al. Comparative analysis method of permanent metallic stents (XIENCE) and bioresorbable poly-L-lactic (PLLA) scaffolds (Absorb) on optical coherence tomography at baseline and follow-up. *EuroIntervention : journal of*

EuroPCR in collaboration with the Working Group on Interventional Cardiology of the European Society of Cardiology. 2016;12(12):1498-509.

16. Serruys PW, Onuma Y, Ormiston JA, de Bruyne B, Regar E, Dudek D, et al. Evaluation of the second generation of a bioresorbable everolimus drug-eluting vascular scaffold for treatment of de novo coronary artery stenosis: six-month clinical and imaging outcomes. *Circulation*. 2010;122(22):2301-12.
17. Papafaklis MI, Bourantas CV, Theodorakis PE, Katsouras CS, Naka KK, Fotiadis DI, et al. The effect of shear stress on neointimal response following sirolimus- and paclitaxel-eluting stent implantation compared with bare-metal stents in humans. *JACC Cardiovascular interventions*. 2010;3(11):1181-9.
18. Bourantas CV, Papafaklis MI, Kotsia A, Farooq V, Muramatsu T, Gomez-Lara J, et al. Effect of the endothelial shear stress patterns on neointimal proliferation following drug-eluting bioresorbable vascular scaffold implantation: an optical coherence tomography study. *JACC Cardiovascular interventions*. 2014;7(3):315-24.
19. Stone PH, Saito S, Takahashi S, Makita Y, Nakamura S, Kawasaki T, et al. Prediction of progression of coronary artery disease and clinical outcomes using vascular profiling of endothelial shear stress and arterial plaque characteristics: the PREDICTION Study. *Circulation*. 2012;126(2):172-81.
20. Carew TE, Vaishnav RN, Patel DJ. Compressibility of the arterial wall. *Circulation research*. 1968;23(1):61-8.
21. Chuong CJ, Fung YC. Compressibility and constitutive equation of arterial wall in radial compression experiments. *Journal of biomechanics*. 1984;17(1):35-40.
22. Sadat U, Teng Z, Gillard JH. Biomechanical structural stresses of atherosclerotic plaques. Expert review of cardiovascular therapy. 2010;8(10):1469-81.
23. Timmins LH, Meyer CA, Moreno MR, Moore JE. Effects of stent design and atherosclerotic plaque composition on arterial wall biomechanics. *Journal of endovascular therapy : an official journal of the International Society of Endovascular Specialists*. 2008;15(6):643-54.
24. Salunke NV, Topoleski LD, Humphrey JD, Mergner WJ. Compressive stress-relaxation of human atherosclerotic plaque. *Journal of biomedical materials research*. 2001;55(2):236-41.
25. Ohayon J, Mesnier N, Broisat A, Toczek J, Riou L, Tracqui P. Elucidating atherosclerotic vulnerable plaque rupture by modeling cross substitution of ApoE^{-/-} mouse and human plaque components stiffnesses. *Biomechanics and modeling in mechanobiology*. 2012;11(6):801-13.
26. Hayashi K. Experimental approaches on measuring the mechanical properties and constitutive laws of arterial walls. *Journal of biomechanical engineering*. 1993;115(4b):481-8.
27. Koniari I, Mavrilas D, Papadaki H, Karanikolas M, Mandellou M, Papalois A, et al. Structural and biomechanical alterations in rabbit thoracic aortas are associated with the progression of atherosclerosis. *Lipids in health and disease*. 2011;10:125.
28. Farrar DJ, Riley WA, Bond MG, Barnes RN, Love LA. Detection of early atherosclerosis in M. fascicularis with transcutaneous ultrasonic measurement of the elastic properties of the common carotid artery. *Texas Heart Institute journal*. 1982;9(3):335-43.
29. Weissman NJ, Palacios IF, Weyman AE. Dynamic expansion of the coronary arteries: implications for intravascular ultrasound measurements. *American heart journal*. 1995;130(1):46-51.
30. Pericevic I, Lally C, Toner D, Kelly DJ. The influence of plaque composition on underlying arterial wall stress during stent expansion: the case for lesion-specific stents. *Medical engineering & physics*. 2009;31(4):428-33.
31. Tang D, Yang C, Zheng J, Woodard PK, Saffitz JE, Sicard GA, et al. Quantifying Effects of Plaque Structure and Material Properties on Stress Distributions in Human Atherosclerotic Plaques Using 3D FSI Models. *Journal of biomechanical engineering*. 2005;127(7):1185-94.
32. Sprague EA, Luo J, Palmaz JC. Endothelial cell migration onto metal stent surfaces under static and flow conditions. *Journal of long-term effects of medical implants*. 2000;10(1-2):97-110.
33. Tenekecioglu E, Bourantas CV, Onuma Y, Serruys PW. Sealing of calcified plaques after bioresorbable scaffold implantations: a five-year follow up. *The international journal of cardiovascular imaging*. 2017;33(4):451-2.

34. Chatzizisis YS, Coskun AU, Jonas M, Edelman ER, Feldman CL, Stone PH. Role of endothelial shear stress in the natural history of coronary atherosclerosis and vascular remodeling: molecular, cellular, and vascular behavior. *Journal of the American College of Cardiology*. 2007;49(25):2379-93.
35. Phelps JE, DePaola N. Spatial variations in endothelial barrier function in disturbed flows in vitro. *American journal of physiology Heart and circulatory physiology*. 2000;278(2):H469-76.
36. Foin N, Gutierrez-Chico JL, Nakatani S, Torii R, Bourantas CV, Sen S, et al. Incomplete stent apposition causes high shear flow disturbances and delay in neointimal coverage as a function of strut to wall detachment distance: implications for the management of incomplete stent apposition. *Circulation Cardiovascular interventions*. 2014;7(2):180-9.
37. Tenekecioglu E, Torii R, Bourantas C, Crake T, Zeng Y, Sotomi Y, et al. Preclinical assessment of the endothelial shear stress in porcine-based models following implantation of two different bioresorbable scaffolds: effect of scaffold design on the local haemodynamic micro-environment. *EuroIntervention : journal of EuroPCR in collaboration with the Working Group on Interventional Cardiology of the European Society of Cardiology*. 2016;12(10):1296.
38. Tenekecioglu E, Torii R, Bourantas C, Sotomi Y, Cavalcante R, Zeng Y, et al. Difference in hemodynamic microenvironment in vessels scaffolded with absorb BVS and mirage BRMS: Insights from a pre-clinical endothelial shear stress study. *EuroIntervention : journal of EuroPCR in collaboration with the Working Group on Interventional Cardiology of the European Society of Cardiology*. 2017.
39. Tenekecioglu E, Poon EK, Collet C, Thondapu V, Torii R, Bourantas CV, et al. The Nidus for Possible Thrombus Formation: Insight From the Microenvironment of Bioresorbable Vascular Scaffold. *JACC Cardiovascular interventions*. 2016;9(20):2167-8.

Chapter 9

Five-year follow-up of underexpanded and overexpanded bioresorbable scaffolds: self-correction and impact on shear stress

Improvement in local hemodynamics 5 years after implantation of a coronary bioresorbable scaffold: a pulsatile non-Newtonian shear stress analysis

Endothelial shear stress 5 years after implantation of a coronary bioresorbable scaffold

Early strut protrusion and late neointima thickness in the Absorb bioresorbable scaffold: a serial wall shear stress analysis up to five years

Five-year follow-up of underexpanded and overexpanded bioresorbable scaffolds: self-correction and impact on shear stress

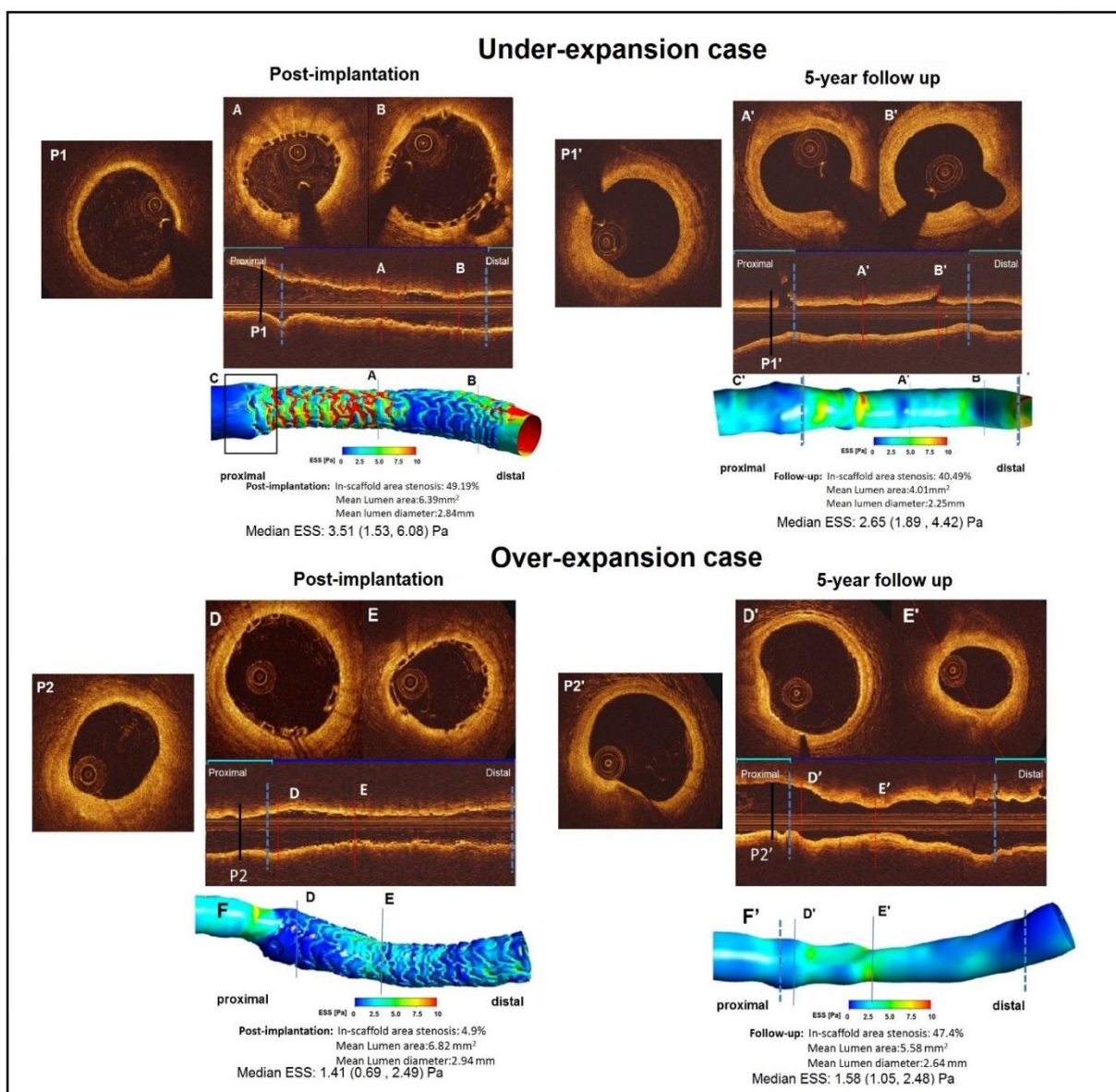
Ryo Torii*, Erhan Tenekecioglu*, Christos Bourantas, Eric Poon, Vikas Thondapu, Frank Gijzen, Yohei Sotomi, Yoshinobu Onuma, Peter Barlis, Andrew S. H. Ooi, Patrick W Serruys

* These authors equally contributed to this work

EuroIntervention. 2017;12(17):2158-2159.

INTERVENTIONAL FLASHLIGHTS

Two patients received 3.0x18mm Absorb bioresorbable vascular scaffolds (Abbott Vascular, USA) one in the left-anterior descending coronary artery, the other patient in circumflex coronary artery. Post-implantation OCT (pullback speed: 20mm/s, acquisition rate: 200 frames/s) and angiographic data were fused to reconstruct coronary anatomy and computational fluid dynamic (CFD) techniques were used to simulate Newtonian steady blood flow and estimate endothelial shear stress (ESS) distributions.¹ In **Figure**, Panels-A, -B and -C show underexpansion of the scaffold (Mean expansion index: 0.51). Panels-D, -E and -F show an over-expanded bioresorbable scaffold. (Mean Expansion index= 1.32).



In CFD model of underexpanded case (Figure, panel-C), high ESS (*in red*) was noted on top-of the struts which disrupted the flow, creating recirculation zones and low ESS (*in dark blue*) in

the inter-strut zones. Scaffold underexpansion caused a “step-down” at the proximal-edge of the scaffolded segment (Figure, black box in panel-C). On the five-year OCT, there was attenuation of the *step-down* appearance with normalized ESS in the proximal edge segment; the luminal surface was smoother and overall, the shear stress was more homogeneous and physiological (1.5-3.0 Pa) (Figure, panel-A’ and-B’).

In CFD model of the over-expanded case (Figure, panel-F’), low ESS was detected not only in the inter-strut areas but also on top-of-the struts. Scaffold over-expansion caused an “step-up” at the proximal-edge of the scaffolded segment. At the five-year follow up, the *step-up* became less prominent and the areas of very low shear stress regressed considerably.

These two cases of over- and under-expansion at baseline resulted acutely in two different shear stress distribution. Both increased and decreased ESS appear to induce biological mechano-transduction process that aims at normalizing ESS levels at long-term follow-up to values close to the physiological ranges (1.5-2.5 Pa). The mechanism of “normalization” seems to be related to a dynamic remodeling, which presumably resulted from shear stress, wall stress, cyclic strain and other important biologic factors.^{2,3}

Practical implication

Under-expansion and over-expansion have been incriminated as causative factors of adverse cardiac events. However, dynamic biological interaction between vessel wall and scaffold may attenuate the adverse hemodynamic impact of over- or under-expansion.

REFERENCES

1. Tenekecioglu E, Poon EK, Collet C, et al. The Nidus for Possible Thrombus Formation: Insight From the Microenvironment of Bioresorbable Vascular Scaffold. *JACC Cardiovasc Interv.* 2016;9(20):2167-2168.
2. Koskinas KC, Chatzizisis YS, Antoniadis AP, Giannoglou GD. Role of endothelial shear stress in stent restenosis and thrombosis: pathophysiologic mechanisms and implications for clinical translation. *J Am Coll Cardiol.* 2012;59(15):1337-1349.
3. Stone PH, Saito S, Takahashi S, et al. Prediction of progression of coronary artery disease and clinical outcomes using vascular profiling of endothelial shear stress and arterial plaque characteristics: the PREDICTION Study. *Circulation.* 2012;126(2):172-181.

Improvement in local hemodynamics 5 years after implantation of a coronary bioresorbable scaffold: a pulsatile non-Newtonian shear stress analysis

Erhan Tenekecioglu, Vikas Thondapu, Eric K. W. Poon, Yoshinobu Onuma, Patrick W Serruys

Eur Heart J Cardiovasc Imaging. 2017;18(11):1294.

IMAGE FOCUS

A 3.0 × 18 mm Absorb bioresorbable vascular scaffold (Abbott Vascular, Santa Clara, California) was implanted in the left circumflex coronary artery of patient with stable angina pectoris. Optical coherence tomography (OCT) revealed a well-expanded and apposed scaffold (pullback-speed:18 mm/s, acquisition rate:180 frames/s). A patient-specific 3-dimensional geometry of the scaffolded lumen was generated by fusing OCT with coronary angiography. Pulsatile computational fluid dynamic (CFD) simulations were carried out by solving the Navier-Stokes equations. Blood was modeled as non-Newtonian fluid. Endothelial shear stress (ESS) at lumen and scaffold surfaces was calculated as product of local blood viscosity and near-wall velocity gradient.

During low coronary flow in systole, low-ESS predominates (Figure, Panel-A and -C) whereas at peak diastolic flow vessel is exposed to high ESS (Figure, Panel-B and -D). Irrespective of systolic or diastolic phase, post-implantation vessel appears highly corrugated with an alternans of high ESS on struts tops and low ESS between struts (Figure, Panel-A and -B), that has been associated with blood micro-recirculation, fibrin deposition and platelet aggregation. By 5-years, heterogeneity in ESS has largely dissipated (Figure, Panel-C and -D, online video supplement) while ESS distribution narrows and becomes more homogenous in both systole and diastole (Figure, Panel-E). Histograms depicting the overall percent area of the simulated vessel exposed to varying levels of ESS during each of studied flow conditions and time-points (Figure, Panel-E) demonstrate that vessel exposure to very low and very high ESS decreases, leading to an overall increase in mid-range values of ESS generally considered to be more physiologic.

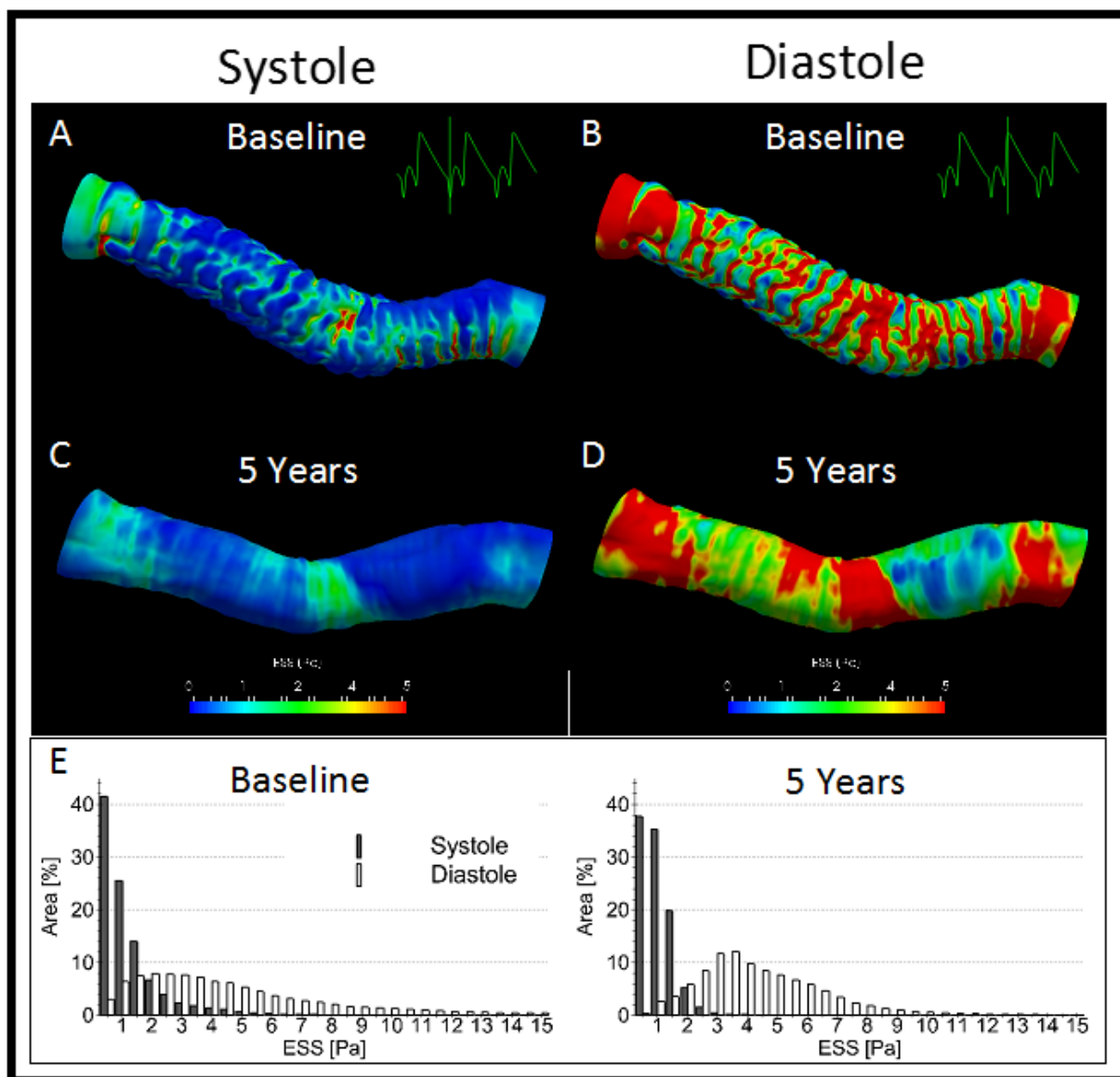


Figure. Post-implantation vessel appears highly corrugated with an alternans of high ESS on the strut-tops and low-ESS between the struts (Panel-A and -B). By 5 years, heterogeneity in ESS has largely dissipated along with the scaffold (Panel-C and -D) while the ESS distribution becomes more homogenous in both systole and diastole (Panel-E). Histograms shows the overall percent area of the simulated vessel exposed to varying levels of ESS during each time points (Panel E). ESS: endothelial shear stress; Area %: percent of lumen area

Video. Post-implantation vessel appears highly corrugated with an alternans of shear stress between inter-strut zones and top of the struts. By 5 years, heterogeneity in ESS has largely disappeared along with the scaffold.

Endothelial shear stress 5 years after implantation of a coronary bioresorbable scaffold

Vikas Thondapu*, Erhan Tenekecioglu*, Eric K W Poon, Carlos Collet, Ryo Torii, Christos V Bourantas, Cheng Chin, Yohei Sotomi, Hans Jonker, Jouke Dijkstra, Eve Revalor, Frank Gijzen, Yoshinobu Onuma, Andrew Ooi, Peter Barlis, Patrick W Serruys

* These authors equally contributed to this work

Eur Heart J. 2018;39(18):1602-1609.

ABSTRACT

Aims: As a sine qua non for arterial wall physiology, local hemodynamic forces such as endothelial shear stress (ESS) may influence long-term vessel changes as bioabsorbable scaffolds dissolve. The aim of this study was to perform serial computational fluid dynamic (CFD) simulations to examine immediate and long-term haemodynamic and vascular changes following bioresorbable scaffold placement.

Methods and results: Coronary arterial models with long-term serial assessment (baseline and five years) were reconstructed through fusion of intravascular optical coherence tomography (OCT) and angiography. Pulsatile non-Newtonian computational fluid dynamic simulations were performed to calculate the ESS and relative blood viscosity. Time-averaged, systolic, and diastolic results were compared between follow-ups. Seven patients (seven lesions) were included in this analysis. A marked heterogeneity in ESS and localised regions of high blood viscosity were observed post-implantation. Percent vessel area exposed to low averaged ESS (<1 Pa) significantly decreased over five years (15.92% vs 4.99%, $p < 0.0001$) whereas moderate (1-7 Pa) and high ESS (>7 Pa) did not significantly change (moderate ESS: 76.93% v 80.7%, $p = 0.546$; high ESS: 7.15% v 14.31%, $p = 0.281$), leading to higher ESS at follow up. A positive correlation was observed between baseline ESS and change in lumen area at five years ($p < 0.0001$). Maximum blood viscosity significantly decreased over five years (4.30 ± 1.54 versus 3.21 ± 0.57 , $p = 0.028$).

Conclusion: Immediately after scaffold implantation, coronary arteries demonstrate an alternans of extremely low and high ESS values and localized areas of high blood viscosity. These initial local haemodynamic disturbances may trigger fibrin deposition and thrombosis. Also, low ESS can promote neointimal hyperplasia, but may also contribute to appropriate scaffold healing with normalisation of ESS and reduction in peak blood viscosity by five years.

Key words: bioabsorbable scaffold, shear stress, blood viscosity

INTRODUCTION

The fundamental concept of a stent and its complications has not changed greatly since pioneering work in the early 20th century.¹ The technology underlying these devices, however, has undergone great and rapid advances that seem, perhaps, to be accelerating.

Despite excellent clinical outcomes with current generation of metallic drug-eluting stents, their permanent nature remains a theoretical limitation. In that sense, the adoption of bioresorbable materials is one recent leap forward in stent technology. The ideal bioresorbable stent is meant to fulfil a temporary function as a vascular scaffold to aid vessel healing and stabilisation, and then disappear.

The Absorb BVS (Abbott Vascular, Santa Clara, California) has been the most implanted and studied bioresorbable scaffold. The longest-term clinical data currently available indicates five-year outcomes similar to standard comparator metallic drug-eluting stents.^{2, 3} Resorption of the Absorb may also be accompanied by a partial and gradual return of normal vasomotion, late lumen enlargement, and plaque stabilisation.⁴⁻⁸ However, recent evidence from larger trials shows that while rare, late thrombosis occurs more frequently with the Absorb scaffold.⁹⁻¹¹ There remain many unanswered questions regarding the mechanisms of late scaffold complications, but certain clues may lie in the dynamics of blood flow after scaffolding.

Fluid shear stress exerted by blood flow directly regulates vascular physiology and pathology.^{12, 13} Changes in arterial geometry induced by stent or scaffold placement can significantly change blood flow throughout the vessel,^{14, 15} thereby altering the macro-level shear stress distribution. Individual stent struts may themselves disturb flow at an even smaller scale near the endothelium,¹⁶⁻¹⁹ creating so-called micro-level disturbances. After implantation, such macro- and micro-level flow disturbances may have repercussions not only for the development of scaffold thrombosis and restenosis, but also for appropriate neointimal healing and vessel remodelling.

The aim of this study was to perform serial high-fidelity computational fluid dynamic (CFD) simulations to examine immediate and long-term haemodynamic and vascular changes following bioresorbable scaffold placement.

METHODS

Patient Selection and Study Design

Patients with serial imaging from the ABSORB Cohort B clinical trial were retrospectively identified for further computational analysis. The original study design and protocol have been previously described.²⁰ Patients underwent serial invasive imaging with coronary angiography and OCT immediately after scaffold implantation and again at five years.

Exclusion criteria were lack of 2 angiographic views separated by $>25^\circ$, excessive vessel foreshortening, suboptimal OCT images, and side branches $>2\text{mm}$ within the scaffold which prohibited three-dimensional reconstruction. Angiography and OCT images from each time point were fused to reconstruct three-dimensional models of the scaffolded artery at baseline and 5 years. CFD analysis was then performed to calculate ESS and local blood viscosity at baseline and five years.

Image acquisition and data analysis

OCT is an intravascular imaging technique providing high-resolution ($10\text{-}20\mu\text{m}$) cross-sectional images of coronary arteries and scaffolds.²¹ OCT was performed immediately after scaffold implantation and at five years in all treated coronary arteries using a frequency-domain OCT system (C7-XR or C8XR OCT Intravascular Imaging System; St. Jude Medical, St. Paul, Minnesota). All image acquisitions were performed using non-occlusive contrast flushing according to standard guidelines.²¹ Angiography was performed as previously described.²⁰

Three-dimensional Arterial Reconstruction

For each time point, OCT and angiography were fused to reconstruct patient-specific 3D models of the scaffolded artery at baseline and five years (**Figure 1**).²² Briefly, dual plane end-diastolic angiographic images (orthogonal views $>25^\circ$ difference) were used to extract the 3D luminal centreline (QAngio XA 3D, Medis Specials Bv, the Netherlands). The radiopaque scaffold markers and side branches were used as landmarks to co-register angiography with OCT. The OCT lumen and scaffold contours were semi-automatically detected (QCU-CMS v4.69, LKEB, Leiden University, the Netherlands). The contours were placed onto the angiographic centreline using scaffold markers and vessel landmarks to correct the rotational and longitudinal orientation of the OCT frames (MATLAB R2015b, MathWorks Inc., Natick,

Massachusetts), and the baseline and five year scaffolded vessel surfaces were generated (MeshLab, Visual Computing Lab ISTI-CNR, Pisa, Italy).²³

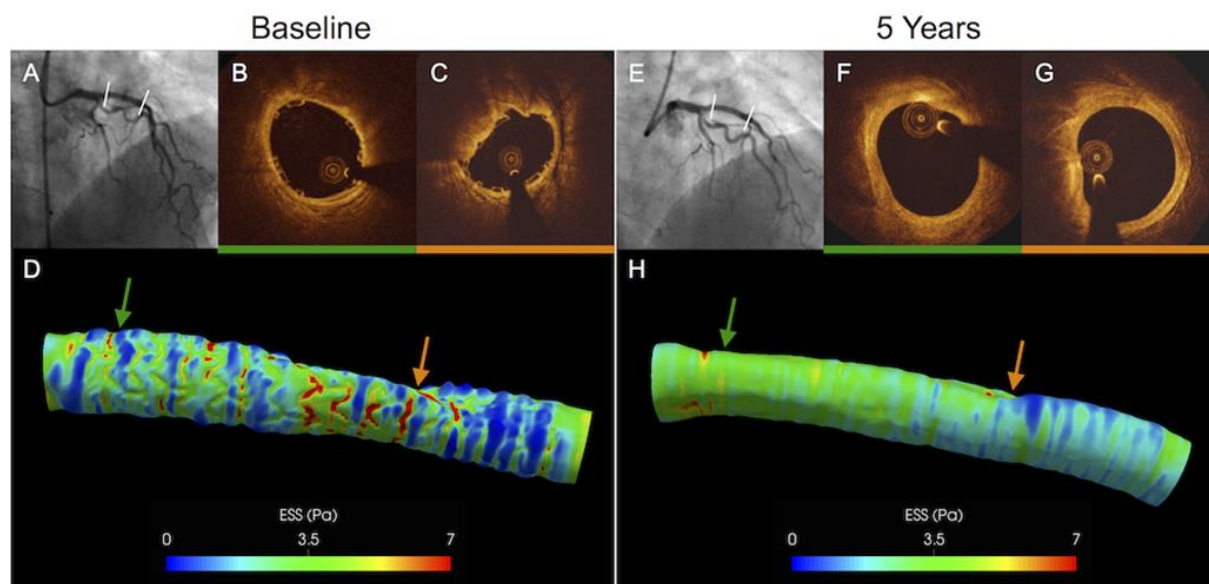


Figure 1. Three-dimensional arterial models were reconstructed from the fusion of angiography and OCT. (A, E) Angiography was used to extract the vessel centerline in the scaffolded segment (between white lines). (B, C, F, G) OCT images were used to generate the detailed lumen and scaffold surface. Representative OCT images show the same locations at baseline and five years (green and orange arrows). (D, H) CFD simulations were performed to calculate endothelial shear stress and local blood viscosity. OCT, optical coherence tomography. CFD, computational fluid dynamics.

Computational fluid dynamic simulation

Each reconstruction was discretised into approximately 30 million tetrahedral elements using ICEM CFD v15.0 (ANSYS Inc., Canonsburg, Pennsylvania). CFD analysis was accomplished through direct solution of the incompressible Navier–Stokes equations describing fluid motion (OpenFOAM-2.1.1, OpenCFD Ltd, ESI group, Bracknell, UK). A time-varying (pulsatile) parabolic velocity profile with a mean inlet flow of 1.3cc/second was applied at the inlet. The arterial wall was considered rigid with a no-slip boundary and a non-specific distal vascular resistance was applied at the outlet. Blood density was assumed 1060kg/m^3 and haematocrit 45%. Non-Newtonian blood behaviour was modelled using the Quemada equation, in which viscosity varies depending on shear rate and haematocrit.²⁴ OpenFOAM was run on the Victorian Life Sciences Computation Initiative (VLSCI) supercomputer consisting of 1024 IBM Blue Gene/Q CPUs at 1.6 GHz (IBM Research Australia).

ESS was calculated as the product of viscosity and velocity gradient (shear rate) at the wall. For quantitative calculations ESS was classified as low (<1 Pa), moderate (1-7 Pa), or high (>7

Pa) (see online-supplement).²⁵⁻²⁷ Percent lumen area exposed to low, moderate, and high ESS at systolic, diastolic, and time-averaged flow was determined at baseline and five years. In order to assess the change in lumen dimensions, the baseline and five-year arterial reconstructions were matched by using the scaffold markers and anatomical landmarks. The impact of baseline ESS on the change in lumen area was investigated.

Due to its shear-thinning properties, blood exhibits higher viscosity at low shear rates and approaches a constant low viscosity at high shear rates. CFD simulations using a Newtonian model of blood behaviour assume that shear rate is high enough that viscosity is constant (0.0035 Pa.s). However, the non-Newtonian model used in this study allowed direct calculation of local blood viscosity,²⁴ which was expressed as a ratio of non-Newtonian to constant Newtonian viscosity^{28, 29} and henceforth referred to as relative viscosity. Maximum relative blood viscosity was determined at systolic, diastolic, and time-averaged flow at baseline and 5 years.

Statistical analysis

Continuous variables were reported as mean (SD) if they followed a Gaussian distribution. Binary variables were reported as counts and percentages. Changes in ESS between baseline and five years were compared with a generalized linear mixed-effect model with a random intercept. To examine the association between baseline shear stress and changes in luminal area a one-level hierarchical linear model was used. No formal hypothesis testing was planned. A Wilcoxon rank sum test was used to evaluate the change in relative blood viscosity. All p-values were two-sided. However, the p-values presented are exploratory analyses only, and should therefore be interpreted cautiously. A non-parametric Robust method (CLSI C28-A3) method was used to calculate 95% CI. Data analysis was performed using SPSS, version 24 (Chicago, Illinois, United States).

RESULTS

Seven patients (seven lesions) fulfilled the study criteria and were included in the present analysis. The scaffold was implanted the left anterior descending coronary artery (5), left circumflex artery (1), and right coronary artery (1). Patient characteristics are demonstrated in **Table 1**. Procedural characteristics are shown in **Table 2**. None of the patients developed

adverse clinical events including death, myocardial infarction, revascularisation, or scaffold thrombosis during five years of clinical observation (**Online Table 1**).

Table 1. Baseline Characteristics of the Studied Population (N = 7, Lesions=7)

Age	62 ± 9
Male	4 (57)
Hypertension	3 (43)
Hypercholesterolemia	5 (71)
Diabetes mellitus	0 (0)
Current smoking	1 (14)
Prior percutaneous coronary intervention	2 (29)
Prior myocardial infarction	2 (29)
Stable angina	5 (71)
Unstable angina	1 (14)
Silent ischemia	0 (0)
Treated vessel	
Left anterior descending artery	5 (71)
Left circumflex artery	1 (14)
Right coronary artery	1 (14)
Ramus intermedius	0 (0)

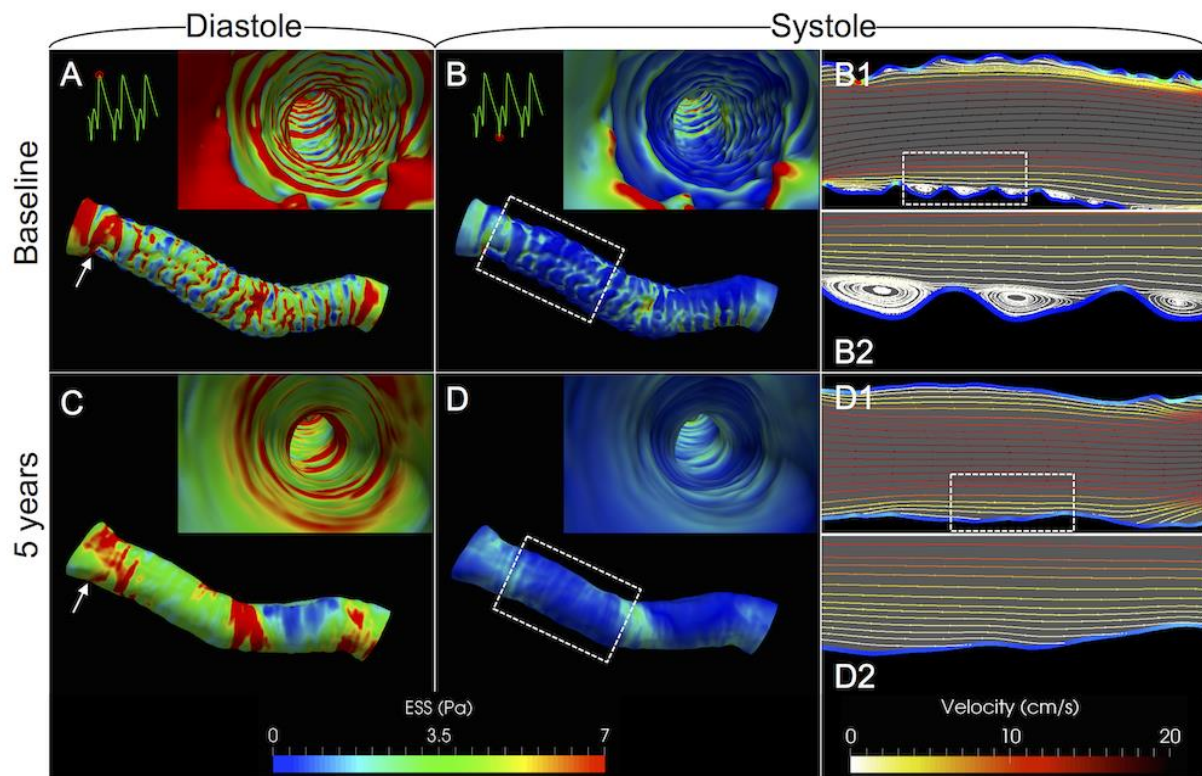
Values are mean ± SD or n (%).

Since peak coronary flow occurs during diastole, the vessel was exposed to predominantly high ESS (**Take home figure A and C**) without evidence of micro-recirculation. During systole, a rapid drop in coronary flow results in exposure to very low ESS (**Take home figure B and D**) and, due to the steep negative flow gradient, unmasks micro-recirculation of blood between

scaffold struts at baseline (**Take home figure B1 and B2**). By five years, ESS has homogenised to more physiologic values and systolic micro-recirculation has dissipated (**Take home figure D1 and D2**).

Table 2. Procedural Characteristics

		N=7, lesions=7
ACC/AHA lesion class	A	0% (0)
	B1	71% (5)
	B2	29% (2)
	C	0% (0)
Pre-dilatation		100% (7/7)
Mean Pre-dilatation pressure, atm		11.77 ± 2.56
Diameter of scaffolds, mm		3.00 ± 0.0
Expected scaffold diameter, mm		3.26 ± 0.10
Total length of study devices, mm		18.0 ± 0.0
Nominal Scaffold area, mm ²		7.07 ± 0.0
Expected scaffold area, mm ²		8.37 ± 0.53
Mean Deployment pressure, atm		13.00 ± 3.01
Post-dilatation		57% (4/7)
Mean Post-dilatation pressure, atm		17.64 ± 5.28
Procedural complications		0% (0/7)
Clinical device success		100% (7/7)
Clinical procedure success		100% (7/7)



Take home figure. Pulsatile CFD simulation provides detailed local hemodynamics in diastole and systole. (A, B) At baseline, the vessel has a corrugated appearance arising from high ESS on top of scaffold struts and low ESS in between. (C, D) At five years, only broad swaths of low, moderate, and high ESS remain. (B1, D1) Cut-plane views of the area within the dashed white box in Panels B and D, respectively, demonstrate laminar flow at the center of the artery but micro-recirculation near the wall. By five years systolic micro-recirculation has been eliminated. (B2, D2) Enlarged view of area within the dashed white box in Panels B1 and D1, respectively, show that micro-recirculation occurs only at baseline between scaffold struts. ESS, endothelial shear stress.

Quantitative measurements demonstrate that although ESS distribution varied considerably through the cardiac cycle, the mean percent lumen area exposed to ESS <1 Pa significantly decreased between baseline and five years during diastolic, systolic, and time-averaged conditions (diastole: 6.90% to 2.78%, $p=0.008$; systole: 53.31% to 38.37%, $p=0.042$; time-averaged: 15.92% to 4.99%, $p<0.0001$) (**Table 3**). Although individual cases demonstrated slightly different patterns of increases in moderate and high ESS (**Figure 2**) (**Online Table 2**), overall mean vessel exposure to moderate and high ESS did not significantly change over five years in diastolic, systolic, or time-averaged flow conditions (**Table 3**).

Table 3. Pulsatility-dependent ESS at baseline and five-years, all cases combined

	Systole			Diastole			Time-averaged		
	Baseline	5 Years	p- value	Baseline	5 Years	p- value	Baseline	5 Years	p- value
ESS<1	53.31	38.37	0.042	6.9	2.78	0.008	15.92	4.99	<0.0001
95% CI	14.23- 102.61	-24.11- 99.05		-5.02- 17.74	-10.72- 12.83		1.06- 27.89	-10.42- 18.16	
1<ESS<7	46.23	58.98	0.067	68.79	61.28	0.434	76.93	80.7	0.546
95% CI	-0.88- 84.10	6.01- 116.29		36.82- 91.75	1.66- 122.01		58.67- 94.70	46.40- 123.14	
ESS>7	0.46	2.65	ns	24.31	35.94	0.218	7.15	14.31	0.281
95% CI	-1.65- 2.03	0-9.89		-6.06- 58.17	-30.82- 102.02		-8.16- 20.21	-31.11- 49.68	

Values are expressed as percent lumen area exposed to low, moderate, and high ESS.

Figure 3 represents the relationship between post-implantation ESS and the change in lumen area over five years. A positive association was observed ($y=0.32x-1.49$; $p<0.0001$), indicating that higher baseline ESS values after scaffold implantation were correlated with an increase in lumen area. A serial point-by-point analysis was also performed to investigate the change in lumen radius, and demonstrated a similar qualitative relationship to baseline ESS (**Figure 4**).

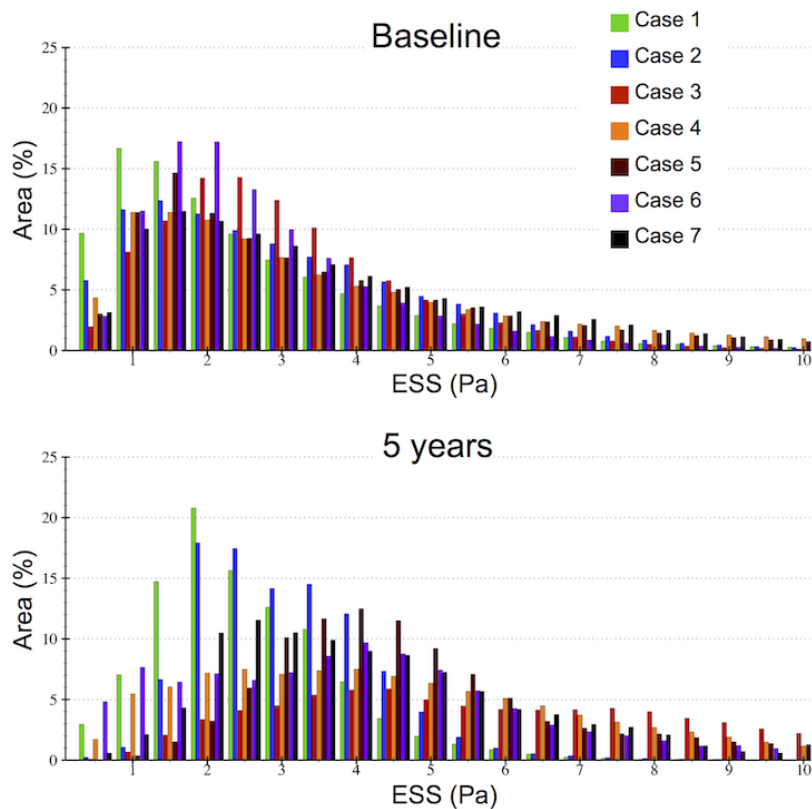


Figure 2. Histogram demonstrating percent of the lumen area exposed to various levels of ESS at baseline and five years for each case.

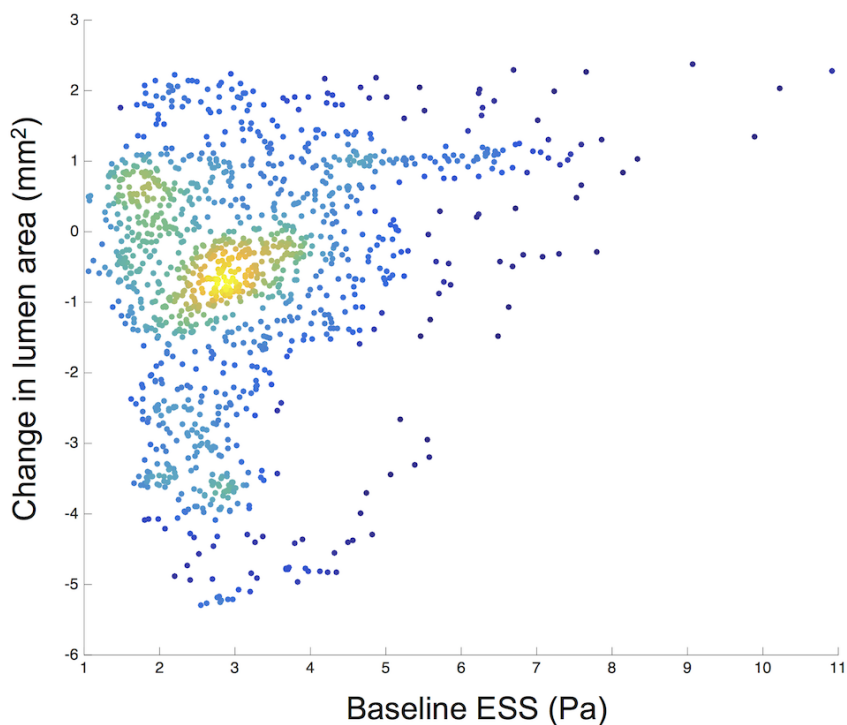


Figure 3. Scatterplot of baseline ESS versus the interval change in lumen area over five years for all cases combined, colored by the relative density of data points (yellow indicates high density, blue indicates low density). Baseline and five-year arterial reconstructions were precisely aligned and compared on a frame-by-frame basis. Higher baseline ESS values are correlated with an increase in lumen area over five years.

High blood viscosity was apparent in two broadly distinctive regions: at the centre of the artery where shear rate is low but blood velocity is high, and at specific locations near the lumen surface where both shear rate and blood velocity are low. Notably, near-wall regions of high blood viscosity were observed in the vicinity of scaffold struts (**Figure 5**), corresponding to locations of micro-recirculation and low ESS.

Quantitative analysis of all seven cases demonstrated an approximately 35% higher time-averaged blood viscosity throughout the arteries than is conscribed by the Newtonian model. Although mean viscosity did not change, maximum relative viscosity significantly decreased over five years (systole: 8.84 versus 5.33, $p=0.043$; diastole: 4.46 versus 3.18, $p=0.063$; time-averaged: 4.30 versus 3.21, $p=0.028$) (**Table 4**). Like ESS, viscosity also fluctuated considerably throughout the cardiac cycle, peaking in systole for all cases at both baseline and five years (**Online Table 3**). Remarkably, in Cases 1, 5 and 7 the maximum relative viscosity approached a ten-fold increase in some locations at baseline.

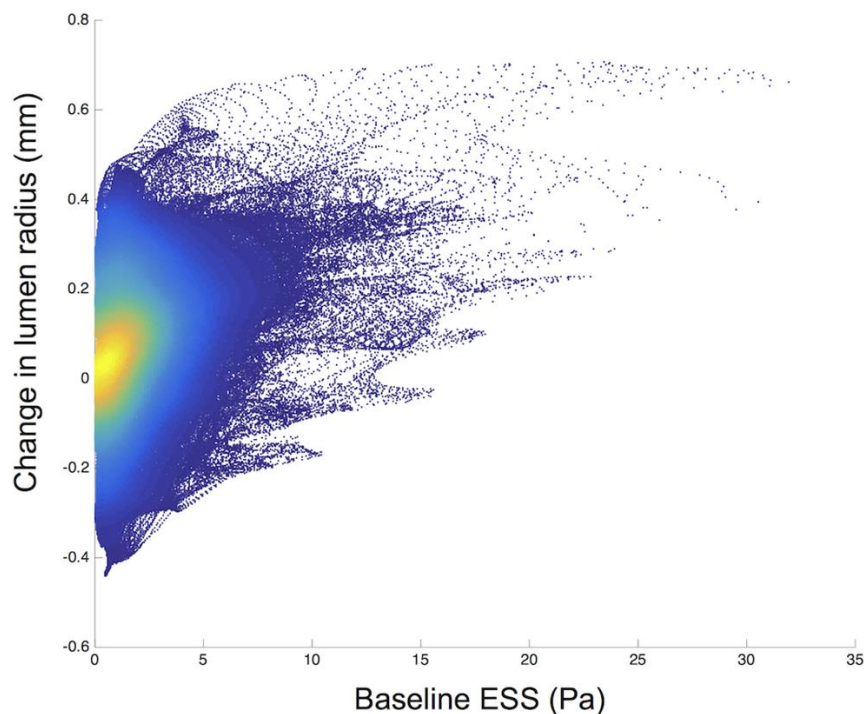


Figure 4. After optimal alignment, baseline and five-year arterial reconstructions were compared on a point-by-point basis. A scatterplot of baseline ESS versus the interval changes in lumen radius over five years from a single representative case, colored by density of data points (yellow indicates high density; blue indicates low density). Qualitatively, higher baseline ESS values are correlated with an increase in lumen radius at that point over five years.

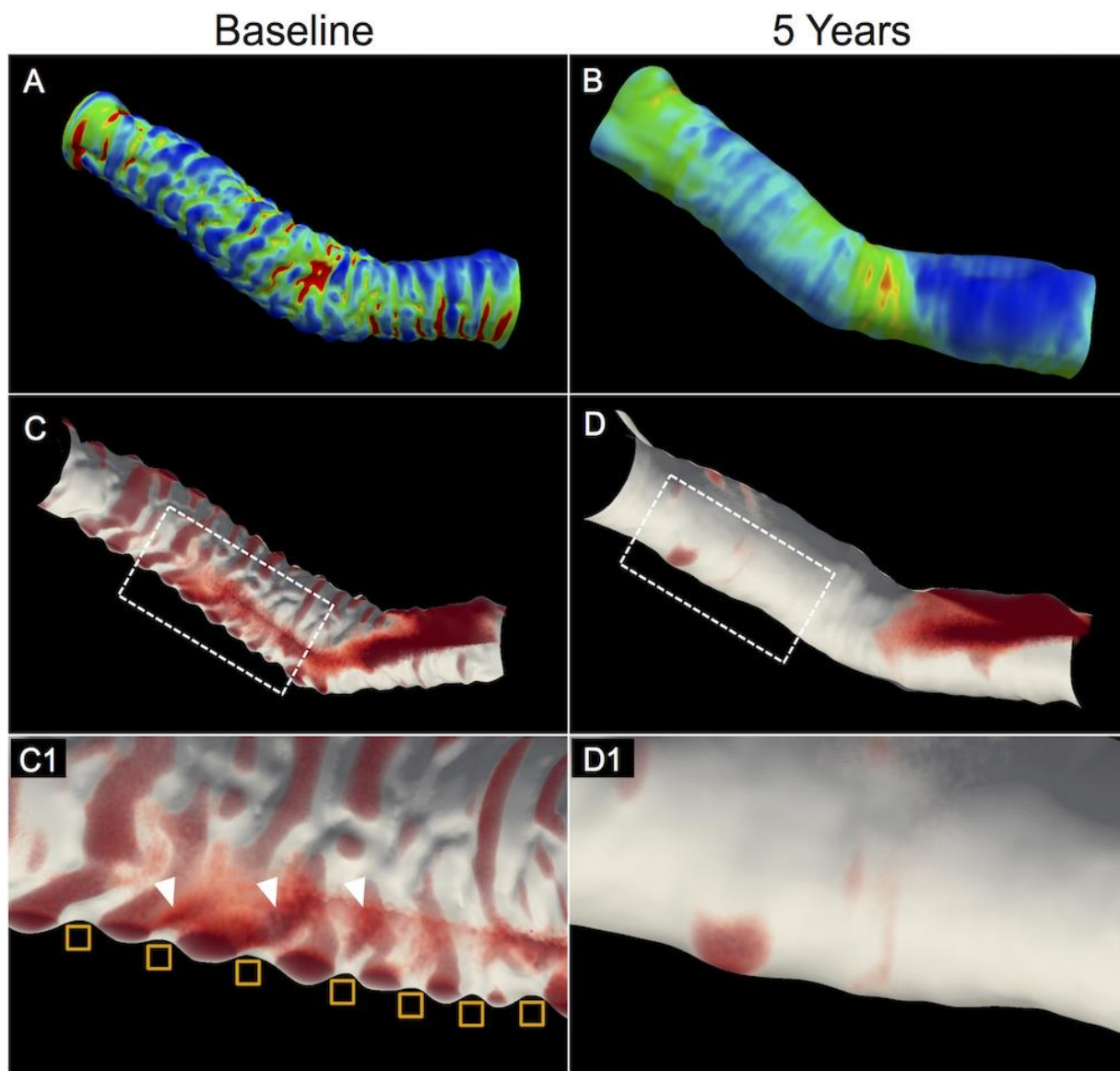


Figure 5. (A, B) Time-averaged ESS within the scaffolded segment. (C, D) Longitudinal cut-plane view of the scaffolded segment, with volume-rendered near-wall regions of high blood viscosity. The lumen surface is solid white in colour. Regions of red indicate relative viscosity >1.4 . (C) At baseline, regions of high viscosity localize to the inter-strut region and the distal segment of the curved artery. (C1) A closer view shows that after implantation, high viscosity may extend over struts and further into the lumen (**white arrowheads**). (D, D1) By five years, a region of high viscosity persists at the distal curvature, however the inter-strut regions of high viscosity have largely disappeared.

Table 4. Local blood viscosity at baseline and 5 years, all cases combined

	Systole			Diastole			Time-Averaged		
	Baseline	5 Years	p-value	Baseline	5 Years	p-value	Baseline	5 Years	p-value
Maximum Viscosity	8.84±1.79	5.33±3.63	0.043	4.46±1.50	3.18±0.90	0.063	4.30±1.54	3.21±0.57	0.028
95% CI	4.01-13.70	-5.31-13.25		0.23-7.88	0.58-5.52		-0.08-7.82	1.51-4.84	

Relative viscosity is expressed as a ratio of non-Newtonian viscosity to the constant Newtonian viscosity (0.0035 Pa s). Maximum viscosity values are presented as relative viscosity \pm SD. Pa, pascal

DISCUSSION

The high fidelity CFD simulations conducted in this study revealed that hemodynamics in scaffolded coronary arteries are marked by wide fluctuation in ESS throughout the cardiac cycle, resulting in transient micro-recirculation and pockets of high blood viscosity in the scaffolded region that largely disappear as the scaffold dissolves. This process was accompanied by vessel exposure to more physiologic levels of ESS, reduced peak blood viscosity, and late lumen enlargement over five years.

Bioresorbable medical devices have gained exceptional attention over recent years but there remain many unanswered questions about how these devices perform over time. These questions have been particularly relevant with the Absorb coronary scaffold, which has been hampered by late scaffold thrombosis.^{2, 10, 11, 30} The mechanisms are thought to involve late scaffold dismantling and inflammation,^{8, 31} but other factors governing scaffold outcomes could include local blood flow dynamics. Fluid dynamic phenomena of blood flow directly regulate vascular biology and influence the development of atherosclerosis.^{12, 13} Abnormally low and high ESS have been correlated with atherosclerotic plaque progression, vulnerability, and perhaps even disruption, platelet activation, and subsequent thrombosis.³²⁻³⁵ Similarly, changes in arterial geometry induced by stent or scaffold placement can also significantly alter blood flow and ESS distribution at the strut and vessel scale.³⁶ Such post-intervention flow

disturbances may have repercussions for the development of scaffold thrombosis and restenosis.^{15, 18, 37}

In order to gain new insights into local hemodynamics within scaffolded arteries, this study employed serial OCT imaging over five years as the basis for CFD analysis. Due to the use of pulsatile flow conditions and a non-Newtonian model of blood behaviour, these simulations are of unprecedented scope and detail. This methodology has allowed several key observations.

First, higher ESS values immediately after scaffold implantation are significantly correlated with lumen enlargement by five years. Several IVUS-based studies in native arteries and OCT-based studies in scaffolded arteries suggest a similar relationship between ESS and subsequent vessel change.^{35, 38-41} Whether this phenomenon is unique to polymeric bioresorbable devices is unknown, but the consistent upward shift in ESS values observed in this study may continue to push the balance toward positive Glagovian remodelling and late lumen enlargement.^{8, 42-44}

Second, there is significant fluctuation in ESS and relative blood viscosity throughout the cardiac cycle, indicating that coronary arteries experience extreme absolute values and sudden shifts in local hemodynamics with each heartbeat. Exceptionally high ESS values identified in diastole are notable given the putative role of high ESS in platelet activation, plaque destabilisation, and perhaps even rupture.^{32, 34, 45} Conversely, the rapid drop in coronary flow at the onset of systole unmasks micro-recirculation of blood between scaffold struts, reflecting areas prone to momentary blood stagnation and high viscosity in every cardiac cycle. In fact, after scaffold implantation blood manifested up to a ten-fold increase in relative viscosity around scaffold struts during systole. Some regions of high viscosity persisted even in diastole.

Third, regardless of time point within the cardiac cycle, all cases demonstrated homogenisation of ESS over five years, with less exposure to atherogenic low ESS and increased exposure to moderate and high ESS which are generally thought to be more atheroprotective. Critically, this was accompanied by a significant reduction in maximum blood viscosity. Immediately after implantation, micro-recirculation, low ESS, and high peak viscosity within the scaffolded region may contribute to early accumulation of fibrin, platelets, and other blood components just distal to each strut.⁴⁶ In a sense, the scaffold may act as a

template for neointimal growth between struts as these aggregated materials organize. Once neointimal tissue has grown to cover the struts and the lumen surface becomes smooth, the alternans of high and low ESS dissipates, overall, ESS increases, and peak viscosity is reduced. In such an ideal scenario there is no longer strong stimulus for thrombosis or neointimal hyperplasia. Remarkably, as bioresorbable devices dissolve, underlying arteries have demonstrated a partial and gradual return of normal arterial vasoreactivity and plaque stabilisation in addition to late lumen gain.⁴⁻⁷ We postulate that some of these observations may be related to the normalisation of hemodynamics after scaffold implantation.

Although none of the patients in the current study developed adverse clinical events during five years of follow up, our findings may add to previous work in explaining certain mechanisms of scaffold thrombosis and the potential mechanisms of long-term benefit. Factors associated with very late scaffold thrombosis include poor neointimal healing, uncovered struts, and persistent scaffold malapposition.³¹ In some cases, suboptimal local hemodynamics immediately after scaffold implantation may contribute to poor neointimal growth and persistently uncovered or malapposed struts.¹⁷ Such struts protruding into the lumen are exposed to high ESS, which is associated with platelet activation.⁴⁵ Regions distal to protruding struts are prone to low ESS and high viscosity, where activated platelets can aggregate.

Non-Newtonian simulations provide uniquely complementary haemodynamic data about blood viscosity. Blood is a non-Newtonian fluid with primarily shear-thinning properties: at low shear rates blood is thick, but at high shear rates it becomes thinner with viscosity approaching a constant. Although most arterial CFD simulations safely assume that blood behaves as a Newtonian fluid with a constant viscosity, under certain flow conditions the local shear rate can drop enough that the Newtonian assumption no longer holds.⁴⁷⁻⁵⁰ This appears to be the case in coronary arteries under pulsatile flow and harbouring curvatures and scaffolds: even after averaging viscosity throughout each entire simulated artery, relative blood viscosity was approximately 35% greater than the Newtonian model, a finding consistent with previous studies in unstented arteries.^{29, 51-53} That we have demonstrated discrete and consistent increases in blood viscosity in patient-specific scaffolded coronary arteries suggests that the Newtonian assumption may not always be accurate in this setting.

The ability to measure local blood viscosity *in vivo* has the potential to add an entirely new dimension to the study of local arterial hemodynamics. Although some clinical evidence points to a correlation between higher plasma viscosity and coronary disease,⁵⁴ whether and how local blood viscosity relates to clinical outcomes will require much larger dedicated studies. Additionally, previous CFD studies suggest that neglecting non-Newtonian behaviours of blood may reduce the accuracy of ESS measurements.⁴⁷⁻⁴⁹ This may partially explain the persistent limitation of ESS to detect and predict progressive atherosclerosis.⁵⁵ It is possible that in combination with traditional wall-based haemodynamic metrics, non-Newtonian simulations and viscosity calculations may improve the accuracy and specificity of CFD simulations by identifying areas at risk for platelet activation, blood stagnation, plaque growth, neointimal hyperplasia, and thrombosis.

Limitations

This study has several limitations that must be acknowledged. First is the retrospective design, which means that OCT acquisition techniques to optimise arterial reconstruction were not specified in the original protocol. Second is the low number of cases studied. This was related to the low number of patients with serial OCT in the original study, but also to the absence of pre-defined OCT acquisition standards leading to several OCT studies that were suboptimal for arterial reconstruction. Due to our strict exclusion criteria, all such cases were excluded from CFD analysis, contributing to the low number of cases. Despite a small sample size, the overall consistency of our results suggests that the observations may indeed merit further investigation through dedicated pre-specified substudies of larger clinical device trials. Third, our analysis only included interval changes in lumen dimensions—it did not explicitly evaluate tissue characteristics. Quantitative OCT tissue characterisation is currently in development, and will provide further insights into the relationship between local hemodynamics and tissue changes in the future.⁵⁶ Fourth, although differences in scaffold architecture, connector design, and strut geometry will alter the haemodynamic micro-environment, CFD principles are universal and remain operational in the analysis of other scaffold designs.⁵⁷ Using CFD, our group has investigated two other scaffold designs with different strut thicknesses, the Mirage Bioresorbable Microfiber Scaffold (125µm) and the ArterioSorb scaffold (95µm). In both preclinical and randomized clinical trials, we have demonstrated that the circular struts of the Mirage become better embedded such that the area of laminar flow disturbances and low ESS were reduced from 49.30% in Absorb to 24.48% in Mirage ($p < 0.0001$).⁵⁸⁻⁶⁰ In addition,

using pulsatile and non-Newtonian CFD, we have shown that the ArterioSorb scaffold exhibits major reductions in area of low ESS area compared to Absorb, and in fact shear stress assessment has been reported as “a method to differentiate bioresorbable scaffold platforms”.⁵⁷

CONCLUSION

In conclusion, high fidelity pulsatile non-Newtonian CFD simulations reveal micro- and macro-level hemodynamics in scaffolded coronary arteries. Early haemodynamic disturbances induced after scaffold implantation may direct subsequent neointimal growth as the scaffold degrades, leading to more physiologic ESS, reduced peak blood viscosity, and in some cases lumen enlargement. The ability to identify intravascular regions of high blood viscosity may have implications for further clinical characterisation of thrombosis, neointimal growth, and vessel healing.

Funding

This work has been partially supported by the Victorian Life Sciences Computation Initiative (VLSCI grant number VR0210) on its Peak Computing Facility at the University of Melbourne, an initiative of the Victorian Government, Australia; the Australian Research Council through ARC Linkage Project LP120100233; and Abbott Vascular. ET is supported by a research grant from TUBITAK (The Scientific Council of Turkey).

Conflicts of Interest

PWS and YO are members of the International Advisory Board of Abbott Vascular. All other authors declare no competing interests.

REFERENCES

1. Carrel A. *Suture of Blood Vessels and Transplantation of Organs*. Amsterdam: Elsevier; 1912.
2. Ellis SG, Kereiakes DJ, Metzger DC, Caputo RP, Rizik DG, Teirstein PS, Litt MR, Kini A, Kabour A, Marx SO, Popma JJ, McGreevy R, Zhang Z, Simonton C, Stone GW, Investigators AI. Everolimus-Eluting Bioresorbable Scaffolds for Coronary Artery Disease. *N Engl J Med* 2015;**373**(20):1905-15.
3. Serruys PW, Ormiston J, van Geuns RJ, de Bruyne B, Dudek D, Christiansen E, Chevalier B, Smits P, McClean D, Koolen J, Windecker S, Whitbourn R, Meredith I, Wasungu L, Ediebah D, Veldhof S, Onuma Y. A Polylactide Bioresorbable Scaffold Eluting Everolimus for Treatment of Coronary Stenosis: 5-Year Follow-Up. *J Am Coll Cardiol* 2016;**67**(7):766-76.
4. Brugaletta S, Heo JH, Garcia-Garcia HM, Farooq V, van Geuns RJ, de Bruyne B, Dudek D, Smits PC, Koolen J, McClean D, Dorange C, Veldhof S, Rapoza R, Onuma Y, Bruining N, Ormiston JA, Serruys PW. Endothelial-dependent vasomotion in a coronary segment treated by ABSORB everolimus-eluting bioresorbable vascular scaffold system is related to plaque composition at the time of bioresorption of the polymer: indirect finding of vascular reparative therapy? *Eur Heart J* 2012;**33**(11):1325-33.
5. Brugaletta S, Radu MD, Garcia-Garcia HM, Heo JH, Farooq V, Girasis C, van Geuns RJ, Thuesen L, McClean D, Chevalier B, Windecker S, Koolen J, Rapoza R, Miquel-Hebert K, Ormiston J, Serruys PW. Circumferential evaluation of the neointima by optical coherence tomography after ABSORB bioresorbable vascular scaffold implantation: can the scaffold cap the plaque? *Atherosclerosis* 2012;**221**(1):106-12.
6. Gomez-Lara J, Brugaletta S, Farooq V, van Geuns RJ, De Bruyne B, Windecker S, McClean D, Thuesen L, Dudek D, Koolen J, Whitbourn R, Smits PC, Chevalier B, Morel MA, Dorange C, Veldhof S, Rapoza R, Garcia-Garcia HM, Ormiston JA, Serruys PW. Angiographic geometric changes of the lumen arterial wall after bioresorbable vascular scaffolds and metallic platform stents at 1-year follow-up. *JACC Cardiovasc Interv* 2011;**4**(7):789-99.
7. Lane JP, Perkins LE, Sheehy AJ, Pacheco EJ, Frie MP, Lambert BJ, Rapoza RJ, Virmani R. Lumen gain and restoration of pulsatility after implantation of a bioresorbable vascular scaffold in porcine coronary arteries. *JACC Cardiovasc Interv* 2014;**7**(6):688-95.
8. Otsuka F, Pacheco E, Perkins LE, Lane JP, Wang Q, Kamberi M, Frie M, Wang J, Sakakura K, Yahagi K, Ladich E, Rapoza RJ, Kolodgie FD, Virmani R. Long-term safety of an everolimus-eluting bioresorbable vascular scaffold and the cobalt-chromium XIENCE V stent in a porcine coronary artery model. *Circ Cardiovasc Interv* 2014;**7**(3):330-42.
9. Cassese S, Byrne RA, Ndrepepa G, Kufner S, Wiebe J, Repp J, Schunkert H, Fusaro M, Kimura T, Kastrati A. Everolimus-eluting bioresorbable vascular scaffolds versus everolimus-eluting metallic stents: a meta-analysis of randomised controlled trials. *The Lancet* 2016;**387**(10018):537-544.
10. Serruys PW, Chevalier B, Sotomi Y, Cequier A, Carrié D, Piek JJ, Van Boven AJ, Dominici M, Dudek D, McClean D, Helqvist S, Haude M, Reith S, de Sousa Almeida M, Campo G, Iñiguez A, Sabaté M, Windecker S, Onuma Y. Comparison of an everolimus-eluting bioresorbable scaffold with an everolimus-eluting metallic stent for the treatment of coronary artery stenosis (ABSORB II): a 3 year, randomised, controlled, single-blind, multicentre clinical trial. *The Lancet* 2016;**388**(10059):2479-2491.
11. Wykrzykowska JJ, Kraak RP, Hofma SH, van der Schaaf RJ, Arkenbout EK, AJ IJ, Elias J, van Dongen IM, Tijssen RY, Koch KT, Baan J, Jr., Vis MM, de Winter RJ, Piek JJ, Tijssen JG, Henriques JP, Investigators A. Bioresorbable Scaffolds versus Metallic Stents in Routine PCI. *N Engl J Med* 2017.

12. Martorell J, Santoma P, Kolandaivelu K, Kolachalama VB, Melgar-Lesmes P, Molins JJ, Garcia L, Edelman ER, Balcells M. Extent of flow recirculation governs expression of atherosclerotic and thrombotic biomarkers in arterial bifurcations. *Cardiovasc Res* 2014;**103**(1):37-46.
13. Nam D, Ni CW, Rezvan A, Suo J, Budzyn K, Llanos A, Harrison D, Giddens D, Jo H. Partial carotid ligation is a model of acutely induced disturbed flow, leading to rapid endothelial dysfunction and atherosclerosis. *Am J Physiol Heart Circ Physiol* 2009;**297**(4):H1535-43.
14. LaDisa JF, Jr., Olson LE, Douglas HA, Warltier DC, Kersten JR, Pagel PS. Alterations in regional vascular geometry produced by theoretical stent implantation influence distributions of wall shear stress: analysis of a curved coronary artery using 3D computational fluid dynamics modeling. *Biomed Eng Online* 2006;**5**:40.
15. Wentzel JJ, Whelan DM, van der Giessen W, van Beusekom HMM, Andhyiswara I, Serruys PW, Slager CJ, Krams R. Coronary stent implantation changes 3-D vessel geometry and 3-D shear stress distribution. *J Biomechanics* 2000;**33**:1287-1295.
16. Balossino R, Gervaso F, Migliavacca F, Dubini G. Effects of different stent designs on local hemodynamics in stented arteries. *J Biomechanics* 2008;**41**(5):1053-61.
17. Foin N, Gutierrez-Chico JL, Nakatani S, Torii R, Bourantas CV, Sen S, Nijjer S, Petraco R, Kouser C, Ghione M, Onuma Y, Garcia-Garcia HM, Francis DP, Wong P, Di Mario C, Davies JE, Serruys PW. Incomplete stent apposition causes high shear flow disturbances and delay in neointimal coverage as a function of strut to wall detachment distance: implications for the management of incomplete stent apposition. *Circulation. Cardiovascular interventions* 2014;**7**(2):180-9.
18. Kolandaivelu K, Swaminathan R, Gibson WJ, Kolachalama VB, Nguyen-Ehrenreich KL, Giddings VL, Coleman L, Wong GK, Edelman ER. Stent thrombogenicity early in high-risk interventional settings is driven by stent design and deployment and protected by polymer-drug coatings. *Circulation* 2011;**123**(13):1400-9.
19. Poon EK, Barlis P, Moore S, Pan WH, Liu Y, Ye Y, Xue Y, Zhu SJ, Ooi AS. Numerical investigations of the haemodynamic changes associated with stent malapposition in an idealised coronary artery. *Journal of biomechanics* 2014;**47**(12):2843-51.
20. Serruys PW, Onuma Y, Ormiston JA, de Bruyne B, Regar E, Dudek D, Thuesen L, Smits PC, Chevalier B, McClean D, Koolen J, Windecker S, Whitbourn R, Meredith I, Dorange C, Veldhof S, Miquel-Hebert K, Rapoza R, Garcia-Garcia HM. Evaluation of the second generation of a bioresorbable everolimus drug-eluting vascular scaffold for treatment of de novo coronary artery stenosis: six-month clinical and imaging outcomes. *Circulation* 2010;**122**(22):2301-12.
21. Tearney GJ, Regar E, Akasaka T, Adriaenssens T, Barlis P, Bezerra HG, Bouma B, Bruining N, Cho JM, Chowdhary S, Costa MA, de Silva R, Dijkstra J, Di Mario C, Dudek D, Falk E, Feldman MD, Fitzgerald P, Garcia-Garcia HM, Gonzalo N, Granada JF, Guagliumi G, Holm NR, Honda Y, Ikeno F, Kawasaki M, Kochman J, Koltowski L, Kubo T, Kume T, Kyono H, Lam CC, Lamouche G, Lee DP, Leon MB, Maehara A, Manfrini O, Mintz GS, Mizuno K, Morel MA, Nadkarni S, Okura H, Otake H, Pietrasik A, Prati F, Raber L, Radu MD, Rieber J, Riga M, Rollins A, Rosenberg M, Sirbu V, Serruys PW, Shimada K, Shinke T, Shite J, Siegel E, Sonoda S, Suter M, Takarada S, Tanaka A, Terashima M, Thim T, Uemura S, Ughi GJ, van Beusekom HM, van der Steen AF, van Es GA, van Soest G, Virmani R, Waxman S, Weissman NJ, Weisz G. Consensus standards for acquisition, measurement, and reporting of intravascular optical coherence tomography studies: a report from the International Working Group for Intravascular Optical Coherence Tomography Standardization and Validation. *Journal of the American College of Cardiology* 2012;**59**(12):1058-72.
22. Bourantas CV, Papafaklis MI, Lakkas L, Sakellarios A, Onuma Y, Zhang YJ, Muramatsu T, Diletti R, Bizopoulos P, Kalatzis F, Naka KK, Fotiadis DI, Wang J, Garcia Garcia HM, Kimura T, Michalis LK, Serruys PW. Fusion of optical coherence tomographic and angiographic data for more accurate

evaluation of the endothelial shear stress patterns and neointimal distribution after bioresorbable scaffold implantation: comparison with intravascular ultrasound-derived reconstructions. *Int J Cardiovasc Imaging* 2014;**30**(3):485-94.

23. Cignoni P, Callieri M, Corsini M, Dellepiane M, Ganovelli F, Ranzuglia G. MeshLab: an Open-Source Mesh Processing Tool. In: Scarano V, De Chiara R, Erra U, (eds). *Sixth Eurographics Italian Chapter Conference*; 2008, 129-136.

24. Quemada D. Rheology of concentrated disperse systems II. A model for non-newtonian shear viscosity in steady flows. *Rheologica Acta* 1978;**17**:632-642.

25. Dewey CFJ. Fluid Mechanics of Arterial Flow. In: Wolf S, Werthessen NT, (eds). *Advances in Experimental Medicine and Biology*. New York and London: Plenum; 1979, 55-103.

26. Levesque MJ, Sprague EA, Schwartz CJ. Influence of Shear Stress on Cultured Vascular Endothelial Cells: The Stress Response of an Anchorage-Dependent Mammalian Cell. *Biotechnology Progress* 1989;**5**:1-8.

27. Malek AM, Alper SL, Izumo S. Hemodynamic Shear Stress and its Role in Atherosclerosis. *JAMA* 1999;**282**:2035-2042.

28. Ballyk PD, Steinman DA, Ethier CR. Simulation of non-Newtonian blood flow in an end-to-end anastomosis. *Biorheology* 1994;**31**:565-586.

29. Johnston BM, Johnston PR, Corney S, Kilpatrick D. Non-Newtonian blood flow in human right coronary arteries: steady state simulations. *J Biomech* 2004;**37**(5):709-20.

30. Collet C, Asano T, Miyazaki Y, Tenekecioglu E, Katagiri Y, Sotomi Y, Cavalcante R, de Winter RJ, Kimura T, Gao R, Puricel S, Cook S, Capodanno D, Onuma Y, Serruys PW. Late thrombotic events after bioresorbable scaffold implantation: a systematic review and meta-analysis of randomized clinical trials. *Eur Heart J* 2017.

31. Raber L, Brugaletta S, Yamaji K, O'Sullivan CJ, Otsuki S, Koppala T, Taniwaki M, Onuma Y, Freixa X, Eberli FR, Serruys PW, Joner M, Sabate M, Windecker S. Very Late Scaffold Thrombosis: Intracoronary Imaging and Histopathological and Spectroscopic Findings. *J Am Coll Cardiol* 2015;**66**(17):1901-14.

32. Bark DL, Jr., Ku DN. Wall shear over high degree stenoses pertinent to atherothrombosis. *J Biomechanics* 2010;**43**(15):2970-7.

33. Bark DL, Para AN, Ku DN. Correlation of Thrombosis Growth Rate to Pathological Wall Shear Rate During Platelet Accumulation. *Biotechnol Bioeng* 2012;**109**:2642-2650.

34. Fukumoto Y, Hiro T, Fujii T, Hashimoto G, Fujimura T, Yamada J, Okamura T, Matsuzaki M. Localized elevation of shear stress is related to coronary plaque rupture: a 3-dimensional intravascular ultrasound study with in-vivo color mapping of shear stress distribution. *J Am Coll Cardiol* 2008;**51**(6):645-50.

35. Stone PH, Coskun AU, Kinlay S, Popma JJ, Sonka M, Wahle A, Yeghiazarians Y, Maynard C, Kuntz RE, Feldman CL. Regions of low endothelial shear stress are the sites where coronary plaque progresses and vascular remodelling occurs in humans: an in vivo serial study. *Eur Heart J* 2007;**28**(6):705-10.

36. Foin N, Torii R, Mattesini A, Wong P, Di Mario C. Biodegradable vascular scaffold: is optimal expansion the key to minimising flow disturbances and risk of adverse events? *EuroIntervention* 2015;**10**(10):1139-42.

37. Bourantas CV, Raber L, Zaugg S, Sakellarios A, Taniwaki M, Heg D, Moschovitis A, Radu M, Papafaklis MI, Kalatzis F, Naka KK, Fotiadis DI, Michalis LK, Serruys PW, Garcia Garcia HM, Windecker S. Impact of local endothelial shear stress on neointima and plaque following stent implantation in

patients with ST-elevation myocardial infarction: A subgroup-analysis of the COMFORTABLE AMI-IBIS 4 trial. *Int J Cardiol* 2015;**186**:178-85.

38. Corban MT, Eshtehardi P, Suo J, McDaniel MC, Timmins LH, Rassoul-Arzrumly E, Maynard C, Mekonnen G, King S, 3rd, Quyyumi AA, Giddens DP, Samady H. Combination of plaque burden, wall shear stress, and plaque phenotype has incremental value for prediction of coronary atherosclerotic plaque progression and vulnerability. *Atherosclerosis* 2014;**232**(2):271-6.

39. Bourantas CV, Papafaklis MI, Kotsia A, Farooq V, Muramatsu T, Gomez-Lara J, Zhang YJ, Iqbal J, Kalatzis FG, Naka KK, Fotiadis DI, Dorange C, Wang J, Rapoza R, Garcia-Garcia HM, Onuma Y, Michalis LK, Serruys PW. Effect of the endothelial shear stress patterns on neointimal proliferation following drug-eluting bioresorbable vascular scaffold implantation: an optical coherence tomography study. *JACC Cardiovasc Interv* 2014;**7**(3):315-24.

40. Eshtehardi P, McDaniel MC, Suo J, Dhawan SS, Timmins LH, Binongo JN, Golub LJ, Corban MT, Finn AV, Oshinski JN, Quyyumi AA, Giddens DP, Samady H. Association of coronary wall shear stress with atherosclerotic plaque burden, composition, and distribution in patients with coronary artery disease. *J Am Heart Assoc* 2012;**1**(4):e002543.

41. Samady H, Eshtehardi P, McDaniel MC, Suo J, Dhawan SS, Maynard C, Timmins LH, Quyyumi AA, Giddens DP. Coronary artery wall shear stress is associated with progression and transformation of atherosclerotic plaque and arterial remodeling in patients with coronary artery disease. *Circulation* 2011;**124**(7):779-88.

42. Glagov S, Weisenberg E, Zarins CK, Stankunavicius R, Kolettis G. Compensatory Enlargement of Human Atherosclerotic Coronary Arteries. *NEJM* 1987;**316**:1371-1375.

43. Zarins CK, Zatina MA, Giddens DP, Ku DN, Glagov S. Shear stress regulation of artery lumen diameter in experimental atherogenesis. *Journal of Vascular Surgery* 1987;**5**(3):413-420.

44. Onuma Y, Collet C, van Geuns RJ, de Bruyne B, Christiansen E, Koolen J, Smits P, Chevalier B, McClean D, Dudek D, Windecker S, Meredith I, Nieman K, Veldhof S, Ormiston J, Serruys PW, Investigators A. Long-term serial non-invasive multislice computed tomography angiography with functional evaluation after coronary implantation of a bioresorbable everolimus-eluting scaffold: the ABSORB cohort B MSCT substudy. *Eur Heart J Cardiovasc Imaging* 2017.

45. Holme PA, Orvim U, Hamers MJAG, Solum NO, Brosstad FR, Barstad RM, Sakairassen KS. Shear-Induced Platelet Activation and Platelet Microparticle Formation at Blood Flow Conditions as in Arteries With a Severe Stenosis. *Arterioscler Thromb Vasc Biol* 1997;**17**:646-653.

46. Jimenez JM, Prasad V, Yu MD, Kampmeyer CP, Kaakour AH, Wang PJ, Maloney SF, Wright N, Johnston I, Jiang YZ, Davies PF. Macro- and microscale variables regulate stent haemodynamics, fibrin deposition and thrombomodulin expression. *J R Soc Interface* 2014;**11**(94):20131079.

47. Karimi S, Dabagh M, Vasava P, Dadvar M, Dabir B, Jalali P. Effect of rheological models on the hemodynamics within human aorta: CFD study on CT image-based geometry. *Journal of Non-Newtonian Fluid Mechanics* 2014;**207**:42-52.

48. van Wyk S, PrahL Wittberg L, Bulusu KV, Fuchs L, Plesniak MW. Non-Newtonian perspectives on pulsatile blood-analog flows in a 180° curved artery model. *Physics of Fluids* 2015;**27**(7):071901.

49. van Wyk S, PrahL Wittberg L, Fuchs L. Wall shear stress variations and unsteadiness of pulsatile blood-like flows in 90-degree bifurcations. *Comput Biol Med* 2013;**43**(8):1025-36.

50. Gijsen FJH, van de Vosse FN, Janssen JD. The influence of the non-Newtonian properties of blood on the flow in large arteries: steady flow in a carotid bifurcation model. *J Biomech* 1999;**32**:601-608.

51. Soulis JV, Giannoglou GD, Chatzizisis YS, Seralidou KV, Parcharidis GE, Louridas GE. Non-Newtonian models for molecular viscosity and wall shear stress in a 3D reconstructed human left coronary artery. *Med Eng Phys* 2008;**30**(1):9-19.
52. Johnston BM, Johnston PR, Corney S, Kilpatrick D. Non-Newtonian blood flow in human right coronary arteries: transient simulations. *J Biomech* 2006;**39**(6):1116-28.
53. Soulis JV, Farmakis TM, Giannoglou GD, Hatzizisis IS, Giannakoulas GA, Parcharidis GE, Louridas GE. Molecular Viscosity in the Normal Left Coronary Arterial Tree. Is It Related to Atherosclerosis? *Angiology* 2006;**57**:33-40.
54. Junker R, Heinrich J, Ulbrich H, Schulte H, Schonfeld R, Kohler E, Assmann G. Relationship Between Plasma Viscosity and the Severity of Coronary Heart Disease. *Arterioscler Thromb Vasc Biol* 1998;**18**:870-875.
55. Peiffer V, Sherwin SJ, Weinberg PD. Does low and oscillatory wall shear stress correlate spatially with early atherosclerosis? A systematic review. *Cardiovasc Res* 2013;**99**(2):242-50.
56. Liu S, Sotomi Y, Eggermont J, Nakazawa G, Torii S, Ijichi T, Onuma Y, Serruys PW, Lelieveldt BPF, Dijkstra J. Tissue characterization with depth-resolved attenuation coefficient and backscatter term in intravascular optical coherence tomography images. *J Biomed Opt* 2017;**22**(9):1-16.
57. Tenekecioglu E, Torii R, Bourantas CV, Al-Lamee R, Serruys PW. Non-Newtonian pulsatile shear stress assessment: a method to differentiate bioresorbable scaffold platforms. *Eur Heart J* 2017;**38**(33):2570.
58. Tenekecioglu E, Torii R, Sotomi Y, Collet C, Dijkstra J, Miyazaki Y, Crake T, Su S, Costa R, Chamie D, Liew HB, Santoso T, Onuma Y, Abizaid A, Bourantas CV, Serruys PW. The Effect of Strut Protrusion on Shear Stress Distribution: Hemodynamic Insights From a Prospective Clinical Trial. *JACC Cardiovasc Interv* 2017;**10**(17):1803-1805.
59. Tenekecioglu E, Serruys PW, Onuma Y, Costa R, Chamie D, Sotomi Y, Yu TB, Abizaid A, Liew HB, Santoso T. Randomized Comparison of Absorb Bioresorbable Vascular Scaffold and Mirage Microfiber Sirolimus-Eluting Scaffold Using Multimodality Imaging. *JACC Cardiovasc Interv* 2017;**10**(11):1115-1130.
60. Tenekecioglu E, Torii R, Bourantas C, Sotomi Y, Cavalcante R, Zeng Y, Collet C, Crake T, Suwannasom P, Onuma Y, Serruys PW. Difference in hemodynamic microenvironment in vessels scaffolded with absorb BVS and mirage BRMS: Insights from a pre-clinical endothelial shear stress study. *EuroIntervention* 2017.

ONLINE SUPPLEMENT

METHODS

Selection of ESS thresholds

Since a normal range of ESS values are exceedingly difficult to measure directly in vivo, there are no definitively established thresholds for “low” and “high” ESS. However, estimates calculated from experimental data suggest a normal range between 1-7 Pa, and perhaps a great deal higher in complex geometries. Similarly, ESS values below 0.5-1 Pa seem to be associated with endothelial dysfunction. To our knowledge, there is no such empirically-derived threshold for what is considered high ESS. Therefore, with the understanding that these are somewhat arbitrary thresholds, ESS was classified as low (<1 Pa), moderate (1-7 Pa), or high (>7 Pa).

RESULTS

Changes in ESS over five years in individual cases

During diastole, all cases showed a decrease in exposure to low ESS over five years, which was balanced by increases in either moderate or high ESS, and in some cases both. Whereas Cases 1 and 2 demonstrated increased exposure to moderate ESS, Cases 3-7 demonstrated greater increases in high ESS (**Online Table 2**). This accounted for the mean increase in diastolic exposure to high ESS. In systole, Cases 1 and 2 demonstrated a very slight increase in exposure to low ESS but cases 3-7 consistently demonstrated a decrease in exposure to low ESS that, except for Case 6, was mainly accounted for by increases in moderate ESS. Time averaged results largely reflect the systolic and diastolic ESS patterns: every case demonstrated a decrease in exposure to ESS<1 Pa, with a concomitant increase in moderate and/or high ESS. Again, Cases 1 and 2 showed large increases in exposure to moderate ESS, whereas 3-7 demonstrated greater increases in exposure to high ESS.

Online Table 1. Five-year clinical outcomes

	N=7, lesions=7
All deaths	0 (0%)
Cardiac deaths	0 (0%)
Myocardial infarction per protocol	0 (0%)
Target vessel myocardial infarction	0 (0%)
Non-target vessel myocardial infarction	0 (0%)
All target-lesion revascularisation	0 (0%)
All target-vessel revascularisation	0 (0%)
Non-target-vessel revascularisation	0 (0%)
All revascularisation	0 (0%)
Definite scaffold or stent thrombosis	0 (0%)
Definite or probable scaffold or stent thrombosis	0 (0%)

Online Table 2. Pulsatility-dependent ESS at baseline and five-years, each case

Case	ESS (Pa)	Systole		Diastole		Time-averaged	
		Baseline	5 Years	Baseline	5 Years	Baseline	5 Years
1	<1	70.95	72.88	11.02	2.91	26.34	10.01
	1<ESS<7	28.81	27.12	70.02	87.71	69.18	89.42
	>7	0.24	0	18.96	9.38	4.48	0.57
2	<1	60.35	61.52	8.23	0.3	17.4	1.32
	1<ESS<7	39.65	38.48	63.85	83.16	78	98.02
	>7	0	0	27.92	16.54	4.6	0.66
3	<1	55.06	17.29	3.04	0.51	10.08	0.79
	1<ESS<7	44.94	72.82	78.47	25.79	87.38	53.07
	>7	0	9.89	18.49	73.7	2.54	46.14
4	<1	53.94	35.2	5.27	2.84	15.74	7.22
	1<ESS<7	45.37	64.66	61.15	50.27	70.17	75.06
	>7	0.69	0.14	33.58	46.89	14.09	17.72
5	<1	60.65	22.91	3.12	0.02	14.4	0.38
	1<ESS<7	39.28	77.09	63.73	47.12	75.18	83.81
	>7	0.07	0	33.15	52.86	10.42	15.81
6	<1	15.61	13.08	13.07	12.09	14.34	12.48
	1<ESS<7	82.42	78.38	83.94	76.47	83.17	77.22
	>7	1.97	8.54	2.99	11.44	2.49	10.29
7	<1	56.59	45.71	4.53	0.79	13.15	2.73
	1<ESS<7	43.15	54.29	60.38	58.42	75.45	88.32
	>7	0.26	0	35.09	40.79	11.4	8.95

Values are expressed as percent of lumen area exposed to low, moderate, and high ESS

Online Table 3. Relative viscosity at baseline and 5 years, each case

Relative viscosity is expressed as a ratio of non-Newtonian viscosity to the constant Newtonian viscosity (0.0035 Pa s).

Case	Baseline					5 Years				
	Mean	Median	Min	Max	St Dev	Mean	Median	Min	Max	St Dev
1 Time- Diastole Systole										
	1.390	1.369	1.224	7.292	0.105	1.418	1.386	1.237	4.041	0.152
	1.330	1.318	1.219	3.990	0.067	1.369	1.332	1.228	4.444	0.163
2 Time- Diastole Systole										
	1.365	1.347	1.222	4.785	0.082	1.372	1.362	1.236	3.455	0.067
	1.317	1.306	1.217	6.310	0.062	1.332	1.313	1.228	3.111	0.074
3 Time- Diastole Systole										
	1.364	1.352	1.217	2.364	0.060	1.331	1.314	1.226	2.557	0.076
	1.318	1.310	1.213	2.156	0.044	1.305	1.284	1.217	2.423	0.076
4 Time- Diastole Systole										
	1.359	1.337	1.219	4.184	0.084	1.360	1.338	1.234	2.969	0.082
	1.311	1.299	1.215	4.089	0.053	1.326	1.302	1.227	2.965	0.070
5 Time- Diastole Systole										
	1.387	1.365	1.218	3.655	0.096	1.346	1.333	1.232	2.884	0.067
	1.325	1.313	1.214	3.749	0.065	1.311	1.296	1.224	2.556	0.058
6 Time- Diastole Systole										
	1.363	1.347	1.221	4.392	0.070	1.349	1.325	1.224	3.846	0.085
	1.360	1.345	1.220	6.449	0.069	1.348	1.323	1.224	4.440	0.085
7 Time- Diastole Systole										
	1.361	1.341	1.220	3.417	0.076	1.363	1.345	1.234	2.710	0.075
	1.314	1.0300	1.215	4.475	0.058	1.326	1.305	1.227	2.350	0.073
All cases Time- Diastole Systole										
	1.370	1.351	1.220	4.298	0.082	1.363	1.343	1.232	3.209	0.086
	1.325	1.313	1.216	4.460	0.060	1.331	1.308	1.225	3.184	0.085
	1.467	1.420	1.226	8.843	0.168	1.425	1.399	1.242	5.325	0.111

Pa, pascal

Early strut protrusion and late neointima thickness in the Absorb bioresorbable scaffold: a serial wall shear stress analysis up to five years

Erhan Tenekecioglu, Ryo Torii, Yuki Katagiri, Taku Asano, Rodrigo Modolo, Yosuke Miyazaki, Ply Chichareon, Eric K.W. Poon, Frank Gijzen, Vikas Thondapu, David van Klaveren, Hans Jonker, Andrew Ooi, Peter Barlis, Carlos Collet, Yoshinobu Onuma, Christos V. Bourantas, Patrick W. Serruys

EuroIntervention. 2019;15(4): e370-e379.

ABSTRACT

Aim: To evaluate the effect of strut protrusion (SP) on wall shear stress (WSS) and neointimal growth (NG) one- and five-year after implantation of Absorb bioresorbable vascular scaffold.

Methods and Results: Eight patients were selected from first-in-man study. Following three-dimensional(3D) reconstruction of coronaries, WSS was quantified using Newtonian steady-flow simulation in each cross-section at 5°-subunit (sector) of the circumferential luminal surface. At 1-year, neointimal thickness (NT) was measured by optical coherence tomography (OCT) and correlated to WSS and SP post-procedure. Median-SP was 112.9(90.8,133.1) μm post-implantation. Post-procedure, a logarithmic inverse relationship between SP and post-implantation WSS ($r=-0.425$, $p<0.001$; correlation-coefficients range from -0.143 to -0.553) was observed whereas a correlation between baseline logarithmic-transformed-WSS (log-WSS) and NT ($r=-0.451$, $p<0.001$; correlation-coefficients ranged from -0.140 to -0.662) was documented at 1y. Mixed-effects analysis between baseline log-WSS and NT at follow-up yielded a slope of $30\mu\text{m}/\ln \text{ Pascal (Pa)}$ and a γ -intercept of $98\mu\text{m}$. As result of NG, median flow-area decreased from 6.91 (6.53,7.48) mm^2 post-implantation to 5.65 (5.47,6.02) mm^2 at 1-year($p=0.01$) and to $5.75\pm 1.37\text{mm}^2$ at 5-year follow-up($p=0.024$). However, vessel surface exposed to low-WSS($<1\text{Pa}$) decreased significantly post-procedure (42%) to 1y (35.9%) and 5y (15.2%) (p -overall <0.0001).

Conclusions: SP disturbs laminar flow, creates regions of low-WSS ($<1.0 \text{ Pa}$) that are associated with NG and lumen-area reduction. Low-WSS post-implantation significantly reduced at long-term follow-up. Thin strut with effective embedment would substantially reduce NG and accelerate homogenization of WSS towards physiological values.

Key words: Bioresorbable scaffolds; Drug-eluting stent; Optical coherence tomography; Other imaging modalities; Other technique

INTRODUCTION

Bioresorbable scaffolds (BRS) have ushered the interventional cardiology to a new era of percutaneous treatment of coronary artery disease. BRS restores vasomotricity and vessel wall (VW) cyclic strain that are vital for VW metabolism.¹ Local hemodynamics (LH), quantified as wall shear stress (WSS), has fundamental interaction with VW.² Scaffold coverage, strut thickness, protrusion and embedment have influence on local WSS distribution.^{3, 4} Following scaffold implantation, disruption of *laminar-flow* triggers a cascade of reactions that may result in acute/subacute thrombosis, chronic exuberant neointimal tissue (NTi) and neoatherosclerosis.⁵

Optical coherence tomography (OCT) based computational fluid dynamic (CFD) models provide assessment of LH at a detailed level not attainable even with experimental techniques.⁶ In the present study, we investigated the effect of strut protrusion/embedment on post-implantation WSS (post-WSS) distribution and NTi formation at one-year(1y) and five-year(5y) follow-ups.

METHODOLOGY

Study Design

The details of Absorb Cohort-B study [A Clinical Evaluation of the Everolimus-Eluting Bioresorbable Vascular Scaffold System in the Treatment of Patients with De-Novo Native Coronary Artery Lesions;(NCT00856856)] and treatment procedure have been previously described.⁷ Eight cases with serial OCT were selected based on good image quality, minimal foreshortening and relative lack of curvature of the target vessel in two angiograms and clear visualization of struts by OCT without major artifacts due to rotation, elongation and repetition of endoluminal structures due to cardiac motion.⁸

OCT image acquisition

Intracoronary imaging was performed post-procedure, at 1y and 5y in treated coronaries using frequency-domain (FD) OCT system (C7-XR OCT; St. Jude Medical, MN, USA) with a pull-backed speed of 20mm/sec. The details of image acquisition are in on-line supplement.

OCT Data Analysis

OCT data were analyzed off-line, using QCU-CMS software (Medis Medical Imaging Systems, Leiden, Netherlands).⁷ Following data were acquired from OCT; endoluminal intra-scaffold FA, abluminal scaffold area, proximal and distal edge segment FA, percent(%) FA obstruction, neointima area and thickness.⁷ The data acquired post-implantation were used to investigate the relationship between post-implantation strut protrusion/embedment and post-implantation WSS distribution. The data acquired at 1-year follow-up were used to reconstruct 2 separate contours; firstly, the baseline luminal borders defined by splines connecting the abluminal sides of the struts (*retrospective* baseline model) and secondly, the luminal contour at 1-year follow-up (one-year follow-up model) delineating the interstrut neointimal boundary as well the covered struts (**Figure 1**).

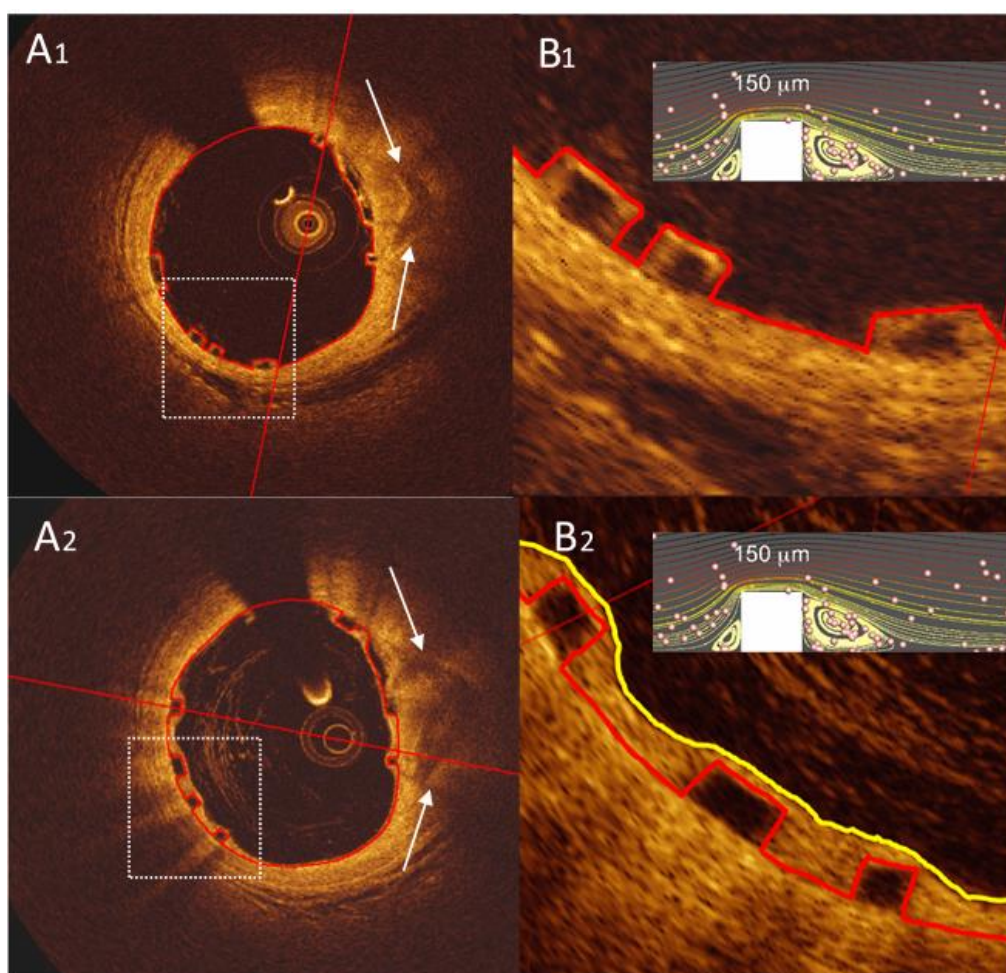


Figure 1. In OCT red-contour superimposed on the lumen and strut boundaries in Panel-A1 and-B1 are actual flow luminal contours post-implantation while in Panel-B2, red-contour still delineates the virtual and retrospective (1y later) flow luminal contours. For 1y retrospective analysis of virtual-WSS post-implantation, virtual post-procedure luminal borders in red were determined by the splines conjoining abluminal sides of the black-core of the struts.¹⁶ In Panel-B2, yellow-contour represents the actual flow luminal contour at 1y once the struts have been covered by neointima. Inserted in Panel-B1 and-B2 (right-upper small panels) are CFD simulations that depict flow streamlines, cell-tracking and flow reversals.

Embedment/protrusion analysis by OCT

The strut embedment and protrusion were measured with a semi-automated method (QCU-CMS, version-4.69) (**Figure 2**).⁹

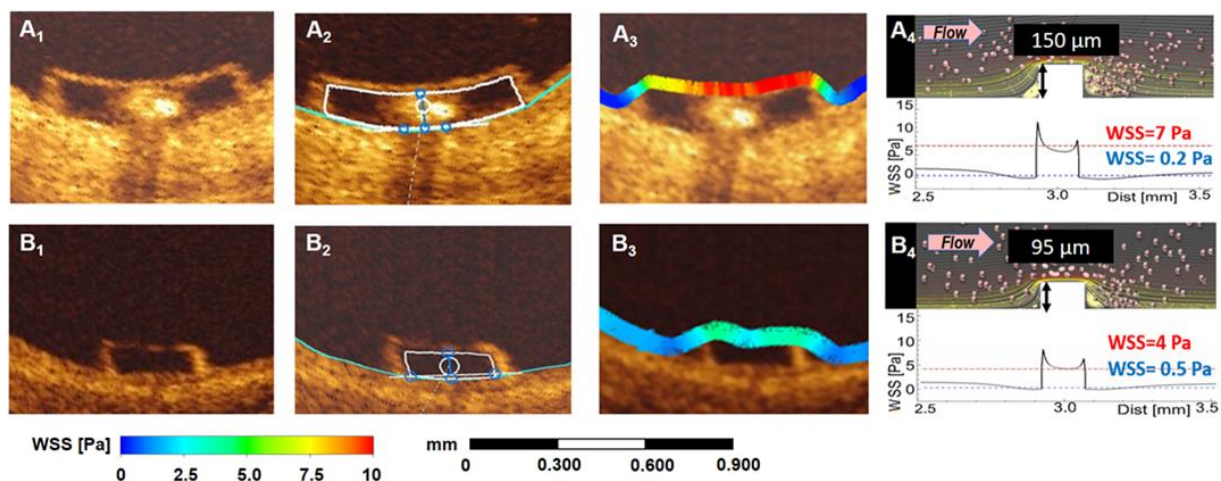


Figure 2. Panels-A1 and-B1 show two struts (Absorb and ArterioSorb) of different thickness (150 μm and 95 μm) and/or protrusion, with in Panel-A2 and-B2 interpolated luminal-contour being located at the backside of the struts.⁹ Panel-A3 and-B3 show color-coded WSS and overlying the strut with high-WSS in red-color on the top of the strut and low-WSS in dark-blue at the bottom of the strut. The thin strut (ArterioSorb) generates less WSS-gradient between top of the strut (indigo color) and bottom of the strut (light blue). CFD simulations shown in Panel-A4 and-B4 depict streamlines, cell-tracking indicating regions of flow-reversal and WSS-gradient (expressed in Pascal [Pa]) between top (WSS value in red) and bottom (WSS value in blue) of the strut.⁴

Coronary Artery Reconstruction

For CFD study, three-dimensional(3D) reconstruction of the coronary artery was performed using a published methodology.¹⁰ The details of 3D-reconstruction are explained in ***on-line supplement***.

Computational Fluid Dynamic Study

WSS was estimated by solving 3D Navier-Stokes equations (ANSYS-CFX, Version-18.0, ANSYS, Inc. Pennsylvania). WSS was measured in native and scaffolded segment in cross-sections along the axial direction per 200 μm interval and in circumferential per 5-degree subunit(sector) in each cross-section, using an in-house algorithm (**Figure 3**). The details of CFD study are explained in ***on-line supplement***.

Statistical analysis

Data are expressed as mean \pm standard deviation or median and inter-quartile range. Pearson correlation coefficient and logarithmic regression analyses were implemented to investigate the association between baseline-WSS, post-implantation protrusion and the neointimal thickness (NT) at follow-up. For WSS comparison between post-implantation, 1y and 5y, mixed-effects model was built on % increase of WSS from post-implantation to 1y and 5y. All analysis were performed using statistical analysis programs SPSS V.23 (SPSS Inc., Chicago, IL), R V.3.2.3 and R package-lme5.¹¹

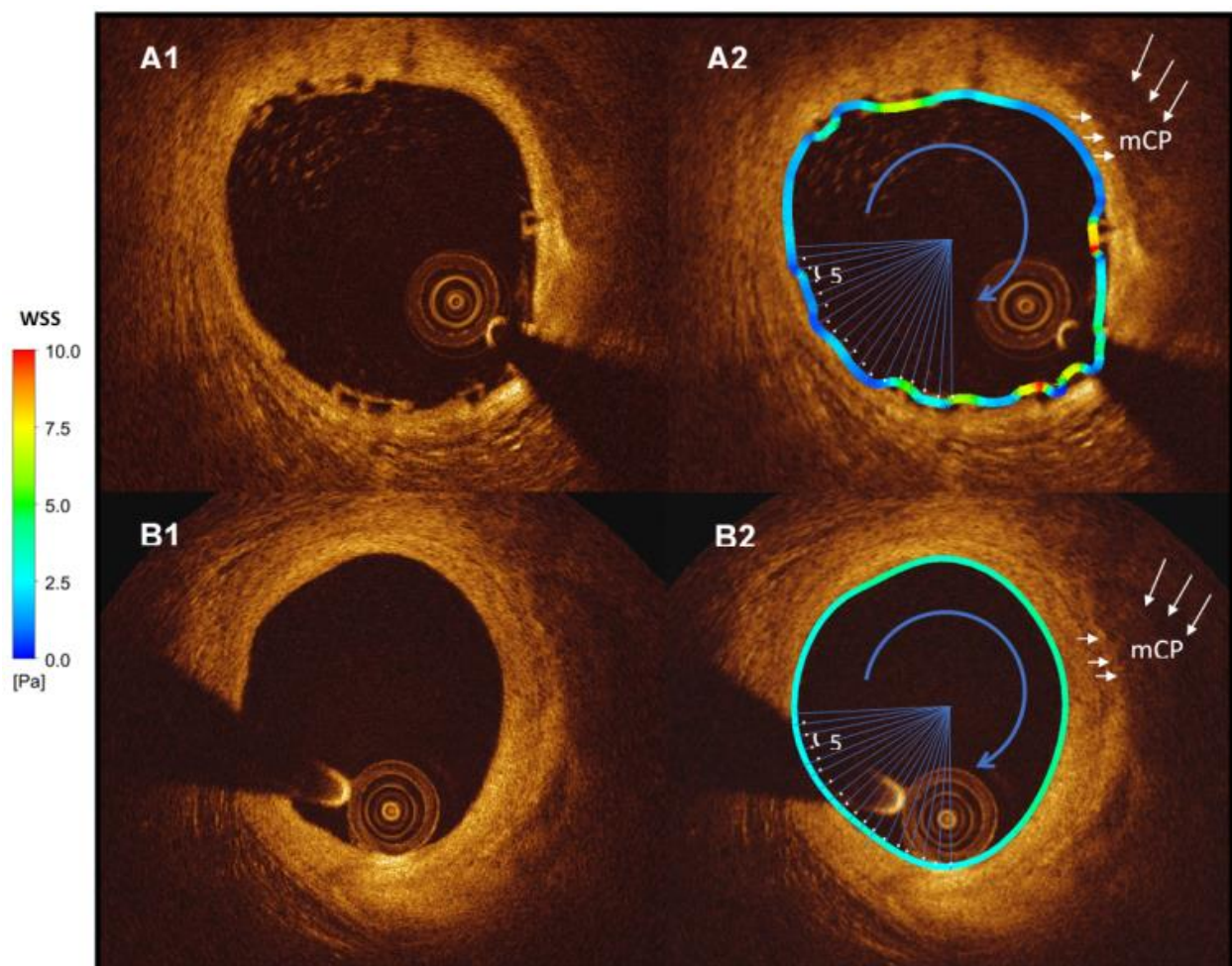


Figure 3. Post-WSS is quantified circumferentially in 5°-subunits (sectors) (Panel-A1 and-A2) and at 5y (Panel-B1 and-B2) over the luminal-perimeter (see colored bar-code for WSS values). Each 5°-subunit has one WSS value. Post-implantation high-WSS is usually observed on top of the strut and low-WSS between the struts. At 5y, WSS is homogeneously in physiological value (see bar-code 2.5-5 Pa in green) (mCP: mixed calcified-plaque).

RESULTS

Patient characteristics

In all cases (n=8), scaffolded segments were relatively straight and had a luminal centerline with <20-degrees angulation.¹² Five left-anterior descending, two left-circumflex and one right coronary artery were treated with an Absorb. All scaffolds had diameter of 3.0mm and length of 18mm. The expected scaffold diameter for the range of deployment pressures was 3.24±0.11mm. Patient characteristics are tabulated in *on-line supplementary Table-1*. Procedural characteristics are shown in *on-line supplementary Table-2*. Pre-implantation, post-implantation, 1y and 5y Quantitative Coronary Angiography (QCA) data are shown in **Table-1**.

Table 1. Results of QCA analysis pre-procedural, post-procedural and at 5-year follow-up.

	Pre-procedure (n:8) Median (Q1, Q3)	Post-procedure (n:8) Median (Q1, Q3)	1y follow-up (n:8) Median (Q1, Q3)	5y follow-up (n:8) Median (Q1, Q3)	p (Pre-Post)	p (Post-1y)	p (1y-5y)	p (Post-5y)	p- overall
In-scaffold lumen diameter, mm	2.21 (2.08, 2.30)	2.68 (2.54, 2.76)	2.42 (2.31, 2.54)	2.67 (2.31, 2.81)	0.001	0.021	0.998	0.212	0.03
In-scaffold minimum lumen diameter, mm	0.98 (0.88, 1.12)	2.33 (2.17, 2.41)	2.00 (1.91, 2.11)	2.23 (1.91, 2.34)	< 0.0001	0.389	0.98	0.149	<0.0001
Interpolated reference vessel diameter, mm	2.54 (2.40, 2.55)	2.60 (2.53, 2.72)	2.45 (2.32, 2.51)	2.62 (2.34, 2.78)	0.353	0.047	0.986	0.997	0.228
In-scaffold percent diameter stenosis, %	63.2 (53.0, 65.8)	13.5 (9.9, 16.3)	16.0 (12.31, 17.8)	16.3 (12.5, 21.2)	< 0.0001	0.985	0.99	0.86	<0.0001
In- scaffold acute absolute gain, mm	-	1.28 (0.98, 1.51)	-	-					
In- scaffold acute absolute recoil, mm	-	0.28 (0.14, 0.37)	-	-					
In- scaffold acute percent recoil, %	-	5.83 (-1.75, 9.25)	-	-					
In-scaffold absolute late lumen loss, mm		-	0.28 (0.14, 0.37)	0.04 (-0.04, 0.31)			0.476		0.476

(Q1: First-Quartile, Q3: Third-quartile, Pre: pre-implantation, Post: post-implantation, 1y:one-year, 5y: five year). Bonferroni adjustment was used for multiple comparisons

OCT analysis results

OCT results are summarized in **Table 2**. The analyses were performed at device-level(n=8). In-scaffold FA decreased from 6.91(6.53, 7.48) mm² to 5.65(5.47, 6.02) mm² at 1y(p=0.01) and to 5.70(5.10, 6.59) mm² at 5y(p=0.024). At 1y, neointimal proliferation [Neointimal

area:1.4(1.20,2.01) mm², NT:0.12(0.06,0.19) mm] was noticed in treated segments and resulted in an increase of %FA stenosis from 4.47(-6.71, 13.25) % post-implantation to 17.1(12.4, 24.3) % at 1y and 15.5(11.7, 26.3) % at 5y. At 5y, the regional differences in FA post-implantation between non-scaffolded proximal/distal-edge and scaffolded segments, disappeared (Table 2).

Table 2.OCT analysis post-procedure, at one-year and five-year follow-up (in-scaffold and in-segment measurement)

	Post-procedural (n _{scaffold} =8) Median (Q1, Q3)	1-y follow-up (n _{scaffold} =8) Median (Q1, Q3)	5-y follow-up (n _{scaffold} =8) Median (Q1, Q3)	p (Post-1y)	p (1y-5y)	p (Post-5y)	p- overall
Flow area, mm ²	6.91 (6.53, 7.48)	5.65 (5.47, 6.02)	5.70 (5.10, 6.59)	0.01	0.998	0.024	0.002
Abluminal scaffold area, mm ²	7.13 (6.86, 7.65)	7.11 (6.71, 7.67)		0.532			0.532
Strut Area, mm ²	0.19 (0.17, 0.20)	0.17 (0.16, 0.18)		0.377		0.377	
Minimum flow area, mm ²	5.80 (5.28, 6.02)	4.16 (4.03, 4.60)	4.27 (3.20, 5.63)	0.021	0.98	0.091	0.010
Percentage flow area stenosis, %	4.47 (-6.71, 13.25)	17.1 (12.4, 24.3)	15.5 (11.7, 26.3)	0.50	0.998	0.466	0.22
Neointimal Area, mm ²		1.4 (1.20, 2.01)					
Flow area In proximal-edge segment, mm ²	6.69 (6.00, 9.91) †	6.22 (5.25, 8.40) #	5.63 (4.98, 6.32) Ω	0.322	0.998	0.951	0.344
Flow area In distal-edge segment, mm ²	5.31 (4.56, 6.13) ‡	5.16 (5.00, 5.74) &	5.68 (4.16, 6.65) Φ	0.99	0.88	0.99	0.72

†p-flow area between scaffolded segment and proximal-edge segment post-implantation=0.056

‡p-flow area between scaffolded segment and distal-edge segment post-implantation <0.005

#p-flow area between scaffolded segment and proximal-edge segment at one-year=0.39

&p-flow area between scaffolded segment and distal-edge segment at one-year=0.47

Ωp-flow area between scaffolded segment and proximal-edge segment at five-year=0.30

Φp-flow area between scaffolded segment and distal-edge segment at five-year=0.64

(Q1: First-Quartile, Q3: Third-quartile, Pre: pre-implantation, Post: post-implantation, 1y:one-year, 5y: five year). Bonferroni adjustment was used for multiple comparisons.

Embedment/protrusion analysis results

The analyses were performed at cross-section and strut-levels. All struts were well apposed to VW. There were 5038-struts analysed for embedment/protrusion in 556 OCT cross-sections. At strut-level, strut embedment was 54.2(34.2, 77.4) μm while the protrusion was

112.9(90.9, 133.1) μm . At cross-section level, strut embedment was 57.8(45.5, 71.1) μm while the protrusion was 109.3(96.4, 121.6) μm . Deployment/post-dilatation balloon pressures were found to have a slight effect on embedment depths ($r=0.14$, $p=0.049$).

WSS analysis post-implantation and at follow-up

Each CFD cross-section was divided into 4-quadrants and in each quadrant WSS was calculated at post-implantation baseline model, at retrospective baseline model, 1y-model and 5y-model. Due to skewed WSS data, logarithmic transformation was implemented. Post-implantation median-WSS was compared with the virtual-WSS in the retrospective baseline model. The actual and virtual-WSS peri-strut were compared at cross-section level ($n=630$) in Bland-Altman approach and by linear-regression analysis ($r=0.827$) (**Online Figure 1a and 1b**). In mixed-effects analysis, WSS based on post-implantation CFD models (*real* post-implantation model) was comparable to WSS at retrospective baseline CFD models derived from 1y OCT data ($p=0.86$).

Post-implantation in-scaffold median-WSS was 1.19(0.84, 1.69) Pa whereas median-WSS in proximal and distal non-scaffolded edges were 1.82(0.95, 3.10) Pa and 1.90(1.03, 5.62) Pa, respectively (P -for difference between proximal non-scaffolded edge and scaffolded segment WSS=0.013, P -for difference in WSS between scaffolded and distal non-scaffolded edge <0.0001). **Figure 4a** shows logarithmic inverse relationships between SP and post-WSS ($r= -0.425$, $p<0.001$; correlation coefficients range from -0.143 to -0.553).

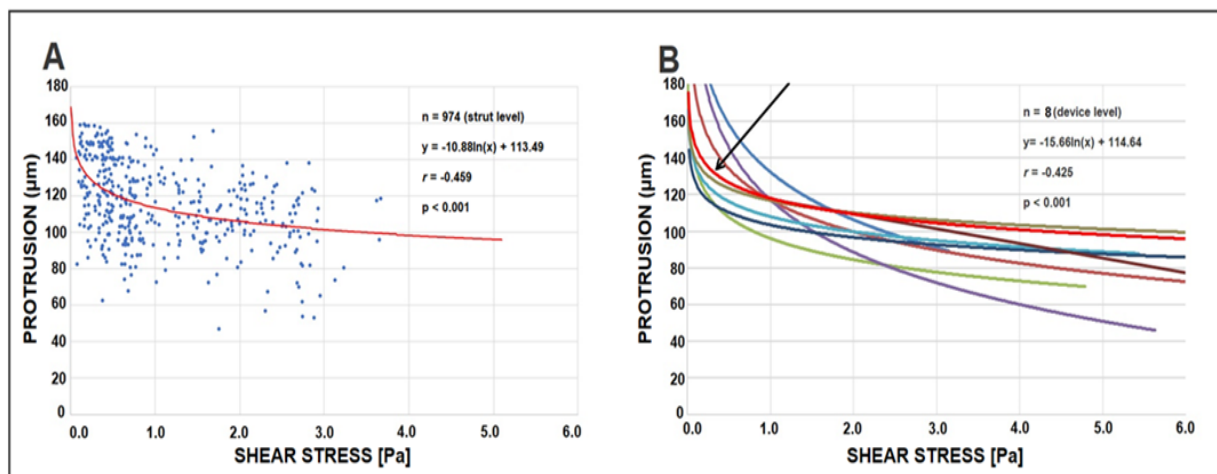


Figure 4a. Panel-A shows significant logarithmic inverse relationship between WSS (Pa) and SP (μm) at strut-level analysis for each cross-section of one device. In Panel-B, the arrow identifies single relationship exhibited in Panel-A among all the other logarithmic inverse relationships.

At 1y, in-scaffold median-WSS was 1.26(0.98, 1.60) Pa whereas median-WSS in proximal non-scaffolded edge segment was 1.17(0.67, 2.01) Pa and 1.81(0.80, 3.44) Pa in distal non-scaffolded edge segment. The median-NT was 0.12(0.06, 0.19) mm (Area of neointima:1.4(1.20, 2.01) mm²). A statistically significant inverse correlation was noted between retrospective baseline log-WSS and neointima thickness (NT) at 1y for all devices ($r = -0.451$, $p < 0.005$; correlation-coefficients range -0.140 to -0.662) (**Figure 4b**). Overall, mixed-linear regression analysis between retrospective baseline log-WSS and NT at follow-up yielded a slope of $30\mu\text{m}/\ln(\text{Pa})$ and a y-intercept of $98\mu\text{m}$.

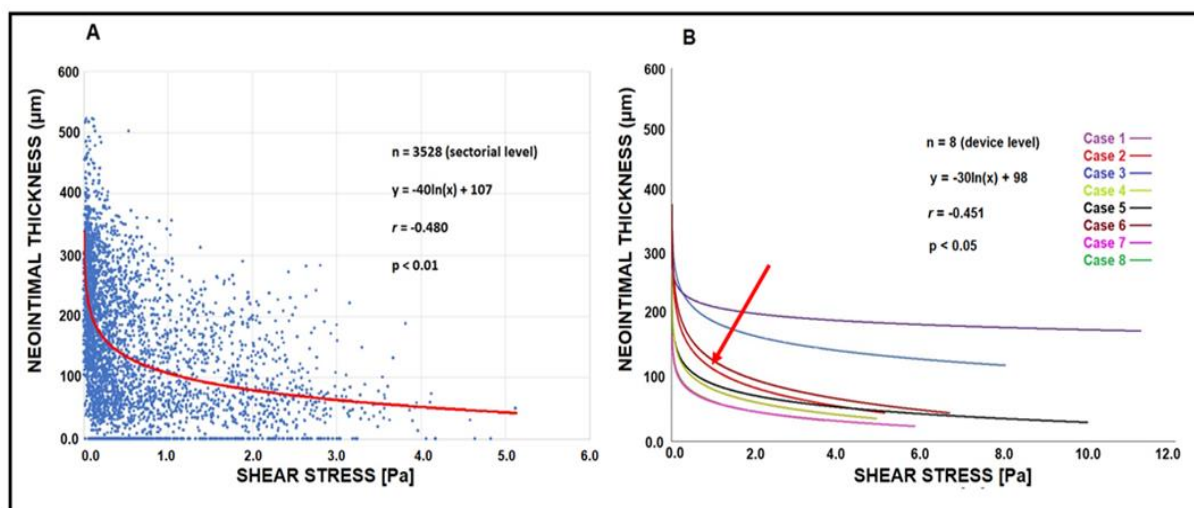


Figure 4b. Panel-A shows significant logarithmic inverse relationship between WSS and NT in one device displaying all the sectorial measurements obtained in that single device. In Panel-B, the arrow identifies the neointima-WSS relationship for that specific device among all the other logarithmic inverse relationship observed in other devices.

At 5y, in-scaffold median-WSS [1.92(1.31, 2.81) Pa] were significantly higher than post-procedure [1.19(0.84, 1.69) Pa] ($p = 0.0016$). Median-WSS in proximal and distal non-scaffolded segments weren't significantly different from scaffolded-segment median-WSS ($p = 0.97$, $p = 0.91$, respectively) (**Table 3**). The model fit with correlation structure was much better than the model fit without (likelihood ratio test $p < 0.0001$) in comparisons between the time points.

Table 3. Results of WSS analysis (median values) post-procedural, at one-year and at 5-year follow-up

	Post-procedural (scaffolded segment,n=2772) (proximal-edge segment,n=2248) (distal-edge segment,n=1108) Median (Q1, Q3)	1-y follow-up (scaffolded segment,n=2744) (proximal-edge segment,n=1920) (distal-edge segment,n=528) Median (Q1, Q3)	5-y follow-up (scaffolded segment,n=2948) (proximal-edge segment,n=2124) (distal-edge segment,n=700) Median (Q1, Q3)	p (Post-1y)	p (1y-5y)	p (Post-5y)
WSS, proximal edge, Pa	† 1.82 (0.95, 3.10)	# 1.17 (0.67, 2.01)	1.63 (1.08, 2.42)	<0.0001	<0.0001	0.145
WSS, in-scaffold, Pa	1.19 (0.84, 1.69)	1.26 (0.98, 1.60)	1.92 (1.31, 2.81)	0.936	<0.0000 1	0.0016
WSS, distal edge, Pa	‡ 1.90 (1.03, 5.62)	ψ 1.81 (0.80, 3.44)	1.82 (1.14, 3.10)	<0.0001	<0.0001	<0.0001
In-scaffold percent	42.0 %	35.9 %	15.2 %	<0.0001	<0.0001	<0.0001

†p<0.05, ‡p<0.0001, #p < 0.05, ψp<0.001, Ωp=0.11, Φp = 0.89 n: total number of circumferential 4 quadrants per cross-section in the pullbacks performed serially in 8 scaffolds. (p-values come from mixed effects analysis) (Q1: First Quartile, Q3: Third quartile, Pre: pre-implantation, Post: post-implantation, 1y: one-year, 5y: five-year)

While post-WSS distribution was heterogeneous with numerous peri-strut zone of low-WSS, at 5y, the distribution became more homogeneous (**Figure 5 and 6**). Vessel surface exposed to low-WSS(<1Pa) decreased significantly from 42.0% at baseline to 35.9% at 1y and 15.2% at 5y (p-overall <0.0001) (**Figure 7**).

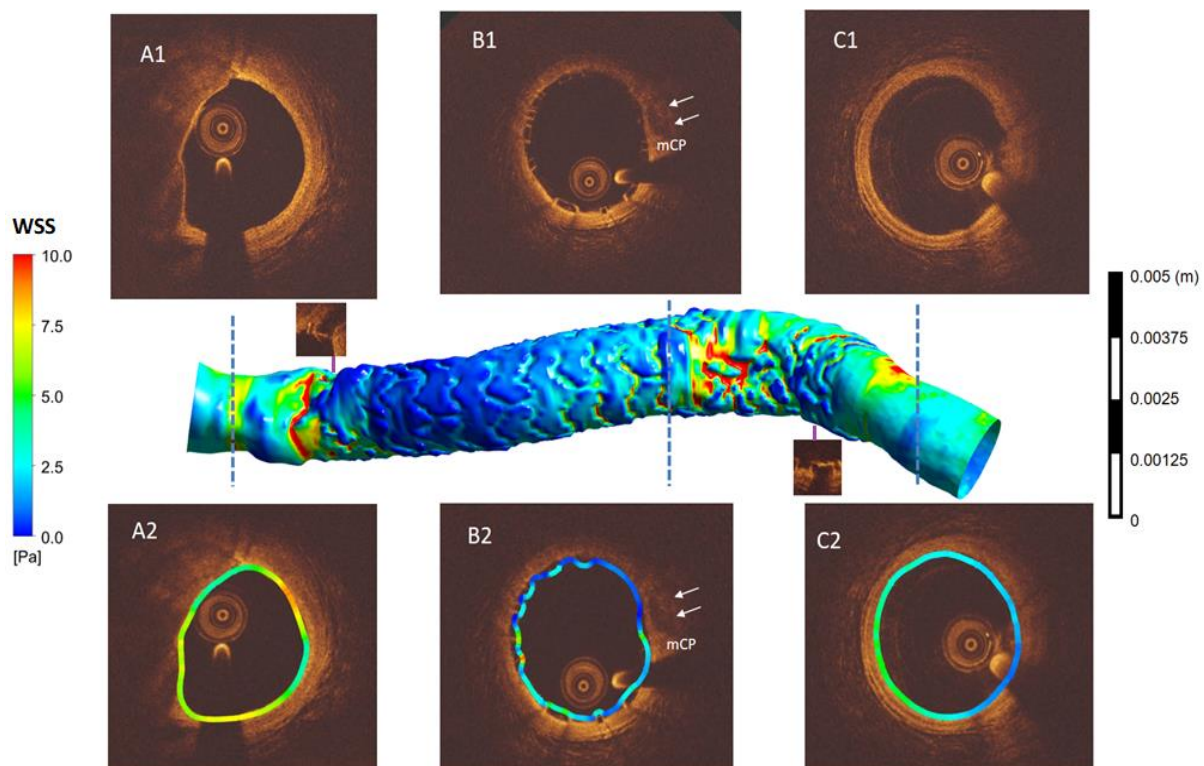


Figure 5. WSS was analyzed post-implantation in the proximal non-scaffolded segment (Panels-A1 and-A2), in scaffolded segments (Panels-B1 and -B2) and in the distal non-scaffolded edge segment (Panels-C1 and-C2). In the scaffolded segment, due to larger luminal area and strut protrusion, WSS in the inter-strut luminal surface shows peri-strut area of very-low-WSS (dark-blue in Panel-B2). At inlet and outlet of the scaffold, the non-scaffolded segment shows short region of high-WSS in red (mCP: mixed calcified-plaque).

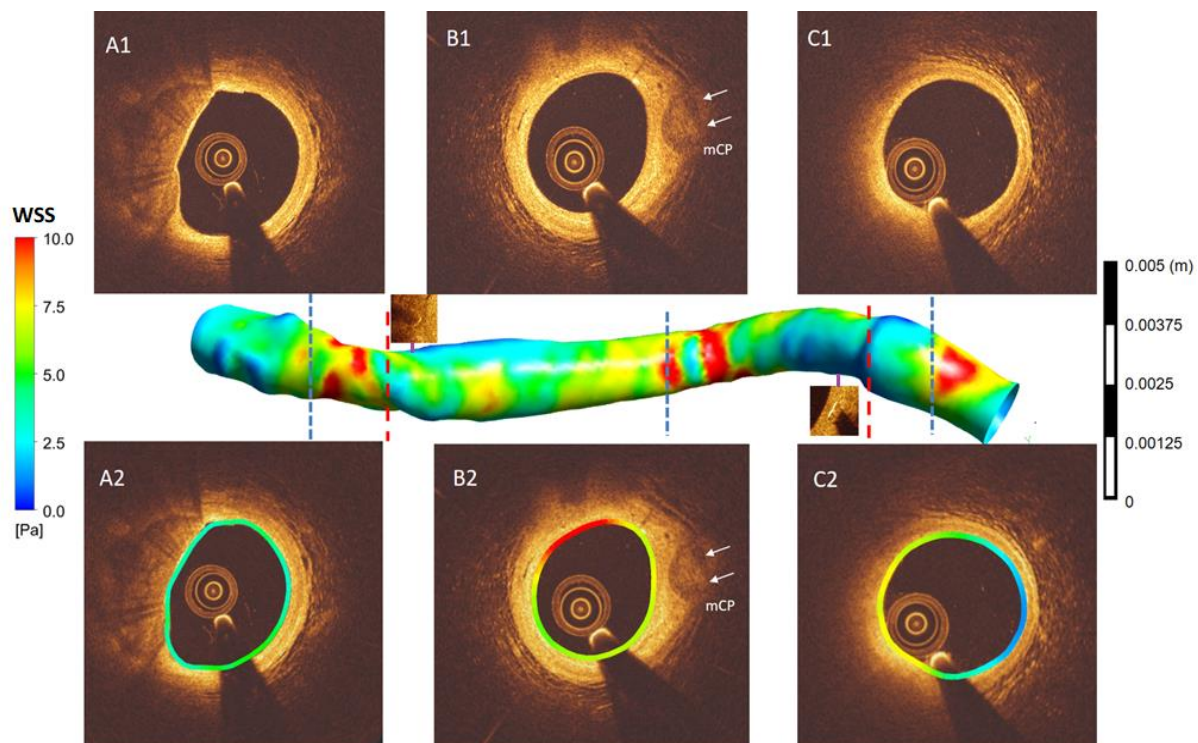


Figure 6. At 5y, WSS was analyzed in the proximal non-scaffolded edge (Panels-A1 and-A2), in scaffolded segments (Panels-B1 and-B2) and in the distal non-scaffolded edge (Panels-C1 and-C2). Compared to the corresponding cross-sections in post-implantation CFD model in Figure-5, WSS distribution becomes more homogeneous and have more physiological values (color-coded green and yellow) ranging between 5 and 7.5Pa in the scaffolded segment identified on OCT by the radiopaque markers. The inlet and outlet of the scaffold still show area of high-WSS in red. At follow-up, the lumen became smooth without significant topographic obstacles which could disrupt the flow (mCP: mixed calcified-plaque).

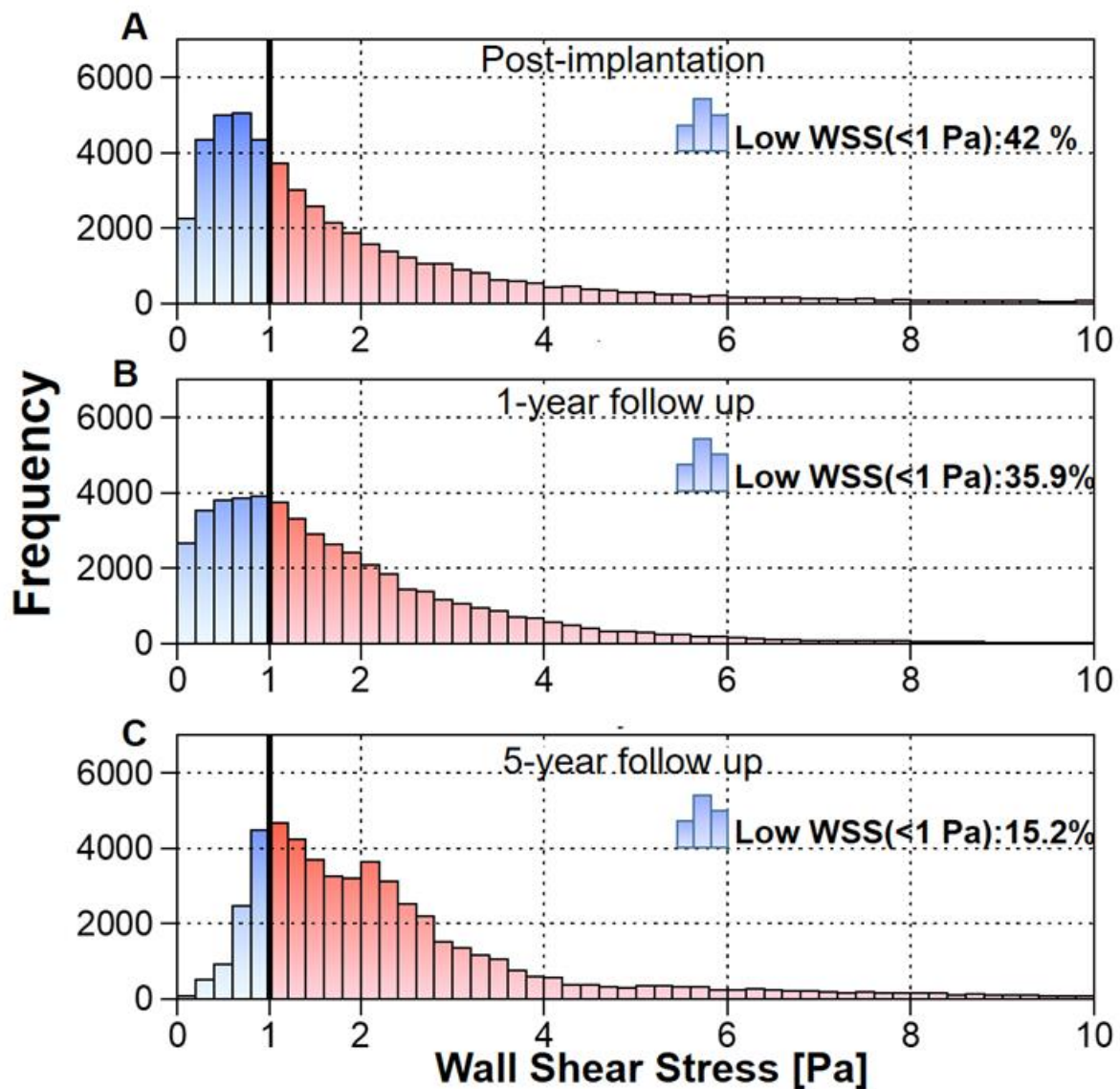


Figure 7. Histograms of WSS post-implantation, at 1y and at 5y. The percentage of low-WSS(<1Pa) was 42% post-implantation (Panel-A), 35.9% at 1y (Panel-B) and 15.2% at 5y (Panel-C).

DISCUSSION

This is the first study to use serial OCT and CFD data to evaluate the effect of SP on WSS and NT at 1y and 5y follow-ups. We have identified: 1) The mean SP is $110 \pm 25 \mu\text{m}$ and only $36 \pm 15\%$ of the strut thickness ($157 \mu\text{m}$) is embedded post-implantation. 2) Due to poor strut penetration, post-implantation thick square-shaped struts induced flow disruptions with regions of very-low-WSS peri-strut. 3) The disrupted laminar-WSS and areas of very-low-WSS with flow reversal at baseline determines the amount of peristrut neointimal proliferation at 1y. 4) At 5y, due to neointimal coverage, WSS recover homogeneous distribution with

physiological values. 5) At the edges of scaffolded region, initial post-procedural *step-up* and *step-down* in WSS disappeared at 5y.

The impact of SP on post-WSS and neointimal regeneration at 1y

Due to wide footprint of Absorb, strut embedment is not easily achievable. The square-shape and initial contact-radius of the struts impede penetration by the principles of *contact mechanics*.¹³ The penetration of the strut is directly related to the strut width which is based on Pascal's law of pressure (Pressure = Force / Area). As the strut width increases, the pressure required for well penetration will increase that may reduce the strut embedment well enough. With poor penetration, thick struts stand as obstacles, creating flow separations, eddies and stasis around the struts resulting in low-WSS peri-strut. On the contrary, strut surface induces higher-WSS creating a gradient in WSS between top and bottom of the struts.¹⁴ The disturbed flow and oscillatory-WSS promotes biological changes producing a well-established environment for thrombus formation and neointimal hyperplasia (NH) through activation of athero-promoting genes.¹⁵ The NTi on the strut surface is much less accentuated than in the inter-strut zones.¹⁶ Over time this mechanobiological modulation of tissue proliferation dissipates the WSS micro-gradient as the proliferating tissue between the struts fills inter-strut zones. NTi continues to develop until it reaches the strut surface and the thicker the struts are, the thicker the neointima will be.

With thinner struts and deeper VW embedment, protrusion is reduced and recirculation and stagnation around the struts will be smaller.⁵ In case of thinner struts with good penetration, neointimal growth(NG) will be inevitably limited with less lumen area reduction.¹⁷

Improvement in WSS at long-term follow-up

Following scaffold implantation, barotrauma -stretch induced arterial injury- changes smooth muscle cells (SMC) phenotype from contractile to synthetic and triggers SMC migration towards subintima where they secrete abundant proteoglycan forming the bulk of stenotic mass.¹⁸ Mechanical stretch also engenders inflammatory reactions in intima and adventitia. The antiproliferative-drug eluted from the scaffold aims at eliminating early inflammatory reaction secondary to the barotrauma. However, 80% of the antiproliferative-drug is eluted from the scaffold by 30-days.⁷ The limited duration of antiproliferative agent release has no significant effect on long-term NG that is influenced by other factors such as LH. Apparently, increased and sustained *laminar-WSS* at follow-up is an *inhibiting-factor* for further cellular proliferation.¹⁹

Step-up and *step-down* in luminal dimensions at inlet and outlet of the scaffold generate macro-changes in WSS and modulates neointimal proliferation that ultimately will homogenize luminal dimensions in proximal, distal and scaffolded segments.²⁰ The morphological improvement in transitional-zones were completed at 1y.²¹

Methodological challenges in assessing WSS and neointima

During implantation, thick struts of Absorb are barely embedded and highly protruding. These protruding struts disturb laminar flow around the struts. At that stage, the best approach to describe flow patterns is proposed by Gogas et al depicting 5 sites of WSS assessment: proximal inter-strut, proximal peristrut, on top of the strut, distal peristrut and inter-strut space distal to the strut.²²

At 1y, translucency and volume of the strut remains essentially unchanged. By interpolating lumen contour from the embedded-struts, it is possible to reconstruct the lumen contour (for retrospective post-implantation model). It has been appealing to compute retrospectively peristrut WSS (virtual baseline WSS) and correlate the current neointima at 1y as this approach enables perfect co-localization and matched assessment of the post-WSS with current NG at 1y (**Figure 2**).¹⁶

At 5y, the struts and initial lumen contour are undetectable and luminal surface is smooth and homogeneous and the only feasible method of surface analysis was to subdivide luminal perimeter in subunit of 5°-sectors. To standardize the analysis method and render the WSS analysis comparable for 3-periods of acquisition: post-implantation, 1y and 5y, we applied subunit-sector approach to post-implantation, 1y and 5y.¹⁶

Impact on Clinical Practice

The fundamental issue of the polymeric struts in PLLA is their lack of tensile strength and radial force that have to be compensated by their thickness and large footprint preempting VW embedment and their quick coverage by neointima. Thereby, SP and its disturbing impact on laminar-flow and WSS predetermine thickness of the neointima. Although present observation is hypothesis-generating, recent pre-clinical and clinical observations with thinner and circular struts have demonstrated causative relationship between embedment(more) and WSS disturbance(less).⁴ Long-term follow-up will confirm or disprove causative relationship between strut thickness and thickness of the neointima with new-generation BRS with thinner and circular struts.

Limitations

The main limitation of the present study is that, to investigate the relationship between post-WSS and NT at 1y, a retrospective 3D vessel model was implemented using 1y OCT data. This was done to overcome potential discrepancies in corresponding OCT frames, regarding the circumferential strut distribution between post-implantation and 1y OCT and to associate post-WSS and follow-up neointima as accurate as possible. Second limitation is small number of observations. Several criteria were implemented for filtering suitable cases to investigate the effect of SP on post-WSS and NH at 1y; 1-To prevent any effect of swirling-flow due to vessel curvature, on the scaffolded segment WSS distribution, we didn't include the cases with curvature. 2-The cases without two angiographic projections at least with >25-degree difference couldn't be reconstructed. 3-To investigate the alteration in WSS at 1y and 5y, the cases with truly serial-OCT imaging post-implantation, at 1y and at 5y were recruited.

CONCLUSIONS

Following Absorb implantation, local flow micro-environment around the protruding struts is characterized by alternance of high and low-WSS. SP and disrupted local-WSS appear to be important determinants of NG. The thickness of the struts and intensity of the flow disturbance predetermine the thickness of the inter-strut neointima.

With time, newly constituted intimal lining improved the luminal surface with homogenization of the WSS towards physiological values at long-term follow-up. Despite the initial bulky structure of the quadratic-struts, VW recovered smooth surface to re-establish a *de-novo laminar WSS* profile, following biointegration of the scaffold into the VW.

Funding statement

P.W. Serruys and Y. Onuma are members of the International Advisory Board of Abbott Vascular. E. Tenekecioglu has a research grant from The Research and Scientific Council of Turkey (TUBITAK).

Conflict of interest

None of the authors have any conflict of interest.

REFERENCES

1. Serruys PW, Garcia-Garcia HM and Onuma Y. From metallic cages to transient bioresorbable scaffolds: change in paradigm of coronary revascularization in the upcoming decade? *Eur Heart J*. 2012;33:16-25b.
2. Slager CJ, Wentzel JJ, Gijzen FJ, Schuurbijs JC, van der Wal AC, van der Steen AF and Serruys PW. The role of shear stress in the generation of rupture-prone vulnerable plaques. *Nature clinical practice Cardiovascular medicine*. 2005;2:401-7.
3. Tenekecioglu E, Torii R, Bourantas C, Crake T, Zeng Y, Sotomi Y, Onuma Y, Yilmaz M, Santoso T and Serruys PW. Preclinical assessment of the endothelial shear stress in porcine-based models following implantation of two different bioresorbable scaffolds: effect of scaffold design on the local haemodynamic micro-environment. *EuroIntervention*. 2016;12:1296.
4. Tenekecioglu E, Torii R, Bourantas CV, Al-Lamee R and Serruys PW. Non-Newtonian pulsatile shear stress assessment: a method to differentiate bioresorbable scaffold platforms. *European heart journal*. 2017;38:2570.
5. Jimenez JM and Davies PF. Hemodynamically driven stent strut design. *Ann Biomed Eng*. 2009;37:1483-94.
6. Murphy J and Boyle F. Predicting neointimal hyperplasia in stented arteries using time-dependant computational fluid dynamics: a review. *Computers in biology and medicine*. 2010;40:408-18.
7. Serruys PW, Onuma Y, Ormiston JA, de Bruyne B, Regar E, Dudek D, Thuesen L, Smits PC, Chevalier B, McClean D, Koolen J, Windecker S, Whitbourn R, Meredith I, Dorange C, Veldhof S, Miquel-Hebert K, Rapoza R and Garcia-Garcia HM. Evaluation of the second generation of a bioresorbable everolimus drug-eluting vascular scaffold for treatment of de novo coronary artery stenosis: six-month clinical and imaging outcomes. *Circulation*. 2010;122:2301-12.
8. Okamura T, Onuma Y, Garcia-Garcia HM, Bruining N and Serruys PW. High-speed intracoronary optical frequency domain imaging: implications for three-dimensional reconstruction and quantitative analysis. *EuroIntervention : journal of EuroPCR in collaboration with the Working Group on Interventional Cardiology of the European Society of Cardiology*. 2012;7:1216-1226.
9. Sotomi Y, Tateishi H, Suwannasom P, Dijkstra J, Eggermont J, Liu S, Tenekecioglu E, Zheng Y, Abdelghani M, Cavalcante R, de Winter RJ, Wykrzykowska JJ, Onuma Y, Serruys PW and Kimura T. Quantitative assessment of the stent/scaffold strut embedment analysis by optical coherence tomography. *Int J Cardiovasc Imaging*. 2016;32:871-83.
10. Bourantas CV, Papafaklis MI, Lakkas L, Sakellarios A, Onuma Y, Zhang YJ, Muramatsu T, Diletti R, Bizopoulos P, Kalatzis F, Naka KK, Fotiadis DI, Wang J, Garcia Garcia HM, Kimura T, Michalis LK and Serruys PW. Fusion of optical coherence tomographic and angiographic data for more accurate evaluation of the endothelial shear stress patterns and neointimal distribution after bioresorbable scaffold implantation: comparison with intravascular ultrasound-derived reconstructions. *The international journal of cardiovascular imaging*. 2014;30:485-94.
11. Bates D, Mächler M, Bolker B and Walker S. Fitting Linear Mixed-Effects Models Using lme4. 2015. 2015;67:48.
12. Gomez-Lara J, Garcia-Garcia HM, Onuma Y, Garg S, Regar E, De Bruyne B, Windecker S, McClean D, Thuesen L, Dudek D, Koolen J, Whitbourn R, Smits PC, Chevalier B, Dorange C, Veldhof S, Morel MA, de Vries T, Ormiston JA and Serruys PW. A comparison of the conformability of everolimus-eluting bioresorbable vascular scaffolds to metal platform coronary stents. *JACC Cardiovascular interventions*. 2010;3:1190-8.
13. Johnson KL and Johnson KL. *Contact Mechanics*: Cambridge University Press; 1987.
14. LaDisa JF, Jr., Olson LE, Molthen RC, Hettrick DA, Pratt PF, Hardel MD, Kersten JR, Warltier DC and Pagel PS. Alterations in wall shear stress predict sites of neointimal hyperplasia after stent implantation in rabbit iliac arteries. *Am J Physiol Heart Circ Physiol*. 2005;288:H2465-75.
15. Chien S. Mechanotransduction and endothelial cell homeostasis: the wisdom of the cell. *American journal of physiology Heart and circulatory physiology*. 2007;292:H1209-24.

16. Bourantas CV, Papafaklis MI, Kotsia A, Farooq V, Muramatsu T, Gomez-Lara J, Zhang YJ, Iqbal J, Kalatzis FG, Naka KK, Fotiadis DI, Dorange C, Wang J, Rapoza R, Garcia-Garcia HM, Onuma Y, Michalis LK and Serruys PW. Effect of the endothelial shear stress patterns on neointimal proliferation following drug-eluting bioresorbable vascular scaffold implantation: an optical coherence tomography study. *JACC Cardiovascular interventions*. 2014;7:315-24.
17. Kastrati A, Mehilli J, Dirschinger J, Dotzer F, Schuhlen H, Neumann FJ, Fleckenstein M, Pfaffert C, Seyfarth M and Schomig A. Intracoronary stenting and angiographic results: strut thickness effect on restenosis outcome (ISAR-STEREO) trial. *Circulation*. 2001;103:2816-21.
18. Russo RJ, Silva PD and Yeager M. Coronary artery overexpansion increases neointimal hyperplasia after stent placement in a porcine model. *Heart (British Cardiac Society)*. 2007;93:1609-15.
19. Carlier SG, van Damme LC, Blommerde CP, Wentzel JJ, van Langehove G, Verheye S, Kockx MM, Knaapen MW, Cheng C, Gijssen F, Duncker DJ, Stergiopoulos N, Slager CJ, Serruys PW and Krams R. Augmentation of wall shear stress inhibits neointimal hyperplasia after stent implantation: inhibition through reduction of inflammation? *Circulation*. 2003;107:2741-6.
20. Tateishi H, Suwannasom P, Sotomi Y, Nakatani S, Ishibashi Y, Tenekecioglu E, Abdelghani M, Cavalcante R, Zeng Y, Grundeken MJ, Albuquerque FN, Veldhof S, Onuma Y and Serruys PW. Edge Vascular Response After Resorption of the Everolimus-Eluting Bioresorbable Vascular Scaffold- A 5-Year Serial Optical Coherence Tomography Study. *Circulation journal : official journal of the Japanese Circulation Society*. 2016;80:1131-41.
21. Torii R, Tenekecioglu E, Bourantas C, Poon E, Thondapu V, Gijssen F, Sotomi Y, Onuma Y, Barlis P, Ooi ASH and Serruys PW. Five-year follow-up of underexpanded and overexpanded bioresorbable scaffolds: self-correction and impact on shear stress. *EuroIntervention : journal of EuroPCR in collaboration with the Working Group on Interventional Cardiology of the European Society of Cardiology*. 2017;12:2158-2159.
22. Gogas BD, Yang B, Piccinelli M, Giddens DP, King SB, 3rd, Kereiakes DJ, Ellis SG, Stone GW, Veneziani A and Samady H. Novel 3-Dimensional Vessel and Scaffold Reconstruction Methodology for the Assessment of Strut-Level Wall Shear Stress After Deployment of Bioresorbable Vascular Scaffolds From the ABSORB III Imaging Substudy. *JACC Cardiovascular interventions*. 2016;9:501-3.

ON-LINE SUPPLEMENT

Patient and procedural characteristics

Patient characteristics are tabulated in *on-line supplementary Table-1*. Procedural characteristics are shown in *on-line supplementary Table-2*.

OCT image acquisition and OCT data analysis:

A non-occlusive flushing technique was obtained by injection of angiographic contrast medium for blood clearance. Flow area (FA) of the scaffolded segment and 5-mm segments adjacent to proximal and distal scaffold edges were analyzed at 200 μ m intervals by an independent core-laboratory (Cardialysis, Rotterdam, Netherlands). The data acquired post-implantation were used to investigate the relationship between post-implantation strut protrusion/embedment and post-implantation WSS distribution. The data acquired at 1-year follow-up were used to reconstruct 2 separate contours; firstly, the baseline luminal borders defined by splines connecting the adluminal sides of the struts (*retrospective* baseline model) and secondly, the luminal contour at-1-year follow-up (one-year follow-up model) delineating the interstrut neointimal boundary as well the covered struts (**Figure-1**). The rationale for this approach is to optimize the topographical relationship between WSS evaluation and neointimal growth at one-year follow-up and avoid complex and inaccurate colocalization and matching on OCT cross-sections of struts visualized post-procedure and at 1-year. After full complete bioresorption, the five-year luminal contours on OCT were used to assess the WSS at five-years.

Coronary Artery Reconstruction:

The radiopaque markers and the anatomical landmarks (i.e. side-branches), identified both on angiography and on OCT, were used to define the scaffolded segment and the 5mm proximal-distal native vessel segments. In the region of interest (ROI), the scaffolded and the proximal-distal non-scaffolded vessel segments were analyzed at a 200 μ m interval. Post-implantation, the FA was delineated in the non-scaffolded segments by the luminal border and in the scaffolded segments by the *endoluminal* side of the struts and by the luminal surface borders between the struts. At one-year follow-up, for the retrospective analysis of the WSS post-

implantation, post-procedure luminal borders were determined by the splines conjoining the *abluminal* sides of the struts. The luminal surfaces at one (one-year follow-up model) and five-year (five-year follow-up model) follow-up were established by the endoluminal borders of the grown neointima.

Two end-diastolic angiographic projections with $>30^\circ$ angles difference were selected that portrayed the most distal and proximal anatomical landmark detected also in the FD-OCT images.⁷ In order to delineate the lumen contours and to estimate the centerline of the lumen, the 2 centerlines from the angiograms were used to form the 3D luminal centerline. In this reconstruction, the 3D luminal centerline derived from the angiographic projections was used as a “backbone”. The center of mass (ie, centroid) of the lumen area in FD-OCT images was established and lumen borders obtained from FD-OCT were placed perpendicularly onto the 3D lumen centerline in equidistant locations, positioning the lumen centroids on the 3D centerline. The orientation of side-branches was used for the absolute rotational orientation of the FD-OCT cross-sections. The lumen 3D boundary points were combined to get the FD-OCT-based lumen geometry in 3D.

Computational Fluid Dynamic Study:

To determine the impact of scaffold designs on the local hemodynamic microenvironment, the mesh density around the struts and in near wall flow boundary zone was elaborated to have an average element edge of $20\mu\text{m}$ (less than $1/7$ of the strut thickness). Blood was treated as a homogeneous, Newtonian fluid with a viscosity of $0.0035\text{ Pa}\cdot\text{s}$ and a density of $1,050\text{ kg}/\text{m}^3$. A steady and parabolic flow velocity profile was imposed at the inlet of the 3D models. Blood flow for each reconstruction was estimated by measuring, in the 2 angiographic projections, the number of frames required for the contrast agent to pass from the inlet to the outlet of the reconstructed segment, the volume of the reconstructed segment and the cine frame rate.⁹ The arterial wall was considered to be rigid. No-slip conditions were imposed at the scaffold surface and vessel luminal surface. At the outlet of the model zero-pressure conditions were imposed. WSS at luminal surface and strut surface was calculated as the product of blood viscosity and the gradient of blood velocity at the wall and strut surface.

Statistical analysis

Normality of distribution was tested by Kolmogorov-Smirnov test. Paired variables were compared using general-linear model with Bonferroni adjustment between multiple time-

points. Categorical variables were compared using Pearson's chi-square test or Fischer's exact test, as appropriate. For WSS comparison between post-implantation, 1-year and 5-year follow-ups, mixed-effects model was built on % increase of WSS from post-implantation to 1-year and 5-year follow-ups. The model was set with fixed-effects on log-WSS with standard deviations and intercept, and random-effects on patient-ID. Since WSS values in adjacent cross-sections are related to each other and are not independent from each other, there are unavoidable correlations between the WSS values in sequential cross-sections. Therefore, a special correlation structure was implemented based on Euclidian-distances between the locations where 5-degree sectorial-WSS were quantified. The correlation structure was incorporated into the mixed-effects model within random-effects.

Supplementary Table 1. Baseline Characteristics of the Studied Population (N = 8, Lesion=8)

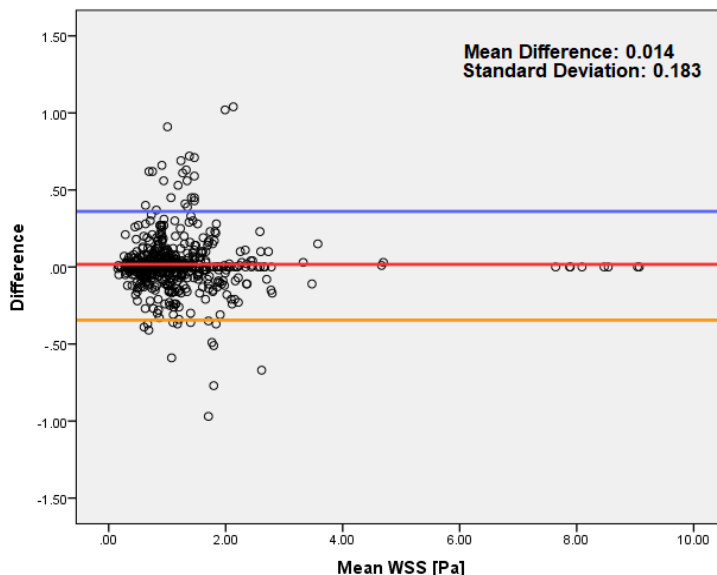
Age, yrs	62 ± 8
Male	5 (63)
Hypertension	5 (63)
Hypercholesterolemia	6 (75)
Diabetes mellitus	0 (0)
Current smoking	3 (38)
Prior percutaneous coronary intervention	1 (12)
Prior myocardial infarction	2 (25)
Stable angina	7 (88)
Unstable angina	1 (12)
Silent ischemia	0 (0)
Treated vessel	
Left anterior descending artery	5 (63)
Left circumflex artery	2 (25)
Right coronary artery	1 (12)
Ramus intermedius	0 (0)

Values are mean ± SD or n (%).

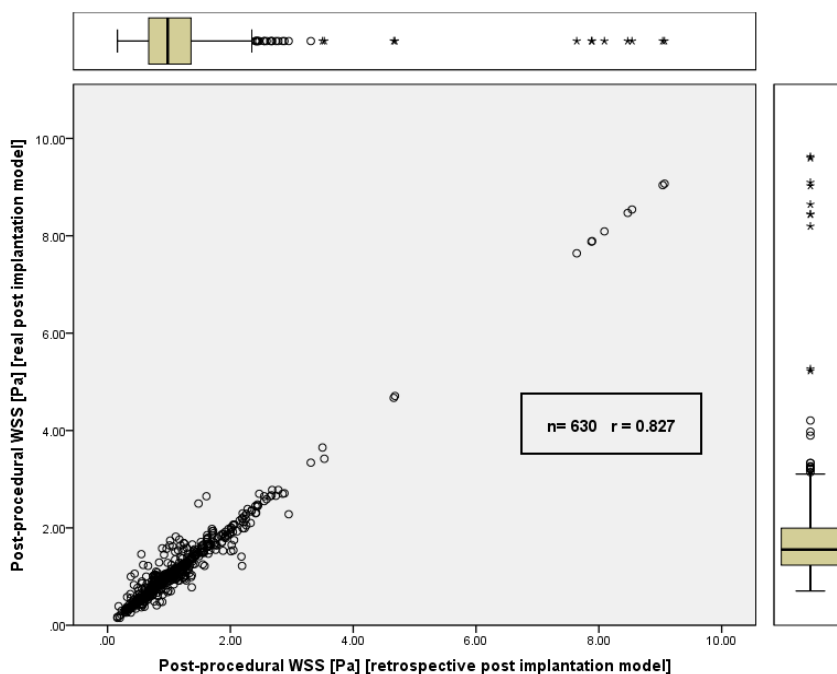
Supplementary Table 2. Procedural Characteristics

	N =8, L=8
ACC/AHA lesion class	
A	0% (0)
B1	63% (5)
B2	38% (3)
C	0% (0)
Pre-dilatation	100% (8/8)
Pre-dilatation pressure, atm	11.00 ± 2.20
Diameter of scaffolds, mm	3.00 ± 0.0
Expected scaffold diameter, mm	3.24 ± 0.11
Total length of study devices, mm	18.0 ± 0.0
Nominal scaffold area, mm ²	8.26 ± 0.56
Deployment pressure, atm	11.50 ± 2.56
Post-dilatation	63% (5)
Post-dilatation pressure, atm	16.0 ± 3.27
Procedure complication	0 (0)
Clinical device success	100% (8/8)
Clinical procedure success	100% (8/8)

Values are mean ± SD or n (%).



Online Figure 1a. Bland-Altman plots show narrow level-of-agreement (LOA) in the cross-section level (n=630) of median-WSS values between the retrospective post-implantation and real post-implantation models. The mean difference was 0.014 and LOAs for WSS were 0.38 and -0.17.



Online Figure 1b. Linear-regression graph shows a high correlation-coefficient($r=0.827$) between cross-section level median-WSS(n=630) from retrospective post-implantation model and real post-implantation mode

Chapter 10

Endothelial Shear Stress and Vascular Remodeling in Bioresorbable Scaffold and Metallic Stent

Endothelial Shear Stress and Vascular Remodeling in Bioresorbable Scaffold and Metallic Stent

Erhan Tenekecioglu*, Yuki Katagiri*, Kuniaki Takahashi, Mariusz Tomaniak, Dariusz Dudek, Angel Cequier, Didier Carrié, Andrés Iñiguez, Rinse Johannes van der Schaaf, Marcello Dominici, Ad J. van Boven, Steffen Helqvist, Manel Sabaté, Andreas Baumbach, Jan J. Piek, Joanna J. Wykrzykowska, Pieter Kitslaar, Jouke Dijkstra, Johan H.C. Reiber, Bernard Chevalier, Dilek Ural, Kerem Pekkan, Christos V. Bourantas, Frank Gijsen, Yoshinobu Onuma, Ryo Torii, Patrick W. Serruys

* These authors contributed equally to this work.

Atherosclerosis. 2020; 312:79-89.

ABSTRACT

Background and Aim: The impact of endothelial shear stress (ESS) on vessel remodeling in vessels implanted with bioresorbable scaffold (BRS) as compared to metallic drug-eluting stent (DES) remains elusive. The aim was to determine whether the relationship between ESS and remodeling patterns differs in BRS from those seen in metallic DES at 3-year follow-up.

Methods: In the ABSORB II randomized trial, lesions were investigated by serial coronary angiography and intravascular ultrasound (IVUS). Three-dimensional reconstructions of coronary arteries post-procedure and at 3-year were performed. ESS was quantified using non-Newtonian steady flow simulation. IVUS cross-sections in device segment were matched using identical landmarks.

Results: Paired ESS calculations post-procedure and at 3 years were feasible in 57 lesions in 56 patients. Post-procedure, median ESS at frame level was higher in BRS than in DES, with marginal statistical significance (0.97 ± 0.48 vs. 0.75 ± 0.39 Pa, $p=0.063$). In the BRS arm, vessel area and lumen area showed larger increases in the highest tercile of median ESS post-procedure as compared to the lowest tercile. In contrast, in DES, no significant relationship between median ESS post-procedure and remodeling was observed. In multivariate analysis, smaller vessel area, larger lumen area, higher plaque burden post-procedure, and higher median ESS post-procedure were independently associated with expansive remodeling in matched frames. Only in BRS, younger age was an additional significant predictor of expansive remodeling.

Conclusions: In a subset of lesions with large plaque burden, shear stress could be associated with expansive remodeling and late lumen enlargement in BRS, while ESS had no impact on vessel dimension in metallic DES.

Keywords: Stenting; bioresorbable scaffold; vessel remodeling; shear stress

INTRODUCTION

Given the transient scaffolding and recovery of vasomotion in the instrumented vessels, bioresorbable scaffolds (BRS) have emerged as a potential solution for drawbacks of metallic drug-eluting stents (DES), that causes permanent vessel straightening and loss of compliance, dynamic vessel remodeling and mechanotransduction.[1] These shortcomings may influence vessel wall metabolism and contribute to late degeneration of intra-device neointima leading to neoatherosclerotic lesion formation. During resorption of polymeric scaffold, late luminal enlargement with expansive remodeling has been documented[2], but biological and/or physiological determinants of this morphological and anatomical processes are still elusive. Arterial remodeling is a complex process depends on several endogenous (plaque characteristics, oxidative stress, inflammation, calcification and collagen deposition) and environmental factors.[3] Homeostatic response of the vessel wall to hemodynamic and mechanical triggers is the main underlying process of arterial remodeling.[4] The relationship between lumen area, plaque-media area, and vessel area is at the foundation of the Glagov's principle of compensatory expansive remodeling of the external elastic membrane(EEM).[4] Regarding the modifications in these three compartments, there are miscellaneous scenarios of expansive or constrictive remodeling, increase or decrease in plaque/media and increase/decrease in lumen area.[2, 5] Endothelial shear stress (ESS), the frictional force at the endothelial surface produced by flowing blood, is a preliminary cue for vessel remodeling. ESS is a dynamic entity related with macroscopic changes in blood flow. [6, 7]

The purposes of the present study were to determine whether ESS post-procedure is associated with vessel remodeling in instrumented arterial segments; and whether the relationship between ESS and remodeling patterns differs in BRS from those seen in metallic DES at 3-year follow-up.

PATIENTS AND METHODS

Study design and patient selection

The ABSORB-II trial was a prospective, single-blind, multicenter trial that randomized 501 patients to percutaneous coronary intervention(PCI) with implantation of either Absorb BRS or Xience metallic DES in a 2:1 fashion.[8] The protocol mandated documentary intravascular ultrasound(IVUS) pre-procedure and post-procedure as well as at 3-year follow-up.

Data acquisition and analysis

Two-dimensional (2D) quantitative coronary angiography (QCA) and IVUS data acquisition have been described previously.[8] For the present study, in order to correspond with the cardiac phase analyzed in QCA, the electrocardiogram(ECG)-gated end-diastolic cross-sectional frames in IVUS were used.

All IVUS pullbacks were analyzed off-line by the independent core lab using commercially available software (QIVUS version 2.2, Medis, Leiden, the Netherlands). The methods for quantitative analysis of IVUS have been reported previously.[9] As in the conventional analysis on IVUS, the device segments as well as the segments 5mm proximal and distal to the device, were analyzed, since beyond these regions, the effect of trauma by the device edge to trigger neointima growth is inexistent.[10] After scanning all the population (n=501 patients with 546 lesions), the 100 cases with 2 time points (n=200 lesions) (post-implantation and 3-years), which fulfilled both criteria of ; 1)suitable coronary angiograms (minimal foreshortening and $\geq 25^\circ$ angle difference between two angiograms) and 2)IVUS-VH (at least 5mm edge segments proximal and distal to the treated segment both post-implantation and at 3-years follow-up), were included into the study.

The increase or decrease in vessel area (or EEM area) defines the type of vascular remodeling, constrictive or expansive. In order to compare the BRS and metallic stent and due to the difficulty to measure the neointima in the biodegraded scaffold at 3-year,the intra-scaffold/stent neointima was incorporated in the metric of "plaque/media=vessel area–lumen area".[2] In a previous study[11], performed on ex vivo human coronary arteries, relative range of inter-observer reproducibilities of measurements for lumen, plaque-media, and vessel cross sectional areas based on two standard deviations of their measurements were $\pm 15\%$, $\pm 22\%$, $\pm 12\%$, respectively. In compliance with these relative values of reproducibility, there have been 9 theoretical patterns of vessel/lumen/plaque remodeling based on increase, no change, and decrease in each of these three parameters.[5] In the present study, vessel remodeling was defined as any positive or negative change in vessel area, assessed in a continuous fashion, without the use of binary cut-off criteria.

Coronary artery reconstruction

Three-dimensional (3D) model reconstruction of coronary artery was based on 3D-QCA of the vessel implanted with the device and co-registration of lumen contour of IVUS onto the centerline of the vessel reconstructed in 3D-QCA.[12] Following the recruitment of the cases

fulfilled the criteria of coronary angiogram and IVUS ($n=200$ lesions), during the 3D vessel reconstruction for CFD work, 34 vessels couldn't be 3D reconstructed due to various technical points during the main vessel-side branch co-registration process.

Three-dimensional QCA was performed using QAngioXA-3D (version-1.3 Medis, Leiden, the Netherlands). Two post-procedural end-diastolic angiographic images with at least 25° -angle difference and with minimal foreshortening were selected. In order to adjust for the effect of vessel curvature on the local hemodynamic forces[13], the proximal native vessel segment from its ostium was incorporated into the 3D-model (**Figure 1A**).

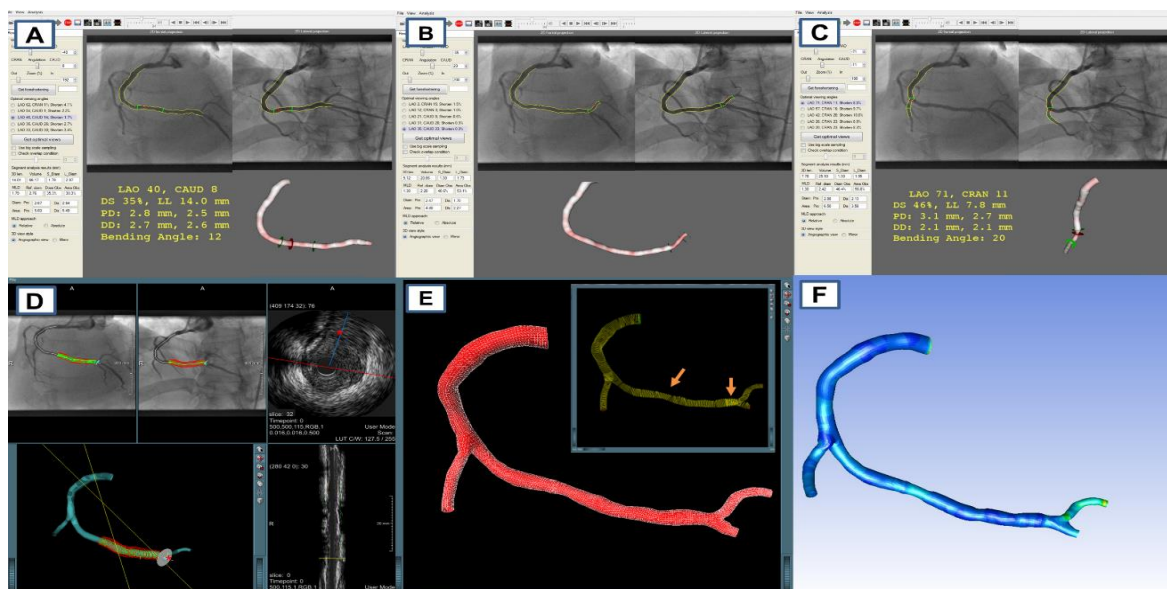


Figure 1. Analysis steps for computational fluid dynamics (CFD) simulation in coronary artery.

This figure demonstrates the steps for CFD simulations in the study. Two orthogonal coronary projections displaying the treated vessel were processed in 3D-QCA software. After defining the reference points for the main vessel (which were the vessel ostium or just after the catheter tip -as in this case- for proximal reference point and one diameter of the main vessel after the distal side branch for distal reference point) for 3D-QCA, the luminal borders and the centerline were automatically detected by the software (**Panel-A**). For proximal and distal side branches, proximal reference point was the same as in main vessel reconstruction. After automatic luminal contour and centerline detection of the distal side-branch (**Panel-B**) and proximal side-branch (**Panel-C**), 3D-QCA models were transferred to the dedicated software for co-registration to mount the IVUS-derived lumen and vessel contours on the 3D-centerline which comes from 3D-QCA of the main vessel (**Panel-D**). During co-registration step, longitudinal position of the IVUS contours was implemented by mapping the IVUS frames including side-branches on the orthogonal angiographic projections. The circumferential orientation of the IVUS cross-sections was adjusted by the side-branches (red asterisks in **Panel-D**). The rotation of cross-sections in-between was linearly interpolated. Following the co-registration, the model was transferred to the 3D workbench software to fuse the 3D-QCA models with IVUS contours in order to get luminal surface models (**Panel-E**). The 3D-QCA segment overlapping with IVUS segment was deleted in order to get the luminal surface data only from IVUS in device segment (right upper panel in **Panel-E**, the arrows show the proximal and distal edge of the IVUS segment). The luminal surface wall data was exported in .stl format. Following the workbench step, luminal volume was meshed and the meshed model was then processed in a CFD software to simulate the flow in the reconstructed vessel model (**Panel-F**). Side-branch (SB) proximal to the device segment (within a distance of 3 times the diameter of proximal-SB), SB in the device segment and SB distal to the device segment (within a distance of one-diameter of the distal-SB) were included to account for the effect of flow division and the effect of any flow disturbance caused by the carina zone of the SB. To achieve a realistic effect of flow division[14], side-branches ≥ 1.5 mm in QCA measurements were reconstructed and incorporated into the 3D-model (**Figure 1B, 1C**).

Following 3D-QCA, lumen contours by IVUS within device segment and segments 5mm proximal and distal to the device were co-registered onto the 3D-QCA centerline using 3D-Angio-IVUS Co-registration (Medis, Leiden, the Netherlands) (**Figure 1D**) and a 3D-surface model was reconstructed using QAngio-CT 3D-Workbench (version-1.3.0.2, Medis, Leiden, the Netherlands) (**Figure 1E**).

Computational Fluid Dynamic study

Following 3D-reconstruction of the coronary artery, the computational fluid dynamics (CFD) mesh was generated by using ANSYS ICEM CFD 17.0 (ANSYS, Inc. Canonsburg, Pennsylvania). A typical cell size of 0.1mm was used and three prism layers at the wall were constructed, resulting in a mesh size of $\sim 2 \times 10^6$ cells. In order to incorporate its shear-thinning behavior, blood was modeled as a non-Newtonian fluid by applying Carreau model with the parameters taken from Seo et al[15]. The blood density was set to $1,060 \text{ kg/m}^3$. The vessel wall was modeled as rigid and no-slip condition was imposed at the wall. For the inflow and outflow conditions in main vessel and side-branches, flow rates were estimated based on the diameter of the main vessel and SB, following the relationship derived from in vivo observations (scaling approach).[14, 16] Poiseuille velocity profile was prescribed at the inlet based on the scaled flow rate. Since the association of ESS with vessel remodeling is based on time-averaged data over 3-years, we focused on steady flow simulations.[17] A finite-volume solver was used to perform steady-state simulations using standard numerical techniques (ANSYS Fluent v17.0, ANSYS, Inc. Canonsburg, Pennsylvania) (**Figure 1F**).

In post-processing the CFD result, cross-sections of the CFD models were located perpendicularly onto the lumen centerline and matched to the IVUS frames using in-house algorithms to be able to export mean, median, minimum, and maximum ESS at frame level (a distance of adjacent frames: median 0.42 [interquartile range 0.38, 0.50]mm). During the co-localization and orientation between the cross-sections from 3D CFD model and IVUS frames, side-branches were utilized incorporating the horizontal angle degree of the SB with the centerline.

During volume meshing, due to geometrical artefacts in bifurcation zones 6 models couldn't be meshed and due to low mesh quality 14 models couldn't be simulated. Following the CFD simulation of 146 lesions, 14 models couldn't be processed during the post-processing step.

At the end, there were 57 patients both with post-implantation and 3y shear stress simulation successfully post-processed.

Matching frames among pre-procedure, post-procedure and 3-year follow-up

IVUS cross-sections were matched for pre-procedure, post-procedure and 3-year follow-up using identical landmarks such as scaffold/stent edges, side-branches and calcium locations so that serial changes of the lumen, plaque, vessel area and ESS from post-procedure to 3-year could be analyzed at a cross-sectional level. Pre-procedural compositional information in IVUS-virtual histology (VH) was also matched with frames at later time points. Matching was performed using dedicated software [QCU-CMS software version-4.69 (Leiden University Medical Center, Leiden, Netherlands)].[18]

Statistical analysis

In patient or device level, categorical variables were compared using Pearson's chi-square test or Fischer's exact test, as appropriate. Continuous variables were compared using Student t-test.

Analyses in the present study were carried out using variables per each cross-section(frame) in device segment. Frame-level ESS between devices or between post-procedure and at 3-year was compared using linear mixed model, taking into account clustering nature of the data within device or patient. Terciles of median-ESS at a frame level were determined based on pooled cross-sectional data. The relationships between terciles of post-procedural median-ESS and cross-sectional changes of the lumen, plaque, vessel area, and plaque burden were analyzed by linear mixed-model adjusted for multiple comparisons by Bonferroni correction. Multivariate linear mixed-model predicting vessel area change was constructed using variables with p-value<0.10 in univariate analysis. Post-procedural median-ESS was forced to enter in the model as a primary variable of interest. A p-value<0.05 was considered statistically significant. Statistical analyses were performed with SPSS version-24.0.0.2(IBM, Armonk, New York).

RESULTS

Baseline patient characteristics, angiographic and IVUS results

Out of 546 lesions in 501 patients enrolled in ABSORB-II trial, paired ESS post-procedure and at 3-years were analyzable in 35 lesions in 35 patients in BRS arm and 22 lesions in 21 patients in DES arm. The study flowchart is shown in **Figure 2**.

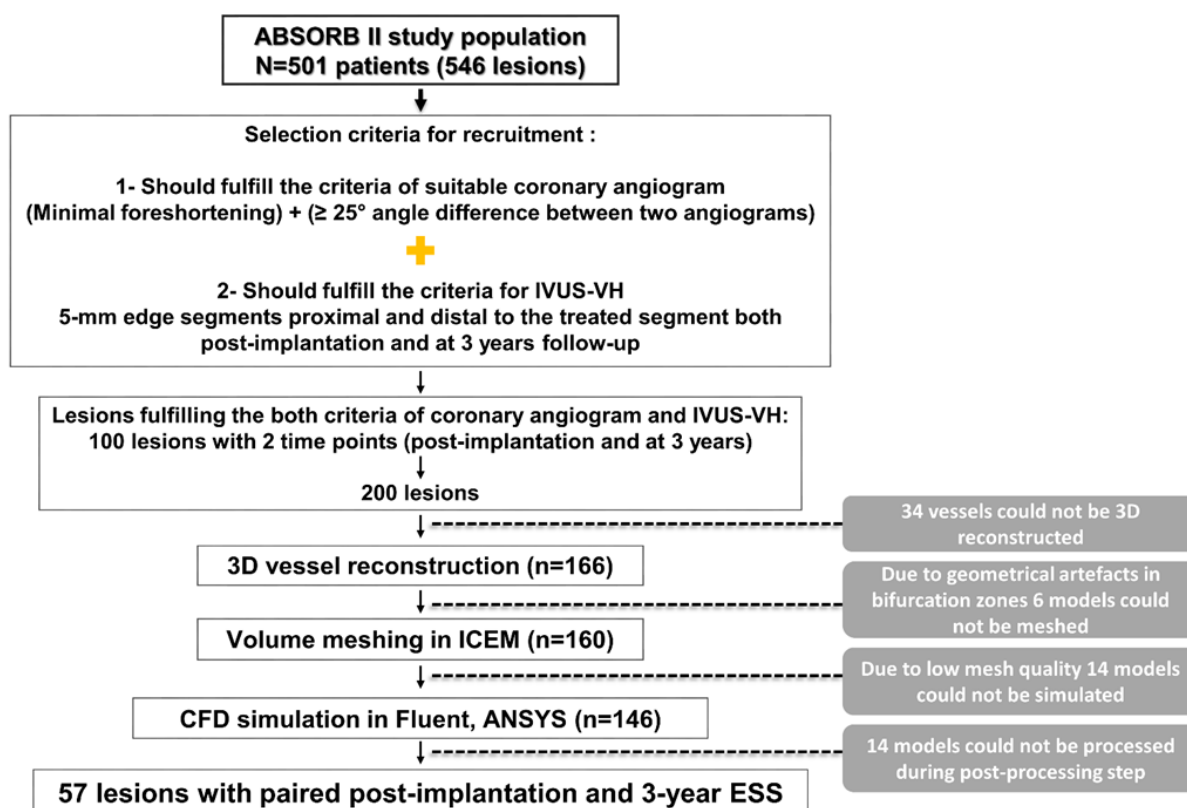


Figure 2. Study flow-chart.

Baseline (pre-procedure) clinical and lesion characteristics are tabulated in **Table 1**. Patient, lesion and procedural features were well balanced between two device groups.

Post implantation and at 3 years, both mean and minimum luminal diameters by QCA were smaller in the BRS arm than in the DES arm (**Online Table 1**). Mean and minimum lumen area post-implantation, as measured by IVUS, were smaller in the BRS arm, when compared to the metallic DES arm (**Online Table 2**). Post-implantation mean vessel area was significantly smaller in BRS arm than in DES arm (12.78 ± 3.20 vs. 14.97 ± 2.98 , $p=0.012$). However, at 3 years follow-up, mean vessel area was no longer statistically different, as a result of expansive

remodeling in BRS arm and constrictive remodeling in DES arm in combination with some loss in lumen area (change in mean vessel area: $+0.78\pm 1.49$ vs. -0.66 ± 1.64 mm², $p=0.001$).

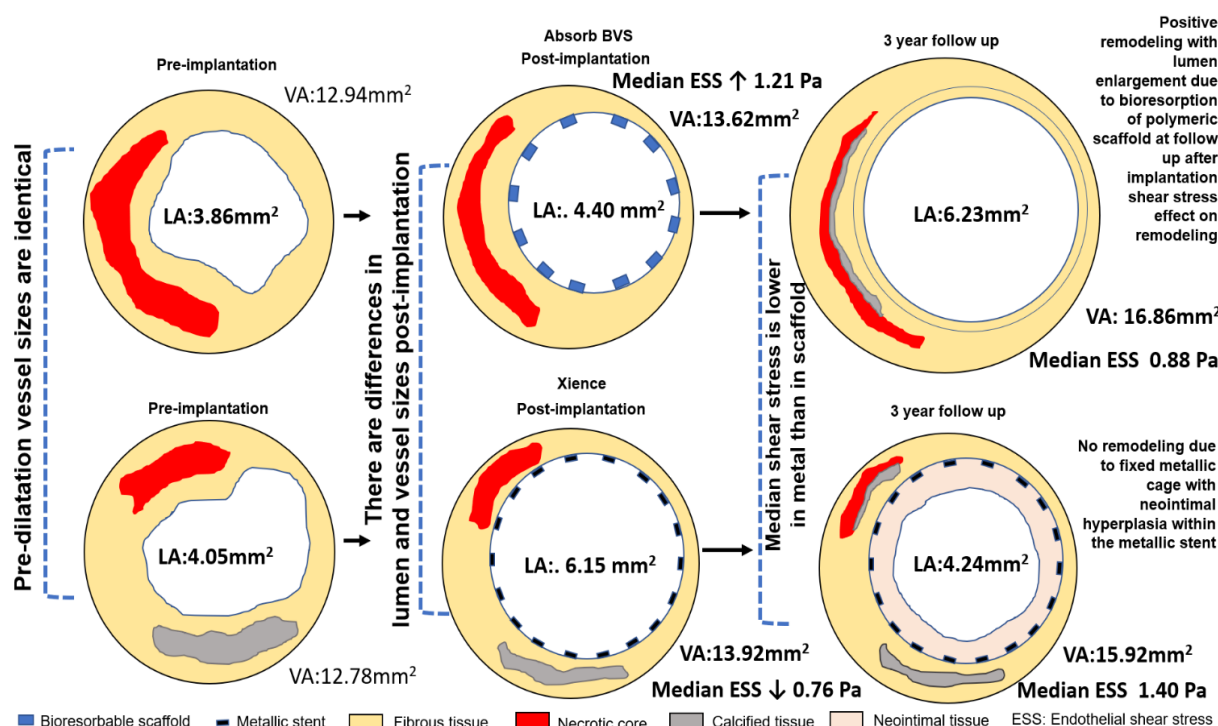
Table 1. Baseline patient, lesion characteristics and procedure details.

	BRS	DES	P
Patient characteristics	35 patients	21 patients	
Age (years)	60.34±8.09	57.57±10.63	0.275
Male	20(57.1)	20(95.2)	0.002
Current smoking	9(25.7)	5(23.8)	1.000
Hypertension requiring medication	27(77.1)	15(71.4)	0.752
Dyslipidemia requiring medication	28(80.0)	13(61.9)	0.212
Diabetes	8(22.9)	1(4.8)	0.132
Unstable angina	4(11.4)	3(14.3)	1.000
Prior MI	8(22.9)	5(23.8)	1.000
Previous PCI	13(37.1)	9(42.9)	0.780
Obesity (BMI≥30kg/m ²)	8(22.9)	7(33.3)	0.534
Lesion characteristics	35 lesions	22 lesions	
Lesion location			
Right coronary artery	10(28.6)	7(31.8)	0.415
Left anterior descending	15(42.9)	12(54.5)	
Left circumflex artery	10(28.6)	3(13.6)	
Lesion classification			
A	1 (2.9)	0 (0.0)	0.628
B1	13 (37.1)	10 (45.5)	
B2	21 (60.0)	12 (54.5)	
Procedural details			
Pre-dilatation performed	35(100.0)	21(95.5)	0.386
Nominal diameter of pre-dilatation balloon(mm)	2.62±0.39	2.63±0.38	0.930
Maximal pressure during pre-dilatation(atm)	12.23±3.25	12.71±2.63	0.565
Nominal diameter of device(mm)	3.01±0.30	3.09±0.20	0.297
Length of implanted device(mm)	21.77±6.79	19.36±3.51	0.085
Maximal pressure during device implantation(atm)	13.91±2.37	13.36±2.56	0.411
Expected device diameter(mm)	3.36±0.32	3.30±0.28	0.523
Post-dilatation performed	23(65.7)	17(77.3)	0.391
Nominal diameter of post-dilatation balloon(mm)	3.16±0.37	3.29±0.30	0.234
Maximal pressure during post-dilatation(atm)	15.65±3.24	16.94±3.88	0.260
Expected diameter of post-dilatation balloon(mm)	3.29±0.39	3.39±0.32	0.431
Expected diameter of post-dilatation/device balloon	3.40±0.33	3.37±0.29	0.732
Expected balloon-artery ratio	1.21±0.13	1.17±0.12	0.176
Post-procedural patient related factors	35 patients	21 patients	
Mean LDL cholesterol(mmol/L)	2.35±0.62	2.52±0.84	0.374

BMI=body mass index, BRS=bioresorbable scaffold, DES=drug-eluting stent, LDL=low-density lipoprotein, MI=myocardial infarction, PCI=percutaneous coronary intervention.

Endothelial shear stress: comparison between devices and serial evolution

Central illustration, Table 2, Figure-3 and Online Figure 1 show changes in the lumen, plaque, vessel area (mm^2) and plaque burden (%) over 3 years among the tertiles of ESS post-procedure (~ 0.658 ; $0.658 \sim 0.953$; $0.953 \sim \text{Pa}$). In BRS arm, the lowest-tertile of ESS showed a decrease in lumen area as opposed to late lumen enlargement in the intermediate- and the highest-tertiles. There is a significant difference in plaque-media area, increasing in BRS ($+0.64 \pm 1.10 \text{mm}^2$) and decreasing in Xience ($-0.46 \pm 1.22 \text{mm}^2$).



Central illustration. Intravascular ultrasound data of patient number 107836-1007 in the ABSRORB II trial translated into a cartoon. In Absorb bioresorbable scaffold (BRS), due to low radial force, the lumen area post-implantation is smaller than in the metallic stent. Due to smaller lumen area in BRS, wall shear stress is relatively higher in BRS than in metallic stent immediately post-implantation. At follow up, with the dismantling of the scaffold higher shear stress may play a more predominant role in the remodeling process of the vessel and lumen area in the Absorb scaffold. On the other hand, in metallic stents, there is no opportunity of such kind of structural modification of the vessel wall due to the fixed metallic cage. Conversely, the neointimal hyperplasia intrastent can only reduce the lumen.

In BRS, increase in plaque area from post-procedure to 3-year follow up was not different among the three tertiles of ESS post-procedure and vessel area showed a larger increase in the highest-tertile as compared to the lowest-tertile of ESS post-procedure. Consequently, the lowest tertile of ESS post-procedure showed an increase in plaque burden ($+5.36 \pm 8.98\%$) significantly larger than intermediate ($1.86 \pm 8.09\%$) or highest ($0.72 \pm 7.46\%$) tertile of ESS post-procedure. In contrast, in DES arm, there was no significant difference in change in the lumen,

plaque vessel areas and plaque burden amongst the 3 tertiles of ESS post-procedure (**Figure 3**).

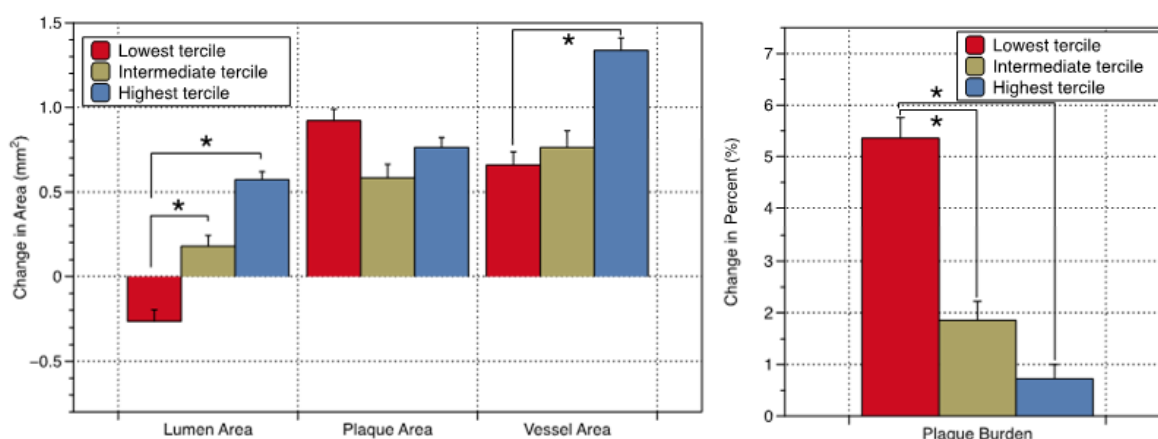
The relationship between vessel area, lumen area and plaque burden at the frame level in case of expansive remodeling is presented in the **Figure 4**.

Table 2. Changes in lumen, plaque, vessel area and plaque burden in matched frames stratified by median ESS.

BRS (n=741 frames)	Range (Pa)	Lowest tercile	Intermediate tercile	Highest tercile	p-value*	
					Lowest vs. Intermediate tercile	Lowest vs. Highest tercile
Median ESS	0.658~0.953	~0.658	0.658~0.953	0.953~		
Number of frames		516	497	728		
Delta Lumen Area (mm ²)		-0.26±1.46	0.18±1.39	0.57±1.28	0.003	<0.001
Delta Plaque Area (mm ²)		0.92±1.54	0.58±1.79	0.76±1.59	0.249	0.283
Delta Vessel Area (mm ²)		0.66±1.79	0.76±2.19	1.34±1.99	0.779	0.036
Delta Plaque Burden (%)		5.36±8.98	1.86±8.09	0.72±7.46	0.011	<0.001
<hr/>						
DES (n=953 frames)	Range (Pa)	Lowest tercile	Intermediate tercile	Highest tercile	p-value*	
					Lowest vs. Intermediate tercile	Lowest vs. Highest tercile
Median ESS	0.658~0.953	~0.658	0.658~0.953	0.953~		
Number of frames		388	397	168		
Delta Lumen Area(mm ²)		-0.04±0.90	-0.16±0.84	-0.23±0.73	1.000	1.000
Delta Plaque Area(mm ²)		-0.01±2.06	-0.30±1.51	-0.21±1.85	0.487	1.000
Delta Vessel Area(mm ²)		-0.05±2.05	-0.46±1.70	-0.43±1.79	0.367	1.000
Delta Plaque Burden (%)		0.77±7.73	0.12±5.53	0.22±6.74	1.000	1.000

*P-values were by linear mixed model, corrected for multiple comparison. ESS=endothelial shear stress.

Absorb (n=1741 frames)



Xience (n=953 frames)

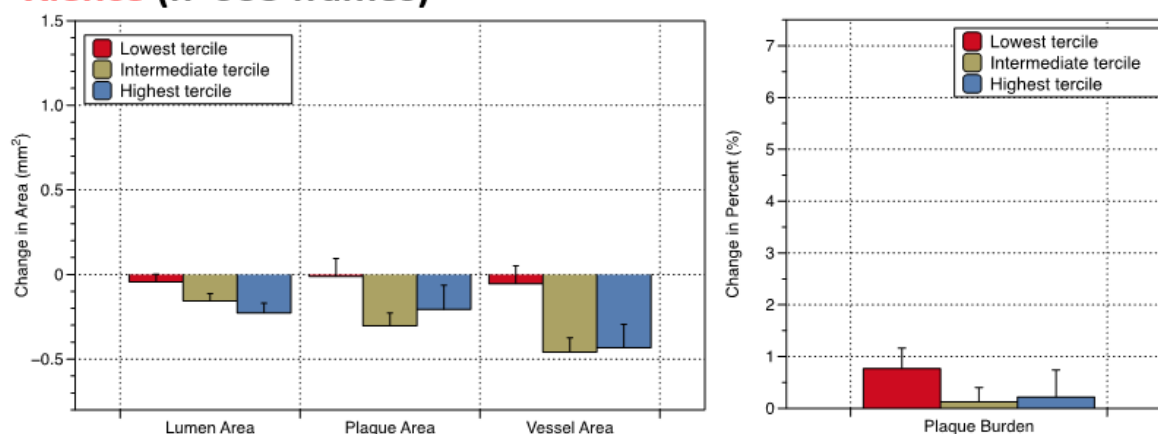


Figure 3. Changes in lumen, plaque, vessel area and plaque burden in matched frame stratified by tertiles of median-ESS post-procedure. Stratification by tertiles of median ESS post-procedure: $\sim 0.658, 0.658 \sim 0.953, 0.953 \sim Pa$. Thresholds of tertiles were derived from frame-level data with all lesions pooled. There were 1741 and 953 frames (2:1 randomization) with paired ESS values post-procedure and at 3 years in the BRS and DES arm, respectively.

*P-value < 0.05 (by linear mixed model, corrected for multiple comparisons) ESS = endothelial shear stress.

Predictors of vessel remodeling

The results of univariate analysis predicting vessel area change (mm²) over 3-years in linear mixed-model were tabulated in **Online Table 3**. Following forced entry of variables with $p < 0.10$ in univariate analyses as well as median-ESS post-procedure, a multivariate model was constructed. Overall, smaller vessel area, larger lumen area, higher plaque burden post-procedure, and higher median ESS post-procedure were independently associated with expansive remodeling in matched frames (**Table 3, Figure 5**). Only in BRS, younger age was an additional significant predictor of expansive remodeling.

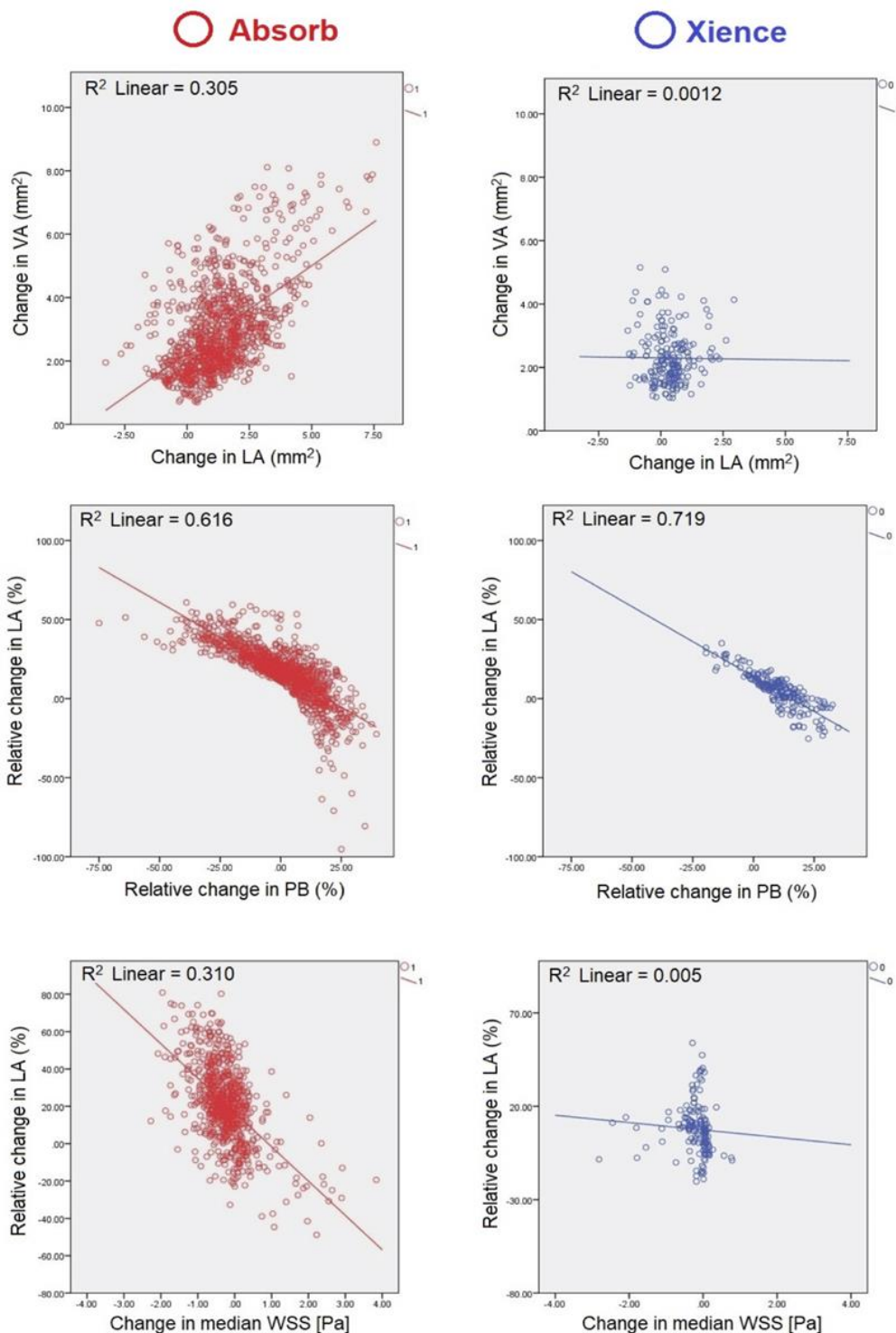


Figure 4. Correlations between change in vessel and lumen area, between relative change in lumen area and relative change in plaque burden, and between relative change in lumen area and change in median shear stress, in patients exhibiting expansive remodeling in Absorb and metallic Xience groups, respectively (analysis at frame level).

Table 3. Multivariate model predicting vessel area change (mm²) over 3 years.

	Overall			Absorb			Xience		
	Coefficient	95% CI	P value	Coefficient	95% CI	P value	Coefficient	95% CI	P value
Age (per year)	-0.07	(-0.21 , 0.07)	0.329	-0.22	(-0.39 , -0.04)	0.016	0.09	(-0.10 , 0.28)	0.330
Female	0.57	(-2.61 , 3.75)	0.715	0.54	(-2.10 , 3.19)	0.676	3.11	(-6.69 , 12.92)	0.510
Absorb implantation	0.04	(-2.67 , 2.75)	0.975				NA		
IVUS post-procedure									
Vessel area (per mm ²)	-0.74	(-0.92 , -0.56)	<0.001	-0.70	(-0.92 , -0.48)	<0.001	-0.92	(-1.27 , -0.56)	<0.001
Lumen area (per mm ²)	0.78	(0.43 , 1.13)	<0.001	0.66	(0.19 , 1.12)	0.006	1.16	(0.59 , 1.73)	<0.001
Plaque area (per mm ²)					NA*				
Plaque burden (per %)	0.10	(0.06 , 0.15)	<0.001	0.10	(0.05 , 0.15)	<0.001	0.14	(0.05 , 0.24)	0.002
Median ESS post-procedure (per Pa)	0.45	(0.01 , 0.89)	0.046	0.59	(0.16 , 1.01)	0.009	0.21	(-1.12 , 1.54)	0.740

* not shown because it is redundant.

CI=confidence interval, ESS=endothelial shear stress, IVUS=intravascular ultrasound, NA=not available

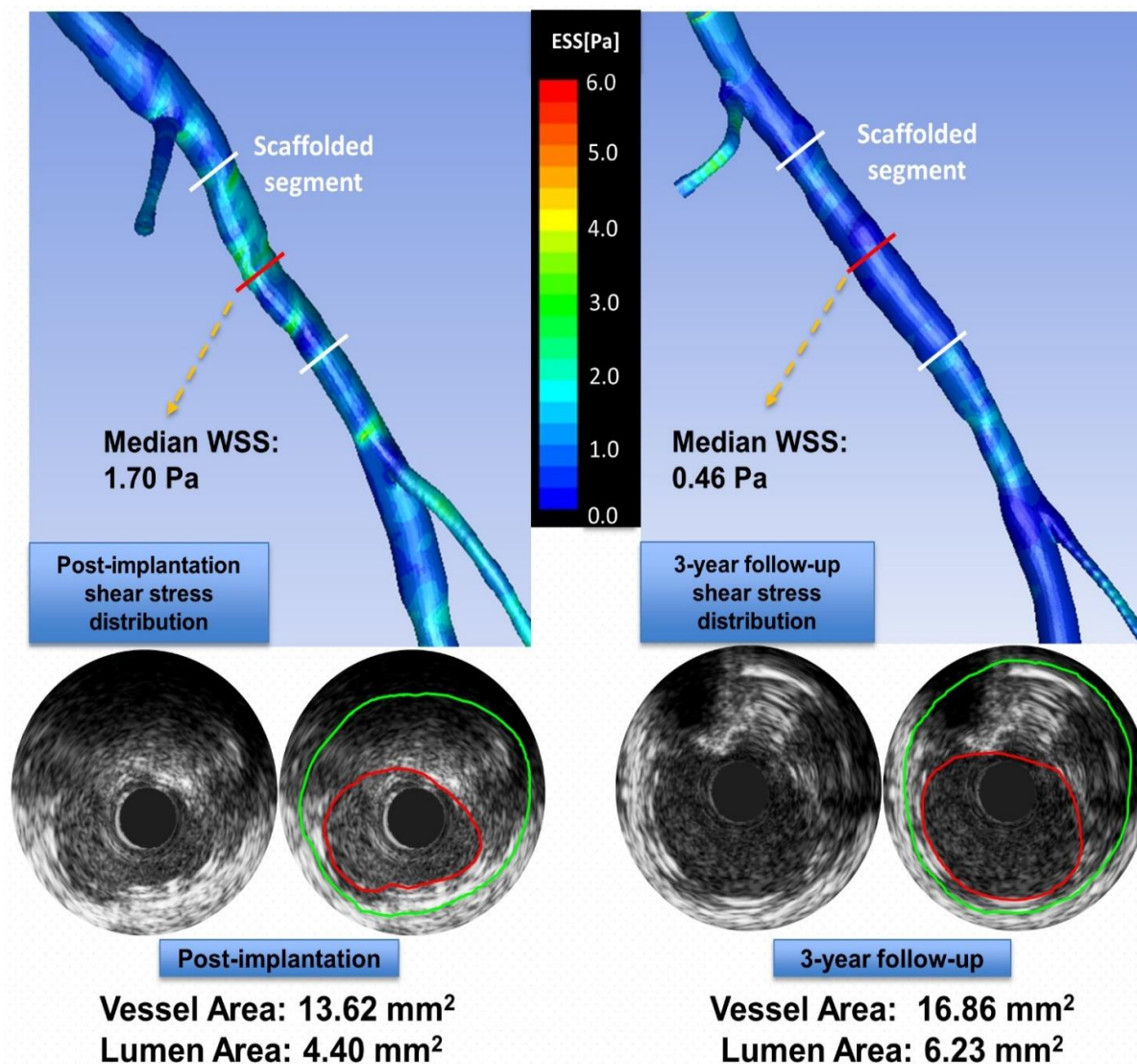


Figure 5. Post-procedural endothelial shear stress and changes in IVUS parameters during 3 years in a case of expansive remodeling in BRS. Upper panels show 3D representation of endothelial shear stress (ESS) distribution post-procedure(left) and at 3-year(right) in a vessel implanted with bioresorbable scaffold (BRS). The scaffolded segment is located between white lines. The red line indicates matched sites whose cross-sectional images are shown in the lower panels. At this cross-section, median ESS post-procedure was 1.70Pa (highest tercile in the analysis population). Subsequently, vessel area increased by 3.24mm² with lumen enlargement of 1.83mm².

DISCUSSION

Although the bioresorbable scaffold Absorb is no longer commercially available, it is the BRS that has been the most widely used and studied, and long-term follow up of COMPARE, AIDA, ABSORB-III and -IV have still to be reported. The Absorb device is representative of a generic or class effect that will be encountered with other BRS. Any fundamental pathophysiological mechanisms investigated on this archetype of BRS, such as dismantling, remodeling, late lumen enlargement, will be probably replicated in novel scaffolds with thinner struts currently in trial. However, the Absorb remains the first historical device in which the effect of shear stress on scaffolded vessel segments has been investigated.

The main findings of the present study were: 1) The vessel segments implanted with BRS demonstrated a higher ESS as compared to those with DES both post-procedure and at 3 years; 2) Overall, higher median-ESS, smaller vessel area, larger lumen area, and higher plaque burden post-procedure were independently associated with expansive remodeling at long term follow-up; 3) Only in BRS, younger age was an additional significant predictor of expansive remodeling. To the best of our knowledge, this is the first study investigating ESS in BRS and DES in the context of a randomized trial.

The implication of “macro” shear stress assessed by IVUS

In ABSORB-II, we tried to unravel the phenotype complexity of the remodeling of the lumen, plaque-media and vessel area. The lower resolution of IVUS (80-150 μ m), as compared to optical coherence tomography (OCT) (10-20 μ m), allowed us to explore ESS only in a “macro” hemodynamic environment rather than in a “micro” environment only analyzable by OCT.[19] OCT was not mandated in the ABSORB-II trial, however, in the pilot study (Absorb Cohort-B) prior to the randomized trial, the assessment of acute and chronic(5 years) shear stress between and on top of the struts had been carefully documented by OCT.[20]

However, remodeling of vessel area and change in plaque burden cannot be captured by OCT that can only analyze endoluminal lining, whereas IVUS can measure plaque, media and vessel area (EEM area). Although bioresorption is not completed at 36 months, comparative analysis of the remodeling in Xience and Absorb at 36 months published by our group and clearly indicated that major constrictive or expansive remodeling already occurred at 3-years.[2] The

current study tried to elucidate impact of the shear stress post implantation on caged and uncaged vessel wall.

When compared to DES, smaller post-procedural lumen area in BRS (**Online Table 2**) was expected to be the main determinant of post-procedural higher “macro” ESS by QCA-IVUS-derived 3D-coronary artery model. At 3-year follow-up, mean lumen area exhibited an increase in BRS and a decrease in DES which resulted in comparable mean lumen area with the two devices (**Central illustration**).

In BRS, significant increase in vessel and lumen area at 3-years follow up was documented in vessels with the highest tercile of shear stress post-procedure. A significant difference in plaque-media area, increasing in BRS ($+0.64 \pm 1.10 \text{ mm}^2$) and decreasing in Xience ($-0.46 \pm 1.22 \text{ mm}^2$), has to be underlined. This difference in behavior is highly significant ($p < 0.001$) and may be explained by the shrinking of the primary and short lasting inflammatory reaction due to the barotrauma in the metallic drug eluting stent[2], while in BRS the secondary long lasting phase of inflammatory reaction is mainly due to the bioresorption of the polymer and generates an increase in plaque-media area (plaque burden) that contributes certainly to the increase in the vessel area.[21]

In contrast, in the DES arm, there was no significant difference in change in the lumen, plaque vessel area and plaque burden amongst the 3 terciles of ESS post-procedure. In BRS, increase in mean lumen area resulted in lowering of the median ESS over 3-years, which is expected from the standard fluid dynamic laws, and illustrated in **Figure 5**.[22]

Predictors of vessel remodeling

Endothelial shear stress post-procedure

Higher ESS was one of the independent predictors of expansive remodeling. This is in line with other previous studies in native vessels.[23-25] High ESS can stimulate the production of metalloproteinases by macrophages, which could contribute to expansive remodeling[26, 27]. On the contrary, in lesions implanted with bare metal stent or DES, ESS did not impact on vessel remodeling in IBIS-4.[28] It is of note that BRS had p -value < 0.10 in univariate analysis; however, in the multivariate model, it was not retained while ESS was with a significant p -value. This fact indicates that, the device type would impose restriction on remodeling (i.e., metallic DES would restrict remodeling whereas BRS would not). The dismantling of the

polymeric structure and the inflammatory reaction around the polymeric struts permit the shear stress to act on the vessel wall in BRS. The durable skeleton of the metallic stent could not provide such a flexible “environment” for the shear stress precluding its influence on the vessel wall. Instead of outward expansive remodeling with potentially late lumen enlargement, seen with the polymeric scaffold, in metallic stents relatively high ESS could only prevent an exuberant intrastent neointimal hyperplasia. Lower ESS had raising effect for vessel area however compared to the higher ESS it was significantly less. Nevertheless, lower ESS had decremental effect on the lumen area contrary to higher ESS.

On the other hand, to explain the vessel long-term behaviors only with ESS value measured at a one-time point *-post-implantation ESS or ESS at 3-years-* may be problematic. Due to its nature, shear stress is not a static entity. It has a dynamic behavior which closely depends on the temporal and spatial changes within the flow area[29]; teleologically, the response to a decreased shear stress post-implantation of the scaffold will be a *narrowing* of the vessel lumen in order to restore the shear stress in its physiological range. Conversely, high post-implantation shear stress will regulate mechanotransduction processes that will result in an enlargement of lumen and vessel area of the scaffold, -as soon as its mechanical integrity has subsided- to eventually decrease the shear stress level back to physiological range (1-7Pa) [30]

Post-procedural vessel, lumen area and plaque burden

Smaller post-procedural vessel area was independently associated with expansive remodeling. A similar relationship was already observed by Zarins et al in pressure-perfusion-fixed postmortem adult human coronary arteries.[31] In other words, the smaller the vessel is, the more capable it is of expansive remodeling. In the Absorb group there is some relationship between change in vessel area and lumen area, between lumen area and plaque burden and relative change in lumen area and ESS($R^2=0.310$). In the Xience group, such relationship between lumen area and wall shear stress($R^2=0.005$) does not exist (**Figure 4**).

Larger lumen area post-procedure is another independent predictor of expansive remodeling. Larger lumen area could be either due to good scaffold/stent expansion or large vessel size. In our previous study, with a sample size of 501 patient, high balloon-artery ratio was a predictor of expansive remodeling[2], and could have resulted in larger lumen area.

Glagov et al. reported that lumen area is preserved until plaque burden reaches 40-50% of the vessel area, as a result of a compensatory expansive remodeling[4]. However, beyond the value of 40-50%, the compensatory expansive remodeling gets exhausted with subsequent

reduction in lumen area, at the pro rata of the increase in plaque burden. Post-procedural plaque burden in the present study population was on average $54.6 \pm 6.0\%$ (BRS) and $54.3 \pm 5.5\%$ (DES) in both arms.

Age and capability of remodeling

The coefficient of age (per year) in the multivariate model was negative with significant p-value only in the stratified analysis in BRS. In other words, younger patients are more prone to show expansive remodeling only in BRS. This could be explained by the fact that matrix metalloproteinase-9, an enzyme which enhances expansive remodeling, decreases as a function of age.[32] Apparently, the relationship of age and remodeling is weaker in the vessel segments caged by metallic DES.

Tissue component

In our previous report analyzing vessel remodeling at the device level, pre-procedural necrotic core was significantly associated with expansive remodeling.[2] However, in the present study, none of the tissue components documented by IVUS-VH was retained as a significant predictor of expansive vessel remodeling. A study with larger sample size may unravel interactions between tissue composition, vessel remodeling and ESS.

Limitations

The retrospective nature of this post-hoc study may be subject to a potential selection bias, and thus, the reported results should be regarded as hypothesis-generating. There were also too few events to allow construction of a comprehensive multivariable model that would have explored the value of ESS in predicting clinical outcomes. Although ESS analyses were attempted on the entire randomized population of ABSORB II (n=501patients), due to eligibility criteria for each step in the study and technical difficulties, a large number of patients had to be excluded. Similarly, in the PROSPECT study, researchers could only include 14% of the original cohort in the ESS sub-study for comparable reasons.[33]

Assumptions are inevitable in computational flow modelling. Our models include side branches and non-Newtonian blood behavior – both of which are often simplified more – and the only major assumption was the steady state flow condition. It has been shown that steady flow condition captures well the time-averaged shear stress [34] and is used as an effective predictor of disease progression.[17] Pulsatile flow condition would be required in case

oscillatory nature of flow and shear stress is of interest [35], which is warranted as our future study.

CFD was applied to compute ESS in the stented segments, and several assumptions were made, potentially effecting the accuracy of the computations. The most prominent assumption deals with applying scaling laws to estimate the flow rates in the main branch and the side branches. This assumption can influence average ESS values up to 8%. [14] It has to be noted though that the largest impact was seen near side branches, so we expect a smaller effect in the stented segments.

In future studies investigating the effect of ESS and vessel remodeling, a hybrid IVUS-OCT catheter may be preferred, as it could measure concomitantly lumen area, vessel area, plaque-media area and micro flow disturbance with precise co-registration, as recommended in the expert consensus on ESS. [30]

What is already known?

In bioresorbable scaffold (BRS) due to lower radial force, the lumen area post-implantation is smaller than metallic stent. Due to smaller lumen area in BRS, endothelial shear stress (ESS) is relatively higher in BRS than in metallic stent. At follow up, with higher shear stress and the degradation of the polymeric scaffold, the vessel remodels and the vessel area starts to expand. On the other hand, in metallic stents, there is no such opportunity of structural modification in the vessel wall due to the fixed metallic cage. Instead, the neointimal hyperplasia increases inside the metallic cage with a reduction in lumen area. Shear stress has impact on neointimal hyperplasia in the metallic caged vessel segments.

What does this study add?

Shear stress had significant influence on the expansive behavior of the BRS implanted vessels whereas no such effect was noted in metallic caged vessel segments. The present study is the first to reveal that high shear stress may have impact on expansion of the vessels instrumented with polymeric scaffolds.

How might this impact on clinical practice?

The development in the 3D vessel reconstruction and 3D CFD modeling may facilitate virtually the planning of stent/scaffold implantation prior to the PCI in the cath-lab. In the future with ultra-high-speed computers, "online CFD simulation" may provide assessment of the optimized implantation of the polymeric scaffold. Virtual stenting enables planning and

selection of optimal treatment strategy. Post-implantation shear stress assessment may provide insights about hemodynamic micro-environment and this may shed light on the potential vascular behaviors at long-term follow up that can alert the clinicians for any potential adverse events.

CONCLUSIONS

Coronary segments implanted with BRS were exposed to higher ESS post-procedure as compared to DES. Post-procedural higher median ESS, smaller vessel area, and higher plaque burden were independent predictors of expansive remodeling and late lumen enlargement at 3 years. Only in the BRS, younger age was an additional significant predictor of expansive remodeling.

Conflict of interest

None of the author declared any conflict of interest related with the current manuscript.

Financial support

Dr. Tenekecioglu has a research grant from TUBITAK (The Research and Scientific Council of Turkey). Dr. Sabaté reports grants and personal fees from Abbott Vascular. Dr. Piek reports non-financial support from Member medical advisory board Abbott Vascular, personal fees and non-financial support from Consultant Philips/Volcano. Dr. Wykrzykowska reports grants and personal fees from Abbott. Johan H.C. Reiber is CEO of; and Pieter Kitslaar is an employee of Medis medical imaging systems Bv, Leiden. Dr. Chevalier reports personal fees from Abbott Vascular; personal fees from Cordis, personal fees from Biotronik, from Medtronic, personal fees from Terumo, other from CERC. Y. Onuma is a member of the advisory board of Abbott Vascular. P.W. Serruys is a member of the advisory board of Abbott Vascular. All the other authors have nothing to declare.

Author contributions

Design of the study: Erhan Tenekecioglu, Yuki Katagiri, Frank Gijzen, Kerem Pekkan, Yoshinobu Onuma, Ryo Torii, Patrick W. Serruys, Kuniaki Takahashi, Pieter Kitslaar, Jouke Dijkstra, Johan H.C. Reiber

Data collection: Dariusz Dudek, Angel Cequier, Didier Carrié, Andrés Iñiguez, Rinse Johannes van der Schaaf, Marcello Dominici, Ad J. van Boven, Steffen Helqvist, Manel Sabaté, Andreas

Baumbach, Jan J. Piek, Frank Gijsen, Kerem Pekkan, Joanna J. Wykrzykowska, Bernard Chevalier, Patrick W. Serruys

Drafting the manuscript: Erhan Tenekecioglu, Yuki Katagiri, Frank Gijsen, Yoshinobu Onuma, Ryo Torii, Patrick W. Serruys

Critical revision of the manuscript: Erhan Tenekecioglu, Yuki Katagiri, Frank Gijsen, Yoshinobu Onuma, Ryo Torii, Mariusz Tomaniak, Dilek Ural, Kerem Pekkan, Christos V. Bourantas, Patrick W. Serruys

Statistical analysis: Yuki Katagiri, Erhan Tenekecioglu, Yoshinobu Onuma

Final revision of the manuscript: Erhan Tenekecioglu, Yuki Katagiri, Frank Gijsen, Yoshinobu Onuma, Dilek Ural, Kerem Pekkan, Ryo Torii, Patrick W. Serruys

REFERENCES

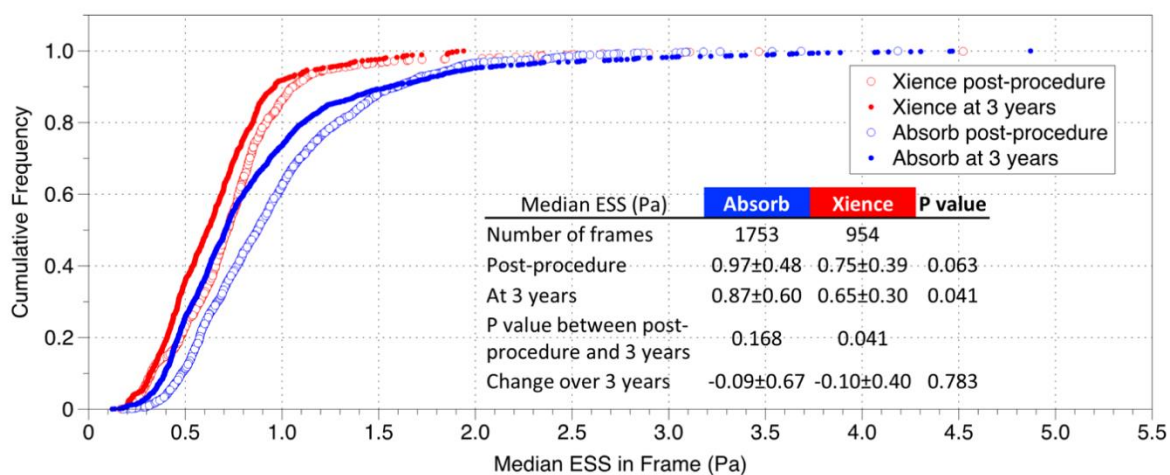
1. Serruys PW, Garcia-Garcia HM, Onuma Y: From metallic cages to transient bioresorbable scaffolds: change in paradigm of coronary revascularization in the upcoming decade? *European heart journal* 2012, 33(1):16-25b.
2. Serruys PW, Katagiri Y, Sotomi Y, Zeng Y, Chevalier B, van der Schaaf RJ, Baumbach A, Smits P, van Mieghem NM, Bartorelli A et al: Arterial Remodeling After Bioresorbable Scaffolds and Metallic Stents. *J Am Coll Cardiol* 2017, 70(1):60-74.
3. Galis ZS, Khatri JJ: Matrix metalloproteinases in vascular remodeling and atherogenesis: the good, the bad, and the ugly. *Circulation research* 2002, 90(3):251-262.
4. Glagov S, Weisenberg E, Zarins CK, Stankunavicius R, Kolettis GJ: Compensatory enlargement of human atherosclerotic coronary arteries. *The New England journal of medicine* 1987, 316(22):1371-1375.
5. Van Mieghem CA, Bruining N, Schaar JA, McFadden E, Mollet N, Cademartiri F, Mastik F, Ligthart JM, Granillo GA, Valgimigli M et al: Rationale and methods of the integrated biomarker and imaging study (IBIS): combining invasive and non-invasive imaging with biomarkers to detect subclinical atherosclerosis and assess coronary lesion biology. *Int J Cardiovasc Imaging* 2005, 21(4):425-441.
6. Resnick N, Yahav H, Shay-Salit A, Shushy M, Schubert S, Zilberman LC, Wofovitz E: Fluid shear stress and the vascular endothelium: for better and for worse. *Progress in biophysics and molecular biology* 2003, 81(3):177-199.
7. Heil M, Schaper W: Influence of mechanical, cellular, and molecular factors on collateral artery growth (arteriogenesis). *Circulation research* 2004, 95(5):449-458.
8. Serruys PW, Chevalier B, Sotomi Y, Cequier A, Carrié D, Piek JJ, Van Boven AJ, Dominici M, Dudek D, McClean D et al: Comparison of an everolimus-eluting bioresorbable scaffold with an everolimus-eluting metallic stent for the treatment of coronary artery stenosis (ABSORB II): a 3 year, randomised, controlled, single-blind, multicentre clinical trial. *The Lancet*, 388(10059):2479-2491.
9. Mintz GS, Nissen SE, Anderson WD, Bailey SR, Erbel R, Fitzgerald PJ, Pinto FJ, Rosenfield K, Siegel RJ, Tuzcu EM et al: American College of Cardiology Clinical Expert Consensus Document on Standards for Acquisition, Measurement and Reporting of Intravascular Ultrasound Studies (IVUS). A report of the American College of Cardiology Task Force on Clinical Expert Consensus Documents. *Journal of the American College of Cardiology* 2001, 37(5):1478-1492.
10. Serruys PW, Degertekin M, Tanabe K, Russell ME, Guagliumi G, Webb J, Hamburger J, Rutsch W, Kaiser C, Whitbourn R et al: Vascular responses at proximal and distal edges of paclitaxel-eluting stents: serial intravascular ultrasound analysis from the TAXUS II trial. *Circulation* 2004, 109(5):627-633.
11. Muramatsu T, Garcia-Garcia HM, Brugaletta S, Heo JH, Onuma Y, Fedewa RJ, Nair A, Ozaki Y, Serruys PW: Reproducibility of intravascular ultrasound radiofrequency data analysis (virtual histology) with a 45-MHz rotational imaging catheter in ex vivo human coronary arteries. *Journal of cardiology* 2015, 65(2):134-142.
12. Papafaklis MI, Bourantas CV, Farooq V, Diletti R, Muramatsu T, Zhang Y, Fotiadis DI, Onuma Y, Garcia Garcia HM, Michalis LK et al: In vivo assessment of the three-dimensional haemodynamic micro-environment following drug-eluting bioresorbable vascular scaffold implantation in a human coronary artery: fusion of frequency domain optical coherence tomography and angiography. *EuroIntervention*

: journal of EuroPCR in collaboration with the Working Group on Interventional Cardiology of the European Society of Cardiology 2013, 9(7):890.

13. Manbachi A, Hoi Y, Wasserman BA, Lakatta EG, Steinman DA: On the shape of the common carotid artery with implications for blood velocity profiles. *Physiological measurement* 2011, 32(12):1885-1897.
14. van der Giessen AG, Groen HC, Doriot PA, de Feyter PJ, van der Steen AF, van de Vosse FN, Wentzel JJ, Gijssen FJ: The influence of boundary conditions on wall shear stress distribution in patients specific coronary trees. *Journal of biomechanics* 2011, 44(6):1089-1095.
15. Seo T, Schachter LG, Barakat AI: Computational study of fluid mechanical disturbance induced by endovascular stents. *Ann Biomed Eng* 2005, 33(4):444-456.
16. Schrauwen JT, Schwarz JC, Wentzel JJ, van der Steen AF, Siebes M, Gijssen FJ: The impact of scaled boundary conditions on wall shear stress computations in atherosclerotic human coronary bifurcations. *American journal of physiology Heart and circulatory physiology* 2016, 310(10):H1304-1312.
17. Stone PH, Saito S, Takahashi S, Makita Y, Nakamura S, Kawasaki T, Takahashi A, Katsuki T, Nakamura S, Namiki A et al: Prediction of progression of coronary artery disease and clinical outcomes using vascular profiling of endothelial shear stress and arterial plaque characteristics: the PREDICTION Study. *Circulation* 2012, 126(2):172-181.
18. Sotomi Y, Ishibashi Y, Suwannasom P, Nakatani S, Cho YK, Grundeken MJ, Zeng Y, Tateishi H, Smits PC, Barragan P et al: Acute Gain in Minimal Lumen Area Following Implantation of Everolimus-Eluting ABSORB Biodegradable Vascular Scaffolds or Xience Metallic Stents: Intravascular Ultrasound Assessment From the ABSORB II Trial. *JACC Cardiovasc Interv* 2016, 9(12):1216-1227.
19. Thondapu V, Tenekecioglu E, Poon EKW, Collet C, Torii R, Bourantas CV, Chin C, Sotomi Y, Jonker H, Dijkstra J et al: Endothelial shear stress 5 years after implantation of a coronary bioresorbable scaffold. *European heart journal* 2018, 39(18):1602-1609.
20. Tenekecioglu E, Torii R, Katagiri Y, Asano T, Modolo R, Miyazaki Y, Chichareon P, Poon EKW, Gijssen F, Thondapu V et al: Early strut protrusion and late neointima thickness in Absorb bioresorbable scaffold: A serial wall shear stress analysis up to five years. *EuroIntervention : journal of EuroPCR in collaboration with the Working Group on Interventional Cardiology of the European Society of Cardiology* 2018.
21. Otsuka F, Pacheco E, Perkins LE, Lane JP, Wang Q, Kamberi M, Frie M, Wang J, Sakakura K, Yahagi K et al: Long-term safety of an everolimus-eluting bioresorbable vascular scaffold and the cobalt-chromium XIENCE V stent in a porcine coronary artery model. *Circulation Cardiovascular interventions* 2014, 7(3):330-342.
22. Klabunde RE: *Cardiovascular physiology concepts*, 2nd edn. Philadelphia, PA: Lippincott Williams & Wilkins/Wolters Kluwer; 2012.
23. Stone PH, Coskun AU, Kinlay S, Popma JJ, Sonka M, Wahle A, Yeghiazarians Y, Maynard C, Kuntz RE, Feldman CL: Regions of low endothelial shear stress are the sites where coronary plaque progresses and vascular remodelling occurs in humans: an in vivo serial study. *European heart journal* 2007, 28(6):705-710.
24. Samady H, Eshtehardi P, McDaniel MC, Suo J, Dhawan SS, Maynard C, Timmins LH, Quyyumi AA, Giddens DP: Coronary artery wall shear stress is associated with progression and transformation of atherosclerotic plaque and arterial remodeling in patients with coronary artery disease. *Circulation* 2011, 124(7):779-788.

25. Corban MT, Eshtehardi P, Suo J, McDaniel MC, Timmins LH, Rassoul-Arzrumly E, Maynard C, Mekonnen G, King S, 3rd, Quyyumi AA et al: Combination of plaque burden, wall shear stress, and plaque phenotype has incremental value for prediction of coronary atherosclerotic plaque progression and vulnerability. *Atherosclerosis* 2014, 232(2):271-276.
26. Death AK, Nakhla S, McGrath KC, Martell S, Yue DK, Jessup W, Celermajer DS: Nitroglycerin upregulates matrix metalloproteinase expression by human macrophages. *J Am Coll Cardiol* 2002, 39(12):1943-1950.
27. Slager CJ, Wentzel JJ, Gijzen FJ, Schuurbiers JC, van der Wal AC, van der Steen AF, Serruys PW: The role of shear stress in the generation of rupture-prone vulnerable plaques. *Nature clinical practice Cardiovascular medicine* 2005, 2(8):401-407.
28. Bourantas CV, Raber L, Zaugg S, Sakellarios A, Taniwaki M, Heg D, Moschovitis A, Radu M, Papafaklis MI, Kalatzis F et al: Impact of local endothelial shear stress on neointima and plaque following stent implantation in patients with ST-elevation myocardial infarction: A subgroup-analysis of the COMFORTABLE AMI-IBIS 4 trial. *International journal of cardiology* 2015, 186:178-185.
29. Koskinas KC, Feldman CL, Chatzizisis YS, Coskun AU, Jonas M, Maynard C, Baker AB, Papafaklis MI, Edelman ER, Stone PH: Natural history of experimental coronary atherosclerosis and vascular remodeling in relation to endothelial shear stress: a serial, in vivo intravascular ultrasound study. *Circulation* 2010, 121(19):2092-2101.
30. Gijzen F, Katagiri Y, Barlis P, Bourantas C, Collet C, Coskun U, Daemen J, Dijkstra J, Edelman E, Evans P et al: Expert recommendations on the assessment of wall shear stress in human coronary arteries: existing methodologies, technical considerations, and clinical applications. *European heart journal* 2019.
31. Zarins CK, Weisenberg E, Kolettis G, Stankunavicius R, Glagov S: Differential enlargement of artery segments in response to enlarging atherosclerotic plaques. *J Vasc Surg* 1988, 7(3):386-394.
32. Bonnema DD, Webb CS, Pennington WR, Stroud RE, Leonardi AE, Clark LL, McClure CD, Finklea L, Spinale FG, Zile MR: Effects of age on plasma matrix metalloproteinases (MMPs) and tissue inhibitor of metalloproteinases (TIMPs). *J Card Fail* 2007, 13(7):530-540.
33. Stone PH, Maehara A, Coskun AU, Maynard CC, Zaromytidou M, Siasos G, Andreou I, Fotiadis D, Stefanou K, Papafaklis M et al: Role of Low Endothelial Shear Stress and Plaque Characteristics in the Prediction of Nonculprit Major Adverse Cardiac Events: The PROSPECT Study. *JACC Cardiovascular imaging* 2018, 11(3):462-471.
34. Tenekecioglu E, Torii R, Bourantas C, Crake T, Zeng Y, Sotomi Y, Onuma Y, Yilmaz M, Santoso T, Serruys PW: Preclinical assessment of the endothelial shear stress in porcine-based models following implantation of two different bioresorbable scaffolds: effect of scaffold design on the local haemodynamic micro-environment. *EuroIntervention : journal of EuroPCR in collaboration with the Working Group on Interventional Cardiology of the European Society of Cardiology* 2016, 12(10):1296.
35. Kok AM, Molony DS, Timmins LH, Ko YA, Boersma E, Eshtehardi P, Wentzel JJ, Samady H: The Influence of Multidirectional Shear Stress on Plaque Progression and Composition Changes in Human Coronary Arteries. *EuroIntervention : journal of EuroPCR in collaboration with the Working Group on Interventional Cardiology of the European Society of Cardiology* 2019.

Online Supplement



Online Figure 1. Cumulative frequency curves of endothelial shear stress (ESS) between devices post-procedure and at follow-up (frame-level statistics with all lesions pooled). Post-procedure median ESS was higher in the bioresorbable scaffold (BRS) arm, although the difference did not reach statistical significance. At 3 years, median ESS at frame level was significantly higher in the BRS arm than in the drug eluting stent (DES) arm. ESS post-procedure was evaluated at the frame level (pooled analysis). Statistical test was performed using linear mixed effect model taking into account clustering within a lesion. ESS= endothelial shear stress.)

Online Table 1. Results of QCA* post-procedure and at 3 years in study population.

	BRS (n=35)	DES (n=22)	P value
Post-procedure			
Mean Lumen Diameter (mm)	2.66±0.30	2.89±0.27	0.006
Minimum Lumen Diameter (mm)	2.22±0.31	2.49±0.31	0.002
Reference Vessel Diameter (mm)	2.67±0.33	2.78±0.29	0.213
Diameter Stenosis (%)	16.7±6.59	10.23±5.68	<0.001
At 3 years			
Mean Lumen Diameter (mm)	2.40±0.38	2.66±0.22	0.003
Minimum Lumen Diameter (mm)	1.96±0.42	2.27±0.27	0.006
Reference Vessel Diameter (mm)	2.49±0.38	2.67±0.27	0.070
Diameter Stenosis (%)	21.27±13.10	14.48±9.03	0.050
Change in 3 years			
Mean Lumen Diameter (mm)	-0.26±0.24	-0.24±0.24	0.713
Minimum Lumen Diameter (mm)	-0.26±0.31	-0.22±0.30	0.695
Reference Vessel Diameter (mm)	-0.19±0.20	-0.13±0.21	0.294
Diameter Stenosis (%)	4.34±13.46	3.81±8.82	0.878

*In-device analysis. BRS = bioresorbable scaffold, DES = drug-eluting stent, QCA = quantitative coronary angiography.

Online Table 2. Results of IVUS post-procedure and at 3 years in study population.

	BRS (n=35)	DES (n=22)	P value
Post-procedure			
Mean Vessel Area (mm ²)	12.78±3.20	14.97±2.98	0.012
Mean Lumen Area (mm ²)	5.73±1.30	6.76±1.25	0.005
Mean Plaque Area (mm ²)	7.05±2.19	8.21±2.09	0.052
Mean Plaque Burden (%)	54.6±6.0	54.3±5.5	0.851
Minimum Lumen Area (mm ²)	4.46±1.16	5.74±1.25	<0.001
At 3 years			
Mean Vessel Area (mm ²)	13.56±3.30	14.32±2.87	0.383
Mean Lumen Area (mm ²)	5.88±1.73	6.57±1.23	0.108
Mean Plaque Area (mm ²)	7.69±2.13	7.75±1.98	0.915
Mean Plaque Burden (%)	56.7±7.5	53.6±5.0	0.098
Minimum Lumen Area (mm ²)	4.27±1.40	5.41±1.48	0.005
Change in 3 years			
Mean Vessel Area (mm ²)	0.78±1.49	-0.66±1.64	0.001
Mean Lumen Area (mm ²)	0.14±1.12	-0.19±0.71	0.174
Mean Plaque Area (mm ²)	0.64±1.10	-0.46±1.22	0.001
Mean Plaque Burden (%)	2.1±5.7	-0.7±3.7	0.031
Minimum Lumen Area (mm ²)	-0.19±0.99	-0.33±1.21	0.641

BRS = bioresorbable scaffold, DES = drug-eluting stent, IVUS = intravascular ultrasound.

Online Table 3. Univariate analysis predicting vessel area change (mm²) in 3 years.

	Coefficient	95% CI	P value*
Patient characteristics			
Age (per year)	0.04	(0.00 , 0.08)	0.078
Female	1.38	(0.54 , 2.21)	0.002
Current smoker	-0.60	(-1.56 , 0.35)	0.202
Hypertension requiring medication	0.32	(-0.61 , 1.25)	0.490
Dyslipidemia requiring medication	-0.02	(-0.92 , 0.87)	0.962
Any diabetes	-0.33	(-1.43 , 0.77)	0.550
Diabetes treated with insulin	-0.56	(-2.35 , 1.23)	0.535
Prior MI	0.07	(-0.89 , 1.02)	0.891
Previous PCI	0.06	(-0.77 , 0.88)	0.889
Unstable angina	0.55	(-0.59 , 1.70)	0.337
BMI >30 (kg/m ²)	0.05	(-0.93 , 1.03)	0.916
Procedural characteristics			
Nominal diameter of pre-dilatation balloon (per mm)	0.44	(-0.56 , 1.43)	0.381
Maximal pressure during pre-dilatation (per atm)	-0.04	(-0.17 , 0.09)	0.550
BRS implantation	1.23	(0.50 , 1.97)	0.001
Nominal diameter of device (per mm)	-0.05	(-1.50 , 1.40)	0.945
Maximal pressure during device implantation (per atm)	0.05	(-0.11 , 0.20)	0.545
Expected diameter of device balloon (per mm)	0.18	(-1.22 , 1.58)	0.799
Post-dilatation performed	-0.50	(-1.36 , 0.37)	0.258
Nominal diameter of post-dilatation balloon (per mm)	0.23	(-1.12 , 1.58)	0.733
Maximal pressure during post-dilatation (per atm)	-0.06	(-0.20 , 0.07)	0.356
Expected diameter of post-dilatation balloon (per mm)	0.37	(-0.92 , 1.67)	0.563
Maximal expected diameter of balloon throughout procedure (per mm)	0.09	(-1.17 , 1.36)	0.883
balloon-artery ratio by maximal expected diameter of balloon throughout procedure > 1.25	0.60	(-0.23 , 1.42)	0.154
Post-procedural patient-related factors			
mean LDL cholesterol over 3 years (per mmol/L)	0.24	(-0.33 , 0.82)	0.402
DAPT continuation	-0.73	(-1.64 , 0.19)	0.117
ACE inhibitor/ARB continuation	-0.18	(-1.03 , 0.67)	0.668
Statin continuation	0.32	(-0.48 , 1.13)	0.425
Post-procedural IVUS			
Vessel area (per mm ²)	-0.35	(-0.43 , -0.27)	<0.001

(continued)

Lumen area (per mm ²)	-0.29	(-0.49	,	-0.09)	0.005
Plaque area (per mm ²)	-0.31	(-0.39	,	-0.22)	<0.001
Plaque burden (per %)	-0.06	(-0.09	,	-0.04)	<0.001
Post-procedural ESS							
Median ESS post-procedure (per Pa)	-0.02	(-0.66	,	0.62)	0.953
Minimum ESS post-procedure (per Pa)	-0.28	(-0.98	,	0.42)	0.419

The analysis was performed by linear mixed model taking into account clustering of frames within vessel. ACE = angiotensin conversion enzyme, ARB = angiotensin receptor blocker, BMI = body mass index, BRS = bioresorbable scaffold, CI = confidence interval, DAPT = dual antiplatelet therapy, DES = drug-eluting stent, ESS = endothelial shear stress, IVUS = intravascular ultrasound, LDL = low-density lipoprotein, MI = myocardial infarction, PCI = percutaneous coronary intervention.

Samenvatting en conclusies (Dutch)

Summary of the thesis

Conclusions

SAMENVATTING EN CONCLUSIES

Deel A: Bioresorbeerbare stents

Met de ontwikkeling van een biocompatibele polymeercoating zijn verschillende veiligheidsproblemen met betrekking tot metalen medicinale stents (=Drug Eluting Stent, DES) verholpen. Echter, late stenttrombose, neo-atherosclerose, allergische reacties en ontbrekende aanhechting blijven belangrijke problemen. Volledig bioresorbeerbare stents (BRS) zijn ontwikkeld om de nadelen van de DES op te lossen. De BRS kan bestaan uit verschillende materialen, met verschillende mechanische eigenschappen, waar de vaatwand na implantatie op verschillende manieren op reageert. De verschillende karakteristieken van verschillende BRS vragen daarom om specifieke implantatiemethodes en nacontroles.

Hoofdstuk 2 beschrijft het concept en de potentiële voordelen van BRS. De volledige resorptie van een volledig polymere stent vermindert het risico op late restenose, die zelfs bij de nieuwere generatie DES is waargenomen. Doordat de BRS minder stijf is kan hij zich beter vormen naar de bloedvatgeometrie. Andere positieve punten van de BRS zijn de mogelijkheid tot herstel van de vasoreactiviteit in het behandelde vaatsegment en de mogelijkheid tot niet-invasieve beeldvorming van de vaatwand zonder enige beeldartefacten. Echter, tijdens het implanteren van een BRS moet wel rekening gehouden worden met de specifieke mechanische kenmerken van de BRS. Dat houdt in dat bij het implanteren van een BRS met name bochtige vaatsegmenten en overmatige verkalking van de laesie vermeden dienen te worden om te voorkomen dat de stent na plaatsing loskomt van de vaatwand. De maat van de stent kan worden geselecteerd met behulp van kwantitatieve coronair angiografische metingen (QCA) waarbij zowel de proximale als distale maximale referentie diameters in acht genomen moeten worden. Voorafgaande aan de BRS-implantatie, is goede voorbereiding van het bloedvat van belang. Als eerste predilatatie van het letsel met behulp van een ballon, die dezelfde diameter heeft als de referentiediameter van het vat (een verhouding van 1:1 tussen ballon en referentie diameter) en daarna post-dilatatie met een niet-compliance ballon tot een diameter maximaal 0,5 mm groter dan de geïmplanteerde BRS. Tijdens de BRS-implantatie is intra-coronaire beeldvorming een *conditio sine qua non*. Optische coherentie tomografie (OCT) is de gerenommeerde visualisatie methode voor het beoordelen van de aanligging van de stent, dissecties van de vaatwand, thrombusvorming en stentbreuk.

Intracoronaire beeldvorming is de hoeksteen van de BRS-implantatie. Om het risico op complicaties na implantatie te beperken, mag de beoordeling van de implantatie met behulp van intracoronaire beeldvorming, in het bijzonder OCT, niet nagelaten worden. In **hoofdstuk 3** bespreek ik intracoronaire OCT als nieuwste intracoronaire beeldvormingstechniek en de klinische en onderzoekstoepassingen van OCT. Analyse van stentexpansie, residuele stenose, excentriciteit en stentasymmetrie zijn de belangrijkste punten waarop stent implantatie beoordeeld moet worden. In dit hoofdstuk geef ik ook informatie over de methodologie van de analyses om de inbedding van een stent te beoordelen. Ik beschrijf de lichtdempingsanalyse die gebaseerd is op absorptie van het licht van de OCT door weefsel en lichtverstrooiing. Een andere OCT-specifieke maat is de lichtintensiteit. De analyse van de lichtintensiteit wordt gebruikt om het absorptieproces van de BRS te beoordelen en geeft informatie over de matrixinfiltratie en de integratie van collageenrijk bindweefsel in de strutkernen. Informatie over de OCT-afgeleide plaquemorfologie helpt in de keuze van strategieën voor een optimale implantatie. Ook plaqueruptuur of erosie als onderliggende oorzaak voor intravasculaire thrombusvorming kan in beeld gebracht worden. Vergeleken met coronaire angiografie, heeft angiografie met OCT assistentie gezorgd voor minder cardiale complicaties in het eerste jaar na stent implantatie (CLI-OPCI-onderzoek). In hoofdstuk 3 heb ik ook een andere nieuwe BRS, de Mirage stent, onderzocht en vergeleken met de Absorb BRS. Op OCT beelden, geeft Mirage behandeling een verhoogde incidentie van resterende bloedvatstenose. Door zijn circulaire gestroomlijnde strutgeometrie werd juist verwacht dat Mirage de in-stent restenose zou verminderen. Onze 1-jaarlijkse resultaten hebben echter het tegengestelde resultaat getoond.

Deel B: Preklinische beoordeling van schuifspanning in bioresorbeerbare vasculaire stents

In **hoofdstuk 4** evalueer ik de hemodynamische eigenschappen van een specifieke BRS, de Absorb BVS, in gezonde vaten van dieren. In die verkennende analyse heb ik aangetoond dat de dikke rechthoekige niet-gestroomlijnde struts van de Absorb BVS aanzetten tot recirculatie en lage afschuifspanning van het bloed aan het endotheel (= endothelial shear stress, ESS) binnen specifieke regio's van het stent-lumenoppervlak. Als gevolg van deze

stromingsverstoringen was er een matige tot ernstige fibrineophoping rond de struts en was de re-endothelialisatie van de geanalyseerde struts onvoldoende. In het volgende deel van dit hoofdstuk evalueerde ik een nieuwe BRS, de Mirage, geïmplanteerd in gezonde vaten van varkens. De Mirage stent heeft twee maten van ovale struts met 125 μm en 150 μm strutdikte respectievelijk. Terwijl de versie met 125 μm strutdikte geïmplanteerd werd in de vaten ≤ 3.0 mm, werd de stent met 150 μm strutdikte geïmplanteerd in de vaten ≥ 3.5 mm. In de Mirage met 125 μm strutdikte was het percentage van het lumaal oppervlak met lage ESS (<1.0 Pa) hoger dan in de versie met 150 μm struts. 45 procent van het lumaal oppervlak werd bedekt door de Mirage stent en waarschijnlijk droeg deze hoge bedekking bij aan het relatief lage percentage lage ESS gebieden in Mirage in vergelijking met de Absorb stent in de vorige studie. In het laatste deel van dit hoofdstuk heb ik het verschil onderzocht tussen de Absorb stent en een andere nieuwe BRS, de ArterioSorb, door middel van stromingssimulatie en afschuifspanningsverdelingsberekeningen. Ik gebruikte niet-Newtoniaanse pulserende stromingssimulaties om de lokale hemodynamica in systolische en diastolische hartfasen te onderzoeken. In beide hartfasen vertoonde ArterioSorb, met dunnere struts, een relatief hogere gemiddelde schuifspanning in vergelijking met de Absorb BVS.

In **hoofdstuk 5** heb ik de lokale stromingskarakteristieken in Absorb BVS en Mirage stent in gezonde varkensvaten geëvalueerd. Ik deed een pulserende stromingssimulatie en toonde aan dat er rond de vierhoekige dikkere struts van Absorb recirculaties waren, terwijl er in Mirage geen recirculatie werd gedetecteerd. De gemiddelde ESS was lager in Absorb BVS in vergelijking met Mirage BRS in steady-flow-simulatie ($0,60 \pm 0,51$ Pa versus $1,09 \pm 0,76$ Pa, respectievelijk; $p < 0,001$); 70% van het behandelde oppervlak in Absorb BVS en 53% in Mirage BRMS werd blootgesteld aan een lage (<1 Pa) atherosclerose bevorderende ESS. In het volgende deel van dit hoofdstuk heb ik seriële afschuifspanningsanalyses uitgevoerd in Absorb- en Mirage stents in gezonde varkensvaten. Er was er een significant verschil in de mate van protrusie van de struts in de vaatholte (152 ± 140 μm voor Absorb, 117 ± 123 μm voor Mirage; $p = 0,003$), een feit dat moet worden toegeschreven aan de verschillende strutdiktes. In deze studie resulteerde een grotere protrusie in Absorb BVS in een hogere ESS bovenop de struts en een lagere ESS tussen de struts in vergelijking met de Mirage stent. Bovenop de struts was de ESS in Absorb $1,69 \pm 1,20$ Pa, en $1,53 \pm 0,91$ Pa in de Mirage ($p < 0,001$), terwijl in de gebieden tussen de struts de gemiddelde ESS-waarden $0,60 \pm 0,51$ Pa en $0,63 \pm 0,50$ Pa respectievelijk waren ($p < 0,001$); 52% van het stentoppervlak in de Absorb en 47% in de Mirage

(125 μ m) werd blootgesteld aan een lage (<1Pa), atherosclerose bevorderende, ESS-omgeving ($p < 0.0001$).

In het laatste deel van dit hoofdstuk voerde ik inbeddings- en protrusiemetingen met daarbij afschuifspanningsanalyses uit van een nieuwe BRS, ArterioSorb naast de Absorb BVS in diermodellen. Er is een significant verschil tussen de twee stenttypes in strutprotrusie (153 \pm 137 μ m voor Absorb, 84 \pm 12 μ m voor ArterioSorb; $p < 0.0001$), dat kan worden toegeschreven aan het verschil in strutdikte. De protrusie was meer in Absorb (97% van de strutdikte) dan in ArterioSorb (88% van de strutdikte). Wanneer de protrusiehoogte aangepast werd aan de lumendiameters, was de verhouding protrusieafstand/gemiddelde lumendiameter hoger in Absorb BVS (0,052 \pm 0,0038) dan in ArterioSorb (0,028 \pm 0,0045) ($p < 0,0001$). ESS was significant hoger in ArterioSorb (1,52 \pm 0,34 Pa) dan in Absorb (0,73 \pm 2,19 Pa) ($p = 0,001$). Daarbij had Absorb BVS vaker een lage ESS (<1,0 Pa) en een zeer lage ESS (<0,5 Pa) heeft dan ArterioSorb. Naast de dunnere struts is de maximale afstand tussen de struts in ArterioSorb (1.4 mm) groter dan in Absorb BVS (1.0 mm), waardoor laminaire stroming zich efficiënt kan herstellen in ArterioSorb.

In **hoofdstuk 6** onderzocht ik het effect van strutvorm en strutprotrusie op de lokale afschuifspanningsverdeling. Ik gebruikte speciale OCT-software om de inbedding/protrusie van de struts te meten. De gemiddelde protrusie was significant verschillend tussen de stentgroepen [156 \pm 137 μ m voor Absorb, 98,97 \pm 16,47% van de strutdikte in Absorb, 139 \pm 153 μ m voor Mirage (95,63 \pm 14,48% van de strutdikte in Mirage-150, 89,52 \pm 17,09% van de strutdikte in Mirage-125); $p = 0,035$]. Na correctie van de protrusieafstand voor de lumenale doorsnede bleef het verschil in protrusieafstanden significant (0,050 \pm 0,038 mm voor Absorb versus 0,041 \pm 0,034 mm voor Mirage; $p < 0,0001$). De gemiddelde schuifspanning (ESS) niveaus waren omgekeerd gecorreleerd met protrusieafstanden in Absorb ($r = 0,369$, $p < 0,0001$), terwijl in Mirage de correlatie in positieve richting was ($r = 0,192$, $p < 0,0001$). De positieve correlatie van ESS met strut protrusie lijkt paradoxaal. De onderliggende oorzaak van een dergelijke paradoxale relatie komt voort uit het feit dat verminderde stromingsverstoringen door de cirkelvormige strutgeometrie met de meer geleidelijke veranderingen in de helling over het strutoppervlak de relatie van ESS met strutprotrusie omkeerden. Het Bernoulli-principe stelt voor dat de stroming over een gestroomlijnde geometrie versnelt, wat de positieve relatie van ESS met protrusieafstand in Mirage verklaart.

ESS heeft de neiging om af te nemen met de protrusieafstand in Absorb, terwijl in Mirage de ESS omgekeerd evenredig is met de protrusieafstand. De omgekeerde relatie tussen de protrusie en de lokale ESS in Absorb, heeft bij de histologie analyses van Absorb dan ook laten zien dat er onvoldoende endotheliale bedekking is, terwijl bij Mirage de struts volledig bedekt waren met neointima. In het volgende deel van dit hoofdstuk heb ik twee ArterioSorb-stents geëvalueerd die serieel zijn geïmplanteerd in één varkensvat. De twee stents hadden verschillende strutdiktes (90 μm en 120 μm). De mediaan ESS was lager in de distale stent (ArterioSorb-120 μm) [1.17 (0.78-1.55) Pa] dan in de proximale stent (ArterioSorb-95 μm) [1.25 (0.92-1.88) Pa] in Newtoniaanse steady flow simulatie ($p < 0.0001$). 37.4% van het stentoppervlak in ArterioSorb-120 μm en 32.6% in ArterioSorb-95 μm werd blootgesteld aan een lage (< 1 Pa) atherosclerose-bevorderende ESS.

Deel C: Klinische beoordeling van schuifspanning in bioresorbeerbare vasculaire stents

In **hoofdstuk 7** heb ik de richtlijnen beschreven voor het juiste gebruik van computational fluid dynamics (CFD) om reproduceerbare en betrouwbare afschuifspanningsanalyses (EES) te krijgen in onbehandelde en behandelde menselijke kransslagaders. Ik bespreek de beschikbare methoden om modellen van de kransslagaders te reconstrueren en heb voorgesteld om angiografie of computertomografie angiografie (CTCA) beelden te fuseren met intravasculaire beeldvormingsmodaliteiten om hoge resolutie modellen van kransslagaders te verkrijgen. Naast de intravasculaire echografie biedt optische coherentietomografie (OCT) bijna microscopische informatie over atherosclerotische plaques, plaquekapdikte, neovascularisatie, macrofaagaccumulatie en intravasculair lumaal oppervlak met of zonder geïmplanteerde stent. Ik heb de meshing-procedures, de randvoorwaarden en de bloedreologie in detail uitgelegd. Rode bloedcellen aggregeren en verlenen onder verschillende stromingsomstandigheden en dit heeft effect op de viscositeit van het bloed en op de grootte van de afschuifspanning aan de wand. Deze afschuifspanning geïnduceerde verandering van de viscositeit maakt bloed tot een niet-Newtoniaanse vloeistof. Echter, in de meeste van de CFD-analyses wordt aangenomen dat bloed zich als een Newtoniaanse vloeistof gedraagt met een viscositeit van 3,5 tot 4,0 mPa.s. Bij CFD is het

belangrijkt dat de tijdens het oplossen van de Navier-Stokes convergeert. De post-processing fase levert verschillende uitkomstparameters op die worden verkregen uit de berekende verdeling van de afschuifspanning van de wand, zoals de oscillerende afschuifindex, de relatieve verblijftijd en de transversale afschuifspanning aan de wand.

In **hoofdstuk 8** heb ik de verdeling van de afschuifspanning in een met Absorb BVS behandelde menselijke kransslagader onderzocht met behulp van pulserende stromingssimulatietechnieken. Door de kromming van de arterie ontstond een scheef snelheidsprofiel waarbij de wervelingen rondom de stent struts minder uitgesproken waren in de buitenbocht, maar relatief groter in de binnenbocht van het behandelde vaatsegment. Verhoogde recirculaties rond de struts in de binnenbocht verhoogd de kans op thrombusvorming rond de struts. In het volgende deel van het hoofdstuk heb ik de impact van de strutprotrusie op de afschuifspanningsverdeling in de BRS behandelde menselijke kransslagaders onderzocht. Ik gebruikte de gegevens van de Mirage first-in-man studie waarbij ik Absorb BVS en Mirage BRS met elkaar vergeleek. In de analyse was de strutprotrusie lager voor Mirage in vergelijking met Absorb en in beide stenttypes werd een lagere protrusie gemeten ter plaatse van fibroatheroma's in vergelijking met andere plaques. Door de verschillen in de strutprotrusie was de ESS relatief hoger in Mirage dan in Absorb en was de ESS-magnitude hoger ter plaatse van fibroatheromatische plaques in vergelijking met de andere plaquetypes. Naast het onderliggende plaquetype geeft contactmechanica enige informatie over een betere inbedding van de struts in Mirage BRS; een lagere contactstraal van het cirkelvormige strutoppervlak van Mirage heeft het voordeel van een betere inbedding door ter plaatse van het dikste gedeelte van de strut de hoogste druk door te geven aan de vaatwand terwijl de rechthoekige struts van Absorb BVS die de druk tijdens implantatie meer verdelen. In het laatste deel van het **hoofdstuk 8** heb ik het effect van de atherosclerotische plaques op de inbedding van de struts en de verdeling van de afschuifspanning in de behandelde menselijke kransslagaders van BRS onderzocht. Ter plaatse van lipidenrijke plaques ($76 \pm 48 \mu\text{m}$) was de strutinbedding significant verhoogd van terwijl ter plaatse van gecalcificeerde plaques deze juist verlaagd ($35 \pm 52 \mu\text{m}$) was. In lijn met strutinbedding was de wandschuifspanning (WSS) significant hoger bij lipidenrijke plaques ($1,50 \pm 0,81 \text{ Pa}$), terwijl deze significant afnam bij gecalcificeerde plaques ($1,05 \pm 0,91 \text{ Pa}$). Na categorisering van WSS als laag ($< 1,0 \text{ Pa}$) of normaal/hog ($\geq 1,0 \text{ Pa}$), was het percentage laag-WSS in de plaquesubtypen respectievelijk 30,1%, 31,1%, 25,4% en 36,2% voor normale vaatwand,

fibrotische plaque, lipidenrijke plaque en gecalcificeerde plaque (p -overall $<0,001$). Het idee om een stenttype te selecteren op basis van specifieke plaque eigenschappen identificeerbaar op intracoronaire beeldvorming en de implantatietechniek aan te passen op basis van CFD-analyse kan het gebruik van deze technieken tijdens PCI ondersteunen. Bij meer gecalcificeerde plaque zijn ovale struts in het voordeel en bij onvoldoende inbedding kunnen extra nadilataties met non-compliant ballonen verricht worden. Bij lipidenrijke plaques waarbij een diepe strutinbedding mogelijk is kan de Absorb-BVS reeds zorgen voor een gunstige afschuifspanningsverdeling.

In **hoofdstuk 9** evalueerde ik het effect van stent onderexpansie en overexpansie op de lokale afschuifspanningsverdeling direct na de implantatie en bij de vijfjaarsfollow-up in patienten. Initiele stent onderexpansie veroorzaakte een "step-down" aan de proximale rand van de stent. Bij de vijfjaarscontrole was die "step-down" verminderd met een meer gelijkmatige verdeling van de afschuifspanning. In het geval van overexpansie ontstond een "step-up" aan de proximale rand. Bij vijfjaarsfollow-up is de step-up afgenomen en zijn de zones met zeer lage schuifspanning -in het behandelde vaatsegment- grotendeels verdwenen.

In het volgende deel van het hoofdstuk heb ik de evolutie van de lokale schuifspanning en de viscositeit in de met Absorb BVS behandelde vaten bij vijfjaarsfollow-up onderzocht. Met behulp van op OCT-gebaseerde CFD-modellen, lieten pulsatile, niet-Newtoniaanse stromingssimulaties zien dat het gedeelte lumen blootgesteld aan een ESS <1 Pa aanzienlijk verminderde tussen post-implantatie en vijfjaarsfollow-up, zowel tijdens diastole, systole als onder tijdgemiddeldeomstandigheden (diastole: 6,90 vs. 2,78%, $p = 0,008$; systole: 53,31 vs. 38,37%, $p = 0,042$; tijdgemiddeld: 15,92 vs. 4,99%, $p < 0,0001$). Er was een positieve correlatie tussen de hogere ESS na de implantatie en het lumenoppervlak na 5 jaar ($y = 0,32x - 1,49$; $p < 0,0001$). Verhoogde viscositeitszones werden waargenomen in de buurt van de struts aan het luminale oppervlak hetgeen overeenkwam met de locaties van de wervelingen en lage ESS. Hoewel de gemiddelde viscositeit niet veranderde, daalde de maximale relatieve viscositeit aanzienlijk over 5 jaar (systole: 8,84 vs. 5,33, $p = 0,043$; diastole: 4,46 vs. 3,18, $p = 0,063$; tijdsgemiddelde: 4,30 vs. 3,21, $p = 0,028$).

In het laatste deel van het hoofdstuk 9 evalueerde ik de impact van strut-protrusie op de distributie van de afschuifspanning direct na implantatie, de vorming van neo-intimaal weefsel na één jaar en de wandschuifspanning (WSS)-distributie bij vijf jaar follow-up. Ik

gebruikte geschikte beelden uit de first-in-man trial van Absorb BVS. Voor de WSS-analyse zijn newtoniaanse steady flow-simulaties uitgevoerd. Er was een logaritmisch omgekeerde relatie tussen strutprotrusie en WSS na implantatie ($r=-0,425$, $p<0,001$; correlatiecoëfficiënten varieerden van $-0,143$ tot $-0,553$). Een significante inverse correlatie werd waargenomen tussen initiele log-WSS en de neointima dikte op é én jaar na implantatie voor alle stents ($r = 0,451$, $p<0,005$; correlatiecoëfficiënten varieerden van $-0,140$ tot $-0,662$). Bij vijf jaar was de mediaan WSS ($1,92$ [$1,31$, $2,81$] Pa) significant hoger dan de mediaan WSS na implantatie ($1,19$ [$0,84$, $1,69$] Pa) ($p=0,0016$). Bij vijf jaar follow-up verdwenen de post-procedurele step-up en step-down in WSS aan de randen van de stentgebieden. De protrusie van de stent strut en de storende invloed daarvan op de laminaire stroming en de WSS voorspelde de dikte van de neointima bij follow-up. Met deze studie heb ik geconcludeerd dat er een oorzakelijk verband is tussen inbedding (meer) en WSS-verstoring (minder). Hieruit volgt de hypothese dat BRS met dunnere (ArterioSorb) en meer cirkelvormige (Mirage) struts de minste neointima zouden ontwikkelen.

In **hoofdstuk 10** heb ik de relatie onderzocht tussen postimplantatie afschuifspanning en vasculaire remodeleringspatronen in met BRS en metalen stents behandelde vaten. In deze studie gebruikte ik IVUS-gebaseerde CFD-modellen voor Newtoniaanse stromingssimulaties. Deze studie was de eerste die de impact van ESS op arteriële remodelering in BRS en metalen stents op een vergelijkende manier onderzocht. Er werden seriële 3D-CFD-modellen uitgevoerd en vervolgens werden er na implantatie en na 3 jaar gepaarde ESS-berekeningen uitgevoerd. Het gemiddelde en minimale lumenoppervlak na de implantatie, zoals gemeten door IVUS, waren kleiner in de BRS in vergelijking met de metalen DES-arm. Het gemiddelde lumenoppervlak na implantatie was aanzienlijk kleiner in de BRS-arm dan in de DES-arm ($12,78\pm 3,20$ mm² vs. $14,97\pm 2,98$ mm², $p=0,012$). Bij 3 jaar follow-up was het gemiddelde lumenoppervlak echter niet meer statistisch verschillend, als gevolg van expansieve remodelering in de BRS groep en vernauwende remodelering in de DES groep in combinatie met enig verlies in lumenoppervlak (verandering in gemiddeld lumenoppervlak: $+0,78\pm 1,49$ mm² vs. $-0,66\pm 1,64$ mm², $p=0,001$). Na het classificeren van ESS na de implantatie in lage, middelhoge en hoge tertielen, in de BRS-arm, vertoonde het laagste tertiel van ESS een afname van het lumengebied in tegenstelling tot de late lumenvergroting in de middelhoge en de hoogste tertielen. Er was een significant verschil in vaatwandoppervlak, toenemend in BRS ($+0,64\pm 1,10$ mm²) en afnemend in Xience ($-0,46\pm 1,22$ mm²) bij driejaars follow-up. Het

laagste tertiel van ESS na de implantatie toonde een toename van de plaquepercentage (+5,36±8,98%) die aanzienlijk groter was dan voor het middelste (1,86±8,09%) of het hoogste (0,72±7,46) tertiel van ESS na de implantatie. Aan de andere kant was er in de DES-arm geen significant verschil in verandering in het lumen, het vaatwandoppervlak en de plaquepercentage tussen de 3 tertielen van ESS na de implantatie. Tot slot heb ik geconstateerd dat een groter lumenoppervlak, een kleiner vaatoppervlak, een hoger plaquepercentage na de procedure en een hogere mediaan ESS na de procedure in verband werden gebracht met meer expansieve remodelering. Een jongere leeftijd was ook gerelateerd aan expansieve remodelering in de BRS-groep. Interessant genoeg was de plaquesamenstelling niet geassocieerd met expansieve remodelering. In de vorige studie van onze groep was de necrotische kern echter wel significant geassocieerd met expansieve remodelering.

CONCLUSIES

Bioresorbeerbare stents vereisen specifieke implantatietechnieken waarmee rekening moet worden gehouden voor een veilige resultaat op de korte en lange termijn. De specifieke materiaaleigenschappen van bioresorbeerbare stents vragen om een nauwkeurige beoordeling van de plaque, een adequate pre-dilatatie van de laesies, optimale positionering van de stent tijdens implantatie en post-dilatatie met een ballonarterieverhouding van $\geq 1,1$.

De inbedding van de struts is één van de kritische punten tijdens de BRS-implantatie. De vaak aanwezige onderexpansie van de stent maakt een optimale inbedding van de struts cruciaal om de stromingsverstoringen te beperken. Wat betreft de stromingsverstoringen over het lumen oppervlak van de stent, geeft de analyse van de protrusie van de struts waardevolle informatie tijdens de implantatie.

Een te hoge afschuifspanning na implantatie van de bioresorbeerbare stent geeft het risico op onvoldoende bekleding terwijl een te lage afschuifspanning juist lokaal veel fibrine ophopingen geeft. Om de behandeling succesvol te doen zijn moeten de struts van de laatste generatie stents worden aangepast om meer bloedstroomcompatibel te zijn om complicaties als stentthrombose en restenose na implantatie te voorkomen. Gestroomlijnde, dunnere struts, niet-trombogene stentmaterialen en een stroomcompatibel macro-ontwerp zijn de verbeterpunten voor nieuwe BRS. Het analyseren van de verdeling van de schuifspanning in

het gestente vaat segment is een belangrijke methode voor het onderzoeken van de hemodynamische effecten van het behandelde vaatsegment met nieuwe type bioresorbeerbare stents. Preklinische CFD-modellen bieden een unieke mogelijkheid om informatie over de lokale micro-hemodynamische omgeving in verschillende BRS te ontrafelen.

SUMMARY AND CONCLUSIONS

Part A: Bioresorbable Scaffolds

Development of biocompatible polymer coating, several safety concerns have been overcome in metallic drug eluting stents (DES). However, late stent thrombosis, neoatherosclerosis, allergic reactions, late acquired malappositions continue to be critical issues. Bioresorbable scaffolds has been introduced to address the drawbacks of the DES. Different structural materials, mechanical characteristics and distinct behaviors in the vessel wall at follow up make BRS unique and demands specific implantation methods and follow-up. In **chapter 2** we described the concept and potential benefits of BRS. Complete resorption of the polymeric scaffold reduces the risk of late catch-up in restenosis which can be detected even in newer generation DES. The mechanical flexibility of BRS increases the conformability of the polymeric scaffold to the vessel geometry. Recovery of the vasomotricity in the treated vessel segment and enabling non-invasive imaging without any image artefacts have been other positive points in BRS. Due to distinct mechanical features of Absorb BVS, some technical considerations should be sought during implantation. To prevent device dislodgement, tortuous vessel segments and excessive calcifications should be avoided during lesion selection. Device size should be selected using QCA-DMax methodology through measuring proximal and distal maximum diameters in QCA. Preceding BRS implantation, target vessel segment preparation, predilatation of the lesion using balloon-reference vessel diameter ratio of 1:1 and post-dilatation with a non-compliant balloon up to a maximum of 0.5 mm larger are indispensables of BRS implantation. During BRS implantation, intra-coronary imaging is a *sine qua non*. Particularly optical coherence tomography the prominent method for assessing and treating the strut apposition, edge dissection, thrombus formation or strut disruptions. Intracoronary imaging is the cornerstone point of BRS implantation. In order to have low risk of major adverse cardiovascular event, assessment of the implantation using intracoronary imaging, in particular OCT, should not be overlooked. In **chapter 3**, we discussed about the intra-coronary OCT and clinical and research applications of OCT. Interpretation of stent expansion, residual area stenosis, eccentricity and stent asymmetry provide assessment of stent/scaffold performance and optimized device implantation. We give information about the methodology of stent/scaffold embedment analysis. We described light attenuation

modality derived from OCT which is based on absorption of the light by tissue and light scattering. Another OCT dedicated software is light intensity. Light intensity analysis is used to assess the BRS strut cores and gives information about the matrix infiltration and integration of collagen-rich connective tissue. OCT derived plaque morphology information provides strategies for optimal implantation. Also determining plaque rupture and erosion may depict the underlying cause for intravascular thrombus formation. Compare to coronary angiography guidance, angiography-plus-OCT guidance has provided less adverse cardiac events at one year post-implantation. (CLI-OPCI study). In chapter 3, we also investigated a novel BRS, Mirage scaffold and compared it with Absorb BVS. On OCT, Mirage cases have demonstrated increased ratio of in scaffold stenosis. Having circular streamlined strut geometry, Mirage was expected to reduce in-stent restenosis. However, our 1-year results have shown an opposite direction.

Part B: Preclinical assessment of shear stress in bioresorbable vascular scaffolds

In **chapter 4** we evaluated the hemodynamic characteristics of Absorb BVS in healthy preclinical vessel models. In that exploratory analysis we demonstrated that thick rectangular non-streamlined struts of Absorb BVS incited recirculations and low shear stress zones within the scaffolded luminal surface. Due to those flow disruptions, there was moderate to severe fibrin accumulation around the struts and re-endothelialization of the analyzed struts were insufficient. In the following section of this chapter, we evaluated a novel BRS, Mirage scaffold implanted in healthy animal vessels. Mirage scaffold has two types of circular struts; 125 μm and 150 μm . While the version with 125 μm strut thickness was implanted to the vessels ≤ 3.0 mm, the scaffold with 150 μm strut thickness was implanted to the vessels ≥ 3.5 mm. In Mirage with 125 μm struts the percent of luminal surface with low ESS (<1.0 Pa) was higher than in the version of 150 μm struts. The percent of luminal surface coverage in Mirage was 45% and probably this high coverage contributed to the relatively lower percentage of low ESS in Mirage compared to the Absorb scaffold in the previous study. In the last section of this chapter, we demonstrated the difference between Absorb scaffold and a novel BRS ArterioSorb by flow simulation and shear stress distribution. We used non-Newtonian

pulsatile flow simulation to unravel the local hemodynamics in systolic and diastolic cardiac phases. In both cardiac phases, ArterioSorb, with thinner struts, exhibited relatively higher mean shear stress magnitudes as compared to the Absorb BVS.

In **chapter 5**, we evaluated local flow characteristics in Absorb BVS and Mirage scaffold in healthy porcine vessels. We did pulsatile flow simulation and demonstrated that around the quadrangle thicker struts of Absorb, there were recirculations whereas in Mirage no recirculation was detected. Mean ESS was lower in Absorb BVS compared to Mirage BRMS in steady flow simulation (0.60 ± 0.51 Pa [n=5,256] vs. 1.09 ± 0.76 Pa [n=6,336], respectively; $p < 0.001$); 70% of the scaffolded surface in Absorb BVS and 53% in Mirage BRMS was exposed to a low (< 1 Pa) athero-promoting ESS. In the following section of this chapter, we performed serial shear stress analyses in Absorb and Mirage scaffolds in healthy porcine vessels. In cross-section level analysis, there was a significant difference between the scaffolds in the protrusion distances (152 ± 140 μ m for Absorb, 117 ± 123 μ m for Mirage; $p = 0.003$), a fact that should be attributed to the different strut thicknesses. In this study, increased protrusion distances in Absorb BVS resulted in higher ESS on top of the struts and lower ESS between the struts as compared to the Mirage scaffold. On top of the struts the ESS in Absorb was 1.69 ± 1.20 Pa, and 1.53 ± 0.91 Pa in the Mirage ($p < 0.001$), while in the areas between struts the mean ESS values were 0.60 ± 0.51 Pa and 0.63 ± 0.50 Pa, respectively ($p < 0.001$); 52% of the scaffolded surface in the Absorb and 47% in the Mirage (125 μ m) was exposed to a low (< 1 Pa) athero-promoting ESS environment ($p < 0.0001$). In the last section of the chapter, we performed embedment/protrusion measurements and shear stress analysis of a novel BRS, ArterioSorb and Absorb BVS in animal models. In cross-section level analysis, there was significant difference between the two scaffolds in strut protrusion (153 ± 137 μ m for Absorb, 84 ± 12 μ m for ArterioSorb; $p < 0.0001$), that can be attributed to difference in strut thicknesses. The protrusion was higher in Absorb (97% of the strut thickness) than in ArterioSorb (88% of the strut thickness). When the protrusion distance was adjusted according to the lumen diameters, the ratio of protrusion distance / mean lumen diameter was higher in Absorb BVS (0.052 ± 0.0038) compared with the ArterioSorb (0.028 ± 0.0045) (< 0.0001). ESS was significantly higher in ArterioSorb (1.52 ± 0.34 Pa) than in Absorb (0.73 ± 2.19 Pa) ($p = 0.001$). In cross-section level analysis, Absorb BVS unraveled low ESS (< 1.0 Pa) and very low ESS (< 0.5 Pa) more frequently than in ArterioSorb. Beside the thinner struts, maximum inter-strut

distance is longer in ArterioSorb (1.4mm) than in Absorb BVS (1.0 mm) that enables laminar flow to recover efficiently in ArterioSorb.

In **chapter 6**, we investigated the effect of strut shape and strut protrusion on local shear stress distribution. We used a dedicated OCT software to measure strut embedment/protrusion. mean protrusion distances were significantly different between the scaffold groups [$156 \pm 137 \mu\text{m}$ for Absorb, $98.97 \pm 16.47\%$ of the strut thickness in Absorb, $139 \pm 153 \mu\text{m}$ for Mirage ($95.63 \pm 14.48\%$ of the strut thickness in Mirage-150, $89.52 \pm 17.09\%$ of the strut thickness in Mirage-125); $p = 0.035$]. After adjusting the protrusion distances according to the luminal cross-section area, the difference in protrusion distances remained significant (0.050 ± 0.038 for Absorb vs. 0.041 ± 0.034 for Mirage; $p < 0.0001$). Mean shear stress levels were inversely correlated with protrusion distances in Absorb ($r = -0.369$, $p < 0.0001$), whereas in Mirage, the correlation was in positive direction ($r = 0.192$, $p < 0.0001$). The positive relation of ESS with strut protrusion seems paradoxical. The underlying cause of such paradoxical relation stems from the fact that reduced flow disruption due to the circular strut geometry and the gradual changes in the slope over the strut surface reversed the relation of ESS with strut protrusion. Bernoulli principle proposes that the fluid flow accelerates over a streamlined geometry which explains the positive relation of shear stress with protrusion distance in Mirage. ESS has a tendency to decrease with the protrusion distance in Absorb, while in Mirage shear stress is inversely proportional to the protrusion distance. Due to the inverse relationship between the strut protrusion and local ESS in Absorb, histology sections from Absorb has shown insufficient neointimal endothelial coverage while in Mirage the struts were fully covered with the neointimal tissue. In the following section of the present chapter, we evaluated two ArterioSorb scaffolds implanted serially in one porcine vessel. The two scaffolds had different strut thicknesses ($90 \mu\text{m}$ and $120 \mu\text{m}$). Median ESS was lower in the distal scaffold (ArterioSorb- $120 \mu\text{m}$) [1.17 (0.78 – 1.55) Pa] than in the proximal scaffold (ArterioSorb- $95 \mu\text{m}$) [1.25 (0.92 – 1.88) Pa] in Newtonian steady flow simulation ($p < 0.0001$). 37.4% of the scaffolded surface in ArterioSorb- $120 \mu\text{m}$ and 32.6% in ArterioSorb- $95 \mu\text{m}$ was exposed to a low (<1 Pa) athero-promoting ESS.

Part C: Clinical assessment of shear stress in bioresorbable vascular scaffolds

In **chapter 7**, we described the guidelines for appropriate use of CFD to get reproducible and reliable shear stress analysis in native and instrumented human coronary arteries. We explained the available methods to reconstruct coronary arteries and proposed to do fusion of angiography or computed tomography angiography and intravascular imaging modalities to reconstruct high resolution models of coronary arteries. Beside the intravascular ultrasound, OCT provides microscopic information about atherosclerotic plaques, fibrous cap thickness, neovessel formations, macrophage accumulation and intravascular luminal surface with or without implanted stent/scaffold. We explained meshing procedures, boundary conditions and blood rheology in detail. Red blood cells aggregate and elongate under different flow conditions and this has effect on blood viscosity and wall shear stress magnitudes. Shear-thinning behavior of viscosity denotes its inverse relationship with the shear rate that makes the blood a non-Newtonian fluid. However, most of the CFD analysis make the assumptions by simplifying the shear-thinning behavior of the blood to a Newtonian fluid using a constant blood viscosity of 3.5~4.0 mPa.s. During the CFD simulations, the key concept in the solution procedure is convergence and the Navier-Stokes equations are solved in an iterative manner. Post-processing phase provides several metrics obtained from the computed wall shear stress distribution such as oscillatory shear index, relative residence time, transverse wall shear stress.

In **chapter 8**, we explored shear stress distribution in an Absorb BVS implanted human coronary artery using pulsatile flow simulation techniques. Arterial curvature created a skewed velocity profile that microcirculations were less pronounced at the outer curve but relatively larger at the inner curve of the treated vessel segment. Increased recirculations around the struts within the inner vessel curve makes tendency for thrombus formations around the struts particularly in the inner vessel curve. In the following section of the chapter, we investigated the impact of strut protrusion on shear stress distribution in the BRS implanted human coronaries. We used the data from the Mirage first-in-man trial comparing Absorb BVS and Mirage BRS. In the analysis, strut protrusion was

lower in Mirage compared with Absorb and in both scaffold types, lower protrusion was detected in fibroatheromas compared with other plaque types. Related to the differences in strut protrusion, ESS was relatively higher in Mirage than in Absorb and ESS magnitude was

higher in fibroatheromatous atherosclerotic plaques compared to the other plaque types. Additional to the underlying plaque type, the contact mechanics provide some information about better embedment of the struts in Mirage BRS; lower contact radius of the circular strut surface in Mirage gives the advantage of better embedment compared to the quadratic struts of Absorb BVS. In the last section of the **chapter 8**, we explored the effect of the atherosclerotic plaque types on strut embedment and shear stress distribution in BRS implanted human coronaries. At cross-section level ($n=1289$), strut embedment was significantly increased in fibroatheromatous plaques ($76\pm 48\mu\text{m}$) and decreased in fibro-calcific plaques ($35\pm 52\mu\text{m}$). Compatible with strut embedment, wall shear stress (WSS) was significantly higher in lipid-rich fibroatheromatous plaques ($1.50\pm 0.81\text{Pa}$), whereas significantly decreased in fibro-calcified plaques ($1.05\pm 0.91\text{Pa}$). After categorization of WSS as low ($<1.0\text{ Pa}$) and normal/high WSS ($\geq 1.0\text{ Pa}$), the percent of low-WSS in the plaque subgroups were 30.1%, 31.1%, 25.4% and 36.2% for non-diseased vessel wall, fibrous plaque, fibro-atheromatous plaque and fibro-calcific plaque, respectively ($p\text{-overall}<0.001$). The idea of designing lesion specific stent and implantation techniques using intravascular imaging modalities may enhance the utility of CFD analysis during PCI. Absorb may provide favorable shear stress distribution in lipid-rich fibroatheromatous plaques enabling deeper strut embedment.

In **chapter 9**, we evaluated the effect of scaffold under-expansion and overexpansion on the local shear stress distribution post-implantation and at five-year follow up in human cases. At long-term follow up, in the under-expansion case, scaffold under-expansion caused a “step-down” at the proximal edge of the scaffolded segment. At five-year follow up, that step-down abated with smoother shear stress distribution. In the over-expanded case, over-expansion of the scaffold caused a “step-up” at the proximal edge. At five-year follow up, the step-up attenuated and the vessel zones with very-low shear stress -within the treated vessel segment- mostly disappeared.

In the following section of the chapter, we investigated the evolution of local shear stress and viscosity in the Absorb BVS implanted vessels at five years follow up. Using OCT-based CFD models, pulsatile non-Newtonian flow simulations unraveled that mean percent lumen area exposed to ESS $<1\text{ Pa}$ considerably decreased between post-implantation and five-years follow up during diastole, systole and time averaged conditions (diastole: 6.90 vs. 2.78%, $p = 0.008$;

systole: 53.31 vs. 38.37%, $p= 0.042$; time-averaged: 15.92 vs. 4.99%, $p< 0.0001$). There was a positive correlation between higher post-implantation ESS and lumen area ($y = 0.32x-1.49$; $p< 0.0001$). Increased viscosity zones were noted in the vicinity of the struts over the luminal surface where corresponded to the locations of micro-recirculations and low ESS. Although mean viscosity did not change, maximum relative viscosity considerably decreased over 5 years (systole: 8.84 vs. 5.33, $p= 0.043$; diastole: 4.46 vs. 3.18, $p= 0.063$; time-averaged: 4.30 vs. 3.21, $p= 0.028$).

In the last section of the chapter 9, we evaluated the impact of strut protrusion post-implantation on shear stress distribution post-implantation, neointimal tissue formation at one year and WSS distribution at five-years follow up. We used appropriate cases from the first-in-man trial of Absorb BVS. Newtonian steady flow simulations were performed for WSS analysis. There was an logarithmic inverse relationships between strut protrusion and WSS post-implantation ($r=-0.425$, $p<0.001$; correlation coefficients ranged from -0.143 to -0.553). A significant inverse correlation was recorded between retrospective baseline log-WSS and neointimal thickness at one year for all devices ($r=-0.451$, $p<0.005$; correlation coefficients ranged from -0.140 to -0.662). At five years, in-scaffold median WSS (1.92 [1.31, 2.81] Pa) was significantly higher than median WSS post-implantation (1.19 [0.84, 1.69] Pa) ($p=0.0016$). At five-years follow up, initial post-procedural step-up and step-down in WSS at the edges of the scaffolded regions disappeared. Strut protrusion and its disturbing impact on laminar flow and WSS predetermine the thickness of the neointimal layer. With this study, we have concluded that, even that study was hypothesis -generating recent preclinical and clinical observations with thinner (ArterioSorb) and circular (Mirage) struts have demonstrated a causative relationship between embedment (more) and WSS disturbance (less).

In **chapter 10**, we investigated the relationship between post-implantation shear stress and vascular remodeling patterns in BRS and metallic stent implanted vessels. In this study, we used IVUS based-CFD models for Newtonian flow simulations. our study was the first exploring the impact of ESS on arterial remodeling in BRS and metallic stents in a comparative fashion. Serial 3D CFD models were performed and then paired ESS calculations post-implantation and at 3 years were conducted. Mean and minimum lumen area post-implantation, as measured by IVUS, were smaller in the BRS, as compared to the metallic DES arm. Post-implantation mean vessel area was substantially smaller in the BRS arm than in the DES arm (12.78 ± 3.20

mm² vs. 14.97±2.98 mm², p=0.012). However, at 3 years follow-up, mean vessel area was no longer statistically different, as a result of expansive remodeling in the BRS arm and constrictive remodeling in the DES arm in combination with some loss in lumen area (change in mean vessel area: +0.78±1.49 mm² vs. -0.66±1.64 mm², p=0.001). After classifying post-implantation ESS to low, intermediate and high terciles, in the BRS arm, the lowest tercile of ESS showed a decrease in lumen area as opposed to late lumen enlargement in the intermediate and the highest terciles. There was a significant difference in plaque-media area, increasing in BRS (+0.64±1.10 mm²) and decreasing in Xience (-0.46±1.22 mm²) at 3 years follow up. The lowest tercile of ESS post-implantation demonstrated an increase in plaque burden (+5.36±8.98%) considerably larger than the intermediate (1.86±8.09%) or the highest (0.72±7.46) tercile of ESS post-procedure. On the other hand, in the DES arm, there was no significant difference in change in the lumen, plaque vessel and plaque burden amongst the 3 terciles of ESS post-implantation. Finally, we have found that larger lumen area, smaller vessel area, higher plaque burden post-procedure, and higher median ESS post-procedure were associated with expansive remodeling. Younger age was also related to expansive remodeling in BRS group. Interestingly, tissue component was not associated with expansive remodeling. However, in the previous study of our group, necrotic core was significantly associated with expansive remodeling.

CONCLUSIONS

Bioresorbable scaffolds require optimal implantation techniques which should be taken into account for a safe follow-up. Different material properties require precious assessment and lesion pre-dilatation pre-implantation, sizing of the scaffold during implantation and post-dilatation using balloon-artery ratio of ≥ 1.1 .

Strut embedment-protrusion is one of the critical points during BRS implantation. Scaffold under-expansion makes strut embedment so pivotal. Regarding flow disruptions over the scaffolded luminal surface, strut protrusion analysis introduces so valuable information throughout the implantation.

Shear stress assessment has been in the cornerstone point in the stent/scaffold technology. Being the latest revolution in stent technology, the bioresorbable scaffolds should be modified to be more hemocompatible to prevent unprecedented cardiac events. Streamline thinner struts, non-thrombogenic scaffold materials, flow compatible macro-design are the points for

new BRS. Analyzing shear stress distribution is the most efficient method for investigating the hemodynamic features of scaffolded vessel segment. Pre-clinical CFD models give unique opportunity to unravel information about local micro-hemodynamic environment in different BRS by providing healthy vessel segments.

Appendices

Authors and affiliations

Curriculum vitae

Portfolio

List of publications

Acknowledgement

AUTHORS AND AFFILIATIONS

Mohammad Abdelghani	Academic Medical Center, University of Amsterdam, Amsterdam, The Netherlands
Alexander Abizaid	Department of Invasive Cardiology, Institute Dante Pazzanese of Cardiology, São Paulo, Brazil
Takashi Akasaka	Department of Cardiovascular Medicine, Wakayama Medical University, Wakayama, Japan
Felipe N. Albuquerque	Montefiore Medical Center, Albert Einstein College of Medicine, New York, New York, USA
Rasha Al-Lamee	Imperial College London, London, UK
Kadem Al-Lamee	Arterius, Leeds, UK
Taku Asano	Academic Medical Center, University of Amsterdam, Amsterdam, The Netherlands
Andreas Baumbach	Department of Cardiology, Barts Heart Centre, London, UK
Peter Barlis	Melbourne Medical School, Faculty of Medicine, Dentistry & Health Sciences, University of Melbourne, Melbourne, Australia
Christos V. Bourantas	Department of Cardiology, University College of London Hospitals, London, United Kingdom
Didier Carrié	Hopital de Rangueil, Toulouse, France
Rafael Cavalcante	ThoraxCenter, Erasmus Medical Center, Rotterdam, The Netherlands
Angel Cequier	Bellvitge University Hôpital, Barcelona, Spain
Daniel Chámie	Instituto Dante Pazzanese, São Paulo, Brazil; Cardiovascular Research Center, São Paulo, Brazil
Ply Chichareon	Academic Medical Center, University of Amsterdam, Amsterdam, The Netherlands
Bernard Chevalier	Institut Jacques Cartier, Massy, France
Cheng Chin	School of Mechanical Engineering, The University of Adelaide, Adelaide, South Australia, Australia.
Carlos Collet	Academic Medical Center, University of Amsterdam, Amsterdam, The Netherlands
Ricardo A. Costa	Instituto Dante Pazzanese de Cardiologia, Sao Paulo, Brazil

Tom Crake	Barts Heart Centre, Barts Health NHS Trust, London, United Kingdom
Carlo Di Mario	National Institute of Health Research Cardiovascular BRU, Royal Brompton & Harefield Foundation Trust & National Heart & Lung Institute, Imperial College, London, United Kingdom
Jouke Dijkstra	Division of Image Processing, Department of Radiology, Leiden University Medical Center, Leiden, The Netherlands
Marcello Dominici	S Maria UniversityHospital,Terni,Italy
Dariusz Dudek	Department of Interventional Cardiology, Jagiellonian University, Krakow, Poland
Jeroen Eggermont	Division of Image Processing, Department of Radiology, Leiden University Medical Center, Leiden, The Netherlands
Jean Fajadet	Department of Cardiology, Pasteur Hospital, Toulouse, France
Vasim Farooq	Manchester Heart Centre, Manchester Royal Infirmary, Central Manchester University, Hospitals NHS Trust, Manchester, UK.
Peter Fitzgerald	Stanford University, Stanford, CA, USA
Nicolas Foin	National Heart Centre Singapore; Duke-NUS Medical School, Singapore
Robert van Geuns	Department of Interventional Cardiology, Erasmus University Medical Center, Thoraxcenter, Rotterdam, The Netherlands
Frank Gijzen	Department of Biomedical Engineering, Erasmus University Medical Center, Thoraxcenter, Rotterdam, the Netherlands
Maik J. Grundeken	Academic Medical Center, University of Amsterdam, Amsterdam, The Netherlands
Giulio Guagliumi	Ospedali Riuniti di Bergamo, Bergamo, Italy
Umair Hayat	Faculty of Medicine, Dentistry and Health Sciences, Department of Medicine, The University of Melbourne, Victoria, Australia
Steffen Helqvist	Rigshospitalet, University of Copenhagen, Copenhagen, Denmark
Andrés Iñiguez	Interventional Cardiology Unit, Cardiology Department, Hospital Alvaro Cunqueiro, University Hospital of Vigo, Vigo, Spain
Yuki Ishibashi	ThoraxCenter, Erasmus Medical Center, Rotterdam, The Netherlands
Hans Jonker	Cardialysis, Rotterdam, The Netherlands
Yuki Katagiri	Academic Medical Center, University of Amsterdam, Amsterdam, The Netherlands
Takeshi Kimura	Department of Cardiovascular Medicine, Kyoto University Hospital, Kyoto, Japan

Peter Kitslaar	Division of Image Processing, Department of Radiology, Leiden University, Leiden, The Netherlands.
David van Klaveren	Department of Bioinformatics, Leiden University Medical Center, Leiden University, Leiden, Netherlands
Neal S. Kleiman	Department of Cardiology, Houston Methodist DeBakey Heart and Vascular Center, Texas, USA
Jaryl Ng Chen Koon	National Heart Centre Singapore; Duke-NUS Medical School, Singapore
Ran Kornowski	Rabin Medical Center, Petah Tikva, Israel
Ken Kozuma	Teikyo University Hospital, Tokyo, Japan
Robin P. Kraak	Heart Center, Department of Clinical and Experimental Cardiology, Amsterdam Cardiovascular Sciences, Amsterdam UMC, University of Amsterdam, Amsterdam, The Netherlands
Ulf Landmesser	Charite Universitätsmedizin Berlin, Berlin, Germany
Houng-Bang Liew	Department of Cardiology, Queen Elizabeth Hospital II, Sabah, Malaysia
Shengnan Liu	Division of Image Processing, Department of Radiology, Leiden University Medical Center, Leiden, The Netherlands
Dougal McClean	Christchurch Hospital, Christchurch, New Zealand
Yosuke Miyazaki	ThoraxCenter, Erasmus Medical Center, Rotterdam, The Netherlands
Rodrigo Modolo	Department of Cardiology, Academic Medical Center, Amsterdam, Netherlands
Stephen Moore	IBM Research Australia, Victoria, Australia
Takashi Muramatsu	Fujita Health University Hospital, Toyoake, Japan
Shimpei Nakatani	ThoraxCenter, Erasmus Medical Center, Rotterdam, The Netherlands
Takayuki Okamura	Department of Cardiology, Yamaguchi University, Yamaguchi, Japan
Yoshinobu Onuma	ThoraxCenter, Erasmus Medical Center, Rotterdam, The Netherlands
Andrew Ooi	Department of Mechanical Engineering, Melbourne School of Engineering, University of Melbourne, Melbourne, Australia
John A. Ormiston	Green Lane Cardiovascular Service, Auckland City Hospital, Auckland, New Zealand
Yukio Ozaki	Department of Cardiology, Fujita Health University Hospital, Toyoake, Japan

Kerem Pekkan	Department of Mechanical Engineering, Koc University, Istanbul, Turkey
Jan J. Piek	Academic Medical Center, University of Amsterdam, Amsterdam, The Netherlands
Eric K.W.Poon	Department of Mechanical Engineering, University of Melbourne, Parkville, Victoria 3010, Australia.
Jeffrey J. Popma	Beth Israel Deaconess Medical Center, Boston, MA, USA
Francesco Prati	San Giovanni Addolorata Hospital, Rome, Italy
Robert T. Pyo	Albert Einstein College of Medicine, Montefiore Medical Center, NY, USA
Lorenz Räber	University Hospital Bern, Bern, Switzerland
Maria D. Radu	Department of Cardiology, The Heart Center, Rigshospitalet, Copenhagen University Hospital, Copenhagen, Denmark
Evelyn Regar	Thoraxcenter, Erasmus Medical Center, Rotterdam, The Netherlands
Johan H. C. Reiber	Department of Radiology, Leiden University Medical Center, Leiden, The Netherlands
Manel Sabaté	Thorax Institute, University Hospital Clinic, Institut d'Investigacions Biome'diques August Pi i Sunyer, University of Barcelona, Barcelona, Spain
Teguh Santoso	Department of Internal Medicine, Faculty of Medicine, Dr. Cipto Mangunkusumo and Medistra Hospitals, University of Indonesia, Jakarta, Indonesia
Patrick W. Serruys	Department of Cardiology, Saolta Group, Galway University Hospital, Health Service Executive and National University of -Ireland Galway, Galway, Ireland. NHLI, Imperial College London, London, United Kingdom
Pieter C. Smits	Maastad Ziekenhuis, Rotterdam, the Netherlands
Yohei Sotomi	Academic Medical Center, University of Amsterdam, Amsterdam, The Netherlands
Rod Stables	Liverpool Heart and Chest Hospital, Liverpool, UK
Gregg W. Stone	Columbia University Medical Center, New York-Presbyterian Hospital, and the Cardiovascular Research Foundation, New York, NY, USA
Solomon Su	DuNing Incorporated, Tustin, California, USA
Pannipa Suwannasom	Academic Medical Center, University of Amsterdam, Amsterdam, The Netherlands

Kengo Tanabe	Division of Cardiology, Cardiac Intensive Care Unit, Mitsui Memorial Hospital, Tokyo, Japan
Hiroki Tateishi	ThoraxCenter, Erasmus Medical Center, Rotterdam, The Netherlands
Erhan Tenekecioglu	Thorax Center, Erasmus Medical Center, Rotterdam, The Netherlands
Vikas Thondapu	Department of Medicine, Faculty of Medicine, Dentistry & Health Sciences, The University of Melbourne, Melbourne, Victoria, Australia.
Jan G. Tijssen	Academic Medical Center, University of Amsterdam, Amsterdam, The Netherlands
Ryo Torii	Department of Mechanical Engineering, University College London, London, United Kingdom
Dilek Ural	Department of Cardiology, Faculty of Medicine, Koc University, Istanbul, Turkey
Ad J Van Boven	Medical Center Leeuwarden, Leeuwarden, Netherlands
Robert-Jan van Geuns	Thorax Center, Erasmus Medical Center, Rotterdam, The Netherlands
Renu Virmani	CVPath Institute, Inc., Gaithersburg, Maryland, USA
Stephan Windecker	Universitätsklinik für Kardiologie, Inselspital, Bern, Switzerland
Robbert J. De Winter	Academic Medical Center, University of Amsterdam, Amsterdam, The Netherlands
Joanna J. Wykrzykowska	Academic Medical Center, University of Amsterdam, Amsterdam, The Netherlands
Mustafa Yilmaz	Department of Cardiology, Bursa Uludag University, Bursa, Turkey
Ting-Bin Yu	DuNing Incorporated, Duning, Tustin, CA, USA
Yaping Zheng	Thorax Center, Erasmus Medical Center, Rotterdam, The Netherlands

CURRICULUM VITAE

Erhan Tenekecioglu, MD

Date and Place of Birth: 05/Sep/1976, Batman, Turkey

Gender: Male

Nationality: Turkish

E-mail : drercardio2@gmail.com

Educational Background: June 2000, M.D., Faculty of Medicine, Ege University, Izmir, Turkey

Postgraduate Training

Period	Position
Aug 2001 - Sep 2006	Cardiology fellowship, Bursa Education and Research Hospital, Bursa, Turkey
Nov 2014 – Feb 2018	<ul style="list-style-type: none"> • PhD student in Thorax Center, Erasmus Medical Center, Rotterdam, the Netherlands • Academic researcher in Cardialysis, Rotterdam, the Netherlands
Feb 2017 –March 2018	Chief Fellow, Department of Cardiology, Bursa Education and Research Hospital, Bursa, Turkey
March 2018 -	Assoc Professor, Department of Cardiology, Health Sciences University, Bursa Education and Research Hospital, Bursa, Turkey

License and Certification

Period	Title
September 2006	Turkish Medical Board
March 2008	Member of Turkish Medical Association
March 2018	Assoc Prof in Cardiology
November 2018	Affiliated in Health Sciences University

Memberships of Academic Societies

- Turkish Society of Cardiology
- European Atherosclerosis Society
- European Society of Cardiology - European Association of Percutaneous Cardiovascular Interventions

PhD PORTFOLIO

PhD student: Erhan Tenekecioglu

PhD period: Nov 2014 – Feb 2018

Supervisors: prof. dr. R. van Geuns and prof. dr. P.W.J.C. Serruys

Co-supervisor: dr. Y. Onuma

PhD training	Year	ECTS
Presentations and international conferences		
12th International Symposium on Biomechanics in Vascular Biology and Cardiovascular Disease, Rotterdam, The Netherlands (oral presentation)	2017	2.0
EuroPCR, Paris, France (2 oral presentations)	2016	4.0
EuroPCR, Paris, France (1 oral presentation)	2017	2.0
EuroPCR, Paris, France (2 oral presentations, 2 poster)	2018	4.0
Certifications		
ANSYS FLUENT, Computational Fluid Dynamics program	2015	
QFR (Quantitative Flow Reserve) analysis program	2017	
Other academic activities		
Local associated editor and regular reviewer for EuroIntervention	2014 -	4.0
Grants		
Abbott Vascular	2016- 2017	
ManLi Cardiology	2015- 2016	
TUBITAK	2014- 2015	

LIST OF PUBLICATIONS

Included in thesis

1. Tenekecioglu E, Farooq V, Bourantas CV, Silva RC, Onuma Y, Yilmaz M, Serruys PW. Bioresorbable scaffolds: a new paradigm in percutaneous coronary intervention. *BMC Cardiovasc Disord*. 2016 Feb 12;16:38.
2. Differential aspects between cobalt-chromium everolimus drug-eluting stent and Absorb everolimus bioresorbable vascular scaffold: from bench to clinical use. Sotomi Y, Suwannasom P, Tenekecioglu E, Tateishi H, Abdelghani M, Serruys PW, Onuma Y. *Expert Rev Cardiovasc Ther*. 2015 Oct;13(10):1127-45.
3. Tenekecioglu E, Bourantas CV, Abdelghani M, Sotomi Y, Suwannasom P, Tateishi H, Onuma Y, Yilmaz M, Serruys PW. Optimisation of percutaneous coronary intervention: indispensables for bioresorbable scaffolds. *Expert Rev Cardiovasc Ther*. 2016 Sep;14(9):1053-70.
4. Intracoronary optical coherence tomography: Clinical and research applications and intravascular imaging software overview. Tenekecioglu E, Albuquerque FN, Sotomi Y, Zeng Y, Suwannasom P, Tateishi H, Cavalcante R, Ishibashi Y, Nakatani S, Abdelghani M, Dijkstra J, Bourantas C, Collet C, Karanasos A, Radu M, Wang A, Muramatsu T, Landmesser U, Okamura T, Regar E, Räber L, Guagliumi G, Pyo RT, Onuma Y, Serruys PW. *Catheter Cardiovasc Interv*. 2017 Mar 1;89(4):679-689.
5. Randomized Comparison of Absorb Bioresorbable Vascular Scaffold and Mirage Microfiber Sirolimus-Eluting Scaffold Using Multimodality Imaging. Tenekecioglu E, Serruys PW, Onuma Y, Costa R, Chamié D, Sotomi Y, Yu TB, Abizaid A, Liew HB, Santoso T. *JACC Cardiovasc Interv*. 2017 Jun 12;10(11):1115-1130.
6. Assessment of the hemodynamic characteristics of Absorb BVS in a porcine coronary artery model. Tenekecioglu E, Torii R, Bourantas C, Abdelghani M, Cavalcante R, Sotomi Y, Crake T, Su S, Santoso T, Onuma Y, Serruys PW. *Int J Cardiol*. 2017 Jan 15;227:467-473.
7. Corrigendum to "Assessment of the hemodynamic characteristics of Absorb BVS in a porcine coronary artery model" [*Int. J. Cardiol*. 227 (2017) 467-473]. Tenekecioglu E, Torii R, Bourantas C, Abdelghani M, Cavalcante R, Sotomi Y, Crake T, Su S, Santoso T, Onuma Y, Serruys PW. *Int J Cardiol*. 2017 May 15;235:206.
8. Hemodynamic analysis of a novel bioresorbable scaffold in porcine coronary artery model. Tenekecioglu E, Torii R, Bourantas CV, Cavalcante R, Sotomi Y, Zeng Y, Collet C, Crake T, Abizaid A, Onuma Y, Su S, Santoso T, Serruys PW. *Catheter Cardiovasc Interv*. 2018 May 1;91(6):1084-1091.
9. Non-Newtonian pulsatile shear stress assessment: a method to differentiate bioresorbable scaffold platforms. Tenekecioglu E, Torii R, Bourantas CV, Al-Lamee R, Serruys PW. *Eur Heart J*. 2017 Sep 1;38(33):2570.
10. Preclinical assessment of the endothelial shear stress in porcine-based models following implantation of two different bioresorbable scaffolds: effect of scaffold design on the local haemodynamic micro-environment. Tenekecioglu E, Torii R, Bourantas C, Crake T, Zeng Y, Sotomi Y, Onuma Y, Yilmaz M, Santoso T, Serruys PW. *EuroIntervention*. 2016 Nov 20;12(10):1296.
11. Difference in haemodynamic microenvironment in vessels scaffolded with Absorb BVS and Mirage BRMS: insights from a preclinical endothelial shear stress study. Tenekecioglu E, Torii R, Bourantas C, Sotomi Y, Cavalcante R, Zeng Y, Collet C, Crake T, Suwannasom P, Onuma Y, Serruys PW. *EuroIntervention*. 2017 Dec 20;13(11):1327-1335.

12. Post-implantation shear stress assessment: an emerging tool for differentiation of bioresorbable scaffolds. Tenekecioglu E, Torii R, Katagiri Y, Chichareon P, Asano T, Miyazaki Y, Takahashi K, Modolo R, Al-Lamee R, Al-Lamee K, Colet C, Reiber JHC, Pekkan K, van Geuns R, Bourantas CV, Onuma Y, Serruys PW. *Int J Cardiovasc Imaging*. 2019 Mar;35(3):409-418.
13. Strut protrusion and shape impact on endothelial shear stress: insights from pre-clinical study comparing Mirage and Absorb bioresorbable scaffolds. Tenekecioglu E, Sotomi Y, Torii R, Bourantas C, Miyazaki Y, Collet C, Crake T, Su S, Onuma Y, Serruys PW. *Int J Cardiovasc Imaging*. 2017 Sep;33(9):1313-1322.
14. The effect of strut thickness on shear stress distribution in a preclinical model. Tenekecioglu E, Torii R, Bourantas C, Miyazaki Y, Collet C, Al-Lamee R, Al-Lamee K, Onuma Y, Serruys PW. *Int J Cardiovasc Imaging*. 2017 Nov;33(11):1675-1676.
15. Expert recommendations on the assessment of wall shear stress in human coronary arteries: existing methodologies, technical considerations, and clinical applications. Gijssen F, Katagiri Y, Barlis P, Bourantas C, Collet C, Coskun U, Daemen J, Dijkstra J, Edelman E, Evans P, van der Heiden K, Hose R, Koo BK, Krams R, Marsden A, Migliavacca F, Onuma Y, Ooi A, Poon E, Samady H, Stone P, Takahashi K, Tang D, Thondapu V, Tenekecioglu E, Timmins L, Torii R, Wentzel J, Serruys P. *Eur Heart J*. 2019 Sep 30. pii: ehz551.
16. Tenekecioglu E, Poon EK, Collet C, Thondapu V, Torii R, Bourantas CV, Zeng Y, Onuma Y, Ooi AS, Serruys PW, Barlis P. 2. The Nidus for Possible Thrombus Formation: Insight From the Microenvironment of Bioresorbable Vascular Scaffold. *JACC Cardiovasc Interv*. 2016 Oct 24;9(20):2167-2168.
16. Tenekecioglu E, Torii R, Sotomi Y, Collet C, Dijkstra J, Miyazaki Y, Crake T, Su S, Costa R, Chamie D, Liew HB, Santoso T, Onuma Y, Abizaid A, Bourantas CV and Serruys PW. The Effect of Strut Protrusion on Shear Stress Distribution: Hemodynamic Insights From a Prospective Clinical Trial. *JACC Cardiovascular interventions*. 2017;10:1803-1805.
17. Erhan Tenekecioglu*, Ryo Torii*, Ernest Spitzer, Yuki Katagiri, Ply Chichareon, Yohei Sotomi, Jouke Dijkstra, Taku Asano, Rodrigo Modolo, Kuniaki Takahashi, Hans Jonker, Yoshinobu Onuma, Christos V. Bourantas, Patrick W. The impact of plaque type on strut embedment/protrusion and shear stress distribution in bioresorbable scaffold. *Eur Heart J Cardiovasc Imaging*. 2019 Jun 19. pii: jez155.
18. Tenekecioglu E*, Torii R*, Bourantas C, Poon E, Thondapu V, Gijssen F, Sotomi Y, Onuma Y, Barlis P, Ooi AS, Serruys PW. 5. Five-year follow-up of underexpanded and overexpanded bioresorbable scaffolds: self-correction and impact on shear stress. *EuroIntervention*. 2017 Apr 20;12(17):2158-2159.
19. Tenekecioglu E*, Thondapu V*, Poon EKW, Onuma Y, Serruys PW. Improvement in local haemodynamics 5 years after implantation of a coronary bioresorbable scaffold: a pulsatile non-Newtonian shear stress analysis. *Eur Heart J Cardiovasc Imaging*. 2017 Nov 1;18(11):1294.
20. Tenekecioglu E*, Thondapu V*, Poon EKW, Collet C, Torii R, Bourantas CV, Chin C, Sotomi Y, Jonker H, Dijkstra J, Revalor E, Gijssen F, Onuma Y, Ooi A, Barlis P, Serruys PW. Endothelial shear stress 5 years after implantation of a coronary bioresorbable scaffold. *Eur Heart J*. 2018 May 7;39(18):1602-1609.
21. Tenekecioglu E, Torii R, Katagiri Y, Asano T, Modolo R, Miyazaki Y, Chichareon P, Poon EKW, Gijssen FJH, Thondapu V, van Klaveren D, Jonker H, Ooi A, Barlis P, Collet C, Onuma Y, Bourantas CV, Serruys PW. Early strut protrusion and late neointima thickness in the Absorb bioresorbable scaffold: a serial wall shear stress analysis up to five years. *EuroIntervention*. 2019 Jul 20;15(4):e370-e379.

22. Tenekecioglu E; Katagiri K; Takashi K; Tomaniak M; Dudek D; Cequier A; Carrié D; Iñiguez A; van der Schaaf RJ; Dominici M; van Boven AJ; Helqvist S; Sabaté M; Baumbach A; Piek JJ; Wykrzykowska JJ; Kitslaar P; Dijkstra J; Reiber HJC; Chevalier B; Bourantas CV; Gijsen F; Onuma Y; Torii R; Serruys PW. Endothelial Shear Stress and Vascular Remodeling in Bioresorbable Scaffold and Metallic Stent. Submitted.

Published articles, not included in thesis (first authorships)

23. Tenekecioglu E, Karabulut A, Yilmaz M. Comparison of tissue Doppler dynamics with Doppler flow in evaluating left atrial appendage function by transesophageal echocardiography in prehypertensive and hypertensive patients.
24. Tenekecioglu E, Karabulut A, Yilmaz M. E-page original images. Accessory mitral valve associated with cerebrovascular thromboembolism. *Anadolu Kardiyol Derg.* 2010 Nov 30;10(6):E27-8.
25. Tenekecioglu E, Agca FV, Karaagac K, Ozluk OA, Peker T, Kuzeytemiz M, Senturk M, Yilmaz M. Left atrial appendage function in prediction of paroxysmal atrial fibrillation in patients with untreated hypertension. *Clin Exp Hypertens.* 2014;36(5):348-53.
26. Tenekecioglu E, Yilmaz M, Karaagac K, Bekler A, Aslan B, Demir S, Kuzeytemiz M. Predictors of coronary collaterals in patients with non ST-elevated acute coronary syndrome: the paradox of the leukocytes. *Cent Eur J Immunol.* 2014;39(1):83-90.
27. Tenekecioglu E, Agca FV, Ozluk OA, Karaagac K, Demir S, Peker T, Kuzeytemiz M, Senturk M, Yilmaz M. Disturbed Left Atrial Function is Associated with Paroxysmal Atrial Fibrillation in Hypertension. *Arq Bras Cardiol.* 2014 Mar;102(3):253-62.
28. Tenekecioglu E, Yilmaz M, Demir S, Bekler A, Ozluk OA, Aydin U, Goncu T, Yontar OC. HDL-cholesterol is associated with systemic inflammation in cardiac syndrome X. *Minerva Med.* 2015 Jun;106(3):133-41. Epub 2014 Jul 16.
29. Tenekecioglu E, Yilmaz M, Bekler A, Demir S. Eosinophil count is related with coronary thrombus in non ST-elevated acute coronary syndrome. *Biomed Pap Med Fac Univ Palacky Olomouc Czech Repub.* 2015 Jun;159(2):266-71.
30. Tenekecioglu E, Yilmaz M, Yontar OC, Karaagac K, Agca FV, Tutuncu A, Kuzeytemiz M, Bekler A, Senturk M, Aydin U, Demir S. Microalbuminuria in untreated prehypertension and hypertension without diabetes. *Int J Clin Exp Med.* 2014 Oct 15;7(10):3420-9.
31. Tenekecioglu E, Yilmaz M, Yontar OC, Bekler A, Peker T, Karaagac K, Ozluk OA, Agca FV, Kuzeytemiz M, Senturk M, Aslan B, Topal D. Red blood cell distribution width is associated with myocardial injury in non-ST-elevation acute coronary syndrome. *Clinics (Sao Paulo).* 2015 Jan;70(1):18-23.
32. Tenekecioglu E, Karaagac K, Yontar OC, Agca FV, Ozluk OA, Tutuncu A, Arslan B, Yilmaz M. Evaluation of Tp-Te Interval and Tp-Te/QT Ratio in Patients with Coronary Slow Flow Tp-Te/QT Ratio and Coronary Slow Flow. *Eurasian J Med.* 2015 Jun;47(2):104-8. doi: 10.5152/eurasianjmed.2015.72.
33. Tenekecioglu E, Bourantas C, Abdelghani M, Zeng Y, Silva RC, Tateishi H, Sotomi Y, Onuma Y, Yilmaz M, Serruys PW. From drug eluting stents to bioresorbable scaffolds; to new horizons in PCI. *Expert Rev Med Devices.* 2016;13(3):271-86.
34. Tenekecioglu E, Farooq V, Bourantas CV, Silva RC, Onuma Y, Yilmaz M, Serruys PW. Bioresorbable scaffolds: a new paradigm in percutaneous coronary intervention. *BMC Cardiovasc Disord.* 2016 Feb 12;16:38.
35. Tenekecioglu E, Tateishi H, Serruys PW. Bioresorbable scaffolds for the treatment of in-stent restenosis: an alternative to double metal layers? *EuroIntervention.* 2016 Apr 20;11(13):1451-3.
36. Tenekecioglu E, Bourantas CV, Onuma Y, Serruys PW. Sealing of calcified plaques after bioresorbable scaffold implantations: a five-year follow up. *Int J Cardiovasc Imaging.* 2017 Apr;33(4):451-452.

Published articles, not included in thesis (co-authorships)

37. Tosu AR, Demir S, Kaya Y, Selcuk M, Asker M, Ozdemir M, Tenekecioglu E. Increased QT dispersion and P wave dispersion in major depressive disorder. *Exp Clin Cardiol*. 2013 Spring;18(2):110-2.
38. Yilmaz M, Tenekecioglu E, Arslan B, Bekler A, Ozluk OA, Karaagac K, Agca FV, Peker T, Akgumus A. White Blood Cell Subtypes and Neutrophil-Lymphocyte Ratio in Prediction of Coronary Thrombus Formation in Non-ST-Segment Elevated Acute Coronary Syndrome. *Clin Appl Thromb Hemost*. 2015 Jul;21(5):446-52.
39. Bekler A, Gazi E, Tenekecioglu E, Karaagac K, Altun B, Temiz A, Barutcu A, Peker T, Aslan B, Yilmaz M. Assessment of the relationship between red cell distribution width and fragmented QRS in patients with non-ST elevated acute coronary syndrome. *Med Sci Monit*. 2014 Mar 13;20:413-9.
40. Karaagac K, Tenekecioglu E, Yontar OC, Kuzeytemiz M, Vatansever F, Tutuncu A, Ozluk OA, Yilmaz M, Demir M. Effect of non-dipper and dipper blood pressure patterns on Tp-Te interval and Tp-Te/QT ratio in patients with metabolic syndrome. *Int J Clin Exp Med*. 2014 May 15;7(5):1397-403. eCollection 2014.
41. Tosu AR, Demir S, Selcuk M, Kaya Y, Akyol A, Ozdemir M, Tenekecioglu E. Comparison of inflammatory markers in non-dipper hypertension vs. dipper hypertension and in normotensive individuals: uric acid, C-reactive protein and red blood cell distribution width readings. *Postepy Kardiol Interwencyjne*. 2014;10(2):98-103.
42. Bekler A, Ozkan MT, Tenekecioglu E, Gazi E, Yener AU, Temiz A, Altun B, Barutcu A, Erbag G, Binnetoglu E. Increased Platelet Distribution Width Is Associated With Severity of Coronary Artery Disease in Patients With Acute Coronary Syndrome. *Angiology*. 2015 Aug;66(7):638-43.
43. Yontar OC, Karaagac K, Tenekecioglu E, Tutuncu A, Demir M, Melek M. Assessment of ventricular repolarization inhomogeneity in patients with mitral valve prolapse: value of T wave peak to end interval. *Int J Clin Exp Med*. 2014 Aug 15;7(8):2173-8.
44. Bekler A, Ozkan MT, Tenekecioglu E, Gazi E, Yener AU, Temiz A, Altun B, Barutcu A, Erbag G, Binnetoglu E. Increased Platelet Distribution Width Is Associated With Severity of Coronary Artery Disease in Patients With Acute Coronary Syndrome. *Angiology*. 2015 Aug;66(7):638-43. Epub 2014 Aug 10.
45. Karaagac K, Yontar OC, Tenekecioglu E, Vatansever F, Ozluk OA, Tutuncu A, Yagcioglu P, Yilmaz M. Evaluation of Tp-Te interval and Tp-Te/QTc ratio in patients with coronary artery ectasia. *Int J Clin Exp Med*. 2014 Sep 15;7(9):2865-70. eCollection 2014.
46. Bekler A, Barutcu A, Tenekecioglu E, Altun B, Gazi E, Temiz A, Kirilmaz B, Ozkan MT, Yener AU. The relationship between fragmented QRS complexes and SYNTAX and Gensini scores in patients with acute coronary syndrome. *Kardiol Pol*. 2015;73(4):246-54. Epub 2014 Nov 5.
47. Bekler A, Tenekecioglu E, Erbag G, Temiz A, Altun B, Barutcu A, Gazi E, Gunes F, Yilmaz M. Relationship between red cell distribution width and long-term mortality in patients with non-ST elevation acute coronary syndrome. *Anatol J Cardiol*. 2015 Aug;15(8):634-9. Epub 2014 Jun 23.
48. Karaagac K, Vatansever F, Tenekecioglu E, Ozluk OA, Kuzeytemiz M, Topal D, Yilmaz M. The Relationship between Non-Dipper Blood Pressure and Thoracic Aortic Diameter in Metabolic Syndrome. *Eurasian J Med*. 2014 Jun;46(2):120-5. doi: 10.5152/eajm.2014.27.
49. Karaagac K, Emul A, Tenekecioglu E, Agca FV, Ozluk OA, Tutuncu A, Yontar OC, Yilmaz M. The Effects of Metabolic Syndrome on TpTe Interval and TpTe/QT Ratio in Patients with Normal Coronary Arteries. *Eurasian J Med*. 2014 Oct;46(3):182-6. Epub 2014 Aug 26.
50. Yavuz S, Toktas F, Goncu T, Eris C, Gucu A, Ay D, Erdolu B, Tenekecioglu E, Karaagac K, Vural H, Ozyazicioglu A. Surgical embolectomy for acute massive pulmonary embolism. *Int J Clin Exp Med*. 2014 Dec 15;7(12):5362-75. eCollection 2014.

51. Arican Ozluk O, Topal D, Tenekecioglu E, Peker T, Yilmaz M, Karaagac K, Vatansever F, Boyraz B, Aydın O. High tenascin-C levels cause inadequate myocardial blush grade in patients with acute myocardial infarction. *Int J Clin Exp Med*. 2015 Feb 15;8(2):2554-61. eCollection 2015.
52. Goncu T, Alur I, Gucu A, Tenekecioglu E, Toktas F, Kahraman N, Vural H, Yavuz S. Clinical and echocardiographic results of the Kalangos biodegradable tricuspid ring for moderate and severe functional tricuspid regurgitation treatment. *Int J Clin Exp Med*. 2015 Feb 15;8(2):2839-45. eCollection 2015.
53. Arican Ozluk O, Ber I, Peker T, Yilmaz M, Tenekecioglu E, Karaagac K, Vatansever F. Mean platelet volume levels in the presence of angiographically documented peripheral artery disease. *Int J Clin Exp Med*. 2015 Feb 15;8(2):2899-904. eCollection 2015.
54. Michail M, Torii R, Crake T, Ozkor M, Garcia-Garcia HM, Tenekecioglu E, Onuma Y, Mathur A, Serruys PW, Bourantas CV. Local Hemodynamics: An Innocent Bystander or a Critical Factor Regulating Neoatherosclerotic Evolution? *JACC Cardiovasc Interv*. 2015 Aug 17;8(9):e149-e150. Epub 2015 Jul 22.
55. Kuzeytemiz M, Tenekecioglu E, Yilmaz M, Senturk M, Demir S, Bekler A, Aslan B. Assessment of left atrial functions in cardiac syndrome X. *Eur Rev Med Pharmacol Sci*. 2015 Aug;19(16):3023-9.
56. Barlis P, Poon EK, Thondapu V, Grundeken MJ, Tu S, Hayat U, Ooi A, Moore S, Tenekecioglu E, Wykrzykowska JJ, Serruys PW. Reversal of flow between serial bifurcation lesions: insights from computational fluid dynamic analysis in a population-based phantom model. *EuroIntervention*. 2015 Sep;11(5):e1-3. doi: 10.4244/EIJV11I5A111.
57. Nakatani S, Sotomi Y, Ishibashi Y, Grundeken MJ, Tateishi H, Tenekecioglu E, Zeng Y, Suwannasom P, Regar E, Radu MD, Räber L, Bezerra H, Costa MA, Fitzgerald P, Prati F, Costa RA, Dijkstra J, Kimura T, Kozuma K, Tanabe K, Akasaka T, Di Mario C, Serruys PW, Onuma Y. Comparative analysis method of permanent metallic stents (XIENCE) and bioresorbable poly-L-lactic (PLLA) scaffolds (Absorb) on optical coherence tomography at baseline and follow-up. *EuroIntervention*. 2016 Dec 20;12(12):1498-1509. doi: 10.4244/EIJY15M10_03.
58. Agca FV, Demircan N, Peker T, Ari H, Karaagac K, Ozluk OA, Yilmaz M, Tenekecioglu E. Infective endocarditis: a tertiary referral centre experience from Turkey. *Int J Clin Exp Med*. 2015 Aug 15;8(8):13962-8. eCollection 2015.
59. Ozluk OA, Yilmaz M, Topal D, Tenekecioglu E, Peker T, Kanat S, Karaagac K, Vatansever F, Parlak U. Neutrophil to lymphocyte ratio is associated with proximal/middle segment of the LAD lesions in patients with ST segment elevation infarction. *Cent Eur J Immunol*. 2016;41(4):386-391. doi: 10.5114/ceji.2016.65138. Epub 2017 Jan 24.
60. Gürdoğan M, Ari H, Tenekecioglu E, Ari S, Bozat T, Koca V, Melek M. Predictors of Atrial Fibrillation Recurrence in Hyperthyroid and Euthyroid Patients. *Arq Bras Cardiol*. 2016 Feb;106(2):84-91. doi: 10.5935/abc.20160013. Epub 2016 Jan 26.
61. Suwannasom P, Sotomi Y, Tateishi H, Tenekecioglu E, Zeng Y, Kraak RP, Wykrzykowska JJ, De Winter RJ, Serruys PW, Onuma Y. Bioresorbable drug-eluting scaffolds for treatment of vascular disease. *Expert Opin Drug Deliv*. 2016;13(5):725-39. doi: 10.1517/17425247.2016.1153062. Epub 2016 Mar 1.
62. Zeng Y, Tateishi H, Suwannasom P, Tenekecioglu E, Silva RC, Sotomi Y, Onuma Y, Serruys PW. Progression of calcification after implantation of a fully bioresorbable scaffold: A serial and combined IVUS-OCT follow-up of 5 years. *Int J Cardiol*. 2016 Apr 15;209:176-8. doi: 10.1016/j.ijcard.2016.01.030. Epub 2016 Jan 7.
63. Sotomi Y, Tateishi H, Suwannasom P, Dijkstra J, Eggermont J, Liu S, Tenekecioglu E, Zheng Y, Abdelghani M, Cavalcante R, de Winter RJ, Wykrzykowska JJ, Onuma Y, Serruys PW, Kimura T. Quantitative assessment of the stent/scaffold strut embedment analysis by optical coherence tomography. *Int J Cardiovasc Imaging*. 2016 Jun;32(6):871-83. doi: 10.1007/s10554-016-0856-6. Epub 2016 Feb 22.
64. Tateishi H, Suwannasom P, Sotomi Y, Nakatani S, Ishibashi Y, Tenekecioglu E, Abdelghani M, Cavalcante R, Zeng Y, Grundeken MJ, Albuquerque FN, Veldhof S, Onuma Y, Serruys PW; investigators of the ABSORB Cohort B study. Edge Vascular Response After Resorption of the Everolimus-Eluting

- Bioresorbable Vascular Scaffold - A 5-Year Serial Optical Coherence Tomography Study. *Circ J*. 2016 Apr 25;80(5):1131-41. doi: 10.1253/circj.CJ-15-1325. Epub 2016 Mar 3.
65. Bourantas CV, Jaffer FA, Gijzen FJ, van Soest G, Madden SP, Courtney BK, Fard AM, Tenekecioglu E, Zeng Y, van der Steen AFW, Emelianov S, Muller J, Stone PH, Marcu L, Tearney GJ, Serruys PW. Hybrid intravascular imaging: recent advances, technical considerations, and current applications in the study of plaque pathophysiology. *Eur Heart J*. 2017 Feb 7;38(6):400-412. doi: 10.1093/eurheartj/ehw097.
66. Ari H, Emlek N, Ari S, Coşar S, Doğanay K, Aydın C, Tenekecioglu E, Tütüncü A, Yontar OC, Gürdoğan M, Bozat T, and Melek M. The Effect of High Dose Cilostazol and Rosuvastatin on Periprocedural Myocardial Injury in Patients with Elective Percutaneous Coronary Intervention. *Acta Cardiol Sin*. 2015 Jul;31(4):292-300.
67. Abdelghani M, Spitzer E, Soliman OII, Beitzke D, Laggner R, Cavalcante R, Tateishi H, Campos CM, Verstraeten L, Sotomi Y, Tenekecioglu E, Onuma Y, Tijssen JG, de Winter RJ, Maisano F, Serruys PW. A simplified and reproducible method to size the mitral annulus: implications for transcatheter mitral valve replacement. *Eur Heart J Cardiovasc Imaging*. 2017 Jun 1;18(6):697-706.
68. Chang M, Ahn JM, Lee CW, Cavalcante R, Sotomi Y, Onuma Y, Tenekecioglu E, Han M, Park DW, Kang SJ, Lee SW, Kim YH, Park SW, Serruys PW, Park SJ. Long-Term Mortality After Coronary Revascularization in Nondiabetic Patients With Multivessel Disease. *J Am Coll Cardiol*. 2016 Jul 5;68(1):29-36.
69. Collet C, Sotomi Y, Cavalcante R, Suwannasom P, Tenekecioglu E, Onuma Y, Serruys PW. Coronary stent thrombosis: what have we learned? *J Thorac Dis*. 2016 Jul;8(7):1398-405.
70. Cavalcante R, Sotomi Y, Lee CW, Ahn JM, Farooq V, Tateishi H, Tenekecioglu E, Zeng Y, Suwannasom P, Collet C, Albuquerque FN, Onuma Y, Park SJ, Serruys PW. Outcomes After Percutaneous Coronary Intervention or Bypass Surgery in Patients With Unprotected Left Main Disease. *J Am Coll Cardiol*. 2016 Sep 6;68(10):999-1009.
71. Ozkan H, Binici S, Tenekecioglu E, Ari H, Bozat T. Atrial Strain and Strain Rate: A Novel Method for the Evaluation of Atrial Stunning. *Arq Bras Cardiol*. 2016 Oct;107(4):305-313. Epub 2016 Sep 12.
72. Cavalcante R, Sotomi Y, Zeng Y, Lee CW, Ahn JM, Collet C, Tenekecioglu E, Suwannasom P, Onuma Y, Park SJ, Serruys PW. Coronary bypass surgery versus stenting in multivessel disease involving the proximal left anterior descending coronary artery. *Heart*. 2017 Mar;103(6):428-433. doi: 10.1136/heartjnl-2016-309720. Epub 2016 Sep 20.
73. Sotomi Y, Onuma Y, Suwannasom P, Tateishi H, Tenekecioglu E, Zeng Y, Cavalcante R, Jonker H, Dijkstra J, Foin N, Koon JN, Collet C, de Winter RJ, Wykrzykowska JJ, Stone GW, Popma JJ, Kozuma K, Tanabe K, Serruys PW, Kimura T. Is quantitative coronary angiography reliable in assessing the lumen gain after treatment with the everolimus-eluting bioresorbable polylactide scaffold? *EuroIntervention*. 2016 Oct 10;12(8):e998-e1008.
74. Sotomi Y, Cavalcante R, Shlofmitz RA, Suwannasom P, Tateishi H, Tenekecioglu E, Zheng Y, Abdelghani M, de Winter RJ, Wykrzykowska JJ, Onuma Y, Serruys PW. Quantification by optical coherence tomography imaging of the ablation volume obtained with the Orbital Atherectomy System in calcified coronary lesions. *EuroIntervention*. 2016 Oct 20;12(9):1126-1134.
75. Sotomi Y, Onuma Y, Dijkstra J, Eggermont J, Liu S, Tenekecioglu E, Zeng Y, Asano T, de Winter RJ, Popma JJ, Kozuma K, Tanabe K, Serruys PW, Kimura T. Impact of Implantation Technique and Plaque Morphology on Strut Embedment and Scaffold Expansion of Polylactide Bioresorbable Scaffold - Insights From ABSORB Japan Trial. *Circ J*. 2016 Oct 25;80(11):2317-2326. Epub 2016 Oct 8.
76. Collet C, Sotomi Y, Cavalcante R, Asano T, Miyazaki Y, Tenekecioglu E, Kistlaar P, Zeng Y, Suwanasson P, de Winter RJ, Nieman K, Serruys PW, Onuma Y. Accuracy of coronary computed tomography angiography for bioresorbable scaffold luminal investigation: a comparison with optical coherence tomography. *Int J Cardiovasc Imaging*. 2017 Mar;33(3):431-439. doi: 10.1007/s10554-016-1018-6. Epub 2016 Nov 28.
77. Cavalcante R, Onuma Y, Sotomi Y, Collet C, Thomsen B, Rogers C, Zeng Y, Tenekecioglu E, Asano T, Miyasaki Y, Abdelghani M, Morel MA, Serruys PW. Non-invasive Heart Team assessment of multivessel coronary disease with coronary computed tomography angiography based on SYNTAX

score II treatment recommendations: design and rationale of the randomised SYNTAX III Revolution trial. *EuroIntervention*. 2017 Mar 20;12(16):2001-2008.

78. Suwannasom P, Sotomi Y, Asano T, Koon JN, Tateishi H, Zeng Y, Tenekecioglu E, Wykrzykowska JJ, Foin N, de Winter RJ, Ormiston JA, Serruys PW, Onuma Y. Change in lumen eccentricity and asymmetry after treatment with Absorb bioresorbable vascular scaffolds in the ABSORB cohort B trial: a five-year serial optical coherence tomography imaging study. *EuroIntervention*. 2017 Apr 7;12(18):e2244-e2252.

79. Lee CW, Ahn JM, Cavalcante R, Sotomi Y, Onuma Y, Suwannasom P, Tenekecioglu E, Yun SC, Park DW, Kang SJ, Lee SW, Kim YH, Park SW, Serruys PW, Park SJ. Coronary Artery Bypass Surgery Versus Drug-Eluting Stent Implantation for Left Main or Multivessel Coronary Artery Disease: A Meta-Analysis of Individual Patient Data. *JACC Cardiovasc Interv*. 2016 Dec 26;9(24):2481-2489.

80. Zeng Y, Cavalcante R, Tenekecioglu E, Suwannasom P, Sotomi Y, Collet C, Abdelghani M, Jonker H, Digne F, Horstkotte D, Zehender M, Indolfi C, Saia F, Fiorilli R, Chevalier B, Bolognese L, Goicolea J, Nie S, Onuma Y, Serruys PW; investigators of Absorb II study. Comparative assessment of "plaque/media" change on three modalities of IVUS immediately after implantation of either everolimus-eluting bioresorbable vascular scaffold or everolimus-eluting metallic stent in Absorb II study. *Int J Cardiovasc Imaging*. 2017 Apr;33(4):441-449.

81. Miyazaki Y, Suwannasom P, Sotomi Y, Abdelghani M, Tummala K, Katagiri Y, Asano T, Tenekecioglu E, Zeng Y, Cavalcante R, Collet C, Onuma Y, Serruys PW. Single or dual antiplatelet therapy after PCI. *Nat Rev Cardiol*. 2017 May;14(5):294-303.

82. Patel K, Tarkin J, Serruys PW, Tenekecioglu E, Foin N, Zhang YJ, Crake T, Moon J, Mathur A, Bourantas CV. Invasive or non-invasive imaging for detecting high-risk coronary lesions? *Expert Rev Cardiovasc Ther*. 2017 Mar;15(3):165-179. doi: 10.1080/14779072.2017.1297231. Epub 2017 Mar 1.

83. Sotomi Y, Onuma Y, Miyazaki Y, Asano T, Katagiri Y, Tenekecioglu E, Jonker H, Dijkstra J, de Winter RJ, Wykrzykowska JJ, Stone GW, Popma JJ, Kozuma K, Tanabe K, Serruys PW, Kimura T. Is quantitative coronary angiography reliable in assessing the late lumen loss of the everolimus-eluting bioresorbable polylactide scaffold in comparison with the cobalt-chromium metallic stent? *EuroIntervention*. 2017 Aug 4;13(5):e585-e594.

84. Michail M, Serruys PW, Stettler R, Crake T, Torii R, Tenekecioglu E, Zeng Y, Onuma Y, Mathur A, Bourantas CV. Intravascular multimodality imaging: feasibility and role in the evaluation of coronary plaque pathology. *Eur Heart J Cardiovasc Imaging*. 2017 Jun 1;18(6):613-620.

85. Zeng Y, Tateishi H, Cavalcante R, Tenekecioglu E, Suwannasom P, Sotomi Y, Collet C, Nie S, Jonker H, Dijkstra J, Radu MD, Räber L, McClean DR, van Geuns RJ, Christiansen EH, Fahrni T, Koolen J, Onuma Y, Bruining N, Serruys PW. Serial Assessment of Tissue Precursors and Progression of Coronary Calcification Analyzed by Fusion of IVUS and OCT: 5-Year Follow-Up of Scaffolded and Nonscaffolded Arteries. *JACC Cardiovasc Imaging*. 2017 Oct;10(10 Pt A):1151-1161.

86. Sotomi Y, Onuma Y, Collet C, Tenekecioglu E, Virmani R, Kleiman NS, Serruys PW. Bioresorbable Scaffold: The Emerging Reality and Future Directions. *Circ Res*. 2017 Apr 14;120(8):1341-1352.

87. Collet C, Asano T, Miyazaki Y, Tenekecioglu E, Katagiri Y, Sotomi Y, Cavalcante R, de Winter RJ, Kimura T, Gao R, Puricel S, Cook S, Capodanno D, Onuma Y, Serruys PW. Late thrombotic events after bioresorbable scaffold implantation: a systematic review and meta-analysis of randomized clinical trials. *Eur Heart J*. 2017 Sep 1;38(33):2559-2566.

88. Stettler R, Dijkstra J, Räber L, Torii R, Zhang YJ, Karanasos A, Lui S, Crake T, Hamshere S, Garcia-Garcia HM, Tenekecioglu E, Ozkor M, Windecker S, Serruys PW, Regar E, Mathur A, Bourantas CV. Neointima and neoatherosclerotic characteristics in bare metal and first- and second-generation drug-eluting stents in patients admitted with cardiovascular events attributed to stent failure: an optical coherence tomography study. *EuroIntervention*. 2018 Feb 2;13(15):e1831-e1840.

89. Miyazaki Y, Abdelghani M, de Boer ES, Aben JP, van Sloun M, Suchecki T, van 't Veer M, Collet C, Asano T, Katagiri Y, Tenekecioglu E, Soliman OII, Onuma Y, de Winter R, Tonino P, van de Vosse FN, Rutten MCM, Serruys PW. A novel synchronised diastolic injection method to reduce contrast volume during aortography for aortic regurgitation assessment: in vitro experiment of a transcatheter heart valve model. *EuroIntervention*. 2017 Dec 20;13(11):1288-1295.

90. Ahn JM, Park DW, Lee CW, Chang M, Cavalcante R, Sotomi Y, Onuma Y, Tenekecioglu E, Han M, Lee PH, Kang SJ, Lee SW, Kim YH, Park SW, Serruys PW, Park SJ. Comparison of Stenting Versus Bypass Surgery According to the Completeness of Revascularization in Severe Coronary Artery Disease: Patient-Level Pooled Analysis of the SYNTAX, PRECOMBAT, and BEST Trials. *JACC Cardiovasc Interv.* 2017 Jul 24;10(14):1415-1424.
91. Collet C, Chevalier B, Cequier A, Fajadet J, Dominici M, Helqvist S, Van Boven AJ, Dudek D, McClean D, Almeida M, Piek JJ, Tenekecioglu E, Bartorelli A, Windecker S, Serruys PW, Onuma Y. Diagnostic Accuracy of Coronary CT Angiography for the Evaluation of Bioresorbable Vascular Scaffolds. *JACC Cardiovasc Imaging.* 2018 May;11(5):722-732.
92. Sotomi Y, Suwannasom P, Tenekecioglu E, Collet C, Nakatani S, Okamura T, Muramatsu T, Ishibashi Y, Tateishi H, Miyazaki Y, Asano T, Katagiri Y, von Zur Muehlen C, Tanabe K, Kozuma K, Ozaki Y, Serruys PW, Onuma Y. Imaging assessment of bioresorbable vascular scaffolds. *Cardiovasc Interv Ther.* 2018 Jan;33(1):11-22.
93. Bourantas CV, Tenekecioglu E, Radu M, Räber L, Serruys PW. State of the art: role of intravascular imaging in the evolution of percutaneous coronary intervention - a 30-year review. *EuroIntervention.* 2017 Aug 25;13(6):644-653.
94. Asano T, Katagiri Y, Collet C, Tenekecioglu E, Miyazaki Y, Sotomi Y, Amoroso G, Aminian A, Brugaletta S, Vrolix M, Hernandez-Antolín R, van de Harst P, Íñiguez-Romo A, Janssens L, Smits PC, Wykrzykowska JJ, Ribeiro VG, Pereira H, da Silva PC, Piek JJ, Reiber JHC, von Birgelen C, Sabaté M, Onuma Y, Serruys PW. Functional comparison between the BuMA Supreme biodegradable polymer sirolimus-eluting stent and a durable polymer zotarolimus-eluting coronary stent using quantitative flow ratio: PIONEER QFR substudy. *EuroIntervention.* 2018 Aug 3;14(5):e570-e579.
95. Ng J, Bourantas CV, Torii R, Ang HY, Tenekecioglu E, Serruys PW, Foin N. Local Hemodynamic Forces After Stenting: Implications on Restenosis and Thrombosis. *Arterioscler Thromb Vasc Biol.* 2017 Dec;37(12):2231-2242.
96. Katagiri Y, Tenekecioglu E, Serruys PW, Collet C, Katsikis A, Asano T, Miyazaki Y, Piek JJ, Wykrzykowska JJ, Bourantas C, Onuma Y. What does the future hold for novel intravascular imaging devices: a focus on morphological and physiological assessment of plaque. *Expert Rev Med Devices.* 2017 Dec;14(12):985-999.
97. Zeng Y, Cavalcante R, Collet C, Tenekecioglu E, Sotomi Y, Miyazaki Y, Katagiri Y, Asano T, Abdelghani M, Nie S, Bourantas CV, Bruining N, Onuma Y, Serruys PW. Coronary calcification as a mechanism of plaque/media shrinkage in vessels treated with bioresorbable vascular scaffold: A multimodality intracoronary imaging study. *Atherosclerosis.* 2018 Feb;269:6-13.
98. Kerkmeijer LS, Tenekecioglu E, Wykrzykowska JJ. Stent thrombosis in patients with drug-eluting stents and bioresorbable vascular scaffolds: the feared complication. *Pol Arch Intern Med.* 2018 Jan 31;128(1):52-59.
99. Modolo R, Miyazaki Y, Chichareon P, Asano T, Collet C, Tenekecioglu E, Katagiri Y, Soliman O, Garg S, Onuma Y, Serruys PW. Interventional cardiology: review of the year 2017. *EuroIntervention.* 2018 Apr 20;13(17):2083-2096.
100. Collet C, Miyazaki Y, Ryan N, Asano T, Tenekecioglu E, Sonck J, Andreini D, Sabate M, Brugaletta S, Stables RH, Bartorelli A, de Winter RJ, Katagiri Y, Chichareon P, De Maria GL, Suwannasom P, Cavalcante R, Jonker H, Morel MA, Cosyns B, Kappetein AP, Taggart DT, Farooq V, Escaned J, Banning A, Onuma Y, Serruys PW. Fractional Flow Reserve Derived From Computed Tomographic Angiography in Patients With Multivessel CAD. *J Am Coll Cardiol.* 2018 Jun 19;71(24):2756-2769.
101. Katagiri Y, Serruys PW, Tenekecioglu E, Asano T, Collet C, Miyazaki Y, Katsikis A, Piek JJ, Wykrzykowska JJ, Chevalier B, Mintz GS, Stone GW, Onuma Y. Acute and long-term relocation of minimal lumen area after bioresorbable scaffold or metallic stent implantation. *EuroIntervention.* 2019 Sep 20;15(7):594-602.
102. Asano T, Serruys PW, Collet C, Miyazaki Y, Takahashi K, Chichareon P, Katagiri Y, Modolo R, Tenekecioglu E, Morel MA, Garg S, Wykrzykowska J, Piek JJ, Sabate M, Morice MC, Chevalier B, Windecker S, Onuma Y. Angiographic late lumen loss revisited: impact on long-term target lesion revascularization. *Eur Heart J.* 2018 Sep 21;39(36):3381-3389.

103. Collet C, Onuma Y, Sonck J, Asano T, Vandeloo B, Kornowski R, Tu S, Westra J, Holm NR, Xu B, de Winter RJ, Tijssen JG, Miyazaki Y, Katagiri Y, Tenekecioglu E, Modolo R, Chichareon P, Cosyns B, Schoors D, Roosens B, Lochy S, Argacha JF, van Rosendael A, Bax J, Reiber JHC, Escaned J, De Bruyne B, Wijns W, Serruys PW. Diagnostic performance of angiography-derived fractional flow reserve: a systematic review and Bayesian meta-analysis. *Eur Heart J*. 2018 Sep 14;39(35):3314-3321.
104. Miyazaki Y, Modolo R, Abdelghani M, Tateishi H, Cavalcante R, Collet C, Asano T, Katagiri Y, Tenekecioglu E, Sarmiento-Leite R, Mangione JA, Abizaid A, Soliman Oll, Onuma Y, Serruys PW, Lemos PA, Brito FS Jr. The Role of Quantitative Aortographic Assessment of Aortic Regurgitation by Videodensitometry in the Guidance of Transcatheter Aortic Valve Implantation. *Arq Bras Cardiol*. 2018 Aug;111(2):193-202.
105. Torii R, Stettler R, Räber L, Zhang YJ, Karanasos A, Dijkstra J, Patel K, Crake T, Hamshere S, Garcia-Garcia HM, Tenekecioglu E, Ozkor M, Baumbach A, Windecker S, Serruys PW, Regar E, Mathur A, Bourantas CV. Implications of the local hemodynamic forces on the formation and destabilization of neoatherosclerotic lesions. *Int J Cardiol*. 2018 Dec 1;272:7-12.
106. Kanat S, Çakır H, Tütüncü A, Tenekecioglu E. Successful cryoablation of atrial fibrillation from jugular approach in patient with interrupted inferior vena cava and azygos continuation. *Pacing Clin Electrophysiol*. 2019 Mar;42(3):309-312.
107. Asano T, Katagiri Y, Chang CC, Kogame N, Chichareon P, Takahashi K, Modolo R, Tenekecioglu E, Collet C, Jonker H, Appleby C, Zaman A, van Mieghem N, Uren N, Zueco J, Piek JJ, Reiber JHC, Farooq V, Escaned J, Banning AP, Serruys PW, Onuma Y. Angiography-Derived Fractional Flow Reserve in the SYNTAX II Trial: Feasibility, Diagnostic Performance of Quantitative Flow Ratio, and Clinical Prognostic Value of Functional SYNTAX Score Derived From Quantitative Flow Ratio in Patients With 3-Vessel Disease. *JACC Cardiovasc Interv*. 2019 Feb 11;12(3):259-270.
108. Chichareon P, Katagiri Y, Asano T, Takahashi K, Kogame N, Modolo R, Tenekecioglu E, Chang CC, Tomaniak M, Kukreja N, Wykrzykowska JJ, Piek JJ, Serruys PW, Onuma Y. Mechanical properties and performances of contemporary drug-eluting stent: focus on the metallic backbone. *Expert Rev Med Devices*. 2019 Mar;16(3):211-228.
109. Asano T, Hytönen J, Chichareon P, Taavitsainen J, Kogame N, Katagiri Y, Miyazaki Y, Takahashi K, Modolo R, Komiyama H, Tenekecioglu E, Sotomi Y, Wykrzykowska JJ, Piek JJ, Martin J, Baumbach A, Mathur A, Onuma Y, Ylä-Herttuala S, Serruys PW. Serial Optical Coherence Tomography at Baseline, 7 Days, and 1, 3, 6 and 12 Months After Bioresorbable Scaffold Implantation in a Growing Porcine Model. *Circ J*. 2019 Feb 25;83(3):556-566.
110. Çakır H, Kaymaz C, Tanboga İH, Çakır H, Tokgöz HC, Hąkgör A, Akbal ÖY, Er F, Topal D, Mutluer FO, Demir M, Tenekecioglu E. Increased exercise-related platelet activation assessed by impedance aggregometry in diabetic patients despite aspirin therapy. *J Thromb Thrombolysis*. 2019 Apr;47(3):396-402.
111. Kanat S, Mutluer FO, Tütüncü A, Karaduman BD, Bozkaya VO, Keskin M, Uslu A, Çay S, Tenekecioglu E. Left Atrial Function Is Improved in Short-Term Follow-Up after Catheter Ablation of Outflow Tract Premature Ventricular Complexes. *Medicina (Kaunas)*. 2019 Jun 3;55(6). pii: E241.
112. Katagiri Y, Torii R, Takahashi K, Tenekecioglu E, Asano T, Chichareon P, Tomaniak M, Piek JJ, Wykrzykowska JJ, Bullett N, Ahmed N, Al-Lamee K, Al-Lamee R, Leclerc G, Kitslaar P, Dijkstra J, Reiber JHC, Poon EKW, Bourantas CV, Gijzen FJH, Serruys PW, Onuma Y. Preclinical evaluation of a thin-strut bioresorbable scaffold (ArterioSorb): acute-phase invasive imaging assessment and hemodynamic implication. *EuroIntervention*. 2019 Jul 9. pii: EIJ-D-18-01190.
113. Kanat S, Duran Karaduman B, Tütüncü A, Tenekecioglu E, Mutluer FO, Akar Bayram N. Effect of Echocardiographic Epicardial Adipose Tissue Thickness on Success Rates of Premature Ventricular Contraction Ablation. *Balkan Med J*. 2019 Oct 28;36(6):324-330.
114. Uslu A, Kup A, Dogan C, Sari M, Cersit S, Aksu U, Kanat S, Demir M, Tenekecioglu E. Relationship between epicardial adipose tissue thickness and coronary thrombus burden in patients with ST-elevation myocardial infarction. *Biomed Pap Med Fac Univ Palacky Olomouc Czech Repub*. 2019 Sep 16.

115. Chichareon P, Modolo R, Collet C, Tenekecioglu E, Vink MA, Oh PC, Ahn JM, Musto C, Díaz de la Llera LS, Cho YS, Violini R, Park SJ, Suryapranata H, Piek JJ, de Winter RJ, Wykrzykowska JJ, Spaulding C, Kang WC, Slagboom T, Hofma SH, Wijnbergen IF, Di Lorenzo E, Pijls NH, Räber L, Brugaletta S, Sabaté M, Stoll HP, Stone GW, Windecker S, Onuma Y, Serruys PW. Efficacy and Safety of Stents in ST-Segment Elevation Myocardial Infarction. *J Am Coll Cardiol*. 2019 Nov 26;74(21):2572-2584.
116. Bozkaya VÖ, Yumusak OH, Ozaksit G, Tenekecioglu E, Gül Ibrişim E, Alkan M, Oskovi-Kaplan ZA, Erel Ö. The role of oxidative stress on subclinical atherosclerosis in premature ovarian insufficiency and relationship with carotid intima-media thickness. *Gynecol Endocrinol*. 2020 Aug;36(8):687-692.
117. Rezaeimoghaddam M, Oguz GN, Ates MS, Bozkaya TA, Piskin S, Samaneh Lashkarinia S, Tenekecioglu E, Karagoz H, Pekkan K. Patient-Specific Hemodynamics of New Coronary Artery Bypass Configurations. *Cardiovasc Eng Technol*. 2020 Dec;11(6):663-678.
118. Kuzeytemiz M, Tenekecioglu E. Effect of renin-angiotensin system blocker on COVID-19 in young patients with hypertension. *J Investig Med*. 2022 Mar;70(3):786-791.
119. Çakır H, Güneş A, Er F, Çakır H, Karagöz A, Yılmaz F, Öcal L, Zehir R, Emiroğlu MY, Demir M, Kaymaz C, Tenekecioglu E. Evaluating the relationship of sleep quality and sleep duration with Framingham coronary heart disease risk score. *Chronobiol Int*. 2022 May;39(5):636-643.
120. Keskin M, Dogan S, Kaya A, Tenekecioglu E, Ocal L, Cersit S, Seker M, Yavuz S, Orhan AL. The prognostic value of time from symptom onset to thrombolysis in patients with pulmonary embolism. *Int J Cardiol*. 2022 Apr 1;352:131-136.
121. Galimzhanov A, Tenekecioglu E, Rustamova F, Tun HN, Mamas MA. The Prognostic Utility of Mean Platelet Volume in Patients With Acute Coronary Syndrome: A Systematic Review With Meta-Analyses. *Angiology*. 2022 Jan 21;33197211070908.
122. Topal D, Mutluer FO, Aydin O, Cakir H, Kanat S, Aslan B, Er F, Uslu A, Bozkaya VO, Keskin M, Karşı R, Yılmaz M, Aksakal E, Demir M, Tenekecioglu E. The relationship between hemoglobin A1c levels and thrombus load in patients with type 2 diabetes mellitus and non-ST-segment elevation myocardial infarction. *J Res Med Sci*. 2021 Nov 29;26:118.
123. Abdelshafy M, Caliskan K, Guven G, Elkoumy A, Elsherbini H, Elzomor H, Tenekecioglu E, Akin S, Soliman O. Temporary Right-Ventricular Assist Devices: A Systematic Review. *J Clin Med*. 2022 Jan 26;11(3):613.
124. Çakır H, Kanat S, Çakır H, Tenekecioglu E. Lower Serum Fetuin-A Levels are Associated with a Higher Ten-Year Mortality Risk in Patients with ST-Elevation Myocardial Infarction. *Arq Bras Cardiol*. 2022 Jan;118(1):14-21.
125. Keskin M, Borklu EB, Doğan S, Öztürk B, Kaya A, Öcal L, Çerşit S, Tenekecioglu E, Keskin Ü, Keser N, Orhan AL. Effect of the number of parity on right heart chamber quantification. *Echocardiography*. 2022 Apr;39(4):592-598.
126. Aslan B, Özbek M, Aktan A, Boyraz B, Tenekecioglu E. Factors associated with all-cause mortality in patients with coronary artery chronic total occlusions undergoing revascularization (percutaneous coronary intervention or surgery) or medical treatment. *Kardiologija*. 2022 Mar 31;62(3):49-55.
127. Çakır H, Kanat S, Karagöz A, Tütüncü A, Yılmaz F, Öcal L, Toprak C, Emiroğlu MY, Demir M, Kaymaz C, Tenekecioglu E. The effects of catheter ablation of outflow tract premature ventricular complexes on atrial electromechanical delay. *Echocardiography*. 2022 May 16.

*Authors contributed equally

ACKNOWLEDGMENT

This thesis would not have been accomplished without huge supports from my family, promoters, co-promoters, colleagues, and friends. I would like to express my sincere appreciation to all from the bottom of my heart.

Promoters

Dear Prof. Patrick W. Serruys,

Great father of all fellows, great leader of interventionists all over the world.

It was my ultimate dream to come to Rotterdam to work together with you. It took 9 years since the first email contact with you till starting my research in Rotterdam, but was worth it. During my cardiology fellowship training, on March 2005 when I received the invitation email for the interviews from Prof Serruys, I was so excited and felt honored...nobody has believed me but I was trusting myself. Due to fellowship training, public service following completion of the fellowship, I could go for the interviews at 2009. My father's health problems couldn't allow me to begin my research till 2014. During that 9-years period, in the congresses when I met Prof, I always said I will come and Prof was always kind and saying "Yes, Waiting!"

The dream came true on Nov 2014...started my research under supervision of Prof Serruys... I started working with a legend. an alive legend...at each fellow meeting Prof was so kind trying to improve our skills...skills in English pronunciation, improving our English vocabulary, articulation, research strategy, life vision and so on... I do really respect your patience to fellows, great passion for education, and passion for work. Working with fellows may be sometime stressful and tough. However, you never give up teaching us and working together.

Your intellectual curiosity and spirit for clinical research is absolutely at top of the world. As the people in the audience said in one of the cardiology congresses, Prof was the most inspiring academician I've ever seen. It's like a school for the fellows to do research with Prof; not only a high-grade scientific school but also a life school. I will never forget the days I worked with Prof. Dear Prof, you will be always father of us, of fellows. Even years later, it will

be the same, father of us, father of fellows >200 all around the world. Please take care of yourself. I will never forget the great days with you.

Dear Prof. Robbert van Geuns,

Thank you for letting me join your great team. This thesis would not be accomplished without your invaluable supports. I hope to continue our global collaboration in the future.

Co-promoter

Dear Yoshinobu Onuma sensei,

The great Japanese mentor... I learned a lot of things from you, such as your intellectual knowledge in the clinical research field, speed of work, and inspiring alternative thinking methods for solutions. You always tried to be so kind and helpful during my research. After Prof, you were my second idol in cardiology and research. I was so impressed seeing the deep respect and courtesy of Japanese junior fellows to you. Always so nice inviting me to LaBru every Friday evenings.

Paranymph

Dear Marie-Angèle Morel,

It was really pleasure to meet you in Rotterdam. I will never forget your kind support during my research in Rotterdam, especially when Prof was angry :) Always so nice to invite me to drink at Friday evenings and to football matches of Feyenoord with Prof and research fellows.

Dear Ms. Hanny Boutkan,

Dearest Hanny, an elder sister of all fellows. You always supported me on a variety of issues, such as reservation of city hall, registration in AMC, drafting emails in English, tough times during research, etc. Your advice is always critical and supportive. Always trying to make supportive bullets after each crazy time during research. The best friend, like a member of family in Rotterdam. I will not forget your invaluable support. I do look forward to see you in Turkey in one of your vacations and want to invite to our house in my home city, Bursa, Turkey.

Great fellows from all over the world,

It was great pleasure to meet you and work with you my great friends. I will never forget your great supports during my research in Rotterdam. It was really the most enjoyable part of the life in Rotterdam for me. As I encountered a trouble, you always tried to help me and I could overcome those difficulties with your invaluable supports. I do feel as a part of this great team and see myself so lucky to have you, Prof, Hanny, Yoshi and other fellows all around the world. We are a great family of Prof. Always remembering the legendary sentence of Prof team is much more powerful than individual. "L'union fait la force."

Dear Dr. Osama Soliman,

My great friend and brother...always inviting me to the dinners but couldn't attend due to tough crazy workload. Sitting with you always make me feel as if in my country even not speaking Turkish. You will be always a great friend a brother for me.

Dear Dr. Mohammad Abdelghani,

I appreciate your heartfelt supports. I really admire your kind attitude to the works. Your brilliant vision and enthusiasm during research always impressed me. You always are a brother for me.

Dear Dr Pannipa Suwannasom

Thank you for your kind friendship and patience for long conversations.

Dear Dr. Rafael Cavalcante,

My great intelligent Brazilian friend. Many thanks for your kind help and support.

Dear Dr. Yaping Zeng,

I clearly remember the first day in Cardialysis. We started at the same day and didn't know what to do. Always supported and tried to encourage each other. I cannot forget your kind supports during our research in Rotterdam.

The Great Japanese Team always inspiring me

Dear Hiroki Tateishi sensei,

Great Japanese Samurai...Thank you for our enjoyable discussion about works and a lot of various topics. I really enjoyed talking with you about Japanese history and Japanese lifestyle.

Dear Yosuke Miyazaki sensei,

Great Japanese friend...always patient and tried to stay calm even in tough times...You were always so kind to my bombarding questions. I always tell that there're two stars shining in Yamaguchi...Hiroki sensei and Yosuke sensei

Dear Taku Asano sensei,

Many thanks for your kind and invaluable supports on my works. You didn't forget my name and had learnt my long surname in correct.

Dear Yuki Katagiri sensei,

I appreciate your continuous and invaluable supports on my works. I'm really grateful to you for your great supports in statistics. I was really impressed your perseverance in front of troubles during research.

Experts in Leiden University Medical Center,

Dear Dr. Jouke Dijkstra, Dr. Pieter Kitslaar, Prof Hans J.C. Reiber

I appreciate the great opportunity to work with you all. You always kindly replied my crazy questions for the softwares. With your invaluable support, I could finalize shear stress and vessel remodeling project.

EuroIntervention team,

Dear Paul Cummins, Sylvie Lhoste, Amy McDowell, Devia Bijkerk,

I'm sure you get crazy several times since I never follow the author instruction... Thank you very much for your patience, and being kind always. It was so funny to talk about Turkish female singer Selda Bagcan with Paul.

Specialists in Cardialysis,

Dear Hans Jonker, Ravindra Pawar, Jamal Khachabi, Gerrit-Anne van Es, Dr. Ernest Spitzer and Prof. Jan G.P. Tijssen,

Thank you so much for your great and invaluable supports. You're always so kind and patient when I dive into your rooms suddenly as I encounter a technical problem about softwares, statistics or image analysis. Your special knowledge always gives us an effective solution for our research problems. Always trying to solve the problems by smiling.

Family

I cannot express my feelings for my lovely wife Canan and my daughters Burcu and Buket. I love you all so much that I can't even describe with words. You struggle all the problems with me and moved to Rotterdam for me. I could not complete my projects during my research without your invaluable supports. Despite several troubles you always keep your calmness and stand with me. Always proud of you to be so strong in front of several difficulties living in a foreign country.

I would like to dedicate this thesis to all of my beloved family.